Experimental studies of phospholipid self assembly in hydrocarbon liquids: Reverse vesicles as possible compartmentalisation strategies for hydrocarbon-based life on Titan

by

Lucy Helen Norman

Department of Space and Climate Physics

University College London

A thesis submitted in fulfilment of a Doctorate in:

Astrobiology and Soft Condensed Matter

February 2015

I, Lucy Helen Norman, confirm that the work presented in this thesis is my own. Where information has been derived from other sources, I confirm that this has been indicated in the thesis. I can confirm this thesis has a 79,202 word count.

Abstract

The goal of this thesis was to determine the nature of phosphatidylcholine self assembly within hydrocarbon liquids. This study was enacted in order to investigate the potential use of amphiphiles in compartmentalisation strategies for putative organisms inhabiting the hydrocarbon lakes of Titan (the largest moon of Saturn). The backbone of terrestrial cell membranes are vesicular structures composed of a phospholipid bilayer, with the hydrophilic head groups arranged around the periphery, and simple lipid vesicles are thought to be akin to the first terrestrial protocells. It may be possible that reverse vesicles, surrounding a nonpolar core and composed of a bilayer with the hydrophilic head groups arranged internally, may be ideal model cell membranes for putative hydrocarbon-based biota inhabiting Titan's hydrocarbon lakes. Compounds that are shown to form reverse vesicles in conditions comparable to those of Titan's lakes could be potential 'biomarkers' and searched for in future missions to Titan.

In order to discover whether certain phosphatidylcholines can exhibit vesicular behaviour within hydrocarbon liquids, and to analyse their structure, I have carried out experimental studies using environmental conditions that are increasing comparable to those found on the surface of Titan. Studies of macroscopic and microscopic phase behaviours were used to determine the presence of self assembled particles, including reverse vesicles. These studies included the use of microscopy, confocal laser scanning fluorescence microscopy, transmission electron microscopy (TEM), dynamic light scattering (DLS), small-angle neutron scattering (SANS) and small-angle x-ray scattering (SAXS). The systems studied included: the hydrocarbon solvents cyclohexane, octane, heptane, hexane, pentane and butane; various amphiphilic ratios of PC4:0, PC18:2 and lysoPC18 at dilute, ≤30 mM, concentrations; inclusion or exclusion of NaCl as a stabiliser; methanol or direct preparation methods; variation of sonication intensities and times; and a variety of temperatures.

Results of this research demonstrate that unilamellar, multilamellar and multi-chambered reverse vesicles can form in a wide range of phosphatidylcholine-hydrocarbon systems. Small concentrations of NaCl and lyso-phosphatidylcholines were found to facilitate reverse vesicle formation. A reduction in temperature (down to the freezing point of the solvent) did not change the structural phase behaviour of most systems, but often increased the size of reverse vesicles. Decreasing the molecular weight of the alkanes was found to effect which amphiphilic ratios formed reverse vesicles; pentane solvent molecules were particularly effective at bilayer penetration.

These results support the feasibility of further cryogenic self assembly experiments as analogues to the hydrocarbon environments found on Titan.

Acknowledgments

I would like to thank the Origins program at UCL for funding this project, the STFC for funding the small angle scattering studies and my family for their financial support after the scholarship finished.

I would like to thank the many people that have helped this project along by allowing me access to the space and equipment required for these studies; Jayesh Gor, John Ward, Neal Skipper, Jawwad Darr, Simon Barrass, John Bowles, Christoph Salzmann, Sam Ranasinghe, Mark Turmaine, Steve Firth, Nick Terrill, Andrew Smith, Lionel Porcar and Anne Martel.

Thank you to: Ian Crawford who always knew what questions to ask; Dominic Fortes for allowing me to pursue this project; Neal Skipper for his wide-ranging support; and Shih-Huang Tung who was always happy to answer questions regarding his research.

A very grateful thank you to those that helped with editing the thesis: Neal Skipper, Jennifer Harris, Richard Evans, and Angela Norman (aka Mum). And a big, thankful hug goes out to Louise Alexander, Jennifer Harris, and Adam Martins for all their much needed support throughout the years.

Finally I would like to thank the musicians responsible for keeping me somewhat sane and energised during long periods in the lab and during the thesis write up: Pharrell Williams for ‘Happy’, Journey for ‘Don’t stop believing’, Nirvana for ‘Smells like teen spirit’ and Marilyn Manson for his version of ‘Tainted love’. Also, big love to the cute mouse that lives in the Planetary Office and has kept me company on many a lonely night… and all the other lovely daytime creatures of the office.

Contents

Accompanying CD: 'DLS raw results' folder, 'SAXS proposal' document, 'SANS proposal' document, 'SANS Experiment report' document, 'SAXS Experiment report' document, and electronic copy of thesis.

List of Figures

List of Tables

Chapter 1: An introduction to the habitability of Titan

1.1 Rationale for studying compartmental structures for putative hydrocarbon-based biota

In addition to studying life on Earth, astrobiological predictions arise from studying universal constraints on chemistry in association with environments on other planetary bodies. These studies can range from observations of the atmospheric chemistry of exoplanets to measurements of physical samples by rovers on the surface of Mars. However, there is one central question which must be answered preceding these studies, and that is "What are we looking for?" Detection of macroscopic life on exoplanets is impossible with present technology and finding extraterrestrial macroscopic life in our own solar system seems unlikely (unless they are situated in the subsurface oceans of icy moons). Therefore, we are left to concentrate on the hunt for microscopic biota and associated biosignatures that may indicate the presence of extant or extinct life.

In order to search for these we must equip missions appropriately based upon plausible theoretical biochemistries and biological processes. For example, astrobiologists looking for exoplanets with an oxygen rich atmosphere assume that photosynthetic organisms would have existed over a long period of time and are still present on that body (Cockell *et al.* 2009). Also, events such as the seasonal bursts of methane in specific locations on Mars have been proposed to be a biosignature of methanogenic type of Martian biota (Mumma *et al.* 2009). In order to search for 'exotic' life – that which is significantly different from our own – we must first study potential exotic habitats, then theorize how life could thrive in these habitats and then research these possibilities. Therefore, we require theories that can be explored using experimental or computational research to discover plausible biochemistries and processes for biota to metabolise, repair, grow, replicate, and compartmentalise in exotic habitats.

One of the most basic requirements for any life is a mode of compartmentalisation – the development of a capsule which allows the organism to concentrate nutrients, to conduct metabolism under controlled conditions, and to store genetic information. Terrestrial life compartmentalises by utilizing a bilayer of amphiphiles, predominantly phospholipids, to create cell (or intracellular) membranes. So for exotic life what type of compartmentalisation strategies would be possible? To answer this question we first need to choose or theorize a type of exotic habitat and employ either experimental or modelling techniques in order to find chemistries that can self assemble into capsules within which exotic life may thrive.

The hydrocarbon lakes found on the icy surface of Saturn's giant satellite Titan present themselves as a possible habitat for exotic life that may have evolved to thrive in a very cold, nonpolar solvent. Therefore, the compartmentalisation strategies for any exotic life in these lakes are likely to be significantly different from any found here on Earth.

1.2 Saturn's giant moon Titan

1.2.1 Titan's organic-rich surface and atmosphere

Titan is unique because it is the only moon in the solar system with a substantial atmosphere; it is approximately 880 ± 60 km from Titan's surface to the top of its stratosphere (Mori *et al.* 2004). The atmosphere predominantly consists of nitrogen with a methane mole fraction ranging from 1 to 10% (Mahjoub et al. 2012; Strobel 2012) and ~6% at the surface (Nixon et al. 2012) which is abnormally high for an icy moon. The atmosphere was first detected by ground-based telescope in 1944 (Kuiper 1944) and subsequently observed by the Voyager spacecrafts in the 1980s.

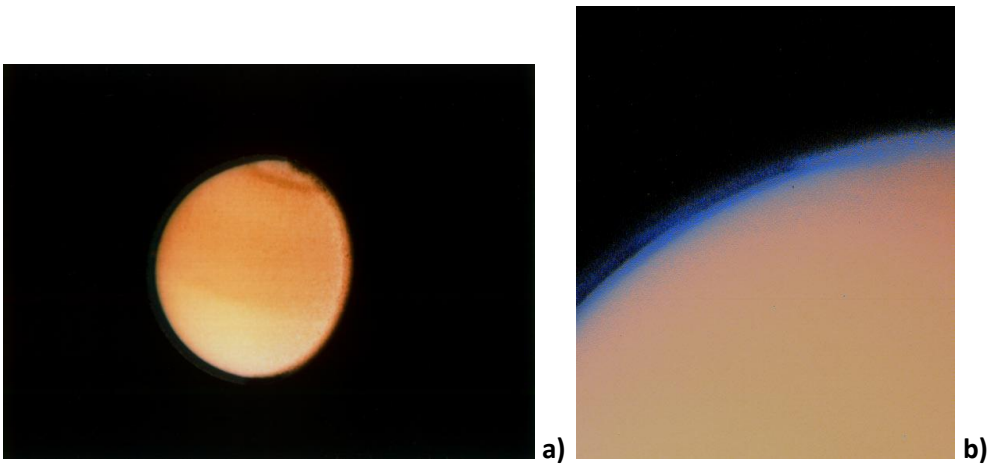

Figure 1: Image Credit: NASA/JPL. a) Voyager 2 image of Titan taken 23rd August 1981 (range 2.3 million km) showing the hemispherical divide and polar hood of the atmospheric haze; and b) Voyager 1 image of Titan's atmosphere taken 12th November 1980 (range 435,000 km).

The surface of Titan was initially inaccessible for study due to the orange haze that characteristically surrounds this moon (see Figure 1). Titan is approximately 9.5 AU from the Sun and the incident solar radiation on the upper atmosphere is only 1.1% of that at the Earth; of this light, the shorter wavelengths are primarily absorbed by N_2 and CH_4 in the upper atmosphere and the longer wavelengths by C_2H_2 and C_4H_2 in the stratosphere (Clarke & Ferris 1997).However, that did not stop theories forming about what was under the orange veil and models arose of a surface covered by an ocean of methane and ethane, kept in liquid form by the low surface temperature of 94 K (Jennings *et al.* 2009), along with hydrocarbon solutes (Lunine *et al.* 1983; Raulin *et al.* 1992; Sagan & Dermott 1982). This theory arose from two avenues of thought; firstly, once ethane has been formed and precipitated to the surface it will stay in liquid

form and therefore gradually accumulate to form an ocean; and secondly, as methane should be lost to space and also irreversibly photolyzed by solar radiation (and being recombined to form complex hydrocarbons) with time, a large reservoir of methane should be feeding the high levels of atmospheric methane. The current levels of methane would vanish within some tens of millions of years without a reservoir (Wilson & Atreya 2004); so in theory a hydrocarbon ocean could act as a large reservoir feeding the methane rich atmosphere with a subsequent stable methane condensation/evaporation cycle (similar to the water-cycle on Earth) and the loss of methane being minimal compared to that of the reservoir volume.

Near IR observations through Titan's haze by telescopes such as the Canada France Hawaii Telescope (CFHT) in Hawaii (e.g. Coustenis *et al.* 2001) and the Hubble Space Telescope (e.g. Smith *et al.* 1996) showed differentiated albedos over large regions. These were thought to be bright highlands surrounded by a dark hydrocarbon ocean. However, the spatial resolution of these images (~300 km) was insufficient to uniquely identify the cause of the albedo inconsistencies.

With the arrival of Cassini (a Saturn orbiter) in 2004 and the launch of the Huygens probe from Cassini onto Titan's surface in 2005, the mysteries of Titan began to truly unravel. This included the absence of the expected widespread hydrocarbon ocean, which opened up new avenues of thought as to the source of the abnormally high percentage of atmospheric methane. This is still a contested subject (Gautier 1995; Stoker *et al.* 1990) and current theories range from input from methanogenic biota (Fortes 2000; McKay & Smith 2005) to episodic outgassing of methane stored in clathrates within the icy shell forming the surface of Titan (Tobie *et al.* 2006).

Destruction of atmospheric methane, powered by photolysis, is the origin of many complex compounds on Titan including heavier hydrocarbons and nitriles (such as HCN, HC_3N etc) and aerosols and so-called tholins (Atreya *et al.* 1978; Carrasco *et al.* 2009; Chassefiere & Cabane 1995; Owen 1982; Owen 2005; Teanby *et al.* 2008a; Teanby *et al.* 2008b; Trainer *et al.* 2006). Tholins are organic rich compounds (containing complex C- H- O-, and N-rich polymers) which have been synthesised in laboratory conditions by numerous methods including; high-energy electric discharges into simulated Titan atmospheres (Coll *et al.* 2001; Ruiz-Bermejo *et al.* 2009; Sagan *et al.* 1992), soft X-ray irradiation of methane-bearing ices (Pilling *et al.* 2009) and plasma radio frequency discharges into a nitrogen-methane atmosphere (Carrasco *et al.* 2009). These tholins are thought to represent Titan haze analogues.

The haze of Titan is the most dominating feature of this moon as it gives Titan its distinctive orange appearance and is optically thick which obscures the surface at visible wavelengths (McKay *et al.* 2001). However, far from being static, the haze itself has distinctive features which have been found to change with time; there is a hemispherical divide, a detached layer

around 300-400 km altitude and also a polar hood (Hutzell *et al.* 1996; Penteado *et al.* 2010; Trainer *et al.* 2006) (see Figure 1a).

The change in heat energy transmitted by sunlight during alternate seasons drives the flow of the haze from one hemisphere of the moon to the other creating the hemispherical divide. During the summer season on one hemisphere the heat generated in this area drives a convecting current which pushes the haze towards the winter hemisphere (a Hadley circulation pattern). The greater density on the winter side is indicated by a low albedo of the winter hemisphere, lower by 10-20 % than that of the summer hemisphere, and reverses in about five years which is faster than the seven year season (Roos-Serote 2005).

Images taken during 1999-2002 (late southern spring on Titan) with the Keck telescope at 8-13 μm showed a significant accumulation of ethylene (C_2H_4) in the stratosphere to latitudes south of 60degrees (Roe *et al.* 2004). This high concentration of ethylene was also detected by Voyager 1 over the north pole in early northern spring with an enrichment of ethane (C_2H_6), acetylene (C_3H_8), propane (C_4H_{10}), ethylene (C_2H_4), diacetylene (C_4H_2), and methylacetylene (C_3H_4) (Coustenis & Bezard 1995). This implies the polar hood forms in the south or north hemisphere depending on the season. Analysis of Titan's north polar hood has shown a uniform cloud of small particles permeating the lower stratosphere at altitudes between 58 and 90 km. These are composed of condensed organics with radii between 1μm and 5μm, the majority of which are likely to be HCN and condensed hydrocarbons (such as ethane); with the later constrained to regions nearer the tropopause (Mayo & Samuelson 2005).

Microphysical models, photochemical models, and laboratory simulations all imply that the haze production rate (if similar to laboratory tholins with a C/N ratio ~ 2-4) is in the range of 0.5-2 x 10^{-14} g cm^{-2} s^{-1} (McKay *et al.* 2001). This haze has a dominant influence on the propagation of solar radiation through Titan's atmosphere and thereby affects the temperature structure of the atmosphere, cooling the surface by an estimated 9 K (Danielso *et al.* 1973; McKay *et al.* 1989; McKay *et al.* 1991; Samuelson & Mayo 1991). Although the temperature at the surface is close to 94 K it decreases to about 71 K at the tropopause, which is located at an altitude of 40 km, above which the temperature rises to 180 K and proceeds to fluctuate by approximately 20 K (Lellouch *et al.* 1989a; Lindal *et al.* 1983; Samuelson & Mayo 1991) as illustrated in Figure 2. It is also likely that the surface temperatures will rise by only a few Kelvin in the summer season compared to the winter season (Jennings *et al.* 2011; Tokano 2005a).

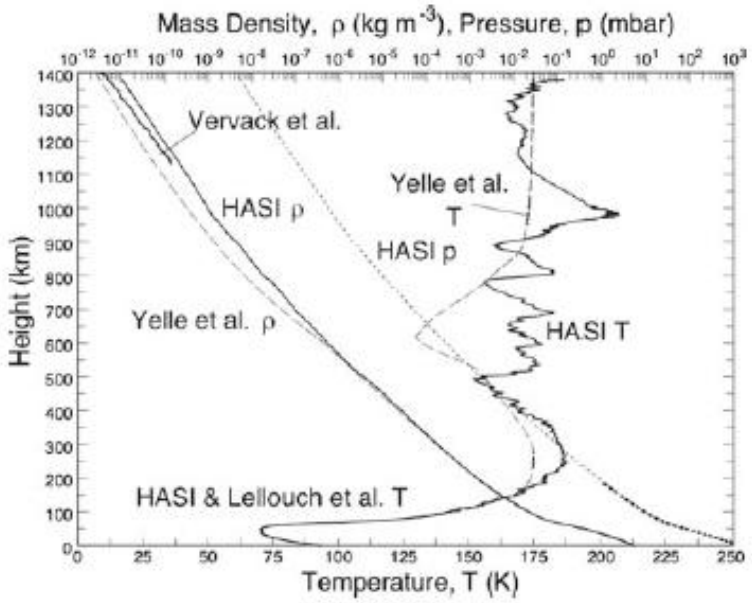

Figure 2: The temperature profile obtained by Huygens' HASI (Huygens Atmosphere Structure Instrument), alongside previously published profiles (Lellouch *et al.* 1989b; Vervack *et al.* 2004; Yelle *et al.* 1997). Image credit (Lebreton *et al.* 2009).

The detailed images from Cassini's synthetic aperture RADAR and Visual and Infrared Mapping Spectrometer (VIMS), along with the Huygens' DISR (Descent Imager Spectral Radiometer) images and direct sampling, has opened up Titan to true geological research. Instead of the expected global hydrocarbon ocean, an incredible array of geological features, resembling those found on Earth, have been found formed from ices rather than silicate rocks. These features include extensive dune fields (e.g. Barnes *et al.* 2008; Lorenz *et al.* 2006b), mountain ranges (e.g. Barnes *et al.* 2007; Mitri *et al.* 2010), craters (e.g. Artemieva 2003; Le Mouelic *et al.* 2008; Lorenz *et al.* 2007) and possible cryovolcanoes (e.g. Le Corre *et al.* 2009; Lopes *et al.* 2007), alongside features that resemble an earth-like 'hydrological' cycle; as illustrated in Figure 3.

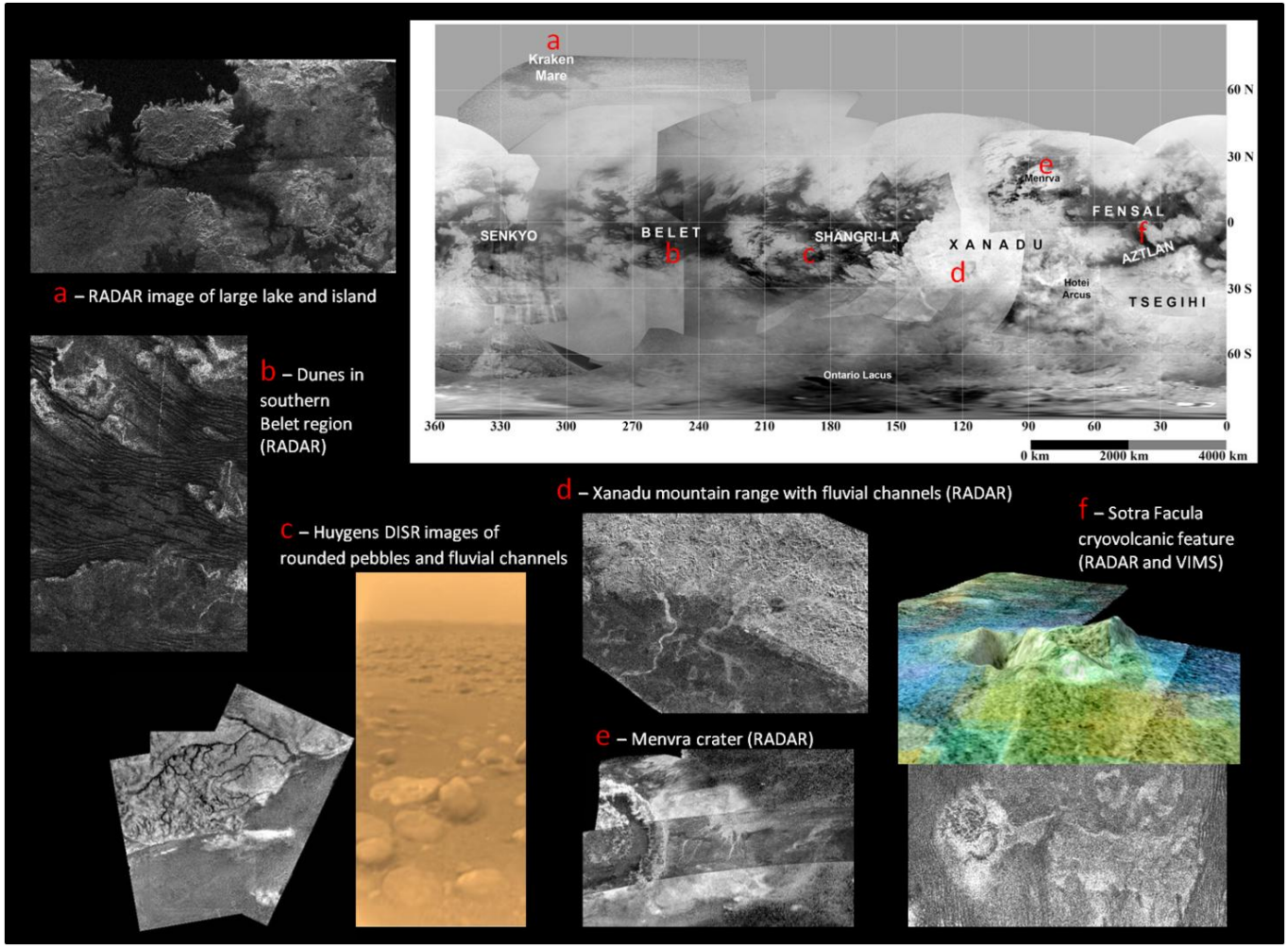

Figure 3: Compilation image of Titan's surface features and their respective locations. Image credits NASA/JPL-Caltech/ASI/Uni. of Arizona/ESA.

Due to the low temperatures on Titan and the amount of hydrocarbons in the atmosphere, the liquids on Titan's surface are methane and ethane, with a small mole fraction of propane (discussed in the next section). This was predicted by pre-Cassini models of Titan, but in smaller overall quantities than the global oceans which had been considered. There is increasing evidence for a hydrocarbon cycle on Titan including; cloud activity and rainfall (Karkoschka & Tomasko 2009; Tokano *et al.* 2006; e.g. Tomasko *et al.* 2005), extensive dendritic networks that are likely to be fluvial systems (e.g. Elachi *et al.* 2005; Soderblom *et al.* 2007), images of the surface scattered with rounded pebbles which are indicative of fluvial erosion (Tomasko *et al.* 2005), and many lakes and seas in the polar regions (e.g. Lopes *et al.* 2010; Stofan *et al.* 2007) (see Figure 3).

In addition to the dynamic surface, the subsurface may also exhibit interesting properties, especially for astrobiological research. Beneath the icy and organic rich surface there is expected to be a thick layer of ice which extends down to around 50 km to a subsurface ocean. Beneath this is a layer of high-pressure ice, which is in contact with the silicate core (see Figure 4). The outer icy shell is where methane clathrate deposits are theoretically located, which could be resupplying the methane lost from the atmosphere. Although the subsurface ocean has not been directly sampled, its presence has been inferred from the observed moment of inertia (Bills & Nimmo 2008; Iess et al. 2010) and the Schumann-like resonance (spectral peaks in the low frequency part of the electromagnetic field – this field being present on Titan due to the Saturnian magnetosphere) observed by Huygens (Beghin *et al.* 2010). The aqueous composition of this subsurface ocean has been modelled to be either ammonia rich (Tobie *et al.* 2005) or rich in ammonium sulfate (Fortes *et al.* 2007; Grindrod *et al.* 2008).

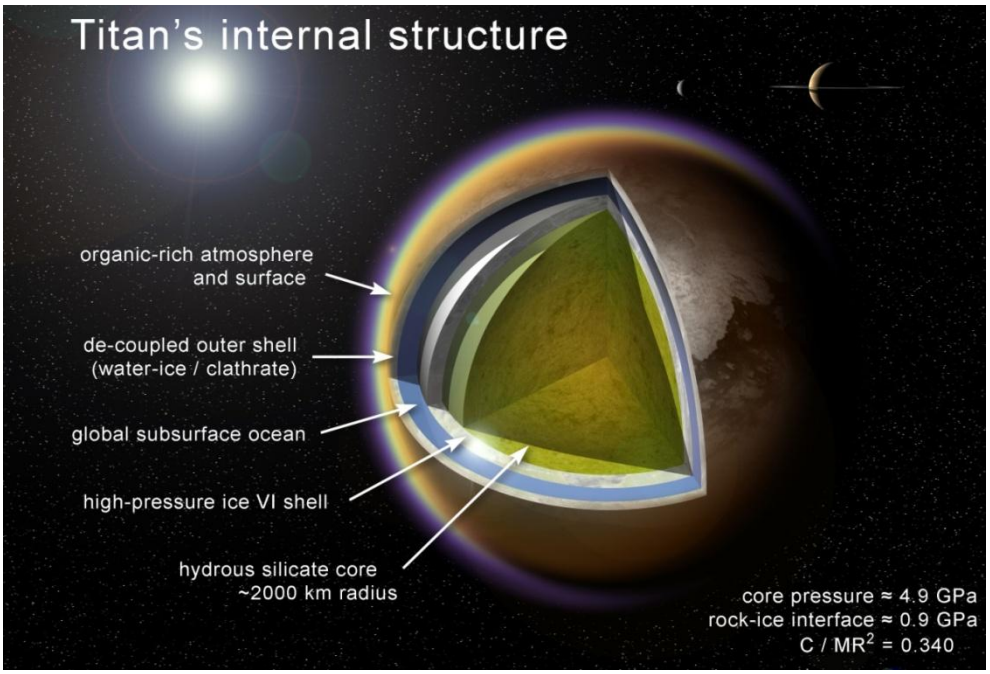

Figure 4: Cross section of Titan (Norman & Fortes 2011). Image credit Fortes, A.D.

1.2.2 Liquid hydrocarbons; rain, rivers and lakes

The liquid hydrocarbon environments on Titan include the large (possibility permanent) hydrocarbon seas such as Kraken Mare and smaller semi-permanent hydrocarbon lakes in the polar regions, small tropical lakes supplied by a source of underground hydrocarbon liquids (Griffith *et al.* 2012), subsurface hydrofers (Hayes *et al.* 2008), and hydrocarbon-saturated regoliths (Czechowski & Kossacki 2009; Hayes *et al.* 2008; Lorenz *et al.* 2006a). Evidence for the ubiquitous presence of liquids on Titan's surface includes: the very low radar backscatter of the purported lakes and seas e.g. (Lopes *et al.* 2010; Stofan *et al.* 2007) see Figure 5 a and b; the identification of a specular reflection in the near-infrared from the feature named Kraken Mare - Titan's largest sea, located near the moon's north pole (Stephan *et al.* 2010) see Figure 6; the identification of near-IR absorption features due to ethane, propane and butane in Ontario Lacus - a large south polar lake (Brown *et al.* 2008); and evidence for liquid methane in the near-surface regolith by the Huygens probe (Niemann *et al.* 2005). The standing bodies of hydrocarbon liquids are quite common in polar regions and are estimated to cover approximately ~ 15 % of Titan's surface above 65° N (during the northern winter season which ended in 2009) (Lunine 2009).

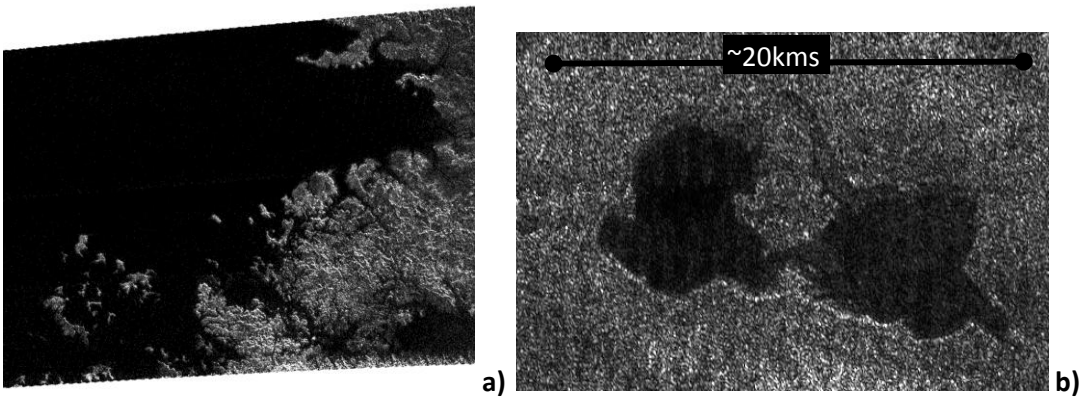

Figure 5: a) Radar image of a very smooth surface, indicated by dark rendering, representing one of the polar lakes on Titan with a distinct shoreline, small islands, and flow channels. Image taken 12th May 2007. Image credit: NASA/JPL-Caltech/ASI; and, b) Radar image of some of the smaller polar lakes found on Titan, taken on 23rd September 2006. Image credit: NASA/JPL-Caltech/ASI.

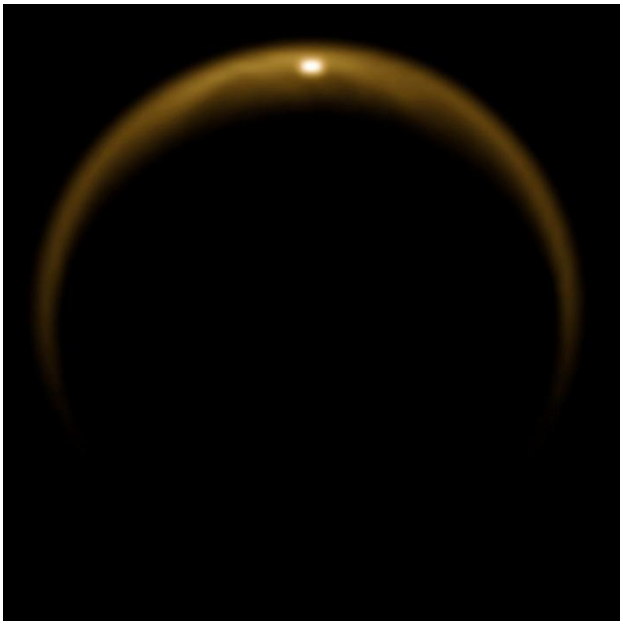

Figure 6: Specular reflection the northern polar region at ~72°N/342°W, corresponding to the location of Kraken Mare (Stephan *et al.* 2010), image taken on 8th July 2009 (range 200,000 km). Image credit: NASA/JPL/University of Arizona/DLR.

The origin and longevity of the high atmospheric methane content is an important issue as this affects the entire carbon cycle on Titan's surface including the history of the hydrocarbon lakes and their suitability as a habitat through time. Numerous models have been published on this subject based on differing premises. Tobie *et al.* (2006) used a model based on the evolution of the interior and predicted that a major outgassing episode happened 400 million years ago. Results from the models by Horst *et al.* (2008), which used CO production as a measure of time, determined that the minimum duration for atmospheric methane was 300 million years. In a recent model by Nixon *et al.* (2012) the isotopic ratio of ^{12}C and ^{13}C (as measured by Cassini's CIRS infrared spectroscopy) was utilised to determine how long the high methane content of the atmosphere had been present by presuming a constant rate of isotopic fractionation over time. Their model showed that, if the atmosphere had not been resupplied with methane, then the atmospheric methane was 60-1600 million years old as measured by depletion by chemical processes and photolysis; compared to only 10 million years old if hydrodynamic escape (loss of methane to space) was also depleting the methane store. However, if the methane has been continuously and substantially replenished (being equal to, or greater than, the depletion rate) over the history of Titan the isotopic ratios can no longer indicate the history of the methane in the atmosphere and therefore it could have been present throughout much of Titan's history. For example, any surface methanogens would be recycling the atmospheric methane, and so although they cannot be the original source of the atmospheric methane they could be perpetuating the existence of a methane rich atmosphere by converting organics back into methane.

These atmospheric models and possible biological influences indicate the vast range of values for the estimated age of atmospheric methane on Titan and consequently also the age of the

hydrocarbon lakes. This will undoubtedly affect the likelihood of life being present in these lakes as the longer these lakes have been present the more time there has been for complex chemistries to evolve into a functioning hydrocarbon-based organism. And also, the greater the longevity of the lakes the more likely any organisms that evolved would have speciated into a diverse and intricate ecosystem. Therefore, future work into the history of the atmospheric methane with particular reference to utilising data provided by future missions to Titan will be of much interest to the astrobiological community.

When working to extrapolate the physiology of putative exotic biota one must first consider the habitat. In addition to the longevity of liquid hydrocarbons on the surface, environmental variables between locations may affect their individual habitability. Such variables that may alter the habitability of a location may include: the change of precipitation type e.g. ethane, methane-ethane or methane, and quantity over latitude, seasons, and hemispheres; any changes in solute quantities from photolysis generation; the frequency of cryo-volcanic liquids entering the system; and any flow of liquids to or from hydrofers/aquifers and the surface lakes.

We currently do not have sufficient evidence to theorize the frequency that subterranean aqueous solutions from aquifers and cryovolcanism may infiltrate the lakes. However, using porous media properties inferred from Huygens probe observations and the size and location of hydrocarbon lakes to provide constraints on parameters for subsurface transport, Hayes *et al.* (2008) suggested flow timescales between hydrofers and observed lakes to be in the range of tens of years; and therefore may be a reaction to seasonal cycles. This type of seasonal flux may induce vegetative-growth life cycles, with seasonal influx of nutrient rich liquids from hydrofers having undergone a longer history of chemical alteration due to contact with subsurface aqueous cryolavas.

During the early years of the study of Titan it was believed by some that Titan was unable to support clouds (Hunten *et al.* 1984). However, there were theories about rain on Titan without the need for clouds with seed nuclei believed to be rare so that CH_4 droplets would rapidly grow (to large sizes up to 100 μm) and quickly precipitate (Toon *et al.* 1988). Ever since clouds were spotted by ground-based telescopes (such as Keck) there have been an ever increasing number of people interested in studying the cloud formations of Titan; with nucleation by haze particles possibly catalyzing this cloud generation (Curtis *et al.* 2005). Observations are undertaken in two ways, regular monitoring of clouds formations from ground based telescopes and by observing cloud formations *via* equipment (such as the VIMS) aboard Cassini (Curtis *et al.* 2008). The type of clouds that have been found to date vary from: the occasional high altitude, transient, tropospheric clouds in tropical latitudes (Griffith *et al.* 2009; McDonald *et al.* 1991; Schaller *et al.* 2009); to relatively frequent polar tropospheric cloud systems some of which present layering (Brown *et al.* 2002; Brown *et al.* 2010; Griffith *et al.* 2000; Schaller *et*

al. 2006; Wang *et al.* 2010); stratospheric clouds of condensed nitriles and hydrocarbons in the polar regions (McKay *et al.* 2001); and 'fogs' (Brown *et al.* 2009). These 'fogs' are believed to form by evaporation of the lakes or a methane-soaked regolith and have been observed within only a few kilometres of the surface, however, are not considered able to produce precipitation (Brown *et al.* 2009). Although there have been attempts to estimate the average amount of rainfall on Titan per terrestrial-year (e.g. Barth & Toon 2006), many factors, including an observed hemispheric difference in the atmosphere and seasonal differences in cloud types and frequency, may play a important role in precipitation that is not fully understood yet.

The range of compositions that are feasible for precipitation capable clouds (those high enough in the atmosphere to be able to produce precipitation), and whether these droplets can reach the surface intact, is still contested. Droplets may comprise of an aerosol, tholin, or ethane nucleus covered with either ethane, methane, or a mixture of hydrocarbon liquids at atmospheric equilibrium e.g. methane-ethane-propane near the surface. The main contention with methane covered tholin droplets is whether they can reach the surface without the methane evaporating. Depending on modelling parameters, such as the atmospheric methane saturation level at near surface altitudes, the destination of droplets can be the surface or evaporation before touchdown (McKay *et al.* 2001). However, observational evidence of methane cloud presence and subsequent changes of the surface topography suggests that methane rain does frequently reach the surface on Titan (Turtle *et al.* 2011). Pure ethane droplets are believed to be present in clouds which have been found to contain small, micrometer sized, particles due to the absence of a large tholin nucleus (Rodriguez *et al.* 2009). These are more likely to reach the ground without vaporizing, although, it is unknown how they would be able to travel through the atmosphere without adsorbing other hydrocarbon liquids such as methane before reaching the surface. With an originally mixed droplet the methane may evaporate at low altitudes and leave a pure ethane droplet (McKay *et al.* 2001) or a droplet composed of ethane plus higher hydrocarbons such as propane. The type and variety of rainfall, some of which may have geographical or temporal limitations e.g. ethane clouds may be restricted to polar locations and to winter seasons (Griffith *et al.* 2006), is likely to have a large impact on liquid composition and therefore form compositionally different habitats stretched across Titan.

There are observations of numerous large tropical clouds; these appear to have produced precipitation that carved out fluvial channels indicating globally prevalent precipitation. However, the absence of surface liquids implies that there are also other factors such as geology that may need to be taken into account in determining the conditions of liquid habitats on Titan. For example, in the seemingly very porous and hydrocarbon saturated regolith at the equatorial location where Huygens landed (Griffith *et al.* 2008) there is the potential for a greater subsurface flow than at the location of the polar lakes which possibly lie on semi-permeable

basins, and hence, we could expect liquid subsurface habitats that are identical over a wide area in the equatorial regions.

Seasonal changes on Titan can have an impact on many different environmental variants and consequently chemical processes in Titan's hydrocarbon liquids. The tilt of Saturn's spin axis (26.7°) provides Titan with strong shifts of solar insolation as a function of season and latitude. It is expected that this will lead to changes in the distribution of lakes in the polar regions as seasons change over the Titan year (~30 terrestrial years) with the possibility of methane lakes entirely evaporating during dry seasons (Aharonson *et al.* 2009; Turtle *et al.* 2009a). Although some thermodynamic models of the lakes show they are quite stable without any evaporation e.g. (Mitri *et al.* 2007) there has been observations of the shoreline at Ontario Lacus receding inward by ~10 km which is indicative of an evaporation sequence (Wall *et al.* 2010). It has been hypothesized that in the summer months variables such as 'land breezes' - that cause a moisture convergence over the seas - could enhance precipitation in locations with lakes; however, 'sea breezes' – that blow moisture from the lake rich polar regions – could draw precipitation away from regions dominated by lakes (Tokano 2009). Also, seasonal models are conflicted with some concluding the summer months are the wet season on Titan due to methane accumulation by Hadley circulation (Schneider *et al.* 2012).

It has been estimated that lake temperature may vary by up to 7 K with season, particularly at high latitudes, which in turn controls the solubility of minor species (Tokano 2005a). Thermodynamic equilibrium between the gas and liquid states of hydrocarbons close to the surface is sensitive to temperature and composition changes of surface liquids, and therefore, this seasonal variation may also alter near-surface methane mixing ratios (Tokano 2005b). This in turn may influence the evaporation rates of methane precipitation at low altitudes and evaporation rates of the hydrocarbon lakes. A rise in temperature may also increase evaporation rates for methane in methane-ethane liquid bodies thereby increase the ethane percentage in the lakes or saturated regolith during the summer. These seasonal factors may coalesce to create significant yearly cycles of lake composition. Therefore, any biota in the lakes may require coping mechanisms to deal with this changing environment or undergo a type of life cycle which alters the physiology of the biota with the seasons.

In addition to seasonal effects there may be hemispherical differences in cloud activity, precipitation quantity and evaporation rates as there is high abundance of lakes in the Northern hemisphere compared to that of the Southern hemisphere. This may be explained by the aphelion (when Titan is farthest from the Sun due to Saturn's eccentric orbit) occurring during the Northern summer season and therefore the Southern hemisphere receives more insolation which increases evaporation rates (Schneider *et al.* 2012). This would make the northern hemisphere a more stable habitat for biota.

These liquid deposits have long been speculated to be a mixture of methane, ethane, and propane with solutes of heavier hydrocarbons, complex organics, nitriles, and atmospheric gases (Dermott & Sagan 1995; Dubouloz *et al.* 1989; Raulin *et al.* 1986; Raulin 1987; Raulin *et al.* 1989). Many chemical potential models of the lakes have used a constant drizzle of liquid hydrocarbon and tholin precipitation to formulate their models, using the 'rain without clouds model' first theorized by Toon *et al.* (1988). However, evidence is mounting for large quantities of precipitation from storm events, including pockets of river dominated terrains strewn across the surface of Titan and direct imaging of changes in lake bathymetry after storm events (Turtle *et al.* 2009b), which may also indicate changes in solute concentrations depending on precipitation type and quantity with each storm. An attempt to employ environmental variables and hemispherical differences in precipitation to chemical potential models of the lakes to determine compositional changes has resulted in ranges of up to 8500% for solute concentrations between models (Cordier *et al.* 2012) and shows just how important environmental variables are to the availability of solutes as a potential nutrient supply for any organisms on Titan.

Titan simulation studies have revealed hundreds of complex chemistries within aerosols and tholins. Complex aerosols in Titan's atmosphere are produced by free radicals interacting with hydrocarbons. Nitrogen may be fixed as organic macromolecular aerosols in Titan's atmosphere (Imanaka & Smith 2010) which could then be utilised by biota as it is precipitated onto the surface. Analogs of Titan's aerosols have been produced in different N_2-Hydrocarbon gas mixtures (Berteloite *et al.* 2010a; Berteloite *et al.* 2010b; Sciamma-O'Brien *et al.* 2010) for example, vinyl acetylene production from reactions between unsaturated hydrocarbons ethene (C_4H_4), propene (C_3H_6), 1-butene and 2-butene, with isobutene (C_4H_8), trimethylethene (C_5H_{10}), tetramethylethene (C_6H_{12}) and the ethynyl radical (C_2H) at low pressures and temperatures (Woon & Park 2009). Also, ethynylbenzene ($C_6H_5C_2H$) and cyanobenzene (C_6H_5CN) can be produced by the reaction of benzene and the ethynyl (C_2H) or cyano (CN) radicals at low temperatures (Woon 2006).

It could be that lakes or hydrofers may play an important role in Titan's chemical evolution because they would protect organic material from photochemical destruction and may enable the production of new organic species therein (Tokano 2005b). Hydrolysing tholins has also been shown to produce amino acids including racemic protein amino acids (Khare *et al.* 2008). Even oxygen ions have been detected entering Titan's atmosphere which can react to form compounds bearing oxygen such as CO, CO_2 or methanol (Horst *et al.* 2008) which potentially increases the range of chemistries available for any biota. These works reveal that the building blocks of proteins and other biochemistries may be produced in the atmosphere and on the surface of Titan; it may be hypothesized that these processes could have proceeded as far as the emergence of life.

1.2.3 The possibility of life on Titan's surface

On Earth there are extremophiles that have different intracellular conditions, such as *Picrophilus torridus* (an acidophilic Archaean) that maintains an intracellular pH of 4.6 (Stan-Lotter & Fendrihan 2012). How this organism copes with the bombardment of free hydrogen atoms in its membrane is not fully understood, but it provides insight into the ability of life to evolve in partnership with 'extreme' conditions rather than erect barriers to protect itself from a harmful environment. Therefore, the idea of biota depending on a different type of intracellular solution, such as a hydrocarbon liquid, may not require such a leap of the imagination as one would first presume.

We need to try diverging from a purely geocentric line of thinking in order to consider the possibilities for hydrocarbon-based life in Titan's hydrocarbon liquids. It has long been recognised that the organic chemistry in Titan's atmosphere may provide useful insights into the proto-biotic evolution of early Earth (e.g. Clarke & Ferris 1997; Raulin *et al.* 1994). However, there is also the potential for Titan's dynamic and diverse environments to currently support a plethora of different biota types (Fortes 2000; Norman & Fortes 2011). If more than one ecosystem exists, they could be interconnected or isolated, with the potential to have completely independent evolutionary histories and geneses.

To a school student the life cycle starts with photoautotrophs (e.g. plants and algae) metabolising and creating organics though photosynthesis which all other heterotrophic life then is reliant upon consuming. One could therefore assume that nonterrestrial ecosystems would undergo a similar cycle. However, just like the unlit ecosystems found at hydrothermal vents on Earth, any Titan ecosystem is likely to consist of chemoautotrophs due to the limited availability of light on the surface of Titan compared to Earth, or, chemoheterotrophs due to the prevalence of a diverse hoard of organic molecules.

Benner *et al.* (2004) first suggested that the liquid hydrocarbons on Titan could be the basis for life and play the same role as water on Earth; this initiated theories about the metabolism of such hypothetical organisms. McKay & Smith (2005) and Schulze-Makuch & Grinspoon (2006) calculated the energy available from hydrogenation; reacting H_2 with organic material to generate methane as a waste product. They showed that the metabolism of acetylene - $C_2H_2 + 3H_2 = 2CH_4$ - yielded the most energy (100 kJ mol^{-1} under Titan's surface conditions) with the energy stored in the triple bond (Schulz-Makuch & Irwin 2006), although, the high abundance of ethane also makes it a competitive source of energy for Titan biota. It has been suggested by Bains (2004) that hydrolysis or ammonolysis of unsaturated hydrocarbons of organics, such as acetylene, may also prove to be a viable metabolic process if catalyzed by silicon compounds. Metabolism *via* hydrogenation or hydrolysis of organics, e.g. acetylene, unfortunately will not proceed spontaneously; they require either metal or biological catalysts to promote the reaction.

However, the Committee on the Limits of Organic Life in Planetary Systems (2007) noted that "many enzymes function in organic solvents, and many organic reactions fundamental to biochemistry can occur in non-aqueous media", so there appears to be no barrier to the adoption of suitable catalytic enzymes by hypothetical methanogens on Titan's surface.

If hydrocarbon-based organisms were hydrogenating organics for metabolism at the surface it follows that anomalous depletions of hydrogen, acetylene and ethane would develop as they consumed these substances (McKay & Smith 2005; Schulze-Makuch & Grinspoon 2005). Intriguingly, recent Cassini data appears to provide evidence for such depletions. A deep ocean consisting principally of ethane was predicted after the Voyager flybys based on photochemical modelling (Dermott & Sagan 1995; Dubouloz *et al.* 1989; Flasar 1983; Lunine *et al.* 1983; Raulin *et al.* 1986; Raulin 1987; Raulin *et al.* 1989); however, the discovery of limited surface liquids in the form of lakes and seas reveals that there is an unexpected lack of ethane on the surface (Lorenz *et al.* 2008). Secondly, Strobel (2010) modelled the hydrogen concentration in Titan's atmosphere, and found that the observational data are best explained by a strong flux of hydrogen to the surface, for which the one explanation is a gradient in the hydrogen concentration created by metabolism of H_2 by methanogenic organisms. Finally, Clark *et al.* (2010) have reported an apparent depletion of acetylene at the surface compared to the expected rates of atmospheric production and subsequent deposition of acetylene onto the surface; in support of this there was no evidence of acetylene in the gases released from the surface after the Huygens Probe landed (Lorenz *et al.* 2006a; Niemann *et al.* 2005). Although these depletions are intriguing, they do not constitute unambiguous proof of life on Titan's surface as there are abiological counter-explanations in each case - the possibility of subduction of hydrocarbons or abiotic hydrogenation processes on the surface - but they certainly endorse the argument that Titan is a target of high astrobiological interest.

We must also consider other physiological aspects of any biota inhabiting Titan's hydrocarbon liquids. For example, variations in membrane physiologies for terrestrial biota are often related to external environmental characteristics as they manipulate their cell membranes to best cope with the habitat they occupy. This variation would also be expected for compartmentalisation strategies of Titan biota - differing depending on the environmental parameters of their habitat e.g. warmer hydrofer or colder surface hydrocarbon lakes.

For those living in the numerous icy habitats of Titan, strategies similar to those of terrestrial psychrophiles (cold-loving extremophiles) might be used. The *in situ* analysis of microbial activity of some psychrophilic methanogenic Achaea has detected metabolism and growth in permafrost even at temperatures as low as -20 °C (Gilichinsky *et al.* 1992; Gilichinsky *et al.* 1993; Rivkina *et al.* 2000). Psychrophiles have been known to alter the type and chain lengths of the fatty acid components of their membranes as a way to cope with low temperature

environments that increases the rigidity (and therefore interferes with the functions) of their membranes. An example of this is the use of anteiso rather than iso branched chain fatty acids (the anteiso structure has a methyl group on the third carbon from the lipophilic end of the molecule rather than the iso form that has a methyl group at the end), as it has been shown that anteiso-$C_{15:0}$ dominates the composition of a *Listeria monocytogenes* membrane when grown at low temperatures (~5 °C) (Annous *et al.* 1997) due to its lower melting point (Chan & Wiedmann 2009).

A common strategy of psychrophiles to cope with low temperatures is to incorporate polyunsaturated fatty acids - which have a lower melting point than their saturated counterparts - into their cell membrane (Russell 1989). There are two theories for the motivation for this process: a homeoviscous adaptive response – which is when an organism that is subjected to different growth temperatures adjusts its membrane lipid composition to maintain fluidity (Russell 1992), or, a homeophasic adaptive response – which occurs when an organism tries to maintain the membrane biophysical structure i.e. to prevent the occurrence of nonbilayer phases (Russell & Nichols 1999). It is possible that this type of amphiphile is the most appropriate to – form a lower the melting point for the cell membrane whilst also favouring a bilayer phase (Hazel 1995). As the ability to synthesize polyunsaturated fatty acids has been retained by all psychrophiles (Castello & Rogers 2005) it may also be a common strategy among Titan biota in icy habitats to use polyunsaturated species to maintain the efficiency of their cell membranes.

Terrestrial toxitolerant extremophiles are organisms which are adapted to cope with environments with a high percent of organics such as hydrocarbon liquids. A wide range of ecological studies have focused on the terrestrial biotransformation of hydrocarbons by toxitolerant extremophiles by means of biodegradation (the unwanted metabolism of hydrocarbon sources) and bioremediation (the use of toxitolerants to clean up hydrocarbon waste such as oil spills); e.g. (Atlas 1995; Atlas & Bartha 1992; Atlas & Cerniglia 1995; Atlas & Philp 2005; Dimitriou-Christidis *et al.* 2008; Jorgensen *et al.* 2005; Leonov *et al.* 2010; McClay *et al.* 2000; Prince & Atlas 2005; Rosenberg 1993; Zhang *et al.* 2010b). Therefore, the metabolism of toxitolerants is usually at the heart of these biotransformation studies. However, there are toxitolerants that do not metabolise hydrocarbons and yet can withstand high concentrations of hydrocarbons, such as various *Pseudomonas* strains, which can tolerate a 50% toluene solution (Inoue *et al.* 1991) or a 50% aromatic hydrocarbon solution (Cruden *et al.* 1992). There has even been a report of a *Pseudomonas* strain able to grow on alpha-pinene (an isomer of $C_{10}H_{16}$) at concentrations up to 90% (Sikkema *et al.* 1995), the mechanisms of which are still debated but which likely involve modification of the outer membrane.

Although there are a variety of mechanisms for toxitolerants to manage their hydrocarbon-filled habitats, the alteration of membrane features is often seen. Such modifications includes

changing the fatty acids and headgroups of phospholipids, thereby, incorporating surfactants with a greater hydrophilic nature into their cell membrane repelling hydrocarbons more efficiently (Heipieper & Debont 1994; e.g. Higgins & Gottesman 1992; Isken & Debont 1996). Other modifications increase the rate of turnover and change the ordering of membrane components as seen in such biota as *Pseudomonas putida* GM73 (Kim *et al.* 1998). The increase of fatty acid types that can be replaced rapidly when there is damage to the membrane is another coping mechanism (Pinkart *et al.* 1996). Increasing saturated fatty acids enhances the rigidity of the cell membrane when there are toxic solvents such as hydrocarbons present (Heipieper *et al.* 1994). The *cis*-to-*trans* isomerisation of the unsaturated fatty acids moieties of amphiphiles, e.g. *P. putida* exhibits these types of *cis/trans* isomerisations (Weber *et al.* 1994), changes the membrane fluidity in response to the presence of high concentrations of toxic substances such as hydrocarbons (Keweloh & Heipieper 1996). Also modifying the outer membrane lipopolysaccharides (LPS) in gram-negative bacteria from 'smooth' to 'rough' may increase the hydrophilic nature and decreases permeability of the membrane (e.g. Pinkart *et al.* 1996).

The alteration of membrane physiology by changing surfactant types is a coping strategy that can be shared by different types of toxitolerant biota e.g. gram-positive and gram-negative toxitolerant bacteria (Torres *et al.* 2011). However, some terrestrial organisms are naturally better adapted to living in hydrocarbon filled habitats; for example, gram negative bacteria have an additional outer membrane which may confer an advantage to repel any unwanted hydrocarbons (Isken & de Bont 1998). By understanding the coping physiologies of terrestrial toxitolerants, we might gain some insights into the features to look for in water- or hydrocarbon-based Titan biota in hydrocarbon-rich environments and their respective biosignatures.

Terrestrial life as we know it also relies on carbon chemistry, however, it has been suggested that in cold environments, such as those found on Titan, silicon could replace carbon as the main constituent of its biochemistry as it tends to be more reactive than carbon (Brook 2000). For example, a low temperature serpentinisation process, or meteorites impacting a cold body such as Titan, has been suggested as methods to provide silanes (Bains 2004; Schulze-Makuch & Irwin 2006). This could be the foundation of an organism utilising polymerized silicon to comprise larger biochemistry elements and silanols as membrane components. However, an entire organism based on silicon is unlikely on Titan due to relative scarcity of the element compared to carbon, especially on Titan's surface.

1.3 Compartmentalisation for hydrocarbon-based life

The suitability of hydrocarbon liquids for supporting life is often debated. If our terrestrial life-supporting water is not the medium that exotic extraterrestrial organisms use, then the biochemistries that are utilised are unlikely to be the same. For life in hydrocarbon liquids, these would be unique physiologies, especially concerning compartmentalisation as they are

immersed in a nonpolar solvent. All the elements necessary for the creation of cell membrane components may be available on Titan, either from: surface organics, cryovolcanism, or meteoritic delivery of simple fatty acids which is likely to have occurred throughout Titan's history (Deamer & Pashley 1989).

For biota inhabiting the hydrocarbon liquids of the Titan lakes, a hydrocarbon-based cytoplasm may be more practical than a water-based cytoplasm. The Committee on the Limits of Organic Life in Planetary Systems (2007) observed that there is currently no information about the possible alternative membrane structures that would be stable in organic solvents, such as those found in the hydrocarbon lakes of Titan, as there are no known terrestrial analogues. For those Titan biota that are hydrocarbon-based, one possible solution to compartmentalisation is to modify the arrangement of amphiphilic molecules in the cell membrane; inverting a terrestrial cell membrane structure into a 'reverse' vesicle structure and therefore encompassing a cytoplasm of liquid hydrocarbons (Norman & Fortes 2011); see Appendix IV and Figure 7.

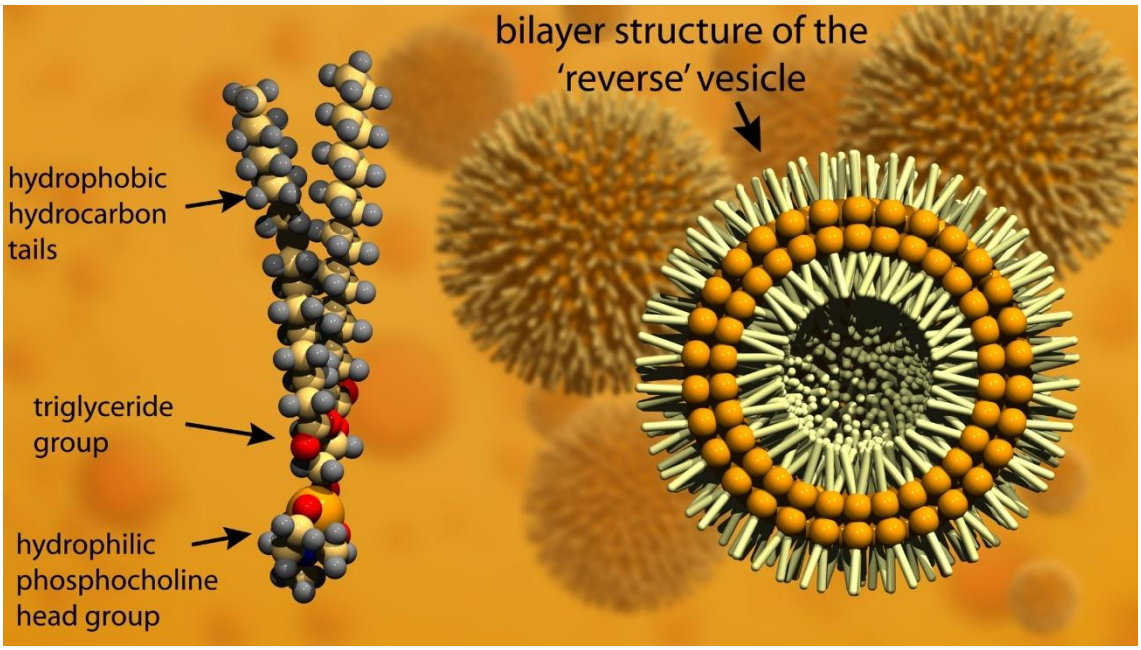

Figure 7: Illustration of the reverse vesicle structure taken from Norman & Fortes (2011) (Appendix IV).

Terrestrial cell membranes are vesicular structures composed primarily of a phospholipid bilayer with the hydrophilic head groups arranged around the periphery. Although this membrane is now an integral part of numerous cell functions, with many species utilising specialised lipids, transport proteins, additional cell walls and external surface structures, the primary responsibility of a cell membrane is compartmentalisation – to keep the organism and environment separate. The backbone of boundary forming compounds then allows other molecules, such as transport proteins, to be attached which can play other biochemical roles. It is believed that the primordial cell membrane on Earth - originating billions of years ago - was

likely to be a simpler type of 'protocell' consisting of a limited variety of lipid amphiphiles (Chen & Walde 2010; Deamer & Dworkin 2005; Deamer & Oro 1980; Hargreaves *et al.* 1977; Kuruma 2007; Luisi *et al.* 1999; Luisi *et al.* 2004; Monnard *et al.* 2007; Monnard & Deamer 2001; Morowitz *et al.* 1988; Segre *et al.* 2001). Artificial analogues of these protocells are called liposomes, or vesicles if prepared from other amphiphiles, and have been extensively utilised in drug delivery systems in the pharmaceutical industry for almost half a century (e.g. Bangham *et al.* 1965; Elsayed *et al.* 2007; Gregoriadis 2008; Ibsen *et al.* 2011; Oda *et al.* 2010; Venkatraman *et al.* 2010). However, there are many other uses for these simple capsules including to optimisation of cheese ripening times in the food industry (e.g. Malheiros *et al.* 2010) and transdermal liposomal delivery of anti-aging creams in the cosmetics industry (e.g. Lee *et al.* 2007).

Therefore, before looking into additional biochemical roles of an exotic type of membrane we must first develop an understanding of chemistries that have the potential to form a basic boundary -; just as in architectural work where the framework of a stable building must be designed before other considerations, such as insulation, is taken into account. In the case of hydrocarbon-based biota on Titan, this may be a reverse vesicle. This is where my research, studying the stability of reverse vesicles at conditions similar to Titan's lakes, begins to unveil the possible morphologies for exotic compartmentalisation strategies.

Chapter 2: A review of reversed micellar structures, focusing on reverse vesicles

Studies into self assembled systems of amphiphiles are generally classified as part of 'soft condensed matter' research. They are complex systems that are associated with the typical physical responses of both liquids and solids. Experimental data on the processes of spontaneous self assembly, and characterising times of existence and interaction for aqueous soft matter assemblies, have been identified as some of the most valuable areas for current research (Khabibullaev & Saidov 2003). Arguably, this may also be the case for experimental work of reversed self assembled structures in nonpolar solvents to determine the habitability of nonpolar mediums on other worlds; such as those found on Titan.

2.1 Classification of 'reversed' micellar structures

Amphiphiles are molecules containing polar and nonpolar moieties; 'amphi' meaning 'double' and 'phile' meaning 'affinity' in Greek which was first termed by Hartley (1936), see Figure 8.

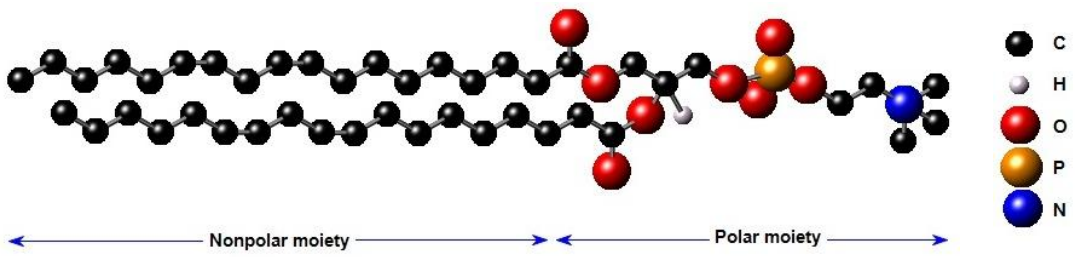

Figure 8: This phosphatidylcholine is an example of an amphiphile that illustrates the polar and nonpolar moieties.

'Normal' self assembly is described as amphiphiles with the polar moieties pointing towards the interface with the polar solvent (usually water). 'Reversed' self assembly is stable in nonpolar solvents, such as organic solvents, as the lipophilic moieties point towards the solvent interface. Therefore reversed micellar particles are inverted versions of normal micellar particles; see Table 1.

Normal structure	**Micelle**	Polar solution with a spherical monolayer of amphiphiles enclosing a nonpolar core	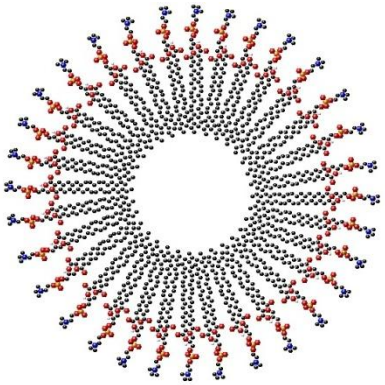
	Cylindrical micelle	Polar solution with a cylindrical monolayer of amphiphiles enclosing a nonpolar core	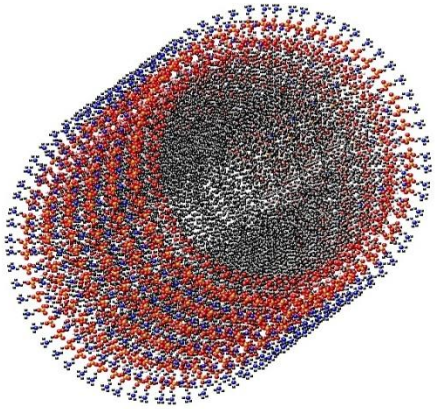
	Vesicle	Polar solution with a bilayer of amphiphiles encapsulating a polar liquid core	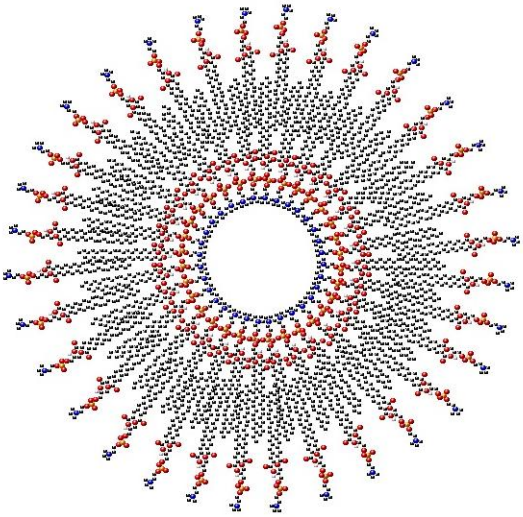
	Sheet	Polar solution with a bilayer sheet of amphiphiles enclosing a nonpolar core	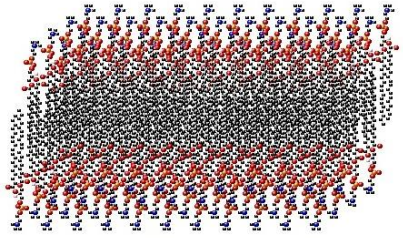

Reversed structure	Reverse micelle	Nonpolar solution with a spherical monolayer of amphiphiles enclosing a polar core	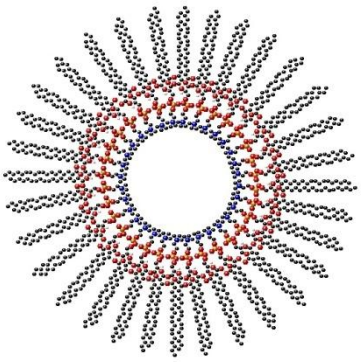
	Reverse cylindrical micelle	Nonpolar solution with a cylindrical monolayer of amphiphiles enclosing a polar core	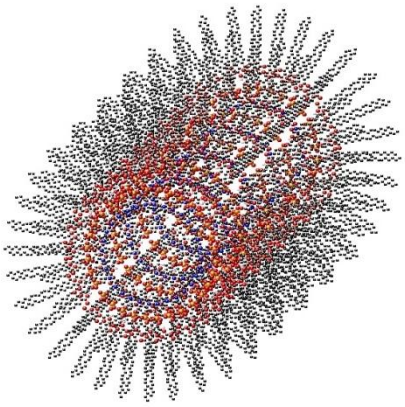
	Reverse vesicle	Nonpolar solution with a bilayer of amphiphiles encapsulating a nonpolar liquid core	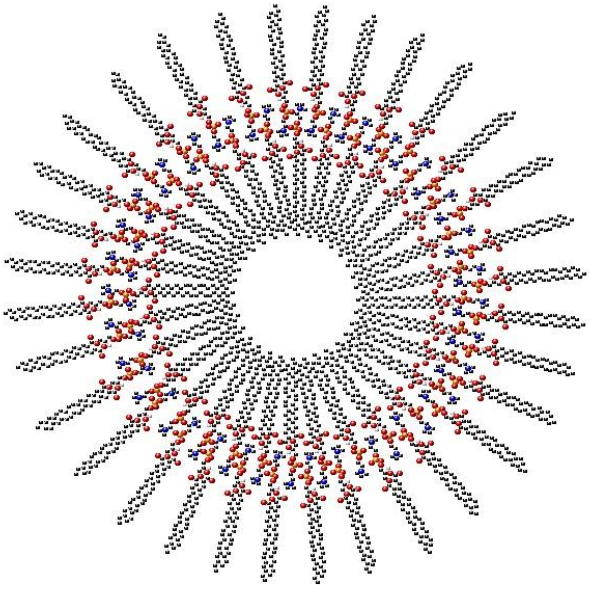
	Reverse sheet	Nonpolar solution with a bilayer sheet of amphiphiles enclosing a polar core	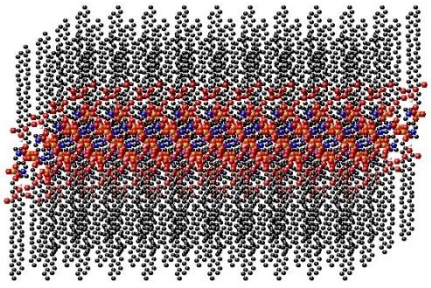

Table 1: List of the common normal and reversed micellar and vesicular particles and their respective structures.

Like normal vesicles, reverse vesicles can be unilamellar or multilamellar; if multilamellar the bilayers are stacked on top of each other sometimes to the point of creating an onion like structure with an internal compartment too small to be imaged with microscopy (e.g. Li *et al.* 2010a). The number of lamellar making up a vesicle can be altered by sonication (using either an ultrasonic probe or water-bath) or extrusion using polycarbonate filters with predetermined pore sizes. This excitation can form either a stable colloidal dispersion or a temporary metastable state after which they may revert to another form after standing for a time.

So far, a variety of different surfactants have been used to create reverse vesicles in nonpolar liquids including; non-ionic ethers (Kunieda *et al.* 1999) and esters (Mollee *et al.* 2000; Shrestha *et al.* 2006); catanionic surfactant mixtures (Li & Hao 2007a); zwitterionic gemini surfactants (Peresypkin *et al.* 2007); coblock polymer surfactants (Rangelov *et al.* 2004); and zwitterionic phospholipid surfactants (Lee *et al.* 2013; Tung *et al.* 2008). Reversed micelles and worms have a wider literature base compared to reverse vesicles; as the reverse vesicles seem to be more difficult to synthesise and there is currently little interest or application. However, a study by Mollee *et al.* (2000) has specifically looked for the potential of reversed vesicles for use in the pharmaceutical industry. However, these reverse vesicles have the potential to be interesting structures for astrobiological research. Research into the stability of reverse vesicles in environments similar to that of Titan is an important step towards understanding the astrobiological potential of compounds to form viable cellular compartments.

2.2 Thermodynamics of micellar particle self assembly

Amphiphiles self assemble into micellar structures in order to minimise the free energy of the system and are driven by weak forces such as coulombic attractions, pi-pi stacking interactions, van der Waals, hydrogen bonding and hydrophobic forces. A bond with a lot of electrostatic energy compared to the thermal energy of the bonded atoms is considered ‘permanent’ (chemical bond) as where a bond that has energy near to the thermal energy is likely to be broken by thermal agitation and therefore is considered ‘temporary’ (physical bond). In micellar systems, chemical bonds generally hold together amphiphile molecules and physical bonds influence the self assembly of a system.

The resultant self assembled structures cannot be fully explained by thermodynamics alone (lowest free energy equilibrium phases) but also requires kinetic processes. For example, when transferring from one phase to another the new minimum free structure might not form instantly and intermediate structures may occur in the interim. The duration of this interim period can sometimes be long enough to be experimentally studied.

Although the exact processes involved in the hydrophobic reaction are still debated, it is generally believed that in aqueous systems a lipophilic moiety causes the alignment of water

molecules around it; therefore decreasing entropy and increasing the free energy of the system. To lower this initial boost of free energy the hydrophilic part of an amphiphilic molecule tries to shield the lipophilic section which reduced the contact between the water and the lipophilic sections.

In systems of amphiphiles within nonpolar solvents it is assumed the chief thermodynamic force is the van der Waals (Tung *et al.* 2008). The lack of hydrogen bonding in these systems may play a role in the reduced reports of reverse vesicles in comparison to liposomes in polar systems and reverse micelles in nonpolar systems.

2.3 Geometric packing considerations for the formation of reverse vesicles

Although thermodynamic forces dominate the occurrence of self assembly, amphiphilic dimensions and geometric packing determine the type of structure formed. The parameter for the geometric packing of amphiphiles is termed the 'packing parameter'. The dimensionless packing parameter relies on geometric information about the *effective* regions of the hydrophilic and lipophilic moieties of the molecules. To determine the packing parameter of a system the amphiphiles are characterised in terms of their hydrocarbon volume 'v' (the volume of the lipophilic tail), critical chain length 'l_c' (maximum effective length of the hydrocarbon chain) and optimum head-group (hydrophilic) area 'a_0': Packing Parameter = v / l_c a_0. This compares the *effective* cross-sectional areas taken up by the hydrophilic and lipophilic sections in order to predict the subsequent particle structure in an amphiphilic rich system; see Table 2.

Packing Parameter Range	Solution Type	Corresponding Illustration of Geometry for Packing Parameter	Predicted Structure
PP < 1/3	Polar	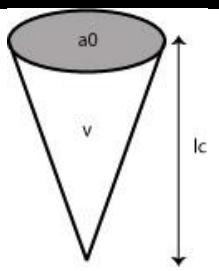	**Spherical micelle** Polar solution with a single spherical layer of surfactants enclosing a nonpolar core
1/3 < PP < 1/2	Polar	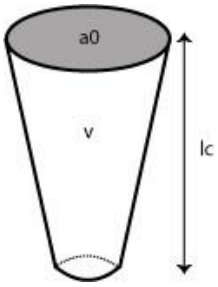	**Cylindrical micelle** Polar solution with a single cylinder of surfactants enclosing a nonpolar core

1/2 < PP < 1	Polar	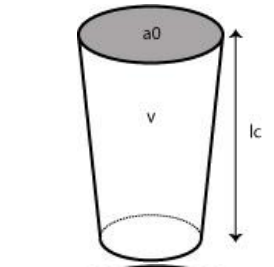	**Vesicles** Polar solution with a bilayer enclosing a polar liquid core
pp = ~1	Polar or nonpolar	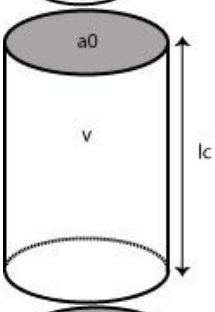	**Bilayer sheets** Flat sheets of bilayers in polar or nonpolar solutions
1 < PP < 1 ½	Nonpolar	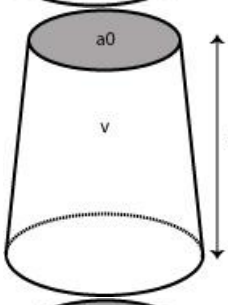	**Reverse vesicles** Nonpolar solution with a bilayer enclosing a nonpolar liquid core
1 ½ < PP < 1 ⅔	Nonpolar	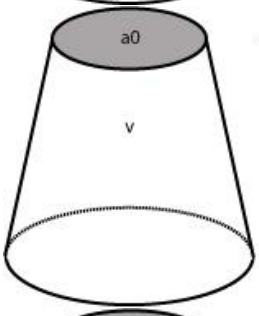	**Reverse cylindrical micelles** Nonpolar solution with a single cylinder of surfactants enclosing a polar core
pp > 1 ⅔	Nonpolar	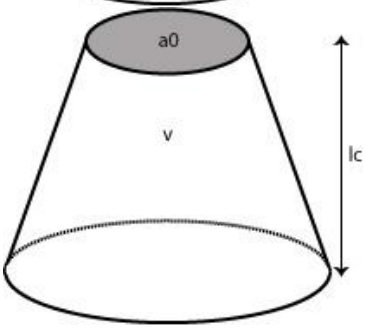	**Reverse spherical micelles** Nonpolar solution with a single spherical layer of surfactants enclosing a polar core

Table 2: Table comparing the packing parameters of amphiphiles with the same effective polar head group area and varied lipid tail volumes, and the resulting particle structures; where 'v' is the hydrocarbon volume, 'l_c' is the critical chain length and 'a_0' is the optimum head-group (hydrophilic) area.

The geometric information about the effective regions of the hydrophilic and lipophilic moieties are a consequence of equilibrium considerations and therefore the interactions between molecules, solution composition and environmental factors affect the packing parameter of a system (Nagarajan 2002). For example, it has been demonstrated that the interaction of the hydrocarbon tails change the microstructures of the molecules when packed into micellar shapes

(Khabibullaev & Saidov 2003). Also, for normal micellar structures in water there is an attractive force between the hydrophilic heads due to their function as shielding around the lipophilic sections; therefore, the *effective* area of the hydrophilic section would be reduced. In organic solvents, the shielding effect draws together lipid tails and therefore reduces the *effective* lipophilic area. Therefore, the packing parameter is not a simple equation relying only upon the geometrical shape and size of the amphiphiles involved but also environmental factors need to be considered.

As can be seen from Table 2 normal vesicles are formed from amphiphiles with a slightly larger hydrophilic moiety than the lipophilic moiety. Examples of the type of amphiphiles that form this structure are phospholipids (e.g. phosphatidylcholines) which are used in cell membranes of terrestrial biota; these have two hydrocarbon tails attached to a large polar head group. To form reverse vesicles with typical phospholipids there needs to be an increase in the effective lipophilic area.

The critical chain length can be estimated from the maximum chain length (l_{max}) of the hydrocarbon chains as they are the same order of magnitude; however, the critical chain length is slightly smaller (Israelachvili 1991). The maximum chain length of a saturated hydrocarbon chain with n atoms, for example, is approximately: $l_{max} = 0.154 + (0.1265n)$ nm. When taking into consideration unsaturated chains it becomes difficult to accurately estimate the critical chain length.

Similarly, the hydrocarbon volume can be estimated for saturated chains: $v = (27.4 + 26.9n) \times 10^{-3} nm^3$ (Tanford 1980). There is also a minimal cross sectional area, $(v/lc) = 0.21\ nm^2$, for saturated hydrocarbon chains with a large number of atoms. However, this formula does not accurately estimate the hydrocarbon volume of unsaturated chains.

Although the area of the lipophilic section may seem to be a distinct geometric parameter the actual space it occupies, in a mono- or bi- layer, can also depend on external factors. For example, a nonpolar liquid with smaller molecules will be more efficient at moving between the lipophilic tails of a reverse micellar structure; this will increase the space between lipophilic sections and therefore increase the *effective* total volume of a cluster of lipophilic tails. Therefore, in these experimental studies solvent penetration needs to be taken into consideration when evaluating systems of different solvents, especially when decreasing the molecular weight of the solvent. So whilst an amphiphilic system in heptane may produce reverse vesicles, the same system in hexane could produce reverse micelles due to an increase in solvent penetration.

The *optimum* head-group area (the point at which repulsive and attractive forces are balanced to give the minimum amount of free energy) is affected by numerous internal and external factors. For reversed particles there can be repulsive forces acting internally between hydrophilic head

groups, such as electrostatic repulsion, which would increase the *effective* area taken up by the polar head groups. The strength or range of these forces can be affected by external factors, such as, temperature or stabilisers that screen repulsive electrostatic forces. These considerations make the optimum head group area parameter difficult to estimate accurately.

Because of the external environmental factors that affect the way the amphiphiles pack together, the packing parameter formula cannot be used independently as an accurate predictive method to determine the way a system will self assemble. So why is it useful? Some benefits come with retrospectively determining the packing parameter range for a system. Once a structural phase has been identified, this information can then be used to predict what aggregate types could form with changes in the system. For example, if a long/short amphiphilic system with a ratio R1 created reversed micelles, then the packing parameter for this system would be ~1.7; therefore, by increasing the amphiphilic ratio we would expect the packing parameter to decrease and eventually produce reverse cylindrical micelles or vesicles. So we can use experimental results to predict structural phase changes with small changes in the system.

2.4 Review of amphiphilic systems that form reverse vesicles

2.4.1 Ionic amphiphiles

Ionic amphiphiles have ionized polar heads, which can be positive (cation) or negative (anion). Balancing the electrostatic interactions is important in ionic systems because two ionic amphiphiles with the same charge will repel one another at close proximities. This is especially significant when trying to achieve a structure with an area of densely packed polar sections, such as, the polar interior of a reversed bilayer. In order to achieve electrostatic stability some reversed systems use ‘stabilisers’; utilising ions to enable bonding between normally repulsive sections or the insertion of small quantities of a polar liquid, such as water, to exponentially weaken the reaction between polar heads with distance.

Anionic reverse vesicles have been made with sodium 1,2-bis(2-ethylhexyloxycarbonyl)-l-ethanesulfonate (AOT) and sodium dodecyl sulphate in decane, using water as a stabiliser (Kunieda *et al.* 1991a). A reverse vesicular ethanol solution utilising didodecyldimethylammonium bromide encapsulating polyoxometalate is an example of a large central stabiliser allowing the formation of stable reverse vesicles without polar solvents like water (Yan *et al.* 2009). Other such systems use internal molecular magnets e.g. $Mn_{12}O_{12}(O_2CCH_3)_{16}(H_2O)_4$, to stabilise ionic amphiphiles e.g. fatty acid CnOOH, in a reversed vesicle formation. This has been shown to work in solvents such as chloroform, dichloromethane, toluene, benzene, and mixed chloroform with methanol (Li *et al.* 2010b).

The only way, theoretically, to make normal or reverse vesicles from ionic amphiphiles without stabilisers is to use a mixture of anionic and cationic amphiphiles, therefore, creating catanionic

systems. However, so far polar solvents have been used to stabilise reverse vesicles in catanionic systems. For example, Zhang *et al.* (2010a) formed a catanionic system where a central section of polyoxometalate was ionically bound to a catanionic mixture of amphiphiles that combined to form reverse vesicles in toluene when using a polar solvent stabiliser. Also, reverse vesicles were formed in salt-free catanionic systems utilising tetradecyltrimethylammonium hydroxide (cation) and tetradecyltrimethylammonium laurate (catanion solution) in toluene, tert-butylbenzene and cyclohexane solvents with water as a necessary stabiliser (Li *et al.* 2008a; Li *et al.* 2010a; Li & Hao 2007a).

2.4.2 Nonionic amphiphiles

Nonionic amphiphiles are characterised by the hydrophilic area of the molecule being an uncharged polar segment i.e. the total net charge for the segment is zero but the individual atoms have partial charges**.** Some nonionic amphiphiles are frequently used in the food and pharmaceutical industries because they are edible e.g. polyglycerol fatty acid esters.

The types of hydrophilic areas utilised by nonionic amphiphiles includes polyhydroxyls (employing many –OH moieties), such as, sugars ($C_nH_{2n}O_n$, n=3 to 7) and polyethers (employing many ether groups 'R-O-R'). Polyethers, utilising multiple oxyethylene units (O-C-C), are the most frequent form of hydrophilic group in nonionic amphiphiles because many different species can be ethoxylated. Common types include sucrose esters, sorbitan esters and polyglycerol esters.

These amphiphiles are very useful for reversed micellar structures because the internal polar heads are less likely to suffer from electrostatic repulsion, and therefore, will not require any stabilisers to counteract the repulsive forces. Also, due to their neutral electrostatic state, nonionic amphiphiles can be used as a type of stabiliser if added to ionic amphiphilic systems in order to negate issues of electrostatic repulsion.

Sorbitan monostearate is a nonionic surfactant that has been shown to form metastable reverse vesicles in hexadecane, isopropyl myristate and vegetable oils (found at 41-44 °C when cooling from 60 °C) without the need for any stabilisers (Murdan *et al.* 1999). Esters, such as glycerol, diglycerol monooctanoate, monodecanoate, and monododecanoate, have been shown to produce reverse vesicles in a variety of hydrocarbon solvents, such as hexadecane, octane, decane, tetradecane, paraffin, and squalane, without the need for any stabilisers (Shrestha *et al.* 2006; Shrestha & Aramaki 2007; Shrestha *et al.* 2009). Also combinations of sucrose ester surfactants have been shown to produce reverse vesicles in silicon oil; with a stability increase with the addition of cholesterol (Mollee *et al.* 2000).

However, in numerous nonionic reverse vesicle systems water has been required as a stabiliser. Reverse vesicle system utilising sucrose alkonates (e.g. fatty acid-C14 10% = sucrose

monomyristate, C16 40% = sucrose monopalmitate, C18 50%; sucrose monolaurate; sucrose dilaurate) required stabilisers, such as water and hexanol, to form reverse vesicles that were stable for periods of over 6 months in the hydrocarbon solutions decane, cyclohexane, hexamethyldisilane and hexadecane (Kunieda *et al.* 1993a; Kunieda *et al.* 1993b; Kunieda *et al.* 1993c; Kunieda *et al.* 1994; Nakamura *et al.* 1995; Olsson *et al.* 1996). Water has also been shown to be required in tetra- or penta- aethylene glycol dodecyl ether systems in dodecane in order to produce reverse vesicles (Kunieda et al. 1991b; Kunieda et al. 1991c; Kunieda et al. 1992; Sanchez-ferrer & Garcia-carmona 1992; Sanchez-ferrer & Garcia-carmona 1994). Even polyoxyethylene ether amphiphiles, which can make reverse vesicles in m-xylene at room temperature using a wide range of polyoxyetheylene sizes (the chain length of the polar EO units ranges between 10-55), requires small amounts of water (ranging from 0.2 to 2 H_2O molecules per EO unit) (Kunieda *et al.* 1999).

This indicates that some nonionic systems either require stabilisers to counteract repulsive forces within the polar interior of reversed bilayers, or, are required to allow the formation of the correct of packing parameter to create reverse vesicular systems. If the later is correct, utilising a range of short and long nonionic surfactants at various ratios may initiate the spontaneous formation of reverse vesicles without water in these systems.

2.4.3 Zwitterionic amphiphiles

Amphiphiles that are zwitterionic contain a positive and negative charge within the hydrophilic moiety of the molecule, and therefore, produces a net charge of zero (similar to nonionic amphiphiles). Typical examples of this are phospholipids that are utilised to construct cell membranes by terrestrial biota and derivatives of amino acids. Due to phospholipids being utilised by organisms they can be effectively used by the pharmaceutical industry.

Zwitterionic systems composed of phospholipid surfactants in high molecular-weight hydrocarbons and other non-polar liquids, such as cyclohexane, squalane, heptane, triglyceride triolein and hexadecane, have produced reverse vesicles at room temperature when utilising such stabilisers as NaCl (Tung *et al.* 2008) and water (Kunieda *et al.* 1992; Mays *et al.* 1999). Also, amino acid derived zwitterionic amphiphiles (N-dodecanoyl-L(or D)-serine) have been shown to produce reverse vesicles in toluene by using water as a stabiliser (Boettcher *et al.* 2001).

A significant result of these projects demonstrated that if very hydrophilic zwitterionic amphiphiles are used alone the dispersal of the liquid crystals are too poor to form reverse vesicles in nonpolar solvents. Therefore, the combination of hydrophilic and lipophilic zwitterionic amphiphiles is important in the creation of reverse vesicles.

A subset of zwitterionic amphiphiles, termed 'Gemini', is formed by conjoining two amphiphiles. They are joined in the hydrophilic group by a short chain often in the form of a hydrocarbon group, and in contrast to what the name suggests, the amphiphiles do not need to be identical. Some cation and anion amphiphiles have been conjoined to form a zwitterionic Gemini amphiphile that has produced reverse vesicles in cyclohexane, hexane, toluene, chlorocyclohexane, and dodecane without the need for stabilisers when the lipophilic chains are either longer than 14-carbon atoms or fluorinated (Peresypkin *et al.* 2007).

2.4.4 Block copolymer amphiphiles

A polymer is a large molecule made up of a string of smaller molecules (termed monomers) joined together. A copolymer is formed when more than one type of monomer is utilised within a string in a structured, often repetitive, fashion, e.g. with monomer types A and B a copolymer could form as an ABABAB or an AAABBB structure. A block copolymer is composed of different copolymer types which would usually phase separate in solution, however, are covalently bonded which prevents phase separation.

When these block copolymers are amphiphilic structure they can self assemble into micellar structures including reverse vesicles. Depending on the type of hydrophilic section, an amphiphilic block copolymer is a subset of either the ionic (e.g. poly oxyethylene polar moiety) or nonionic (e.g. poly acrylate polar moiety) groups. The lipophilic tails tend to be a chain with a large radius – utilising cyclic chains with monomers such as styrene – rather than typical aliphatic hydrocarbon chains. For example, the nonionic diblock and triblock copolymers of 1,3-didodecyloxy-2-glycidyl-glycerol have been shown to produce reverse vesicles in heptane without the need for any stabilisers (Rangelov *et al.* 2004).

2.4.5 Dimeric resorcinarene amphiphiles

Even large dimeric resorcinarene surfactants (hydrogen bonded macrocycles with lipophilic tails) have been stacked to produce reverse vesicles in chloroform, and the binary systems of chloroform/hexane and cyclohexane/decane (Ebbing *et al.* 2002; Xu *et al.* 2009). These do not form the standard bilayer structure but are rather like stacked circular units creating a shell with a nonpolar exterior and polar interior.

2.4.6 Lipophilic sections of amphiphiles

The lipophilic tails of amphiphiles are usually an aliphatic chain – a string of covalently bonded carbon atoms stabilised by hydrogen atoms. However, this carbon chain can also be stabilised by fluorine or a mixture of hydrogen and fluorine atoms e.g. (Peresypkin *et al.* 2007). These chains can vary in number, length and the number of unsaturation points; and unsaturated chains can be in a *cis* or *trans* formation. The differences in lipophilic chains have a strong impact on their use in terrestrial cell membranes and on the packing parameters of the amphiphiles.

Unlike the hydrophilic head groups where the bond types are often different between different amphiphilic systems, the same type of force is prevalent between adjacent lipophilic tails. This is the van der Waals force which is the mediator of the attractive force holding the lipophilic chains of the amphiphiles together, and for reversed structures, the tails with the nonpolar solvent.

2.5 Factors affecting micellar structures

2.5.1 Solute concentration

The concentration of amphiphiles within a solution plays an important role in the characterisation of self assembly within that system. It has been shown in the preceding sections that amphiphiles end up in a particular orientation due to certain moieties being affiliated with the solution; and the type of amphiphiles used and their packing parameter characteristics indicate what type of particle will form. However, in order for the amphiphiles to form any particles the critical micelle concentration (CMC) must be reached. Below the CMC, the amphiphiles will simply adsorb to the solution-air or solution-container interfaces, so that the solvent-phobic sections align themselves away from the solution whilst the solvent-philic sections point into the solution (LeBard *et al.* 2012; e.g. Zdziennicka *et al.* 2012). The CMC indicates the concentration at which the interfaces are saturated; above this point the free-floating amphiphiles are required to self assemble in order to lower the free energy of the system.

There has been conflicting data concerning the existence of a CMC for reversed structures in non-aqueous solvents due to the diminished solvophobic effect. In some systems there has been evidence of a gradual increase in aggregation numbers with increasing amphiphilic concentration (Ruckenstein & Nagarajan 1980); however, a sharp transition distinguishing a CMC has been observed in other systems (Smith *et al.* 2013). In order to mitigate this issue, and increase the probability of self assembly, this study focuses on concentrations of amphiphiles larger, or equal to, those which that have been shown to form reversed structures in cyclohexane (Tung *et al.* 2008). However, the CMC is not only affected by the type of amphiphiles but is also affected by the temperature and the solvent type. Therefore, the CMC for a particular system is often found experimentally rather than being computed from theory.

Over the CMC, the concentration influences the type of micellar structures that are formed. Low concentrations often form isotropic solutions (free floating particles) or liquid crystalline solutions (particles are orientated in a semi-stable 3D pattern). With increased concentration, a solution of isotropic micelles or bicelles (disc-shaped micelles) can go on to form a cubic lattice, and then into micellar worms in a hexagonal pattern. At higher amphiphilic concentrations a lamellar phase of liquid crystal bilayers often forms.

2.5.2 Amphiphilic mixtures

Vesicle formation is often facilitated by using amphiphiles with a variety of fatty acid chain lengths. When using a single amphiphile type the curvature found in vesicles conveys energy to the bilayer because if one leaflet has a favourable curvature the other leaflet would have to bend in an unfavourable direction. Therefore using two, or more, amphiphile sizes enables favourable curvature by utilising more of one amphiphile type in each leaflet and therefore the bilayer can contain both concave and convex layers.

It has been shown that using a soluble and insoluble amphiphile facilitates vesicular forms (e.g. Tung *et al.* 2008). However, whether this is due to the creation of favourable curvature alone or whether the asymmetry of the amphiphiles lowers the melting temperature (e.g. Menger & Peresypkin 2001) and facilitates a liquid crystal phase is uncertain.

2.5.3 Temperature

Amphiphiles usually form lyotropic systems (liquid crystal state where aggregation is induced by solvent type) rather than thermotropic systems (liquid crystal state induced thermally by either heating a solid or cooling a liquid). However, temperature is still a factor that affects the type of structure that is formed from a lyotropic liquid crystal solution. For example, lamellar-micelle transformations are often seen with changes in temperatures (Katsaras *et al.* 2005; e.g. Silva *et al.* 2008).

The effect of temperature on solubility depends on the type of solute; nonionic surfactants increase whilst ionic surfactants decrease in solubility with decreasing temperature. Therefore, hypothetically, a reverse vesicle with a small, very soluble, nonionic amphiphile and a larger, insoluble, ionic amphiphile might keep the solubility ratios in the correct region for a stable reverse vesicle when taking the system down in temperature.

Below the Krafft temperature amphiphiles (that are soluble as monomers) have solidified hydrocarbon chains and often micellar structures will no longer form because the hydrocarbon tails cannot bend to allow favourable curvature (Pershan 1982). However, whether the Krafft temperature prevents the formation of micellar structures depends on the amphiphiles in the system; for example, a combination of amphiphiles that reduce the energy of curvature may remain as particles such as vesicles below the Krafft temperature (Takajo *et al.* 2010).

The change of a micellar structure from a liquid crystalline (Lc) to solid (sol) state due to temperature depression can be hindered by adding smaller surfactants to the mixture which will naturally have a lower Lc-sol transition temperature.

Although the particle might be in a sol phase the particle may retain its overall structure; for example, some normal vesicles have shown to retain their form after a Lc-sol transition phase

(Takajo *et al.* 2010). However, research on the effect of low temperatures on a normal vesicular arrangement is necessarily limited to the freezing temperature of the most commonly used solvent, water, and therefore the temperature range of studies often does not often fall below 0 °C. Since studies of reverse vesicles in systems at cryogenic temperatures are logistically difficult, there have been no published reports on the effect of low temperatures on reverse vesicles to date. However, analogue studies that have been undertaken in normal bilayers and vesicles showed the hydrocarbon chain and head groups of phosphocholines in a multilamellar bilayer went from a liquid crystal to sol state at 37 °C and -34 °C, respectively (Wu *et al.* 1991).

Low temperatures in water obviously have effects on terrestrial biota since the medium the cells inhabit freezes at around 0°C (depending on the solutes present). Low temperatures are not as problematic in low molecular weight hydrocarbons as they often have large liquid phase ranges at low temperatures, for example, ethane's liquid range at ambient pressure is -182.5 °C to -89 °C. However, the relatively high freezing point of water would be expected to influence low temperature studies of those reverse vesicular systems that have used water to stabilise the internal polar region of the bilayer. Depending on the amount of water used there will be bound water (water molecules that are bound by hydrogen bonds to the polar moieties) and there may also be 'free' water (unbound between the two layers of polar heads creating a 'screen' for electrostatic repulsion). If this water freezes there maybe undesirable consequences of this bilayer being used as a cell membrane; including the inability to uptake nutrients or expel waste materials. Although currently there has been no research the internal water of bilayers of reverse vesicles, freezing of 'free' water at -11 °C and bound water at -70 °C has been shown to occur between normal multilamellar bilayers. This can be seen as analogous to a reversed bilayer made of amphiphiles stabilised with water (Wu *et al.* 1991).

2.5.4 Stabilising additives

Many amphiphilic species require a stabiliser in order to balance the electrostatic forces between polar head groups in a confined area and promote a stable, self assembled, reversed micellar structure. However, when using stabilisers we must also consider the possible effects on the kinetics of self assembly; for example, some spherical reverse micelles have been shown to change to reverse cylindrical worms when using divalent cations (such as Ca^{2+} and Mg^{2+}), whereas, trivalent cations (such as Fe^{3+}) had no effect (Lee *et al.* 2010). This indicates how important stabilisers can be in determining the resultant structure by altering the geometric packing parameter of a system.

Although the inclusion of an internal stabiliser into reverse vesicles could decrease the mobility of the membrane this problem is lessened if the stabilisers are small or low concentrations are used e.g. NaCl or trace amounts of water (<~0.5 molecules per amphiphile).

2.6 Choice and justification for systems studied in this thesis

This project studies phospholipids but phosphorus is likely to be an uncommon element on the surface of Titan. However, phosphorus containing molecules may be transported to Titan's surface from meteoritic impact ejecta or cryolavas loaded with species derived from the rocky core. Also, phosphorus containing molecules such as phosphine (PH_3 negative charge) can be dissolved in ethane and methane (Pasek *et al.* 2011). Phosphine becomes increasingly soluble with decreasing temperature and is more soluble in hydrocarbons, compared to that of water, by a factor of 100 (Young *et al.* 1985). Pasek *et al.* (2011) calculated that in the methane/ethane lakes of Titan PH_3 would be soluble up to ~1 mol/kg (mole fractions of 1.6 % for methane and 2.9 % for ethane); which corresponds to the highest solubilities of organics in these lakes (Cordier *et al.* 2009). However, as no phosphine has been observed in meteorites or comets it is probably formed from accumulated rocky bodies and therefore would only get into the lakes on Titan *via* cryovolcanism. There has been one study that shows phosphates can be changed into phosphines *via* lightning (Glindemann *et al.* 2004), however, lightning has not yet been observed on Titan. Pasek *et al.* (2011) estimated that all the PH_3 would be incorporated into clathrates or in the subsurface ocean on Titan, and therefore either cryovolcanism or impacts could liberate the phosphine at a concentration of ~10-10 mol/mole in the resultant melt. So assuming there is cryovolcanic delivery to the surface of Titan phosphine could be the compound that hydrocarbon-based biota use to access phosphorous. Or the phospholipids could be created from phosphates (PO_4) and organics from any putative, subsurface, water-based life; then expelled to the surface by means of cryovolcanism and utilised by hydrocarbon-based biota.

Phospholipids contain oxygen but free oxygen is not prevalent on Titan. However, there are numerous processes by which oxygenated species, such as amino acids and other oxygen bearing organic compounds, may be present on Titan's surface. These processes include oxygen ions, that have been detected entering Titan's atmosphere, reacting to form compounds bearing oxygen, such as, CO, CO_2 or methanol (Horst *et al.* 2008). Oxygen containing species may also form by the interaction of Titan aerosols with liquid water; this can occur by the subduction of these aerosols to subsurface water deposits and resurfacing by cryovolcanism, or, by impacts creating pools of surface water lasting up to a thousand years (Thompson *et al.* 1992). Temporary surface water deposits may also be taken up by biota and use cryoprotectants, such as antifreeze proteins (polypeptides that inhibit the growth of crystals), to extend the longevity of its liquid state. Furthermore, meteoritic impacts could deliver oxygen containing species directly to the surface, for example, meteorites have been shown to contain carbonyl and hydroxyl (Deamer 1985). These processes may therefore increase the range of biologically important chemistries, specifically oxygen bearing species, for biota.

Due to the rapid resurfacing processes on Titan, we have little knowledge about the historical rates of cryovolcanic or impact events. Therefore, it is currently not possible to estimate the plausible surface quantities of oxygen or phosphorus bearing species. However, it is probable that there is some oxygen or phosphorus bearing species that can be used directly, or converted to useful phospholipids, by biota on Titan's surface. Depending on the solubility of these compounds, they could be taken up passively from the hydrocarbon lakes or brought into dissolution, and actively taken up, by reverse micelles.

2.7 Research aims and scope

There are a few attributes that all terrestrial life share, such as metabolism, replication and compartmentalisation e.g. cell membranes. The intention of this thesis is to study the plausible compartmentalisation methods, and any corresponding physiological traits, of biota that may currently inhabit the hydrocarbon lakes of Titan. Therefore, the first logical step of exploring the physiology of theoretical 'exotic' cell membranes should be to study what chemistries would spontaneously form vesicles in hydrocarbon liquid systems.

Currently reverse vesicles have been formed in nonpolar and high molecular weight hydrocarbon solvents. This study will illuminate whether reverse vesicles are also stable in low molecular weight hydrocarbons and at low temperatures.

This experimental study investigates a range of hydrocarbon liquids and phospholipids to understand whether they form capsules which may provide compartmentalisation for biota in Titan's hydrocarbon habitats. This initial research will be limited to studying the specific zwitterionic amphiphiles called phospholipids. Biocompatible reverse vesicles may be exploited by medicinal, food and cosmetic industries and therefore studying the self assembly of phospholipid amphiphiles may have benefits outside of astrobiological exploitation.

The hydrocarbon liquids being studied will range from cyclohexane, octane, heptane, hexane, pentane, butane, and propane. The temperatures studied will range from room temperature to near the freezing temperatures of many of the solvents.

2.8 Research methods

This experimental study begins with describing the experimental methods. Chapter 3 describes the materials, sample preparation, and analytical methods employed to characterise amphiphilic-hydrocarbon systems under conditions progressively closer to those that occur in Titan's lakes. The following three chapters detail the results of the work undertaken at UCL and the final results chapter details small angle scatter studies undertaken at the Diamond Light Source and the Institut Laue-Langevin. This is followed by a chapter comparing all the results and a final chapter evaluating the astrobiological potential of the information gathered in this study.

Chapter 3: Experimental methods

3.1 Introduction

To determine the prospect of amphiphiles self assembling in hydrocarbon deposits on Titan a variety of experimental studies were undertaken. These studies focused upon the spontaneous self assembly of reverse vesicles in alkanes as this structure can potentially be used for compartmentalisation for putative hydrocarbon-based biota on Titan (see Chapter 1 and 2 for details).

The amphiphilic components of these studies - phosphatidylcholines - were chosen in response to Tung's *et al.* (2008) publication which reported that these phospholipids formed reverse vesicles in cyclohexane. An important factor in this research was the lack of water in the system which has often been used as a stabiliser for reverse vesicles, as it is unlikely for liquid water to be present in Titan's hydrocarbon lakes due to the low temperatures. Therefore, studying a system of amphiphiles that can assemble into reverse vesicles without liquid water is preferable when researching the possibilities of self assembly phenomena in Titan's hydrocarbon lakes.

Tung's *et al.* (2008) publication reported the effects on phase behaviour and the structure of self assembled micellar structures with changes in the amphiphilic molar ratio (Ro) of phosphatidylcholines with alkyl lengths of 18 and 4. The Ro is calculated simply by dividing the total molar concentration of the C4 amphiphiles in the system by the total molar concentration of the C18 amphiphiles in the system: Ro = C4 mM / C18 mM. Stable reverse vesicles were found at amphiphile ratios of 2-4 Ro in systems presenting with strong Tyndall scattering. Below 2 Ro reverse micelles were present in a transparent solution and above 4 Ro the system was macroscopically phase separated (liquid and solid phases); the structures of which were not determined.

This thesis entailed the study of a variety of amphiphilic-hydrocarbon systems at increasingly lower temperature conditions in order to simulate the conditions found in the hydrocarbon deposits on Titan. The variables included the type and ratio of phosphatidylcholines, the inclusion of a stabiliser (NaCl), the hydrocarbon solvent (cyclohexane and alkanes), the sample preparation, and the temperature.

3.2 Overall structure and analyses used in studies

This thesis has been set out into four distinct studies.

- Chapter 4: Study of the amphiphilic-hydrocarbon systems consisting of a binary mixture of phosphatidylcholines with the alkyl lengths 18 and 4. The analytical methods

include macroscopic phase behaviour and microscopic imaging studies of self assembled structures.

- Chapter 5: Study of the amphiphilic-hydrocarbon systems consisting of a ternary mixture of phosphatidylcholines with the alkyl lengths 18 and 4 and a lyso-phosphatidylcholine with an alkyl length of 18. The analytical methods include macroscopic phase behaviour and microscopic imaging studies of self assembled structures.

- Chapter 6: Study of the ternary amphiphilic-hydrocarbon systems with dynamic light scattering (DLS).

- Chapter 7: Study of the ternary amphiphilic-hydrocarbon systems with small angle neutron and X-ray scattering (SANS and SAXS).

3.3 Sample preparation

3.3.1 Types of amphiphiles in these studies

These studies used phosphatidylcholines which are zwitterionic amphiphiles that are part of the glycerophospholipid group. Three Avanti Polar Lipids Ltd products were used: Soy L-α-phosphatidylcholine 95% pure (product number 441601) and 99% pure (product number 840054) which are referred to as C18 95% and C18 99% hereafter; and 1,2-dibutyryl-sn-glycero-3-phosphocholine (product number 850303) which is referred to as C4 hereafter, with the molecule being referred to as PC4:0 hereafter (illustrated in Figure 9).

There is a natural range of fatty acid tails in the C18 99% and C18 95% samples as they have been extracted from Soy. The main constituent of these samples is an unsaturated DLPC called 1,2-dilinoleoyl-sn-glycero-3-phosphocholine or PC(18:2(9Z,12Z)/18:2(9Z,12Z)) which is illustrated in Figure 9 and referred to as PC18:2 hereafter. The majority of the mixed range of phosphatidylcholines is $C_{42}H_{80}NO_8P$ with a PC(16:0/18:0 to 3) configuration as determined by the total fatty acid distribution of these samples shown in Table 3.

Type of fatty acids found in C18 95% and C18 99%	Fatty acid distribution (%)
18:2	63
16:0	14.9
18:1	11.4
18:3	5.7
18:0	3.7
Unknown	1.2

Table 3: Table of the types of fatty acids and their respective weight percentages in the C18 99% and C18 99% products.

In the C18 95% sample there is the additional component of 2.8 wt/wt% of lysophosphatidylcholine. This lysophosphatidylcholine is likely to mimic the total fatty acid distribution; and therefore, PC(18:2(9Z,12Z)/0:0) 1-(9Z,12Z-octadecadienoyl)-sn-glycero-3-phosphocholine will be predominate species, which will be termed lyso-PC18 hereafter (see Figure 9 for illustration).

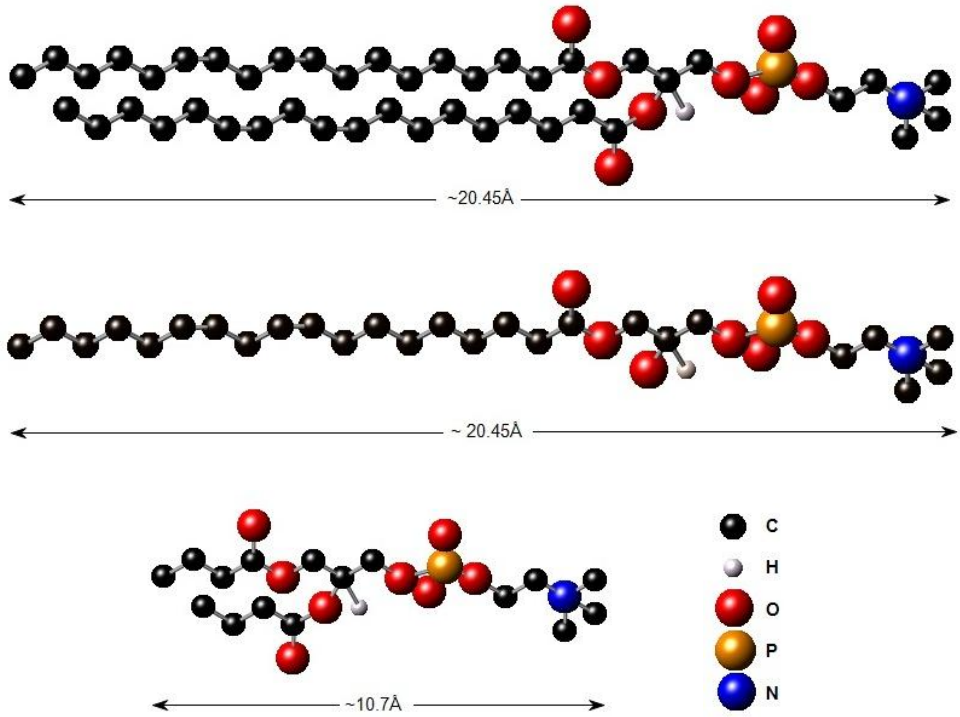

Figure 9: Illustration of molecular structures and approximate molecular lengths of: (top) PC(18:2(9Z,12Z)/18:2(9Z,12Z)) the main constituent of C18 95% and C18 99%, (middle) PC(18:2(9Z,12Z)/0:0) the dominant lysophosphatidylcholine in C18 95%, (bottom) PC(4:0/4:0) the single component of C4.

In summary, the phosphatidylcholine samples consist of:

- C18 99% = mainly PC18:2 with a smaller percentage of PC(16:0/18:0 to 3)
- C18 95% = mainly PC18:2 with a smaller percentage of PC(16:0/18:0 to 3) and 2.8 wt/wt% of lyso-PC18
- C4 = PC4:0

The transition temperatures for bilayers using phosphatidylcholines with alkyl lengths of 18 depended greatly upon the number of saturation points; as illustrated by Table 4.

Phosphatidylcholines	Transition temperature (Tm) °C	Transition temperature (Tm) K
18:0-18:0	54.9 [1]	~328
18:0-18:1	6.3 [1]	~279
18:0-18:2	-16.3 [1]	~257
18:2c9,12	-55.1 ±2.8 [2]	~218

Table 4: Table illustrating the liquid-sol transition temperatures of bilayers with different phosphatidylcholines. [1] (Quinn & Cheery 1992) [2] (Jost & Griffith 1982).

The main components of the phosphatidylcholines used in this thesis are PC18:2c9,12, which has a low transition temperature due to its two unsaturation points, and PC4:0 which has a low transition temperature due to its relatively small size. Therefore, a mixture of these two amphiphiles will produce bilayers with a low transition temperature, however, it is unlikely that the transition temperature of the mixed bilayer will be as low as the temperature found on the surface of Titan (-179°C).

3.3.2 Preparation of amphiphilic mixtures

The mixtures used in these studies consist of phosphatidylcholines and sodium chloride. The samples were named 'Reverse Vesicle experiment 1*g n*' (RVe1*g n*), with *g* labelling the sample group and *n* labelling the sample number in the group. In Chapter 4, mixtures of C18 99% and C4 were prepared with and without methanol - sample groups RVe1b and RVe1a respectively. In Chapter 5, 6, and 7 mixtures of C18 95% and C4 were prepared, usually in methanol, to obtain the sample groups RVe1c, SANS (using deuterated solvents), and SAXS. See Appendices I and II for individual sample preparation and the sample flow charts at the beginning of some results subchapters.

Depending on the system appropriate amounts of C18 99%, C18 95%, C4 and NaCl were weighed separately using scales with a precision of 0.001g. The concentration of amphiphiles was maintained between 15 mM and 30mM and NaCl between 3mM and 10mM. For details on the synthesis of mixtures for each sample please refer to Appendix I.

For samples to be analysed with fluorescence microscopy 2 x 10^{-5} mol L^{-1} of the polar fluorescent dye, Rhodamine B, was added at this stage of sample preparation; in correspondence to the fluorescence imaging of reverse vesicles by Li *et al.* (2010a).

For samples without methanol preparation, the dry products were added directly into the hydrocarbon liquids. To prepare mixtures in methanol the amphiphiles and NaCl were mixed in methanol until entirely dissolved. Appropriate volumes of these methanol solutions were then mixed together depending on the system desired. The methanol was then evaporated with a drying oven (duration for each sample noted in Appendix II) leaving a dry layer of amphiphilic mixture that was ready to be mixed with the hydrocarbon solvent.

3.3.3 Preparation of amphiphilic-hydrocarbon solutions

The solvents used in these studies include the cyclic hydrocarbon cyclohexane and the *n*-alkanes octane, heptane, hexane and pentane (liquid at room temperature) and butane and propane (gas at room temperature); see Table 5 for the liquid temperature range of these hydrocarbons at standard terrestrial atmospheric pressures. For samples to be studied with SANS deuterated hydrocarbon solvents were purchased from Cambridge Isotope Laboratories Inc. The preparations for each sample are detailed in Appendix I.

Material	Melting point (°C)	Boiling point (°C)
Cyclohexane	6.7	80.7
Octane	-56.7	125.6
Heptane	-90.5	98.4
Hexane	-95.3	68.7
Pentane	-129.67	36.06
Butane	-138.3	-0.5
Propane	-187.6	-42.1

Table 5: Liquid temperature range for the hydrocarbon solvents used in this study (Haynes & Lide 2011).

Appropriate volumes of hydrocarbons, that were liquid at room temperature, were pipetted directly into the vials containing the pre-prepared dry amphiphilic mixtures. These were then mixed using a shaking incubator; the temperature, rotation frequency and duration of the mixing for each sample is detailed in Appendix II.

Titan's hydrocarbon liquids are comprised of low molecular weight hydrocarbons, therefore, hydrocarbons that are gases at room temperature were included in this study. The hydrocarbon gases were condensed into a glass vessel surrounded by a coolant using a gas regulator to control the pressure. The coolants used were dry ice (-78 °C) for condensing butane and solid acetone (premixed acetone with liquid nitrogen to obtain a -95 °C coolant) for condensing propane. Once the liquid had been accumulated, it was decanted into vials containing the dry amphiphilic mixtures; which themselves were in a cooling bath containing the same coolant.

3.3.3.1 Sonication

Sonication is a method that can produce unilamellar vesicles from systems containing multilamellar structures. Lower ultrasonic frequency generates bigger cavitation bubbles and higher amplitudes have a higher probability of cavitation generation.

We utilised three devices to produce different intensities of sonication depending on the sample:

Increase in sonication Strength ↓

Weak water bath: Ultrawave U50 ultrasonic bath, ultrasonic frequency operating frequency 44 kHz, ultrasonic power 35 W.

Strong water bath: Fisher FB15050 ultrasonic bath, ultrasonic frequency 37 kHz, ultrasonic power 80 W.

Probe sonicator: MSE Soniprep 150 probe sonicator, with an exponential taper probe, ultrasonic frequency 23kHz, transformation ratio 7:1 multiplied by amplitude microns gives actual probe movement.

The samples containing butane or propane were exclusively sonicated using the weak-water bath containing coolants in order to subdue evaporation. The type and duration of sonication used for each sample is detailed in Appendix II.

3.3.4 Preparation of low-temperature baths for non-ambient phase behaviour

Observing phase behaviour at low temperatures required the use of a variety of cooling baths ranging from ~20 °C to ~-130 °C using as shown in Table 6. A J-KEM digital temperature monitor that was able to operate at low temperatures (250 °C to -200 °C) was used which permitted us to sustain the desired temperatures throughout the duration of the experiments.

	Coolants and approximate temperatures in °C												
	None – Room Temperature	Ice + Water	Ice + Water	Ice + Water	Ice	Potassium Chloride (KCl) + Ice	Sodium chloride (NaCl) + Ice	Magnesium ($MgCl_2$) chloride + Ice	Acetonitrile (CH_3CN) + Dry Ice (CO_2)	Calcium chloride hexahydrate ($CaCl_2$) + Ice	Dry Ice (CO_2)	Solid Acetone ($(CH_3)_2CO$ (Acetone + Liquid Nitrogen)	Solid Pentane (Pentane + Liquid Nitrogen)
Cyclohexane	20	15	10										
Octane	20	15	10	5	0	-10	-20	-30	-42				
Heptane	20	15	10	5	0	-10	-20	-30	-42	-55	-78		
Hexane	20	15	10	5	0	-10	-20	-30	-42	-55	-78		
Pentane	20	15	10	5	0	-10	-20	-30	-42	-55	-78	-95	
Butane							-20	-30	-42	-55	-78	-95	
Propane										-55	-78	-95	-131

Table 6: The range of cooling baths and temperatures used in these studies.

3.4 Sample characterisation methods

Amphiphiles in solution can produce different self assembled structures; as detailed in Chapter 2. In order to determine the structures formed in our samples we needed to use an array of analytical tools according to the type of system present.

The first step to analysing any system is to observe its macroscopic phase behaviour. The ensuing analytical methods chosen for studying the microscopic phase behaviour were influenced by the characteristics of the phase behaviour. These analyses included confocal microscopy, laser scanning fluorescence confocal microscopy, dynamic light scattering (DLS), transmission electron microscopy (TEM), small angle neutron scattering (SANS) and small angle X-ray scattering (SAXS) techniques.

3.4.1 Macroscopic phase behaviour observations

Macroscopic phase behaviour observations guide us in determining the best approach for further analyses to study any self assembled structures in the system; as demonstrated in Table 7. A full list of terms used in describing the phase behaviour and photographic examples can be found in Appendix III.

One of the techniques to determine the presence of self assembled particles in liquid media is to use light scattering. The Tyndall effect is the scattering of white light by particles which produces opalescence and may have a distinct blue or yellow hue (if viewed perpendicular or opposite, respectively, from the direction of the incidence beam) due to the shorter blue light being more refracted. This opalescent feature is produced by colloidal particles that have dimensions close to that of the wavelength of visible light (~40-900 nm) and at a significant concentrations level that enables the generation of observable effects. Rayleigh scattering by particles <40 nm in size can also cause opalescence; however, this effect is only visible with large volumes. Therefore, any opalescence in these samples which were limited to a maximum of 4 ml was attributed to Tyndall scattering. As shown in Table 8 the macroscopic features of the system were used to determine which of the system types – solutions, colloidal dispersions and suspensions, are present and hence the expected particle size range. A variety of micellar structures can form colloidal particles can produce Tyndall scattering, such as unilamellar lipid vesicles or microemulsions, see Figure 10.

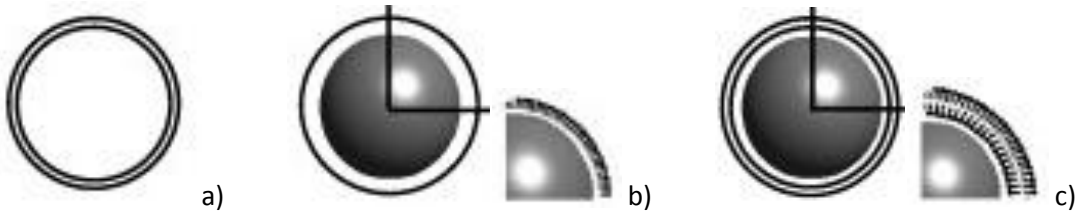

Figure 10: Types of typical colloidal, micellar particles. a) Bilayer vesicle. b) Microemulsion with monolayer (swollen spherical micelle). c) Microemulsion with bilayers. (Salabat *et al.* 2008)

This study works with single solvent systems, so microemulsions, and emulsions (swollen micelles or vesicles surrounding a liquid nucleus of different composition to the medium) will not form, and therefore, are not considered in these analyses. Some colloidal microemulsions, such as milk, can be cloudy but as microemulsions cannot form in our systems cloudy or opaque phase behaviour will be considered a suspension (with large suspended particles) unless rapid precipitation does not occur. This leaves reverse vesicles or compound micelles as the prime suspects for producing Tyndall scattering in our samples.

The intensity of Tyndall scattering increases with higher degrees of dispersion, which is a quantity that varies reciprocally with particle size. Therefore, when analysing the phase behaviour of our samples we will assume those with the greatest intensities of opalescence have the least polydispersity of particles at small size ranges.

The presence of reverse vesicles has been correlated with Tyndall scattering by numerous authors (e.g. Li *et al.* 2008a; Li *et al.* 2010a; Li & Hao 2007b; Tung *et al.* 2008). Some of these have implied the presence or absence of reverse vesicles by Tyndall scattering alone (e.g. Li *et al.* 2008a; Li & Hao 2007a). However, as shown by works like that of Fukuoka *et al.* (2012) large multilamellar reverse vesicles may form a cloudy suspension that quickly precipitate, rather than producing Tyndall scattering. The larger the aggregate in solution the cloudier the solution will appear upon shaken (Pershan 1982). Therefore, although Tyndall scattering is a good indicator of reverse vesicles other turbid phases will be checked for large reverse vesicles with microscopy.

For situations in which systems lack obvious visual indicators of self assembled structures in solution the light scattering of a monochromatic laser was used to clarify their presence. These studies used scatter from a Kaiser red (625-680 nm) laser pointer (<1 mW) in conjunction with the phase behaviour to establish provisional particle characteristics as shown in Table 7. Short laser wavelengths (40-60 nm) can detect monomers in a solution (Ostwald 1917), however, the 625-680 nm range of the laser used in these studies is limited to revealing self assembled structures in solution. Therefore, any laser refraction was taken as evidence of solvated or suspended self assembled structures. An increase in optical heterogeneity increases beam

divergence (Duarte & James 2003), therefore, a widely scattered beam implied a large polydispersity of particles in solution.

Precipitants are expected to form quickly in suspension systems; some of these may consist of settled large uni- or multi- lamellar reverse vesicles. Although, a characteristic of colloidal dispersions is the lack of rapid precipitation, precipitants (alternatively named ‘flocs’) may form over a long period of time due to flocculation in metastable colloidal dispersions. Flocculation is the process of contact adhesion between colloidal particles that create clusters sufficient in size to enable gravitational forces to overcome the Brownian forces that had kept the particles suspended. In our systems, we may expect unilamellar vesicles to cluster due to flocculation over time and form a phase separated system.

It is known that high volume fractions of metastable colloidal dispersions form gels with viscoelastic properties. Although our samples are kept dilute, there may be temporal phase changes as the gravity restricted floc enriched phase could promote the formation of a viscoelastic gel-like phase over time.

Observation	Implication	Laser reaction	Potential structures in our samples	Possible follow up analyses
Transparent	The amphiphiles may have adsorbed onto the glass/solvent or air/solvent interfaces or precipitated out of solution. Any solvated amphiphiles are either isolated monomers or very small (~<40 nm scale) aggregates.	None	• No solutes. • Homogeneous solution of monomers.	None
		Laser refraction	• Reverse spherical micelles. • Short reverse cylindrical micelles. • Small discs (bilayers sheets).	DLS, TEM, SAXS, SANS.
Opaque or cloudy (white)	Turbid solutions where the cloud point has been reached – suspensions of large aggregates >~1 µm. Opaque solutions will have larger aggregates or a higher concentration compared to cloudy solutions.	Laser reflection or diffraction (if over ~ 20 µm)	• Giant or clustered unilamellar reverse vesicles. • Large multilamellar reverse vesicles. • Long reverse cylindrical micelles. • Large compound micelles. • Ribbons or discs (bilayers sheets).	Microscopy
Opalescent	Slight Tyndall scattering effect from a colloidal dispersion (has a greater dilution or polydispersity than 'blue', see below), approximately 40 nm to 1 µm scale.	Laser refraction	Low concentration (compared to 'blue' systems) of: • Unilamellar reverse vesicles. • Limited multilamellar reverse vesicles. • Compound reverse micelles.	Microscopy, DLS, TEM, SANS, SAXS.
		Wide beam divergence	Highly polydisperse: • Unilamellar reverse vesicles. • Limited multilamellar reverse vesicles. • Compound reverse micelles.	
Blue	Strong Tyndall scattering effect from a colloidal dispersion (when viewed perpendicular to light direction). Colloidal particles are approximately 40 nm to 1 µm scale but strong	Strong laser refraction	Low polydispersity of: • Unilamellar reverse vesicles. • Limited multilamellar reverse vesicles. • Compound reverse	DLS, TEM, SANS, SAXS.

	Tyndall scattering implies a homogeneous system of small particles <~500 nm.		micelles.	
Non-viscous precipitant (liquid phase separation)	Precipitant that is easily re-dispersed into solution by shaking implying the absence of a strong network of bonds.	-	Structures forming precipitant: • Large precipitated vesicles. • Clustering of smaller aggregates without bonded coagulation. • Loosely bonded bilayers.	Microscopy.
Gel precipitant	Viscous or viscoelastic precipitant that does not fall under its own gravity implying a network of interlinking bonds between aggregates.	-	Coagulation of precipitated particles: • Network of worm-like structures with interlinking bonds. • Bicontinuous cubic phase (common with coagulated large uni- or multi- lamellar vesicles).	Microscopy.

Table 7: Summary of macroscopic phase behaviour observations, their implications and possible methods for follow up analyses.

Term	Typical particle sizes	Typical phase behaviour	Characteristics of precipitant
Solution	Size of a single molecule, approximately <1 nm.	Transparent, no laser reflection/refraction and no precipitation.	No precipitation.
Colloidal dispersion	Colloidal particles range from approximately 1 nm to 1 µm.	Either transparent or Tyndall scattering, with a strong laser refraction and no rapid precipitation.	Flocculation of colloidal particles can create large aggregates that settle to become precipitants over a long period of time.
Suspension	Suspended particles are approximately >1 µm.	Ephemeral cloudy/opaque phase (heterogeneous), with laser reflection / diffraction and rapid precipitation.	Isolated particles that are too large to fully dissolve rapidly settle due to gravity upon standing, forming a precipitant.

Table 8: Summary of terms used in analysing macroscopic phase behaviour (Raymond 2008).

3.4.2 Imaging studies

3.4.2.1 Analyses with confocal microscopy

These studies used an inverted Zeiss 510 META Axiovert confocal laser scanning microscope using 10x, 20x, 40x, and 63x objectives. 20 µl of the samples of interest were transferred to glass bottom wells or microscopy slides with concave depressions.

Cross-polarised microscopy was used to find multilamellar reverse vesicles by detecting Maltese crosses; optical illusions formed from multiple concentric layers next to one another (Fukuoka *et al.* 2012) (see Figure 11). However, these can also form for unilamellar vesicles (Harris *et al.* 2002).

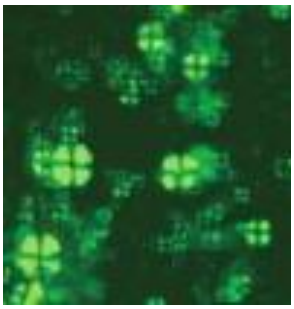

Figure 11: Example of Maltese crosses taken from Li *et al.* (2008b); polarised micrograph of reverse vesicles in toluene (~200µm wide image).

When using microscopy to verify reverse vesicle presence we need to be aware that aggregates can change by the temperature increase during examination by microscopy. This increase in temperature can quicken coagulation or dissolve structures, for example, TTAL/LA reverse vesicles have been reported to vanish due to the use of high magnifications (Li *et al.* 2008b). Therefore, images were taken as quickly as possible and any alterations in structures from prolonged exposure or during use of high magnifications were noted.

3.4.2.2 Analyses with confocal laser scanning fluorescence microscopy

To analyze fluorescence an inverted Zeiss 510 META Axiovert confocal laser scanning fluorescence microscope was used with a He/Ne laser at a 543 nm wavelength.

For samples that were to be analysed with fluorescence microscopy a $2x10^{-5}$ M concentration of Rhodamine b was added to the system. This florescence method was based on the fluorescent observations of reverse vesicles made of tetradecyltrimethylammonium laurate and lauric acid (TTAL and LA respectively) by Li *et al.* (2010a). Fluorescence images were captured using an incidence excitation wavelength of 543 nm which would cause excitation of the Rhodamine B dye and produce a red light.

Fluorescence confocal microscopy can distinguish between some reverse vesicle structures, such as onion, multilamellar and unilamellar reverse vesicles, as the fluorescent dyes attach to

the polar interiors of the reverse vesicles and form a clear contrast between the hydrocarbon solvent and the bilayers (Li *et al.* 2010a).

Raw images were manipulated with Zen lite 2011 software.

3.4.2.3 Analyses with Transmission Electron Microscopy (TEM)

A JEOL 100 keV TEM system was used to produce images on film for the first analysis (RVe1a samples). All other TEM images were taken with a Jeol 1010 TEM system (resolution 0.2nm) as this could take digital images. These images were taken with the standard bright field illumination; sample contrast comes from absorbance of light in the sample so thicker regions (or regions with a higher atomic number) will appear dark. Therefore, for the digital images, the dark areas were considered to represent the regions of condensed (relatively high molecular weight) phospholipids. However, the contrast in the film images was reversed and therefore in these images the bright regions were considered to signify self-assembled phospholipids.

The TEM samples were prepared by applying a 1-2 µl drop onto a carbon-coated copper grid, which was then air-dried before imaging was conducted. Images were manipulated with ImageJ software.

Characterising reverse vesicles with this method is challenging because vesicles are altered when the solvent is evaporated onto the TEM grid. They can aggregate into clusters, bilayer sheets or combine to form larger vesicles than are found by *in situ* analyses (Tung *et al.* 2008). In addition, low molecular weight hydrocarbons were found to dissolve the carbon film of the TEM grids and dried reverse vesicles may be destroyed by the electron beam during analysis.

3.4.3 Scattering techniques

Analysis of samples using scattering techniques provides information about the size, shape, and orientation of components within the sample by measuring the angle and intensity of scattered radiation. The wavelength of the incidence radiation affects what the scattered data tells us about the samples. The three types of scattering methods we used in this study were dynamic light scattering (DLS), small angle neutron scattering (SANS) and small angle X-ray scattering (SAXS). Small angle scattering deals with large particles, usually between the order of 10 and 1000 Å (1 and 100 nm), and can determine the shape and sizes of the aggregates in the system (Dianoux & Lander 2003).

Different radiation types pose limits on the information gathered from samples; see Table 9. X-ray scattering cannot penetrate very thick samples or metal containers. Neutron scattering, however, relies on a substantial difference in scatter length densities between the solvent and components of interest without which no structural data can be received. Small angle scattering is a subgroup which focuses on the study of relatively large components i.e. self assembled

structures potentially up to several tens of thousands of angstroms (a few micrometers) and are similar in their detection methods. Dynamic light scattering correlates variations in scattered light intensity to calculate the Brownian motion of suspended particles, and thereby, deduce the size distribution of particles in solution with the assumption of a spherical shape.

	SANS	SAXS	SALS
Scattered by	Nuclei	Electrons	Electrons
Typical wavelength (nm)	0.15-2.5	0.15	400-700
Typical length scales probed (nm)	0.5-1000	0.1-2500	*250-25000
Typical sample volumes (cm^3)	0.05-3.5	0.0001-0.5	0.05-5
Opaque samples	Yes	Yes	No
Metallic sample containers	Yes	No	No
Radiation damage to sample	Very unlikely	Very likely	Negligible

Table 9: Characteristics of radiation used in small-angle scattering techniques; altered from King (1999).

Both SANS and SAXS produce scatter intensity data that record the intensity of the scattered radiation at particular angles from the incident radiation (similar to static light scattering methods), with either a 1D or a 2D detector**;** see Figure 12.

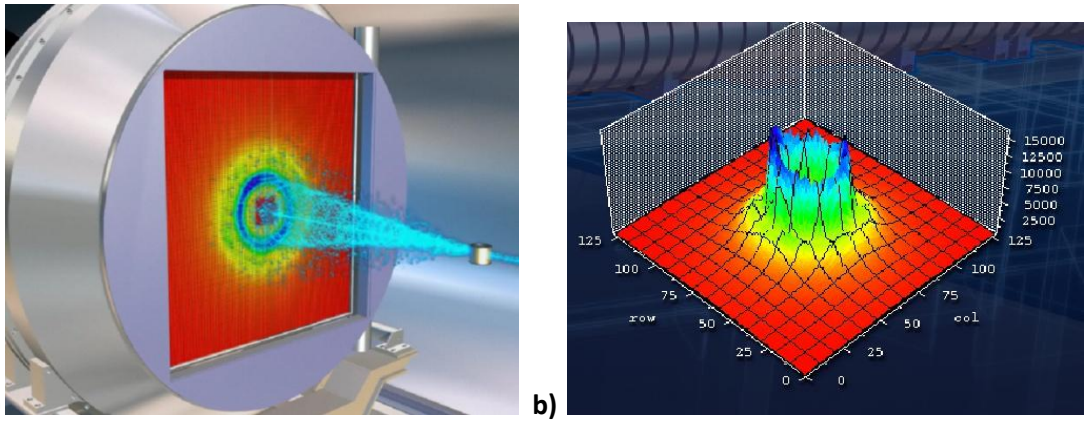

Figure 12: **a)** Illustration of an example for scatter intensity data from small angle scattering using a 2D detector, with blue indicating the highest intensity and red the lowest. Image credit: ILL; **b)** An example of scatter intensity data in graph form with topography related to intensity. Image credit: ILL.

3.4.3.1 Dynamic Light Scattering (DLS)

We used a Malvern Zetasizer Nano S instrument which has particle detection limits of 0.3 nm to 10 µm using a backscatter detector angle of 173 ° and a standard red laser (wavelength 633 nm); see Figure 13. The cuvette that was used to contain the samples being analyzed was quartz with a square aperture. The measurement position was 4.65 mm in order to measure the centre of the specimen and the temperature of the measurements were set to 25 °C.

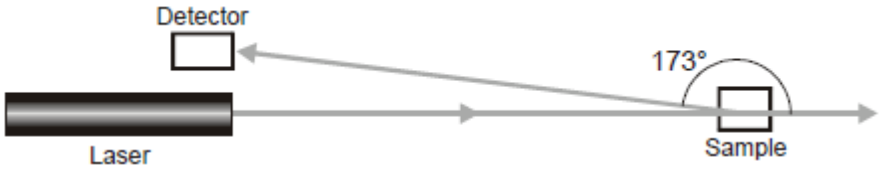

Figure 13: Illustration of the Malvern Zetasizer Nano S DLS detection system.

The measureable Brownian motion of particles in a system is a result of the random fluctuations in the number and direction of collisions of the liquid particles hitting the solute due to thermal agitation. This can be thought of as a diffusive movement, in which Einstein's formula $D = k_BT/\xi$ can be applied – with 'ξ' representing the drag coefficient on the particle. Stokes law shows us that for a sphere with a radius of 'a' within a liquid possessing a viscosity of 'η' the drag coefficient can be found by the equation $\xi = 6\pi\eta a$. By combining the Einstein and Stokes formulae we get the Stokes-Einstein equation $D_{se} = k_BT/6\pi\eta a$ that can accurately relate the diffusive movement, as measured by light scattering techniques, to the radius of spherical aggregates in a solution. This means the radius of particles in our solutions can be calculated by the formula $a = (k_BT/ D_{se})/6\pi\eta$**.** Which requires the diffusive movement (D_{se}), as measured by light scattering, the known viscosity of the liquid (η), temperature (T) and Boltzmann's constant (k_B) ($1.38X10^{-23}JK^{-1}$ = the energy of an individual particle at a certain temperature).

To obtain the diffusive movement (D_{se}) the specimen is illuminated with a laser and the intensity fluctuations in the resulting scattered light is analysed. Although large particles scatter more light – scatter intensity is proportional to the sixth power of its diameter - they have a lower diffuse movement (as can be seen from the Stokes-Einstein equation) and so the incident scatter intensity fluctuations will be low.

There is a specific intensity range within which the detector can produce valid results; therefore, an attenuator is used to reduce the intensity of the laser. This attenuator reduces the laser intensity impact on the sample and consequently reduces the scatter intensity reaching the detector. The attenuator index can be between 0 = full laser block and 11 = all laser transmitted; see Table 10. The level of the attenuator is automatically determined at the beginning of each run.

Attenuator Index	Transmission (% Nominal)	Attenuator Index	Transmission (% Nominal)
0	0	6	0.3
1	0.0003	7	1
2	0.003	8	3
3	0.01	9	10
4	0.03	10	30
5	0.1	11	100

Table 10: Shows the relationship between the attenuator number and the percentage of laser transmission that is passed through the attenuator.

The instrument uses a digital correlator that measures the scatter intensity at the intercept time (t) = 0 and compares this with other scatter intensities over time. We maintained 70 seconds for the total run of each data set, therefore, our correlations were between t = 0 and t = 70 seconds. The larger the particles the longer it takes for the correlation curve to reach the required value of 0 to obtain valid results; see Figure 14. This measured correlation function is then compared to the calculated decay rates for a number of size classes to produce a size distribution graph presenting intensity (%) against diameter (nm).

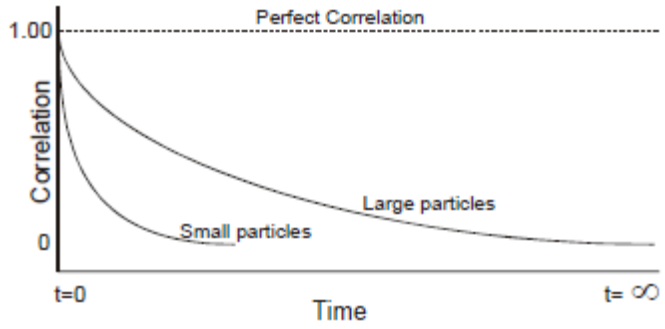

Figure 14: Graph showing two example correlation curves for a small and large particle.

The intensity distribution can be converted using Mie theory to volume distribution, and then, to number distribution; see Figure 15. However, small errors in the correlation function can result in large errors in the number distribution, therefore, we analysed the data using both the intensity and number distributions.

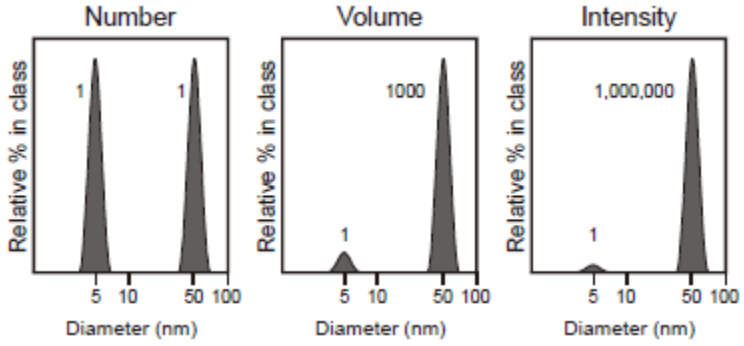

Figure 15: Intensity, volume, and number distribution graphs representing a polydisperse system containing 5 nm and 50 nm particles in equal numbers.

To obtain a zeta-average size a cumulant analysis is completed. A three termed polynomial is fit to the log of the correlation function ($G1$): $\mathrm{Ln}[G1] = a + bt + ct^2$. The zeta-average diffusion coefficient (b) is converted to size using the solvents viscosity and instrumental constants. The polydispersity is derived from term 'c': $PD = 2c/b^2$ and therefore the zeta-averages were only taken as valid for monodisperse systems.

The difficulty with using light scattering techniques for analysing soft matter assemblages, such as reverse vesicle, is that they can be polydisperse, cluster or on the scale of x10 micrometers. This can place reverse solutions out of the detection range of most light scattering methods.

3.4.3.2 Small Angle X-ray Scattering (SAXS)

SAXS is often used when studying biological systems because the sizes of these structures are larger than an angstrom scale used to study many synthetic systems. This technique has already been used to probe reversed bilayer structure and phase by Kunieda *et al.*(1999) and Lee *et al.* (2013). The main issue with X-ray scattering methods is the destructive nature of this highly energized radiation which can destroy specimens during analysis.

3.4.3.2.1 I22 instrument at Diamond

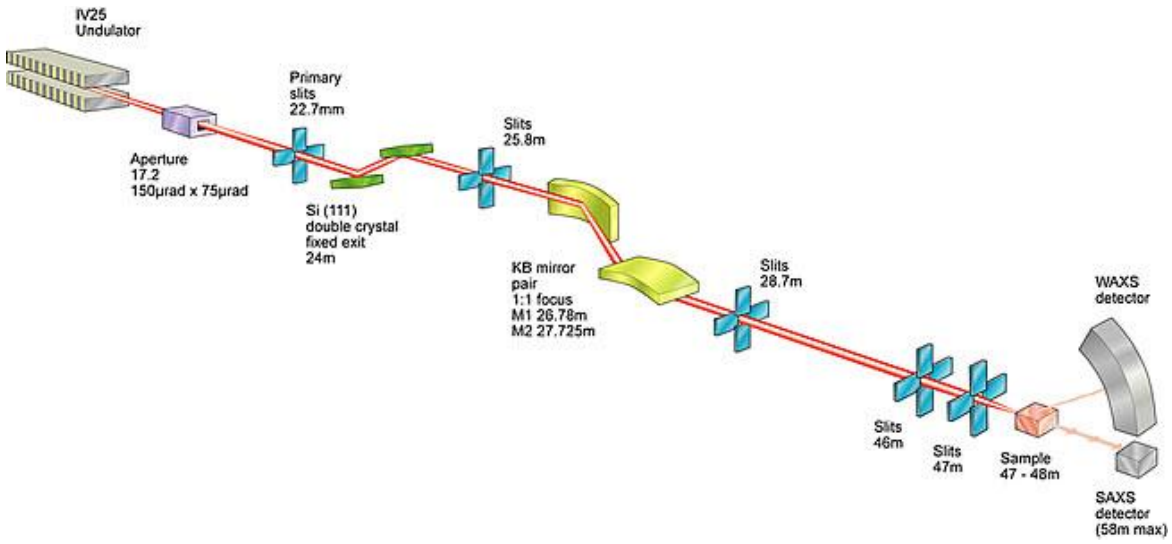

Figure 16: Diagram of I22 apparatus. Image credit: Diamond.

At the I22 beamline at Diamond X-rays with an energy range of 3.7-20 keV are emitted from an in-vacuum undulator source. This radiation is then focused and wavelengths selected using slits and mirrors; see Figure 16.

3.4.3.2.2 SAXS experimental details

The SAXS experiments followed the procedures put forward in the proposal for beamtime; see Appendix V. Samples were then transferred into the 1 mm borosilicate capillaries, sealed with PTFE tape to help prevent evaporation and labelled. These samples were then transferred to the sample ladder and then to the beamline; see Figure 17a. The butane and propane samples were cooled using dry ice/solid pentane cooling baths in order to prevent evaporation during concentration analysis and transferring to the borosilicate capillaries and beamline.

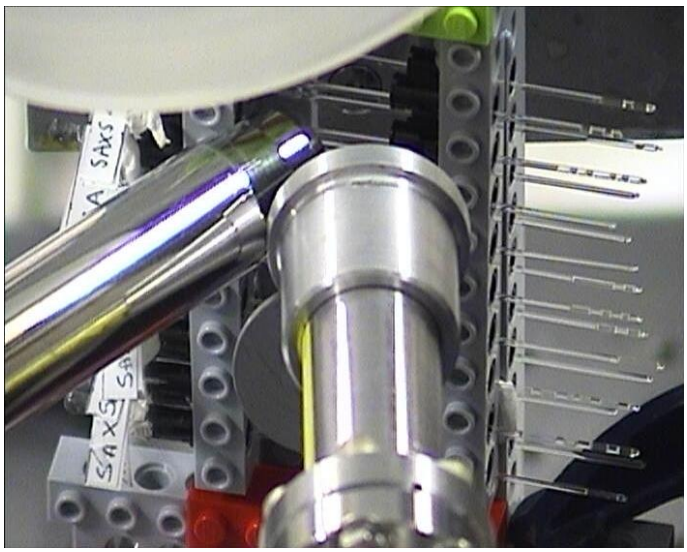

a

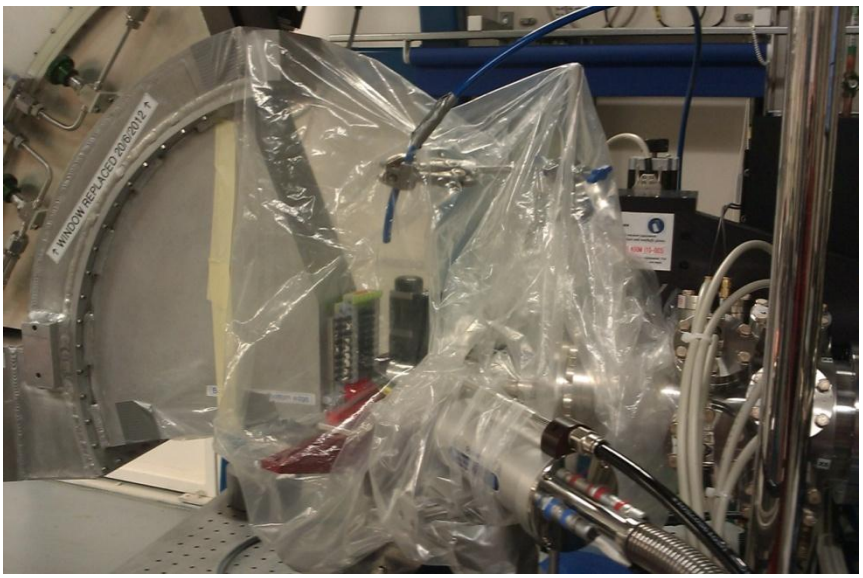

b

Figure 17: Photographs of the SAXS experiment set up. (a) Shows the capillary ladder with the cryojet nozzle (left) and the beamline (centre) aimed at one of the samples. (b) Shows the secured plastic covering enclosing the sample area with the desiccating helium flowing from the black tube (top centre), on the left is the beginning of the detector.

These studies used a 12.4 keV energy beamline and repeat samples were utilised due to the potential radiation damage to samples during analysis. Sets of pure solvent samples were analysed to use in the data reduction process. For the cryogenic studies, the temperatures were reduced using a nitrogen-jet and the samples were allowed to acclimatize for about 10 minutes each. In order to try to prevent ice crystals from forming on the capillaries during the low temperature analyses the sample area was enclosed with a secured plastic covering and a flow of helium was used to keep the sample area desiccated; see Figure 17b.

3.4.3.2.3 SAXS data treatment

A SAXS profile needs to merge data collected from different exposure sets for the same system. The combination of different exposures are utilised in order to measure ultra-low and moderate angles of scattering and thereby produce a single combined SAXS profile. By comparing SAXS

profiles taken at different times, the radiation damage or aggregation of particles over time can also be assessed. The same number of exposure times was replicated for the pure solvent and amphiphilic-hydrocarbon systems in order to produce valid results from the contrast variation method. The scatter intensity data we collected were calibrated using dry collagen.

3.4.3.2.4 SAXS data reduction

To obtain a SAXS profile for the particle the scatter intensity data for the pure solvents were removed from the scatter intensity data of the amphiphilic-hydrocarbon systems for each temperature that was investigated. The data treatment and reduction were performed using Dawn software which was supplied by Diamond.

3.4.3.3 Small Angle Neutron Scattering (SANS)

All neutron scattering requires a focused beam of neutrons to be fired at the sample and the scatter intensity was measured. Nuclear fission or a proton bombarded metal target (spallation utilising particle accelerators), are sources for continual or pulsed beam of neutrons, respectively. SANS utilises long-wavelength neutrons, termed slow or cold neutrons, which have been passed through a moderator e.g. liquid hydrogen. When using a continual beam at such establishments as the Institut Laue-Langevin (ILL) in Grenoble (France) a limited range of wavelengths of the slow neutrons are selected by a bandpass filter. A pulsed beam such as that found at ISIS in Harwell (UK) requires time-of-flight techniques to be used in conjunction with a broad range of slow neutron wavelengths.

The scattering angles and the distance of the sample to the detector can change in order to study systems at particular size ranges, for example, if the system has large particles (on the order of 1000 Å) then large scattering angles and greater distance between the sample and detector would be required.

Neutrons are electrically neutral and therefore can often penetrate samples further than other scattering techniques such as dynamic light scattering. Despite this, the media or solute chemistries need to be deuterated in order to inject heterogeneities between the weight of the media and aggregate nuclei so that scattering information from the aggregates alone can be deduced.

3.4.3.3.1 D11 instrument at the ILL

SANS studies used the D11 beamline at the ILL (Figure 18). The ILL uses nuclear fission of 235-Uranium to produce a continual beam of neutrons. Like our experiments, most of the research done on the D11 SANS instrument studies soft condensed matter systems. The monochromator (ASTRIUM, helical slot velocity selector) takes the polychromatic neutron beam and filters out all but the average wavelength (±9 % about a mean wavelength determined

by the rotation speed of the drum) chosen for study. The beam is then lined up with glass guides (collimators) to the divergence levels required for the experiment.

The beam then passes through the cryostat in which resides the sample chamber. After hitting the sample the scattered neutrons pass through a vacuum to a 3He detector; this distance, which can be between 1.2 and 39 metres, corresponds to a possible momentum transfer range of between $3x10^{-4}$ to 1 $Å^{-1}$. At the detector, the gas undergoes the nuclear reaction $^{1}n_0 + {}^{3}He_2 \rightarrow {}^{1}H_1 + {}^{3}H_1 + 765keV$. These newly formed charged particles liberate electrons which are detected by diodes and translated into the crucial scatter intensity graph (the scattered neutron intensity as a function of the scattering angle). Analyses of the scatter intensity data deliver information about the sample in question.

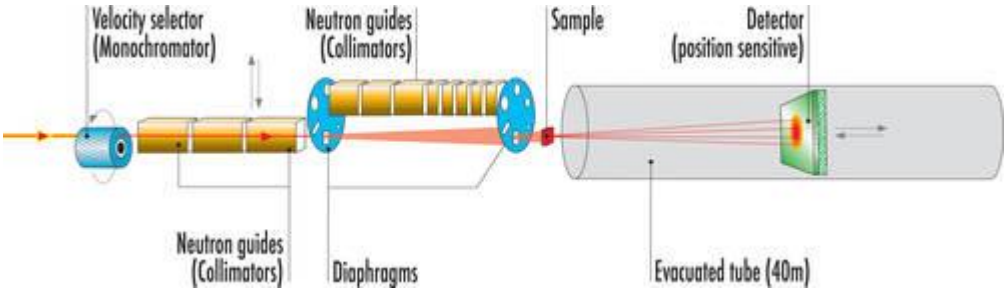

Figure 18: D11 apparatus diagram; the sample chambers in these experiments were also enclosed within a cryostat which could maintain the required temperatures. Image credit: Institut Laue-Langevin.

3.4.3.3.2 SANS experimental details

The SANS samples were prepared in the labs at UCL; as detailed in the previous 'Sample Preparation' section and Appendices I and II. These were transported to the ILL where they were transferred to a Quartz SUPRASIL Hellma cuvette with a 1 mm light path (110-QS, 350 µl volume).

The SANS experiments followed the procedures put forward in the proposal for beamtime; see Appendix VI. 24 hours of beamtime was awarded on the D11 which limited the range of samples and temperatures that could be analyzed in comparison to the proposed experiment.

D11 configurations used:

- Wavelength = 6Å
- Resolution in energy = 10%
- Range of momentum transfer = $8x10^{-4}$ $Å^{-1}$ to 0.5 $Å^{-1}$
- Resolution in moment transfer = 10%

- Environmental equipment = Orange Ø50 cryostat with sapphire windows, a temperature range of 300 K to 1.5 K, large sample top loading, isolated sample area with static exchange gas, and employs a Gifford-McMahon refrigeration cycle; see Figure 19.

- Pressure range: 1 atm

Figure 19: Photo of the Orange Ø50 cryostat used for temperature depression of the samples within the beamline.

Four detector distances were used to obtain the greatest range of scattering vectors – 1.2m, 4m, 8m, and 39m. This large range of scattering vectors can tell us more about the system being studied, rather than concentrating on either the very components (high Q) or the larger components (low Q) of the system. The duration used for accumulative scatter was: 39 m = 20 minutes, 8 m = 3 minutes, 4 m = 5 minutes, and 1.2 m = 5 minutes.

3.4.3.3.3 SANS data

The neutron scattering can be due to nuclear interaction or magnetic interaction due to unpaired electrons of free radicals. As there are no free radicals in our systems, the observed neutron scattering intensity data comes from nuclear interaction alone.

Two types of analysis are available for SANS:

- 'Static' scattering dependence on angle of the average scattered intensity – structural information.

- Absolute magnitude of the scattered intensity - mass or molecular weight of particles.

This research concentrated on static scattering as we want structural information of the aggregates in solution over a range of temperatures.

3.4.3.3.4 SANS data treatment

Treatment corrects the neutron intensity (I) detected to account for background, detector response and geometry effects. This will give us the differential cross-section ($d\sigma/d\Omega$) which may give us structural information about the sample.

The neutron intensity at the detector $I_j(\theta)$ is given by:

$$I_j(\theta) = \int_o^d \Phi_j \Omega_j E_j \, e^{-\mu x} A\rho e^{-\mu(d-x)/\cos\theta} \left\{ \frac{d\sigma_i}{d\Omega} + \frac{d\sigma_c}{d\Omega} \right\} dx$$

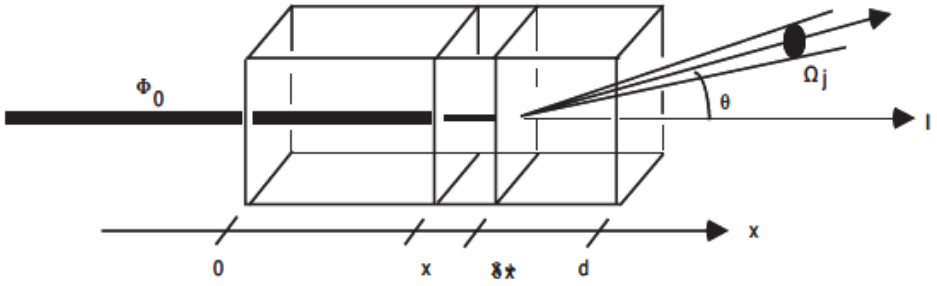

I	Intensity
Q	Scatter vector
Φ_0	Incident flux
A	Area of sample
Ω_j	Solid angle subtended by detector cell ($_j$)
E_j	Efficiency of detector cell ($_j$)
p	Number density of sample
μ	Linear attenuation coefficient
d	Distance to detector
$d\sigma_c/d\Omega$	Coherent differential cross section
$d\sigma_i/d\Omega$	Incoherent differential cross section
T	($e^{-\mu d}$) Sample transmission
N	(Apd) Total number of scattering centres

Although the measured intensity includes information from neutrons that have been scattered more than once this equation ignores this and presumes that the principal scatter comes from the initial scatter. Due to the small angles used, we can take the cosine to equal 1. This gives us a simplified equation to generate neutron intensity data without the effects of interference:

$$I_j(\theta) = \Phi_0 \, \Omega_j \, E_j \, T \, N \left\{ \frac{d\sigma_i}{d\Omega} + \frac{d\sigma_c}{d\Omega} \right\}$$

3.4.3.3.5 SANS data reduction

Our systems presented strong scatter intensity; therefore, removal of scatter intensity from an empty Hellma container was used in the reduction of these results rather than the scatter intensity from the pure solvent.

3.4.3.3.6 SANS data normalisation and removal of erroneous data points

The four scatter intensity curves were spliced together by scaling to the 39 m scatter curve. Scaling was performed by scaling the 8 m data to the 39 m data, then the 4m data to the scaled 8 m data and finally the 1.2 m data to the scaled 4 m data. Then numerous data points from the high Q ends of the detector datasets were removed as they had large errors in contrast to the errors of the overlapping detector datasets. In addition, data higher than $0.3Å^{-1}$ in Q were removed as these points were erroneous for the detection limits of D11. An example of this procedure is presented in the next section.

3.4.3.3.6.1 Example of SANS normalisation and removal of erroneous data points

This example details the normalisation procedure for the d-heptane 3.5 Ro sample (SANS 2) at room temperature. After data treatment and reduction, the data had a scatter vector (Q) range of 0.00132459 $Å^{-1}$ to 0.399147 $Å^{-1}$ and the data swaths were slightly misaligned as is shown in Figure 20.

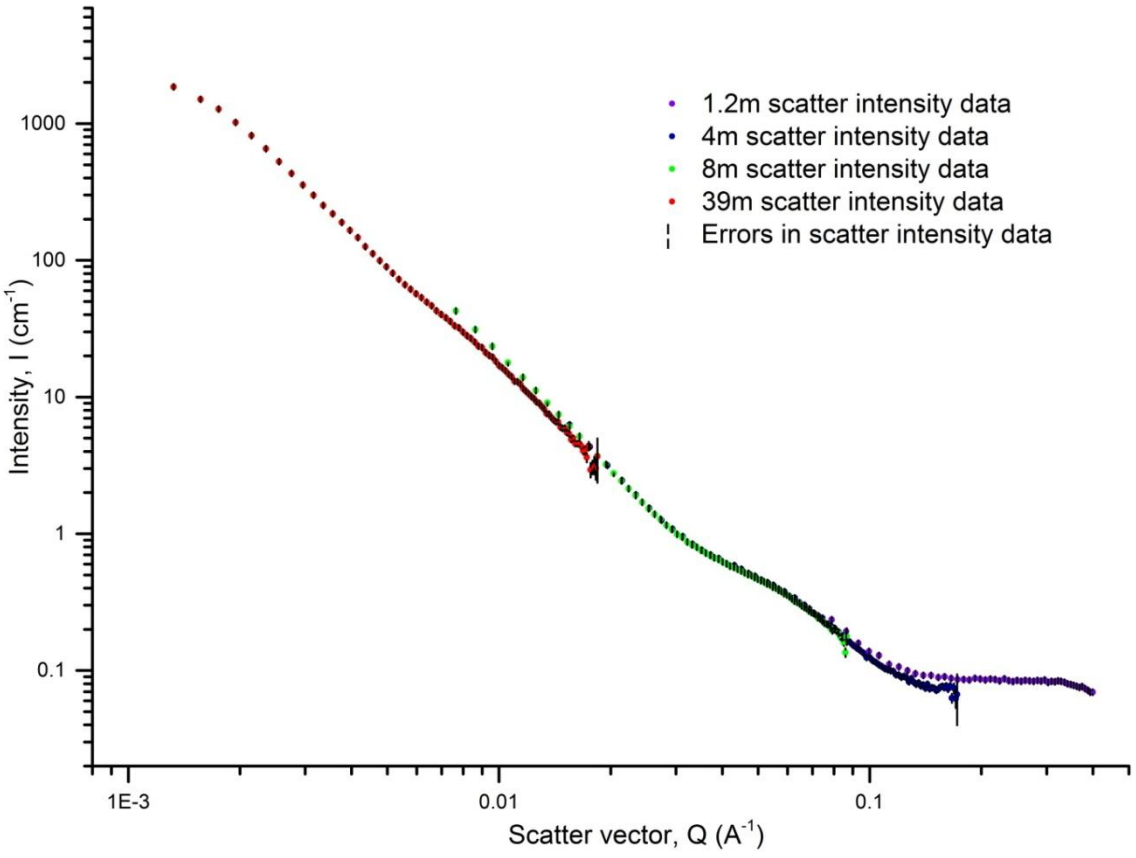

Figure 20: Treated and reduced scatter intensity data for the SANS 2 sample at 290 K.

The data points with the closest Q values between the curves were used for normalising between data swaths. The difference between the corresponding intensity values of these data points was used to determine the scaling factor; see Table 11.

Swaths	Q values of data points used for normalisation ($Å^{-1}$)	Corresponding I values of data points (cm^{-1})
39m	0.0126249	9.2289100
8m	0.0125643	11.1639000
	Scaling factor for 8m	**(**11.1639/9.22891) = **1.209666147**
Scaled 8m	0.0685318	0.226032613
4m	0.0686629	0.2822830
	Scaling factor for 4m	**(**0.282283/0.226032613) = **1.248859606**
Scaled 4m	0.1196830	0.074285532
1.2m	0.1198230	0.1065060
	Scaling factor for 1.2m	**(**0.1065060/0.074285532) = **1.433738137**

Table 11: Scaling values used to calibrate the four datasets of SANS 2 at 290 K.

The resulting range of Q after scaling and removal of high Q points was 0.00132459 $Å^{-1}$ to 0.30273 $Å^{-1}$ as shown in Figure 21.

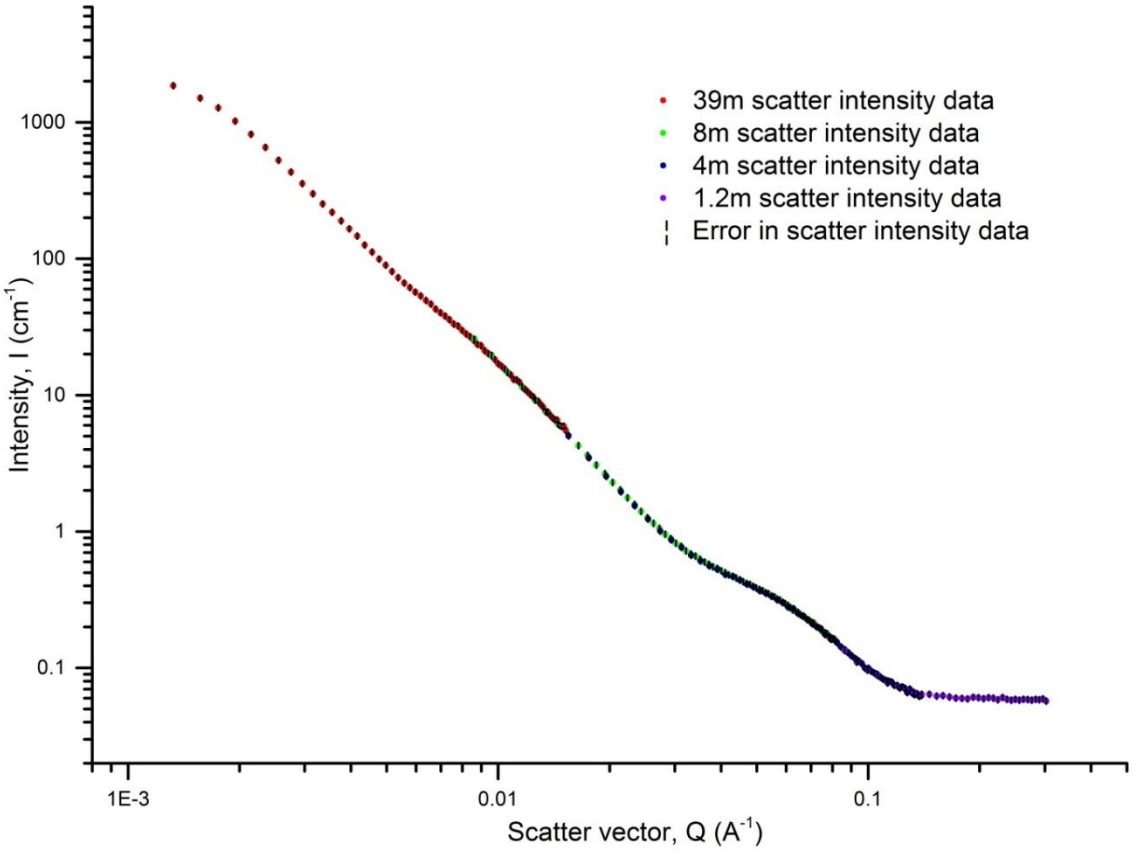

Figure 21: Processed scatter intensity curve for the SANS 2 sample at 290 K.

3.4.3.4 Structural information from SANS and SAXS scatter intensity data

Once the calibrated SAXS and SANS scatter intensity data has been collected this can be compared to the modelled scatter intensity data of different micellar structures in order to determine the shape and whether there are bilayers present.

The momentum transfer, I(q), of the collected data contains information on the types of structures in the system. To reveal the structural information contained within the momentum transfer model form factors, P(q), are fit to the data. For our dilute systems the scatterers are usually presumed to be non-interacting and therefore the structure factors S(q) = 1 and are ignored. However, some of these systems include structure factors within the form factor models, for example, the multilamellar vesicle models include a structure factor to account for lamellar stacking.

As the systems contain a mixture of short and long amphiphiles, the structures are considered polydisperse and a variety of potential shapes due to the prospect of an inhomogeneous distribution of lipids throughout the shell. An example of this would be a disc shaped micelle with the high-curvature edges being comprised of the short, PC4:0, amphiphiles and the long, PC18:2, amphiphiles comprising the planar disc region.

Once the Fourier transform (the mathematical relationship between the scatter intensity data and the object) is correlated to a shape, the dimensions of the aggregates, such as radius and bilayer thickness, can be calculated. For example, for a unilamellar reverse vesicle the radius (R) and bilayer thickness (t) can be equated using the form factor, P(q), equation of that model.

3.4.3.4.1 SASView form factor models

The model form factors, P(q), in SASView were used to analyse the small angle neutron and X-ray scatter intensity data. The types of form factor models and the related micellar structures are detailed in Table 12.

Form factor model	Description of structure
Vesicle	Unilamellar spherical vesicle.
CSEllipsoid	Unilamellar ellipsoidal vesicle.
CSCylinder	Unilamellar long cylinder or short disc (bicelle) vesicles.
CSDiscs	Stacked, unilamellar disc vesicles.
Multishell	Multilamellar vesicles with layers of solvent between bilayers.
CoreMultishell	Multilamellar vesicles without layers of solvent between bilayers.
LamellarPCrystal	Stacking of lamellar without a random distribution so can be used for large multilamellar vesicles.
Sphere	Spherical micelles or 'solid' spherical particles e.g. suspension of gel, compound micelle, or bicontinuous.
Ellipsoid	Ellipsoidal micelles.
Cylinder	Micelle long cylinders or short (bicelle) tactoids.
Lamellar	Disordered bilayer sheets.

Table 12: List of form factor models and their corresponding structures for these systems.

Although micellar systems do not demonstrate the distinct and numerous Bragg peaks of crystalline structures, the width and position of the intensity oscillations relate to the polydispersity and average size of unilamellar vesicles, respectively.

3.4.3.4.1.1 Key for form factor functions

Below is a list of terms used to express components of the form factor functions:

V_{Shell} = Volume of shell

V_1 = Volume of core

V_2 = Total volume of particle

R = Radius of particle

R_1 = Radius of core

R_2 = Radius of shell exterior

p_1 = Scatter length density of the core

p_2 = Scatter length density of the shell

p_{solv} = Scatter length density of the solvent

Δp = Contrast of scatter length densities: particle and solvent

Δp_t = Contrast of scatter length densities: total and solvent

Δp_c = Contrast of scatter length densities: core and solvent

t = Thickness of shell

J_1 = first order Bessel function = $(\sin x - x \cos x)/x^2$

α = Angle between the axis of the cylinder, disc or ellipsoid and the q-vector

L = Length of core

q = q vector = $\sqrt{q_x^2+q_y^2}$

D = Spacing between stacked lamellar or discs

σD = Gaussian standard deviation of the d-spacing

N or n = Number of discs or lamellar per unit volume

background = The incoherent scatter

3.4.3.4.1.2 Vesicle form factor model

This form factor assumes a system of dilute, spherical unilamellar vesicles and therefore does not contain a structure factor. The function is identical to a core-shell structure except the scattering is normalized by the volume of the shell.

$$P(q) = \text{scale factor} / V_{shell} [(3V_1(p_1-p_2)J_1(qR_1)/qR_1)+ (3V_2(p_1-p_{solv})J_1(qR_2)/qR_2)]^2 + \text{background}$$

3.4.3.4.1.3 CSEllipsoid form factor model

This form factor assumes a system of dilute, elliptical unilamellar vesicles (see Figure 22) and therefore does not contain a structure factor. To be used as a model for an elliptical vesicle the core SLD was set to the value of the SLD of the solvent. It is normalised by the particle volume.

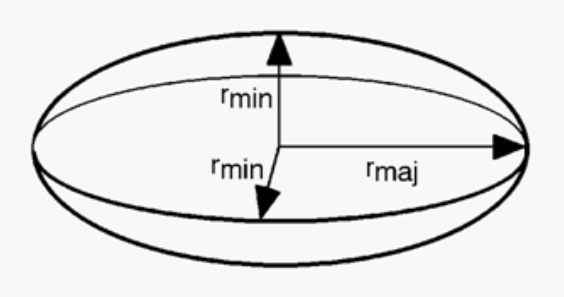

Figure 22: Illustration of elliptical unilamellar vesicle model indicating r_{min} and r_{maj}; illustration from SASView.

$$P(q) = \text{scale factor} * \int_0^1 V\Delta p*(3J_1/q[r_{maj}^2\alpha^2+r_{min}^2(1-\alpha^2)]^{1/2})^2 / V + \text{background}$$

$$V = 4\pi/3*r_{maj}*r_{min}2$$

3.4.3.4.1.4 CSCylinder form factor model

This form factor assumes a system of dilute, cylindrical unilamellar vesicles and therefore does not contain a structure factor. To be used as a model for a cylindrical vesicle the core SLD was set to the value of the SLD of the solvent. It is normalised by the shell volume.

$$P(q) = \text{scale factor} / V_{shell} [2(p_1-p_2)V_1\sin[qL\cos\alpha/2]/[qL\cos\alpha/2]*[J_1[qR_1\sin\alpha]/[qR_1\sin\alpha]]+2(p_1-p_{solv})V_{Shell}\sin[q(L+t)\cos\alpha/2]/[q(L+t)\cos\alpha/2]*(J_1[q(R_1+t)\sin\alpha]/[q(R_1+t)\sin\alpha])]^2 + \text{background}$$

3.4.3.4.1.5 CSDiscs model

This model presumes there are stacked discs (tactoids) in the system with a core/shell structure; see Figure 23. To be used as a model for a stacked vesicle discs the core SLD was set to the

value of the SLD of the solvent. It is normalised by the volume of the cylinder and the d-spacing is assumed to follow a Gaussian distribution.

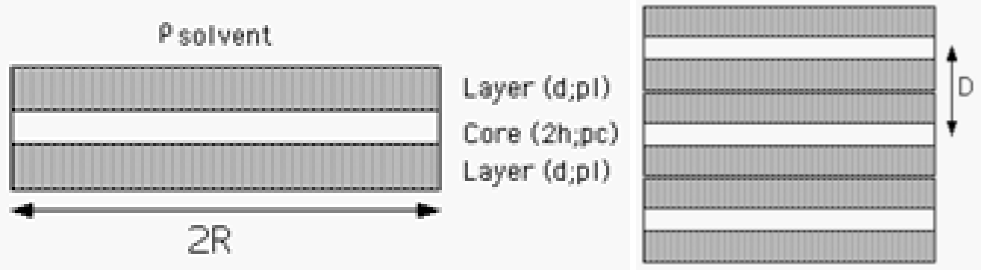

Figure 23: Illustration of stacked vesicular discs modelled with this form factor model; illustration from SASView.

For this model the inclusion of the Kratky and Porod (1949) structure factor S(q) is utilised to account for stacking (Figure 24 illustrates the angles used in this formulae):

$$S(q) = 1 + \frac{2}{n}\sum_{k=1}^{n}(n-k)\cos(kDq\cos\alpha)\exp\left[-k(q\cos\alpha)^2\sigma_D/2\right]$$

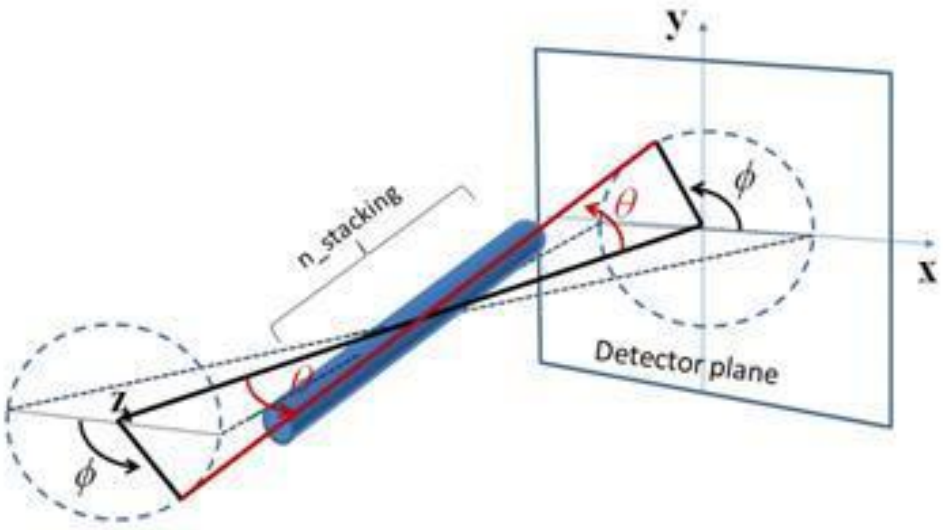

Figure 24: The angles for orientated stacked discs; illustration from SASView.

The scattering intensity, combining the form factor and structure factor, is shown below:

$$I(q) = N\int_0^{\pi/2}[\Delta\rho_t(V_2 f_t(q) - V_1 f_c(q)) + \Delta\rho_c V_1 f_c(q)]^2 S(q)\sin\alpha t\alpha + \text{background}$$

$$\left\langle f_t^2(q)\right\rangle_\alpha = \int_0^{\pi/2}\left[\left(\frac{\sin(q(d+h)\cos\alpha)}{q(d+h)\cos\alpha}\right)\left(\frac{2J_1(qR\sin\alpha)}{qR\sin\alpha}\right)\right]^2\sin\alpha d\alpha$$

$$\left\langle f_c^2(q)\right\rangle_\alpha = \int_0^{\pi/2}\left[\left(\frac{\sin(qh\cos\alpha)}{qh\cos\alpha}\right)\left(\frac{2J_1(qR\sin\alpha)}{qR\sin\alpha}\right)\right]^2\sin\alpha d\alpha$$

3.4.3.4.1.6 Multishell model

This model assumes a spherical particle with a core filled with solvent surrounded by an unlimited number of shells that are interleaved with solvent. The quantity of shells is constrained to integers of 2 or above. The form factor is based on a core/shell sphere form factor:

$$P(q) = \frac{scale}{V_s}\left[\frac{3V_c(\rho_c - \rho_s)j_1(qr_c)}{qr_c} + \frac{3V_s(\rho_s - \rho_{solv})j_1(qr_s)}{qr_s}\right]^2 + bkg$$

3.4.3.4.1.7 CoreMultishell model

This model assumes a spherical particle consisting of a core surrounded by up to four stacked shells (without interleaved solvent). To be used as a model for a multilamellar vesicle the core SLD was set to the value of the SLD of the solvent. The quantity of shells is constrained to integers of 2 or above. The form factor is based on a core/shell sphere form factor (see Multishell model).

3.4.3.4.1.8 LamellarPCrystal model

This model assumes there are stacks of lamellar without a random distribution. The model calculates the scattering from a stack of repeating lamellar structures that are infinite in lateral dimension and are treated as a paracrystal to account for the repeating spacing. Non-integer numbers of stacks were calculated as a linear combination of the lower and higher values. This model can be used for large multilamellar vesicles as their bilayers can be viewed as infinite lamellar structures when the overall structure is larger than the detection range of SANS.

The form factor of the bilayer is approximated as the cross section of an infinite, planar bilayer:

$$P(q)=[\sin(qt/2)/(qt/2)]^2$$

In this model the structure factor, $Z_N(q)$, describes the interference effects for aggregates consisting of more than one bilayer (Bergstrom *et al.* 1999):

$$Z_N(q) = \frac{1 - w^2}{1 + w^2 - 2w\cos(q\langle D\rangle)} + x_N S_N + (1 - x_N)S_{N+1}$$

$$S_N(q) = a_N/N[1 + w^2 - 2w\cos(q\langle D\rangle)]^2$$

$$a_N = 4w^2 - 2(w^3 + w)\cos(q\langle D\rangle) - 4w^{N+2}\cos(Nq\langle D\rangle) + 2w^{N+3}\cos[(N-1)q\langle D\rangle] + 2w^{N+1}\cos[(N+1)q\langle D\rangle]$$

The scattering intensity, combining the form factor and structure factor, is shown below:

$$I(q) = 2\pi(\Delta\rho)^2\Gamma_m(P(q)/q^2)Z_N(q)$$

3.4.3.4.1.9 Sphere form factor model

This model assumes a system of disperse, spherical particles with a uniform scattering length density and is normalised by the total particle volume.

$$P(q) = \text{scale factor} / V_2\,[(3V_2(\Delta\rho)[\sin(qR)-qR\cos(qR))/(qR)^3]^2 + \text{background}$$

3.4.3.4.1.10 Ellipsoid form factor model

This model assumes a system of disperse, elliptical particles with a uniform scattering length density and is normalised by the total particle volume.

$$P(q) = \text{scale factor} / V_2\,[(3V_2(\Delta\rho)[\sin(qR(R_a,R_b,\alpha))-qR\cos(qR(R_a,R_b,\alpha))]/[qR(R_a,R_b,\alpha)]^3]^2 + \text{background}$$

R_a = Radius along the rotation axis of the ellipsoid

R_b = Radius perpendicular to the rotation axis of the ellipsoid

3.4.3.4.1.11 Cylinder form factor model

This model assumes a system of disperse, cylindrical particles with a uniform scattering length density and is normalised by the total particle volume.

$$P(q) = \text{scale factor} / V_2\,[2V_2(\Delta\rho)\sin(qL\cos\alpha/2)/[(qL\cos\alpha/2)*[(J_1(qR\sin\alpha)/(qR\sin\alpha)]]^2 + \text{background}$$

3.4.3.4.1.12 Lamellar form factor model

This model assumes a lyotropic lamellar phase with random distribution; so describes random bilayer sheets in solution.

$$P(q) = (2\Delta\rho^2/q^2)(1-\cos(qt))$$

3.4.3.4.2 Other analyses used in SASView

3.4.3.4.2.1 Absolute Power Law model

The slope of I(Q), Q^{-m}, can identify the systems overall structure as it can indicate the dimensions of growth for a particle. So Q^{-1} corresponds to cylinders as these grow in only one dimension, Q^{-2} corresponds to lamellar and sheets as these grow in two dimensions, Q^{-3} corresponds to spherical objects as they grow in three dimensions, and Q^{-4} corresponds to interactions between particles or sharp interfaces. The position where the transition of the slope takes place (minimum value of Q on slope, Q_{min}): π/Q_{min}, estimates the dimensions that are being described.

Chapter 4: Macroscopic phase behaviour and microscopic imaging studies of self assembled structures in binary amphiphilic-hydrocarbon systems

4.1 Introduction

The focus of this study is to analyze the macroscopic phase behaviour and microscopic structural transitions of self assembled structures in binary amphiphilic-hydrocarbon systems.

This study was based on the presence of reverse vesicles that were reported to consist of the phosphatidylcholines PC4:0 and PC18:2 in the ~2-4 Ro (amphiphilic ratio as described in Chapter 3) range in cyclohexane at room temperature (Tung *et al.* 2008). Therefore, this study was focused upon 2.5 Ro, 3.5 Ro and 4.5 Ro mixtures using the 99% C18 and C4 products, detailed in Chapter 3, in hydrocarbon solvents. In addition to repeating the cyclohexane experiments of Tung *et al.* (2008), this study included the use of alkanes to increase the analogy between the laboratory environment and that of Titan's hydrocarbon lakes.

Tung *et al.* (2008) used 20 mM of surfactants in their work and the samples were faintly blue (pers. comm.) so to try to enhance the Tyndall effects an amphiphilic concentration of 30 mM was mainly studied. They also found that salt, such as NaCl, was necessary for the stabilisation of the reverse vesicles. Tung *et al.* (2008) used 3.5 mM of NaCl in their 20 mM lipid solutions; without NaCl, or at low concentrations (<2 mM for a 20 mM lipid concentration), the bluish homogenous solution phase separates into coexisting liquid phases which were not analyzed. Therefore, in this study we utilised a range of NaCl concentrations ≥3.5 mM for amphiphilic concentrations that ranged from 15 mM to 30 mM. For sample preparation there was a range of sonication intensities used and cold vs. hot mixing; a full list of sample details and preparation methods is outlined in the Appendices I and II.

Included in this study are the RVe1a and RVe1b sample groups; the use of methanol in preparing the amphiphilic-NaCl mixture for the RVe1b samples separate this group from the RVe1a group (see Chapter 3 for method details). Some of these samples include the fluorophore 'Rhodamine b' in order to allow fluorescence microscopy; these are indicated by the symbol (fl) i.e. RVe1a(fl) or RVe1b(fl) followed by the sample number. The sample road map, Figure 25, demonstrates the variety of samples studied in this chapter.

The macroscopic phase behaviour was reported over an extended time period, often for over a year; a key to the abbreviations used in describing phase behaviours is in Table 13 (section 4.1.3) and Appendix III. The imaging techniques used included confocal microscopy, confocal laser scanning fluorescence microscopy, and TEM; details on these imaging techniques can be found in Chapter 3.

4.1.1 Key questions

The key questions we intended to answer in this study were:

- Can we replicate the results published by Tung *et al.* (2008) and create colloidal dispersions containing unilamellar reverse vesicles using PC18:2 and PC4:0 amphiphiles?
- Can PC18:2 and PC4:0 amphiphiles form unilamellar reverse vesicles in alkanes?
- Does the molecular weight of the alkane solvents affect self assembly of PC18:2 and PC4:0 amphiphilic mixtures?
- What is the temporal stability of self assembled structures composed of PC18:2 and PC4:0 amphiphiles in hydrocarbon solvents?
- How do various preparation methods affect self assembled structures in binary PC18:2 and PC4:0 amphiphilic-hydrocarbon systems?

4.1.2 Sample road map

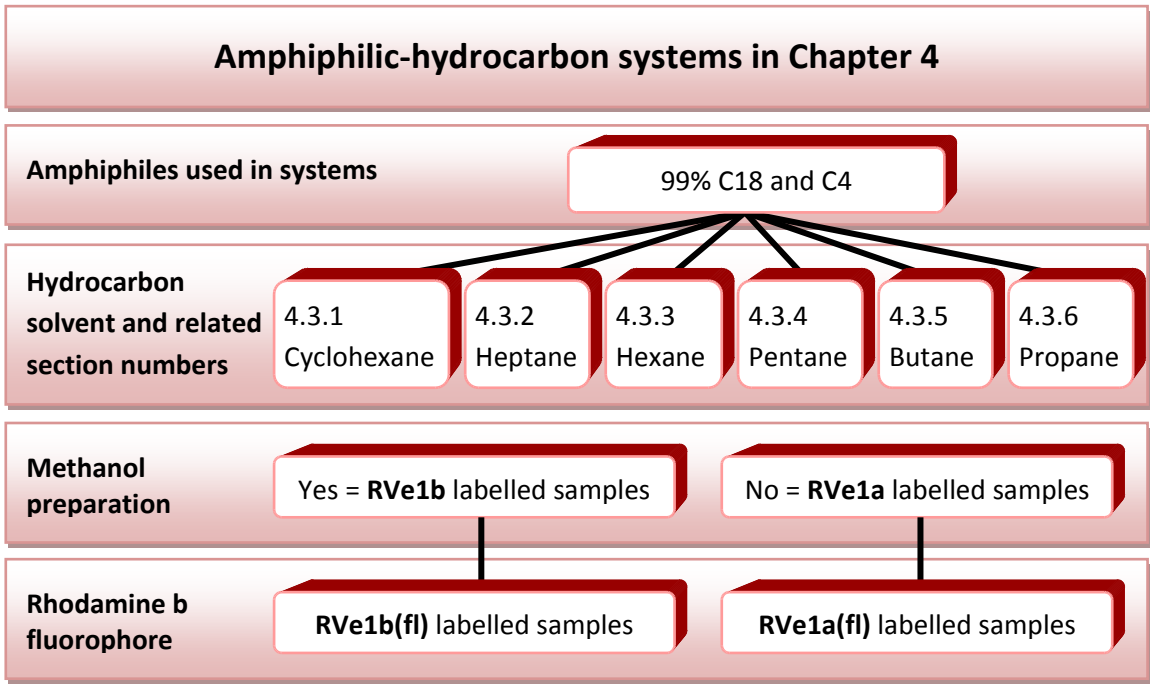

Figure 25: Sample road map illustrating the systems discussed in Chapter 4 and sample labelling.

The following sections of this chapter begin with sample road maps that illustrate the differences in the initial preparation of samples that are discussed in the text.

4.1.3 Key to macroscopic phase behaviour tables

Term	Explanation	Term	Explanation	Term	Explanation
Opaque	White opaque solution. Cannot see through the solution.	SL	Strong laser reflection.	WFP	White (translucent) fluid precipitant.
Cl or Cl(s)	Cloudy solution, (s) symbol signifies after being shaken by hand. A cloudy solution has some transparency unlike those that are characterised as 'Opaque'.	WL	Weak laser reflection.	YFP	Yellow (translucent) fluid precipitant.
O or O(s)	Opalescent solution, (s) symbol signifies after being shaken by hand. Opalescent solution is translucent with an intense shine and can range of slight hues from grey (Gr), grey/yellow (Gr/Y) and grey/blue (Gr/B).	WSL	Widely scattered laser reflection.	TFP	Transparent fluid precipitant.
B	Solution has a blue hue - substantial Tyndall Scattering occurring.	WWSL	Weak widely scattered laser reflection.	WGP	White (translucent) gel precipitant.
T	Transparent solution.	NL	No laser reflection.	YGP	Yellow (translucent) gel precipitant.
Ph	Phase separated solution – the separate phases are characterised individually.			TGP	Transparent gel precipitant.
CLay	White cloudy layer, at the base of the container unless stated otherwise.			YWGP	Milky yellow (translucent) gel precipitant.
BLay	Bluish, opalescent layer, at the base of the container unless stated otherwise.			WSP	White solid precipitant.
Fla(x)	Visible opaque flakes in solution, temporarily after being hand shaken (x=colour; w=white, y=yellow, wy=milky yellow).			Mot	Mottled transparent and white precipitant with solid and fluid characteristics.
Glo	Spherical and translucent gel globules in solution after being shaken by hand.			NaClCem (x)	NaCl crystals cemented with a gel, colour of gel in brackets.

Table 13: Key explaining the abbreviations used in describing the macroscopic phase behaviour of samples.

4.2 Results for independent C18 99% and PC4:0 products in hydrocarbon systems

Creating systems of 20 mM of C18 99% and PC4:0 products independently in hydrocarbon liquids illustrated the difference in solvability between these products. C18 99% phase separated out of solution in cyclohexane, heptane, and pentane to form a liquid crystal precipitant that appeared white and grainy.

In cyclohexane PC4:0 completely dissolved and formed a transparent molecular solution. However, in heptane and pentane there was a strong laser reaction indicative of self assembled micellar particles in solution. Using TEM barbell shaped cylindrical micelles were imaged in the PC4:0 system; see Figure 26.

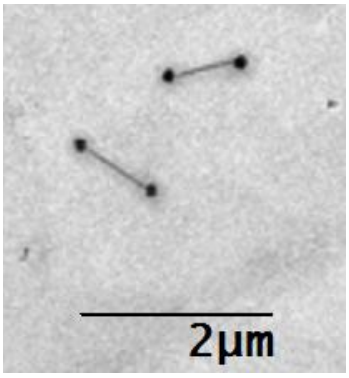

Figure 26: Micellar barbells formed from self assembly of PC4:0 in pentane.

4.3 Results for binary amphiphilic-hydrocarbon systems

In the following section, the results are separated at the highest order by solvent type. These sections are subsequently divided by the amphiphilic ratio which contains analyses of the macroscopic phase behaviour and imaging results of individual samples over time. Each of the solvent defined sections is concluded with a summary comparing these results.

4.3.1 Cyclohexane systems

4.3.1.1 Cyclohexane 2.5 Ro systems

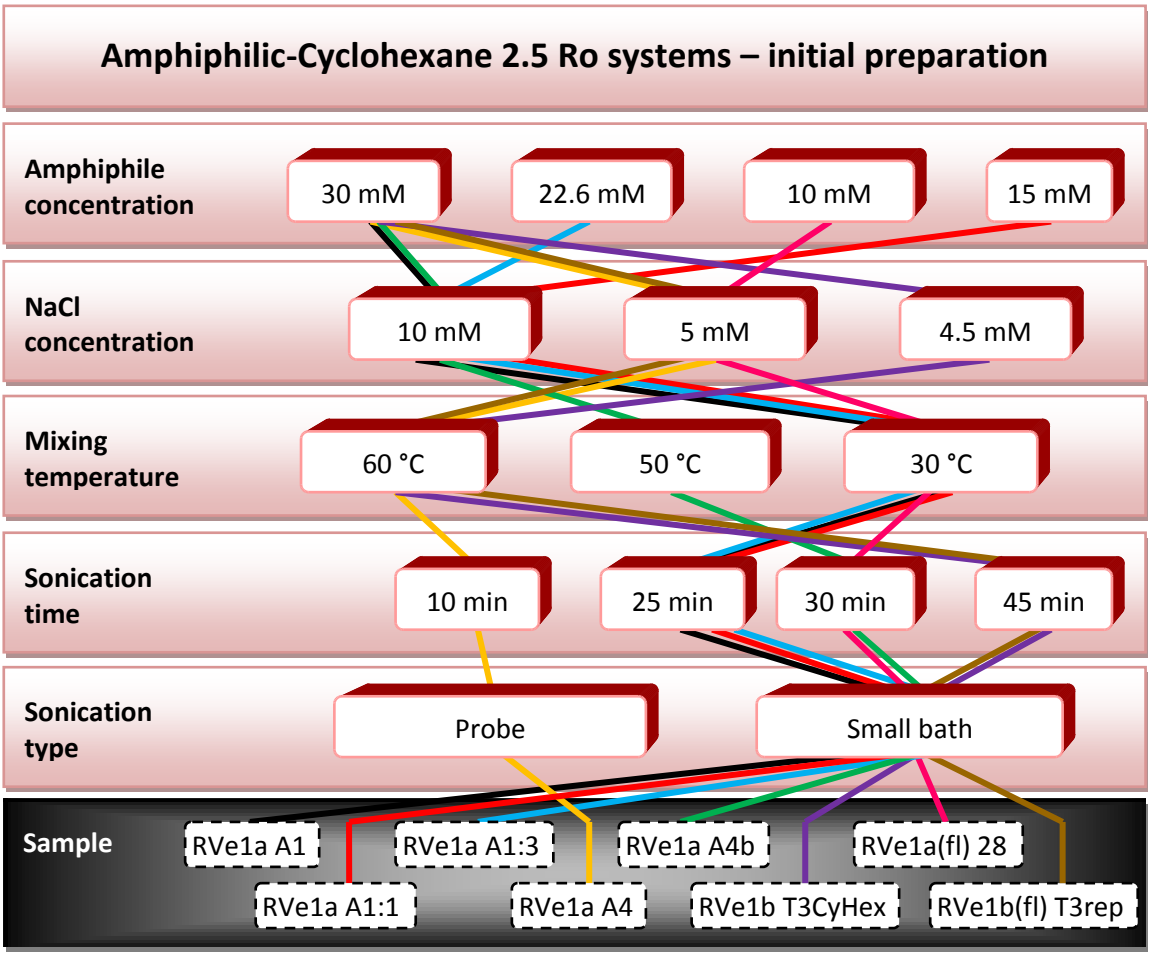

Figure 27: Sample road map illustrating the initial preparation methods for the amphiphilic-cyclohexane 2.5 Ro samples discussed in the text of this section.

The macroscopic phase behaviour of the cyclohexane 2.5 Ro binary amphiphilic mixtures over time are shown in Tables 14 and 15. The first sample prepared, RVe1a A4, used a high (60 °C) mixing temperature and probe sonication (at a high 10 amplitude microns) for intense sonication. This produced a suspension that quickly settled for form a white fluid precipitant. TEM studies reported a high polydispersity of large (micron-sized) structures mainly dominated by particles resembling phase separated liquid crystal particles or compound micelles (Figure 33) but also including some multilamellar reverse vesicles (Figures 34 and 35).

To determine whether the inclusion of more stabilisers would allow the formation of a colloidal system of unilamellar vesicles incremental additions of sodium chloride were added and the sample was re-sonicated. The increase of sodium chloride did not have this effect and at high concentrations began to coalesce with the amphiphilic structures to form a crystalline-gel precipitant. After a year the amphiphilic matrix of the crystalline precipitant had transformed

from white to a yellow colour; signifying a microscopic phase transition of the amphiphilic mixture with time.

Tung *et al.* (2008) sonicated their samples with a water-bath, and therefore, it was possible that the strong probe sonication utilised in RVe1a A4 had caused an increase in particle sizes due to an increase in particle collisions. So RVe1a A4b was initially created with a weak-water bath sonication which created a similar cloudy suspension to RVe1a A4; however, TEM imaging showed an absence of any reversed vesicles.

After two weeks, RVe1a A4b had formed a transparent gel and after 2 months had formed a yellow fluid precipitant; see Figure 28b. Microscopy of this yellow fluid precipitant dispersed by hand shaking revealed large (2 μm to 50 μm) spheres of amorphous liquid crystal (Figure 30).

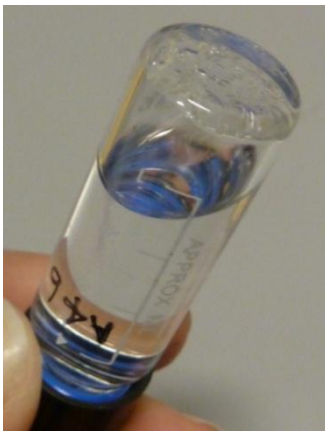
(a)
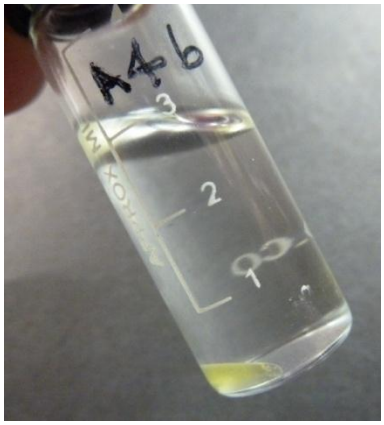

(b)

Figure 28: Images of the macroscopic phase behaviour of RVe1a 4b at: 2 weeks and 4 months after preparation, for images (a) and (b) respectively.

The same macroscopic phase behaviour was observed for systems prepared with a hydrocarbon mixing temperature of 30 ℃ or 60 ℃.

The amphiphilic concentration had been maintained at 30 mM for all the systems mentioned so far; however, Tung *et al.* (2008) used 20 mM amphiphilic concentrations. Therefore, samples with 10 mM, 15 mM, and 22.5 mM amphiphilic concentrations were studied to determine if reduced amphiphilic concentrations would produce the anticipated colloidal dispersion presenting strong Tyndall scattering. The 10 mM and 15 mM systems were translucent without obvious signs of Tyndall scattering and the 22.5 mM system produced a turbid system similar to that of the original 30 mM system; see Figure 29. After two weeks all particle had settled, with the low concentration producing a cloudy precipitant with solid characteristics whilst the high concentration produced a highly viscous cloudy fluid that occupied half of the sample volume; see Figure 29 (b) and (c). This implies that either: the high concentration system contains particles that are larger (maybe swollen with the hydrocarbon solvent) or are rougher, causing

slow settling due to an increase in friction; or the low concentration system contains dense particles (such as crystals or compound micelles). Fluorescence microscopy of the 10 mM system showed 1-8 μm diameter particles of compound reverse micelles; see Figure 36.

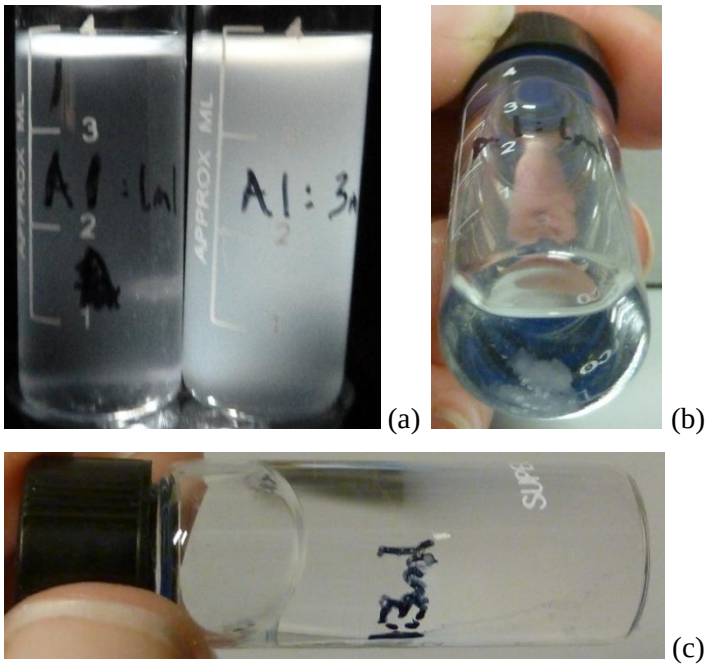

(a) (b)

(c)

Figure 29: Images of the macroscopic phase behaviour for: (a) 7.5 mM and 22.6 mM amphiphilic concentration systems after initial preparation, left to right of image; (b) 7.5 mM amphiphilic concentration system 2 weeks after creation; and (c) and 22.6 mM amphiphilic concentration system 2 weeks after creation, with sample tilted at a 45° angle.

The methanol prepared sample also had a similar macroscopic phase behaviour, that of a rapidly settling suspension. Using fluorescence microscopy on a 1 day old sample showed these amorphous regions were giant unilamellar reverse vesicles; see Figure 37. However, microscopy 6 weeks after preparation revealed these encompassed dense particles which are most likely to be bicontinuous structures from merging lamellar particles; see Figures 31 and 32.

These results imply that neither the temperature during mixing of the amphiphilic-hydrocarbon system or sonication intensity greatly influences the macroscopic phase behaviour of binary amphiphilic-cyclohexane 2.5 Ro system that were not pre-prepared in methanol. These systems are often a suspension dominated by liquid crystal droplets and compound micelles settle that rapidly to form a white fluid.

Although the macroscopic phase behaviour for the systems prepared with methanol is similar to the others the particle structures are very different and produce rapidly settling giant unilamellar reverse vesicles.

4.3.1.1.1 Macroscopic phase behaviour

Sample	Ro	Concentration (mM)	Observations						
			BPS 8/11/2010	APS 8/11/2010	3 hours APS 8/11/2010	After additional NaCl 17/11/2010	3 months APS 2/2/2011	1 yr 5 months APS 22/3/2012	1 yr 10 months APS 21/9/2012
RVe1a A4	2.5	30	T+WSP	Cl+WFP	T+WFP	Cl+NaClCry (W)	T+NaClCry(W)	T+NaClCry(Y) [Tr+ NaClCry(Y) AHS]	T+ NaClCry(Y)+NL [T+ NaClCry(Y)+NL AHS]

			BWS 19/1/2011	AWS 19/1/2011	2 weeks AWS 2/2/2011	1 yr 2months AWS (BSS) 22/3/2012	ASS 22/3/2012	6 months ASS 21/9/2012
RVe1a A1	2.5	30	Cl+WGP	Cl	**Already converted to A1:1 and A1:3.**	-	-	-
RVe1a A1:1	2.5	7.5	**From A1 (see above)**	Tr	T+WSP [T+Fla(W) AHS]	T+YFP [Tr+YFP AHS]	Tr(Y)	T+YGP+NL [Tr+WL AHS]
RVe1a A1:3	2.5	22.6	**From A1 (see above)**	Cl	Ph = Top half: T + Lower half: Cl (high viscosity) [Cl AHS]	T+YFP [Tr+YFP AHS]	Tr(Y)	T+YGP+NL [Tr+YGP+WL AHS]

			AWS 19/1/ 2011	2 weeks AWS 2/2/2011	2 months AWS (BSS) 22/3/2012	ASS 22/3/2012	2 weeks ASS (BPS) 3/4/2012	APS 3/4/2012	5 hours APS 3/4/2012	1 day APS 4/4/2012	1 month APS 1/5/2012	6 months APS 19/9/2012
RVe1a A4b	2.5	30	Cl	T+TGP [T+TGP AHS]	T+YFP [Tr(Y) AHS]	Tr(Y)+YGP(some)	T+YFP+NL [Tr+WL AHS]	Tr+Cl(some)+YFP+WWSL	T+YWFP+NL	T+YWFP+NL	T+YFP+NL	T+YGP+NL [Tr+ Cl(some)+YGP+WWSL AHS]

Table 14: Tables presenting the changes in phase behaviour for RVe1a cyclohexane 2.5 Ro samples.

Sample	Surfactant Ratios (Ro)	Concentration (mM)	Observations										
			AWS 6/2/2012	1 day AWS 7/2/2012	6 weeks AWS 22/3/2012	ASS 22/3/2012	2 weeks ASS (BPS) 3/4/2012	APS 3/4/2012	5 hours APS 3/4/2012	1 day APS 4/4/2012	1 month APS 1/5/2012	6 months APS 19/9/2012	2 years 2 months APS 6/6/2014
RVe1b T3CyHex	2.5	30	Cl	Tr+WGP(some)	T+YWGP [Tr+YWGP AHS]	Cl(Y)+YGP	T+YGP+NL [Tr+ YGP+WL AHS]	Cl+YGP+WSL	T+YWGP+NL	T+YWGP+NL	T+YWGP+NL	T+YGP+NL [Tr+YGP+WWSL AHS]	T+YGP+NL

Table 15: Tables presenting the changes in phase behaviour for the RVe1b cyclohexane 2.5 Ro sample.

4.3.1.1.2 Microscopy

Sample Number	Micrograph	Sample and Micrograph Description
RVe1a A4b	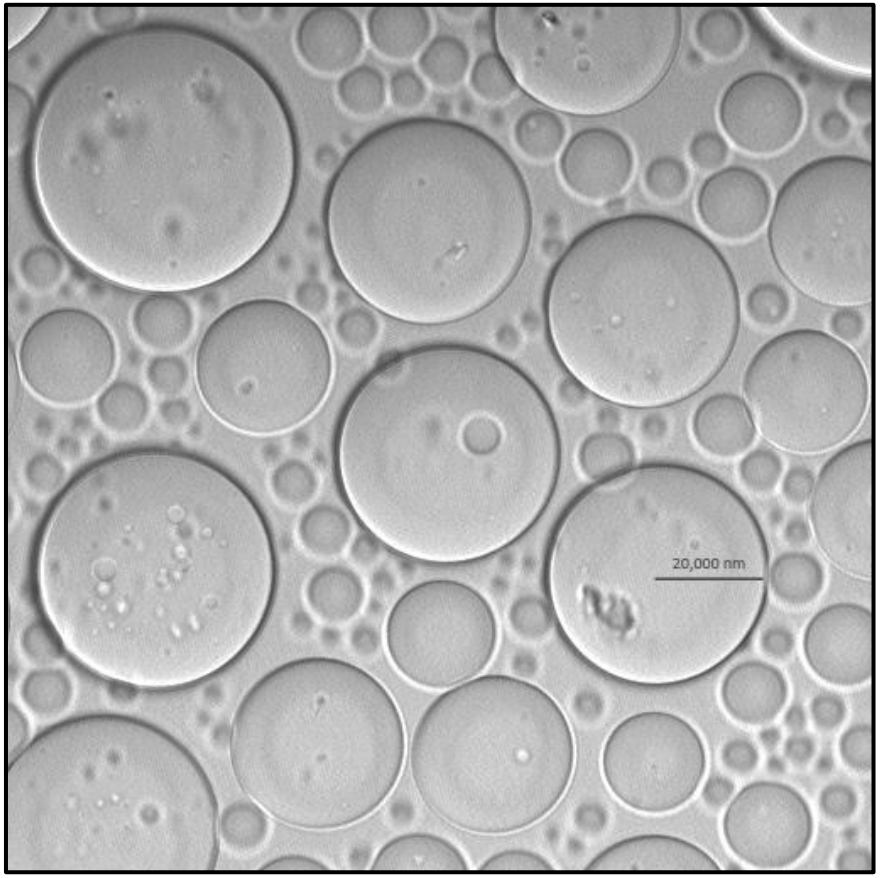	**Figure 30:** 2.5 Ro cyclohexane micrograph **Date of Micrograph**: 21/3/2012 **Sample description**: T+YWGP [Tr+YWGP AHS] 1yr3m after weak water-bath sonication and before probe sonication. Shaken. **Micrograph description**: Homogeneous shape distribution - Spherical particles. Large size distribution – 2 μm to 50 μm. Many large (>20 μm) particles appear to have a wall thickness of > ~5 μm, however, this is probably an optical illusion due to their size.

Sample Number	Micrograph	Sample and Micrograph Description
RVe1b T3CyHex	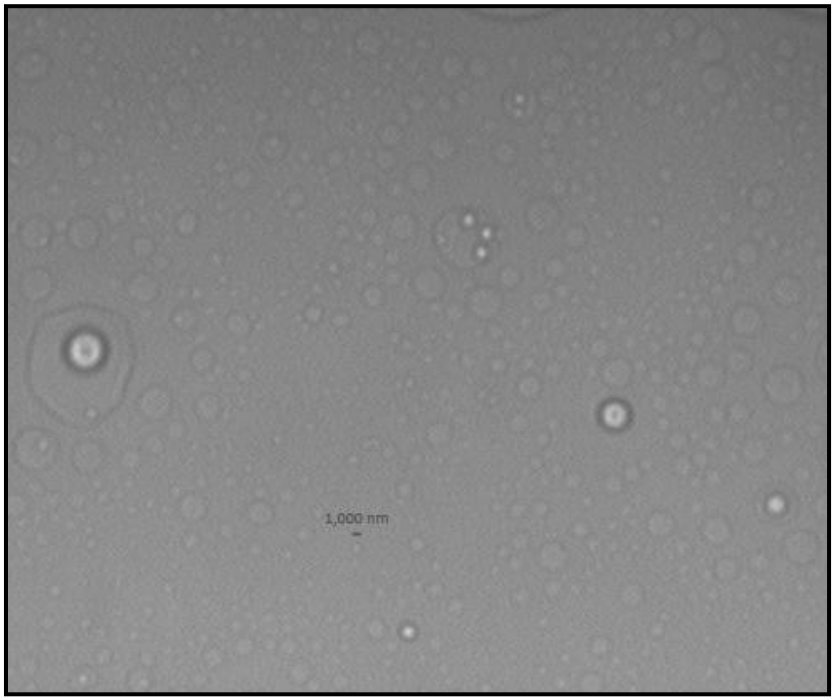	**Figure 31:** 2.5 Ro cyclohexane micrograph **Date of Micrograph**: 21/3/2012 **Sample description**: T+YWGP [Tr+YWGP AHS] 1 month after weak-water bath sonication and before strong-water bath and probe sonication. Shaken. **Micrograph description**: Shape distribution - Spherical to irregular spheroid particles. Size distribution – 1 μm to 15 μm. Most of the structures appear amorphous but are slightly irregular indicating these may be giant unilamellar reverse vesicles. Some of the larger (>5 μm) particles encompass smaller spherical structures.

Sample Number	Micrograph	Sample and Micrograph Description
RVe1b T3CyHex	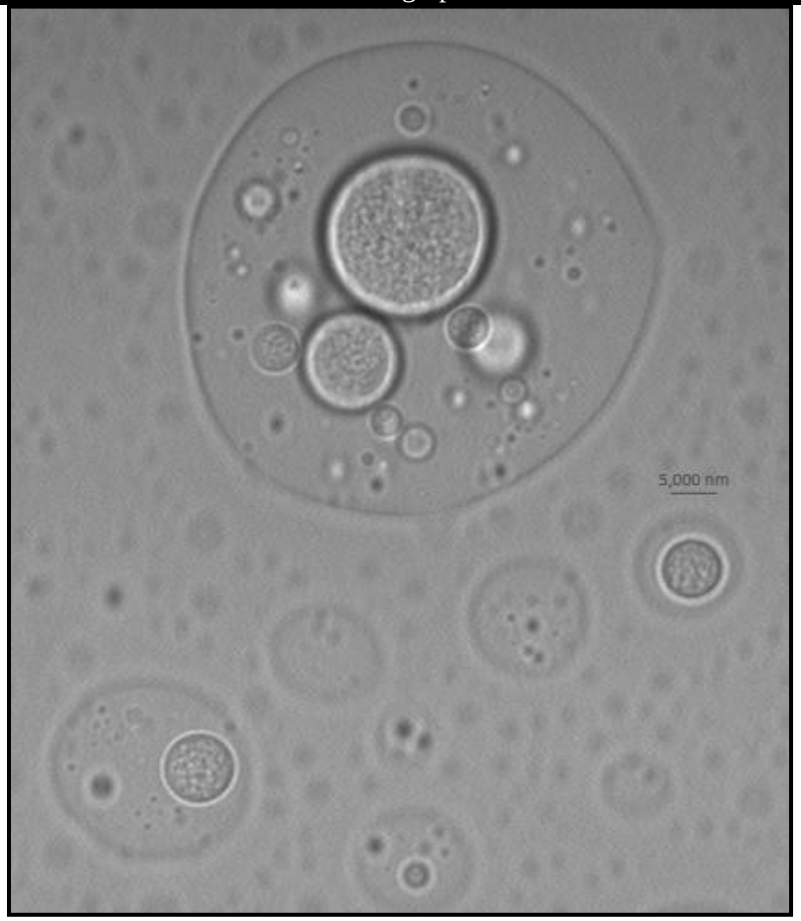	**Figure 32:** 2.5 Ro cyclohexane micrograph **Date of Micrograph**: 21/3/2012 **Sample description**: T+YGP+NL [Tr+YGP+WL AHS] 1 month after weak-water bath sonication and before strong-water bath and probe sonication. Shaken **Micrograph description**: Shape distribution - Spherical to irregular spheroid aggregates. Large size distribution – 1 μm to 50 μm. Most of the structures appear amorphous but are slightly irregular indicating these may be giant unilamellar reverse vesicles. Some of the larger (>5 μm) particles encompass smaller spherical structures. The encompassed smaller structures have a mottled appearance that is likely to represent compound micelles or a bicontinuous structure.

4.3.1.1.3 TEM

Sample Number	Micrograph	Sample and Micrograph Description
RVe1a **A4**	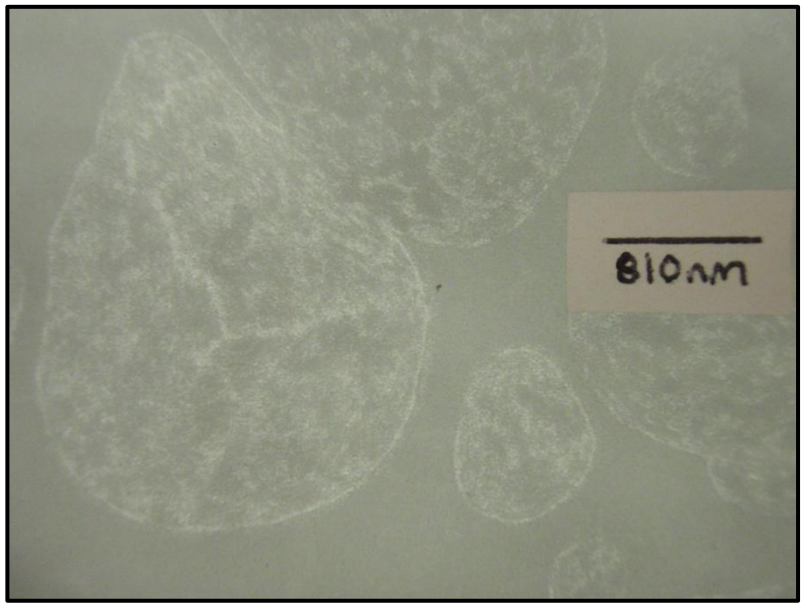	**Figure 33:** 2.5 Ro cyclohexane, Film TEM image **Date of Micrograph**: 9/11/2010 **TEM grid created:** 8/11/2010 **Sample description**: Cl+WFP After probe sonication. **Micrograph description**: Shape distribution – Irregular spheroids. Size distribution – ~200 nm to ~2 μm. These particles have no bilayers and maybe either phase separated liquid crystal particles or compound micelles.

Sample Number	Micrograph	Sample and Micrograph Description
RVe1a A4		**Figure 34:** 2.5 Ro cyclohexane, Film TEM image **Date of Micrograph**: 9/11/2010 **TEM grid created:** 8/11/2010 **Sample description**: Cl+WFP After probe sonication. **Micrograph description**: Shape distribution –Irregular spheroids. Size distribution – large particle ~12 μm. This large particle has irregular bilayers making up a shell thickness between 1 μm and 5 μm and an internal compartment ~5 μm in diameter.

Sample Number	Micrograph	Sample and Micrograph Description
RVe1a A4	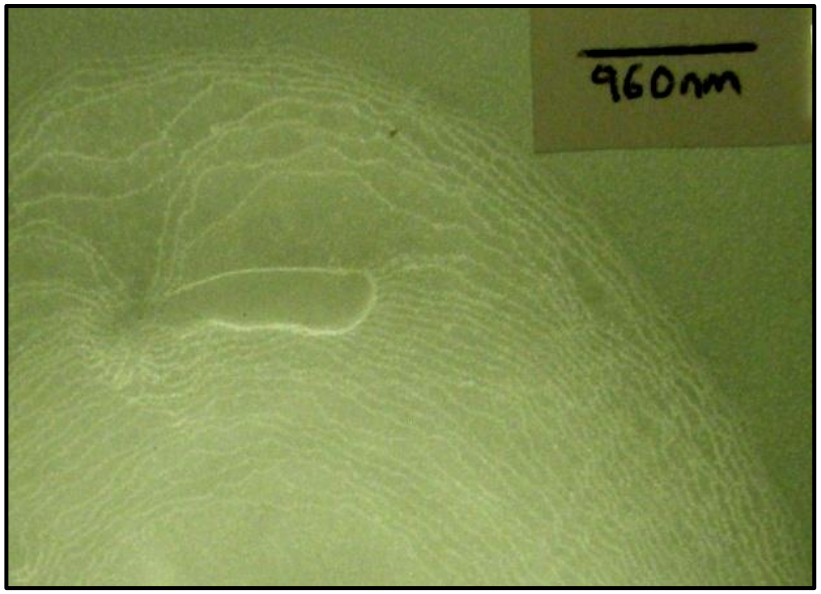	**Figure 35:** 2.5 Ro cyclohexane, Film TEM image **Date of Micrograph**: 9/11/2010 **TEM grid created:** 8/11/2010 **Sample description**: Cl+WFP After probe sonication. **Micrograph description**: This enhanced image of the large ~12 μm particle described in Figure 34 illustrates the irregular nature of the bilayer spacing. The spacing of the bilayers (d-spacing) is most frequently ~1-5 nm but in disturbed regions can increase to ~50 nm.

4.3.1.1.4 Laser scanning confocal fluorescent microscopy

Sample Number	Micrograph	Sample and Micrograph Description
RVe1a (fl) 28	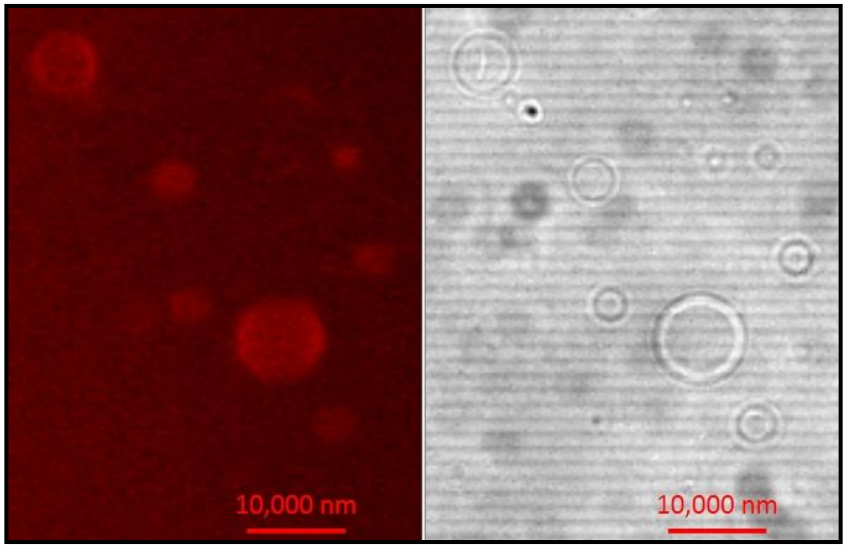	**Figure 36:** 2.5 Ro cyclohexane fluorescence micrograph **Sample description**: Tr 1 day after probe sonication. **Micrograph description**: Shape distribution – Spheroids. Size distribution – ~1-8 μm. The fluorescence image on the left indicates that these spheroids are compound micelles. This image demonstrates how normal microscopy can indicate a thick walled vesicle (image on right) which fluorescence microscopy shows the thick wall is just an optical illusion (image on left).

Sample Number	Micrograph	Sample and Micrograph Description
RVe1a (fl) T3rep	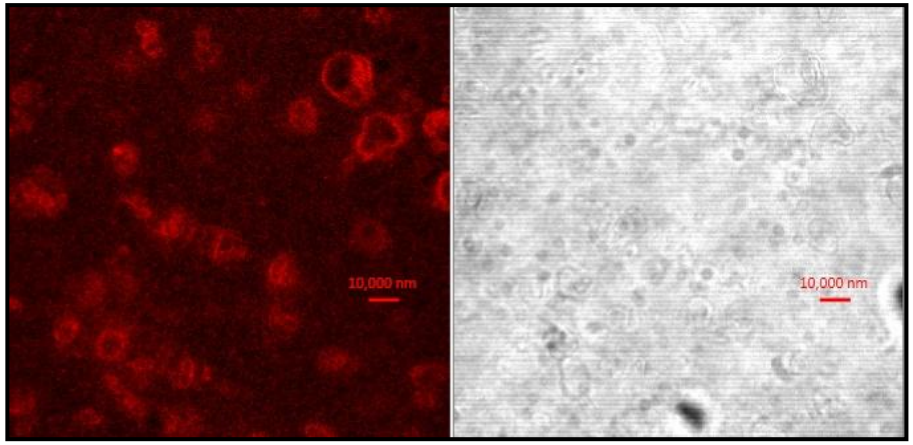 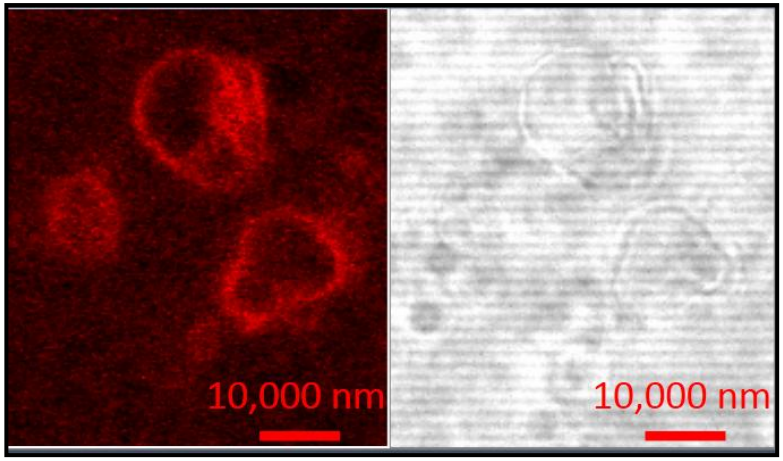	**Figure 37:** 2.5 Ro cyclohexane fluorescence micrograph **Sample description**: Tr 1 day after probe sonication. **Micrograph description**: Shape distribution – Irregular spheroids. Size distribution – ~1-15 μm. The fluorescent images indicate the irregular spheroids are giant unilamellar reverse vesicles which cluster easily.

4.3.1.2 Cyclohexane 3.5 Ro systems, prepared without methanol

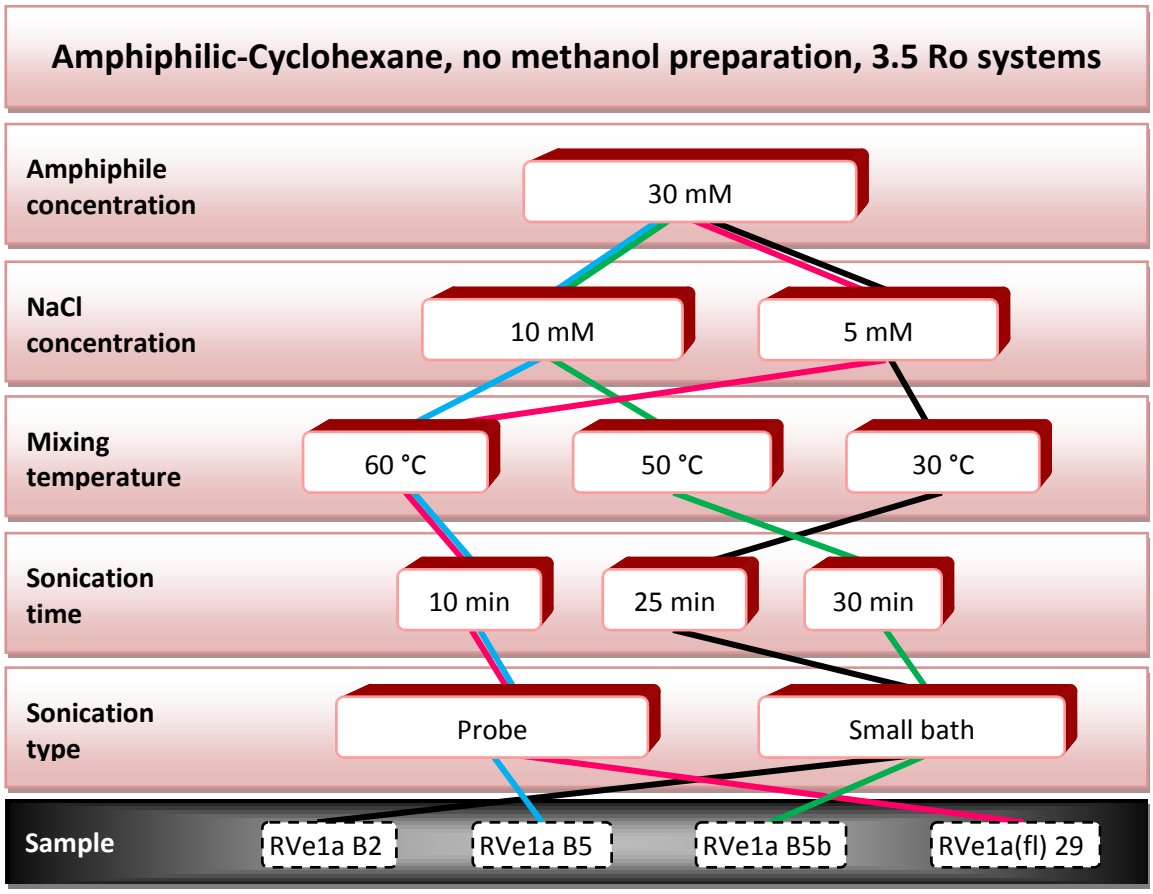

Figure 38: Sample road map illustrating the initial preparation methods for the amphiphilic-cyclohexane 3.5 Ro samples that were not prepared in methanol.

The macroscopic phase behaviour of the cyclohexane 3.5 Ro binary amphiphilic mixtures over time are shown in Table 16. The probe sonicated samples formed a cloudy suspension which settled to form a white fluid precipitant. Fluorescence microscopy showed coexisting phases of some large unilamellar reverse vesicles and dense particles; see Figure 42. TEM imaging showed the dense particles were not lamellar and were either phase separated liquid crystal particles or compound micelles; see Figure 41.

Incremental additions of sodium chloride (with subsequent sonication) did not change this phase behaviour; although at very high concentrations the NaCl crystals coalesced with the amphiphilic particles to form a crystalline precipitant.

All the samples contained precipitants that turned from a white fluid, transparent gel, a yellow fluid and then a yellow gel with time. Microscopy revealed the same amorphous spheres of yellow liquid crystal precipitant in RVe1a 5b (Figures 39 and 40) as those in the yellow fluid precipitant in the cyclohexane 2.5 Ro samples.

4.3.1.2.1 Macroscopic phase behaviour

Sample	Ro	Concentration (mM)	Observations						
			BPS 8/11/2010	APS 8/11/2010	3 hours APS 8/11/2010	After additional NaCl 17/11/2010	3 months APS 2/2/2011	1 yr 5 months APS 22/3/2012	1 yr 10 months APS 21/9/2012
RVe1a B5	3.5	30	T+WSP	Cl	T+WFP	Cl+ NaClCry (W)	T+ NaClCry (W)	T+ NaClCry (Y) [Tr+ NaClCry (Y) AHS]	T+ NaClCry (Y)+NL [T+ NaClCry (Y)+NL AHS]
			BWS 19/1/2011	AWS 19/1/2011	2 weeks AWS 2/2/2011	1 yr 2 months AWS 22/3/2012	1yr 8 months AWS 21/9/2012	3 yrs 5 months AWS 6/6/2014	
RVe1a B2	3.5	30	Cl+WGP	Cl	Ph = Top ¾: T + Lower ¼: Cl (high viscosity)	T+YFP [Tr+YFP AHS]	T+YGP+NL [O(s)+YGP+SL AHS]	T+YGP+Transparent crystals ~1mm long+NL	
			AWS 19/1/2011	2 weeks AWS 2/2/2011	2 months AWS (BSS) 22/3/2012	ASS 22/3/2012	2 weeks ASS (BPS) 3/4/2012	APS 3/4/2012	5 hours APS 3/4/2012	1 day APS 4/4/2012	1 month APS 1/5/2012	6 months APS 19/9/2012
RVe1a B5b	3.5	30	Cl	T+Mot(TFP +WGP) [T+Fla(w)+ WSP AHS]	T+YFP [Tr(Y) AHS]	Cl(Y)+WFP	T+YFP(faint yellow)+NL [Cl(s)+WSL+ AHS]	Cl+YWFP+ WSL	T+YFP+NL	T+YFP+NL	T+YFP+NL	T+ Ph precipitants : TFP+YFP

Table 16: Table presenting the changes in phase behaviour for RVe1a cyclohexane 3.5 Ro samples, prepared without methanol.

4.3.1.2.2 Microscopy

Sample Number	Micrograph	Sample and Micrograph Description
RVe1a B5b	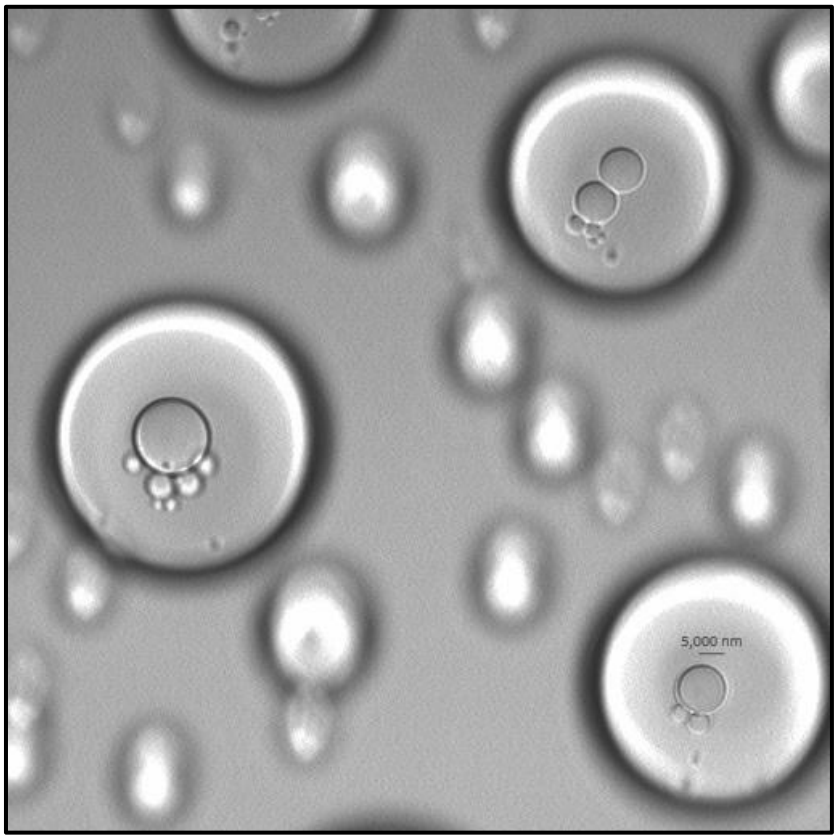	**Figure 39:** 3.5 Ro cyclohexane micrograph **Date of Micrograph**: 21/3/2012 **Sample description**: T+YFP(faint yellow)+NL [Cl+WSL+ AHS] 1yr3m after weak water-bath sonication and before probe sonication. Shaken. **Micrograph description**: Homogeneous shape distribution - Spherical aggregates. Large size distribution – 1 μm to 50 μm. Heterogeneous size distribution - Smaller particles (<10 μm) less frequent. Difficult to distinguish any true walls. All large (>30 μm) particles have smaller particles (<10 μm) attached to their external boundaries.

Sample Number	Micrograph	Sample and Micrograph Description
RVe1a B5b	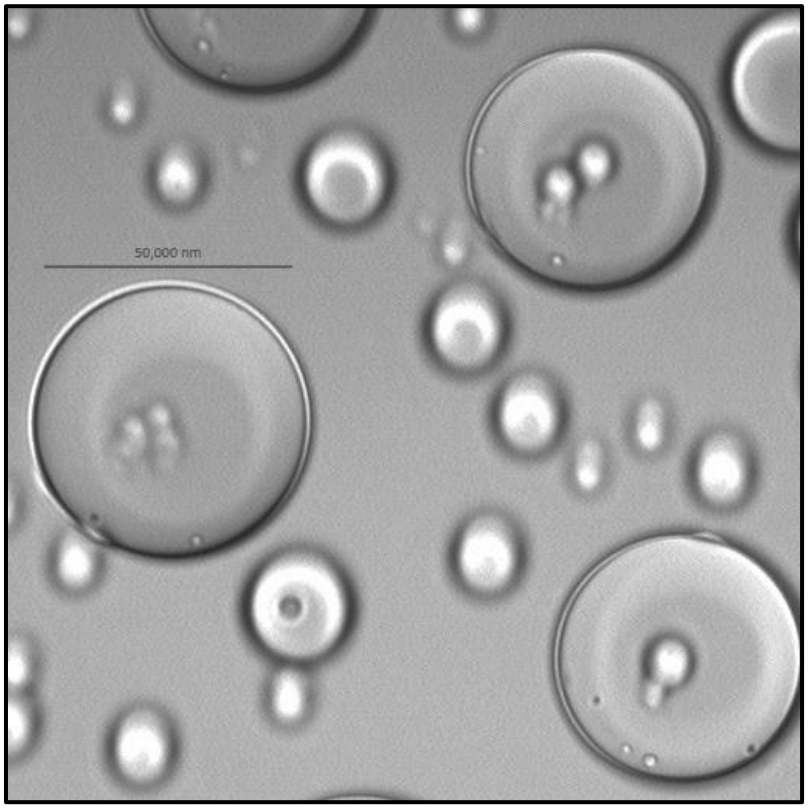	**Figure 40:** 3.5 Ro cyclohexane micrograph **Date of Micrograph**: 21/3/2012 **Sample description**: T+YFP(faint yellow)+NL [Cl+WSL+ AHS] 1yr3m after weak water-bath sonication and before probe sonication. Shaken. **Micrograph description**: Homogeneous shape distribution – Spherical. Large size distribution – 1 μm to 55 μm. Heterogeneous size distribution - Smaller particles (<10 μm) less frequent. The large (>15 μm) particles seem to have thick walls; however, it is likely that this is an optical illusion as the internal boundary is not well defined. All large particles have smaller particles (<10 μm) attached to their external boundaries.

4.3.1.2.3 TEM

Sample Number	Micrograph	Sample and Micrograph Description
RVe1a B5	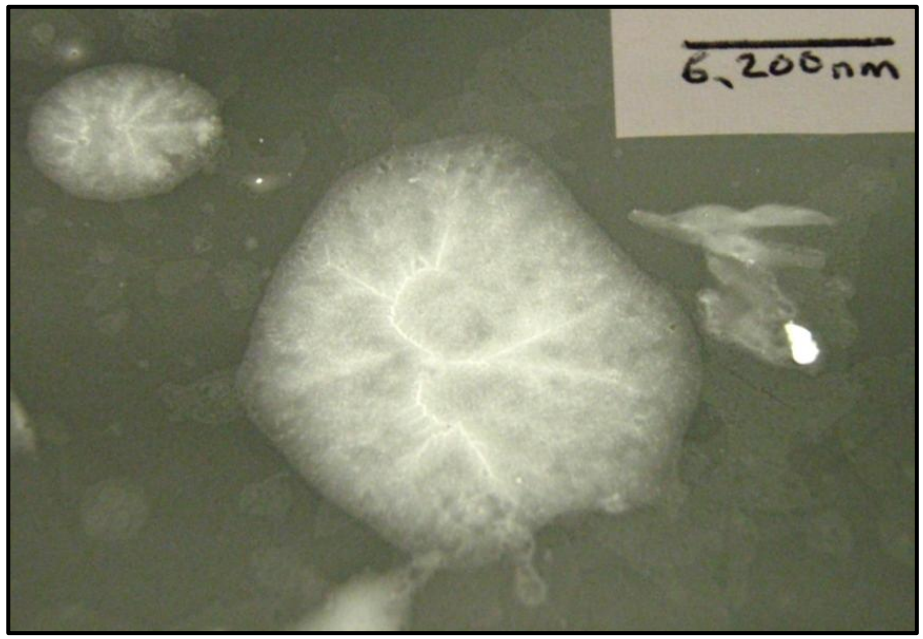	**Figure 41:** 3.5 Ro cyclohexane, Film TEM image **Date of Micrograph**: 9/11/2010 **TEM grid created:** 8/11/2010 **Sample description**: Cl After probe sonication. **Micrograph description**: Shape distribution – Spherical and irregular. Size distribution – ~1-10 μm. These particles have no bilayers and maybe either phase separated liquid crystal particles or compound micelles.

4.3.1.2.4 Laser scanning confocal fluorescent microscopy

Sample Number	Micrograph	Sample and Micrograph Description
RVe1a (fl) 29	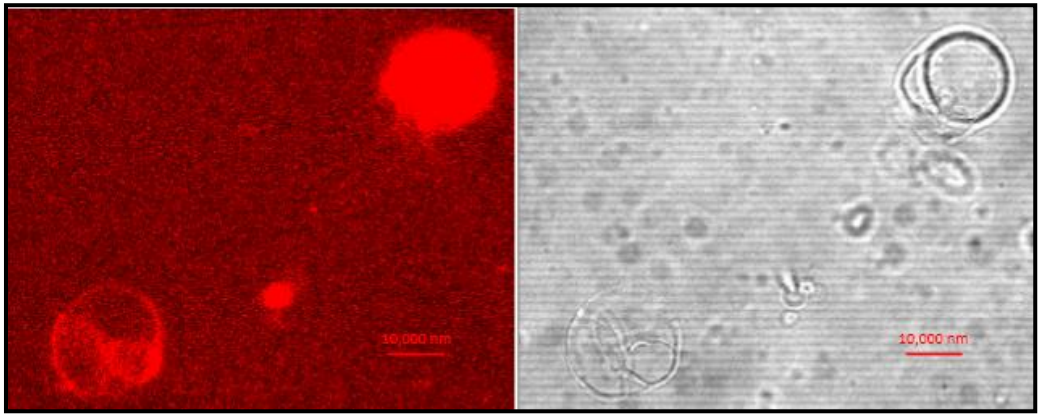	**Figure 42:** 3.5 Ro cyclohexane fluorescence micrograph **Sample description**: Tr 1 day after probe sonication. **Micrograph description**: Shape distribution – Spherical and irregular. Size distribution – ~1-10 μm. These particles are large unilamellar vesicles (lower left) and dense particles without bilayers (upper right) and are either phase separated liquid crystal particles or compound micelles.

4.3.1.3 Cyclohexane 5 Ro, 6.5 Ro, 7 Ro and 8 Ro systems, prepared without methanol

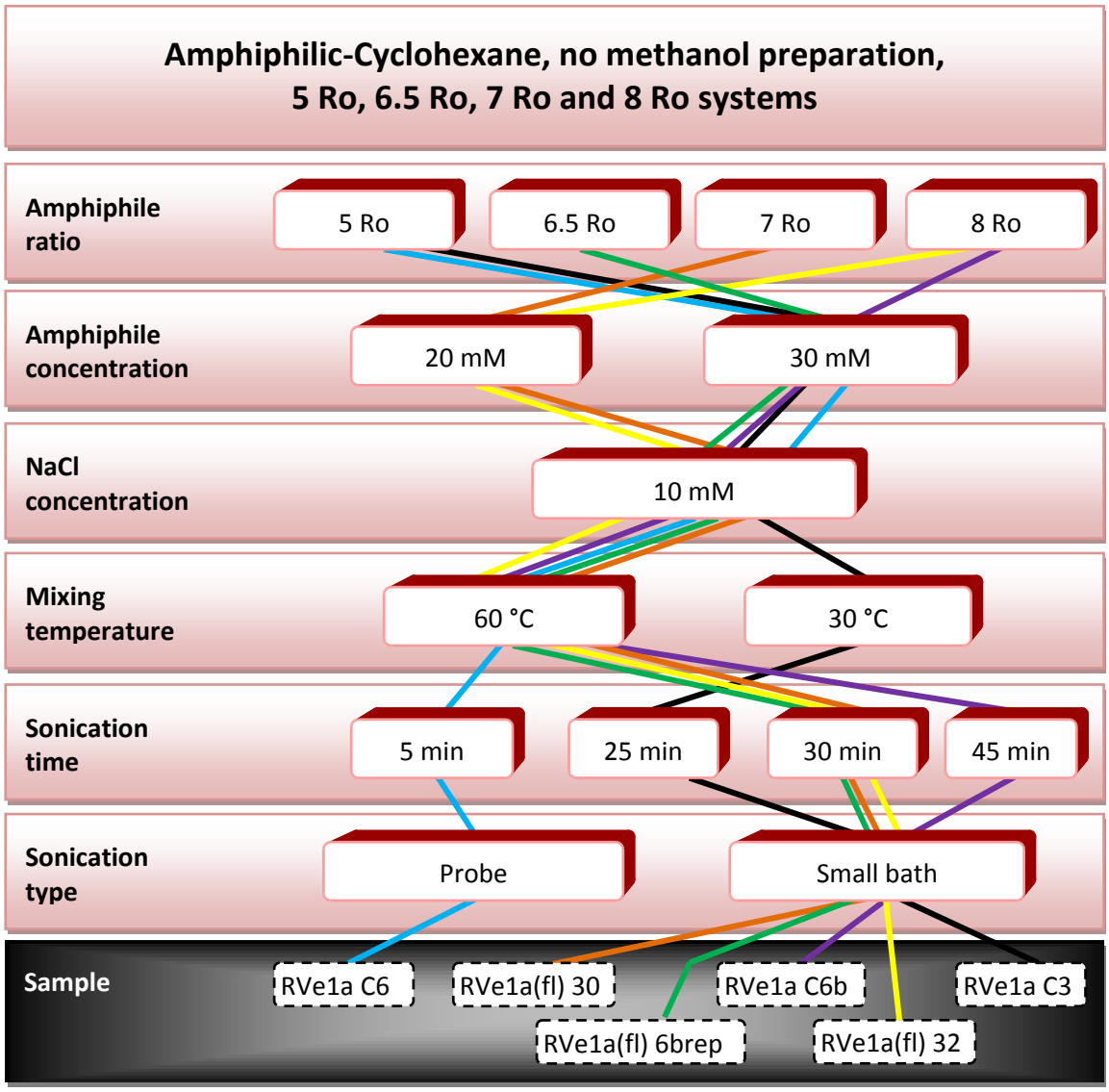

Figure 43: Sample road map illustrating the initial preparation methods for the amphiphilic-cyclohexane 5 Ro, 6.5 Ro, 7 Ro and 8 Ro samples that were not prepared in methanol.

The macroscopic phase behaviour of the cyclohexane 5 Ro and 8 Ro binary amphiphilic mixtures over time are shown in Table 17 and 18 respectively.

Although the 5 Ro systems were all suspensions, there are different opacities and settling rates depending on sonication intensity. Low sonication intensities formed an opaque solution which phase separated into an upper transparent solution and a lower cloudy phase after two weeks. However, the relatively high sonication intensity formed a comparatively more translucent solution that settled to form a transparent solution with a white fluid precipitant within a few hours. This implies that for 5 Ro cyclohexane samples intense sonication causes a decrease in surface area of the particles; however, the particles were too dense to form a colloidal dispersion so the reduction in surface area increased an increase in settling rate.

TEM of the 5 Ro white fluid precipitant of the probe sonicated system showed 0.5 to 4 micrometre sized compound micelles and liquid crystal droplets; see Figure 47 and 48. The systems with weak sonication contained larger and more irregular shaped compound micelles that had slower settling rates due to an increase in surface area.

Fluorescence microscopy of the 6.5 Ro system (RVe1a(fl) 6brep), a day after sonication, showed dense particles that are likely to be compound reverse micelles and cylindrical reverse micelles; see Figure 50.

Fluorescence microscopy of the 7 Ro sample (RVe1a(fl) 30) after weak sonication indicated a phase of large unilamellar reverse vesicles; see Figure 49.

The 8 Ro sample (RVe1a C6b) produced a suspension that phase separated into an upper transparent solution and a lower cloudy phase after two weeks. Fluorescence microscopy of this early stage (RVe1a(fl) 32) presented micrometre sized structures that were uni- and multi-lamellar vesicles, with some of the multilamellar vesicles having a dense reverse onion structure (the internal compartment smaller than a few micrometres); see Figure 51. After all particles settled out of solution a yellow gel precipitant formed and subsequent microscopy, after being shaken by hand, shows multi-chambered unilamellar reverse vesicles or onions; see Figures 44, 45 and 46.

4.3.1.3.1 Macroscopic phase behaviour

Sample	Ro	Concentration (mM)	Observations						
			BPS 8/11/2010	APS 8/11/2010	3 hours APS 8/11/2010	After additional NaCl 17/11/2010	3 months APS 2/2/2011	1 yr 5 months APS 22/3/2012	1 yr 10 months APS 21/9/2012
RVe1a C6	5	30	T+WSP	Cl	T+WFP	Cl+ NaClCry(W)	T+Mot(TGP and NaClCry(W)	**Evaporated** = NaClCry(Y)	**Evaporated** = NaClCry(Y)

			BWS 19/1/2011	AWS 19/1/2011	2 weeks AWS 2/2/2011	1 yr 2months AWS 22/3/2012	1yr 8 months AWS 21/9/2012	3 yrs 5 months AWS 6/6/2014
RVe1a C3	5	30	Cl+WGP	Opa	Ph = Top ⅔ T + Bottom ⅓ Cl (high viscosity)	T+WGP(slightly fluid) [T+Glo(<1mm) AHS]	T+YWGP+NL [T+Fla(YW)+YWGP+NL (except on flakes) AHS]	T+YGP+Transparent crystals ~1mm long+NL

Table 17: Table presenting the changes in phase behaviour for RVe1a cyclohexane 5 Ro samples, prepared without methanol.

Sample	Surfactant Ratios (Ro)	Concentration (mM)	Observations										
			AWS 19/1/2011	2 weeks AWS 2/2/2011	1 yr 2months (BSS) 22/3/2012	ASS 22/3/2012	2 weeks ASS (BPS) 3/4/2012	APS 3/4/2012	5 hours APS 3/4/2012	1 day APS 4/4/2012	1 month APS 1/5/2012	6 months APS 19/9/2012	2 years 2 months APS 6/6/2014
RVe1a C6b	8.1	30	Opa	Ph=Top half T + Lower half Cl (high viscosity)	T+TGP(slight yellow hue) [Tr+TGP(slight yellow hue) AHS]	Tr+TGP(slight yellow hue)	T+YGP+NL [Cl(s)+O(s) +TGP+WL AHS]	Tr+Cl+TFP(faint yellow) +WSL	T+TGP(faint yellow) +NL	T+YGP+ NL	T+YGP+NL	T+YGP+NL [Tr+TGP(faint yellow)+WL AHS]	T+YGP+Transparent crystals ~1mm long+NL

Table 18: Table presenting the changes in phase behaviour for samples prepared without methanol for 8 Ro in cyclohexane.

4.3.1.3.2 Microscopy

Sample Number	Micrograph	Sample and Micrograph Description
RVe1a C6b	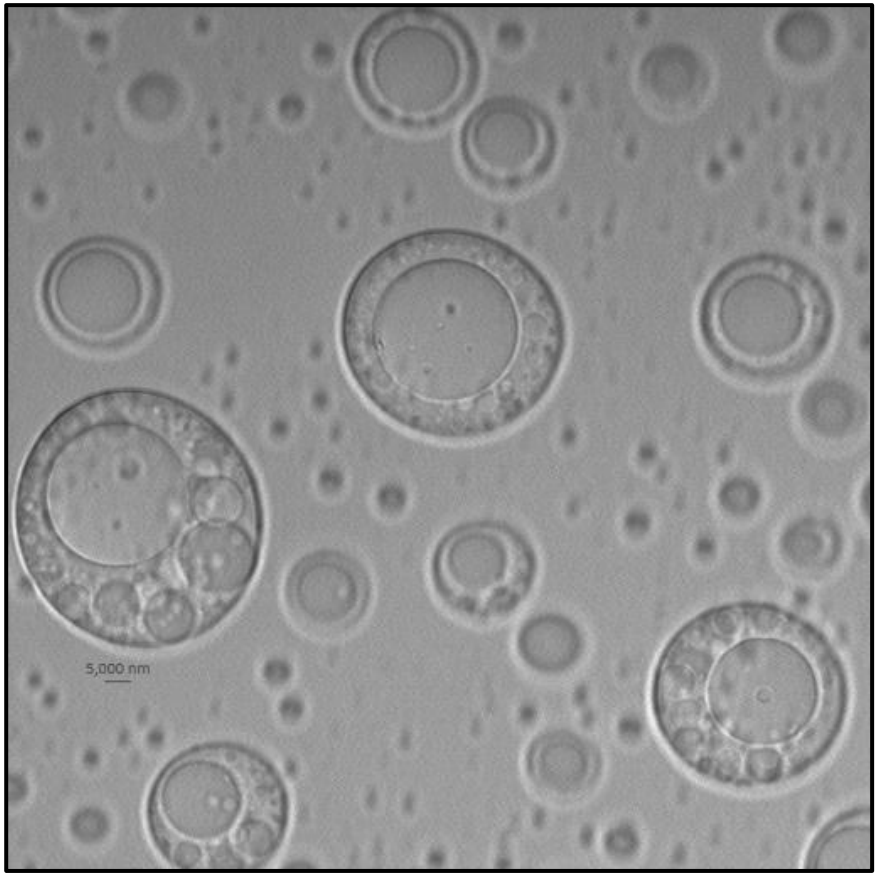	**Figure 44:** 1st z-axis cross section micrograph of 8 Ro cyclohexane **Date of Micrograph**: 21/3/2012 **Sample description:** T+YGP+NL [Cl+O+TGP+WL AHS] 1 year 3 months after weak water-bath sonication and before strong water-bath and probe sonication. Shaken. **Micrograph description**: Shape distribution - Spherical to oblate spheroids. Large size distribution – 1 μm to 40 μm. The large (>15 μm) particles have evident walls and internal compartments. Wall thickness is on average about ⅓ their radius and the internal compartment ⅔. The wall thickness can vary up to x3 around a large aggregate due to the inclusion of smaller spherical structures. The smaller encompassed particles have diameters that can extend up to the wall thickness of the encompassing particle. The smaller (<15μm) encompassed and independent particles often have perceivable but thin walls and large internal compartments.

Sample Number	Micrograph	Sample and Micrograph Description
RVe1a C6b	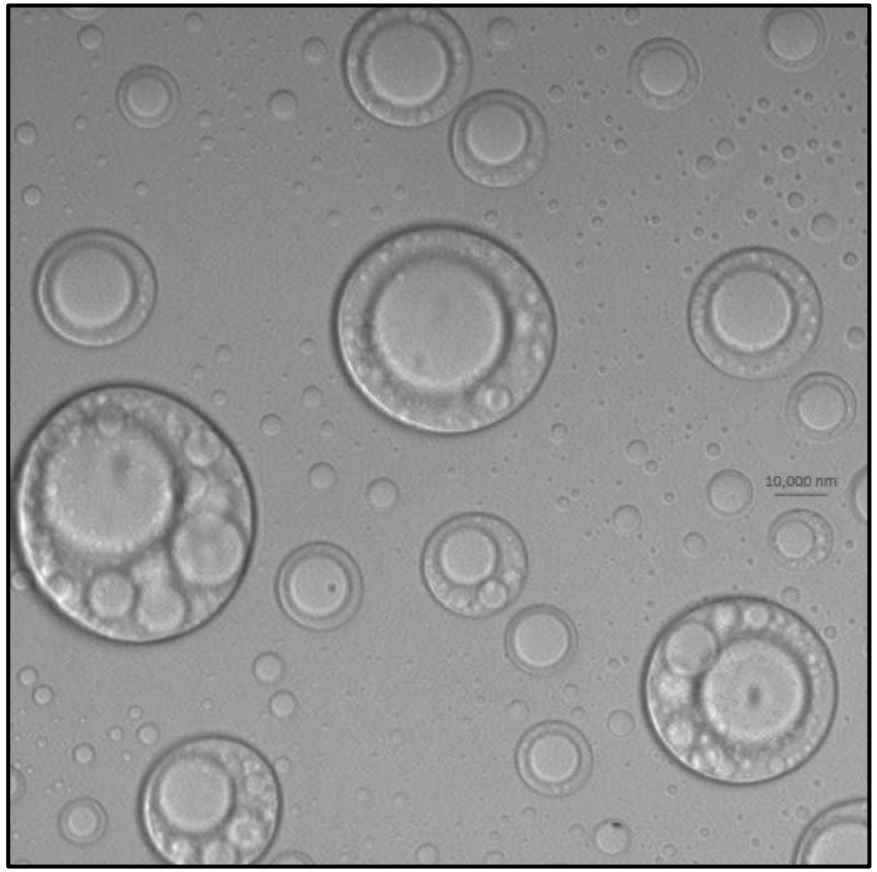	**Figure 45:** 2nd z-axis cross section micrograph of 8 Ro cyclohexane **Date of Micrograph**: 21/3/2012 **Sample description:** T+YGP+NL [Cl+O+TGP+WL AHS] 1 year 3 months after weak water-bath sonication and before strong water-bath and probe sonication. Shaken. **Micrograph description**: Shape distribution - Spherical to oblate spheroid aggregates. Large size distribution – 1 μm to 40 μm. The large (>15μm) particles have evident walls and internal compartments. Wall thickness is on average about ⅓ their radius and the internal compartment ⅔. The wall thickness can vary up to x3 around a large particle due to the inclusion of smaller spherical structures. The smaller encompassed particles have diameters that can extend up to the wall thickness of the encompassing particle. The smaller (<15μm) encompassed and independent particles often have perceivable but thin walls and large internal compartments.

Sample Number	Micrograph	Sample and Micrograph Description
RVe1a C6b	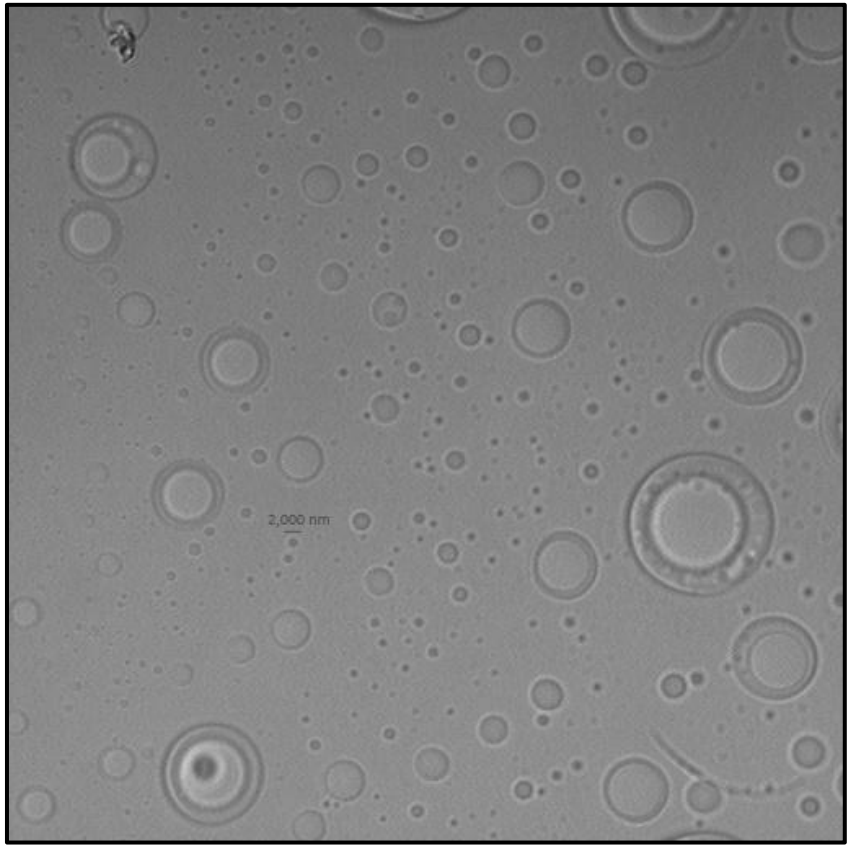	**Figure 46:** 8 Ro cyclohexane micrograph **Date of Micrograph**: 21/3/2012 **Sample description:** T+YGP+NL [Cl+O+TGP+WL AHS] 1 year 3 months after weak water-bath sonication and before strong water-bath and probe sonication. Shaken. **Micrograph description**: Shape distribution - Spherical to oblate spheroid aggregates. Large size distribution – 0.5 μm to 20 μm. The large (>~10 μm) aggregates have evident walls and internal compartments. Wall thickness is on average about ⅓ their radius and the internal compartment ⅔. The wall thickness can vary up to x3 around a large aggregate due to the inclusion of smaller spherical structures. The smaller encompassed particles have diameters that can extend up to the wall thickness of the encompassing particle. The smaller (<~10 μm) encompassed and independent aggregates often have perceivable but thin walls and large internal compartments. Small (<~1vμm) structures are not resolved enough to determine wall/internal compartment structures.

4.3.1.3.3 TEM

Sample Number	Micrograph	Sample and Micrograph Description
RVe1a C6	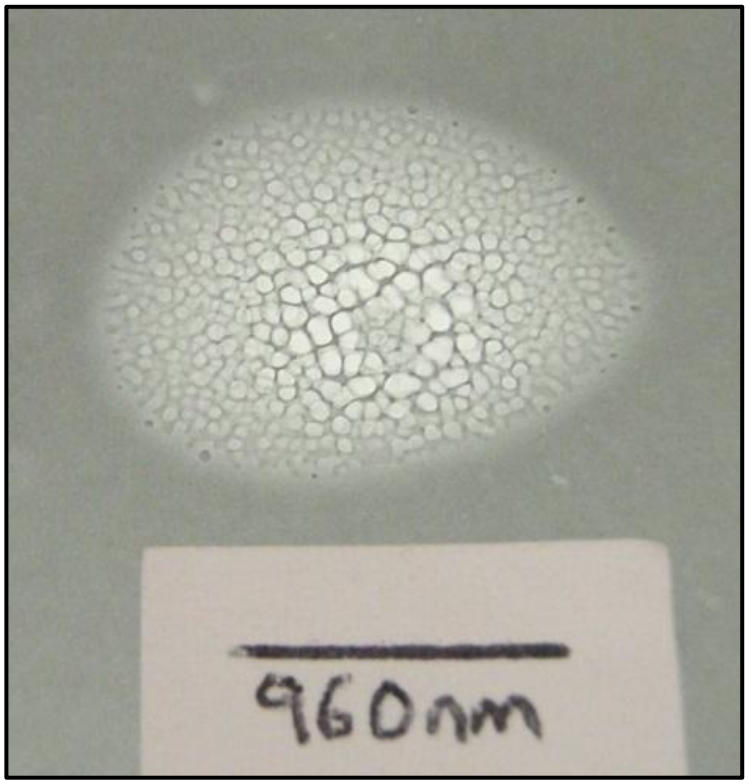	**Figure 47:** 5 Ro cyclohexane, Film TEM image **Date of Micrograph**: 9/11/2010 **TEM grid created:** 8/11/2010 **Sample description**: Cl After probe sonication. **Micrograph description**: Shape distribution – Irregular spheroids. Size distribution – ~1 μm. Likely to be a compound micelle, with micelles ~50 nms in diameter.

Sample Number	Micrograph	Sample and Micrograph Description
RVe1a C6	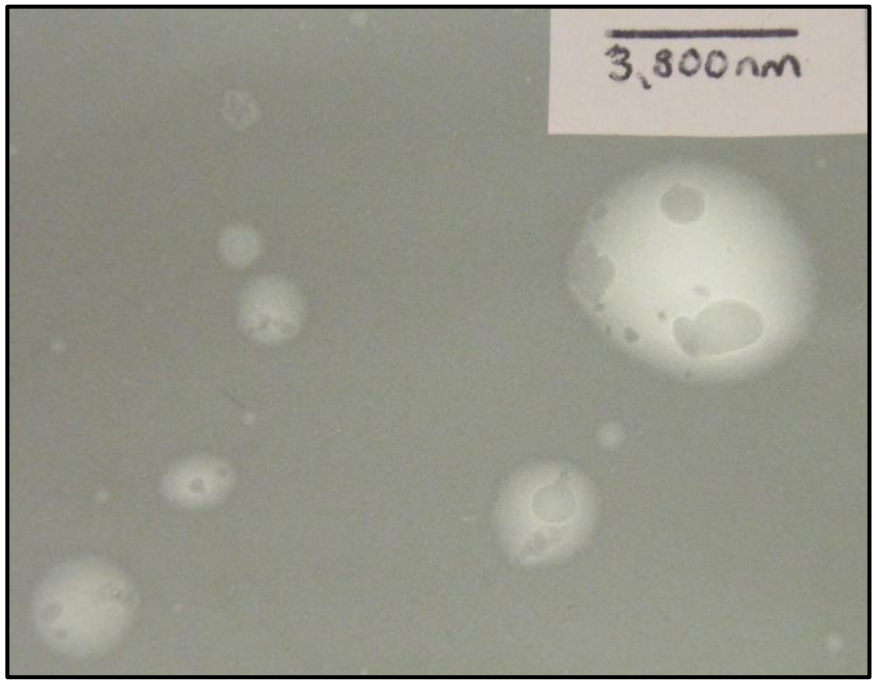	**Figure 48:** 5 Ro cyclohexane, Film TEM image **Date of Micrograph**: 9/11/2010 **TEM grid created:** 8/11/2010 **Sample description**: Cl After probe sonication. **Micrograph description**: Shape distribution – Spherical and irregular spheroids. Size distribution – ~0.5-4 μm. These structures seem to have some internal compartments but no obvious bilayers. Possibly liquid crystal droplets with some fluid inclusions.

4.3.1.3.4 Laser scanning confocal fluorescent microscopy

Sample Number	Micrograph	Sample and Micrograph Description
RVe1a (fl) 30	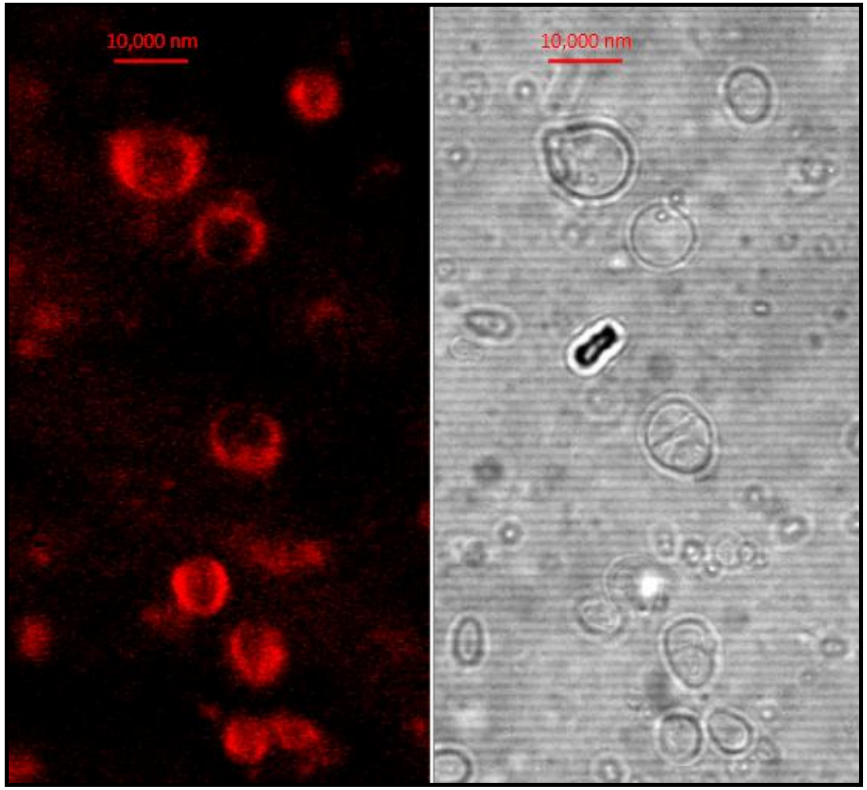	**Figure 49:** 7 Ro cyclohexane fluorescence micrograph **Sample description**: Tr 1 day after weak sonication. **Micrograph description**: Shape distribution – Spherical and irregular spheroids. Size distribution – ~1-13 μm. Unilamellar reverse vesicles.

Sample Number	Micrograph	Sample and Micrograph Description
RVe1a (fl) 6brep	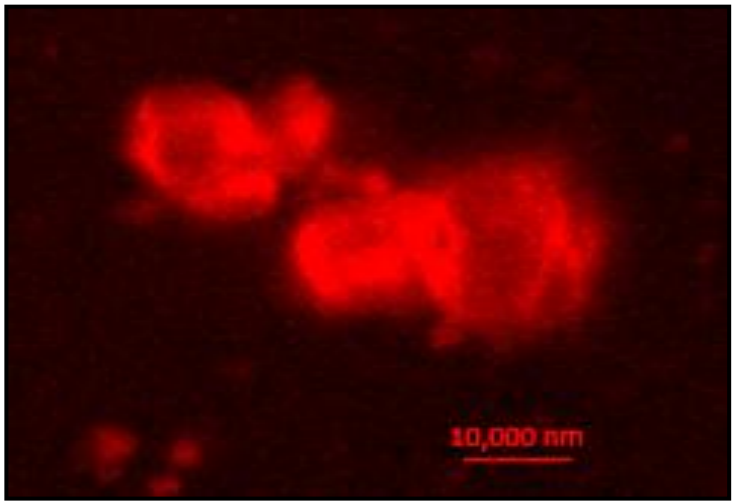 (a) 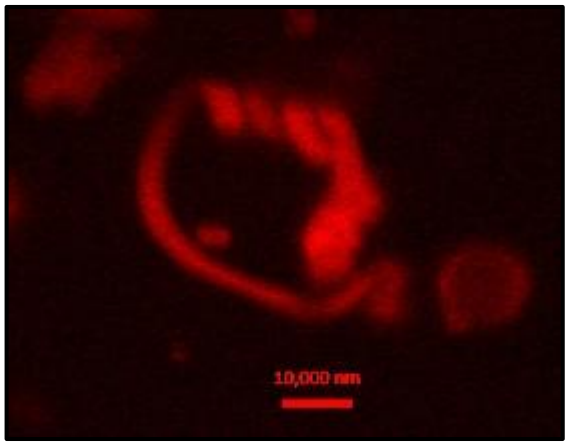 (b)	**Figure 50:** 6.5 Ro cyclohexane fluorescence micrograph **Sample description**: Tr 1 day after probe sonication. **Micrograph description**: Size distribution – ~2-10 μm. (a) The fluorescent image indicates dense particles that are likely to be compound reverse micelles. (b) This image displays a long, twisted cylindrical reverse micelle.

Sample Number	Micrograph	Sample and Micrograph Description
RVe1a (fl) 32	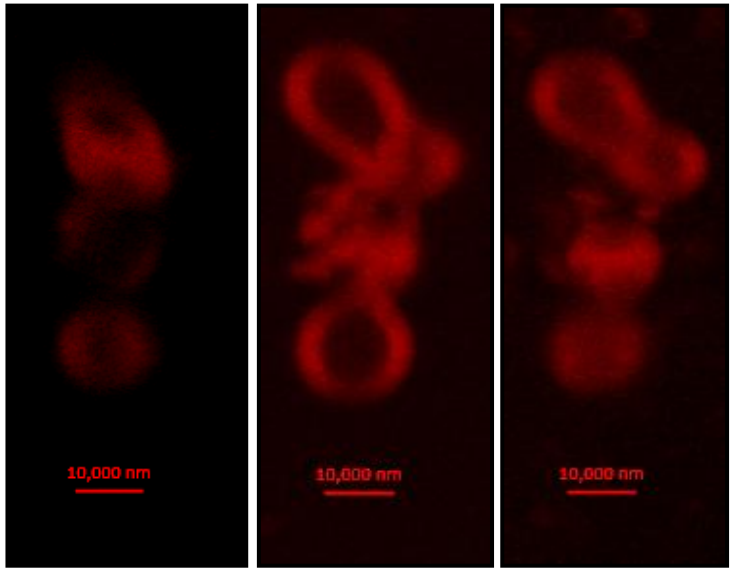	**Figure 51:** 8 Ro cyclohexane fluorescence micrograph **Sample description**: Tr 1 day after probe sonication. **Micrograph description**: Size distribution – ~10-20 μm. The fluorescent images illustrate a z-axis slice through a cluster of reverse vesicles; with the left image being the lowest slice and the right being the highest. The particles in the upper and lower regions of the images show clear, large, internal compartments of a uni- or multi-lamellar vesicle with a ~3 μm shell. However, the central particle appears to be a reverse onion with no large interior cavity.

4.3.1.4 Cyclohexane 4 to 8 Ro systems, prepared with methanol

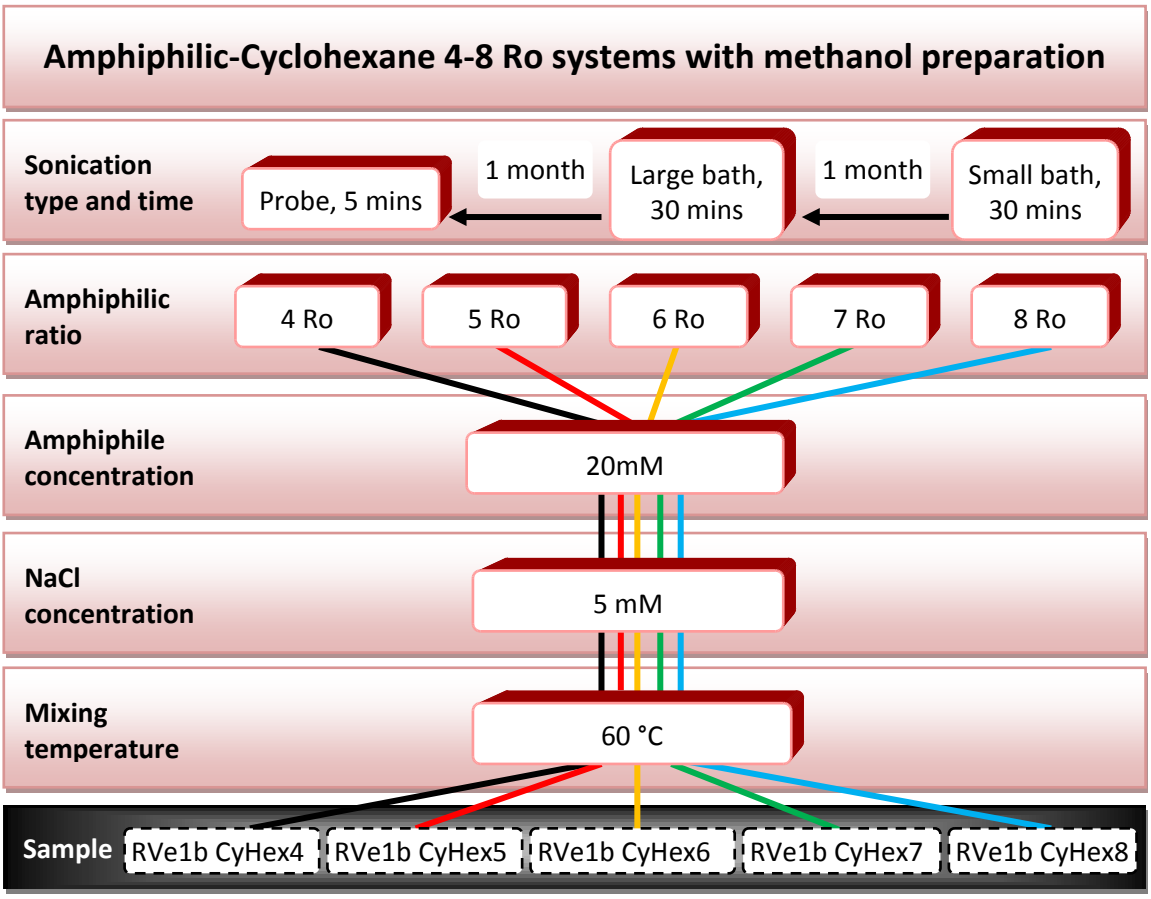

Figure 52: Sample road map illustrating the initial preparation methods for the amphiphilic-cyclohexane 4 to 8 Ro samples that were prepared in methanol.

The use of methanol preparation had shown to promote the formation of giant unilamellar reverse vesicles in the cyclohexane 2.5 Ro samples. Therefore, in an attempt to create the illusive colloidal dispersion of unilamellar reverse vesicles reported by Tung *et al.* (2008), a greater range of amphiphilic ratios were commissioned with methanol preparations; see Figure 52. These showed a range of macroscopic phase behaviours that changed with the strength of sonication as shown in Table 19.

After weak sonication all the samples presented cloudy suspensions, similar to those found in cyclohexane samples with the amphiphilic ratios 2.5 Ro, 3.5 Ro and 4.5 Ro. The strong bath sonication appeared to decrease the size of the structures to produce mainly translucent samples; with 6 Ro and 7 Ro being the first systems to produce an opalescent phase. However, these were still suspensions that settled to form transparent solutions with a transparent fluid precipitant after a couple of weeks. This phase was shaken by hand to produce an opalescent solution which was imaged using TEM. The TEM images in Figures 54, 55, 56, and 57 illustrate the majority of particles were clusters of reverse vesicles (~200-2000 nm cluster diameter) although there were some individual (~100-200 nm in diameter).

The 6 Ro and 7 Ro systems were the first to present colloidal dispersions with the blue hue of strong Tyndall scattering after they were subjected to intense probe sonication; see Figure 53. Microscopy of the 6 Ro system revealed no structures over a micron in size 1 month after probe sonication. However, these colloidal dispersions of unilamellar reverse vesicles were metastable as flocculation caused all particles to settle out of solution within 6 months.

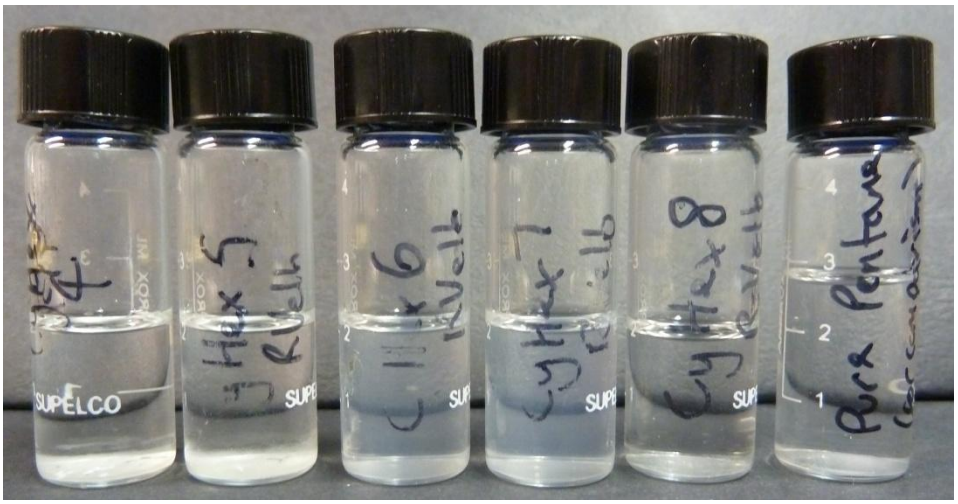

Figure 53: Photograph of macroscopic phase behaviour of samples one month after probe sonication (from left to right); RVe1b 4, RVe1b 5, RVe1b 6, RVe1b 7, RVe1b 8. In comparison, a vial of pure pentane (far right).

As expected the RVe1b CyHex 4 remained as a suspension after probe sonication; which concurs with the phase behaviour of the 3.5 Ro and 4.5 Ro samples studied previously. RVe1b CyHex 5 may be considered a very polydisperse metastable colloidal dispersion system after probe sonication: with a white fluid precipitant forming within hours of probe sonication like a suspension, but some particles taking over a month to settle like a colloidal dispersion. RVe1b CyHex 8 had similar macroscopic phase behaviour to RVe1b CyHex 5 after probe sonication except that more particles were colloids, therefore, after a month the system presented very little precipitation and a strong laser scatter. Fluorescence microscopy of an 8 Ro system (with additional Rhodamine b) indicated the colloidal particles were smaller than the micrometre level; although not entirely conclusive, the lack of prominent Tyndall scattering implied the 8 Ro system was a colloidal dispersion of spherical reverse micelles. This thinking can also be applied to 5 Ro which had the same macroscopic phase behaviour over time to the 8 Ro sample, and therefore, points to the 5 Ro system also containing reverse micelles. Further TEM work on these systems is required in the future to conclusively define the 5 Ro and 8 Ro systems as containing reverse micelles.

4.3.1.4.1 Macroscopic phase behaviour

Sample	Ro	Concentration (mM)	Observations									
			AWS 10/2/2012	1 month AWS (BSS) 22/3/2012	ASS 22/3/2012	1 day ASS 23/3/2012	2 weeks ASS (BPS) 3/4/2012	APS 3/4/2012	5 hours APS 3/4/2012	1 day APS 4/4/2012	1 month APS 1/5/2012	6 months APS 19/9/2012
RVe1b CyHex4	4	20	Cl	T+WFP [O AHS]	Cl	Tr+WFP(some)+SL	T+WGP(some fluidity)+NL [Cl+Fla(w)+WWSL]	Cl+WSL	T+WGP+NL	T+WGP+NL	T+YWGP(wavy pattern)+NL	T+YWGP+NL [T+YWGP+Fla(YW)+NL(only on flakes) AHS]
RVe1b CyHex5	5	20	Cl	T+WFP [O AHS]	Tr	Tr+WFP+WL	T+WGP+WL [Tr+SL AHS]	Tr+SL	Tr+WFP+SL	Tr+WFP+SL	Tr+YWGP+WL	T+YWGP+NL [T+YWGP+Fla(YW) +NL(only on flakes) AHS]
RVe1b CyHex6	6	20	Cl	T+TFP [Tr AHS]	Tr	Tr+SL	T+TFP+NL [Tr+SL AHS]	O+B+SL	O+B+SL	O+B+SL	O+B+SL	T+WGP+NL [T+Fla(w)+WGP+NL (except flakes) AHS]
RVe1b CyHex7	7	20	Cl	T +WFP [O AHS]	O	O+WFP+SL	T+TFP+WL [O+SL AHS]	O+B+SL	O+B+SL	O+B+SL	O+B+SL	T+WGP+NL [T+Fla(w)+WGP+NL (except flakes) AHS]
RVe1b CyHex8	8	20	Cl	T+TFP [O AHS]	Tr	T+TFP+NL	T+TFP+NL [Tr+WL AHS]	Tr	Tr+WFP(some)+SL	Tr+WFP(some)+SL	Tr+WFP(some)+SL	T+TFP+NL

Table 19: Table presenting the changes in phase behaviour for samples prepared with methanol for various amphiphilic ratios in cyclohexane.

4.3.1.4.2 TEM

Sample Number	Micrograph	Sample and Micrograph Description
RVe1b **7** **CyHex**	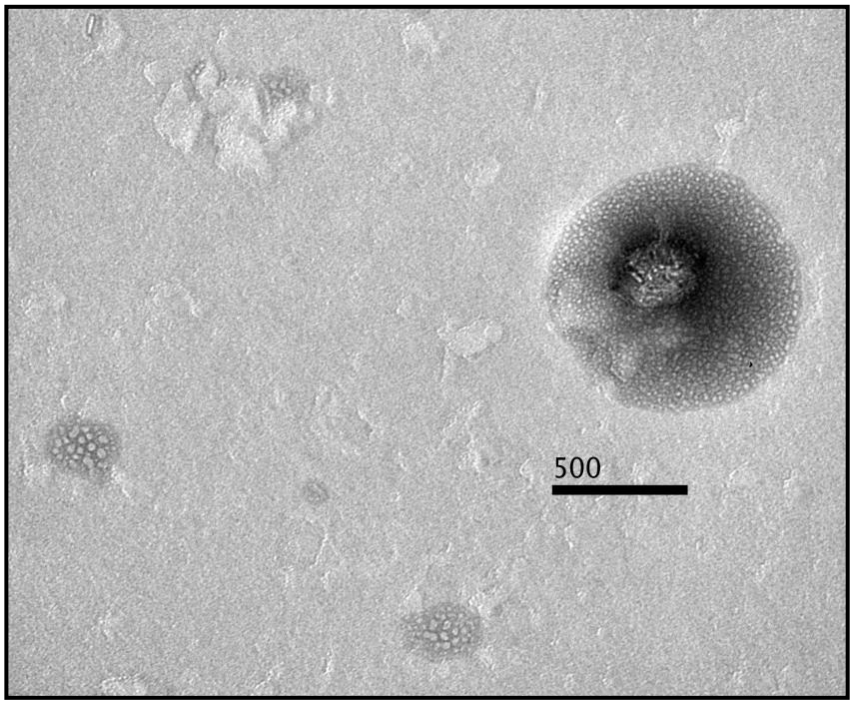	**Figure 54:** 7 Ro cyclohexane, Digital TEM image **Date of Micrograph**: 29/3/2012 **TEM grid created:** 28/3/2011 **Sample description**: T+TFP+WS [O+SL AHS] 1 week after strong water bath sonication but before probe sonication. Shaken. **Micrograph description**: Shape distribution – Irregular spherical features in irregular clusters. Size distribution – ~100 nm and ~200-900 nm clusters. These spherical clusters contain numerous irregular spheres.

Sample Number	Micrograph	Sample and Micrograph Description
RVe1b 7 CyHex	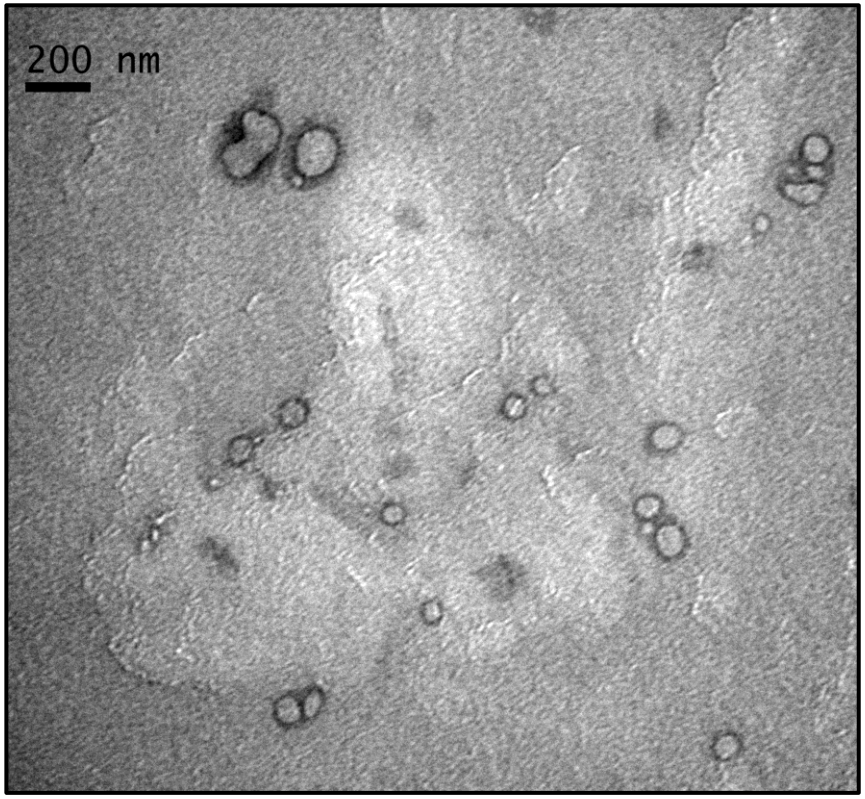	**Figure 55:** 7 Ro cyclohexane, Digital TEM image **Date of Micrograph**: 29/3/2012 **TEM grid created:** 28/3/2011 **Sample description**: T+TFP+WS [O+SL AHS] 1 week after strong water bath sonication but before probe sonication. Shaken. **Micrograph description**: Shape distribution – Irregular spherical features, some in irregular clusters. Size distribution – ~100-200 nm particles and ~200-300 nm clusters. These features have distinct internal walls and compartment, with the external surface often being quite faint. The small spherical clusters contain a few irregular spheres.

Sample Number	Micrograph	Sample and Micrograph Description
RVe1b 7 CyHex	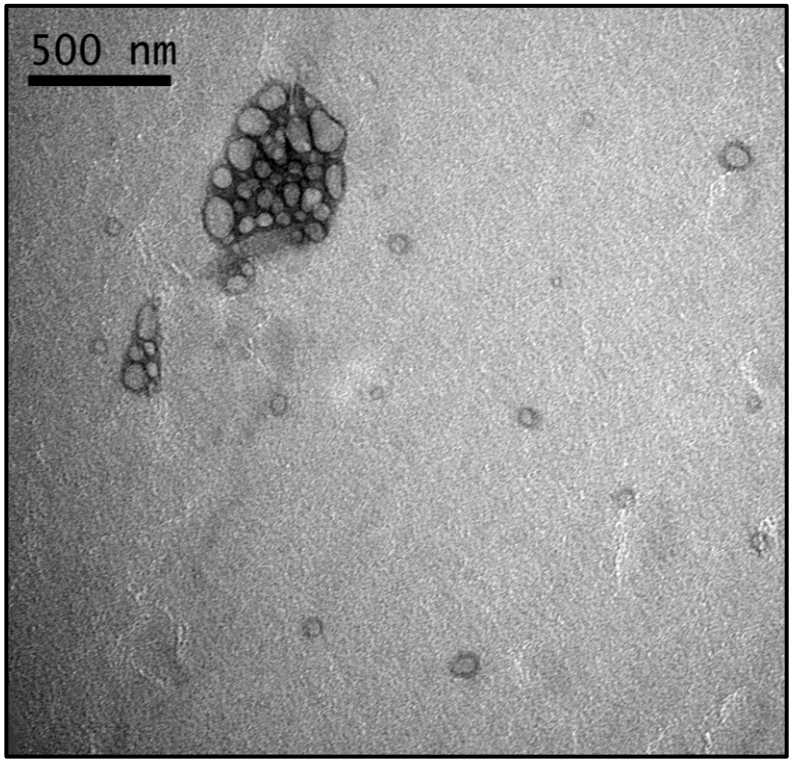	**Figure 56:** 7 Ro cyclohexane, Digital TEM image **Date of Micrograph**: 29/3/2012 **TEM grid created:** 28/3/2011 **Sample description**: T+TFP+WS [O+SL AHS] 1 week after strong water bath sonication but before probe sonication. Shaken. **Micrograph description**: Shape distribution – Irregular spherical features, some in irregular clusters. Size distribution – ~100-200 nm particles and ~200-500 nm clusters. These features have distinct internal walls and compartments, with the external surface often being quite faint. The clusters contain a spheres that are often more irregular in shape than their independent counterparts.

Sample Number	Micrograph	Sample and Micrograph Description
RVe1b 7 CyHex	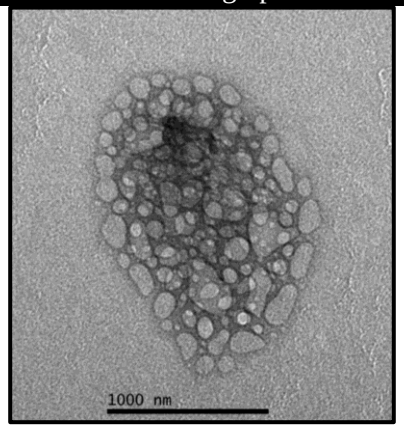 (a) 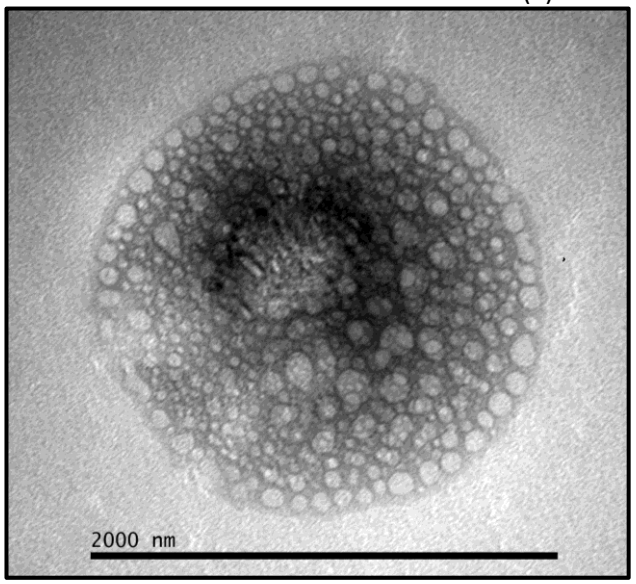 (b)	**Figure 57:** 7 Ro cyclohexane, Digital TEM image **Date of Micrograph**: 29/3/2012 **TEM grid created:** 28/3/2011 **Sample description**: T+TFP+WS [O+SL AHS] 1 week after strong water bath sonication but before probe sonication. Shaken. **Micrograph description**: Shape distribution – Spherical, irregular and elongated spherical features and clusters. Size distribution – ~100-200 nm particles and ~1500-2000 nm clusters. These features have distinct internal walls and compartments, with the external boundaries merging with others in the cluster.

4.3.1.5 Summary of cyclohexane systems

No colloidal systems consisting of prevalent unilamellar reverse vesicles were found at the amphiphilic ratios (2.5 Ro and 3.5 Ro) that had been reported by Tung *et al.* (2008) to form this type of system in cyclohexane. However, in the 2.5 Ro and 3.5 Ro systems metastable giant unilamellar vesicles were formed; which presented as a limited number in those systems without methanol preparation and became dominate in the methanol prepared 2.5 Ro samples.

All samples in the 2.5, 3.5 and 4.5 Ro amphiphilic ratio range produced turbid suspensions that precipitated a white precipitant which would gradually transform into a transparent, and then yellow, gel with time. The white precipitant was indicative of individual, micrometre sized, particles or clusters of; reverse vesicles, compound micelles or liquid crystal precipitants. The intermediate precipitant stages often presented a range of giant structures encapsulating various particles (the structure of which depended on the particles presenting in the initial white precipitant) and the final yellow gel precipitant was often an amorphous liquid crystal.

The systems presenting unilamellar reverse vesicular colloidal dispersions, with prominent Tyndall scattering, were limited to the amphiphilic ratios higher than 6 Ro. To produce colloidal dispersions of nanometre sized reverse vesicles the systems required methanol preparation.

An increase in sonication intensity was shown to decrease the particle size. In suspensions this reduction in particle surface area decreased friction with the solvent and increased the settling rate. However, in systems that could produce nanometre sized particles strong sonication would produce relatively long lived colloidal dispersions.

4.3.2 Heptane systems

The phase behaviour of a methanol prepared 2.5 Ro heptane system presented a suspension for all sonication intensities, see Table 20. Fluorescence imaging 1 day after sonication presented dense 2-3 μm particles; see Figure 60. Microscopy of the yellow gel precipitant dispersed by hand shaking six weeks after being weakly sonicated showed large clusters (up to ~55 μm) of spherical particles (~3 μm to 20 μm); see Figures 58 and 59. These particles did not appear to contain bilayers, had irregular surfaces, and were surrounded by a halo of smaller spherical particles (~1 μm). The initial particles were too large to be individual spherical micelles; therefore, this system contained 2-3 μm compound micelles which quickly merged to form larger compound micelles which aggregated into clusters with time.

4.3.2.1 Macroscopic phase behaviour

Sample	Ro	Concentration (mM)	Observations										
			AWS 6/2/2012	1 day AWS 7/2/2012	6 weeks AWS 22/3/2012	ASS 22/3/2012	2 weeks ASS (BPS) 3/4/2012	APS 3/4/2012	5 hours APS 3/4/2012	1 day APS 4/4/2012	1 month APS 1/5/2012	6 months APS 19/9/2012	2 years 2 months APS 6/6/2014
RVe1b T2Hep	2.5	30	Cl	Tr+WGP	T+YGP	Tr+YGP	T+YGP+NL [Tr+YGP+WL AHS]	Cl+YGP +WSL	T+YGP+ NL	T+YGP+ NL	T+YGP+NL	T+YGP+NL [Tr+YGP+W SL AHS]	T+YGP+NL

Table 20: Table presenting the changes in phase behaviour for the RVe1b heptane sample.

4.3.2.2 Microscopy

Sample Number	Micrograph	Sample and Micrograph Description
RVe1b T2 Hep	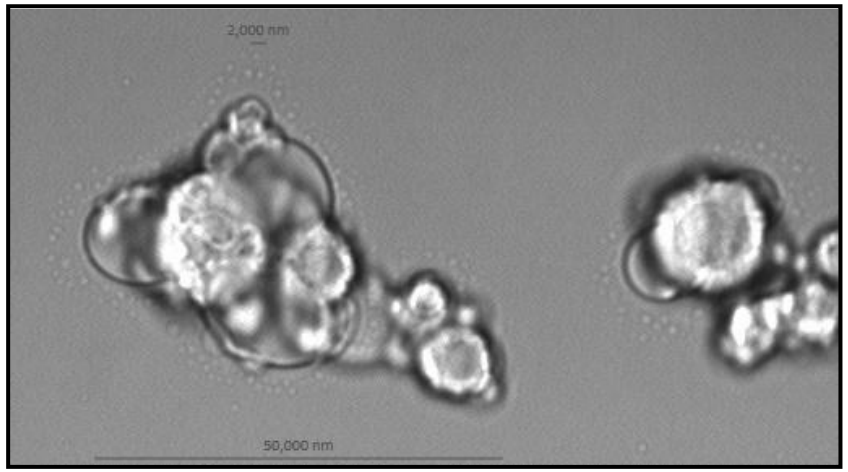 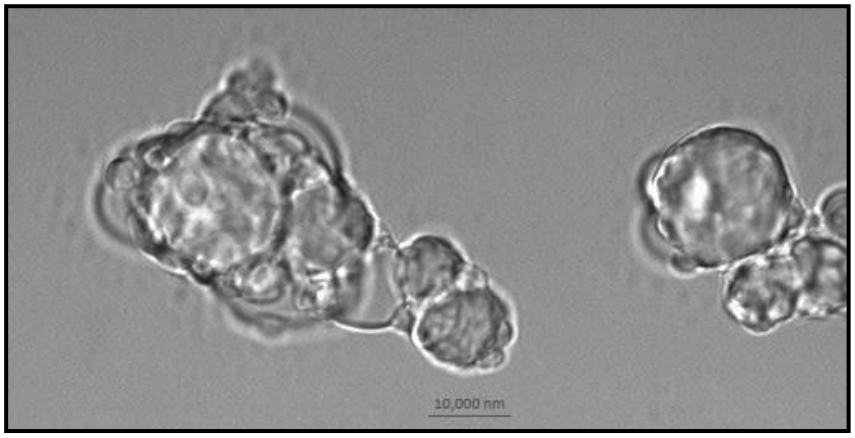	**Figure 58:** 2.5 Ro heptane micrograph **Date of Micrograph**: 21/3/2012 **Sample description**: T+YGP+NL [Tr+YGP+WL AHS] 1 month after weak-water bath sonication and before both strong-water bath and probe sonication. Shaken Two micrographs of the same particles, taken at different z-axis layers **Micrograph description**: Shape distribution – Spherical to irregular spheroid for individual structures. Cluster shapes irregular. Size distribution – ~1 μm to 20 μm individual particles. Clusters up to ~55 μm. Non-clustered particles are spherical and <3 μm. The clusters contain large (~3 μm to 20 μm) spherical to irregular spheroid particles that have irregular surfaces that may be a particle feature or due to cementation of the cluster. They are surrounded by a mesh of small (<2 μm) spherical particles.

Sample Number	Micrograph	Sample and Micrograph Description
RVe1b **T2 Hep**	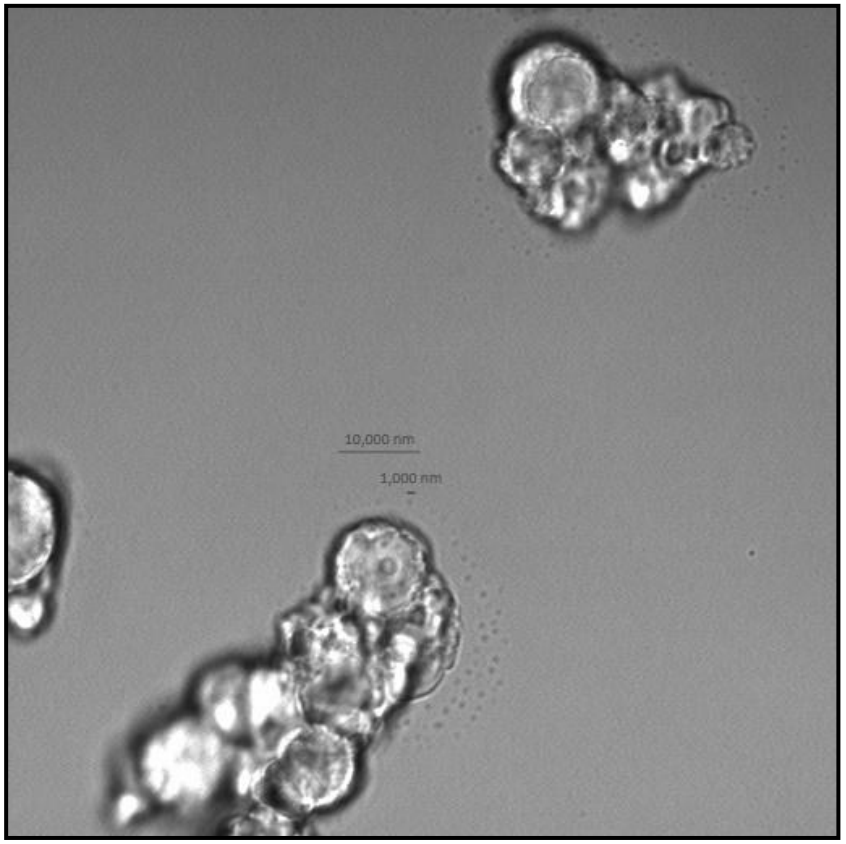	**Figure 59:** 2.5 Ro heptane micrograph **Date of Micrograph**: 21/3/2012 **Sample description**: T+YGP+NL [O(s)+YGP+WL AHS] 1 month after weak-water bath sonication and before both strong-water bath and probe sonication. Shaken **Micrograph description**: Shape distribution – Spherical to irregular spheroid for individual structures. Cluster shapes irregular. Size distribution – ~1 μm to 15 μm individual particles. Clusters up to ~55 μm. The clusters contain large (~3 μm to 20 μm) spherical to irregular spheroid particles that have irregular surfaces that may be a particle feature or due to cementation of the cluster. Clusters are surrounded by a mesh of small (<~2μm) spherical particles. With the overlapping nature of these particles, it is difficult to be confident of any morphological features for individual particles. It is not possible to determine morphological features for the mesh of small particles surrounding the clusters in this image.

4.3.2.3 Laser scanning confocal fluorescent microscopy

Sample Number	Micrograph	Sample and Micrograph Description
RVe1b(fl) T2rep	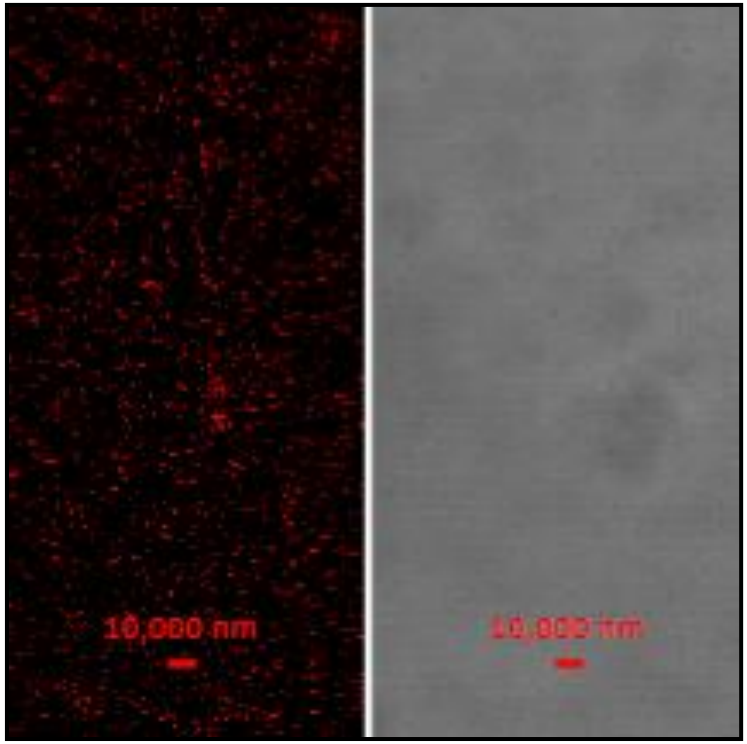	**Figure 60:** 2.5 Ro heptane fluorescence micrograph **Sample description**: Tr 1 day after probe sonication. **Micrograph description**: Size distribution – ~1-3 μm. These particles appear to be dense and uniformly distributed.

4.3.3 Hexane systems

4.3.3.1 Hexane 2.5 Ro systems

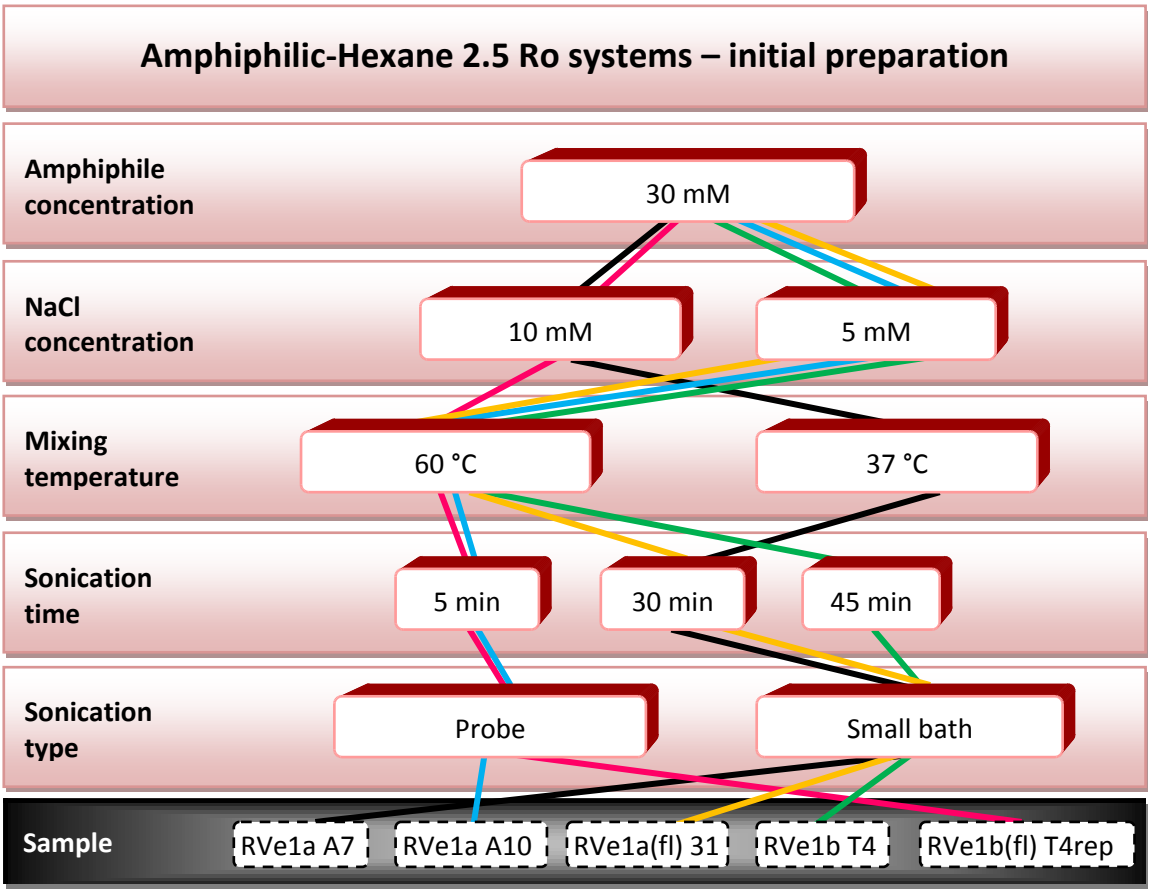

Figure 61: Sample road map illustrating the initial preparation methods for the amphiphilic-hexane 2.5 Ro samples.

The temporal changes in macroscopic phase behaviour of the hexane 2.5 Ro binary amphiphilic mixtures are shown in Tables 21 and 22. All the samples, regardless of sonication type or inclusion of methanol preparation (see Figure 61), were suspensions that rapidly begin to precipitate out the amphiphilic mixtures.

The samples prepared without methanol – RVe1a 10 and RVe1a 7 – differed slightly in their macroscopic phase behaviour over time. RVe1a 10 sample seemed to initially precipitate a white solid rather than the more fluid precipitant viewed in RVe1a 7; this may be due to the sonication differences used in the sample preparation. RVe1a 7 had a low sonication intensity that may have not affected the large particles, and caused slower sedimentation due to their surface area, which in turn made the normal white fluid precipitant. The high sonication intensity of the probe sonication used for RVe1a 10 may have caused particles to break up, causing faster settling due to decreased surface area drag resistance.

Fluorescence imaging of the precipitant (RVe1a(fl) 31) after 1 day of standing of these samples prepared without methanol show a bicontinuous gel; see Figure 65. This indicates that there

may be short lived multilamellar vesicles that quickly merge to form a bicontinuous precipitant or the suspended particles are already bicontinuous in nature directly after sonication.

Fluorescence microscopy of a methanol prepared system 1 day after probe sonication showed the precipitant consisted of some compartmented particles adhered to large, dense particles; see Figure 64. Microscopy of the white gel precipitant dispersed by hand shaking of the methanol prepared system showed the same large clusters (up to ~55 μm) of spherical particles (~3 μm to 20 μm) that are seen in heptane system (e.g. Figure 58) after the same six weeks standing duration; see Figures 62 and 63. The nature of the larger particles was reminiscent of a bicontinuous structure and the irregular clustering indicates that the bonds between particles are strong. Therefore it is likely that this system makes unstable lamellar system which quickly merges into a stable bicontinuous phase, leaving some larger (reverse vesicle type) compartments adhered to the outside of the bicontinuous particles.

4.3.3.1.1 Macroscopic phase behaviour

Sample	Ro	Concentration (mM)	Observations					
			APS 8/11/2010	3 hours APS 8/11/2010	After additional NaCl 17/11/2010	3 months APS 2/2/2011	1 yr 5 months APS 22/3/2012	1 yr 10 months APS 21/9/2012
RVe1a A10	2.5	30	Cl	T+WSP	Cl+NaClCry (W)	T+NaClCry(W)	**Evaporated:** NaClCry(Y)	**Evaporated:** NaClCry(Y)
			BWS 20/1/2011	AWS 20/1/2011	1 hour AWS 20/1/2011	2 weeks AWS 2/2/2011	1 yr 2months AWS 22/3/2012	1yr 8 months AWS 25/9/2012
RVe1a A7	2.5	30	Opa AHS	Opa	Cl+WSP	T+WGP	T+YGP [Cl+YGP AHS]	T+YGP+NL [Cl+YGP+SL AHS]

Table 21: Table presenting the changes in phase behaviour for RVe1a hexane 2.5 Ro samples.

Sample	Ro	Concentration (mM)	Observations										
			AWS 6/2/2012	1 day AWS 7/2/2012	6 weeks AWS 22/3/2012	ASS 22/3/2012	2 weeks ASS (BPS) 3/4/2012	APS 3/4/2012	5 hours APS 3/4/2012	1 day APS 4/4/2012	1 month APS 1/5/2012	6 months APS 19/9/2012	2 years 2 month APS 6/6/2014
RVe1b T4Hex	2.5	30	Cl	Tr+WGP	T+WGP	Cl+WGP	T+YGP(grainy in places)+NL [Tr+YGP(grainy in places)+WL AHS]	Tr+YGP+WL	T+YWGP+NL	T+YWGP+NL	T+YGP+NL	T+YGP+NL [Tr+YGP+WSL]	T+YGP+NL

Table 22: Table presenting the changes in phase behaviour for RVe1b hexane 2.5 Ro samples.

4.3.3.1.2 Microscopy

Sample Number	Micrograph	Sample and Micrograph Description
RVe1b **T4 Hex**	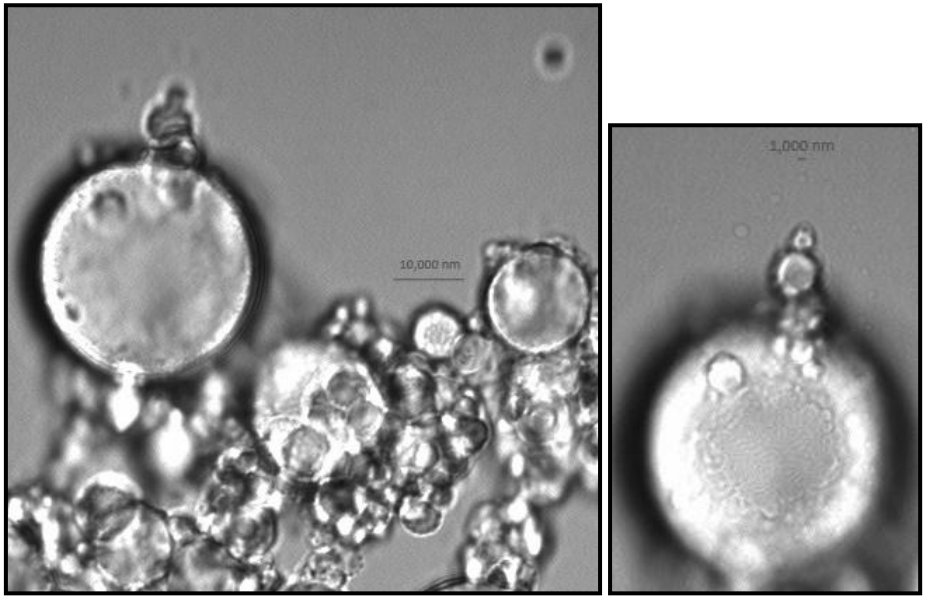 	**Figure 62:** 2.5 Ro hexane micrograph **Date of Micrograph**: 21/3/2012 **Sample description**: T+WGP 6 weeks after weak-water bath sonication and before both strong-water bath and probe sonication. Shaken **Micrograph description**: Shape distribution – Spherical and irregular spheroids as individual structures. Clusters irregular. Size distribution – ~1 μm to 30 μm individual particles. >70 μm clusters. There are no clearly defined walls and the surfaces appear irregular. The largest particle appears to have bicontinuous structure. The small <2 μm particles surround the clusters to around 5 μm from the cluster boundary

Sample Number	Micrograph	Sample and Micrograph Description
RVe1b T4 Hex	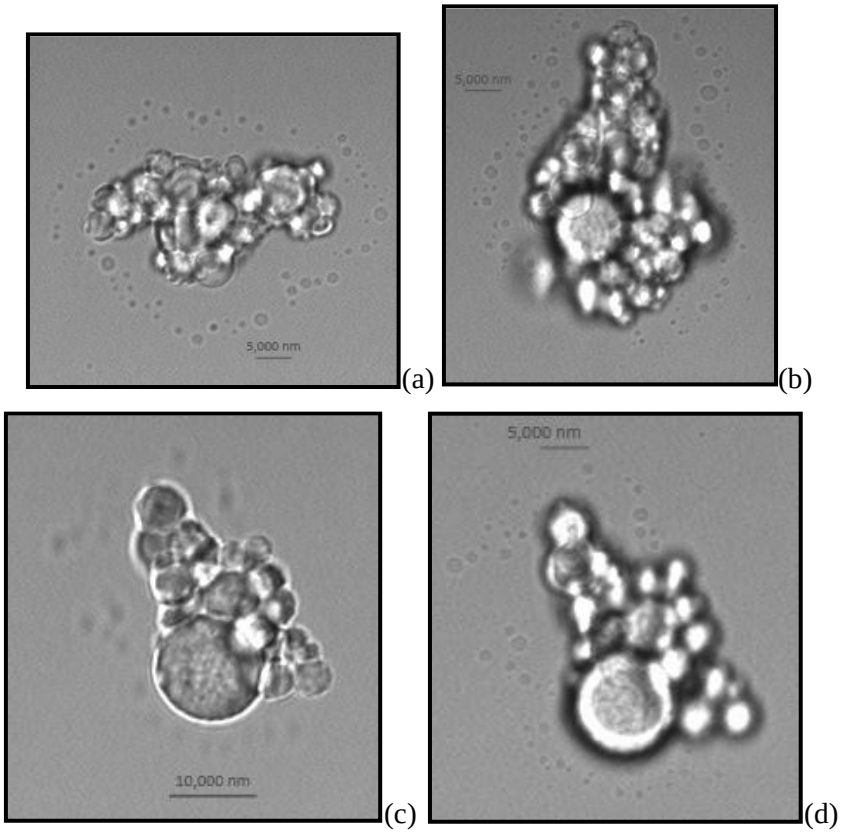 (a) (b) (c) (d)	**Figure 63:** 2.5 Ro hexane micrograph **Date of Micrograph**: 21/3/2012 **Sample description**: T+WGP 1 month after weak-water bath sonication and before both strong-water bath and probe sonication. Shaken **Micrograph description**: Shape distribution – Spherical and irregular spheroids as individual structures. Clusters irregular. Size distribution – ~1 μm to 6 μm individual particles. Up to 35 μm clusters. There are no clearly defined walls and the surfaces appear irregular. The largest particle appears to have bicontinuous structure. The small <2 μm particles surround the clusters to around 5 μm from the cluster boundary

4.3.3.1.3 Laser scanning confocal fluorescent microscopy

Sample Number	Micrograph	Sample and Micrograph Description
RVe1b (fl) T4rep	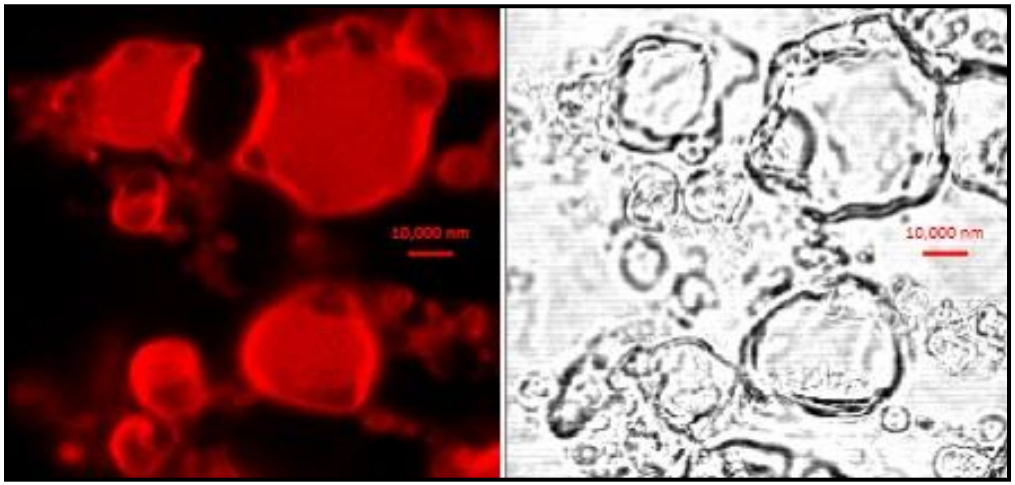	**Figure 64:** 2.5 Ro hexane (with methanol prep) fluorescence micrograph **Sample description**: Tr+WGP 1 day after probe sonication. Shaken. **Micrograph description**: Shape distribution – spherical to irregular spheroids. Size distribution – ~5-40 μm. Most of the larger particles appear amorphous with some of the smaller particles having vesicular features. Even though this system was re-disbursed into solution by hand shaking, many of the particles remain merged; sharing walls.

Sample Number	Micrograph	Sample and Micrograph Description
RVe1a (fl) 31	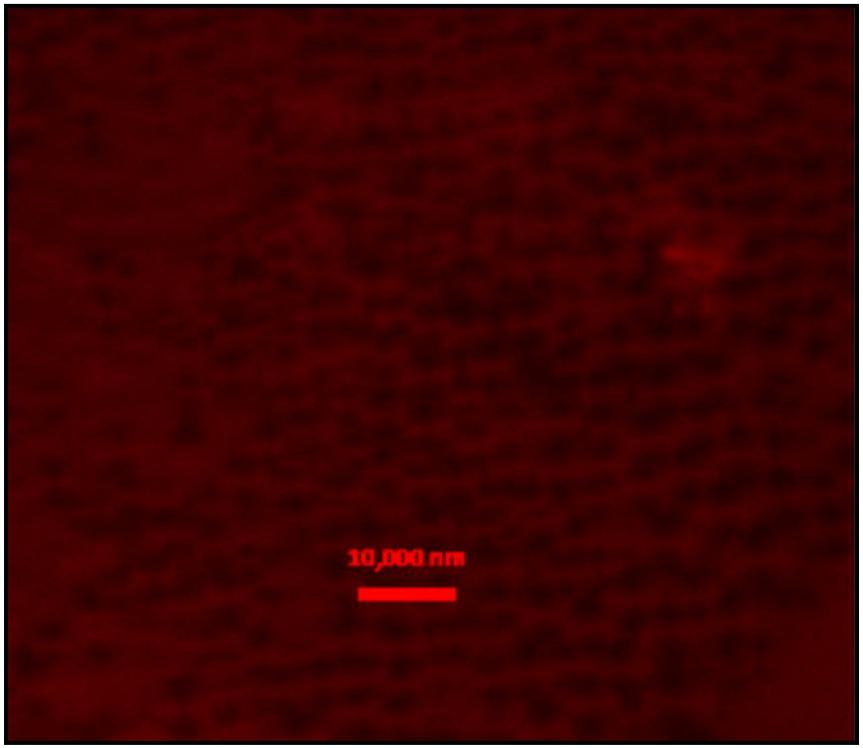	**Figure 65:** 2.5 Ro hexane (without methanol prep) fluorescence micrograph **Sample description**: Tr+WGP 1 day after probe sonication. Shaken. **Micrograph description**: Bicontinuous gel – walls are fluorescent.

4.3.3.2 Hexane 3.5 Ro, 4.5 Ro and 7 Ro systems

The suspensions formed from hexane 3.5 Ro and 4.5 Ro binary amphiphilic mixtures (without methanol preparation) settled rapidly; see Tables 23 and 24. Fluorescence microscopy, after 1 day, revealed no structures in solution and after being shaken (by hand) a rapidly coalescing, amorphous liquid crystal precipitant was seen; see Figure 66. The TEM images taken at temperatures down to -60 °C indicated no change in this phase.

A 7 Ro hexane system prepared using methanol and probe sonication produced complete phase separation with a yellow gel precipitant, which was interpreted to reflect the same liquid crystal precipitants seen in the 3.5 Ro and 4.5 Ro systems prepared without methanol.

4.3.3.3 Summary of hexane systems

The equilibrium phase of the 2.5 Ro hexane systems was bicontinuous particles. Amphiphilic ratios at 3.5 Ro or above produced phase separated liquid crystal precipitants.

4.3.3.3.1 Macroscopic phase behaviour

Sample	Ro	Concentration (mM)	Observations					
			APS 8/11/2010	3 hours APS 8/11/2010	After additional NaCl 17/11/2010	3 months APS 2/2/2011	1 yr 5 months APS 22/3/2012	1 yr 10 months APS 21/9/2012
RVe1aB11	3.5	30	Cl	T+WSP	Cl+NaClCry (W)	T+NaClCry(W)	T+NaClCry(Y)	T+NaClCry(Y) [Cl+NaClCry(Y)+SL AHS]
			BWS 20/1/2011	AWS 20/1/2011	1 hour AWS 20/1/2011	2 weeks AWS 2/2/2011	1 yr 2months AWS 22/3/2012	1yr 8 months AWS 25/9/2012
RVe1aB8	3.5	30	Opa AHS	Opa	Cl+WSP	T+WGP	T+YGP [Cl+YGP AHS]	T+YGP+Transparent crystals ~1mm long+NL [Tr+YGP+WL AHS]

Table 23: Table presenting the changes in macroscopic phase behaviour for RVe1a Hexane 3.5 Ro samples.

Sample	Ro	Concentration (mM)	Observations					
			APS 8/11/2010	3 hours APS 8/11/2010	After additional NaCl 17/11/2010	3 months APS 2/2/2011	1 yr 5 months APS 22/3/2012	1 yr 10 months APS 21/9/2012
RVe1aC12	4.5	30	Cl	T+WSP	Cl+NaClCry (W)	T+NaClCry(W)	**Evaporated:** NaClCry(Y)	**Evaporated:** NaClCry(Y)
			BWS 20/1/2011	AWS 20/1/2011	1 hour AWS 20/1/2011	2 weeks AWS 2/2/2011	1 yr 2months AWS 22/3/2012	1yr 8 months AWS 25/9/2012
RVe1aC9	4.5	30	Ph: Top 1/10 Cl + Lower 9/10 Opa AHS	Opa	Cl+WSP	T+Mot(TFP + some WGP)	T+YGP [Cl+YGP AHS]	T+YGP+Transparent crystals ~1mm long+NL [Tr+YGP+ Transparent crystals ~1mm long+WL AHS]

Table 24: Table presenting the changes in macroscopic phase behaviour for RVe1a Hexane 4.5 Ro samples.

4.3.3.3.2 Laser scanning confocal fluorescent microscopy

Sample Number	Micrograph	Sample and Micrograph Description
RVe1a (fl) 33	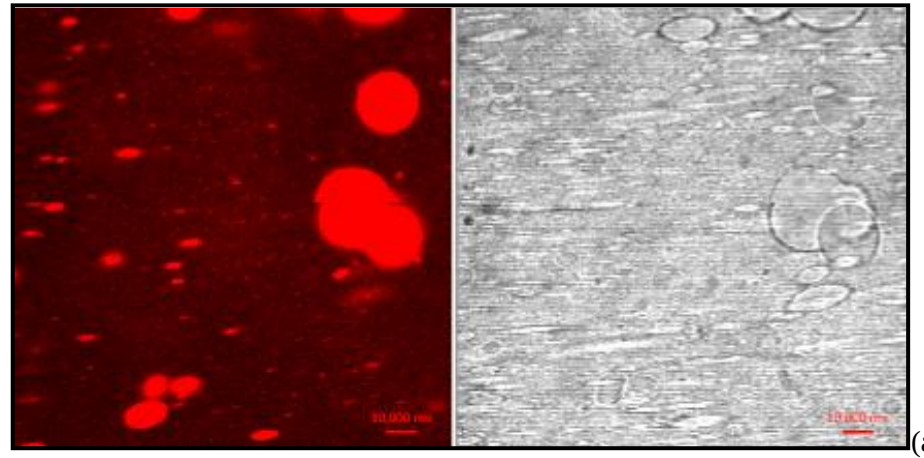 (a) 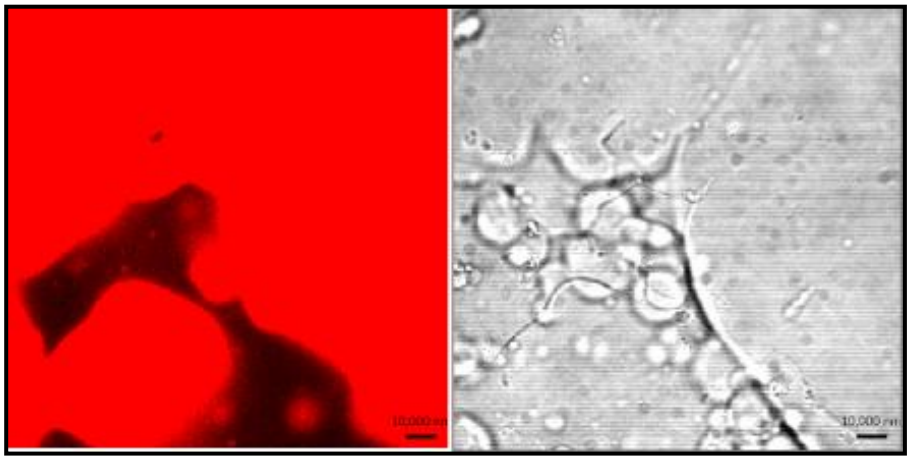 (b)	**Figure 66:** 4.5 Ro hexane fluorescence micrograph **Sample description**: T+WGP 1 day after probe sonication. Shaken. **Micrograph description**: Shape distribution – spherical to irregular spheroids. Size distribution – ~2 μm to >100 μm. These are very dense amorphous particles. They rapidly coalesce as can be seen by the fast movement of the particles in image (**a)** and the resulting huge >100 μm dense phase illustrated in image (**b)**.

4.3.4 Pentane

4.3.4.1 Pentane 2.5 Ro, 3.5 Ro and 4.5 Ro systems

As indicated in Tables 25, 26 and 27 the 2.5 Ro, 3.5 Ro and 4.5 Ro systems presented suspensions with rapid settling rates. Fluorescence microscopy of the 2.5 Ro system revealed a phase separated liquid crystalline precipitant; see Figure 72.

The TEM images of the 3.5 Ro systems revealed a lamellar system of stacked sheets at relatively high temperatures (between room temperature and -30 °C); see Figure 67. However, a reduction in temperature to -95 °C resulted in a phase transition to ~ 50 nm spherical micelles; see Figure 68. Microscopy of this system after a yellow gel had formed indicated an amorphous liquid crystalline precipitant.

The precipitant of the 4.5 Ro systems was interesting as the white precipitant transformed into a heterogeneous state of a white gel with dispersed, macroscopic, transparent spheres. This precipitant remained in this phase for over 3 years without forming the common yellow gel phase. Microscopy of this phase after being dispersed into solution by hand shaking shows a background of 1-2 μm particles that probably formed the white gel and huge spheres (hundreds of micrometres across) that have a bicontinuous structure that probably formed the macroscopic transparent spheres; see Figures 69, 70 and 71.

4.3.4.2 Pentane 7 Ro

A 7 Ro pentane system prepared using methanol and probe sonication produced complete phase separation with a yellow gel precipitant; implying a liquid crystal precipitant. This would need to be confirmed with future experiments.

4.3.4.3 Summary of RVe1a pentane systems

Although all pentane systems settle out of solution quickly in the ratio ranges studied there were a range of microscopic phase behaviours. At room temperature for increased amphiphilic ratios the phase changed from: a phase separated liquid crystal, to stacked lamellar sheets, to a stable heterogeneous bicontinuous phase, and at the highest ratio is theorised to have returned back to a phase separated liquid crystal phase. Temperature reduction was also shown to change the structure of some systems (3.5 Ro) when very low temperatures (-95 °C) were reached.

4.3.4.3.1 Macroscopic phase behaviour

Sample	Ro	Concentration (mM)	Observations					
			APS 8/11/2010	3 hours APS 8/11/2010	After additional NaCl 17/11/2010	3 months APS 2/2/2011	1 yr 5 months APS 22/3/2012	1 yr 10 months APS 21/9/2012
RVe1a A16	2.5	30	Cl	T+WSP	Cl+NaClCry (W)	T+NaClCry(W)	**Evaporated:** NaClCry(Y)	**Evaporated:** NaClCry(Y)
			BWS 20/1/2011	**AWS 20/1/2011**	**1 hour AWS 20/1/2011**	**1 week AWS 2/2/2011**	**1 yr 2months AWS 22/3/2012**	**1yr 8 months AWS 25/9/2012**
RVe1a A13	2.5	30	T+WSP [Opa+WSP AHS]	Opa + WSP(a little)	Cl+WSP	T+WSP(1 ml volume)	T+YGP [Cl+YGP AHS]	T+YGP+Transparent crystals ~1mm long+NL [Tr+YGP+ Transparent crystals ~1mm long+WL AHS]

Table 25: Table presenting the changes in phase behaviour for RVe1a pentane 2.5 Ro samples.

Sample	Ro	Concentration (mM)	Observations					
			APS 8/11/2010	3 hours APS 8/11/2010	After additional NaCl 17/11/2010	3 months APS 2/2/2011	1 yr 5 months APS 22/3/2012	1 yr 10 months APS 21/9/2012
RVe1a B17	3.5	30	Cl	T+WSP	Cl+NaClCry (W)	T+NaClCry(W)	T+NaClCry(Y)	T+ NaClCry(Y)+NL [Tr+ NaClCry(Y)+SL AHS]
			BWS 20/1/2011	**AWS 20/1/2011**	**1 hour AWS 20/1/2011**	**1 week AWS 2/2/2011**	**1 yr 2months AWS 22/3/2012**	**1yr 8 months AWS 25/9/2012**
RVe1a B14	3.5	30	T+WSP [Opa+WSP AHS]	Opa + WSP(a little)	Tr+WSP	T+Mot(TGP + some WGP)	T+YGP [Cl+YGP AHS]	T+YGP+Transparent crystals ~1mm long+NL [Tr+YGP+ Transparent crystals ~1mm long+WL AHS]

Table 26: Table presenting the changes in phase behaviour for RVe1a Pentane 3.5 Ro samples.

Sample	Ro	Concentration (mM)	Observations					
			APS 8/11/2010	3 hours APS 8/11/2010	After additional NaCl 17/11/2010	3 months APS 2/2/2011	1 yr 5 months APS 22/3/2012	1 yr 10 months APS 21/9/2012
RVe1aC18	4.5	30	Cl	T+WSP	Cl+NaClCry (W)	T+NaClCry(W)	**Evaporated:** NaClCry(WY)	**Evaporated:** NaClCry(Y)

			BWS 20/1/2011	AWS 20/1/2011	1 hour AWS 20/1/2011	1 week AWS 2/2/2011	1 yr 2months AWS 22/3/2012	1yr 8 months AWS 25/9/2012	3 years 5 months AWS 6/6/2014
RVe1aC15	4.5	30	T+WSP [Opa+WSP AHS]	Opa + WSP(a little)	Cl+WSP	T+WSP(grainy)	T+Mot(WGP+ some TGP spheres) [Cl+ Mot(WGP+ some TGP spheres)+Fla(w) AHS]	T+Mot(WGP+ some TGP spheres)	T+Mot(WGP+ some TGP spheres)

Table 27: Table presenting the changes in phase behaviour for RVe1a pentane 4.5 Ro samples.

4.3.4.3.2 Microscopy

Sample Number	Micrograph	Sample and Micrograph Description
RVe1a 14	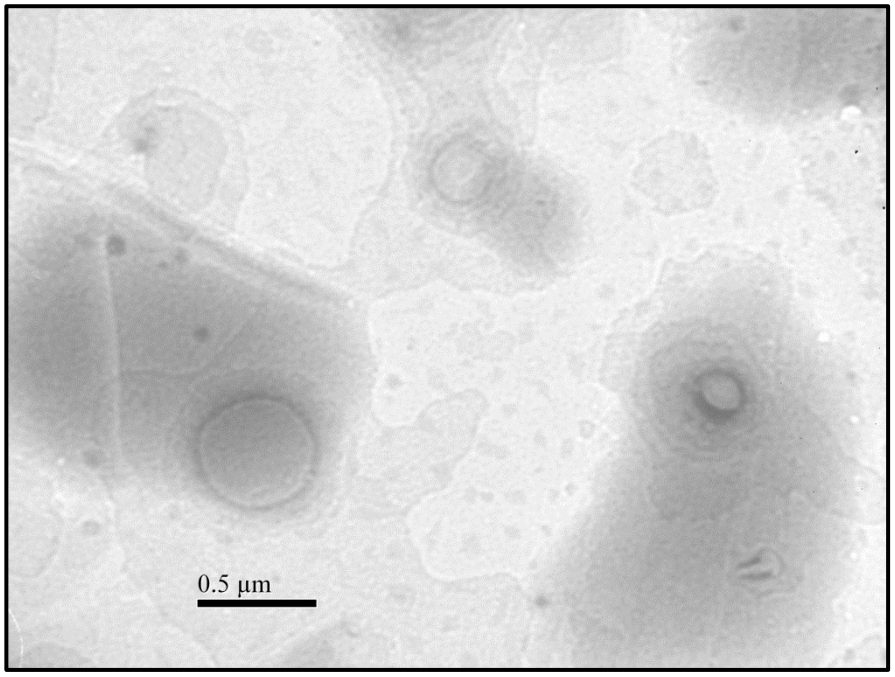	**Figure 67:** 3.5 Ro pentane, Digital TEM micrograph **Date of Micrograph**: 28/1/2011 **TEM grid created:** 27/1/2011 **Temperature:** -30°C **Sample description**: Cl After probe sonication. **Micrograph description**: This image shows a range of stacked bilayer sheets.

Sample Number	Micrograph	Sample and Micrograph Description
RVe1a 14	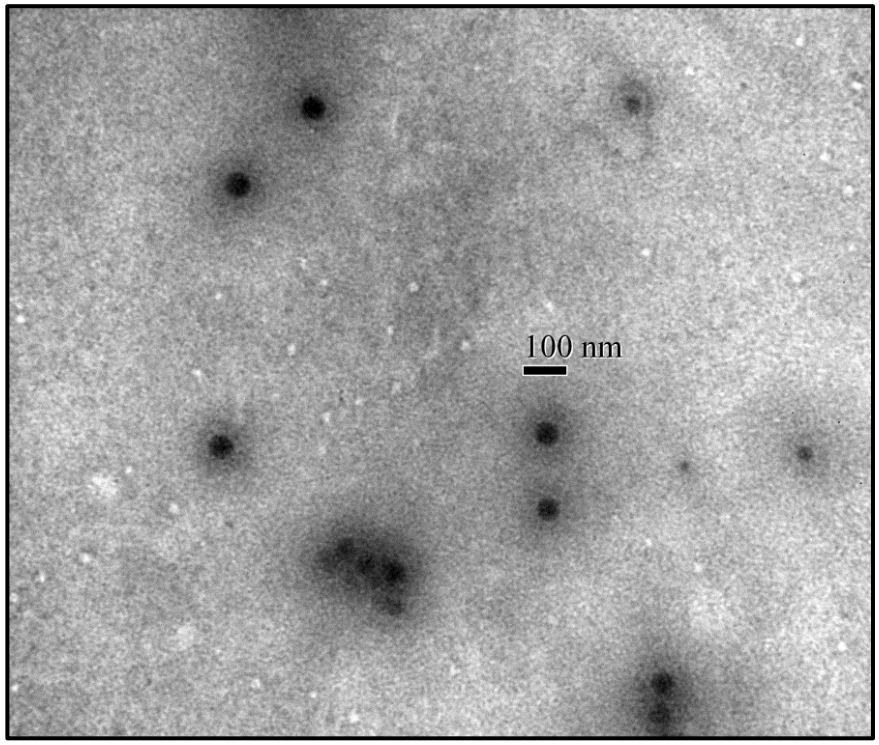	**Figure 68:** 3.5 Ro pentane, Digital TEM micrograph **Date of Micrograph**: 28/1/2011 **TEM grid created:** 27/1/2011 **Temperature:** -95°C **Sample description**: Cl After probe sonication. **Micrograph description**: Shape distribution – Spherical. Size distribution – ~50-60 nm. These structures appear to be spherical micelles.

Sample Number	Micrograph	Sample and Micrograph Description
RVe1a 15	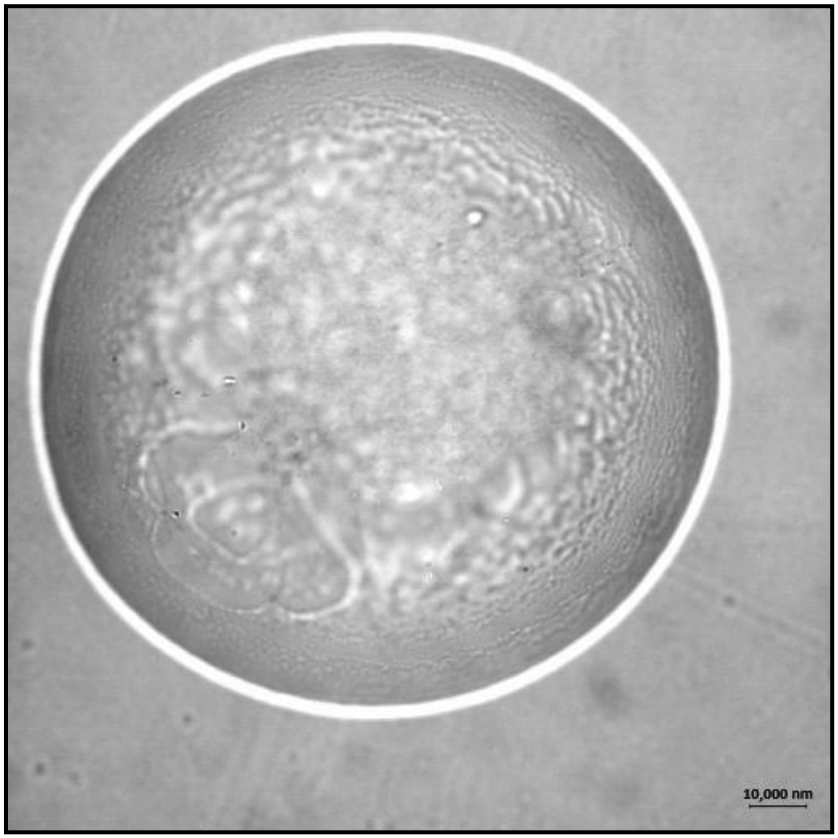	**Figure 69:** 4.5 Ro pentane micrograph **Date of Micrograph**: 17/5/2012 **Sample description**: T+Mot(WGP+ some TGP spheres) 1 year 4 month after weak sonication. Shaken. **Micrograph description**: Shape distribution – Spherical aggregates. Size distribution – Background homogeneous 1-2 μm particles. Large particle ~100 μm. All background aggregates are too small to distinguish morphological features and are out of focus in this image. The large particle appears to have a bicontinuous structure or formed of concentric layers.

Sample Number	Micrograph	Sample and Micrograph Description
RVe1a 15	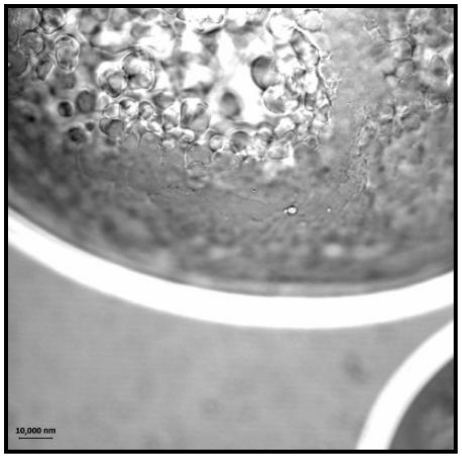 (a) 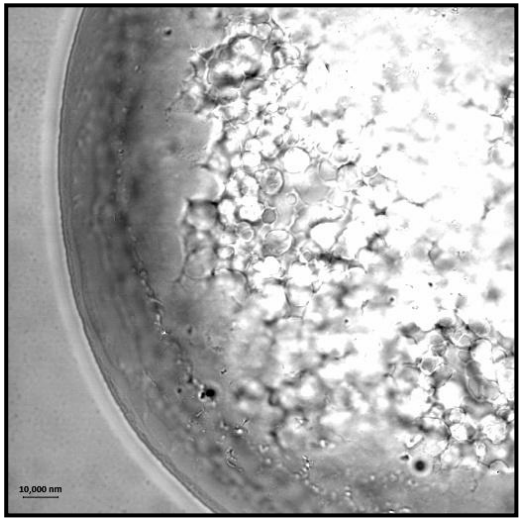 (b)	**Figure 70:** 4.5 Ro pentane micrograph **Date of Micrograph**: 17/5/2012 **Sample description**: T+Mot(WGP+ some TGP spheres) 1 year 4 month after weak sonication. Shaken. **Micrograph description**: Shape distribution – Spherical aggregates. Size distribution – Background homogeneous 1-2 μm. Large aggregate >100 μm (probably ~200 μm). All background aggregates are too small to distinguish morphological features and are out of focus in these images. The large spherical particles seem to have a bicontinuous structure with large ~5 μm to 10 μm internal compartments. As can be seen at the edge of the large particle in image (b), these compartments line up and often merge into concentric circles surrounding the particle edge.

Sample Number	Micrograph	Sample and Micrograph Description
RVe1a 15	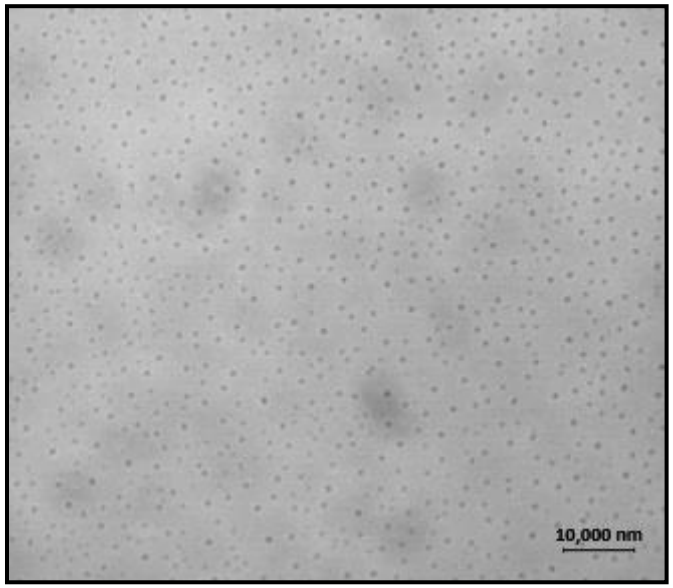	**Figure 71:** 4.5 Ro pentane micrograph **Date of Micrograph**: 17/5/2012 **Sample description**: T+Mot(WGP+ some TGP spheres) 1year 4months after weak sonication. Shaken. **Micrograph description**: Shape distribution - Spherical aggregates. Size distribution – Homogeneous 1-2 μm. All particles are too small to distinguish morphological features.

4.3.4.3.3 Laser scanning confocal fluorescent microscopy

Sample Number	Micrograph	Sample and Micrograph Description
RVe1a (fl) 16rep	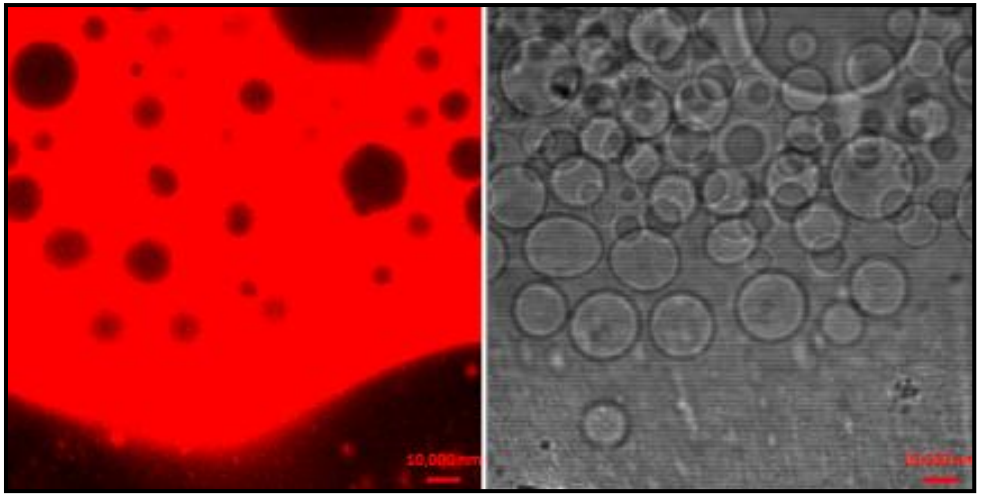	**Figure 72:** 2.5 Ro pentane fluorescence micrograph **Sample description**: T+WGP 1 day after probe sonication. Shaken. **Micrograph description**: The shaking of this sample has caused the encapsulation of solvent within this liquid crystal precipitant (shown as bright red).

4.3.5 Butane systems

As indicated in the list of observations of phase behaviour (Table 28) the butane systems presented an opaque suspension that quickly settled to form a transparent solution with a white solid precipitant. The precipitant may have had a greater viscosity due to the low temperatures that the butane systems were subjected to during preparation. TEM images of this system indicated that there were no obvious internal structures to these particles at a variety of temperatures indicating phase separated liquid crystal and gel phases.

4.3.6 Propane systems

Similar to the butane macroscopic phase behaviour the propane systems presented an opaque suspension that quickly settled to form a transparent solution with a white solid precipitant; see Table 29. TEM imaging revealed this precipitant to consist of a solid crystalline phase; see Figure 73.

4.3.6.1 Macroscopic phase behaviour

Sample	Ro	Concentration (mM)	Observations			
			AWS (NaCl+Ice bath) 1/2/2011	1 day AWS 2/2/2011	1 yr 2 months AWS 22/3/2012	3 yrs AWS 21/2/2014
22	2.5	30	Opaque+WSP	T+WSP [Cl+WSP AHS]	**Evaporated:** YGP+Transparent crystals ~1mm long	**Evaporated:** YGP+Transparent crystals ~1mm long
23	3.5	30	Opaque +WSP	T+WSP [Cl+WSP AHS]	**Evaporated:** YGP+Transparent crystals ~1mm long	**Evaporated:** YGP+Transparent crystals ~1mm long
24	4.5	30	Opaque +WSP	T+WSP [Cl+WSP AHS]	T+YGP [Tr AHS]	T+YGP+NL [Tr+WL AHS]

Table 28: Table presenting the changes in macroscopic phase behaviour for RVe1a butane samples.

Sample	Ro	Concentration (mM)	Observations		
			AWS (Acetonitrile+Dry Ice bath) 1/2/2011	1 day AWS 2/2/2011	3 yrs AWS 21/2/2014
25	2.5	65	Cl	**Evaporated:** WSP	**Evaporated:** YGP+Transparent crystals ~1mm long
27	4.5	40	Cl	**Evaporated:** WSP	**Evaporated:** YGP+Transparent crystals ~1mm long

Table 29: Table presenting the changes in macroscopic phase behaviour for RVe1a propane samples.

4.3.6.2 TEM

Sample Number	Micrograph	Sample and Micrograph Description
RVe1a **27**		**Figure 73:** 4.5 Ro propane, Digital TEM micrograph **Date of Micrograph**: 1/2/2011 **TEM grid created:** 1/2/2011 **Temperature:** -55°C **Sample description**: Cl After weak sonication. **Micrograph description**: Shape distribution – Spherical and irregular or elongated spheroids. Size distribution – ~1.5 µm. This appears to be a solid crystalline phase.

4.4 Summary of macroscopic and microscopic phase behaviour

4.4.1 Answers to key questions

- Can we replicate the results published by Tung *et al.* (2008) and create colloidal dispersions containing unilamellar reverse vesicles using PC18:2 and PC4:0 amphiphiles?

Colloidal dispersions of unilamellar reverses are limited to 6 and 7 amphiphilic ratios in cyclohexane systems prepared with methanol; see Figure 53 and 55. Although, large micron sized multilamellar reverses are found in a wider range of amphiphilic ratios in cyclohexane solvents such as; methanol prepared 2.5 Ro, see Figure 37; and without methanol preparation 7 Ro and 8 Ro, see Figures 49 and 50 respectively. Therefore, this does not concur with the ~2 Ro to 4 Ro amphiphilic range reported to form a phase of colloidal dispersions of unilamellar reverse vesicles in cyclohexane by Tung *et al.* (2008).

- Can PC18:2 and PC4:0 amphiphiles form unilamellar reverse vesicles in alkanes?

The alkane mixtures did not present any systems dominated by unilamellar or multilamellar reverse vesicles in the amphiphilic ranges studied. Instead these systems were dominated by micellar phases (e.g. Figure 68), bicontinuous phases (e.g. Figure 65) and phase separated liquid crystals (e.g. Figure 72). However, at room temperature pentane 3.5 Ro systems presented a lamellar system of stacked bilayers; see Figure 67.

- Does the molecular weight of the alkane solvents affect self assembly of PC18:2 and PC4:0 amphiphilic mixtures?

Yes. Although these systems produced similar macroscopic phase behaviour there were distinct differences in the structural phases between different solvents with the same amphiphilic ratios. For example, 2.5 Ro hexane and pentane (without methanol preparation) presented cloudy suspensions that rapidly settled to form white solid precipitants but those precipitants had different structure characteristics; see Table 21 and Figure 65, and Table 25 and Figure 72, respectively.

- What is the temporal stability of self assembled structures composed of PC18:2 and PC4:0 amphiphiles in hydrocarbon solvents?

Most of the particles in these systems settled out of solution within a few days (see macroscopic phase behaviour Tables 14-29); with the exception of the colloidal dispersions of the methanol prepared 6-7 Ro cyclohexane systems which remained in solution for months (see Table 19). These precipitants were always initially a white fluid, solid or gel which eventually transformed into a desolvated, amorphous liquid crystal phase within a month of settling. Although the

pentane 4.5 Ro system shows a remarkably stable precipitant that retains a heterogeneous white and transparent precipitant containing bicontinuous spheres for over 3 years; see Table 27.

These initial white precipitants were usually able to be redistributed into solution *via* simple hand shaking; implying that although these particles have settled due to gravity to form a separate macroscopic phase the particles remain as individuals any attractive forces were weak. This white to yellow precipitant change is likely to represent merging of particles and desolvation over time. This is supported by the yellow gel being harder to redistribute into solution by hand shaking the sample, a reduction in precipitant volume with time and the yellow gel phase also forming when the solvent has been evaporated.

- How do various preparation methods affect self assembled structures in binary PC18:2 and PC4:0 amphiphilic-hydrocarbon systems?

The effect of methanol was particularly apparent in the cyclohexane systems where it would facilitate the formation of giant or nanometre size unilamellar reverse vesicles depending on the system; see Tables 14-19, and Figures 33 and 35 - example TEM images of structures in samples without and with methanol preparation respectively. The methanol preparation breaks the NaCl crystals into Na^+ and Cl^- ions and promotes the attachment of these to the polar head group of the phospholipids. This recombination of atoms helps to counter the repulsive forces between polar heads that would be found in a polar interior of a reverse bilayer or micelle. For samples without methanol preparation, the NaCl is likely to be incorporated into the polar areas whilst remaining as crystals or individual molecules and are therefore not as efficient as stabilisers.

Also, it was noted that after years of standing many of the systems without methanol preparation had transparent crystals form in the yellow gel precipitant which did not occur in the methanol prepared samples; see Tables 16, 18, 17, 23, 24, 25 and 26. This indicates that the NaCl in these systems were not chemically bonded to the amphiphiles and with time the NaCl crystals phase separated from the amphiphilic mixture.

As predicted a reduction in intensity of sonication could be correlated with an increase in the average particle size for many of the systems presenting self assembled particles. In the micellar systems this decrease in particle size actually increased the settling rate of the particles due to a decreased surface area, for example, the cyclohexane 5 Ro sample (without methanol preparation); see Table 17. However, in systems presenting reverse vesicles (which are less dense that their micellar counterparts) the reduction of reverse vesicle size decreased precipitation rates as stable colloidal dispersions were formed, so precipitation occurred due to flocculation over time; see Table 19.

4.5 Conclusions leading to further analyses

The amphiphilic ratios to obtain a colloidal system of unilamellar vesicles were far higher than reported by Tung *et al.* (2008). This leads us to conclude that their assumption of studying a system containing only the phosphatidylcholines 18:2 and 4:0 along with NaCl was inaccurate. This leads us onto the study contained in Chapter 5 which uses identical products used by Tung *et al* (2008). The difference in this following study is the replacement of the 99% pure PC18 product with a 95% pure PC18 product that includes 2.8 wt% of lyso-phosphatidylcholine. The presence of the lyso-phosphatidylcholine had not been considered in the published research; however, this study indicates that the presence of the lyso-phosphatidylcholine may be an important factor in the formation of colloidal dispersions of unilamellar reverse vesicles.

Chapter 5: Macroscopic phase behaviour and microscopic imaging studies of self assembled structures in ternary amphiphilic-hydrocarbon systems

5.1 Introduction

The focus of this study is to analyze the phase behaviour and imaging of self assembled structures for a multi-component system of amphiphiles in hydrocarbon solvents.

Tung *et al.*(2008) concluded that the reverse vesicles were made from a binary system of PC18 and PC4 which prompted the use of the C18 99% product in the initial experiments covered in Chapter 4. However, due to the differences in the results published by Tung *et al.* (2008) and those of the first study covered in Chapter 4 this second study was commissioned. In this study, identical products and preparation methods of Tung *et al.* (2008) were used with the aim of forming colloidal systems containing unilamellar reverse vesicles and discover the cause of the unexpected results revealed in Chapter 4. The main difference in this study is the replacement of the C18 99% product with the C18 95% product. The difference in these products is the inclusion of 2.8 wt/wt% lysophosphatidylcholine (lyso-PC18:2) in C18 95% (see Chapter 3 for details). The presence of lyso-PC18:2 was not considered by Tung *et al.*(2008); however, lyso-phosphatidylcholines are known to form micellar solutions and when mixed with other lipids can form lamellar phases (Quinn & Cheery 1992). Therefore, this study will determine the effect of lyso-PC18:2 on these amphiphilic-hydrocarbon systems.

In order to replicate the work by Tung *et al.* (2008) to create unilamellar reverse vesicles this study concentrated on samples containing 20 mM total concentration of amphiphiles and 3.5 mM concentration of NaCl. Chapter 4 showed that probe sonication was the most effective method for producing unilamellar reverse vesicles so this type of sonication was dominant in the preparation of samples used in this study. Included in this study are the RVe1c and SAXS sample groups; see Appendix I and II for sample details and preparation methods.

The macroscopic phase behaviour was reported over an extended time period, often for over a year; a key to the abbreviations used in describing phase behaviours is in Appendix III. The imaging techniques used included confocal microscopy and TEM; details on these imaging techniques can be found in Chapter 3.

The results section is followed by a discussion presenting comparisons between systems with different solvents and contains an overview of the main conclusions.

5.1.1 Key questions

The key questions we intended to answer in this study were:

- Can we replicate the results published by Tung *et al.* (2008) and create colloidal dispersions containing unilamellar reverse vesicles using mixtures of C18 95% and C4?
- What is the effect on phase behaviour and microscopic structures of systems containing lyso-PC18:2 compared to systems lacking lyso-PC18:2 as detailed in Chapter 4?
- Can unilamellar reverse vesicles form from C4 and C18 95% products in alkanes?
- Does the molecular weight of the alkane solvents affect the self assembly of C4 and C18 95% products?
- What is the temporal stability of self assembled structures composed of C4 and C18 95%?

5.1.2 Key to macroscopic phase behaviour tables

Term	Explanation	Term	Explanation	Term	Explanation
Opaque	White opaque solution. Cannot see through the solution.	SL	Strong laser reflection.	WFP	White (translucent) fluid precipitant.
Cl or Cl(s)	Cloudy solution, (s) symbol signifies after being shaken by hand. A cloudy solution has some transparency unlike those that are characterised as 'Opaque'.	WL	Weak laser reflection.	YFP	Yellow (translucent) fluid precipitant.
O or O(s)	Opalescent solution, (s) symbol signifies after being shaken by hand. Opalescent solution is translucent with an intense shine and can range of slight hues from grey (Gr), grey/yellow (Gr/Y) and grey/blue (Gr/B).	WSL	Widely scattered laser reflection.	TFP	Transparent fluid precipitant.
B	Solution has a blue hue - substantial Tyndall Scattering occurring.	WWSL	Weak widely scattered laser reflection.	WGP	White (translucent) gel precipitant.
T	Transparent solution.	NL	No laser reflection.	YGP	Yellow (translucent) gel precipitant.
Ph	Phase separated solution – the separate phases are characterised individually.			TGP	Transparent gel precipitant.
CLay	White cloudy layer, at the base of the container unless stated otherwise.			YWGP	Milky yellow (translucent) gel precipitant.
BLay	Bluish, opalescent layer, at the base of the container unless stated otherwise.			WSP	White solid precipitant.
Fla(x)	Visible opaque flakes in solution, temporarily after being hand shaken (x=colour; w=white, y=yellow, wy=milky yellow).			Mot	Mottled transparent and white precipitant with solid and fluid characteristics.

Table 30: Key explaining the abbreviations used in describing the macroscopic phase behaviour of samples.

5.2 Results for C18 95% in hydrocarbon solvents

20 mM of the C18 95% product in cyclohexane formed a transparent molecular solution. However, weak and strong laser reactivity, in heptane and pentane respectively, indicated colloidal dispersions of self assembled micelles. These results are completely different to those of C18 99% but very similar to those of PC4:0 as reported in Chapter 4.

5.3 Results for multi-component amphiphilic-hydrocarbon systems

The following results are separated at the highest level by solvent type and then by the amphiphilic ratio. Each section with a particular solvent and amphiphilic ratio contains results of the macroscopic phase behaviour and imaging analyses for individual samples over time. At the end of each solvent defined section there is a summary comparing the results for all the amphiphilic ratios studied.

5.3.1 Multi-component amphiphilic-cyclohexane systems

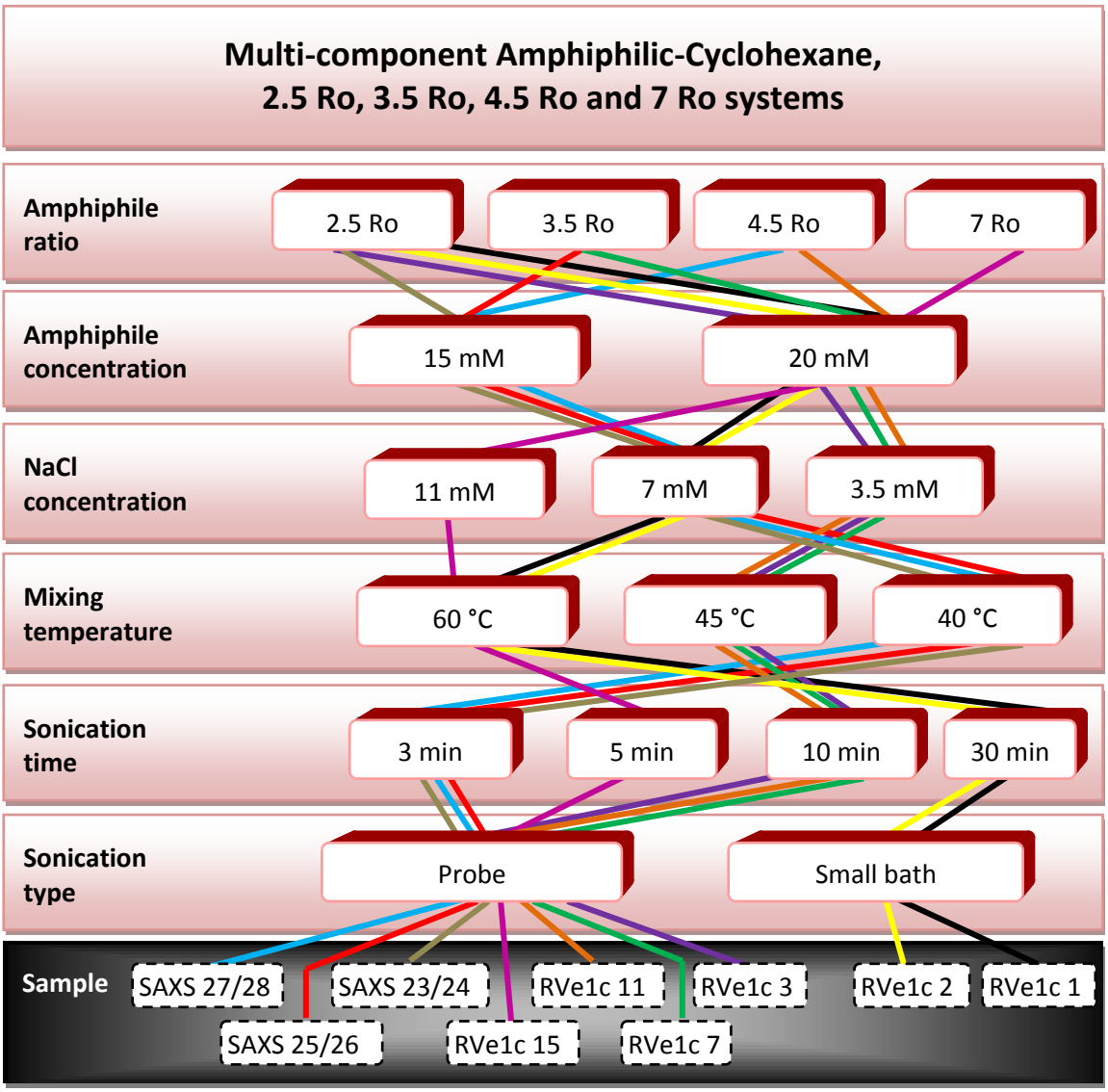

Figure 74: Sample road map illustrating the initial preparation methods for the amphiphilic-cyclohexane 2.5 Ro, 3.5 Ro, 4.5 Ro, and 7 Ro samples.

5.3.1.1 Cyclohexane 2.5 Ro

The difference in phase behaviour of the RVe1c and SAXS samples (see Table 31) indicates that sonication strength has a significant effect on the particle distribution. A weak sonication (RVe1c 2) produced a solution with short lived opalescence and stronger sonication produced a long lived blue hue (RVe1c 1, RVe1c 3 and SAXS 23/24); see Figure 75 for illustration.

Figure 75: Photographs illustrating the phase behaviour of RVe1c 1 (transparent with blue hue, left photo), RVe1c 2 (opalescent, central photo) and RVe1c 3 (opalescent with blue hue, right photo).

The RVe1c3 and SAXS 23/24 are different concentrations; however, the lower concentration sample presents an initial precipitation of white fluid precipitant. A reduction in concentration is unlikely to provoke this reaction and therefore this is probably caused by the increase of relative NaCl in system. RVe1c 3 has 3.5 mM NaCl in relation to 20 mM of amphiphiles and the SAXS 23/24 system has 7.5 mM NaCl in relation to 15 mM of amphiphiles; which corresponds to almost 3 times the respective amphiphile to NaCl ratio. Therefore, it is likely that an increase in NaCl concentration can be related to an initial agglomeration of some reverse vesicles due to excess NaCl forming an attractive force between particles.

Microscopy of the RVe1a 1 system after weak sonication and redistributing the white fluid precipitant by hand shaking revelled clusters of <1 μm to 4 μm, spherical to elongated, structures many of which had thick walls; see Figures 76 and 77. These would quickly settle back into a white fluid precipitant a few hours after hand shaking.

After strong sonication this same RVe1a 1 sample showed Tyndall scattering and no structures could be observed with microscopy. TEM of this system after a month revealed 100-200 nm diameter unilamellar reverse vesicles; see Figures 78 and 79. Checking RVe1c 3 with microscopy after a month revealed the unilamellar vesicles had not clustered into particles large enough (> 1 μm) to be observed with this technique and pointed to a stable colloidal dispersion.

After 6 month some white fluid precipitant had formed in all the strongly sonicated samples indicating a slow rate of flocculation in these samples. The difference in the samples using strong water bath sonication (RVe1a 1) and the higher intensity probe sonication (RVe1c3 and SAXS 23/24) only became evident after two years of standing. At this point most of the particles had precipitated out of solution in the strong water bath sonicated sample and the probe sonicated samples had kept strong laser reactivity. This shows that, although these systems have the same similar macroscopic and microscopic phase behaviours, the systems the flocculation

rate is slightly lower when using the intense probe sonication; implying a greater proportion of smaller unilamellar reverse vesicles.

The precipitants remained as a white fluid or gel like consistency until all the particles had settled out of solution. After which the precipitant gradually transforms into a yellow gel indicating the merging of vesicles. Microscopy of the yellow gel of the probe sonicated samples presented multi-compartmented reverse vesicles.

A probe sonicated specimen without methanol preparation had different macroscopic phase behaviour, producing a transparent solution with some course laser reactivity. Microscopy revealed some large (x100 μm) particles dominantly in a worm-like formation indicative of reverse cylindrical micelles. This shows that pre-mixing the amphiphiles and NaCl in methanol is required to form reverse vesicles. This methanol preparation would facilitate the disassociation of NaCl and combining of the ions into the polar head regions of the amphiphiles to counteract any electrostatic repulsion interactions.

Sample	Surfactant Ratios (Ro) Concentration (mM)	Observations							
		AWS 1/3/2012	3 weeks AWS (BSS) 22/3/2012	ASS 22/3/2012	3 hours ASS 22/3/2012	1 day ASS 23/3/2012	6 months ASS 11/9/2012	1 year 7 months ASS 19/11/2013	2 years 3 months ASS 8/6/2014
RVe1c 1	2.5	20	O+Sl	T+WFP+NL [O+SL AHS]	Tr+B+SL	Tr+B+SL	Tr+B+SL	Tr+WFP(some)+SL [O+SL AHS]	Tr+WGP+SL [O+SL AHS]	Tr+TGP+WL [Cl+O+WWSL]
		AWS 8/3/2012	2 weeks AWS 22/3/2012	No further sonication	1 day AWS 23/3/2012	3 weeks AWS 29/3/2012	6 months AWS 11/9/2012	1 year 7 months AWS 19/11/2013	2 years 3 months AWS 8/6/2014	
RVe1c 2	2.5	20	O+SL	T+WFP+NL [O+SL AHS]	-	T+WFP+NL [O(s)+SL AHS]	T+WFP+NL [O+SL AHS]	T+YGP+NL [Cl+TGP(some)+WS AHS]	T+YGP+NL [Cl+TGP(some)+WSL AHS]	T+YGP+NL [Cl+WSL AHS]
		BPS 30/3/2012	APS 30/3/2012	3 hours APS 30/3/2012	1 day APS 31/3/2012	1 month APS 1/5/2012	5 months APS 11/9/2012	1 year 6 months APS 19/11/2013	2 years 2 months APS 8/6/2014	
RVe1c 3	2.5	20	Cl+SL	O+B+SL	O+B+SL	O+B+SL	O+B+SL	O+B(some)+WFP(some)+SL [O+SL AHS]	Tr+B(some)+CLay(some)+WFP+SL [O+B+SL AHS]	Tr+B(some)+WFP+SL [O+B+SL AHS]
		APS 16/11/2012	3 days APS 19/11/2012	1 year APS 29/10/2013	1 year 7 months APS 8/6/2014					
SAXS 23/24	2.5	15	O+SL	O +WFP(some) + SL	Tr+WFP+SL	Tr+WFP(high viscosity)+SL				

Table 31: Tables presenting the changes in macroscopic phase behaviour for RVe1c and SAXS cyclohexane 2.5 Ro samples

Sample Number	Micrograph	Sample and Micrograph Description
RVe1c 1 CyHex	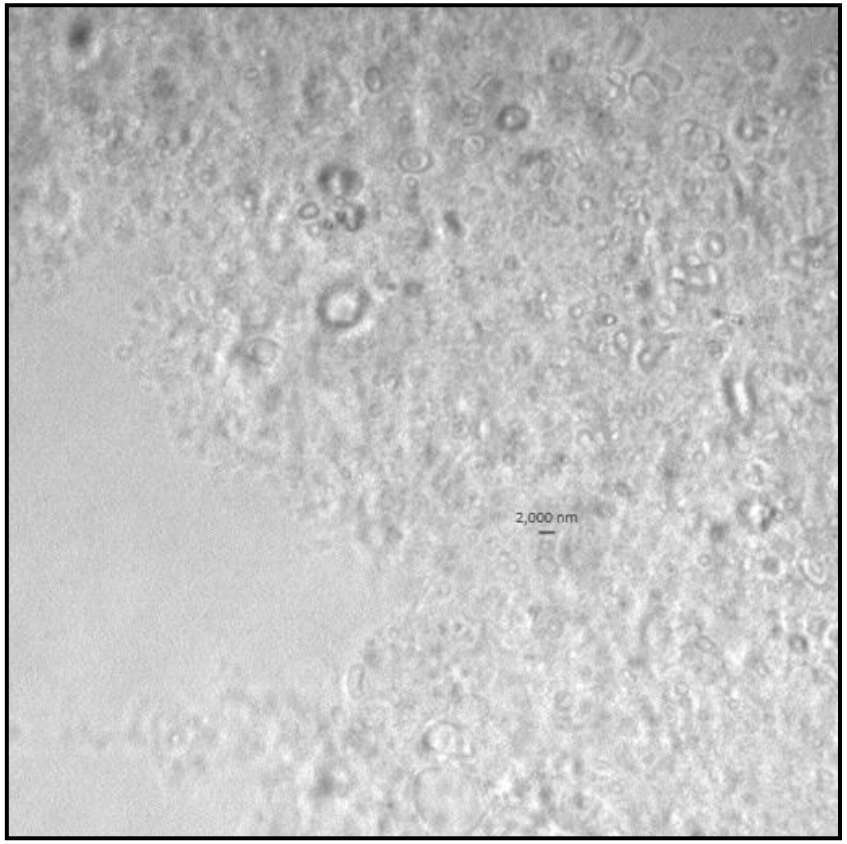	**Figure 76:** 2.5 Ro cyclohexane micrograph **Date of Micrograph**: 21/3/2012 **Sample description**: T+WFP [O handshaken] 1 day after weak-water bath sonication but before strong water-bath sonication. Shaken. **Micrograph description**: Shape distribution – Spherical to irregular spheroid particles. Most are irregular, elongated spheroids. Size distribution – <1 μm to 4 μm. Most of the particles are <1 μm. Most of the distinguishable vesicular structures have thick walls that can take up half of the vesicle volume; the other half allocated to an internal compartment. The particles quickly accumulate into clumps. Image difficult to focus due to constant movement of the aggregates and the 3D clump structure. These are mainly multilamellar irregular spheroid reverse vesicles.

Sample Number	Micrograph	Sample and Micrograph Description
RVe1c 1 CyHex	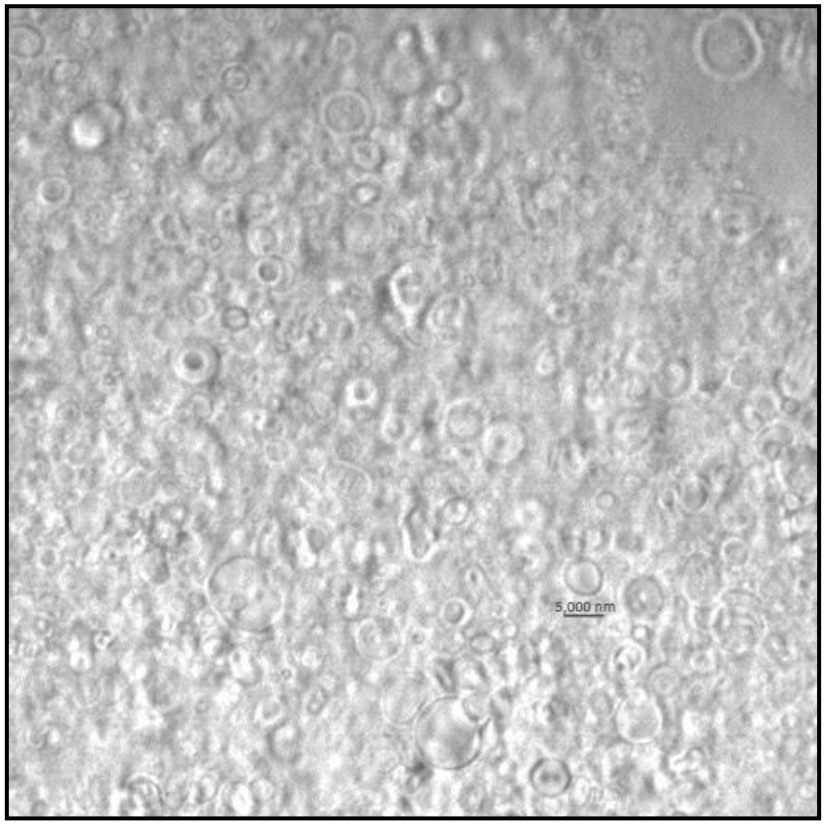	**Figure 77:** 2.5 Ro cyclohexane micrograph **Date of Micrograph**: 21/3/2012 **Sample description**: T+WFP [O handshaken] 1 day after weak-water bath sonication but before strong water-bath sonication. Shaken. **Micrograph description**: Shape distribution – Spherical to irregular spheroid particles. Most are irregular, elongated spheroids. Size distribution – <1 μm to 10 μm. Most of the particles are ~3 μm. Most of the distinguishable vesicular structures have thick walls that can take up half of the vesicle volume; the other half allocated to an internal compartment. The particles quickly accumulate into clumps. Image difficult to focus due to constant movement of the particles and the 3D clump structure. These are mainly multilamellar irregular spheroid reverse vesicles.

Sample Number	TEM Micrograph	Sample and Micrograph Description
RVe1c 1 CyHex	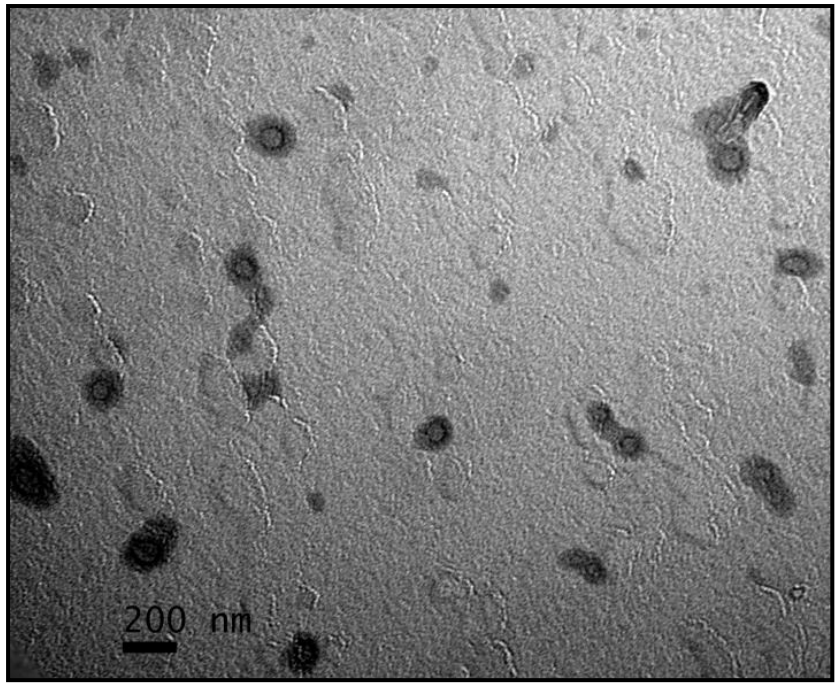	**Figure 78:** 2.5 Ro cyclohexane, Digital TEM micrograph **Sample description**: T+B+SL 1 week after strong water-bath sonication. **Micrograph description**: Shape distribution – Spherical and irregular spheroids. Size distribution – ~100-200 nm. These structures appear to have a boundary that distinguishes an internal compartment, although the external boundary is not as well defined. These features are likely to be unilamellar reverse vesicles.

Sample Number	TEM Micrograph	Sample and Micrograph Description
RVe1c 1 CyHex	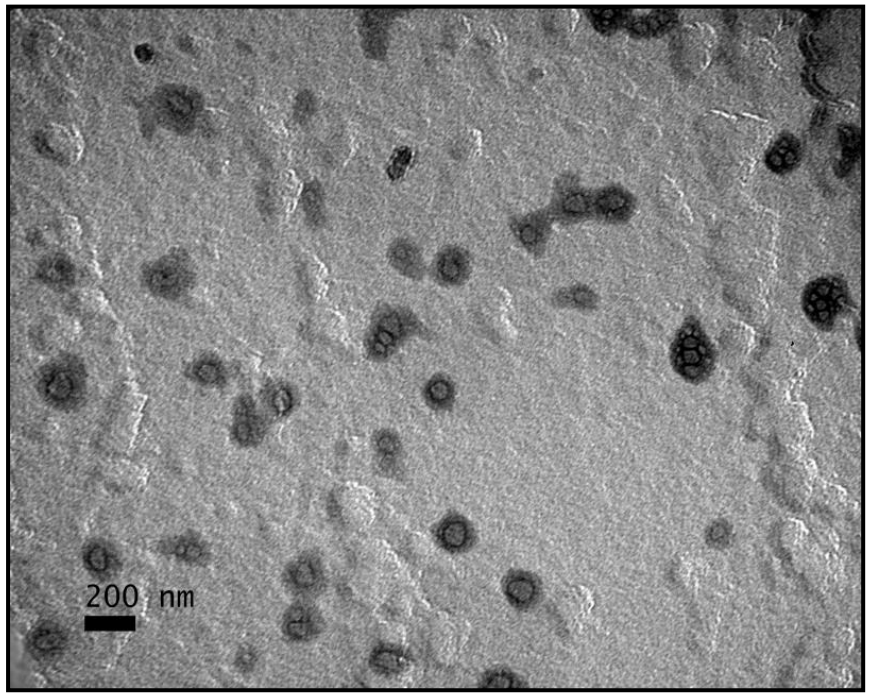	**Figure 79:** 2.5 Ro cyclohexane, Digital TEM micrograph **Sample description**: T+B+SL 1 week after sonication. **Micrograph description**: Shape distribution – Spherical and irregular spheroids. Irregular spheroid clusters. Size distribution – ~100-200 nm with ~200 nm clusters. These structures seem to have a boundary for an internal compartment. Although the external boundary is not as well defined. There are numerous clusters that contain up to ten vesicular structures. These features are likely to be unilamellar reverse vesicles. With some clusters that may have formed during the evaporation process in the TEM slide preparation.

5.3.1.2 Cyclohexane 3.5 Ro

This system produces a colloidal dispersion presenting an opalescent solution with a distinct blue hue for a system with a 20 mM amphiphilic concentration. Although when the amphiphilic concentration is reduced to 15 mM the blue hue is not obvious and only opalescence is observed (as seen in SAXS 25/26); see Table 32. Microscopy confirmed that the majority of particles in the system must be under a micrometer in size.

A small volume of white fluid precipitates early in both the 15 mM and 20 mM concentrations; however, a slow flocculation rate results in a colloidal dispersion for over a year before all the particles settle to form a transparent solution overlying a yellow gel precipitant.

As the phase behaviour is similar to that of the probe sonicated 2.5 Ro cyclohexane samples we can infer that these 3.5 Ro cyclohexane samples also contain unilamellar reverse vesicles.

5.3.1.3 Cyclohexane 4.5 Ro

This system produces a colloidal dispersion presenting opalescence for both 15 mM and 20 mM amphiphilic concentrations; with a distinct blue hue when the amphiphilic concentration is 20 mM (see Table 33).

Similar to the cyclohexane 2.5 Ro and 3.5 Ro results the fast initial precipitation of some particles in the 15 mM sample is probably related to an increase in amphiphilic-NaCl ratio causing excess NaCl that forms an attractive force between particles.

The majority of particles stayed in suspension for an extended period of time; small quantities of solvated particles were even present 1 year and 7 months after preparation. This indicates that flocculation rate of these systems was very slow; especially for the lower amphiphilic concentration sample.

As the phase behaviour is similar to that of the probe sonicated 2.5 Ro cyclohexane samples we can infer that these 3.5 Ro cyclohexane samples also contain unilamellar reverse vesicles.

Microscopy of the 15 mM amphiphilic concentration sample after 1 year and 8 months revealed the suspended particles were below a micron in size; however, the white fluid precipitant contained clustered, micron sized reverse vesicles. Many of these presented Maltese crosses with polarized light indicative of multilamellar reverse vesicles.

After all the particles have settled out of solution the precipitant gradually becomes a desolvated yellow gel.

Sample	Surfactant Ratios (Ro)	Concentration (mM)	Observations							
			BPS 3/4/2012	APS 3/4/2012	3 hours APS 3/4/2012	1 day APS 4/4/2012	1 month APS 1/5/2012	5 months APS 21/9/2012	1 year 7 months APS 19/11/2013	2 years 2 months APS 8/6/2014
RVe1c 7	3.5	20	T+WFP+NL [Cl+WSL AHS]	O+B+SL	O+B+SL	O+B+WFP(some)+SL	O+B+WFP(some)+SL	O+WFP(some) +SL [O+B+SL AHS]	T+YGP+NL [Cl+TGP(some)+ WL AHS]	T+YGP+NL [Cl+YGP+WL AHS]
			APS 16/11/2012		3 days APS 19/11/2012		1 year APS 29/10/2013		1 year 7 months APS 8/6/2014	
SAXS 25/26	3.5	15	O+SL		O +WFP(some) + SL		Tr+WFP+SL		Tr+WFP(high viscosity)+SL	

Table 32: Tables presenting the changes in macroscopic phase behaviour for RVe1c and SAXS cyclohexane 3.5 Ro samples.

Sample	Surfactant Ratios (Ro)	Concentration (mM)	Observations							
			BPS 3/4/2012	APS 3/4/2012	3 hours APS 3/4/2012	1 day APS 4/4/2012	1 month APS 1/5/2012	5 months APS 21/9/2012	1 year 7 months APS 19/11/2013	2 years 2 months APS 8/6/2014
RVe1c 11	4.5	20	T+WFP+NL [Cl+WSL AHS]	O+B+SL	O+B+SL	O+B+SL	O+B(some) +CLay+SL	Tr+WFP+SL [Cl+ WSL AHS]	T+WFP+NL [Cl+ WSL AHS]	T+YGP+NL [Cl+ WSL AHS]
			APS 16/11/2012		3 days APS 19/11/2012		1 year APS 29/10/2013		1 year 7 months APS 8/6/2014	
SAXS 27/28	4.5	15	O+SL		O +WFP(some) + SL		Tr+WFP+SL		Tr+WFP(high viscosity)+SL	

Table 33: Tables presenting the changes in macroscopic phase behaviour for RVe1c and SAXS cyclohexane 4.5 Ro samples.

5.3.1.4 Cyclohexane 7 Ro

The 7 Ro cyclohexane systems presented a transparent molecular solution with no laser reflectivity and a very small amount of precipitation. Microscopy showed this precipitation to consist of large crystals and no self assembled particles. This macroscopic phase behaviour is completely different to the 7 Ro systems of the C18 99% sample presented in Chapter 4, but resemble those of the pure PC4:0 and C18 95% components in cyclohexane. This shows us that for these C18 95% cyclohexane systems the high amphiphilic ratios prevent self assembly.

5.3.1.5 Summary of cyclohexane systems

The results of the 2.5 Ro and 3.5 Ro multi-component amphiphilic-cyclohexane systems are principally equivalent to those of Tung *et al.* (2008); long lived colloidal dispersions presenting Tyndall scattering and containing unilamellar reverse vesicles. Tung *et al.* (2008) noted that their systems began to phase separate at amphiphilic ratios higher than 4 Ro, and therefore, we would have expected suspensions to form in our 4.5 Ro results. However, our 4.5 Ro samples presented the same initial phase behaviour as those of the 2.5 Ro and 3.5 Ro systems. This implies that the boundary for a macroscopic and structural phase transition is actually at a higher amphiphilic ratio than published previously.

For the 20 mM concentrations of the 3.5 Ro and 4.5 Ro systems all particles had precipitated out of solution after a year and a half. However, some particles still remained in solution after a year and a half in the same systems containing a 15 mM amphiphile concentration. This indicates that the flocculation process occurs faster in systems with higher concentrations. This is logical concatenation because the colloids would be further apart in a system with a low concentration and therefore random collisions between particles would occur less frequently.

However, the reduced amphiphilic concentration of 15 mM in the SAXS samples made viewing the effects of Tyndall scattering very difficult in these 4 ml samples. Although opalescence was observed a distinct blue hue was absent from the cyclohexane SAXS samples. This is likely to be a result of the reduced quantity of light scattering particles; although the reduction in amphiphilic concentration may also have caused a structural phase transition or change in particle size ranges. The DLS and SAXS results of these samples (Chapters 6 and 7 respectively) will determine if the particle size or structures have changed due to this 5 mM reduction in amphiphilic concentration.

Sonication differences in the 2.5 Ro samples indicated that an intense sonication, *via* either a strong ultrasonic water-bath (industrial grade) or a probe sonicator, is required to break multilamellar reverse vesicles into unilamellar reverse vesicles.

High amphiphilic ratios cause the system to revert back to a molecular solution state like those exhibited by the pure C18 95% and PC4:0 cyclohexane systems.

5.3.2 Multi-component amphiphilic-octane systems

5.3.2.1 Octane 2.5 Ro

This system appears cloudy when it is sonicated; however, within a few days the system appears opalescent with a blue hue that is very reactive to laser excitation and overlies some white fluid precipitant (see Table 34). This system remains in this state for an extended period with a low flocculation rate gradually increasing the volume of white fluid precipitant. This implies that the system is initially very polydisperse with the large suspended particles settling rapidly and the smaller colloidal particles remaining solvated for years and slowing forming flocs.

After a year a heterogeneous state forms consisting of several layered regions with graduated boundaries; with a translucent phase at the top, an opalescent phase with Tyndall scattering in the centre and a cloudy phase near the base (overlying the white fluid precipitant). This indicates that either the velocity of settling particles is very slow to produce regions of different particle concentrations or there is an interaction between the condensed white fluid precipitant phase and the overlying, relatively dilute, phase. Once a particle has reached a density great enough to overcome the Brownian forces keeping the particle suspended it should settle to the base of the container. Although the different particle settling velocities may cause a heterogeneous striated system it is unlikely for this state to be maintained over seven months in low viscosity solvent such as octane (normal viscosity 0.5080cP at 25 °C) with a maximum distance of 4 cm (presuming an uniform flow from the top of the solution to the base of the vial). It is therefore probable that the particles are cycling between settling and suspension due to the interplay between the forces of gravity and diffusion from concentration gradients. This implies any positive forces between particles are very weak.

After 1 year and 7 months the white fluid precipitant was shown to contain micrometre sized multilamellar reverse vesicles by the presence of Maltese crosses when using polarized microscopy.

5.3.2.2 Octane 3.5 Ro

This system appears cloudy when it is sonicated; however, within a few hours the system appears opalescent with a blue hue, very reactive to laser excitation, and some viscous white fluid precipitant (see Table 35). This implies that the system is initially very polydisperse with large suspended particles settling rapidly and the smaller colloidal particles remaining solvated.

After a year all the particles have settled to form a yellow gel precipitant and the solution is transparent, with no laser reactivity. This implies that the cycling of particles found in the octane 2.5 Ro sample does not occur in this system. The increased quantity and viscosity of the initial precipitant formed from the relatively dense particles indicate this system may have a

different polydispersity to that of the octane 2.5 Ro sample. This is evaluated further with DLS data in Chapter 6.

5.3.2.3 Octane 4.5 Ro

This system appears cloudy when it is sonicated; however, within a few hours the system appears opalescent with a blue hue, very reactive to laser excitation, and some viscous white fluid precipitant (see Table 36). This implies that the system is initially very polydisperse with large suspended particles settling rapidly and the smaller colloidal particles remaining solvated.

After a year the particles in the solution gradually precipitate out to form a transparent solution with a thin, white, fluid precipitant layer overlying a yellow gel precipitant. The white fluid layer was easily dispersed back into solution by hand shaking; however, the yellow gel precipitant remained separate. This implies that the particles that had precipitant out initially had not interacted with the overlying solution and had formed a desolvated yellow gel structure; and that the flocs of colloidal particles had gradually settled over a year in agglomerates with weak bonds between the particles.

After a year and a half, these two precipitant types merged to form one gel with an opaque yellow colouration.

Sample	Surfactant Ratios (Ro)	Concentration (mM)	Observations			
			Directly APS 16/11/2012	3 days APS 19/11/2012	1 year APS 19/11/2013	1 year 7 months APS 8/6/2014
SAXS 41/42	2.5	20	Cl	O+B+WFP(some)+SL	Tr+BLay with CLay underneath+WFP+SL [O+B+SL]	Tr+BLay with CLay underneath+WFP+SL

Table 34: Table presenting the changes in macroscopic phase behaviour for SAXS octane 2.5 Ro samples.

Sample	Surfactant Ratios (Ro)	Concentration (mM)	Observations			
			Directly APS 16/11/2012	3 days APS 19/11/2012	1 year APS 19/11/2013	1 year 7 months APS 8/6/2014
SAXS 43/44	3.5	20	Cl	O+B+WFP(high viscosity)+SL	T+YGP+NL [T+YGP(flakes)+NL AHS]	T+YGP+NL

Table 35: Table presenting the changes in macroscopic phase behaviour for SAXS octane 3.5 Ro samples.

Sample	Surfactant Ratios (Ro)	Concentration (mM)	Observations			
			Directly APS 16/11/2012	3 days APS 19/11/2012	1 year APS 19/11/2013	1 year 7 months APS 11/6/2014
SAXS 45/46	4.5	20	Cl	O+B+ WFP(high viscosity)+SL	T+WFP thin layer over a YGP thin layer +NL [O+YGP+SL]	T+WYGP+NL

Table 36: Table presenting the changes in macroscopic phase behaviour for SAXS octane 4.5 Ro samples.

5.3.2.4 Summary of octane systems

Initially all amphiphilic ratios had similar macroscopic phase behaviour; polydisperse systems with large suspended particles initially causing a cloudy appearance but rapidly settling to form a white precipitant with an overlying opalescent colloidal dispersion presenting a blue hue.

The white fluid precipitants were made of micron sized multilamellar reverse vesicles making it likely that the colloidal dispersion is formed of nanometre sized reverse vesicles.

The 2.5 Ro sample had a very low flocculation rate compared to the 3.5 Ro and 4.5 Ro systems indicating this system is more stable. The stability may reside from a decreased average size of colloids or a lower polydispersity.

5.3.3 Multi-component amphiphilic-heptane systems

5.3.3.1 Heptane 2.5 Ro

After sonication the heptane 2.5 Ro system becomes cloudy but this transforms within a few hours into a colloidal dispersion displaying opalescence and a blue hue overlying a white precipitant; see Table 37. This implies that the system is initially very polydisperse with large suspended particles settling rapidly and the smaller colloidal particles remaining solvated. Microscopy of this white precipitant, after being shaken by hand, showed large clusters up to ~120 μm in size of spherical to oblong uni- and multi- lamellar reverse vesicles with ~1 μm to 4 μm diameters; see Figures 80, 81, 82 and 83. Microscopy of the white fluid precipitant after a 1 year and 7 months revealed a similar range of highly polydispersity of reverse vesicles, ranging from 1 μm to 200 μm. Polarised microscopy revealed most of these to be multilamellar reverse vesicles.

This strong scattering system remains stable for months, with only some of the solution settling to form a thin bluish and/or cloudy layer near the base after about 6 months. This heterogeneous striated system is maintained over several months indicating that the particles are probably cycling between settling and suspension due to the interplay between the forces of gravity and diffusion from concentration gradients. This implies any positive forces between particles are very weak.

Microscopy of the bluish and cloudy layers showed only a few micron sized reverse vesicles. Therefore, most of the particles in these phase regions remain nanometre sized.

Sample	Surfactant Ratios (Ro)	Concentration (mM)	Observations						
			BPS 30/3/2012	APS 30/3/2012	3 hours APS 30/3/2012	1 day APS 31/3/2012	1 month APS 1/5/2012	6 months APS 25/9/2012	1 year 9 months APS 14/1/2014
RVe1c 4	2.5	20	Tr+WFP(grainy)+WL AHS	Cl+WSL	O+B+WGP+SL	O+B+WGP+SL	O+B+WGP+SL	O+B+CLay+WFP(high viscosity)+SL(very strong in CLay) [Cl(s)+O(s)+WSL AHS]	T+YGP+NL
			Directly APS 16/11/2012	3 days APS 19/11/2012		1 year APS 29/10/2013		1 year 7 months APS 11/6/2014	
SAXS 2/3	2.5	20	Cl	O+B+WFP(high viscosity)+SL		O+BLay+CLay+ WFP(high viscosity)+SL		Tr+O/BLay+CLay+ WFP(high viscosity)+SL (increasing strength towards base)	

Table 37: Tables presenting the changes in phase behaviour for RVe1c and SAXS heptane 2.5 Ro samples.

Sample Number	Micrograph	Sample and Micrograph Description
RVe1c 4 Hep	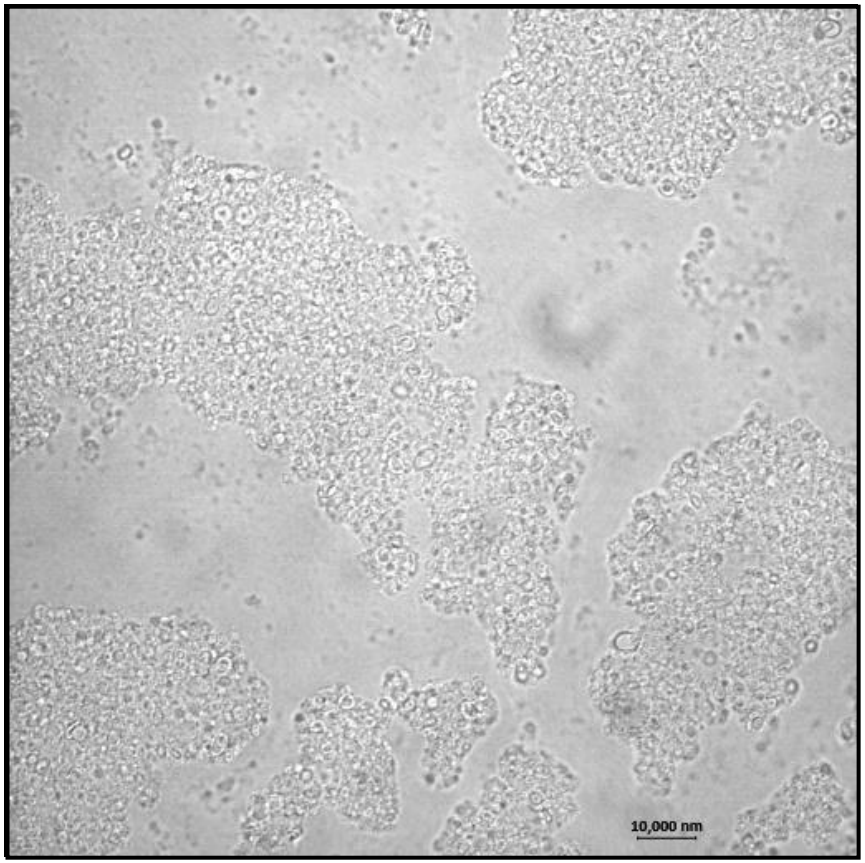	**Figure 80:** 2.5 Ro heptane micrograph **Date of Micrograph**: 17/5/2012 **Sample description**: O+B+WGP+SL 1 month after probe sonication. Shaken **Micrograph description**: Shape distribution – Spherical to irregular spheroids individual structures. Clusters irregular. Size distribution – ~1 μm to 4 μm individual particles. Irregular clusters of aggregates up to ~120 μm. The clusters contain ~1 μm to 4 μm spherical to irregular spheroid particles and consist dominantly of the larger (>2 μm) particles. These particles have perceivable walls and internal compartments; some have walls that occupy most of the volume but most have thin walls. The individual a particles in this image are not in focus but are generally <2 μm in size.

Sample Number	Micrograph	Sample and Micrograph Description
RVe1c **4 Hep**	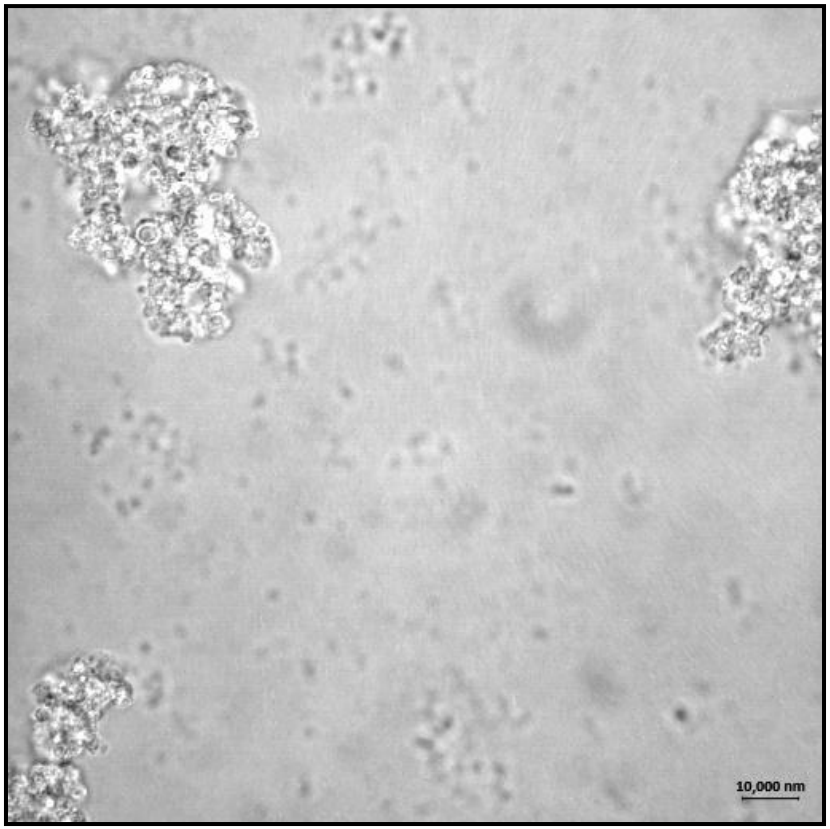	**Figure 81:** 2.5 Ro heptane micrograph **Date of Micrograph**: 17/5/2012 **Sample description**: O+B+WGP+SL 1 month after probe sonication. Shaken **Micrograph description**: Shape distribution – Spherical to irregular spheroids individual structures. Clusters irregular. Size distribution – ~1 μm to 4 μm individual particles. Irregular clusters of aggregates up to ~ 50 μm. The clusters contain ~1 μm to 4 μm spherical to irregular spheroid particles and consist dominantly of the larger (>2 μm) particles. These particles have perceivable, but thin, walls and large internal compartments. The individual particles in this image are not in focus but are generally <3 μm in size.

Sample Number	Micrograph	Sample and Micrograph Description
RVe1c 4 Hep	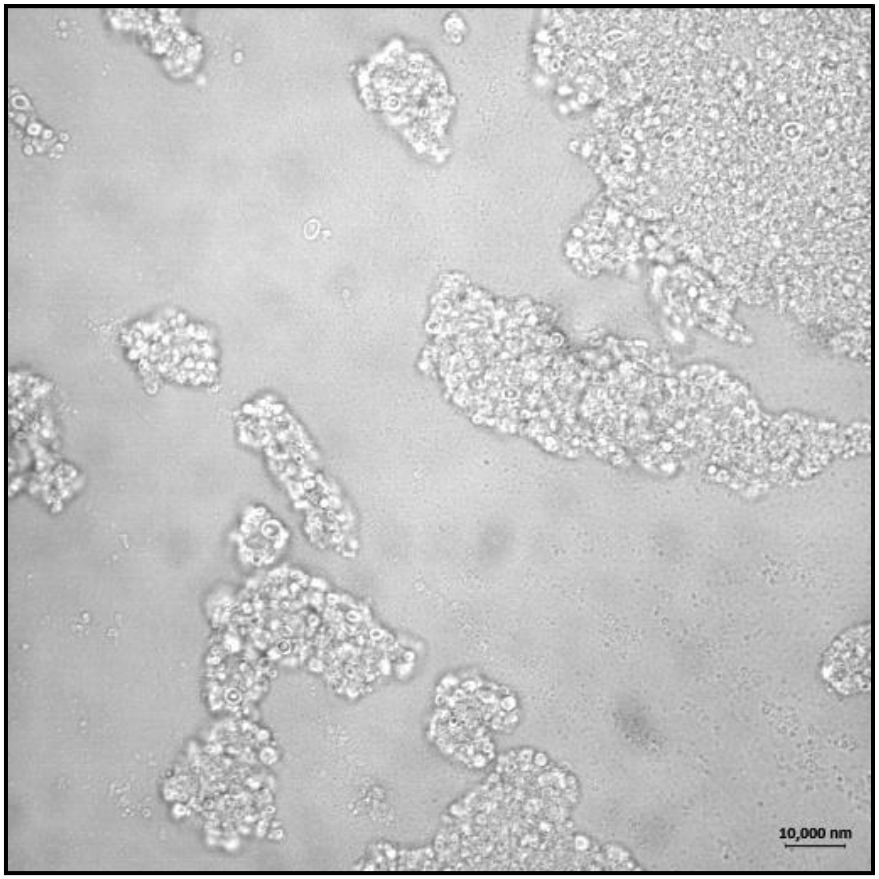	**Figure 82:** 2.5 Ro heptane micrograph **Date of Micrograph**: 17/5/2012 **Sample description**: O+B+WGP+SL 1 month after probe sonication. Shaken **Micrograph description**: Shape distribution – Spherical to irregular spheroids individual structures. Clusters irregular. Size distribution – ~1 μm to 4 μm individual particles. Irregular clusters of aggregates up to ~80 μm. The clusters contain ~1 μm to 4 μm spherical to irregular spheroid particles and are dominantly the larger (>2 μm) particles. These particles usually have perceivable, but thin, walls and large internal compartments, although for some aggregates this proportion of features is inverted. The individual particles in this image are <3 μm in size, principally <1μm. Particles >1 μm show wall/internal compartments. The particles below 1 μm cannot be resolved using this equipment; however, they are continuous throughout the image and are spherical.

Sample Number	Micrograph	Sample and Micrograph Description
RVe1c 4 Hep	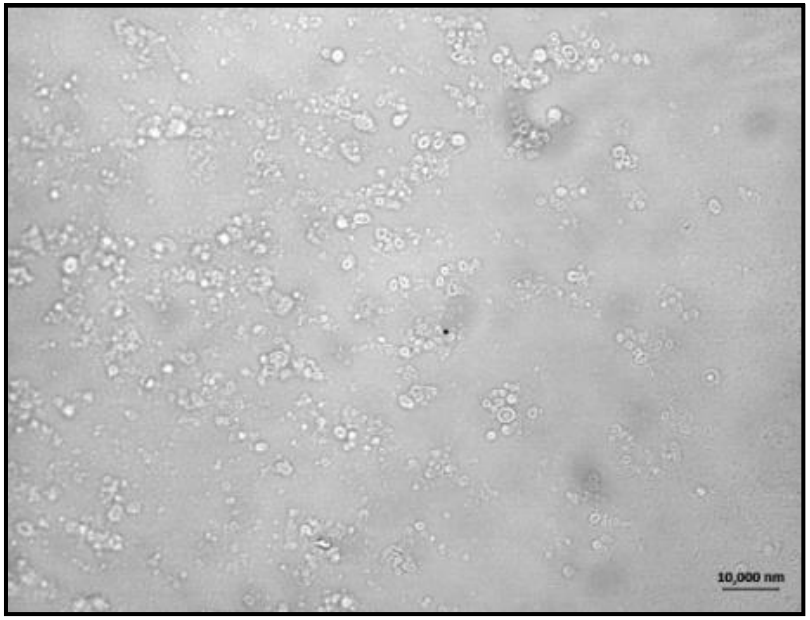	**Figure 83:** 2.5 Ro heptane micrograph **Date of Micrograph**: 17/5/2012 **Sample description**: O+B+WGP+SL 1 month after probe sonication. Shaken **Micrograph description**: Shape distribution – Spherical to irregular spheroids individual structures. Clusters irregular. Size distribution – ~1 μm to 4 μm individual particles. Irregular clusters of particles up to ~30 μm. Small clusters are common and consist dominantly of the larger (>2 μm) aggregates. The particles above 1 μm usually have perceivable, but thin, walls and large internal compartments, although for some particles this proportion of features is inverted. The particles below 1 μm were not able to be resolved to determine specific features using this equipment, however, they are shown to be spherical and are continuous throughout the images.

5.3.3.2 Heptane 3.5 Ro

After sonication the system becomes cloudy but this transforms within a few hours into a colloidal dispersion displaying opalescence and a blue hue overlying a viscous white precipitant; see Table 38. This implies that the system is initially very polydisperse with large suspended particles settling rapidly and the smaller colloidal particles remaining solvated. A relatively fast flocculation rate agglomerates the colloidal particles and these too settle out of solution within 6 months.

Microscopy of a one month old sample, after being shaken by hand, show that the white gel precipitant is made from polydisperse cluster of reverse vesicles ~1 μm to 14 μm; see Figures 84, 85, 86, 87 and 88. These reverse vesicles range from unilamellar to multilamellar and onions, and spherical to elongated shapes. Large (>1 μm) reverse vesicles cluster quickly into large networks causing some deformation of reverse vesicle shapes. The micrographs also showed some single long cylindrical worms that may present in the precipitant or in solution. The micrographs also showed non-clustered spherical particles <1 μm that may have been present in the solution rather than as a precipitant. Although, it was not possible to determine whether these <1μm particles were vesicular.

Sample	Surfactant Ratios (Ro)	Concentration (mM)	Observations						
			BPS 3/4/2012	APS 3/4/2012	5 hours APS 3/4/2012	1 day APS 4/4/2012	1 month APS 1/5/2012	6 months APS 25/9/2012	1 year 9 months APS 14/1/2014
RVe1c8	3.5	20	T+WFP(grainy)+NL	Cl+WSL	O+B+ WFP(some and high viscosity)+SL	O+B+WFP(high viscosity)+SL	O+B+CLay+ WGP+SL	T+YWGP+NL [T+YWGP+Fla(w)+NL(except flakes) AHS]	T+YGP+NL
			Directly APS 16/11/2012	3 days APS 19/11/2012		1 year APS 29/10/2013		1 year 7 months APS 11/6/2014	
SAXS 4/5	3.5	20	Cl	O+B+WFP(high viscosity)+SL		T+YWGP+NL		T+ YWGP+NL	

Table 38: Tables presenting the changes in phase behaviour for RVe1c and SAXS heptane 3.5 Ro samples

Sample Number	Micrograph	Sample and Micrograph Description
RVe1c **8 Hep**	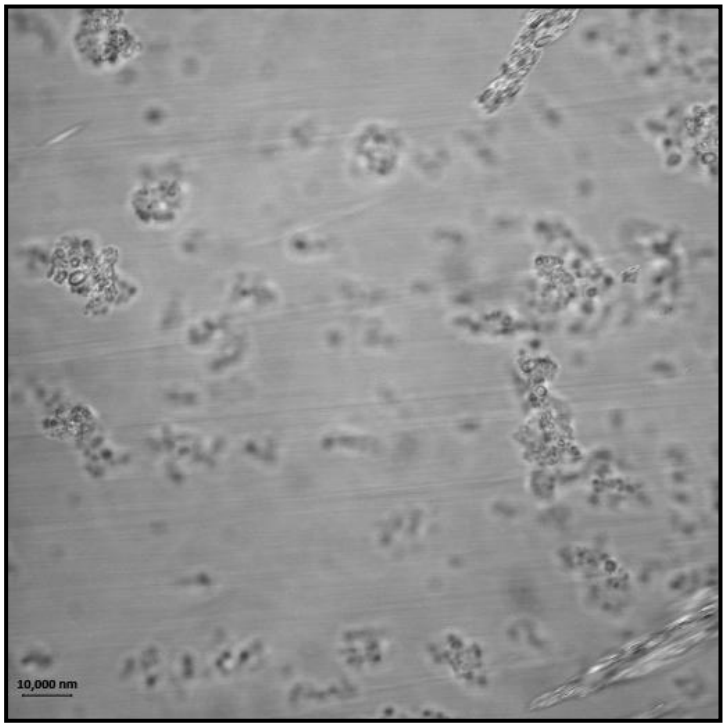	**Figure 84:** 3.5 Ro heptane micrograph **Date of Micrograph**: 17/5/2012 **Sample description**: O+B+CLay+WGP+SL 1 month after probe sonication. Shaken - Minutes after sample shaken **Micrograph description**: Shape distribution – Spherical to irregular spheroids individual structures. Clusters irregular. Size distribution – ~1 μm to 4 μm individual particles. Irregular clusters of particles up to ~30 μm. Small clusters are common and consist dominantly of the larger (>2 μm) particles. The particles above 1μm have perceivable walls and internal compartments. The walls range from thin to thick (taking up over half of the volume). During viewing, the particles (especially the aggregates) were moving and therefore distorted some of the image. This is likely due to the larger particles being drawn together to cluster after the initial shaking of the sample. This was the first image to be taken; the others (Figures 85, 86, 87, and 88) were taken after the solution began to settle.

Sample Number	Micrograph	Sample and Micrograph Description
RVe1c 8 Hep	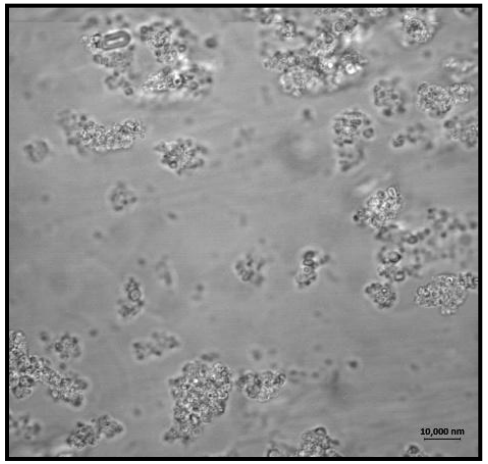 (a) 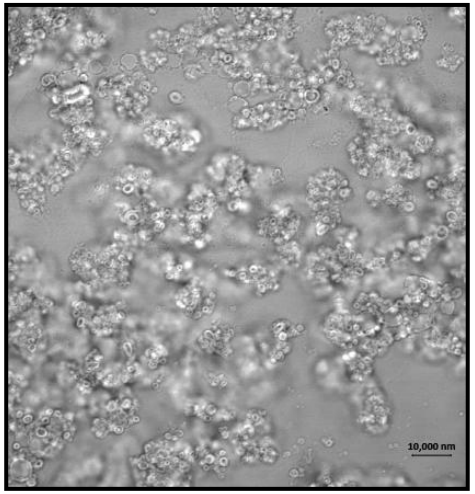 (b)	**Figure 85:** 3.5 Ro heptane micrograph **Date of Micrograph**: 17/5/2012 **Sample description**: O+B+CLay+WGP+SL 1 month after probe sonication. Shaken. **Micrograph description**: Minutes after sample shaken- Shape distribution – Spherical, irregular spheroids to tubular individual structures. Clusters irregular. Size distribution – ~1 μm to 4 μm individual particles. One tabular structure 10 μm by 5 μm. Irregular clusters of particles, eventually making a network that extends beyond the viewing area. The particles above 1 μm have perceivable walls and internal compartments. The walls range from thin to thick (taking up over half of the aggregate volume). There was only one minute between taking these images. Figure **(a)** shows some distortion due to the movement of the clusters. Figure **(b)** shows that after a minute of the smaller clusters moving and amassing a large network of clustered particles form. Between these images, it is also shown that the large elongated particle (top left corner) increases its curvature with time.

Sample Number	Micrograph	Sample and Micrograph Description
RVe1c 8 Hep	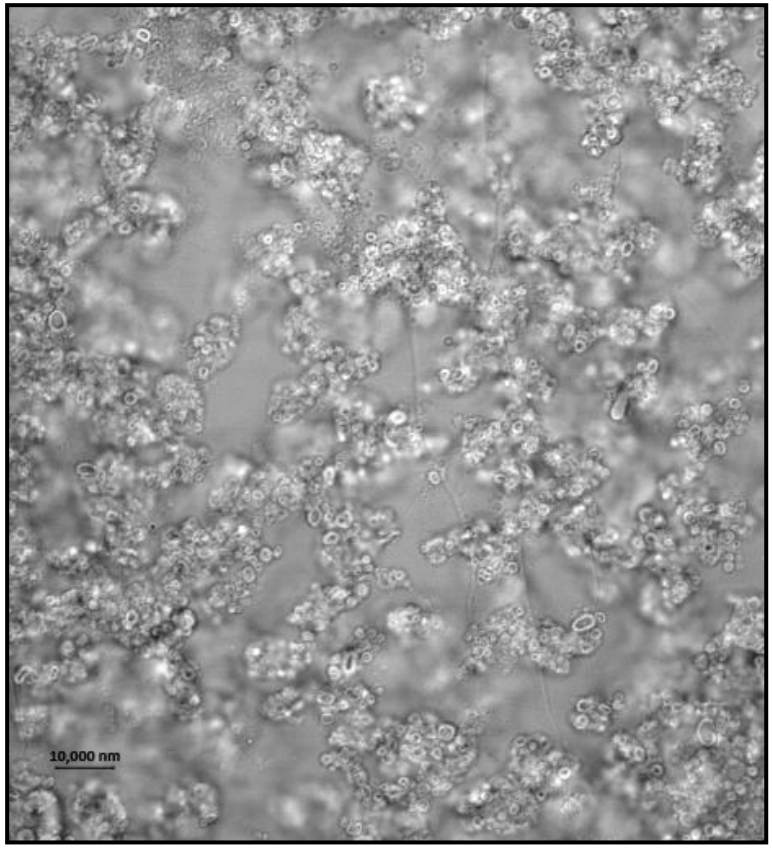	**Figure 86:** 3.5 Ro heptane micrograph **Date of Micrograph**: 17/5/2012 **Sample description**: O+B+CLay+WGP+SL 1 month after probe sonication. Shaken **Micrograph description**: Minutes after sample shaken- Shape distribution – Spherical, irregular spheroids, curved tubular and wavy lines as individual structures. Clusters irregular network. Size distribution – ~1 μm to 4 μm individual spherical particles. The particles above 1 μm have perceivable walls and internal compartments. The walls range from thin (just perceivable) to thick (taking up over half of the particles volume) but most frequently lie between these extremes. There is a heterogeneous size and shape distribution within the clusters.

Sample Number	Micrograph	Sample and Micrograph Description
RVe1c 8 Hep	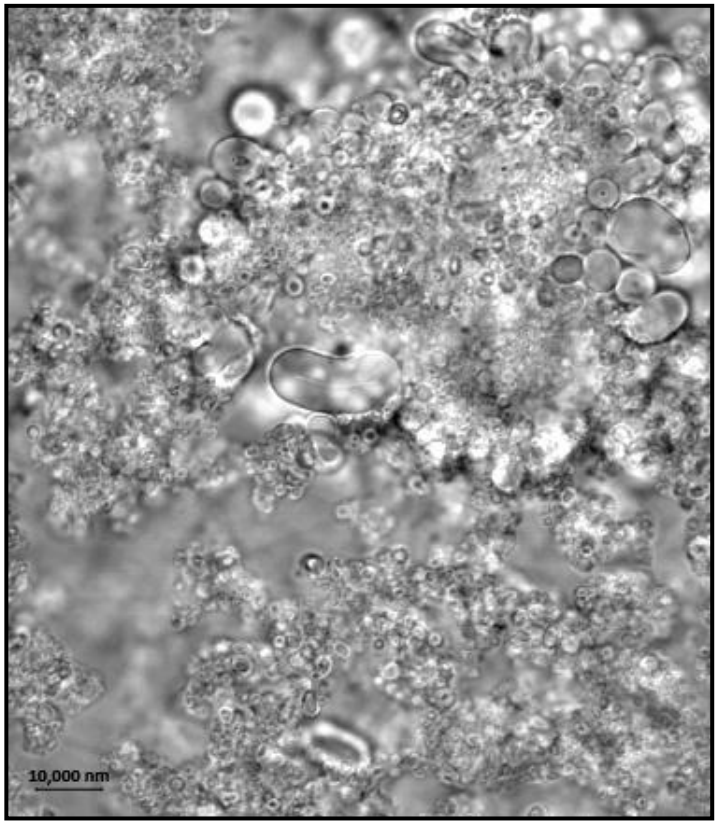	**Figure 87:** 3.5 Ro heptane micrograph **Date of Micrograph**: 17/5/2012 **Sample description**: O+B+CLay+WGP+SL 1 month after probe sonication. Shaken **Micrograph description**: Minutes after sample shaken- Shape distribution – Spherical, irregular spheroids, curved tubular and wavy lines as individual structures. Clusters irregular network. Size distribution – ~1 μm to 14 μm individual spherical particles. There is a heterogeneous size and shape distribution within the clusters. The particles above 1 μm have perceivable walls and internal compartments. The walls range from thin (just perceivable) to taking up most of the aggregate volume, but most frequently they lie between these extremes. One large (10 μm) irregular spheroid (centre right of the image) does not appear to have an internal compartment. There is at least one obvious large reverse vesicular onion structure in the centre right of the image. This onion structure was probably formed from large revere vesicles merging; one example of this occurring is the figure of eight feature (directly left the large 14 μm curved tabular reverse vesicle).

Sample Number	Micrograph	Sample and Micrograph Description
RVe1c **8 Hep**	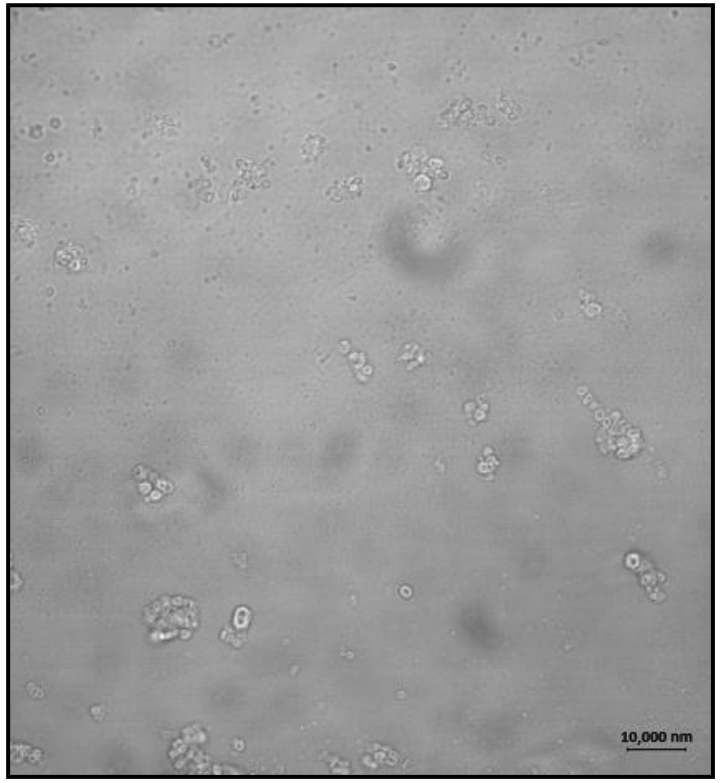	**Figure 88:** 3.5 Ro heptane micrograph **Date of Micrograph**: 17/5/2012 **Sample description**: O+B+CLay+WGP+SL 1 month after probe sonication. Shaken. **Micrograph description**: Minutes after sample shaken- Shape distribution – Spherical and irregular spheroids as individual structures. Clusters irregular. Size distribution – ~1 μm to 4 μm individual particles. ~30 μm clusters. The clusters are mainly made of 2-4 μm particles. The particles above 1 μm have perceivable walls and internal compartments. The walls range from thin (just perceivable) to thick (taking up over half of the particles volume), but most frequently they lie between these extremes. Those aggregates that are not clustered are mainly <1 μm and are quite frequent in the sample; but these are too small to distinguish their characteristics with this method.

5.3.3.3 Heptane 4.5 Ro

The solution appeared cloudy after probe sonication. The cloud forming particles quickly settled within a few hours to leave an opalescent solution with a bluish hue and a white viscous precipitant; see Table 39. This implies that the system is initially very polydisperse with large suspended particles settling rapidly and the smaller colloidal particles remaining solvated.

Within a month an overlying cloudy layer would form over the precipitant and the opalescence of the sample would fade to a transparent state. However, the colloidal particles remain suspended for 6 months in the RVe1c 12 sample in comparison to 1 year and 7 months in the SAXS 6/7 sample. This difference may be due to the slightly less 4.2 Ro value of the RVe1c 12 sample making the temporal stability similar to the 3.5 Ro results.

Microscopy of a handshaken sample containing a white gel precipitant shows a mass formed of clustered particles (multilamellar to onion reverse vesicles) approximately 1 μm to 3 μm in diameter; see Figures 89 and 90. Some of these particles have the defined boundary expected of a reverse vesicle; however, the lack of well defined boundaries between most of these particles shows that many of the once separated bilayers between reverse vesicles have merged to form an interconnected network. This interconnected network bestows the gel-like characteristic upon the precipitant.

5.3.3.4 Summary of heptane systems

All systems had co-existing phases of a suspension of highly polydisperse, micron sized multilamellar reverse vesicles that quickly settled out of solution and a colloidal dispersion presenting Tyndall scattering. However, flocculation rates are faster in the 3.5 Ro samples compared to the 2.5 Ro and 4.5 Ro samples. This may be related to a high polydispersity of colloidal particles in the 3.5 Ro sample; or due to a higher percentage of amphiphiles forming the micron sized multilamellar reverse vesicles in the 2.5 Ro and 4.5 Ro systems leaving a relatively lower concentration of colloidal particles. This reduced concentration of colloidal particles would increase the space between particles and cause a reduction in the rate of random collisions between particles.

Sample	Surfactant Ratios (Ro)	Concentration (mM)	Observations						
			BPS 3/4/2012	APS 3/4/2012	5 hours APS 3/4/2012	1 day APS 4/4/2012	1 month APS 1/5/2012	6 months APS 25/9/2012	1 year 9 months APS 14/1/2014
RVe1c12	4.5	20	T+WFP(grainy)+NL	Cl+WSL	O+B+WFP(high viscosity)+SL	O+B+ WFP(high viscosity)+SL	O+B+CLay+ WGP+SL	T+WYGP+NL [O(s)+WYGP+SL AHS]	T+YGP+NL

			Directly APS 16/11/2012	3 days APS 19/11/2012	1 year APS 29/10/2013	1 year 7 months APS 11/6/2014
SAXS 6/7	4.5	20	Cl	O+B+ WFP(high viscosity)+SL	T+WFP(0.5ml overlying) +WGP(0.5ml)+SL	T+WFP(high viscosity 1ml)+WL

Table 39: Tables presenting the changes in phase behaviour for RVe1c and SAXS heptane 4.5 Ro samples.

Sample Number	Micrograph	Sample and Micrograph Description
RVe1c **12 Hep**	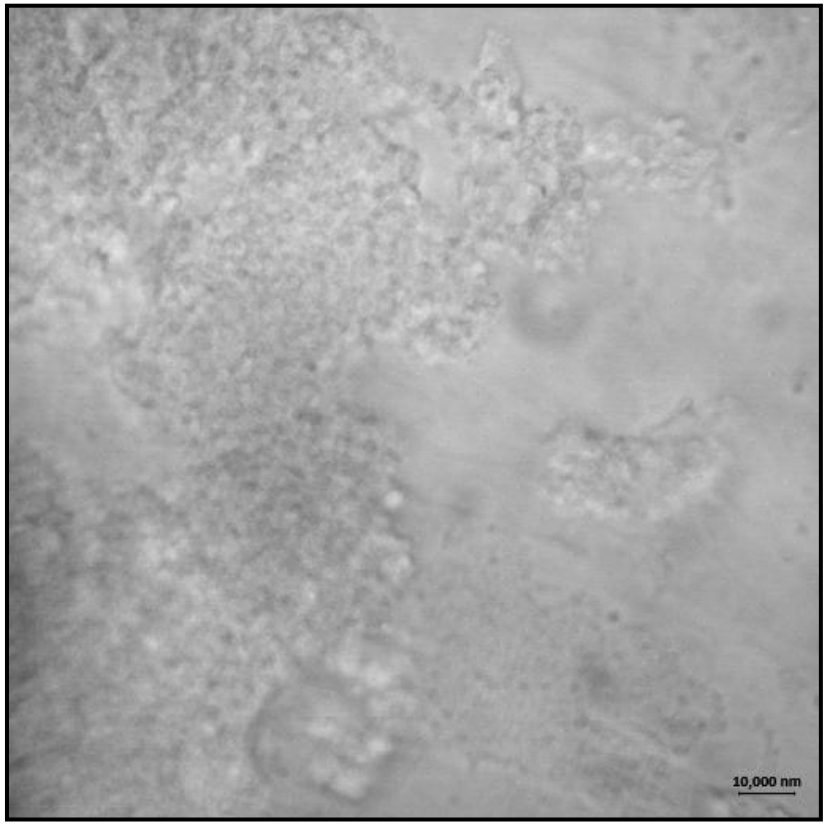	**Figure 89:** 4.5 Ro heptane micrograph **Date of Micrograph**: 17/5/2012 **Sample description**: O+B+CLay+WGP 1 month after probe sonication. Shaken **Micrograph description**: Shape distribution – Irregular spheroids as individual structures. Clusters irregular. Size distribution – ~1 μm to 3 μm individual particles. >70 μm clusters. The particle walls seem to be irregular, although, this effect may be caused from overlapping or interconnecting particles.

Sample Number	Micrograph	Sample and Micrograph Description
RVe1c **12 Hep**	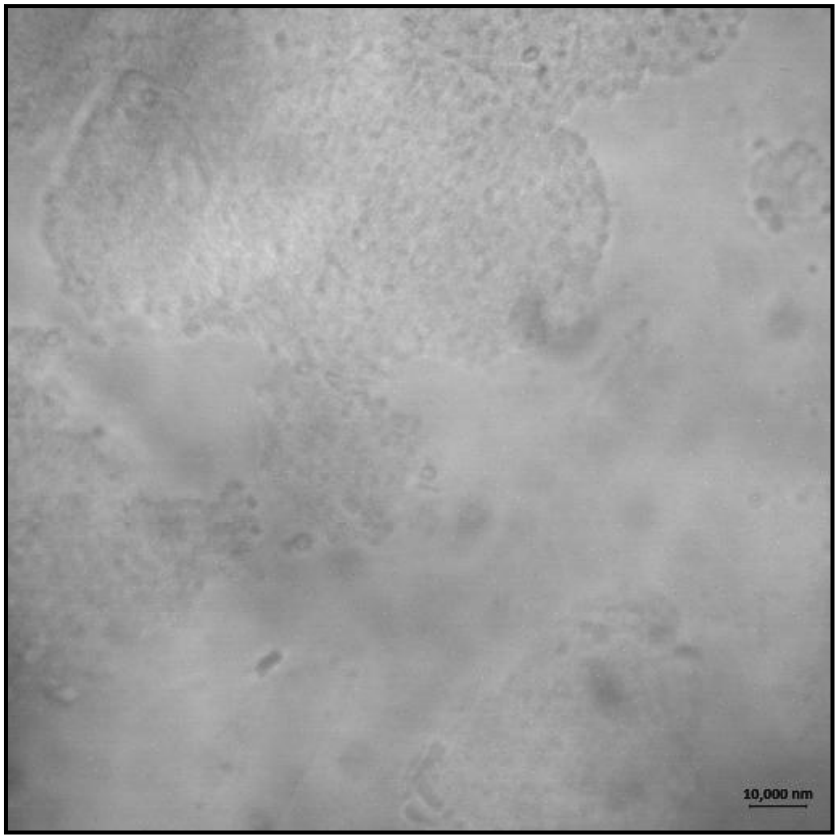	**Figure 90:** 4.5 Ro heptane micrograph **Date of Micrograph**: 17/5/2012 **Sample description**: O+B+CLay+WGP 1 month after probe sonication. Shaken **Micrograph description**: Shape distribution – Irregular spheroids and ellipsoids as individual structures. Clusters irregular. Size distribution – ~1 μm to 3 μm individual particles. >70 μm clusters. The particle walls seem to be irregular, although, this effect may be caused from overlapping or interconnecting aggregates.

5.3.4 Multi-component amphiphilic-hexane systems

5.3.4.1 Hexane 2.5 Ro

After sonication the system becomes cloudy but this transforms within a few hours into a colloidal dispersion displaying opalescence and a blue hue overlying a white gel precipitant; see Table 40. This state remains stable for some months and implies that the system is initially very polydisperse with large suspended particles settling rapidly and the smaller colloidal particles remaining solvated.

Microscopy of a one month old sample shaken by hand shows a mass of structures making up the white gel precipitant that appear to be interconnected particles 1 μm to 10 μm in diameter; with the structures presenting coexisting phases of spherical onions and multilamellar vesicle and phase separated crystals; see Figures 91and 92.

After a year the solution tends to fade to a slight opalescence or transparent but keeps some laser reflection indicating a small quantity of particles still in solution indicating a slow flocculation rate. At this point the precipitant begins to change into a yellow gel.

5.3.4.2 Hexane 3.5 Ro

After sonication the system becomes cloudy but this transforms within a few hours into a colloidal dispersion displaying opalescence and a blue hue overlying a white fluid precipitant; see Table 41. This implies that the system is initially very polydisperse with large suspended particles settling rapidly and the smaller colloidal particles remaining solvated.

Depending on the amount of sonication time the solution either: becomes transparent with no laser reaction after 6 months and the precipitant becomes a yellow gel over a year, for a 10 min probe sonication; or remains opalescent without any Tyndall scattering but has a large amount of white fluid precipitation for over a year, for a 3 min probe sonication.

Microscopy of the SAXS 18/19 system after 1 year and 8 months reveals 2-5 μm rough spheres with no obvious walls, reminiscent of compound reverse micelles, and the opaque yellow precipitant is formed of the same rough spheres interconnected into larger clusters.

Sample	Surfactant Ratios (Ro)	Concentration (mM)	Observations						
			BPS 3/4/2012	APS 3/4/2012	3 hours APS 3/4/2012	1 day APS 4/4/2012	1 month APS 1/5/2012	6 months APS 25/9/2012	1 year 8 months APS 2/12/2013
RVe1c 5	2.5	20	Cl+SL AHS	Cl+WSL	O+B+WGP+SL	O+B+WGP+SL	O+B+WGP+SL	Tr+Mot(YGP+ some WGP)+WL [Cl+O+YGP(some)+WSL AHS]	T (3ml: 1 ml lost due to evaporation) +YGP+WL(very weak)
			Directly APS 16/11/2012		3 days APS 19/11/2012		1 year APS 28/11/2013		1 year 7 months APS 11/6/2014
SAXS 16/17	2.5	20	Cl+TGP		O+WGP+SL		O+BLay(overlying)CLay+WYGP+SL(increasing strength towards base)		Tr+WYGP+WL

Table 40: Tables presenting the changes in phase behaviour for RVe1c and SAXS hexane 2.5 Ro samples.

Sample	Surfactant Ratios (Ro)	Concentration (mM)	Observations						
			BPS 3/4/2012	APS 3/4/2012	5 hours APS 3/4/2012	1 day APS 4/4/2012	1 month APS 1/5/2012	6 months APS 25/9/2012	1 year 8 months APS 2/12/2013
RVe1c9	3.5	20	Cl+WSL AHS	Cl+WSL	O+B+WFP+SL	O+B+WFP+SL	O+B+CLay+WGP+SL	T+Mot(WGP with T spheres)+NL [O+WGP+WL AHS]	T+YGP+NL
			Directly APS 16/11/2012		3 days APS 19/11/2012		1 year APS 28/11/2013	1 year 7 months APS 11/6/2014	1 year 8 months APS 11/7/2014
SAXS 18/19	3.5	20	Cl+TGP		O+WFP+SL		Tr+WSP(0.4ml)+SL	Tr+WSP(0.5ml)+SL	Tr+WYGP+SL

Table 41: Tables presenting the changes in phase behaviour for RVe1c and SAXS hexane 3.5 Ro samples.

Sample Number	Micrograph	Sample and Micrograph Description
RVe1c **5 Hex**	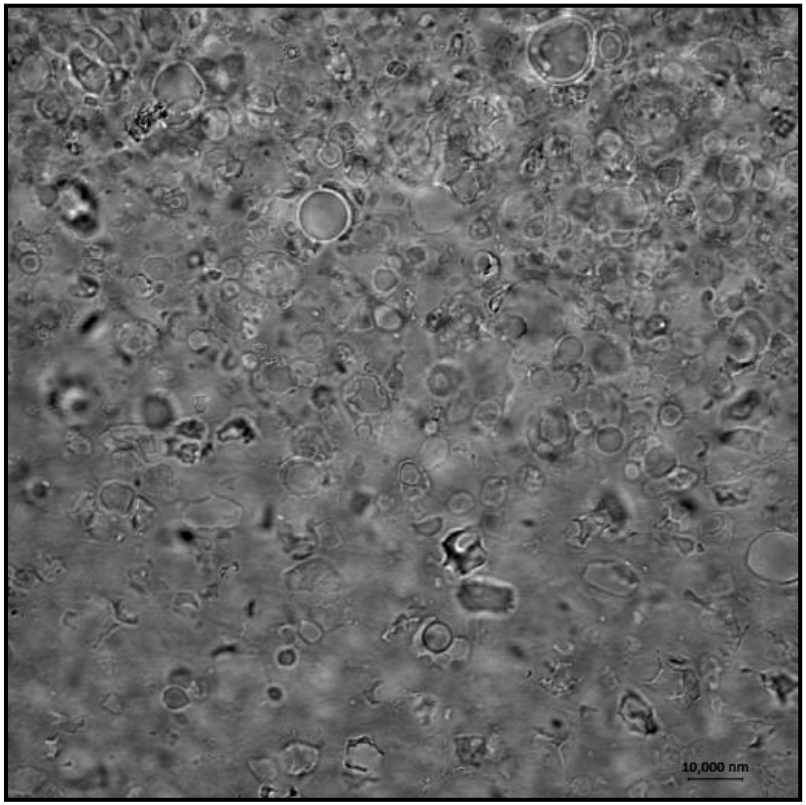	**Figure 91:** 2.5 Ro hexane micrograph **Date of Micrograph**: 17/5/2012 **Sample description**: O+B+WGP+SL 1 month after probe sonication. Shaken **Micrograph description**: Shape distribution – Spherical, irregular spheroids and rectangular individual structures. Size distribution – ~1 μm to 10 μm individual particles. The spherical particles are often a clearly defined, thick wall and internal compartment. Although, the wall thicknesses are often irregular within a particle. The rectangular features (centre/bottom of image) do not seem to have walls and resemble crystals.

Sample Number	Micrograph	Sample and Micrograph Description
RVe1c **5 Hex**	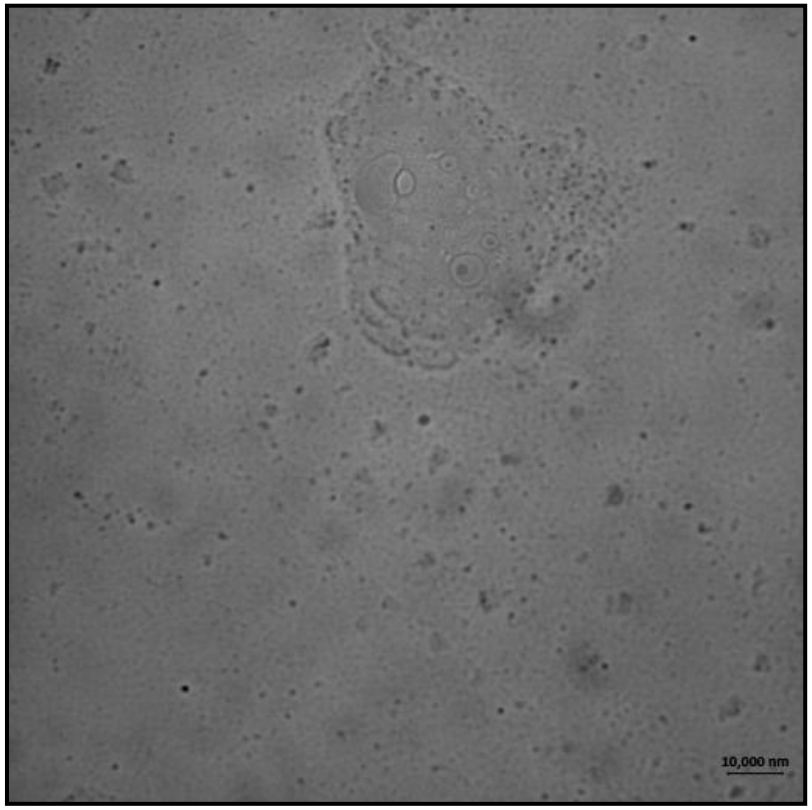	**Figure 92:** 2.5 Ro hexane micrograph **Date of Micrograph**: 17/5/2012 **Sample description**: O+B+WGP+SL 1 month after probe sonication. Shaken **Micrograph description**: Shape distribution – Spherical and irregular spheroid individual structures. Size distribution – ~1 μm to 5 μm individual particles. One ~50 μm cluster. The background mesh of independent aggregates <2 μm are too small to determine morphological features. There is one large cluster that seems to consist of particles with definable wall/internal compartments but also appear to have merged into one interconnected aggregate.

5.3.4.3 Hexane 4.5 Ro

The system becomes cloudy after sonication but this transforms within a few hours into a colloidal dispersion displaying opalescence and a blue hue overlying a white fluid precipitant; see Table 42. This implies that the system is initially very polydisperse with large suspended particles settling rapidly and the smaller colloidal particles remaining solvated.

Microscopy of a shaken RVe1c 13 after 1 month (gel precipitant) seems to show no small particles but large (x100 μm) rough spheres of either; a bicontinuous phase, or, aggregated 3-4 μm micellar or vesicular spherical particles; see Figure 93.

The sample prepared with 4 min probe sonication (SAXS20/21) remains stable for over a year. However, increased flocculation is observed for the 10 min probe sonicated sample (RVe1c 13) that presents a cloudy layer and white gel precipitant after a month, and all particles have settled after 6 months.

5.3.4.4 Summary of hexane systems

The prevalent multilamellar vesicles and onions in the 2.5 Ro systems indicate that this system is dominated by lamellar structures. However, the rough surfaces and absence of clear walls in the micrometre sized particles in the 3.5 Ro and 4.5 Ro systems indicate micellar systems.

Sample	Surfactant Ratios (Ro)	Concentration (mM)	Observations						
			BPS 3/4/2012	APS 3/4/2012	5 hours APS 3/4/2012	1 day APS 4/4/2012	1 month APS 1/5/2012	6 months APS 25/9/2012	1 year 8 months APS 2/12/2013
RVe1c 13	4.5	20	Cl+WSL AHS	Cl+WSL	O+B+WFP+SL	O+B+WFP+SL	O+B+CLay+WGP+SL	T+TGP(very faint yellow)+NL [Tr+TGP(very faint yellow)+WL AHS]	T+YGP+NL
			Directly APS 16/11/2012		3 days APS 19/11/2012		1 year APS 28/11/2013	1 year 7 months APS 11/6/2014	
SAXS 20/21	4.5	20	Cl+TGP		O+WFP+SL		Tr+WSP(0.3ml)+SL	T+WSP(0.5ml)+NL	

Table 42: Tables presenting the changes in phase behaviour for RVe1c and SAXS hexane 4.5 Ro samples.

Sample Number	Micrograph	Sample and Micrograph Description
RVe1c **13 Hex**	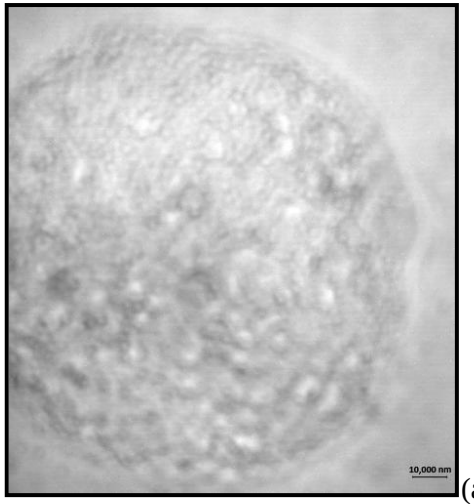 (a) 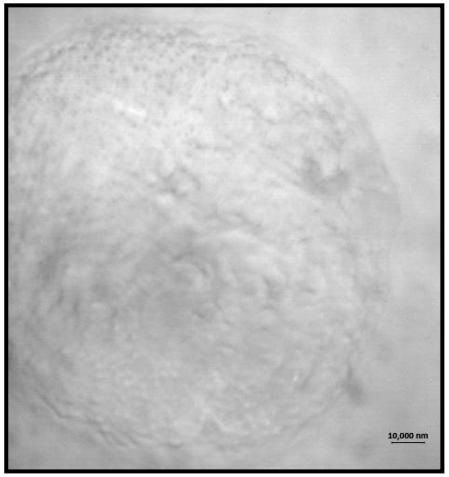 (b)	**Figure 93:** 4.5 hexane micrograph **Date of Micrographs**: 17/5/2012 **Sample description**: O+B+CLay+WGP+SL 1 month after probe sonication. Shaken **Micrograph description**: Shape distribution – Spherical and irregular spheroid individual structures. Irregular spherical cluster. Size distribution – Homogenous ~3-4 μm individual particles. <100 μm cluster. The spherical cluster has a rough surface and is either a bicontinuous phase or consists of aggregated spherical particles that may have either micellar or vesicular structures.

5.3.5 Multi-component amphiphilic-pentane systems

5.3.5.1 Pentane 2.5 Ro

The system is cloudy after sonication but within a few hours transforms into a colloidal dispersion displaying opalescence overlying a grainy, white precipitant with solid characteristics; see Table 43. This implies that the system is initially very polydisperse with large suspended particles settling rapidly. After six months all the colloidal particles have formed flocs and settled out of solution forming a desolvated yellow gel precipitant.

Microscopy results of a month old, shaken sample containing a white gel precipitant shows some 5 – 10 micrometer sized reverse vesicular onions and a high quantity of phase separated crystal regions.

5.3.5.2 Pentane 3.5 Ro

The system is cloudy after sonication but transforms within a few hours into a colloidal dispersion displaying opalescence overlying a white fluid precipitant; see Table 44. This implies that the system is initially very polydisperse with large suspended particles settling rapidly and the smaller colloidal particles remaining solvated for months.

After a day the precipitant becomes grainy and after a month it has coalesced to obtain solid characteristics. Microscopy after one month shows an equally dispersed phase of 1 μm particles and numerous 10-60 μm particles in the solution; see Figure 94. The 1 μm particles were too small to distinguish morphological features, but these particles may form the colloidal dispersion. The large particles appear to have very thick walls surrounding either a compartment or a particle with unknown morphology. The thick walls have internal irregularities that do not correspond to bilayers. This might be a unique structure, with reverse bicontinuous or reverse compound micelles forming the walls of a compartment surrounding a pocket of solvent (similar to that of a vesicle). This requires further investigation using fluorescence microscopy or TEM.

Sample	Surfactant Ratios (Ro)	Concentration (mM)	Observations						
			BPS 3/4/2012	APS 3/4/2012	5 hours APS 3/4/2012	1 day APS 4/4/2012	1 month APS 1/5/2012	6 months APS 25/9/2012	1 year 8 months APS 1/12/2013
RVe1c 6	2.5	20	T+WSP(grainy and flaky)+NL [Cl+WSL AHS]	Cl+WSL	O+WSP(grainy flakes)+SL	Tr+WSP(grainy)+SL	Tr+WSP+SL	T+YGP+NL [O+YGP+WSL handshaken]	T+YGP+NL
			Directly APS 16/11/2012	3 days APS 19/11/2012				1 year APS 2/12/2013	
SAXS 9/10	2.5	20	Cl	O+ WSP(grainy)+SL				**Evaporated**: YGP	

Table 43: Tables presenting the changes in phase behaviour for RVe1c and SAXS pentane 2.5 Ro samples.

Sample	Surfactant Ratios (Ro)	Concentration (mM)	Observations					
			BPS 3/4/2012	APS 3/4/2012	5 hours APS 3/4/2012	1 day APS 4/4/2012	1 month APS 1/5/2012	6 months APS 25/9/2012
RVe1c 10	3.5	20	T+WGP+NL [Cl+WSL AHS]	Cl+SL	O+B+WFP+SL	O+ WFP(grainy)+SL	O+ WSP(grainy)+SL	**Evaporated**: YGP
			Directly APS 16/11/2012	3 days APS 19/11/2012			1 year APS 2/12/2013	
SAXS 11/12	3.5	20	Cl	O(slightly)+WFP(grainy)+SL			T+WGP(with some yellow patches)+NL	

Table 44: Tables presenting the changes in phase behaviour for RVe1c and SAXS pentane 3.5 Ro samples.

Sample Number	Micrograph	Sample and Micrograph Description
RVe1c **10 Pent**	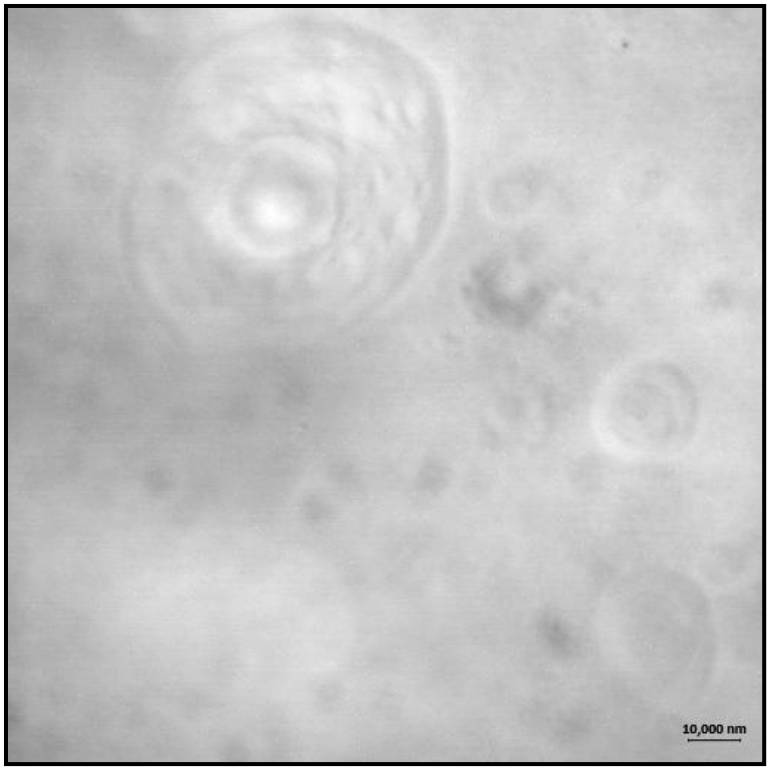	**Figure 94:** 3.5 Ro pentane micrograph **Date of Micrographs**: 17/5/2012 **Sample description**: T+O(slightly)+WGP(grainy)+SL 1 month after sonication. Non-shaken, precipitation. **Micrograph description**: Shape distribution – Rough spherical particles. Size distribution – Background homogeneous 1 μm particles. Large particles ~10 μm to 60 μm in diameter. All background aggregates were too small to distinguish morphological features and are out of focus in this image. The large particles appear to have very thick walls surrounding either a compartment or a particle with unknown morphology. The thick walls have internal irregularities that do not correspond to bilayers.

5.3.5.3 Pentane 4.5 Ro

After sonication the system becomes a cloudy suspension; most of the particles settle out of solution within a few hours to form a viscous, white fluid precipitant and coalesces to become a white gel precipitant within a day; see Table 45. Most particles have settled out of solution after a week and all particles have settled within a month.

Microscopy of the intermediate, one month old, yellow white gel precipitant indicates large stacked sheets or ribbons; see Figure 95. This suggests the precipitant is a layer of stacked, multilamellar bilayer sheets and therefore is in a lamellar phase.

5.3.5.4 Summary of pentane systems

Although a few micrometre sized multilamellar reverses are present in the 2.5 Ro system they are not the dominant structures and there are no large reverse vesicles in the 3.5 Ro and 4.5 ro systems. The 3.5 Ro system appears to be complicated and requires further anaylsis to be fully anaylsed. The 4.5 Ro system appears to be lamellar, however, the packing parameter must be close to 1 to form stacked sheets rather than curved vesicles.

Sample	Surfactant Ratios (Ro)	Concentration (mM)	Observations						
			BPS 3/4/2012	APS 3/4/2012	5 hours APS 3/4/2012	1 day APS 4/4/2012	1 month APS 1/5/2012	6 months APS 25/9/2012	1 year 8 months APS 1/12/2013
RVe1c 14	4.5	20	T+WSP(grains)+WGP+NL [Cl+WSL AHS]	Cl+WSL	Tr+WFP(high viscosity)+WL	Tr+WGP+WL	T+YWGP+NL	T+YGP+NL [Tr+YGP+SL AHS]	T+YGP+NL
			Directly APS 16/11/2012		3 days APS 19/11/2012	1 year APS 2/12/2013		1 year 7 months APS 11/6/2014	
SAXS 13/14	4.5	20	Cl		Tr+WGP+WL	T+Mot(TGP, WGP and YGP patches)+ NL		T+Mot(WGP+YGP, grainy)+NL	

Table 45: Tables presenting the changes in phase behaviour for RVe1c and SAXS pentane 4.5 Ro samples.

Sample Number	Micrograph	Sample and Micrograph Description
RVe1c **14 Pent**	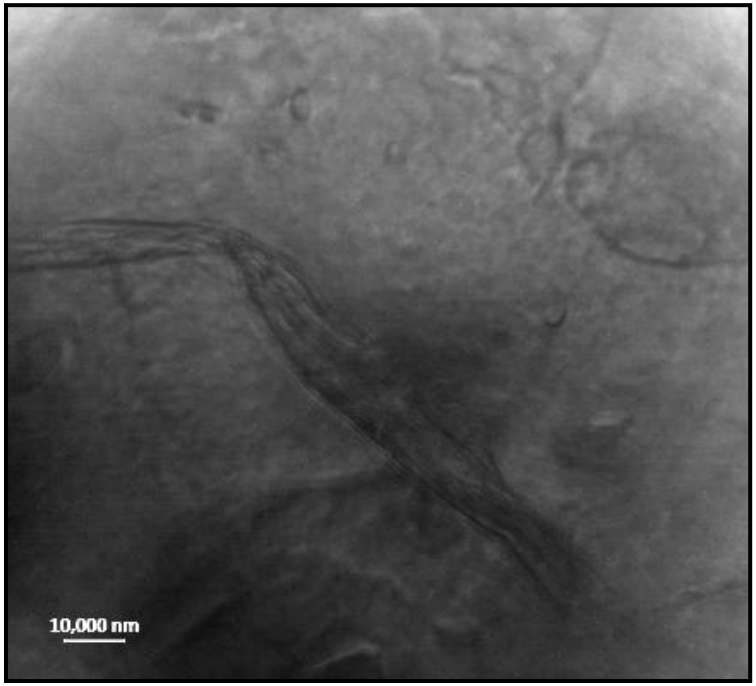	**Figure 95:** 4.5 Ro pentane micrograph **Date of Micrograph**: 17/5/2012 **Sample description**: T +YWGP+NL 1 month after sonication. Non-shaken, precipitation. **Micrograph description**: The precipitation is made of stacked sheet or ribbons.

5.4 Summary of macroscopic and microscopic phase behaviour

5.4.1 Answers to key questions

The key questions we intended to answer in this study were:

- Can we replicate the results published by Tung *et al.* (2008) and create colloidal dispersions containing unilamellar reverse vesicles using C18 95%?

Yes. Unlike the C18 99% systems studied in Chapter 4 long-lasting colloidal dispersions of unilamellar reverse vesicles were present in 2.5 Ro, 3.5 Ro and 4.5 Ro cyclohexane systems; for example, see Figure 75 and 78 and Tables 31, 32 and 33. However, Tung *et al.* (2008) noted that their systems began to phase separate at amphiphilic ratios higher than 4 Ro; this implies the boundary for a macroscopic phase transition is actually at a higher amphiphilic ratios than published.

- Can unilamellar reverse vesicles form from C4 and C18 95% products in alkanes?

Yes. Unilamellar reverse vesicles are prevalent across the 2.5 Ro to 4.5 Ro systems of high molecular weight alkanes, however, these systems were had a large size polydiversity with giant (over a micrometre diameter) uni- and multi- lamellar reverse vesicles settling out of solution early. This was evidenced by long lived Tyndall scattering, see Table 34-39, and microscopy of the larger settled reverse vesicles; for example, see Figures 80, 86 and 87.

- Does the molecular weight of the alkane solvents affect self assembly of C4 and C18 95% products?

Yes. With a reduction in molecular weight of alkane solvents the amphiphilic ranges within which reverse vesicles are found is reduced (within the amphiphilic ranges studied). Reverse vesicles dominate the 2.5 Ro to 4.5 Ro range of high molecular weight alkanes, reducing to 2.5 Ro for mid range alkanes (see Tables 40-42 and Figure 91) and do not dominate any of the low molecular weight alkanes (see Table 43-45).

Micelles begin to dominate the high amphiphilic ratios of the mid molecular weight alkane, hexane, systems. And phase separated lamellar sheets dominate the high amphiphilic ratio of the pentane system (lowest molecular weight solvent in this study); see Figure 95.

- What is the temporal stability of self assembled structures composed of C4 and C18 95%?

Particles over a few microns in size tended to settle out of solution within a week. Smaller particles formed stable colloidal dispersions that remained in solution for months or years depending on the system. Nanometre sized unilamellar reverse vesicles often remained

suspended for years with a low flocculation rate (e.g. see Table 31). After settling to form a precipitant, reverse vesicles could be easily re-dispersed into the solution by hand shaking. However, after standing for a few months the particles would merge to form an interconnected gel-like precipitant which could not be easily re-dispersed into solution by hand shaking. These gels were either a mesh-like or formed multi-compartmented particles.

- What is the effect on phase behaviour and microscopic structures of systems containing lyso-PC18 compared to systems lacking lyso-PC18 as detailed in Chapter 4?

Across the 2.5 Ro to 4.5 Ro amphiphilic ratio range the systems containing lyso-PC18 often produced stable colloidal dispersions of reverse vesicles, but in this same range the systems without the lyso-PC18 mainly produced micellar suspensions. However, 7 Ro cyclohexane systems produced colloidal dispersions of reverse vesicles in lyso-PC18 absent systems but with lyso-PC18 a 7 Ro cyclohexane system produced phase separated crystals. This indicates that the inclusion of a small quantity of lyso-PC18 has a strong effect on the amphiphilic ratio range over which reverse vesicles can form.

5.5 Conclusions leading to further analyses

Many of these systems present stable colloidal dispersions that can be studied with scattering techniques. There were difficulties with studying structures on a nanometre scale using TEM imaging due to the disruption from the evaporation procedure and the fast distortion of particles by the electron emission. Therefore, to obtain *in situ* information regarding the size, shape and polydispersity of the colloids studies using DLS, SANS and SAXS techniques were undertaken and are presented in Chapters 6 and 7. For the lamellar systems the SANS and SAXS techniques were also employed to evaluate bilayer thickness and spacing between lamellar. Another endeavour for these small angle scattering techniques were for *in situ* evaluation of the systems at low temperatures to further simulate the environmental conditions of Titan's surface.

Chapter 6: Advanced analyses: Study of amphiphilic-hydrocarbon systems with dynamic light scattering

6.1 Introduction

In order to characterise soft matter systems with nanometre-sized structures, dynamic light scattering (DLS) analyses can be a useful tool. Phosphatidylcholine liposomes (and liposomes in general) are often characterised using DLS (Pereira-Lachataignerais *et al.* 2006) as they often fall within the appropriate size range and are commonly produced using sonication, which generates the low polydispersity systems that are required to acquire valid DLS data. Reversed forms of soft matter systems found in amphiphilic-nonpolar systems have already been characterised with dynamic light scattering - including reversed vesicles formed in amphiphilic-hydrocarbon systems (e.g. Rangelov *et al.* 2004; Tung *et al.* 2008) .

The equipment settings and theory for the dynamic light scattering method are set out in the methods chapter. The multi-component systems were selected as research subjects for this study; this included the RVe1c and SAXS sample groups – see Appendix I and II for sample details and preparation methods. Results of the phase behaviour and microscopy evidence for these samples can be found in Chapter 5. Appendix III contains the description for terms used in the sample descriptions. All of the raw DLS data can be found on the accompanying CD to this thesis.

The main purpose for these DLS results was to characterise the potential unilamellar reverse vesicles in the multi-component samples presenting Tyndall scattering as described in Chapter 5. These systems contained solvated structures too small (<1 μm) to be imaged by microscopy. Also, due to the evaporation effect clustering and/or merging structures during TEM preparation (as well as some of the low molecular weight hydrocarbons dissolving much of the carbon grids) obtaining images of these nanometre-sized structures was difficult. DLS gives us information on these structures in-situ, which can give us a better understanding of the true diameter and polydispersity of any unilamellar reverse vesicles in solution.

6.2 Analytical methods

6.2.1 Correlation curve

The first step of the analysis is to check the correlation curve (see Chapter 3 for description of correlation curve). The correlation curve needs to start between ~0.85 and ~0.95 (appropriate

intercept values) and reach ~0 to obtain valid size measurements. If the intercept (times (t) = 0) values are lower than ~0.85 this could imply the sample is scattering too weakly, or the background scattering is too high, to obtain valid DLS data. Normally, a correlation curve reaches 0 within seconds and therefore, a run time of 70 seconds was used for each data set to give the process a generous opportunity to produce a correlation curve that reaches 0.

If the count rate dramatically decreases with each measurement, it shows that the particles are quickly sedimenting or dissolving. In our systems, it would be unlikely for the particles to undergo spontaneous dissolution during the DLS measurements as the measurements were taken over a day after the initial preparation of the samples. Therefore, a dramatic count rate decrease was associated with quick sedimentation for these results. Although this gives us some information about the system, the intensity distribution curves will be invalid, which will prevent further analysis by DLS.

Contaminants, such as dust, cause large fluctuations in count rate and therefore can also produce correlation values over 1; see Figure 96. If these characteristics were observed the first step was to clean the outside of the cuvette. If this did not improve the correlation curve, the inside of the cuvette was cleaned and the sample reanalysed. If the correlation curve was still too rough it signified that the solution was either too polydisperse/multimodal or contained particles that are too large for DLS analysis.

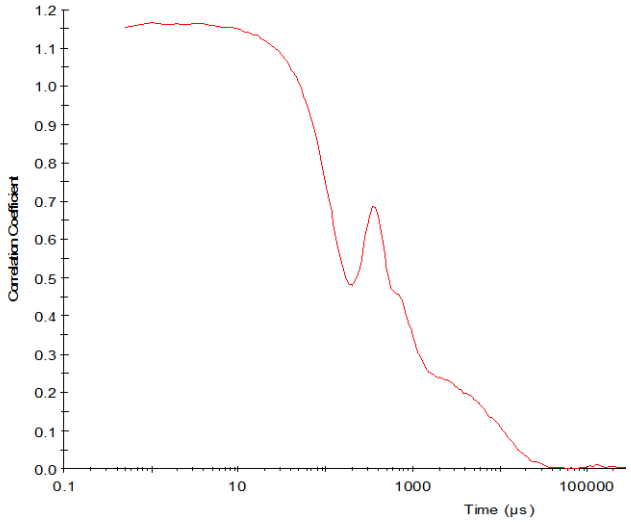

Figure 96: Example of a correlation curve with coefficient values over 1 and fluctuations that might indicate contamination, high polydispersity/multimodal, or large particles that prevent accurate DLS analyses.

Some highly polydisperse/multimodal systems also produce a correlation curve with a plateauing feature near the centre of the curve, see Figure 97.

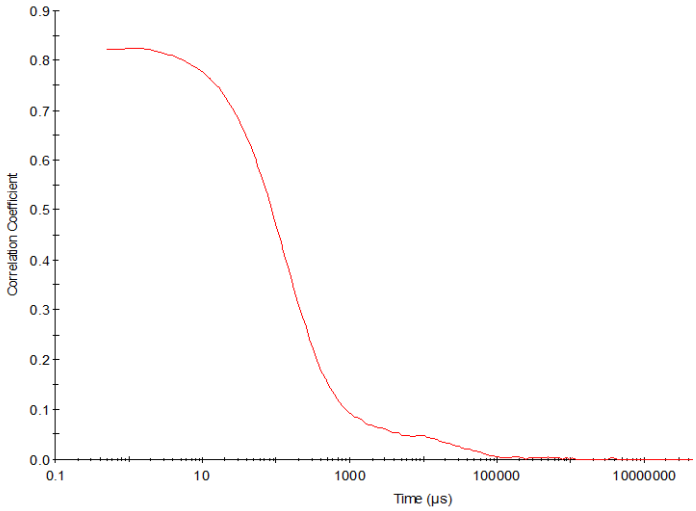

Figure 97: Example of a correlation curve with appropriate intercept values, low fluctuations but plateauing feature beyond 1000µs indicating a high polydispersity/multimodal system preventing accurate DLS analyses.

The difficulty with using light scattering techniques for soft matter assemblages is that some characteristics can incur invalid results; these include assemblages with a high polydispersity, rapid clustering, or incorporate particles beyond the detectable size range. For any of the systems in this study that have these characteristics we may not obtain valid size measurements using DLS. The Malvern instrumentation was set to the default analysis range (the maximum size range) of 0.3 nm to 10 µm. This range encompasses the detection of numerous structures including reverse micelles ~5 nm, unilamellar reverse vesicle sizes x100 nm and some of the smaller, micrometer sized multilamellar reverse vesicles.

Results presenting smooth correlation curves with appropriate intercept values (see Figure 98 for an example) indicated valid intensity fluctuation data had been gathered. Therefore, for these valid results underwent further analysis using intensity and number distribution curves to determine the size, polydispersity, and number of structures in solution.

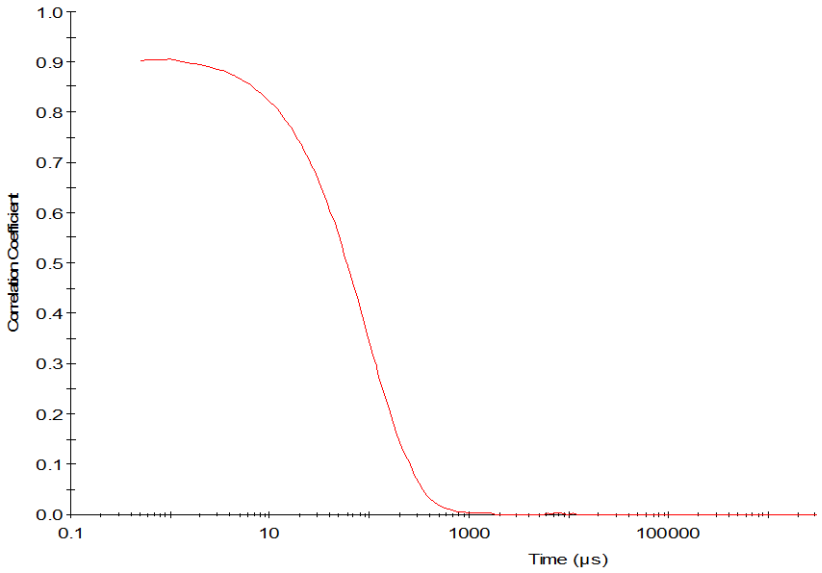

Figure 98: Example of a correlation curve with appropriate intercept, smooth curve, and distinct termination that indicates valid size measurements have been produced using DLS technique.

6.2.2 Intensity and Number distribution curves

The intensity distribution shows the relative intensity against the diameter in nanometres (d. nm). This is a good indicator of a monodisperse or polydisperse system. However, because bigger particles cause larger intensity signals, the intensity values are directly correlated to the size of the structure rather than reflecting the quantity of those particles. To get an idea of the percentage of each size class in solution a number distribution is generated. However, small errors in the correlation function may result in large number distribution errors so these results were considered approximations.

6.2.3 Settings for analysis

The viscosity and refractive index values for the solvents are shown in Table 46. The amphiphilic compounds were given the approximate refractive index of 1.45 and 0.001 absorption that is typical for lipid bilayers of PC (Ardhammar *et al.* 2002). The refractive index of the amphiphiles is used to change the intensity distribution results to a number distribution using Mie theory. Variations in refractive index between 1 and 2 were checked to evaluate their effect on the number distribution, and although the mean size peak changed by a few nanometres, there was no discernible effect on the mode size peak. So, in order to evaluate the number distribution the least variable mode peak values (with varying refractive indices) were analysed.

Material	Viscosity (cP)	Refractive index (589nm λ)	Dielectric Constant
Cyclohexane	0.6250 (at 25°C)	1.423	2.02 (at 20°C)
Octane	0.5080 (at 25°C)	1.394	2 (at 20°C)
Heptane	0.3870 (at 25°C)	1.385	1.92 (at 20°C)
Hexane	0.3000 (at 25°C)	1.373	1.89 (at 20°C)
Pentane	0.2240 (at 20°C)	1.357	1.84 (at 20°C)

Table 46: Viscosity and refractive index values for the hydrocarbon solvents used in the DLS study, taken from the CRC handbook of Chemistry and Physics (Haynes & Lide 2011).

6.2.4 Zeta-average and polydispersity (PD)

The zeta average diameter (D_z) is insensitive to noise: $D_z = \Sigma S_i/\Sigma(S_i/D_i)$, where S_i is the scattered intensity and D_i is the diameter of particle i. However, as this value gives an average diameter for all the particles in solution, and the cumulant analysis is limited to three terms, a highly polydisperse system (<0.5 PD) would not be truly represented by this value. Therefore, this needed to be evaluated in conjunction with the polydispersity index and the intensity distribution curve.

6.3 Size distribution results

A database containing all of the raw DLS data taken during this study can be found in the 'DLS raw results' folder in the accompanying CD. The following sections are separated by solvent types, each containing individual analyses of samples, and terminating with a summary of comparisons between the samples.

6.4 Cyclohexane C18 95% DLS results

The sample road map for these multi-component amphiphilic-cyclohexane samples is Figure 74 and can be found in section 5.3.1.

6.4.1 Cyclohexane 2.5 Ro

Record / Repeat Num	Sample Name	Sample Description	Date	Attenuator	Correlation curve intercept	PD	PD width d. nm	Zeta-Average d. nm	Mode of Intensity Peak 1 d. nm (%)	Mode of Intensity Peak 2 d. nm (%)	Mode of Number Peak 1 d. nm (%)	Mode of Number Peak 2 d. nm (%)
227/1	SAXS 23/24 Cyclohex. 2.5Ro	O+WFP+SL **Unshaken**	22/11/2012 (6 days after prep)	7	0.960	0.274	93.71	178.9	220.2 (96.8)	5560 (3.2)	42.82 (100)	0
228/2				7	0.960	0.312	98.22	175.9	220.2 (97.8)	5560 (2.2)	37.84 (100)	0
229/3				7	0.958	0.275	93.69	178.8	190.1 (97)	5560 (3)	58.77 (100)	0
Mean of 1-3				7	0.960	0.287	95.27	177.9	220.2	5560	43.82	0
235/1	RVe1C 3 Cyclohex. 2.5Ro	O+B+SL **1min bath sonication**	9/5/2012 (6 weeks after prep)	7	0.952	0.281	86.15	162.5	105.7 (51.1)	342.0 (48.9)	68.06 (100)	0
236/1				7	0.949	0.277	86.41	164.3	295.3 (63)	91.28 (37)	68.06 (97.8)	255 (2.2)
237/1				7	0.948	0.274	85.13	162.5	295.3 (62.5)	91.28 (37.5)	78.82 (97.1)	255 (2.9)
				7	0.952	0.277	85.90	163.1	295.3 (59.1)	91.28 (40.9)	68.06 (97.6)	255.0 (2.4)
231/1	RVe1C 3 Cyclohex. 2.5Ro	O+B+SL **3min bath sonication**	4/7/2012 (3 months after prep)	8	0.874	N/A	N/A	N/A	N/A	N/A	N/A	N/A
232/2				8	0.882	N/A	N/A	N/A	N/A	N/A	N/A	N/A
233/3				8	0.910	N/A	N/A	N/A	N/A	N/A	N/A	N/A
Mean of 1-3				8	0.874	N/A	N/A	N/A	N/A	N/A	N/A	N/A

Table 47: DLS results for cyclohexane (C18 95%) 2.5 Ro samples.

Table 47 lists the complete and smooth curve correlation curves, with appropriate intercepts for SAXS 23/24 and RVe1C 3 (May result), which indicate valid intensity distribution results for these measurements. However, the fluctuations and obvious plateauing in the correlation curve of the RVe1C 3 (July result) show these results to be invalid, see Figure 99c. As there was no observable precipitation before the sonication, it is unlikely that the particles in solution were too large for valid measurements. Therefore, either the self-assembled structures became too polydisperse to permit valid DLS measurements during the time between the two DLS measurements taken for the RVe1C 3 sample. Or, the 3 minute water-bath sonication may have separated any structures, bringing them out of equilibrium, and therefore, the particles were self-assembling too quickly during the DLS measurement to enable valid results. However, the acquisition of valid results from the same sample 6 weeks after initial preparation and after 1 minute of sonication (record number 235,236 and 237), implies that it is more likely the structures have become too polydisperse with time.

6.4.1.1 SAXS 23/24

Due to the multimodal nature of the system, the zeta-average may not be the most appropriate value for an accurate evaluation (see Figure 100). Rather, a review of the modal values of the intensity peaks gives a better description of the system.

There is a separate peak at the large size scale of 5560 nm which appears as though it has been limited by the maximum detection size of this DLS equipment. Therefore, this larger peak is probably a hint of larger structures, possibly clusters of x100s nanometre-sized reverse vesicles that may make up the white fluid precipitant of the solution. The smaller peak has some fluctuations between measurements, which indicate that with time all the <60 nm diameter particles merge to form larger particles and a few of the ~200-400 nm particles merge to form more ~400-900 nm sized particles. This has an effect on the main intensity curve with a modal value that changes from 220 nm to 190 nm in the third measurement. However, these values remain larger than the zeta-average values. The averaged intensity curve shows a smooth, Gaussian curve for this smaller peak similar to measurement 3 (see Figure 100c). This information implies that the disturbance of moving the sample from its container to the sample holder broke up a small percent of the self-assembled structures into smaller components, which then reassembled to form a state of equilibrium by the time the third measurement was taken. This is supported by the number distribution which shows the mode of the peak increasing from 38-43 nm in the first two measurements to 59 nm in the final measurement.

6.4.1.2 RVe1c 3 (May result)

Data for RVe1c3, 6 weeks after preparation, showed a bimodal intensity curve; see Figure 101. The distinction between these two peaks grew with time (see Figure 101a) which formed peaks with modes of 295 nm and 91 nm and low polydispersities of 0.11 and 0.08 respectively. It is

likely that the initial amalgamation of the two peaks is caused by the disruption of the system when moving the sample into the DLS sample holder. Because this system is bimodal, the zeta-average value and accompanying polydispersity is invalid. The number distribution broadly follows the smaller peak of the intensity curve, with the larger peak mainly diminished showing that in terms of number there may be a large number of structures in the ~50-150 nm range.

6.4.1.3 Comparison of cyclohexane 2.5Ro results

The difference in the results between the RVe1C 3 and SAXS 23/24 samples at 6 weeks after preparation give some rationale behind their differing observational results; see Figure 102. The SAXS 23/24 sample showed opalescence with white fluid precipitation and the DLS measurements show self-assembled structures that are likely connected with these observations. It is likely that the main intensity peak of SAXS 23/24 are reverse vesicles with a 190-200 nm diameter which cause the opalescence, and the peak in the multiple micrometre range is connected with the structures forming the white fluid precipitant. As the larger peak is distinctly separated from the smaller peak, it is likely that these aggregates are different in some way from the smaller aggregates, rather than the larger aggregates simply being a progressively larger version of the smaller aggregates. The difference in these peaks probably indicates the difference between the smaller unilamellar reverse vesicles and either larger multilamellar reverse vesicles shown to be present in the white fluid precipitants or clusters.

The RVe1C 3 sample showed opalescence and Tyndall scattering without any precipitation. The lack of micrometre sized structures found in the DLS results reinforces the lack of large particles in the solution that would settle and form a precipitant. The two distinct peaks with modal values of 295 nm and 91 nm are not as polydisperse as the main peak found in the SAXS 23/24 sample with a 190 nm modal value. However, the overall size range of structures present were similar, although did not extend to the large sizes found in the SAXS 23/24 sample (SAXS 23/24 has a ~50-955 nm range for the 190 nm mode peak and RVe1C 3 peaks having an overall range of ~60-530 nm). Therefore, the opalescence in the RVe1C 3 sample is likely due to the overall range of these two peaks.

The occurrence of the Tyndall scattering may be due to either of the maximum peak values and/or the increased concentration of particles in the RVe1C 3 sample compared to that of the SAXS 23/24 sample. To produce an obvious bluish colour there needs to be sufficient colloids of a particular size to scatter light. Therefore, concentration of particles has a large effect on the intensity of the bluish colour that we can observe. The lack of an obvious blue colouring in the SAXS 23/24 sample may only be due to the 15 mM concentration which is 5 mM below that of the RVe1c 3 sample. However, the difference in the distribution of particle sizes may be also be influencing the intensity of the Tyndall scattering. The intensity percentages of the RVe1C 3 peaks reach 11% at 92 nm and 13% at 295 nm, compared to 5% and 7% for the same size

ranges in the SAXS 23/24 sample, respectively. Tung *et al.* (2008) related the presence of particles with diameters of ~60 nm and ~79 nm (determined by DLS) to transparent solutions and ~138 nm and ~260 nm particles to solutions with Tyndall scattering. Therefore, it may be that the structures forming the high 13% intensity at the 295 nm modal value peak in the RVe1C 3 sample are the predominate cause for the blue colouring of this sample.

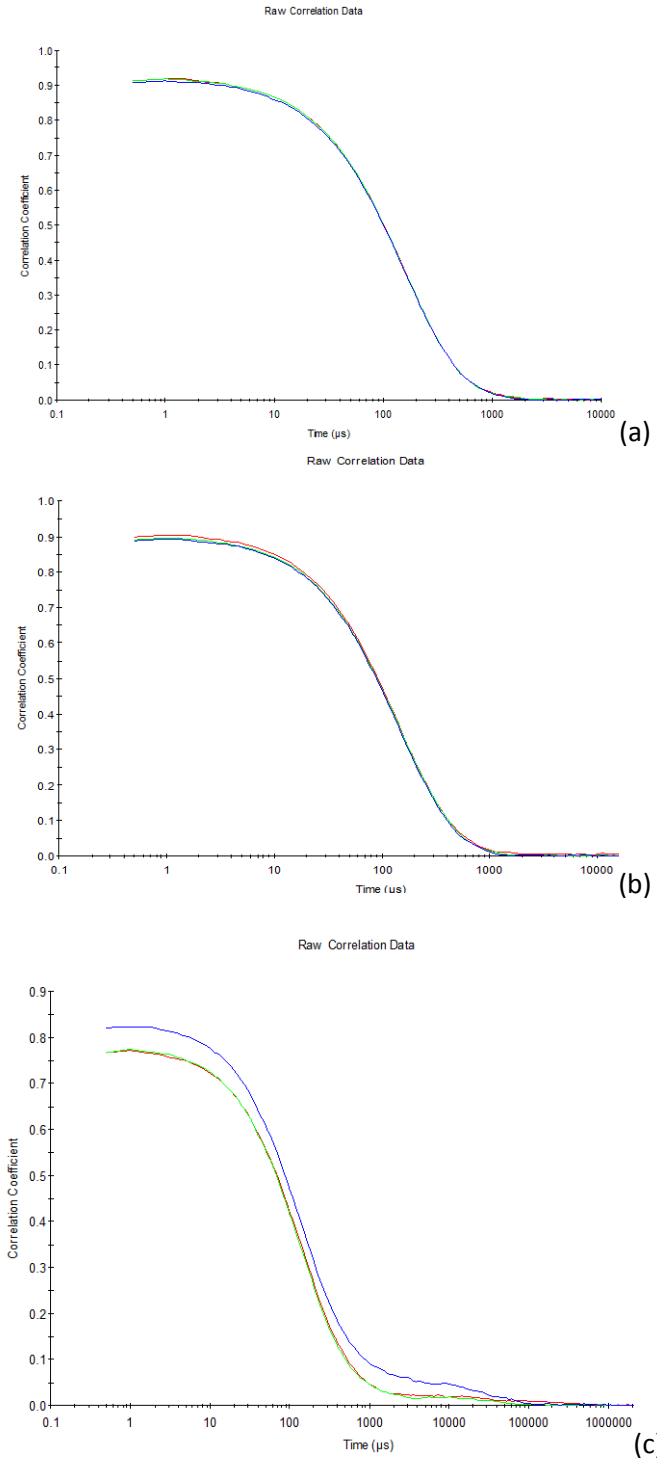

Figure 99: Correlation curves for DLS measurements of cyclohexane 2.5Ro, (a) red line record 227, green line record 228 and blue line record 229, (b) red line record 235, green line record 236 and blue line record 237, (c) red line record 231, green line record 232 and blue line record 233.

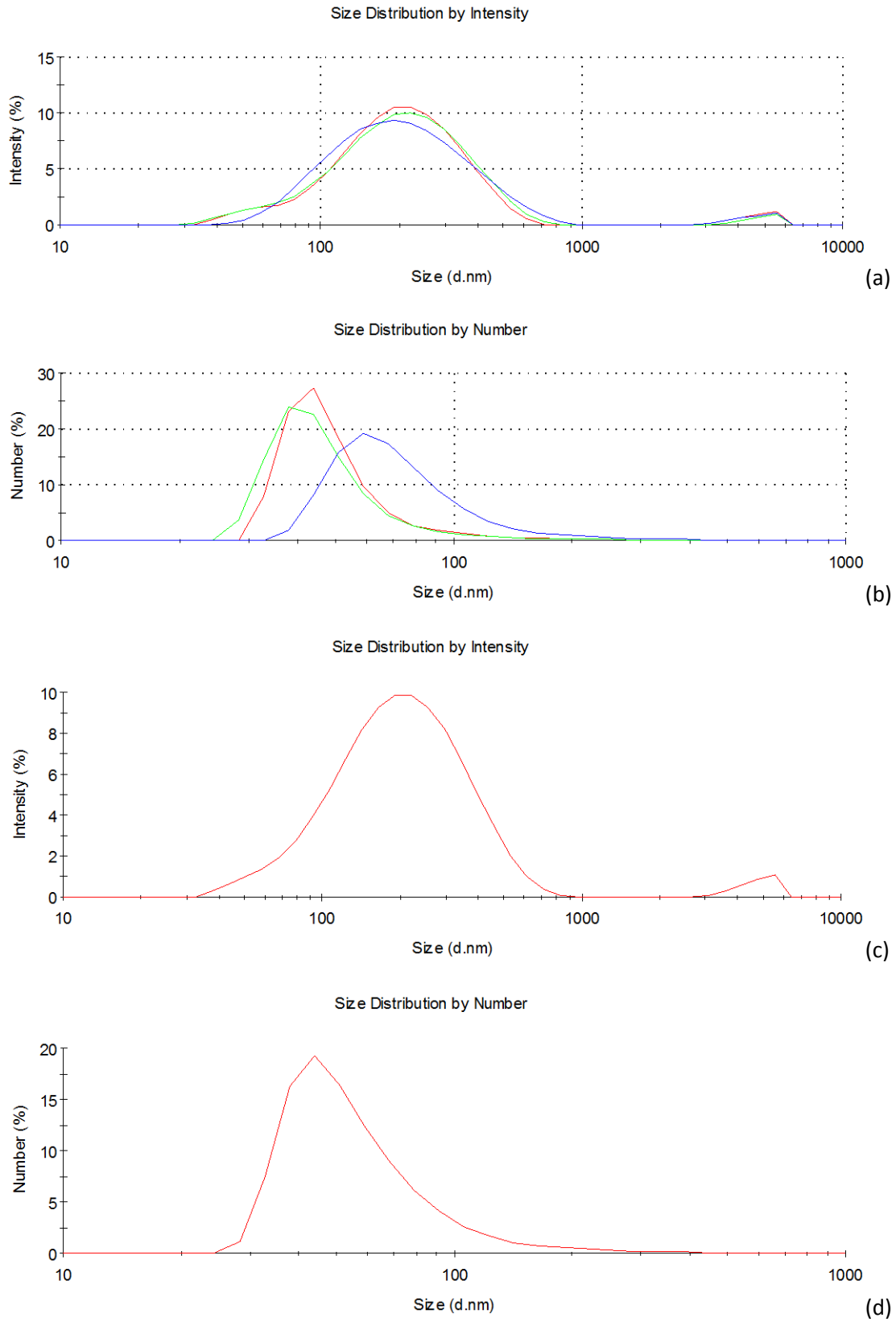

Figure 100: Intensity (a) and number (b) distribution curves for three successive DLS data runs on SAXS 23/24 cyclohexane 2.5Ro - red line record 227, green line record 228 and blue line record 229. Averaged intensity (c) and number (b) distribution curves for records 227, 228 and 229.

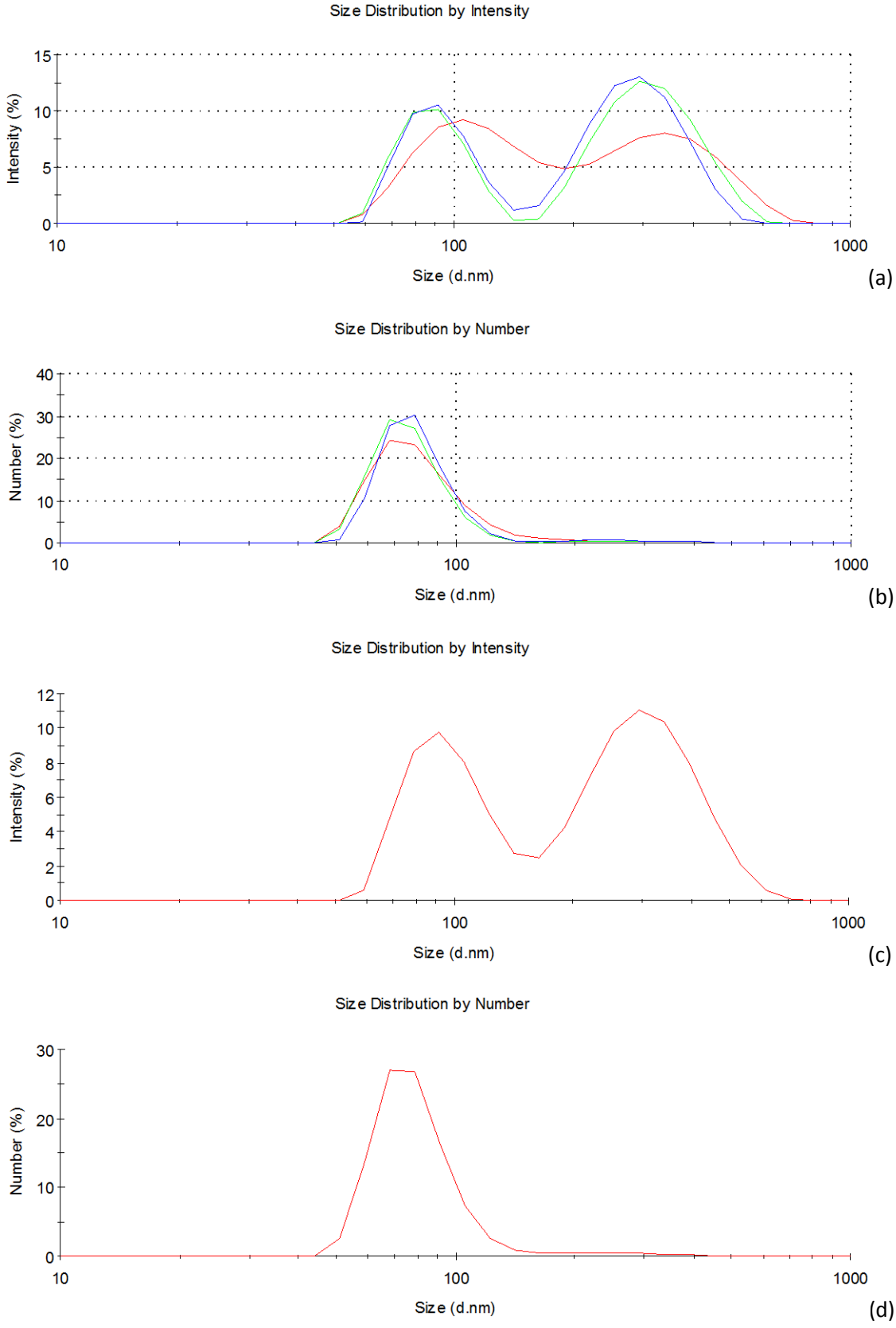

Figure 101: Intensity (a) and number (b) distribution curves for three successive DLS data runs on RVe1C 3 cyclohexane 2.5Ro (6 weeks after prep, 1 minute water-bath sonication) - red line record 235, green line record 236 and blue line record 237. Averaged intensity (c) and number (b) distribution curves for records 235, 236 and 237.

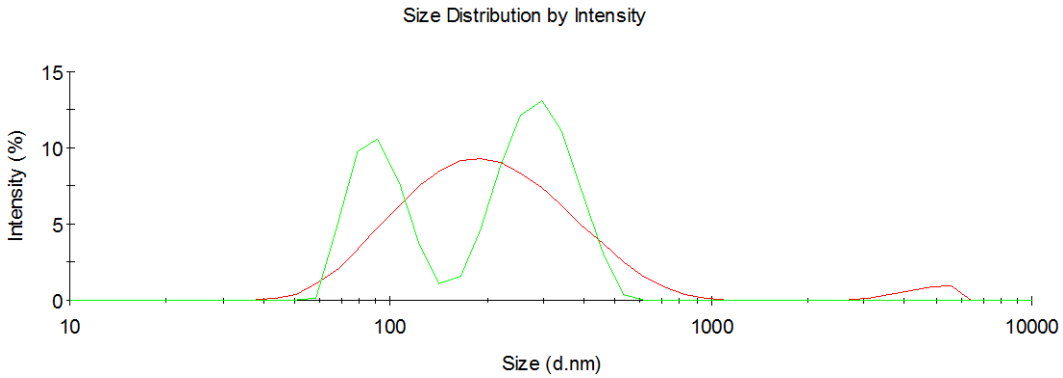

Figure 102: Graph comparing the intensity distribution curves for the 3rd measurements taken 6 weeks after initial preparation for – red line SAXS 23/24 and green line RVe1C 3.

6.4.2 Cyclohexane 3.5 Ro

Record / Repeat Num	Sample Name	Sample Description	Date	Attenuator	Correlation curve intercept	PD	PD width d. nm	Zeta-Average d. nm	Mode of Intensity Peak 1 d. nm (%)	Mode of Intensity Peak 2 d. nm (%)	Mode of Intensity Peak 3 d. nm (%)	Mode of Number Peak 1 d. nm (%)	Mode of Number Peak 2 d. nm (%)
238/1	SAXS 25/26 Cyclohex. 3.5Ro	O + some WFP+SL **Unshaken, top of solution**	22/11/2012 (6 days after prep)	7	0.960	0.269	105.6	203.5	220.2 (94.7)	4801 (4.1)	37.21 (1.1)	32.67 (93.7)	78.82 (6.3)
239/2				7	0.961	0.252	102.8	204.6	220.2 (98.3)	5560 (1.7)	0	37.84 (100)	0
240/3				7	0.960	0.271	106.0	203.7	255.0 (98.9)	5560 (1.1)	0	68.06	0
Mean of 1-3				7	0.960	0.264	104.8	203.9	220.2	5560		32.67	68.06
242/1	RVe1C 7 Cyclohex. 3.5Ro	O+B+WFP+SL	4/7/2012 (3 months after prep)	8	0.935	0.342	116.7	199.5	255.0 (98.6)	5560 (1.4)	0	43.82 (100)	0
243/2				8	0.939	0.360	117.4	195.5	295.3 (98.7)	5560 (1.3)	0	50.75 (100)	0
244/3				8	0.940	0.386	121.4	195.4	295.3 (98.2)	5560 (1.8)	0	50.75 (100)	0
Mean of 1-3				8	0.935	0.363	118.5	196.8	295.3	5560	0	50.75	0

Table 48: DLS results for cyclohexane (C18 95%) 3.5 Ro samples.

The complete and smooth curve correlation curves, with appropriate intercepts, for the all measurement runs for cyclohexane 3.5Ro indicate valid results; see Table 48 and Figure 103.

6.4.2.1 SAXS 25/26

In viewing the intensity curves for SAXS 25/26, we can see that the zeta-average values (along with the corresponding polydispersity values) do not well describe this type of multimodal system. The difference in the three intensity distributions for SAXS 25/26 show that the particles are either combining to form larger particles or clustering. The peak at ~37nm seen in the first measurement seems to move to the higher class size of over 50 nm that merges with the largest intensity peak by the third measurement (Figure 104a). This change in the smaller size range dominates the number distribution curves, with defined mode peaks increasing with each measurement from ~33 nm, ~38 nm, and ~62 nm (Figure 104b). The movement of the other intensity peaks show a similar change with modal value of the main peak increasing from ~220 nm to ~255 nm (mean 261 nm 0.25 PD and 283 nm 0.27 PD respectively) and the peak at the very large class regimes changing from ~4801 nm to ~5560 nm (mean 3973 nm 0.12 PD and 4986 nm 0.05 PD respectively). The rate of clustering/combining of particles is strange as there was no sonication or shaking of the sample previous to the measurements. However, the disturbance of the solution due to the movement of the sample from storage to the DLS (including the pipetting action to move the sample to the cuvette) may have broken up and solubilised some of the larger structures originally found in the precipitant. These DLS measurements would therefore represent observations of the recombination of these structures.

6.4.2.2 RVe1c 7

The results of RVe1C 7 do not have the obvious clustering of the SAXS 25/26 results; however, the overall size and range of intensity peaks are comparable (Figure 104a and 105a). There is a consistent small peak at the large size class range of 5560 nm the same as found in the SAXS 25/26 sample. The largest intensity peak has a consistent zeta-average of 195-199 nm, and although the peak mode values increase from 255 nm to 295.3 nm, the averages for this peak range (measurements 1 = 261.4 nm, 2 = 276.2 nm, 3 = 255.4 nm) represent the fluctuation of the curve more appropriately. This fluctuation in the average of the largest intensity peak is associated with the smaller size class peak around ~60-100 nm. This peak has not automatically been allocated as a separate peak by the software, hence the lack of information of a ‘peak 3’ in Table 48 and has been calculated as part of the larger intensity peak at ~200 nm. However, visual analysis of the intensity curves indicates a peak at this smaller size range dominating the number distribution curve similar to that of the results of SAXS 25/26, see Figure 105b. If viewing this curve as two separate intensity peaks at ~70-100 nm and ~220-280 nm we can see a slight fluctuation that implies that some of the ~70-100nm particles may be randomly coming together and then breaking apart.

6.4.2.3 Comparison

The overall results for the SAXS 25/26 and RVe1C sample indicate a polydisperse system containing three particles size ranges - ~70-100 nm, ~220-280 nm and ~5560 nm. The relative stability of the ~5560 nm range implies that these larger particles are not involved in the apparent fracturing and clustering of the small ~70-100nm size class ranges. A logical deduction of this data is that the particles in the micrometre range are those that settle to form the white fluid precipitant (flocs of either unilamellar vesicles or multilamellar reverse vesicles) and the particles in the nanometres range are unilamellar reverse vesicles that cause the opalescence/Tyndall scattering of the solution. This concurs with the microscopy results, stated in Chapter 5, which showed the majority of particles must be under a micrometre in diameter.

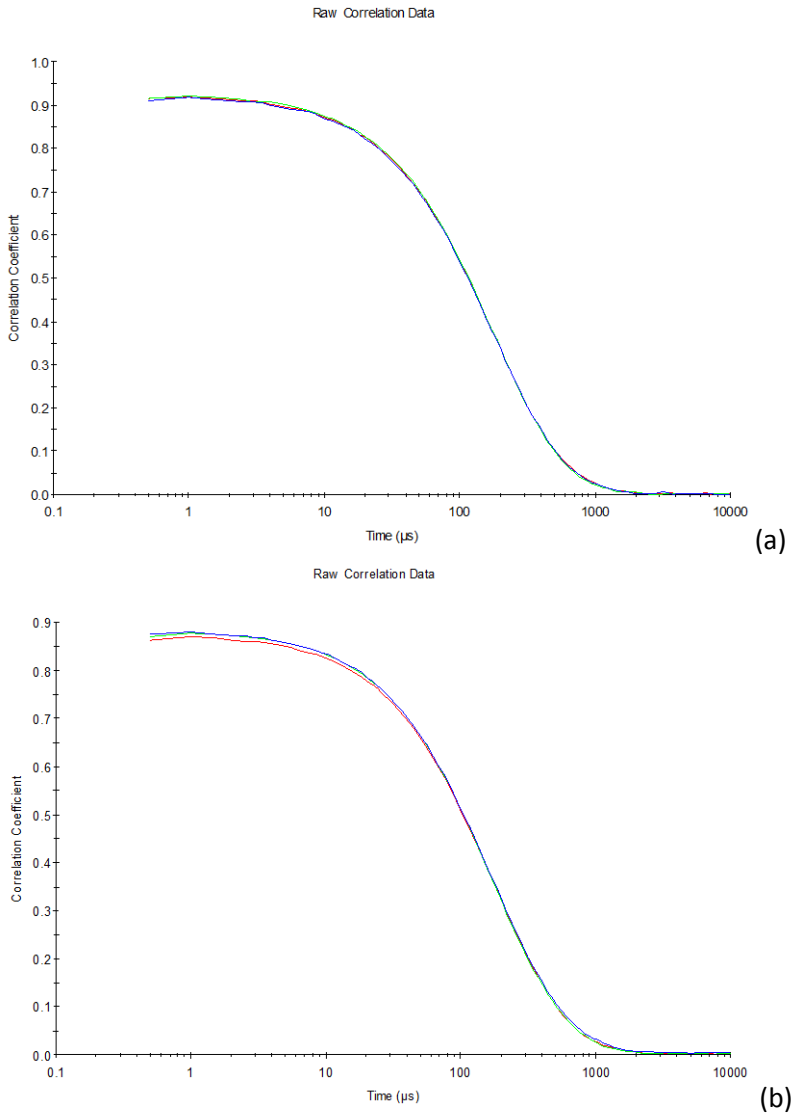

Figure 103: Correlation curves for DLS measurements of cyclohexane 3.5Ro, (a) red line record 238, green line record 239 and blue line record 240, (b) red line record 242, green line record 243 and blue line record 244.

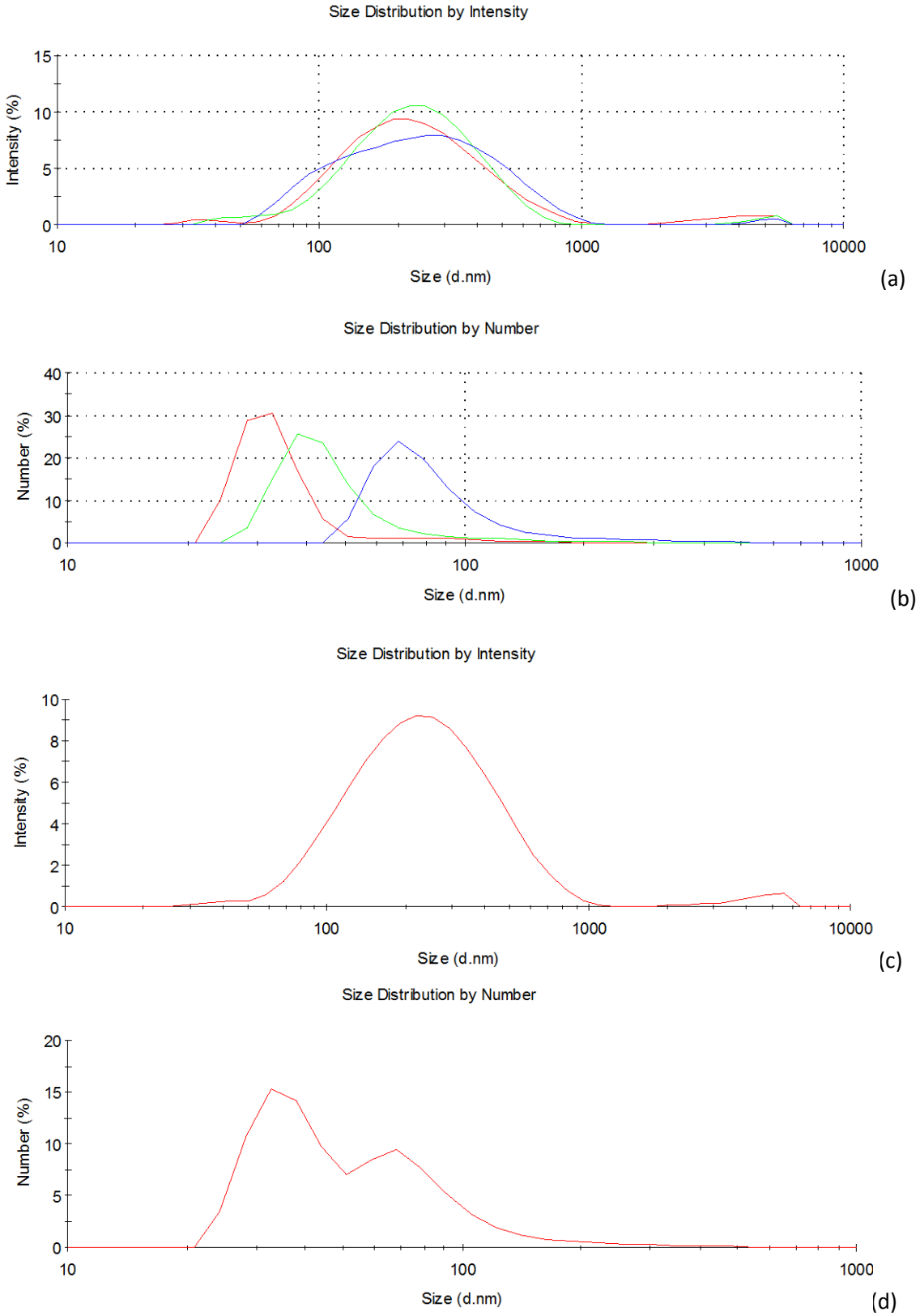

Figure 104: Intensity (a) and number (b) distribution curves for three successive DLS data runs on SAXS 25/26 cyclohexane 3.5Ro - red line record 238, green line record 239 and blue line record 240. Averaged intensity (c) and number (b) distribution curves for records 238, 239 and 240.

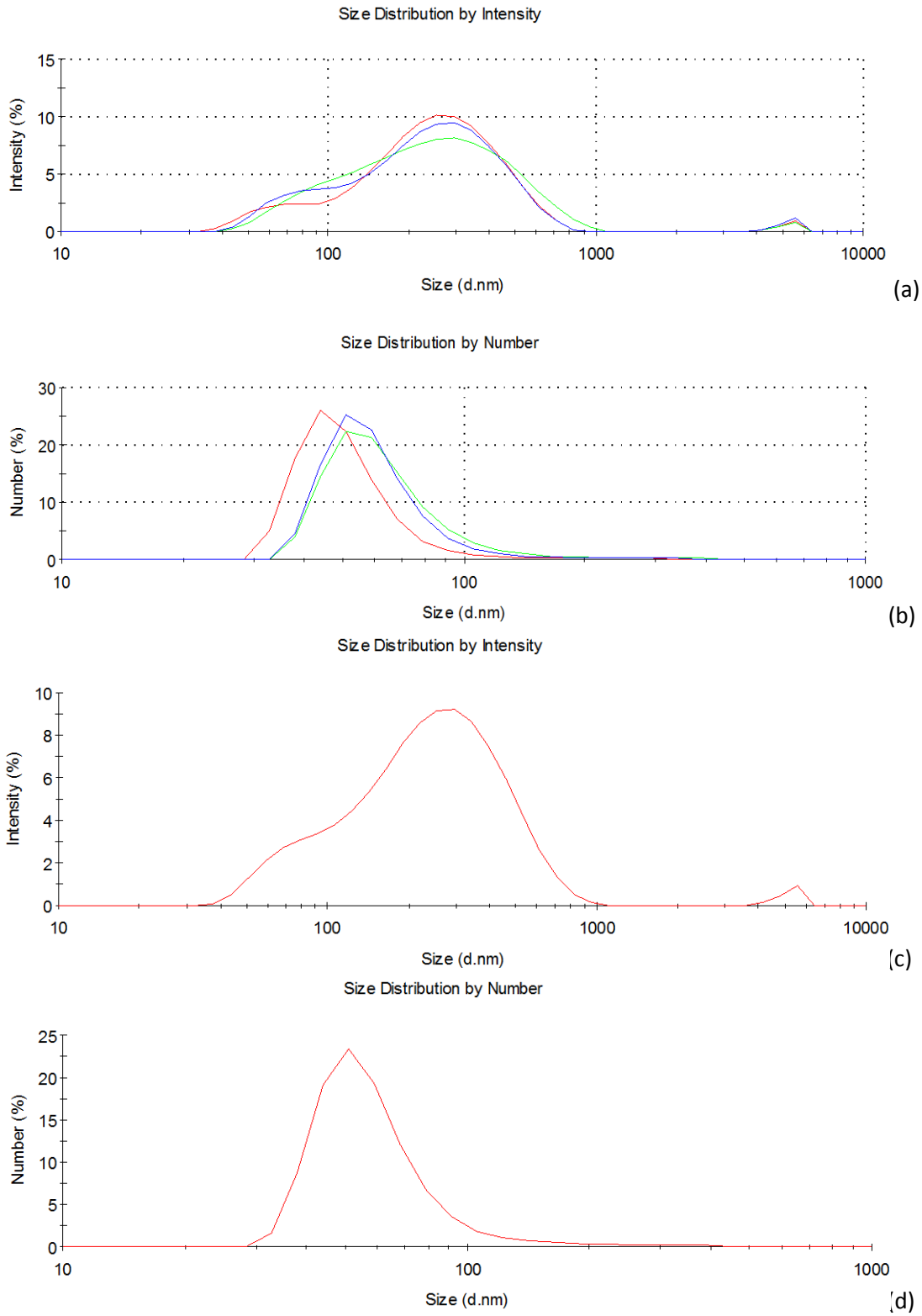

Figure 105: Intensity (a) and number (b) distribution curves for three successive DLS data runs on RVe1C 7 cyclohexane 3.5Ro - red line record 242, green line record 243 and blue line record 244. Averaged intensity (c) and number (b) distribution curves for records 242, 243 and 244.

6.4.3 Cyclohexane 4.5 Ro

Record / Repeat Num	Sample Name	Sample Description	Date	Attenuator	Correlation curve intercept	PD	PD width d. nm	Zeta-Average d. nm	Mode of Intensity Peak 1 d. nm (%)	Mode of Intensity Peak 2 d. nm (%)	Mode of Intensity Peak 3 d. nm (%)	Mode of Number Peak 1 d. nm (%)	Mode of Number Peak 2 d. nm (%)
246/1	SAXS 27/28 Cyclohex. 4.5Ro	O + WFP + SL **Unshaken, top of solution**	22 Nov 2012 (6 days after prep)	8	0.948	0.245	96.54	195.0	220.2 (97.1)	37.84 (1.5)	5560 (1.4)	32.67 (100)	0
247/2				8	0.944	0.246	95.78	193.1	220.2 (100)	0	0	68.06 (100)	0
248/3				8	0.945	0.246	95.45	192.5	295.3 (100)	0	0	68.06 (100)	0
Mean 1-3				8	0.948	0.246	193.5	193.5	220.2 (99.1)	37.84 (0.5)	5560 (0.4)	32.67 (29.2)	68.06 (70.8)
250/1	RVe1c 11 Cyclohex. 4.5Ro	O+B+CLay+SL **3 min water-bath sonication**	4 July 2012 (3 months after prep)	8	0.950	0.254	92.22	182.9	220.2 (98.6)	5560 (1.4)	0	37.84 (100)	0
251/2				8	0.952	0.261	96.02	188.1	220.2 (98.9)	5560 (1.1)	0	32.67 (100)	0
252/3				8	0.953	0.261	94.73	185.5	220.2 (98.7)	5560 (1.3)	0	50.75 (100)	0
Mean 1-3				8	0.950	0.259	94.32	185.5	220.2	5560	0	37.84	0

Table 49: DLS results for cyclohexane (C18 95%) 4.5 Ro samples.

The complete and smooth curve correlation curves, with appropriate intercepts, for the all measurement runs for cyclohexane 4.5Ro indicate valid results; see Table 49 and Figure 106.

6.4.3.1 SAXS 27/28

There are minute intensity signals at ~38 nm and ~5560 nm (consisting of 1.5% and 1.4% of the total intensity signal respectively) in the first run for the SAXS 27/28 sample. These signals vanish by the second and third measurement runs and are replaced by a single, but slightly more polydisperse, curve (increasing from 0.23 to 0.25 PD); see Figure 107a. Therefore, the second and third measurements can be described as a monomodal solution with a zeta-average diameter of 193nm and a polydispersity index of 0.25.

The number distribution curve for the first SAXS 27/28 measurement is overwhelmed by the small ~38 nm intensity peak, and therefore, in the first measurement produced a single peak with a ~32 nm modal value (see Figure 107b). However, the number distribution curves of the second and third measurements show a peak at a higher class size with ~84-92 nm average values as they were not influenced by any signals for particles under 5 nm or over 1000 nm. This distinct difference in the number distribution curves has produced a bimodal averaged result (see Figure 107d); however, this does not describe a real phenomenon.

6.4.3.2 RVe1c 11

The RVe1c 11 sample shows similar intensity distribution curves for all three measurements, with mode peak values at 220 nm and 5560 nm; see Figure 108. However, the average of the main peak trends slightly towards a higher class size - 228.3 nm, 242.6 nm and 247.4 nm (respective to measurements taken). The main difference in these results reside in the lower size range (30-50 nm particles) that are either aggregating or merging into one another to produce a final measurement with no signal under 40 nm and an increased signal in the 50-100 nm range. This may imply that small (<50nm diameter) structures were created by the 3 minute sonication just before analysis which subsequently merged with other small structures to form stable unilamellar reverse vesicles >50 nm in diameter. This difference in the intensity signal at low class sizes is also picked up in the number distribution curves, where the peak jumps from a mode value in the 30-40 nm range (average 40-50 nm) to 50 nm (average ~70 nm) in the final measurement. The zeta-average values remains stable at around 182-8 nm which implies the system as a whole is quite stable.

6.4.3.3 Comparison

Similar to the other DLS results for cyclohexane samples, the particles over a micrometre in diameter are likely to be related to the structures that settle to form the white fluid precipitant in the SAXS 27/28 sample and the cloudy layer in the RVe1c 11 sample. These white, cloudy precipitants are likely to be the same multilamellar reverse vesicles/onions found in the white

fluid precipitant of those with a 2.5Ro ratio e.g. RVe1c 1. The range of particles under 1000 nm in diameter is similar for both samples, implying that the obvious blue hue in the RVe1c 11 sample comes from the 5mM higher concentration compared to that of the SAXS 27/28 sample.

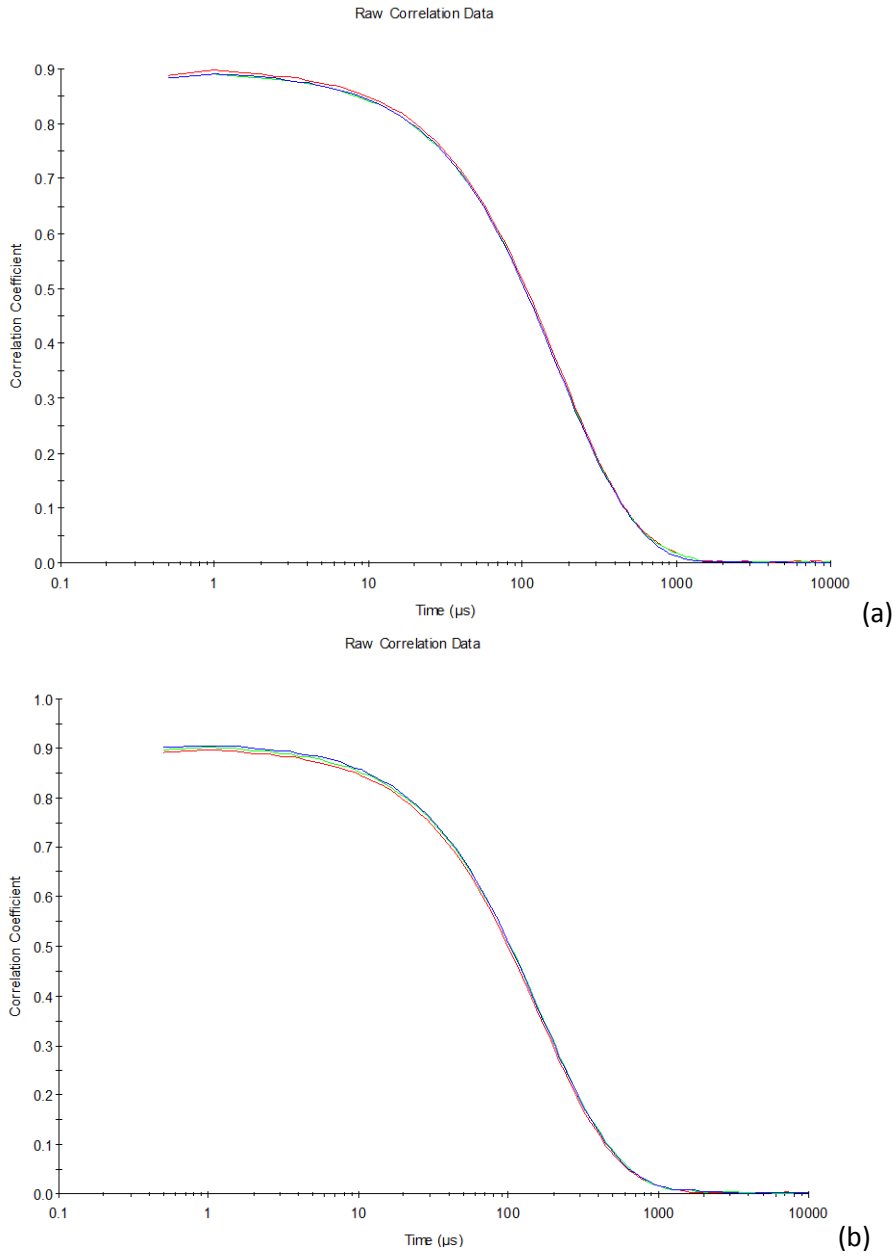

Figure 106: Correlation curves for DLS measurements of cyclohexane 4.5Ro, (a) red line record 246, green line record 247 and blue line record 248, (b) red line record 250, green line record 251 and blue line record 252.

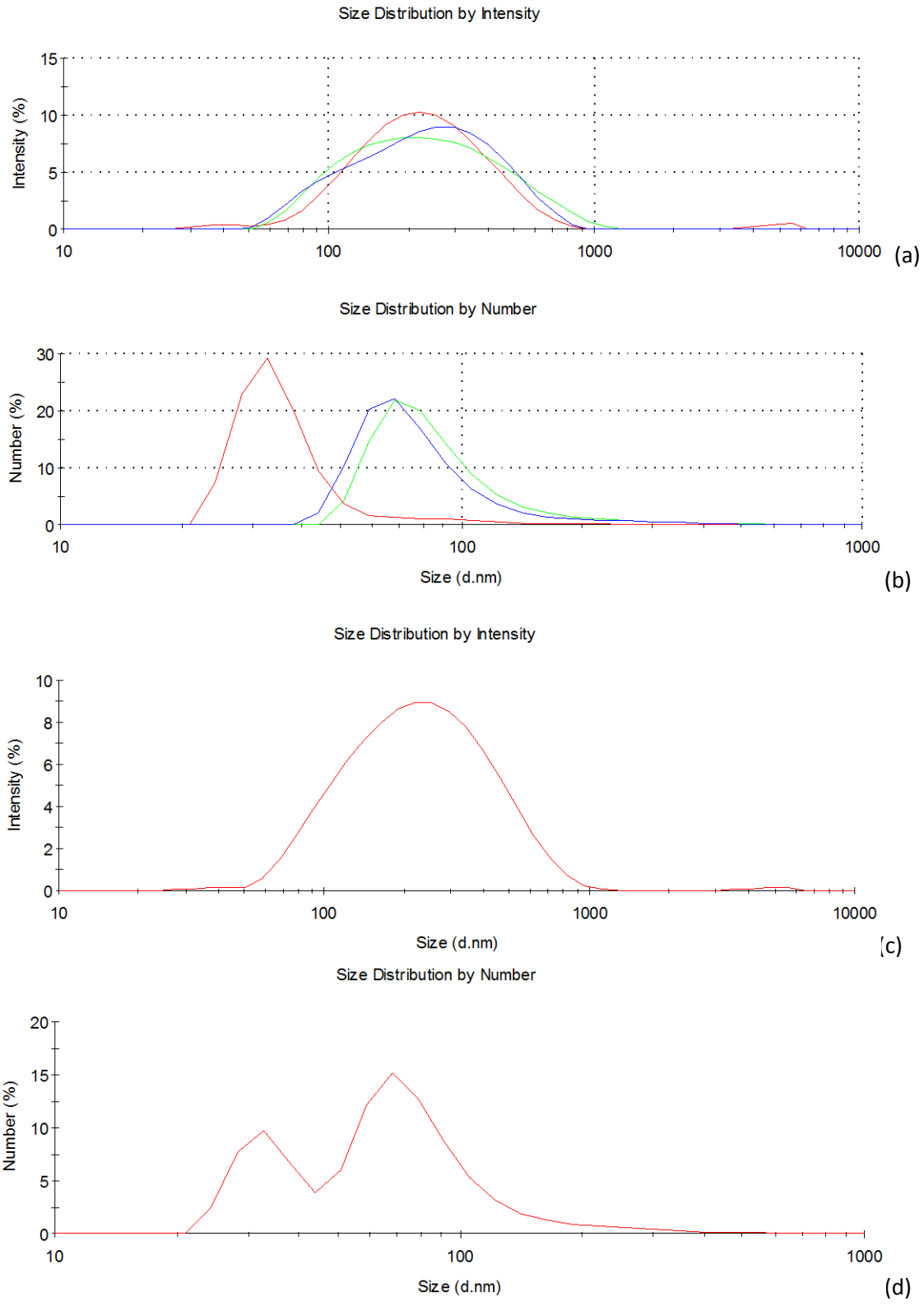

Figure 107: Intensity (a) and number (b) distribution curves for three successive DLS data runs on SAXS 27/28 cyclohexane 4.5Ro - red line record 246, green line record 247 and blue line record 248. Averaged intensity (c) and number (b) distribution curves for records 246, 247 and 248.

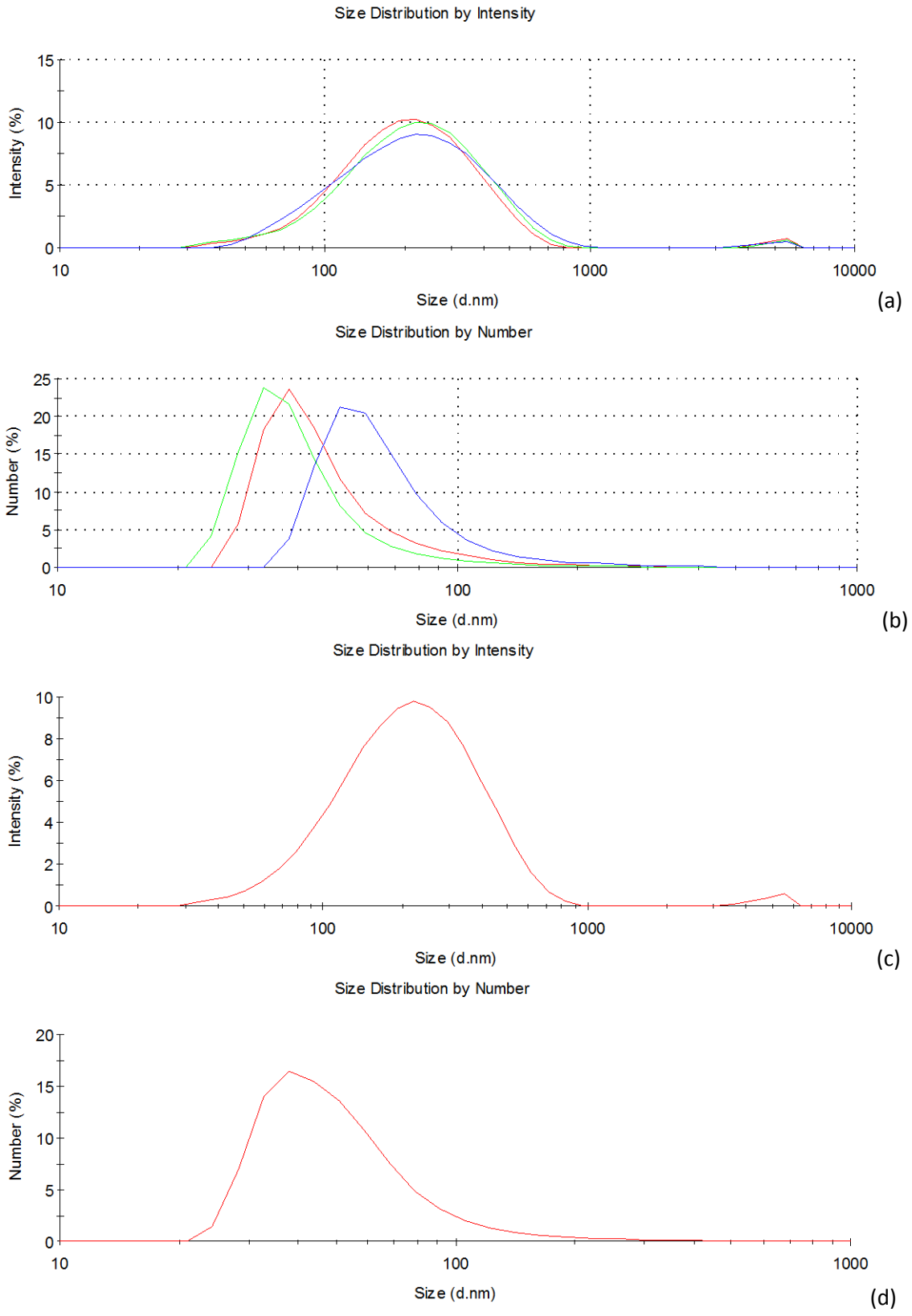

Figure 108: Intensity (a) and number (b) distribution curves for three successive DLS data runs on RVe1c 11 cyclohexane 4.5Ro - red line record 250, green line record 251 and blue line record 252. Averaged intensity (c) and number (b) distribution curves for records 250, 251 and 252.

6.4.4 Cyclohexane C18 95% DLS summary

The DLS results for the cyclohexane systems show the peak intensity signal in the 100s of nanometre range across all the ratios studied. The mean value for these highest intensity peaks range from ~100-300 nm with ~0.1-0.3 polydispersity values. This corresponds with the range of sizes associated with the unilamellar reverse vesicles with in solutions presenting Tyndall scattering published by Tung *et al.* (2008) (137 nm and 260 nm diameters for 1.6 Ro and 2.6 Ro samples respectively).

The larger particles were always over ~3500 nm and had a small intensity signal. These are likely to be associated with the structures forming precipitants or cloudy layers in these samples. This micrometre size range corresponds with the multilamellar reversed vesicles/onions found in the white fluid precipitants of cyclohexane systems using microscopy in Chapter 5.

Particles smaller than ~50 nm were unstable and were often seen to cluster or merge quickly. The initial formation of these particles were associated with disturbance, either by transference to the DLS analyser or pre-sonication, which quickly formed larger particles so were not usually observed in the final DLS measurements. This very low class size is within the range of a single bilayer thickness and therefore may indicate unstable open bilayers or micelles in solution.

Comparing samples with similar size ranges of particles that present different phase behaviour such as opalescence or a blue hue (e.g. SAXS 27/28 and RVe1c 11) indicate examples where the difference was due to a difference in concentration. In particular, those samples with >20 mM in amphiphilic concentration tended to exhibit a blue hue but those with <15 mM were opalescent.

6.5 Octane C18 95% DLS results

6.5.1 Octane 2.5 Ro

Record / Repeat Num	Sample Name	Sample Description	Date	Attenuator	Correlation curve intercept	PD	PD width d. nm	Zeta-Average d. nm	Mode of Intensity Peak 1 d. nm (%)	Mode of Intensity Peak 2 d. nm (%)	Mode of Number Peak 1 d. nm (%)	Mode of Number Peak 2 d. nm (%)
254/1	SAXS 41/42 Octane 2.5Ro	O+B+WFP(some)+SL **Unshaken, top of solution**	19 Nov 2012 (3 days after prep)	6	0.956	0.229	60.32	126.1	164.2 (100)	0	32.67 (100)	0
255/2				6	0.956	0.218	59.08	126.6	141.8 (98.4)	28.21 (1.6)	24.36 (100)	0
256/3				6	0.956	0.222	59.77	126.8	164.2 (100)	0	37.84 (100)	0
Mean 1-3				6	0.956	0.223	58.02	122.9	164.2	0	32.67	0

Table 50: DLS results for octane (C18 95%) 2.5 Ro samples.

The complete and smooth curve correlation curves, with appropriate intercepts, for SAXS 41/42 octane 2.5Ro indicate valid results; see Table 50 and Figure 109.

The mainly monomodal intensity distribution curves for the three measurement runs correlate well with one another except in the small class size regions where there are variations, see Figure 110a. This has resulted in a consistent zeta-average diameter result of 126 nm with a polydispersity of 0.22-0.23 and a stable average for the main intensity peak ranging from 163 nm to 168 nm. The zeta-average of 126 nm diameter with 0.22-0.23 polydispersity fits the description of a soft matter system containing unilamellar reverse vesicles. However, there are signal fluctuations mainly within the 20 nm to 100 nm region, implying that the smaller particles are unstable and are merging or clustering. Therefore, these smaller vesicles are likely to have been created either from the sonication process performed 3 days previously or from disturbance of the sample during transference to the DLS equipment.

This instability at low sizes is reflected in the number distribution curves (which have a tendency to have a greater influence from smaller class size intensity signals) so the modal peaks fluctuate from 33 nm to 24 nm and then increases to 38 nm (see Figure 110b). This change is even more prominent in the average of the peaks that change from 38 nm to 27 nm and then to 48 nm.

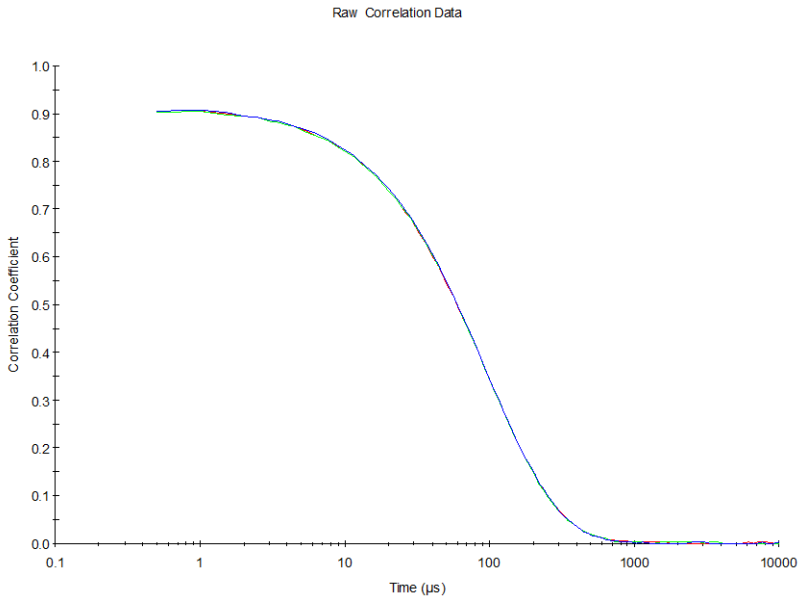

Figure 109: Correlation curves for DLS measurements of octane 2.5Ro, (a) red line record 254, green line record 255, and blue line record 256.

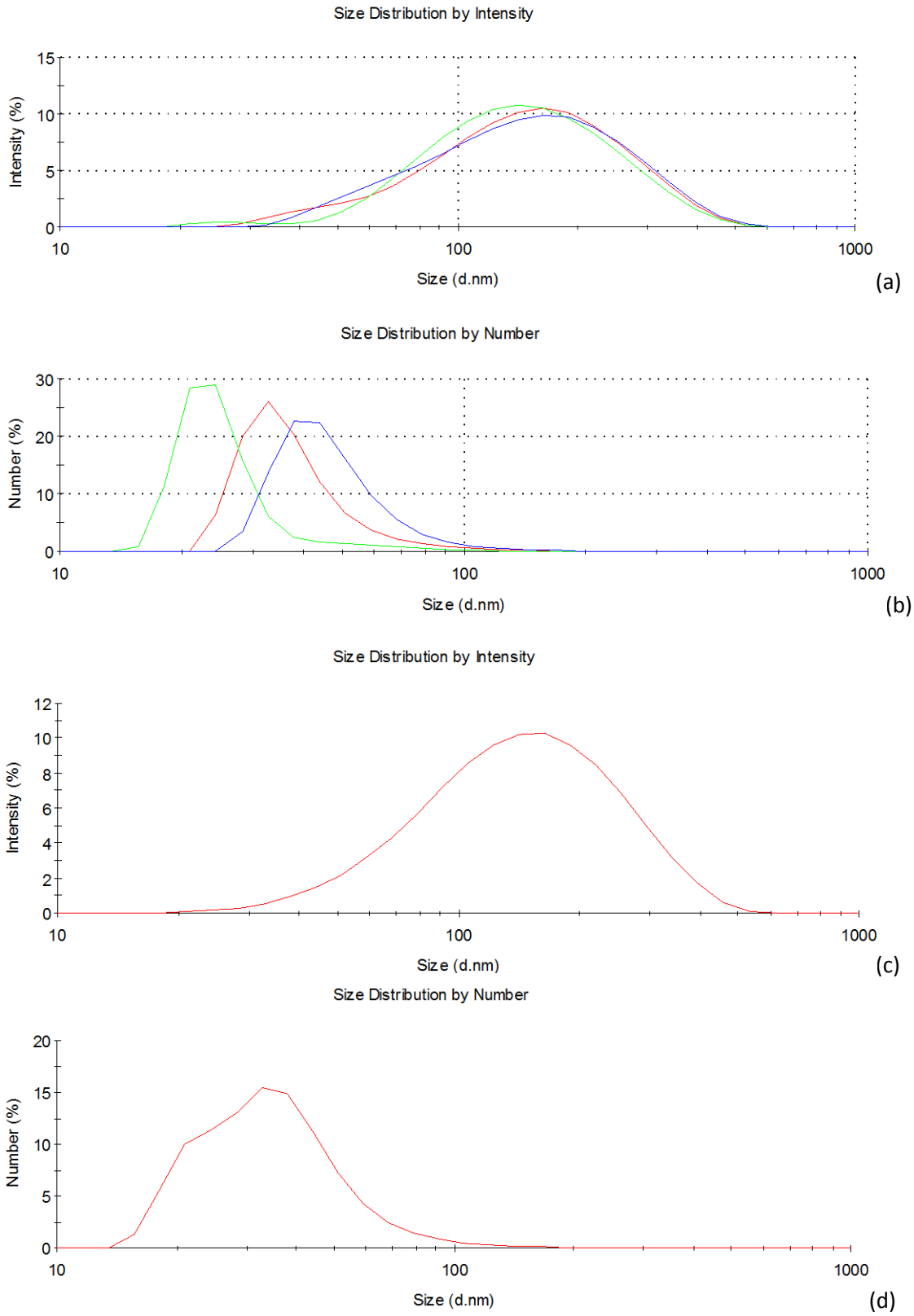

Figure 110: Intensity (a) and number (b) distribution curves for three successive DLS data runs on SAXS 41/42 octane 2.5Ro - red line record 254, green line record 255 and blue line record 256. Averaged intensity (c) and number (b) distribution curves for records 254, 255 and 256.

6.5.2 Octane 3.5 Ro

Record / Repeat Num	Sample Name	Sample Description	Date	Attenuator	Correlation curve intercept	PD	PD width d. nm	Zeta-Average d. nm	Mode of Intensity Peak 1 d. nm (%)	Mode of Intensity Peak 2 d. nm (%)	Mode of Number Peak 1 d. nm (%)	Mode of Number Peak 2 d. nm (%)
258/1	SAXS 43/44 Octane 3.5Ro	O+B+WGP+SL **Unshaken, top of solution**	19 Nov 2012 (3 days after prep)	6	0.965	0.196	69.45	157.1	164.2 (100)	0	68.06 (100)	0
259/2				6	0.964	0.175	66.37	158.5	190.1 (100)	0	58.77 (100)	0
260/3				6	0.960	0.199	70.67	158.6	141.8 (96.1)	5560 (3.9)	91.28 (100)	0
Mean 1-3				6	0.964	0.190	66.88	153.5	164.2 (98.7)	5560 (1.3)	78.82	0

Table 51: DLS results for octane (C18 95%) 3.5 Ro samples.

All of the correlation curve intercepts for octane 4.5 Ro are within the appropriate values and the curves are mainly smooth (see Table 51 and Figure 111). However, the third measurement run has some small fluctuations in the 1 µs to 10 µs time range. This may indicate clustering or a limited number of large (over a micrometre) sized particles are in solution.

The intensity distribution curves (Figure 112 a) indicate that the bulk of the particles in solution are stable and produce a zeta-average of 157-159 nm with a polydispersity of 0.18-0.2 (Table 51). However, there are fluctuations in the intensity signals at the low class sizes (~40-80 nm) especially in the 40-60 nm size range where the signals are shown to appear and disappear (Figure 112 a). The initial reduction in class size between measurement 1 and 2 within the small class size region of the graph might indicate the production of free bilayers or micelles during the merging of unstable smaller particles to the more stable reverse vesicle form >~80 nm. This fluctuation in this small size region is also picked up in the number distribution graph where the mode changes from 68 nm to 59 nm and then increases to 91 nm (Figure 112b).

The intensity signals from the larger class sizes also have an interesting transformation where some of the particles in the ~300-600 nm range may have clustered into large aggregates to form the signal in the ~5560 nm range. Otherwise, these larger particles were already in solution but are so sparse that they were not detected by the first two measurements. As the precipitant in this sample had a gel-like consistency, any of the larger particles in this matrix are less likely to be solubilised by disturbance in the sample after they have settled. Therefore, it is understandable that there would be few micrometre-sized structures in the solution compared to samples containing fluid precipitants, such as many of the cyclohexane samples.

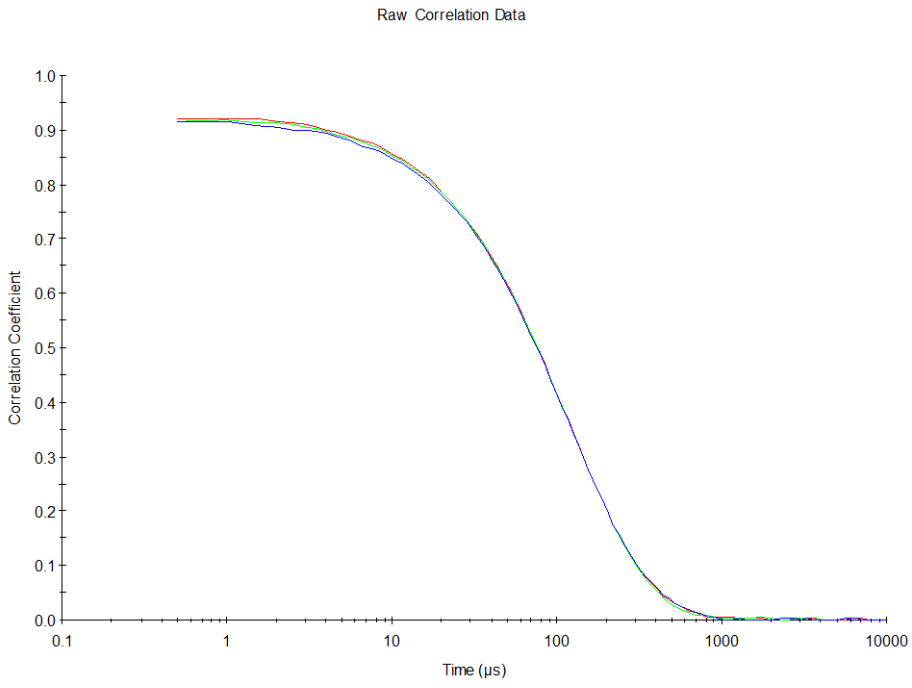

Figure 111: Correlation curves for DLS measurements of octane 3.5 Ro, (a) red line record 258, green line record 259, and blue line record 260.

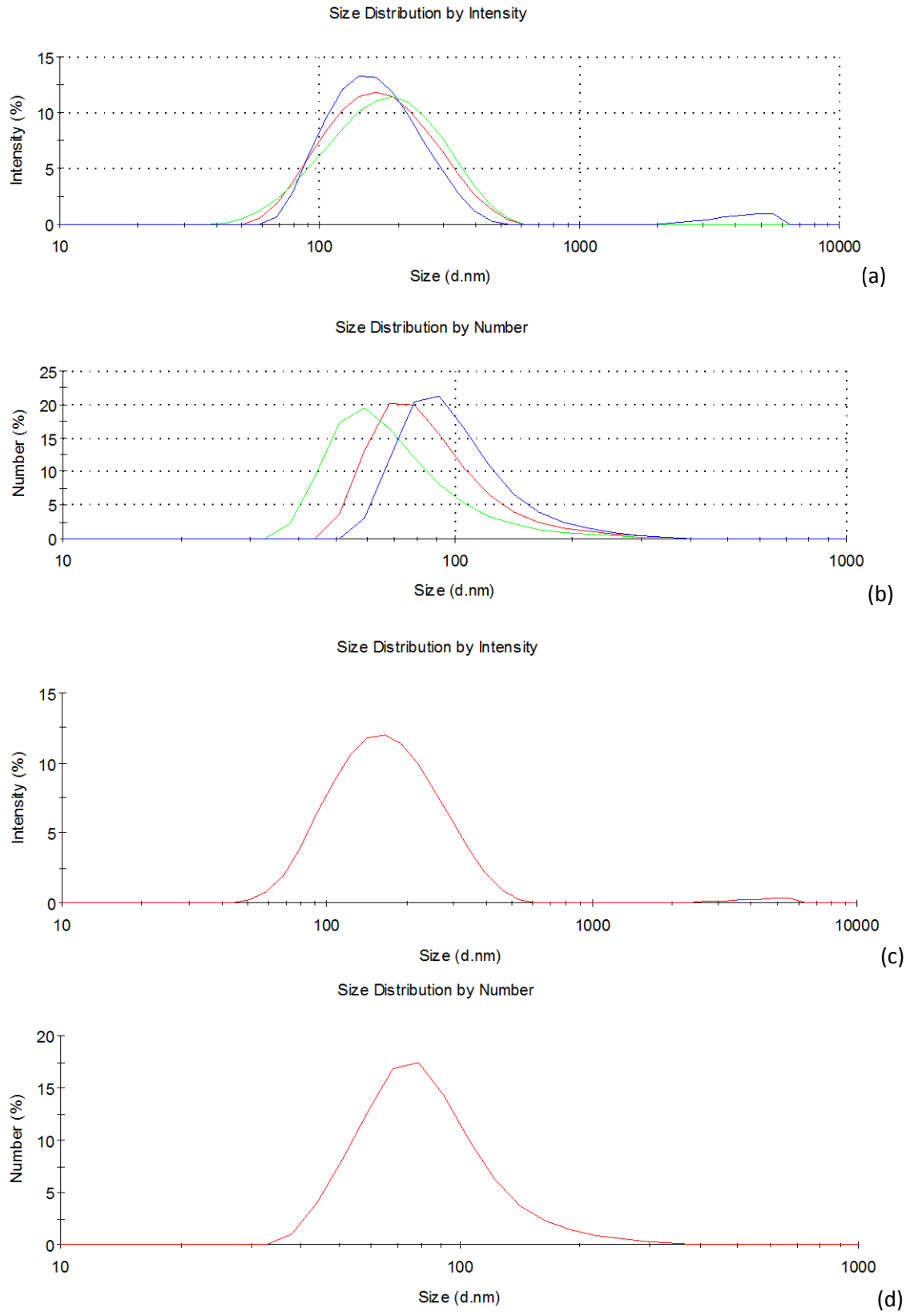

Figure 112: Intensity (a) and number (b) distribution curves for three successive DLS data runs on SAXS 43/44 octane 3.5Ro - red line record 258, green line record 259 and blue line record 230. Averaged intensity (c) and number (b) distribution curves for records 258, 259 and 260.

6.5.3 Octane 4.5 Ro

Record / Repeat Num	Sample Name	Sample Description	Date	Attenuator	Correlation curve intercept	PD	PD width d. nm	Zeta-Average d. nm	Mode of Intensity Peak 1 d. nm (%)	Mode of Intensity Peak 2 d. nm (%)	Mode of Number Peak 1 d. nm (%)	Mode of Number Peak 2 d. nm (%)
263/1	SAXS 45/46 Octane 4.5Ro	O+B+WGP+SL **Unshaken, top of solution**	19 Nov 2012 (3 days after prep)	6	0.959	0.232	64.02	133.0	164.2 (100)	0	43.82 (100)	0
264/2				6	0.962	0.220	62.81	134.0	164.2 (100)	0	43.82 (100)	0
265/3				6	0.962	0.230	64.15	133.6	141.8 (100)	0	43.82 (100)	0
Mean 1-3				6	0.959	0.227	61.84	129.7	141.8 (100)	0	43.82 (100)	0

Table 52: DLS results for octane (C18 95%) 4.5 Ro samples.

The complete and smooth curve correlation curves, with appropriate intercepts, for SAXS 45/46 octane 4.5Ro indicate valid results; see Table 52 and Figure 113.

The matching intensity and number distribution curves for all the measurements of SAXS 45/46 indicate a very stable system with a zeta-average of 133-134nm and a polydispersity of 0.22-0.23 with no observable aggregation factor (Figure 114). This limited variation forms averaged number and intensity distribution curves that imitate the measurement values accurately. This size range and polydispersity falls within the range expected for unilamellar reverse vesicles.

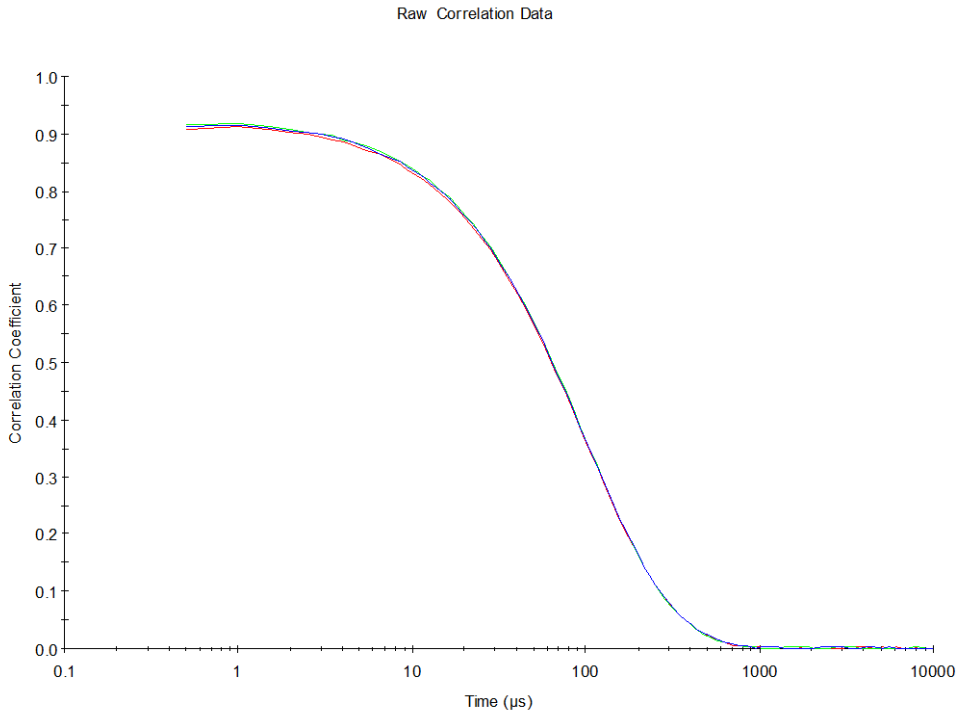

Figure 113: Correlation curves for DLS measurements of octane 4.5Ro, (a) red line record 263, green line record 264, and blue line record 265.

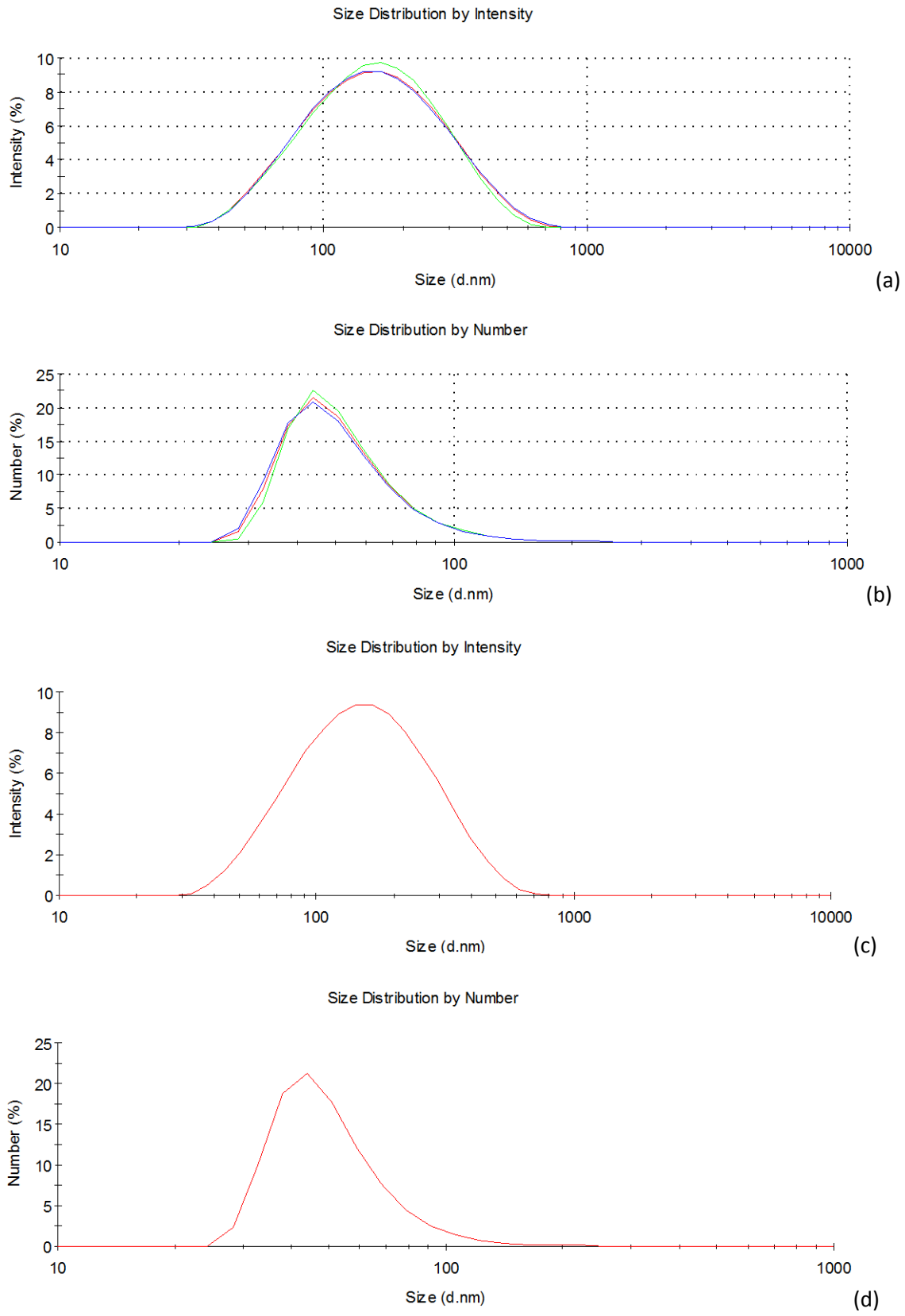

Figure 114: Intensity (a) and number (b) distribution curves for three successive DLS data runs on SAXS 45/46 octane 4.5Ro - red line record 263, green line record 264 and blue line record 265. Averaged intensity (c) and number (b) distribution curves for records 263, 264 and 265.

6.5.4 Octane C18 95% DLS summary

Overall, these systems are stable with the main intensity peak following a size range expected for unilamellar reverse vesicles. The zeta-average for the 2.5 and 4.5 ratios were stable with 127 nm (0.22 PD) and 133 nm (0.23 PD) values, respectively. The zeta-average for the 3.5 ratio sample was slightly higher at 158 nm but this is likely to have been affected by the apparent greater disturbance of this sample as shown by the slight differences between measurement runs.

Due to the gel-like consistency of the precipitants in the 3.5 and 4.5 ratio samples (preventing particle solubilising by sample disturbance) and the lack of much precipitation in the 2.5 sample there were very few intensity signals for particles over a micrometre in size.

6.6 Heptane C18 95% DLS results

6.6.1 Heptane 2.5 Ro

Record / Repeat Num	Sample Name	Sample Description	Date	Attenuator	Correlation curve intercept	PD	PD width d. nm	Zeta-Average d. nm	Mode of Intensity Peak 1 d. nm (%)	Mode of Intensity Peak 2 d. nm (%)	Mode of Number Peak 1 d. nm (%)	Mode of Number Peak 2 d. nm (%)
267/1	SAXS 2/3 Heptane 2.5Ro	O+B+WGP+SL **Unshaken, top of solution**	19 Nov 2012 (3 days after prep)	6	0.964	N/A	N/A	N/A	N/A	N/A	N/A	N/A
268/2				6	0.974	N/A	N/A	N/A	N/A	N/A	N/A	N/A
269/3				6	0.985	N/A	N/A	N/A	N/A	N/A	N/A	N/A
Mean 1-3				6	0.964	N/A	N/A	N/A	N/A	N/A	N/A	N/A

Table 53: DLS results for heptane (C18 95%) 2.5 Ro samples.

The intercept of the SAXS 2/3 correlation curves were within an acceptable range, and therefore, represented a sample with appropriate amounts of scattering from the suspended particles and low amounts of background scattering. However, as can be seen by the 0.02 difference in intercept values and the extended fluctuations in the correlation curves beyond ~500 µs (Figure 115) the sample was either aggregating too quickly or too polydisperse for a valid DLS analysis. This specimen was not pre-sonicated and the precipitant was gel-like which would prevent the temporary solubilisation of precipitants due to disturbance of transferring the sample to the DLS sample holder. Therefore, it is unlikely that the invalid results were due to the solution containing many large, unstable, particles that were quickly settling at the point of measurement; see Table 53. Therefore, the polydispersity of the structures in solution were too high for an accurate DLS analysis with a real value over ~0.4.

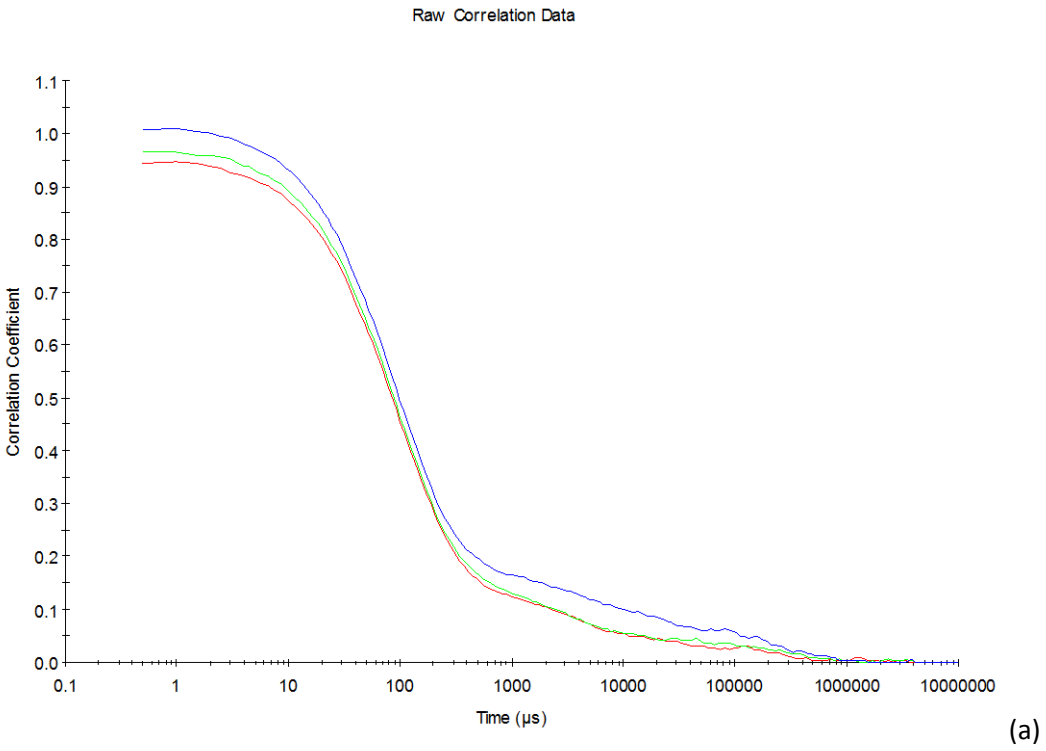

Figure 115: Correlation curves for DLS measurements of heptane 2.5Ro, (a) red line record 267, green line record 268, and blue line record 269.

6.6.2 Heptane 3.5 Ro

Record / Repeat Num	Sample Name	Sample Description	Date	Attenuator	Correlation curve intercept	PD	PD width d. nm	Zeta-Average d. nm	Mode of Intensity Peak 1 d. nm (%)	Mode of Intensity Peak 2 d. nm (%)	Mode of Number Peak 1 d. nm (%)	Mode of Number Peak 2 d. nm (%)
271/1	SAXS 4/5 Heptane 3.5Ro	O+B+WGP+SL **Unshaken, top of solution**	19 Nov 2012 (3 days after prep)	6	0.962	0.173	52.88	127.1	141.8 (100)	0	58.77 (100)	0
272/2				6	0.961	0.165	51.94	127.7	122.4 (100)	0	68.06 (100)	0
273/3				6	0.963	0.169	52.69	128.0	141.8 (100)	0	58.77 (100)	0
Mean 1-3				6	0.962	0.169	52.52	127.7	141.8 (100)	0	58.77 (100)	0

Table 54: DLS results for heptane (C18 95%) 3.5 Ro samples.

The correlation curves for the three measurement runs for heptane 3.5Ro all show a complete, smooth curve with an appropriate intercept indicating valid results; see Table 54 and Figure 116.

There is a single intensity peak which indicates a monomodal solution; see Figures 117 a and b. The zeta-average for the diameter of the particles is 127-128 nm with a 0.17 polydispersity, which is in the expected size range for unilamellar reverse vesicles. The number distribution shows a mode peak at 59-68 nm which implies the majority of particles may be at this smaller size range, however, the expected diameter when comparing to other scattering methods will be the zeta-average values. Over the three results, the zeta-average grows by 0.9 nm indicating a slow aggregation processes.

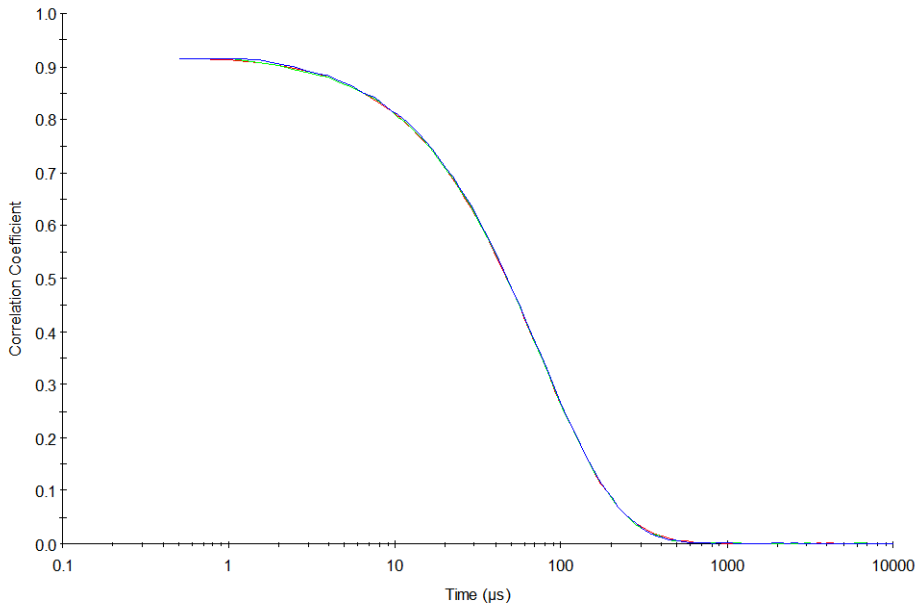

Figure 116: Correlation curves for DLS measurements of heptane 3.5Ro, red line record 271, green line record 272, and blue line record 273.

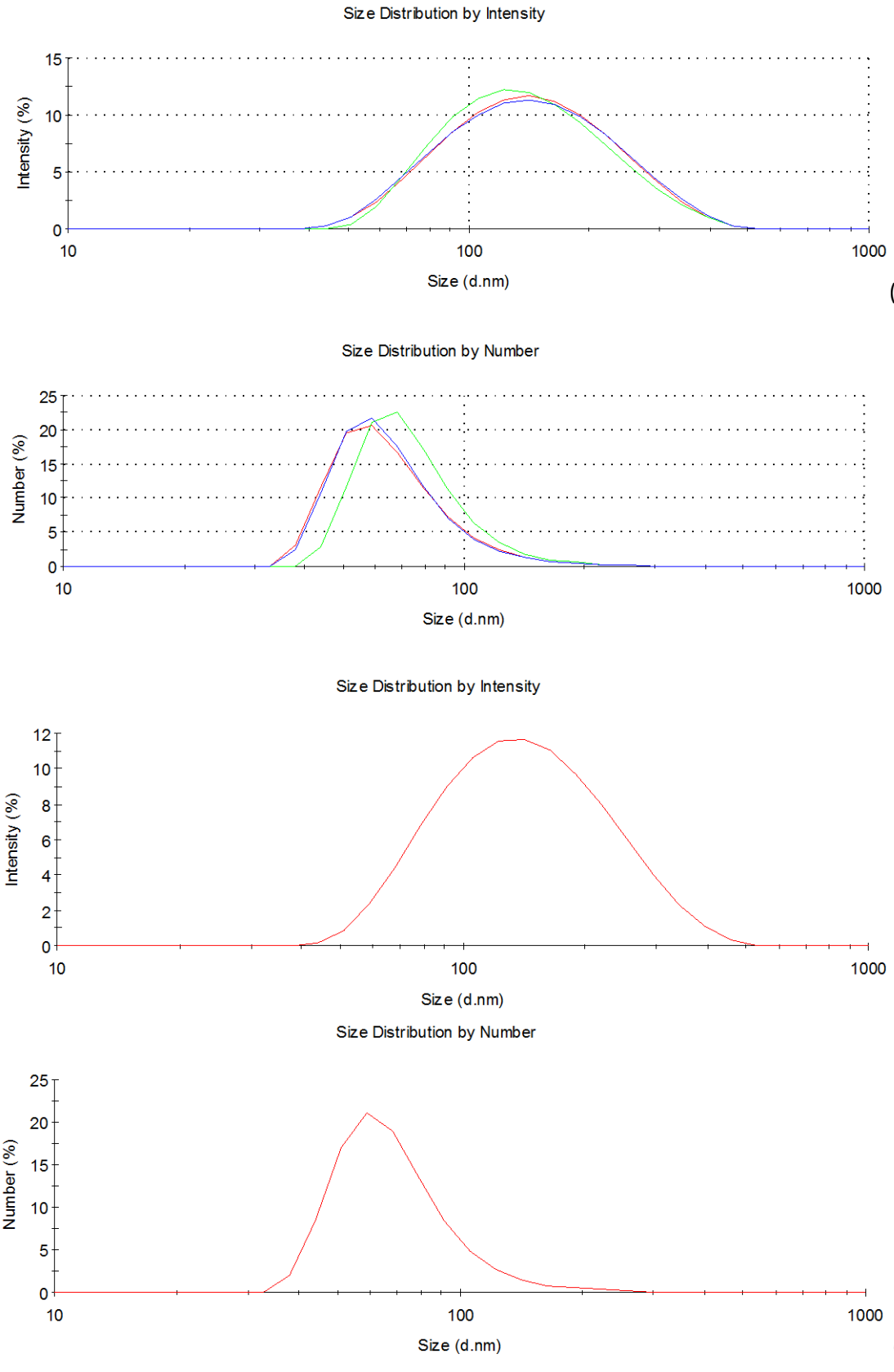

Figure 117: Intensity (a) and number (b) distribution curves for three successive DLS data runs on heptane 3.5Ro - red line record 271, green line record 272, and blue line record 273. Averaged intensity (c) and number (b) distribution curves for records 271, 272 and 273.

6.6.3 Heptane 4.5 Ro

Record / Repeat Num	Sample Name	Sample Description	Date	Attenuator	Correlation curve intercept	PD	PD width d. nm	Zeta-Average d. nm	Mode of Intensity Peak 1 d. nm (%)	Mode of Intensity Peak 2 d. nm (%)	Mode of Number Peak 1 d. nm (%)	Mode of Number Peak 2 d. nm (%)
275/1	SAXS 6/7 Heptane 4.5Ro	O+B+WGP+SL **Unshaken, top of solution**	19 Nov 2012 (3 days after prep)	7	0.946	0.185	53.18	123.8	141.8 (100)	0	50.75 (100)	0
276/2				7	0.946	0.171	51.21	123.8	141.8 (100)	0	50.75 (100)	0
277/3				7	0.948	0.179	52.23	123.4	141.8 (100)	0	50.75 (100)	0
Mean 1-3				7	0.946	0.178	52.20	123.7	141.8 (100)	0	50.75 (100)	0

Table 55: DLS results for heptane (C18 95%) 4.5 Ro samples.

The correlation curves for the three measurement runs for heptane 4.5 Ro show a complete, smooth curve with an appropriate intercept indicating valid results, see Table 55 and Figure 118.

The single intensity peak is repeated throughout the three measurements with little variation indicating a stable, monomodal solution; see Figures 119 a and c. The zeta-average for the diameter of the particles is 123-124nm with a polydispersity of 0.17-0.19, which is in the expected size range for unilamellar reverse vesicles. The number distribution reflects the low polydispersity of the monomodal intensity curve by presenting a modal peak at consistent value of 51 nm and an average of 60-64 nm indicating the majority of particles may be at this smaller size range. However, the expected diameter when comparing to other scattering methods will be the 124nm zeta-average value. As the sample was unshaken, the particles within the white gel precipitant were not included in this analysis.

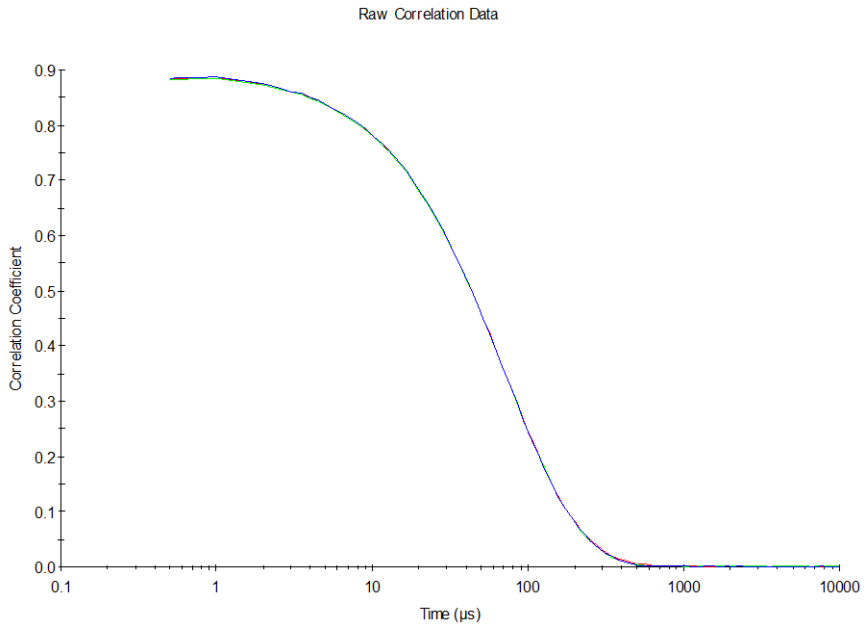

Figure 118: Correlation curves for DLS measurements of heptane 4.5Ro, red line record 275, green line record 276, and blue line record 277.

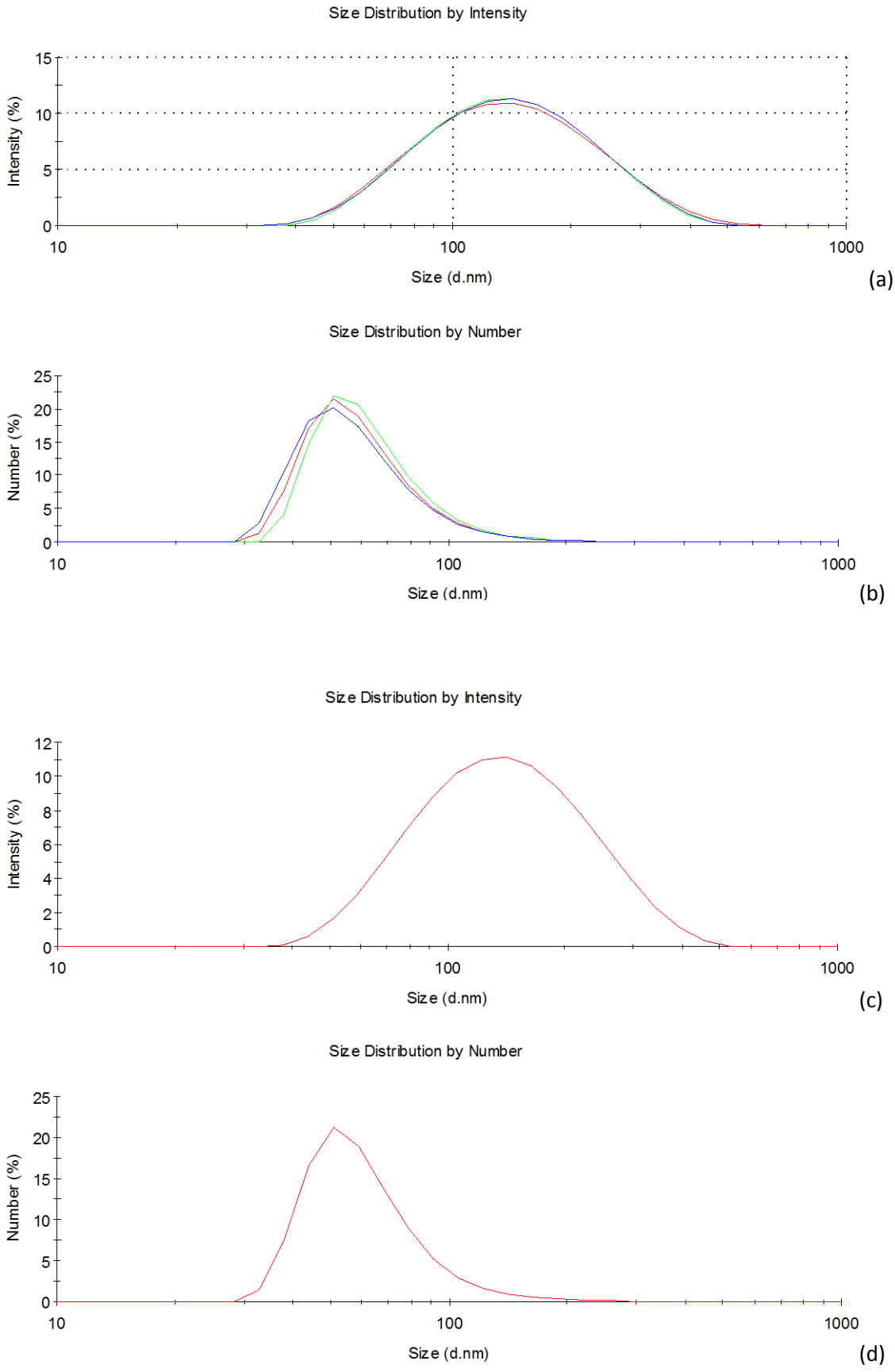

Figure 119: Intensity (a) and number (b) distribution curves for three successive DLS data runs on heptane 4.5Ro - red line record 275, green line record 276, and blue line record 277. Averaged intensity (c) and number (b) distribution curves for records 275, 276 and 277.

6.6.4 Heptane C18 95% DLS summary

Although the DLS data implied a very polydisperse solution at the 2.5 ratio the 3.5 and 4.5 ratios presented very stable, low polydispersity systems with zeta-averages between 123-128 nm and 0.17-0.19 polydispersity. This distribution covers the expected size range for unilamellar reverse vesicles.

These results were taken only three days after the samples were initially prepared, the measurements run were consistent for the 3.5 and 4.5 ratio samples and there was no indication of structures over a micrometre or under 50 nm – this indicates the precipitants that formed from larger structures quickly settle out of solution and that any particles <50 nm quickly aggregate to form larger structures.

6.7 Hexane C18 95% DLS results

6.7.1 Hexane 2.5 Ro

Record / Repeat Num	Sample Name	Sample Description	Date	Attenuator	Correlation curve intercept	PD	PD width d. nm	Zeta-Average d. nm	Mode of Intensity Peak 1 d. nm (%)	Mode of Intensity Peak 2 d. nm (%)	Mode of Number Peak 1 d. nm (%)	Mode of Number Peak 2 d. nm (%)
279/1	RVe1c 5 Hexane 2.5Ro	O+B+WGP+SL **Diluted and 3min bath sonication**	4 July 2012 (3 months after prep)	7	0.960	0.233	66.11	137.1	122.4 (96.7)	5560 (3.3)	68.06 (100)	0
280/2				7	0.963	0.260	70.07	137.5	141.8 (95.8)	5560 (4.2)	68.06 (100)	0
281/3				7	0.961	0.248	68.09	136.6	122.4 (94.7)	5560 (5.3)	58.77 (100)	0
Mean 1-3				7	0.960	0.247	86.41	137.9	164.2 (96.0)	5560 (4.0)	91.28 (100)	0

Table 56: DLS results for hexane (C18 95%) 2.5 Ro samples.

The correlation curves for the three measurement runs for hexane 2.5 Ro show a complete, smooth curve with an appropriate intercept indicating valid results, see Table 56 and Figure 120.

The bimodal pattern is repeated throughout the three measurements indicating a stable solution; see Figures 121 a and c. The consistent 137nm zeta-average with a polydispersity of 0.23-0.26 reflects the main intensity peak, and the distribution is within the range expected for unilamellar reverse vesicles. The second intensity peak indicates the presence of larger particles or clusters in solution that are over ~3000 nm in diameter. The size and asymmetry of this second peak implies there are particles/clusters over ~6000 nm in solution that was prevented from being detected due to the limitations of the equipment used to obtain these measurements. These larger particles are likely to have originally comprised the white gel precipitation. They would then have solubilised into micrometre sized structures following pre-sonication with a weak water bath. In Chapter 5, these micrometre-sized structures are shown to be (interconnected) multilamellar reverse vesicles/onions.

The number distribution shows a mode peak at 59-68 nm and an average of 74-80 nm implying there are a high number of particles at this smaller size range. However, the expected diameter when comparing to other scattering methods will be the 137nm zeta-average value.

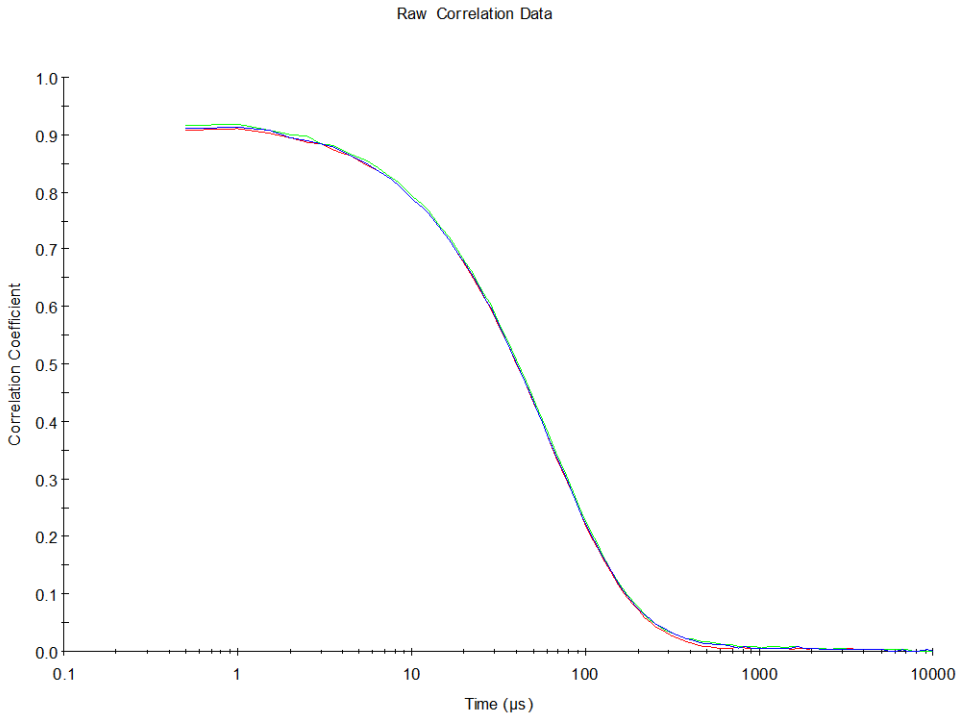

Figure 120: Correlation curves for DLS measurements of hexane 2.5Ro, red line record 279, green line record 280, and blue line record 281.

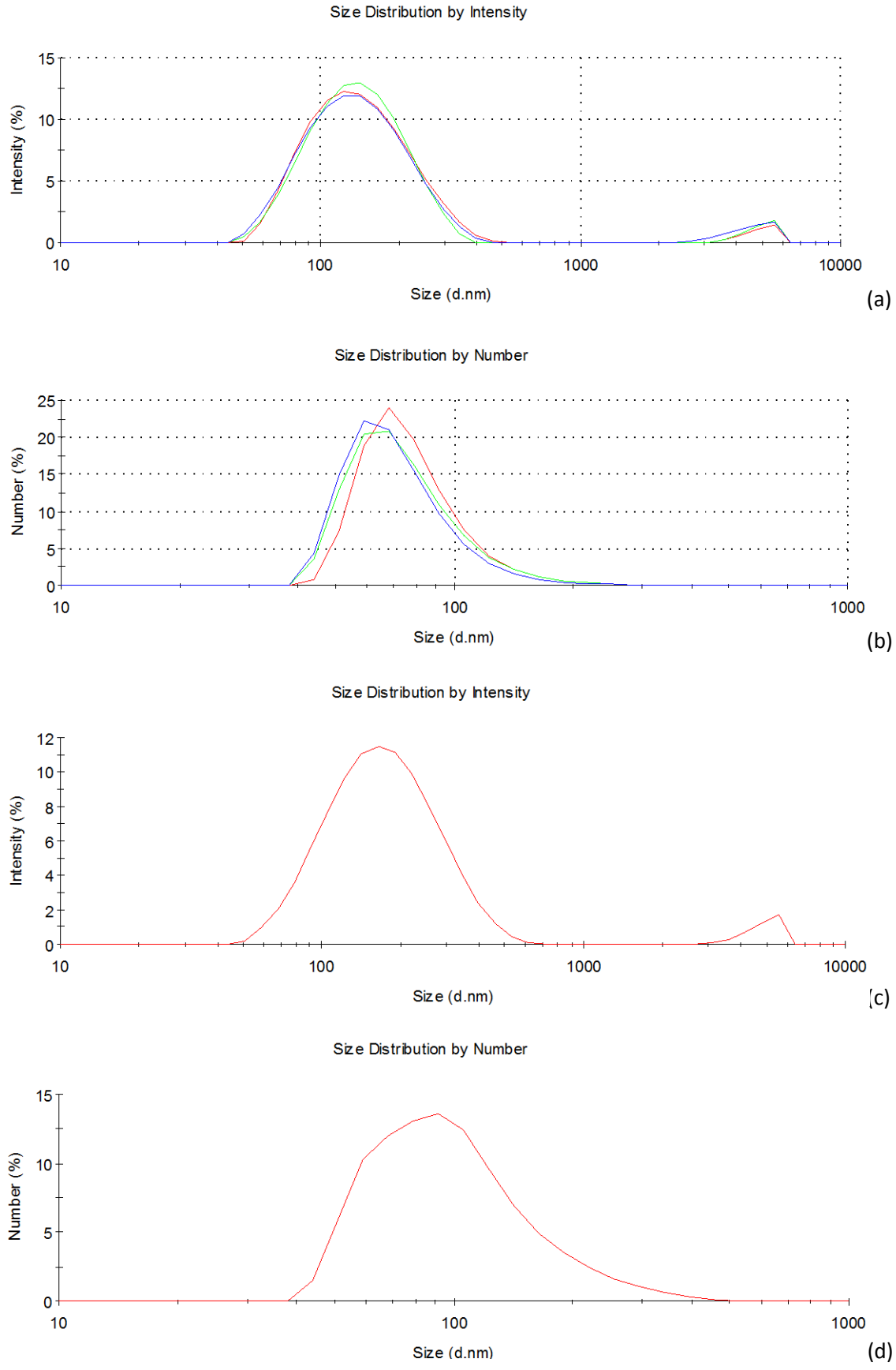

Figure 121: Intensity (a) and number (b) distribution curves for three successive DLS data runs on hexane 4.5Ro - red line record 279, green line record 280, and blue line record 281. Averaged intensity (c) and number (b) distribution curves for records 279, 280 and 281.

6.7.2 Hexane 3.5 Ro

Record / Repeat Num	Sample Name	Sample Description	Date	Attenuator	Correlation curve intercept	PD	PD width d. nm	Zeta-Average d. nm	Mode of Intensity Peak 1 d. nm (%)	Mode of Intensity Peak 2 d. nm (%)	Mode of Number Peak 1 d. nm (%)	Mode of Number Peak 2 d. nm (%)
283/1	RVe1c 9 Hexane 3.5Ro	O+B+CLay+WGP+SL **Diluted and 3min bath sonication**	4 July 2012 (3 months after prep)	7	0.963	N/A	N/A	N/A	N/A	N/A	N/A	N/A
284/2				7	0.953	N/A	N/A	N/A	N/A	N/A	N/A	N/A
285/3				7	0.960	N/A	N/A	N/A	N/A	N/A	N/A	N/A
Mean 1-3				N/A	N/A	N/A	N/A	N/A	N/A	N/A	N/A	N/A

Table 57: DLS results for hexane (C18 95%) 3.5 Ro samples.

The intercept of the RVe1c 9 correlation curves were within an acceptable range, and therefore, represented a sample with appropriate amounts of scattering from the suspended particles and low amounts of background scattering (Table 57). However, the intercepts differ by about 0.01 and the correlation curves have a large deviation after about 200 µs with large fluctuations after 700 µs (Figure 122). As the count rates remain the same this is unlikely to be an effect from the quick sedimentation of particles. The plateauing feature (~700µs to 3000 µs) indicates the sample is too polydisperse for a valid DLS analysis. Therefore, this set of measurements was invalid.

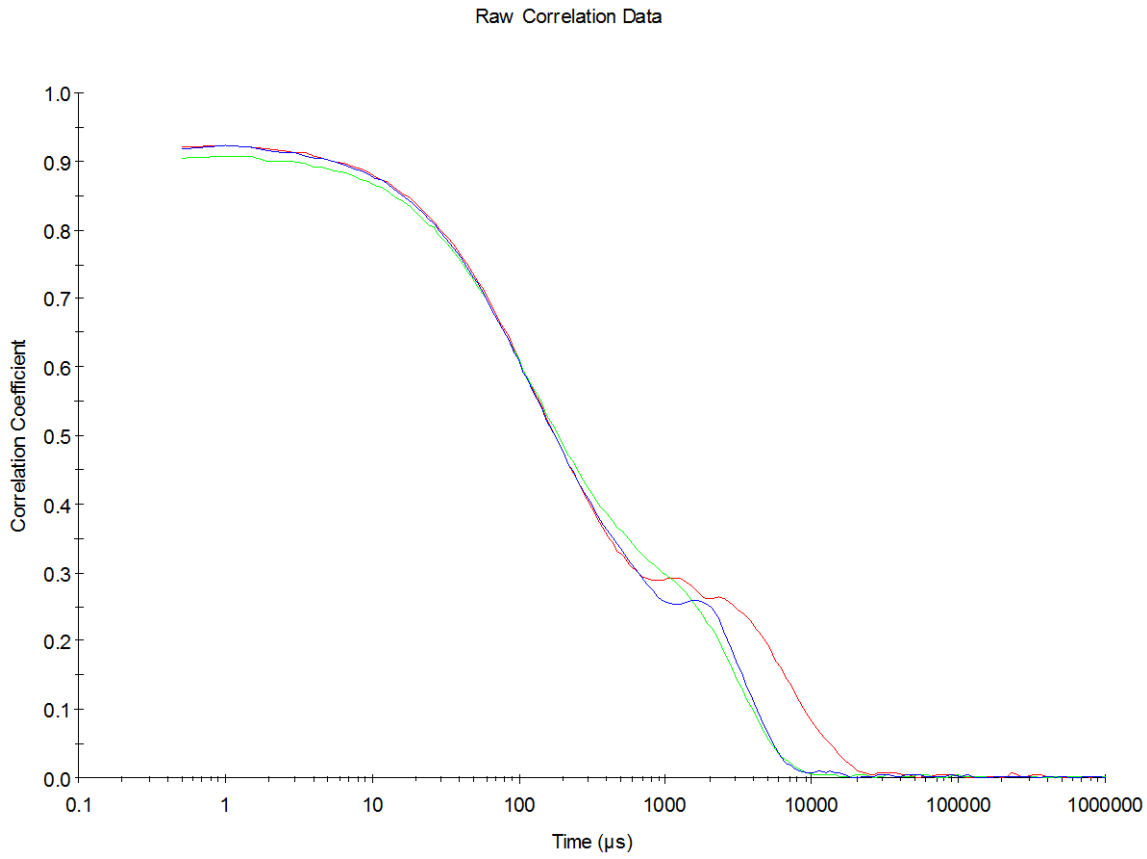

Figure 122: Correlation curves for DLS measurements of hexane 3.5Ro, red line record 283, green line record 284, and blue line record 285.

6.7.3 Hexane 4.5 Ro

Record / Repeat Num	Sample Name	Sample Description	Date	Attenuator	Correlation curve intercept	PD	PD width d. nm	Zeta-Average d. nm	Mode of Intensity Peak 1 d. nm (%)	Mode of Intensity Peak 2 d. nm (%)	Mode of Number Peak 1 d. nm (%)	Mode of Number Peak 2 d. nm (%)
286/1	RVe1c 13 Hexane 4.5Ro	O+B+CLay+WGP+SL **Diluted and 3min bath sonication**	4 July 2012 (3 months after prep)	9	0.966	N/A	N/A	N/A	N/A	N/A	N/A	N/A
287/2				9	0.956	N/A	N/A	N/A	N/A	N/A	N/A	N/A
288/3				9	0.962	N/A	N/A	N/A	N/A	N/A	N/A	N/A
Mean 1-3				N/A	N/A	N/A	N/A	N/A	N/A	N/A	N/A	N/A

Table 58: DLS results for hexane (C18 95%) 4.5 Ro samples.

The intercept of the RVe1c 13 correlation curves were within an acceptable range, and therefore, represented a sample with appropriate amounts of scattering from the suspended particles and low amounts of background scattering (Table 58). However, the intercept values diverge by about 0.01 and correlation curves never fully amalgamate. There is also a large fluctuation at 200-1000µs with smaller fluctuations from 1000µs (Figure 123). These curves indicate the sample is either too polydisperse, sedimenting or has too many large particles, aggregates or dust for a valid DLS analysis. As the count rates decrease significantly across the three measurements, from 268kcps, to 206kcps and then finally 189kcps, this indicates that the sample is sedimenting. Therefore this set of DLS measurements show that a 3 minute bath sonication causes the system to become unstable and particles that have been separated by sonication quickly begin to merge again to become larger particles. Unfortunately, this sedimentation prevents accurate size measurements to be taken; therefore, the intensity distribution and further analyses are invalid.

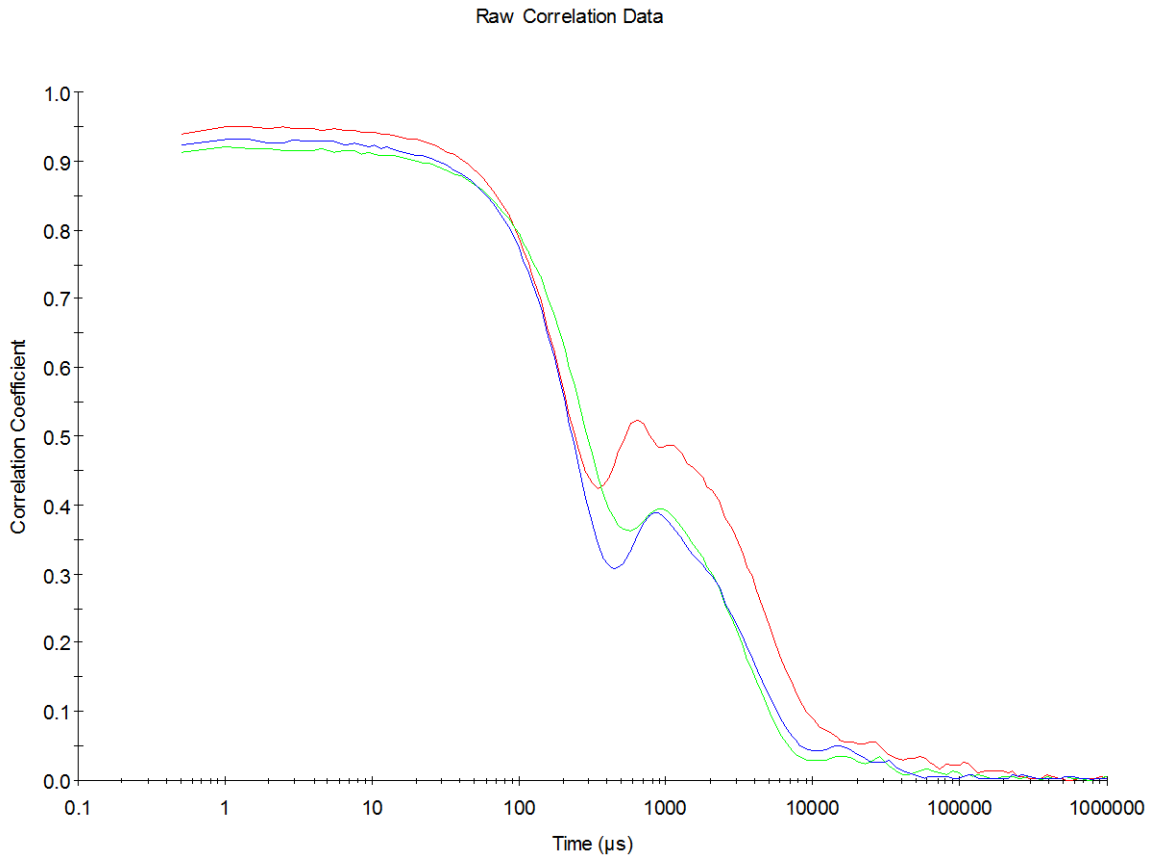

Figure 123: Correlation curves for DLS measurements of hexane 4.5Ro, red line record 286, green line record 287, and blue line record 288.

6.7.4 Hexane C18 95% DLS summary

The high polydispersity caused by the pre-sonication of these systems caused both the 3.5 and 4.5 ratio samples to produce invalid intensity distributions. However, this same pre-sonication in the sample containing a 2.5 ratio did not prevent the DLS analyses. We may be able to attribute this to the nature of the specimens before the pre-sonication as the 2.5 ratio specimen only had a white gel precipitant; however, the other hexane samples had a cloudy layer above this precipitant. This implies that the hexane 2.5 ratio sample consisted of two separate particle types, those in solution (unilamellar reverse vesicles) and those of the precipitant (interconnected multilamellar reverse vesicles/onions). The 3.5 and 4.5 samples on the other hand had a greater range of particle sizes contained in the solution, the cloudy layer and the precipitant, which formed a solution too polydisperse for DLS analyses after mixing occurred.

6.8 Pentane C18 95% DLS results

6.8.1 Pentane 2.5 Ro

Record / Repeat Num	Sample Name	Sample Description	Date	Attenuator	Correlation curve intercept	PD	PD width d. nm	Zeta-Average d. nm	Mode of Intensity Peak 1 d. nm (%)	Mode of Intensity Peak 2 d. nm (%)	Mode of Number Peak 1 d. nm (%)	Mode of Number Peak 2 d. nm (%)
289/1	RVe1c 6 Pentane 2.5Ro	T+O(slightly)+ WGP+SL **Unshaken**	9 May 2012 (1 month after prep)	7	0.964	0.107	35.83	109.6	105.7 (100)	0	91.28 (100)	0
290/2				7	0.962	0.108	35.74	108.8	105.7 (100)	0	91.28 (100)	0
291/3				7	0.962	0.116	37.00	108.5	105.7 (100)	0	78.82 (100)	0
Mean 1-3				7	0.964	0.110	35.02	105.4	105.7 (100)	0	78.82 (100)	0
293/1	SAXS 9/10 Pentane 2.5Ro	T+O(slightly)+ WGP+SL **Unshaken, top of solution**	22 Nov 2012 (1 week after prep)	10	0.873	0.007	8.927	103.5	105.7 (100)	0	78.82 (100)	0
294/2				10	0.873	0.005	7.558	103.7	105.7 (100)	0	78.82 (100)	0
295/3				10	0.874	0.059	25.40	104.1	105.7 (100)	0	78.82 (100)	0
Mean 1-3				10	0.873	0.024	15.58	100.4	105.7 (100)	0	78.82 (100)	0

Table 59: DLS results for pentane (C18 95%) 2.5 Ro samples.

All the correlation curves for the pentane 2.5 Ro samples show complete, smooth curves with appropriate intercept values that indicate valid results, see Table 59 and Figure 124

The results for RVe1c 6 and SAXS 9/10 are similar, presenting a monomodal system with a zeta-average diameter of 109 nm and 104 nm respectively (see Figure 125). These systems have low polydispersities so can be considered monodisperse. This low polydispersity also has an impact on the number distribution; the ~15-25 nm difference between the modal values for the number distribution peaks and the intensity distribution peaks are smaller than in most of the other systems that we have studied in this research. The increase in polydispersity in the zeta-average values between these samples may be due to the clustering of the particles after an additional 3 weeks has passed.

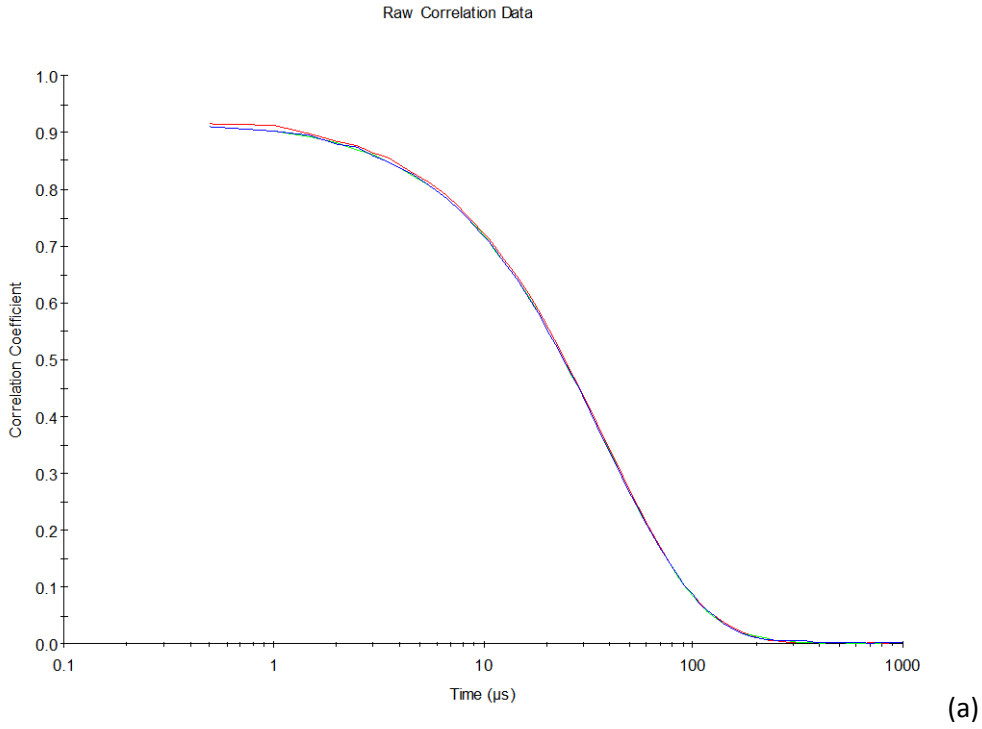

(a)

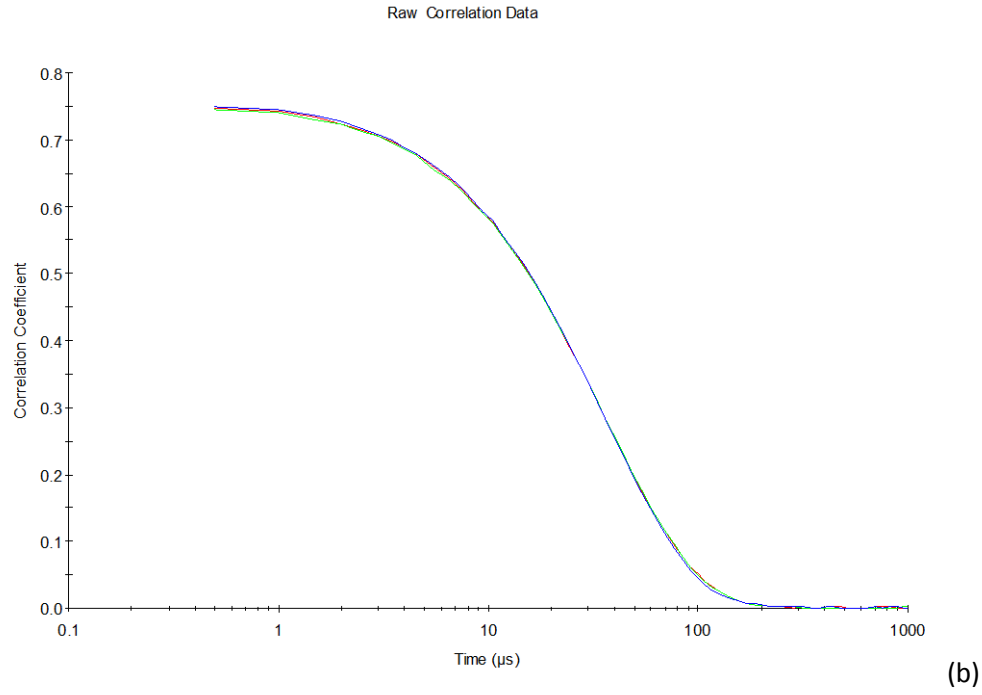

(b)

Figure 124: Correlation curves for DLS measurements of pentane 2.5Ro, (a) RVe1c6: red line record 289, green line record 290, and blue line record 291, (b) SAXS 9/10: red line record 293, green line record 294, and blue line record 295.

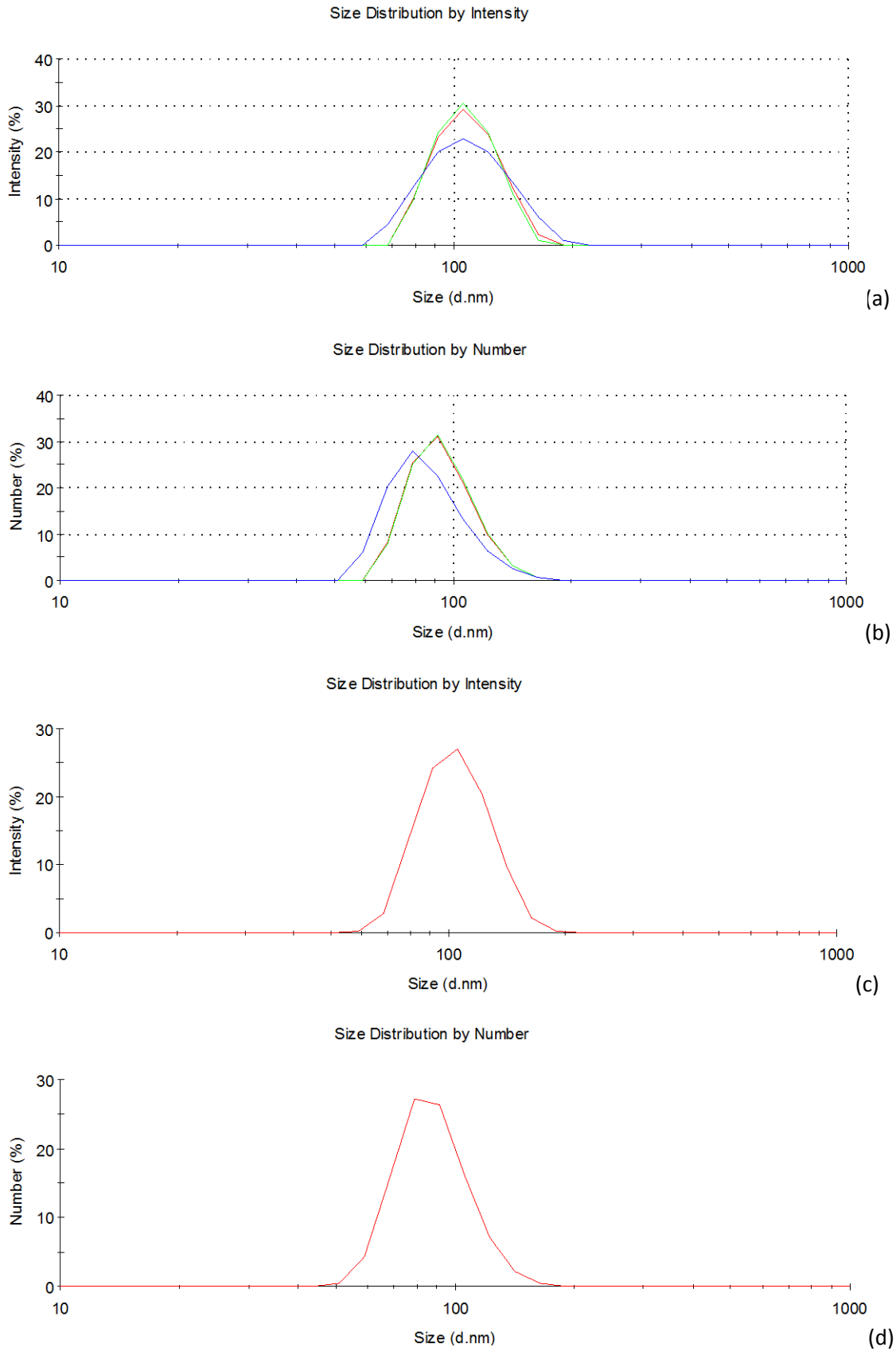

Figure 125: Intensity (a) and number (b) distribution curves for three successive DLS data runs on RVe1c6 pentane 2.5Ro - red line record 289, green line record 290 and blue line record 291. Averaged intensity (c) and number (b) distribution curves for records 289, 290 and 291.

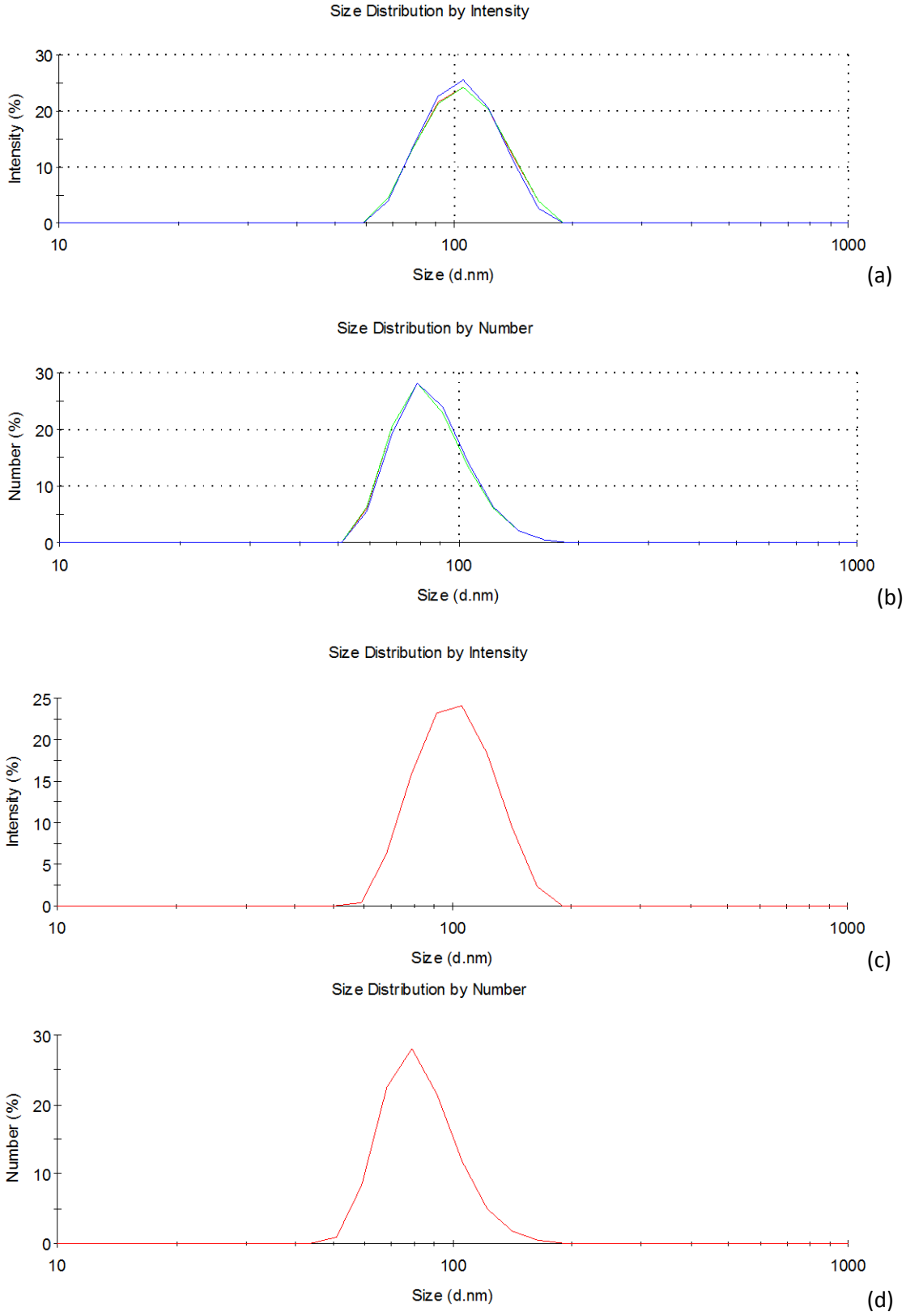

Figure 126: Intensity (a) and number (b) distribution curves for three successive DLS data runs on SAXS 9/10 pentane 2.5Ro - red line record 293, green line record 294 and blue line record 295. Averaged intensity (c) and number (b) distribution curves for records 293, 294 and 295.

6.8.2 Pentane 3.5 Ro

Record / Repeat Num	Sample Name	Sample Description	Date	Attenuator	Correlation curve intercept	PD	PD width d. nm	Zeta-Average d. nm	Mode of Intensity Peak 1 d. nm (%)	Mode of Intensity Peak 2 d. nm (%)	Mode of Number Peak 1 d. nm (%)	Mode of Number Peak 2 d. nm (%)
310/1	RVe1c 10 Pentane 3.5Ro	T+O(slightly)+WGP(grainy)+SL **1 min bath sonication**	9 May 2012 (1 month after prep)	7	0.972	N/A	N/A	N/A	N/A	N/A	N/A	N/A
311/2				7	0.960	0.212	53.34	115.8	105.7 (100)	0	91.28 (100)	0
312/3				7	0.960	0.203	51.36	113.9	105.7 (100)	0	78.82 (100)	0
Mean 1-3				7	0.972	N/A	N/A	N/A	N/A	N/A	N/A	N/A
314/1	SAXS 11/12 Pentane 3.5Ro	T+O(slightly)+WGP(grainy)+SL **Unshaken, top of solution**	22 Nov 2012 (1 week after prep)	9	1.08	N/A	N/A	N/A	N/A	N/A	N/A	N/A
315/2				9	1.08	N/A	N/A	N/A	N/A	N/A	N/A	N/A
316/3				9	1.07	N/A	N/A	N/A	N/A	N/A	N/A	N/A
Mean 1-3				9	1.08	N/A	N/A	N/A	N/A	N/A	N/A	N/A

Table 60: DLS results for pentane (C18 95%) 3.5 Ro samples.

6.8.2.1 SAXS 11/12

The correlation curve intercepts for the SAXS 11/12 sample are over 1 which indicates that there may be dust in the sample (see Table 60). However, the count rates (126 kcps, 123 kcps, and 123 kcps) and the correlation curves do not have the large, random fluctuations that would indicate contamination. Instead, there is a plateauing effect after ~100 μs in all the measurements which lasts until ~2000-3000 μs (see Figure 127b). This plateau may indicate a multimodal system that is unable to be accurately indentified using this technique and would signify that the sample is too polydisperse due to pre-sonication. However, some evaporation occurred during the analysis which would have increased the concentration and this may be the cause of the large intercept value.

6.8.2.2 RVe1c 10

The DLS measurements for RVe1c 10 are also not without their complications, with the correlation curve for the first measurement plateauing after ~200 μs at a very low level (correlation coefficient value of ~0.025). The appropriate intercept values and the validity of the second and third correlation curves indicate that the plateauing is not likely to be due to contamination. Therefore, it is probably an artefact of rapid sedimentation after the pre-sonication. The sonication could have caused suspension of the particles composing the white gel precipitant which quickly settled causing an inaccurate first measurement run.

The second and third measurements describe a monomodal system as having a zeta-average diameter of 114-116 nm with a polydispersity of 0.2-0.21. When viewing the intensity distribution curve this polydispersity seems too large, therefore, this system is better described using the mean diameter of this peak: 111 nm (0.10 PD) and 109 nm (0.08 PD) respective to the measurement run. Both size ranges are plausible for a system of unilamellar reverse vesicles. The modal peaks in the number distribution curve also indicate that most of the particles are near this value at ~79-92 nm.

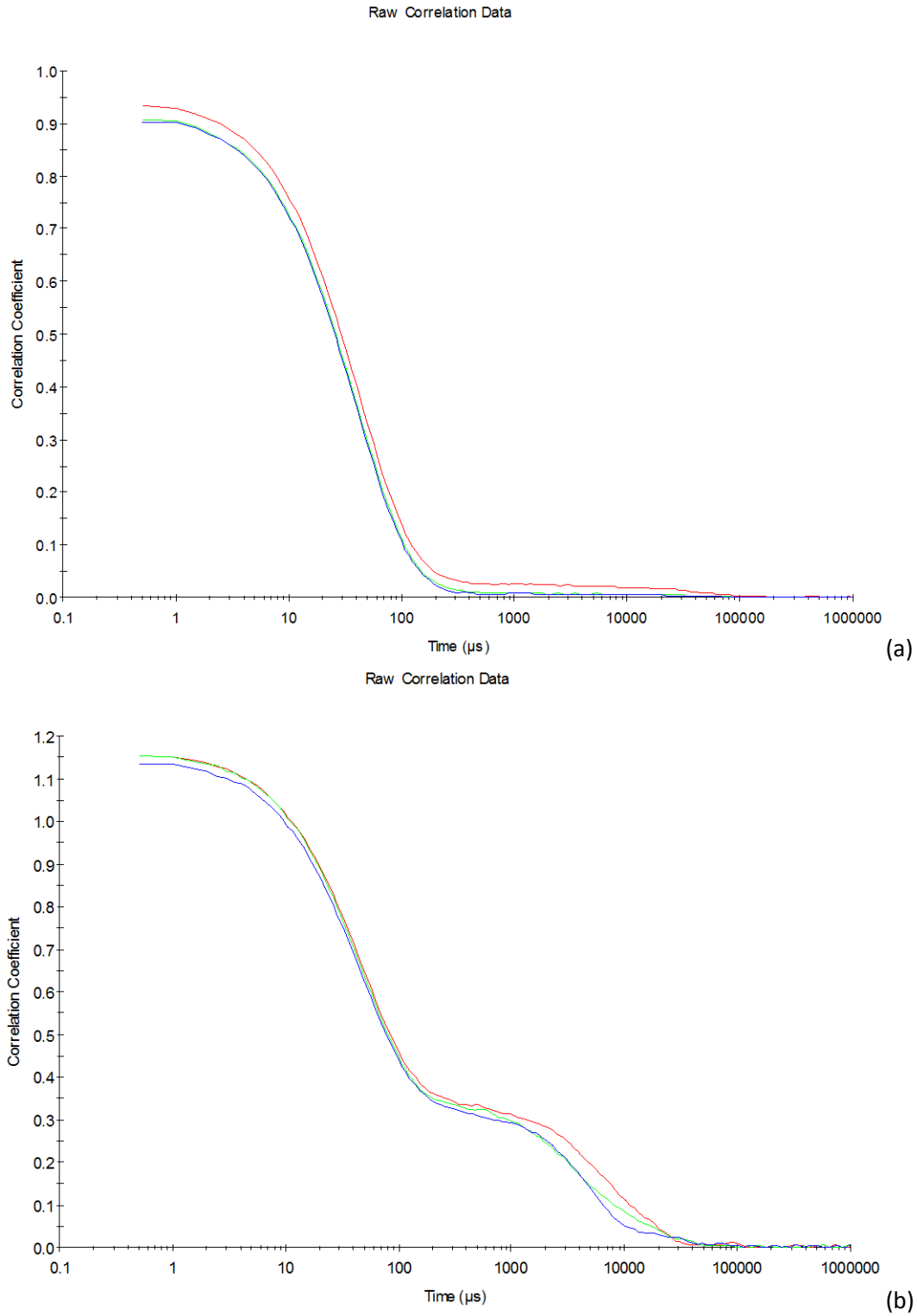

Figure 127: Correlation curves for DLS measurements of pentane 3.5Ro, (a) RVe1c10: red line record 310, green line record 311, and blue line record 312, (b) SAXS 11/12: red line record 314, green line record 315, and blue line record 316.

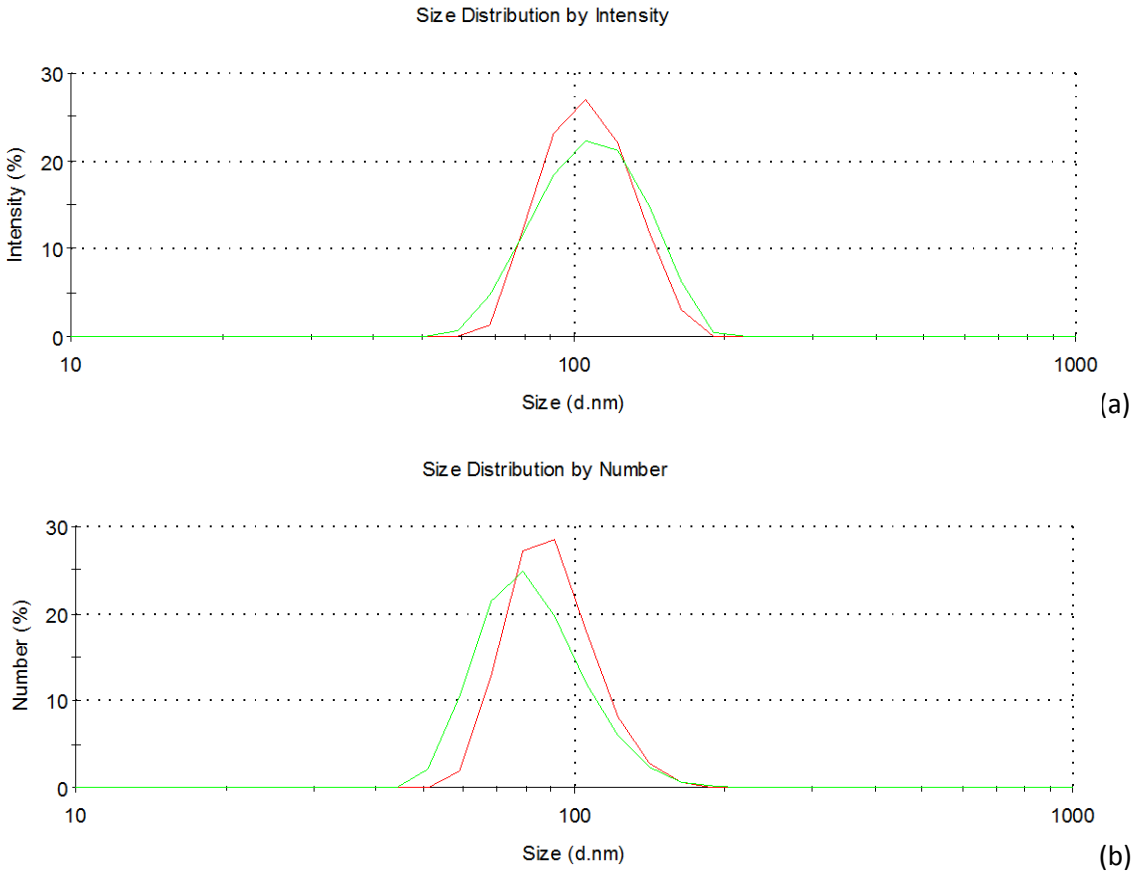

Figure 128: Intensity (a) and number (b) distribution curves for two successive DLS data runs on RVe1c10 pentane 3.5Ro - red line record 311 and green line record 312.

6.8.3 Pentane 4.5 Ro

Record / Repeat Num	Sample Name	Sample Description	Date	Attenuator	Correlation curve intercept	PD	PD width d. nm	Zeta-Average d. nm	Mode of Intensity Peak 1 d. nm (%)	Mode of Intensity Peak 2 d. nm (%)	Mode of Number Peak 1 d. nm (%)	Mode of Number Peak 2 d. nm (%)
318/1	RVe1c 14 Pentane 4.5Ro	T+YWGP+NL **Unshaken, top of solution**	9 May 2012 (1 month after prep)	11	0.778	N/A	N/A	N/A	N/A	N/A	N/A	N/A
319/2				11	0.780	N/A	N/A	N/A	N/A	N/A	N/A	N/A
321/2	RVe1c 14 Pentane 4.5Ro	T+YWGP+NL **3 minutes bath sonication**	4 July 2012 (3 months after prep)	11	3.49	N/A	N/A	N/A	N/A	N/A	N/A	N/A
322/3				11	3.41	N/A	N/A	N/A	N/A	N/A	N/A	N/A
323/1	SAXS 13/14 Pentane 4.5Ro	T+O(slightly)+WGP+WL **After addition of pure pentane (see text)**	22 Nov 2012 (1 week after prep)	8	1.15	N/A	N/A	N/A	N/A	N/A	N/A	N/A
324/2				8	1.08	N/A	N/A	N/A	N/A	N/A	N/A	N/A
325/3				8	1.08	N/A	N/A	N/A	N/A	N/A	N/A	N/A
327/1	SAXS 13/14 Pentane 4.5Ro	T+O(slightly)+WGP+WL **1 min bath sonication**	22 Nov 2012 (1 week after prep)	8	0.967	N/A	N/A	N/A	N/A	N/A	N/A	N/A
328/2				8	0.964	N/A	N/A	N/A	N/A	N/A	N/A	N/A
329/3				8	0.956	N/A	N/A	N/A	N/A	N/A	N/A	N/A

Table 61: DLS results for pentane (C18 95%) 4.5 Ro samples.

6.8.3.1 RVe1c 14

The two DLS results of RVe1c 14, taken two months apart, were used to determine whether DLS could find extremely dilute particles in solution with no laser reflection. As expected, this transparent sample caused the election of the highest attenuator - allowing 100% of the laser to hit the sample (see Table 61). The intercept of RVe1c 14 without sonication was below the lowest eligible limit – 0.85 as a result from lack of scattering particles. The intercept of RVe1c14 after 3 minutes of sonication is far above the acceptable upper limit of 1 and there is a large plateau of the correlation curves that only starts to drop after ~3000μs (see Figure 129b). Therefore, the large or very polydisperse particles from the yellow-white gel precipitant have prevented size analysis with DLS for this sample. These results show us that samples that do not have any laser reaction either have no structures of this size range in solution, or, are so dilute as to not be able to be detected with an observed laser or DLS measurements. We can also determine that yellow-white gel precipitants do not easily split to form distinct uniform particles, but instead weak sonication will form a highly polydisperse solution which was observed to readily resettle.

6.8.3.2 SAXS 13/14

The first DLS measurements of SAXS 13/14 were taken after extensive evaporation had occurred (3/4ths of the solution) and pure pentane added to maintain the correct concentration for the sample. This may have caused a disturbance of the sample causing highly fluctuating correlation curves, along with intercepts over 1 (see Figure 130a). The second set of DLS measurements were made after 1 minute of weak sonication and left to settle for over an hour. The correlation curves for these measurements are closer to resembling a standard correlation curve; however, the plateauing that begins after ~200 μs indicates that the polydispersity of the sample is still too high for a valid analysis (see Figure 130b). The correlation curves can be seen to drop slightly with each measurement which indicates that the system may be gradually becoming more monodisperse as it settles. The only conclusion that we can draw from these results is that a polydisperse range of solubilised particles take over an hour to settle in this system.

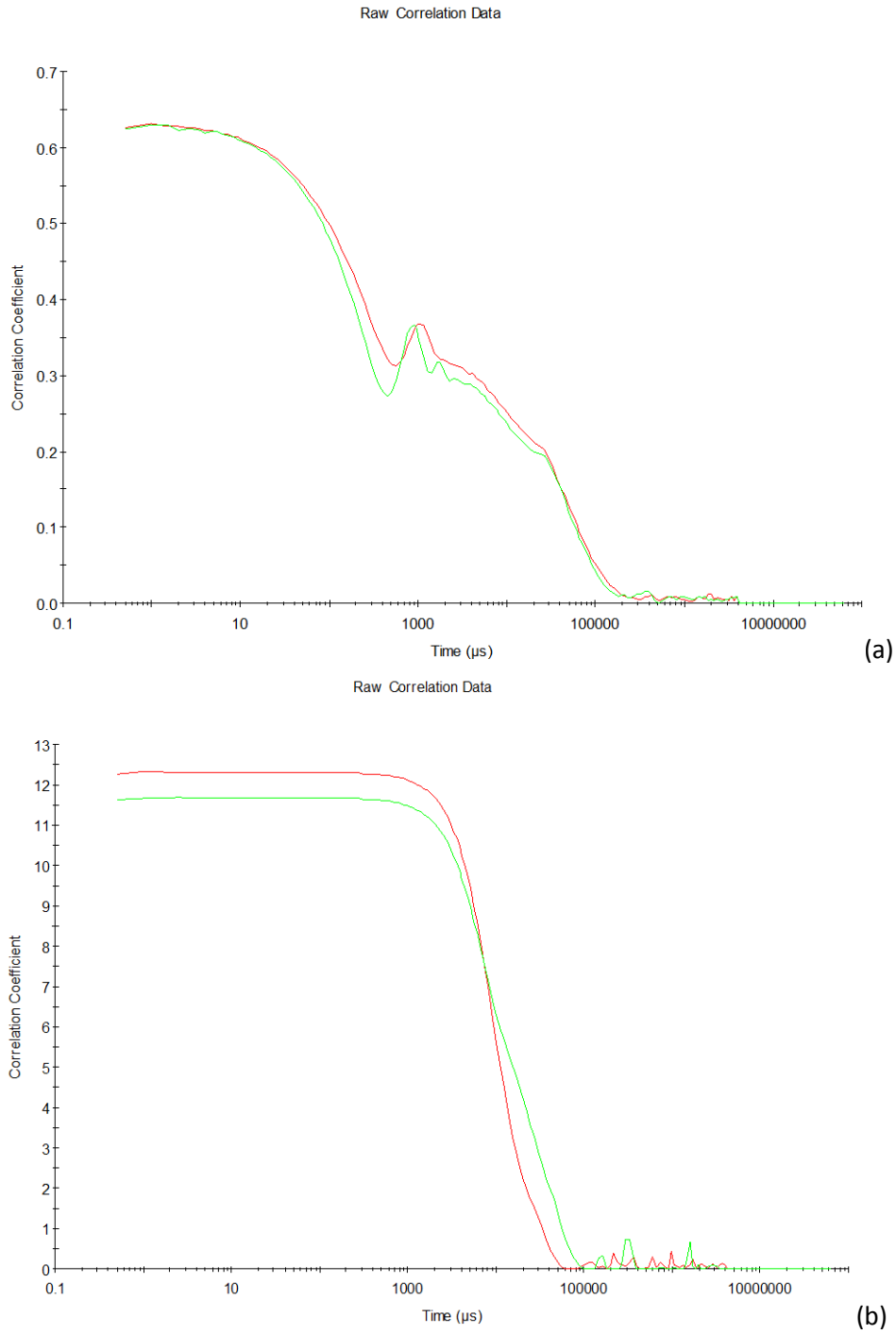

Figure 129: Correlation curves for DLS measurements of RVe1c14 pentane 4.5Ro, (a) RVe1c14: red line record 318 and green line record 319, (b) RVe1c14: red line record 321 and green line record 322.

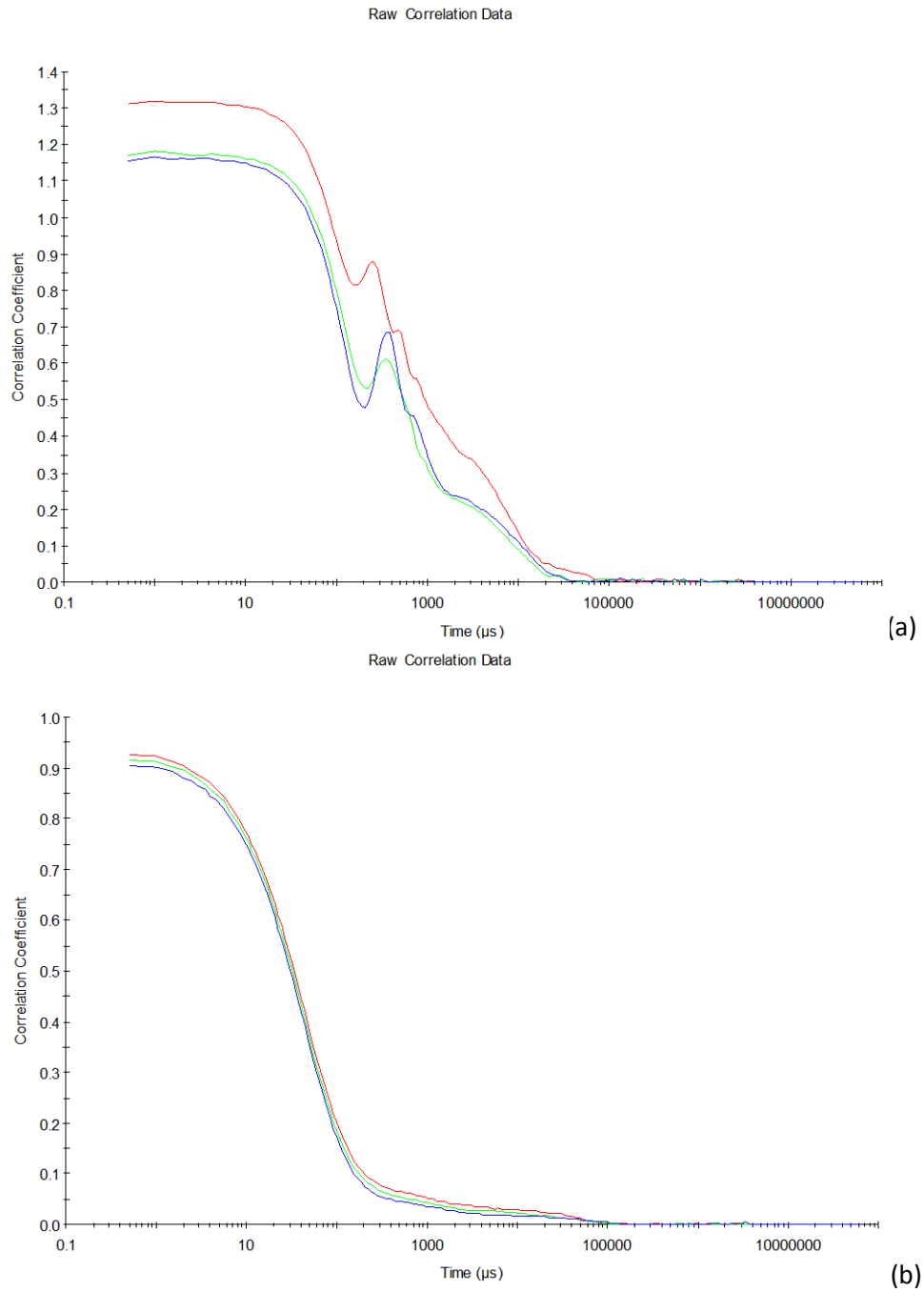

Figure 130: Correlation curves for DLS measurements of SAXS 13/14 pentane 4.5Ro, (a) SAXS 13/14: red line record 323, green line record 324 and blue line record 325, (b) SAXS 13/14: red line record 327, green line record 328 and blue line record 329.

6.8.4 Pentane C18 95% DLS summary

There is evidence for monodisperse (<0.1 PD) unilamellar reverse vesicle systems in both the 2.5 and 3.5 ratio systems with average diameters of ~103-115 nm. The only information gained from the 4.5 ratio samples is that solubilising the precipitants in this type of system forms a highly polydisperse solution.

The heating from laser excitation, and subsequent evaporation of some solvent from these samples within the DLS equipment, may have caused some disruption to the accuracy of the results. Evaporation would have caused increased concentration levels during analysis and may have contributed to some of the invalid result sets. However, no obvious clustering was found to occur in the 2.5 ratio samples, so a small increase in concentration levels are not likely to greatly affect the types of structures in the system.

6.9 Summary of DLS results

The majority of the samples showed particles in a size range that would be applicable to unilamellar reverse vesicles – 50 nm to 200 nm.

6.9.1 Main intensity peak

The mean of the main intensity peak was in the 100-300 nm range with a polydispersity of 0.1-0.3 across all samples that presented valid intensity distribution data. This size range correlates well with systems dominated by unilamellar reverse vesicles (Tung *et al.* 2008).

The form of this main peak tended to have a greater correlation with systems containing the same solvent, rather than systems containing the same amphiphilic ratios. The Figure 131 below illustrates this point with different intensity distributions for the pentane systems compared to cyclohexane systems, and yet the distributions between different ratios in the same solvent are similar.

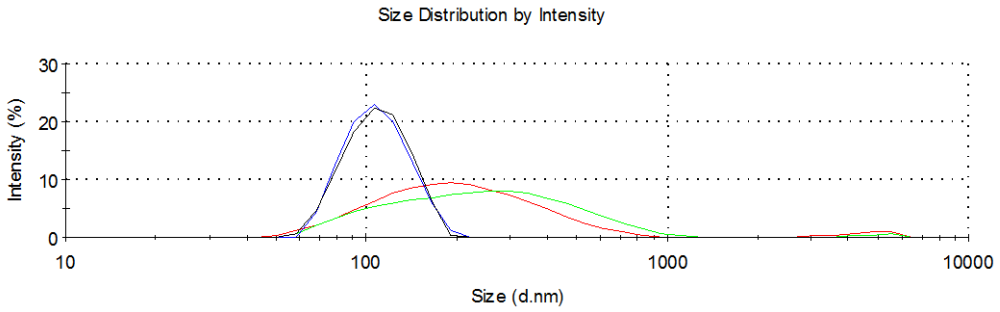

Figure 131: Intensity distribution graph comparing the final measurements of; cyclohexane 2.5Ro (SAXS 23/24, record number 229) red line; cyclohexane 3.5Ro (SAXS 25/26, record number 240) green line; pentane 2.5Ro (RVe1c 6, record number 291) blue line; and pentane 3.5Ro (RVe1c 10, record number 312) black line.

The differences in this main intensity peak also show changes in the range of stable, solubilised particle sizes with the type and molecular weight of the solvent, see Figure 132. The cyclic cyclohexane solvent shows particles of a comparatively wide size range, and the change to an alkane solvent reduces this size range, reflecting the disappearance of 400-1000 nm particles in alkane solvents. The initial reduction of molecular weight of the alkanes, between octane and hexane, causes a gradual shift towards a smaller size range by ~70 nm. However, once we reach the lowest molecular weight alkane (pentane) another large shift is observed. The size range of the particles in pentane are reduced by half compared to those of the higher molecular weight alkanes and therefore form a very monodisperse solution (0.1 PD).

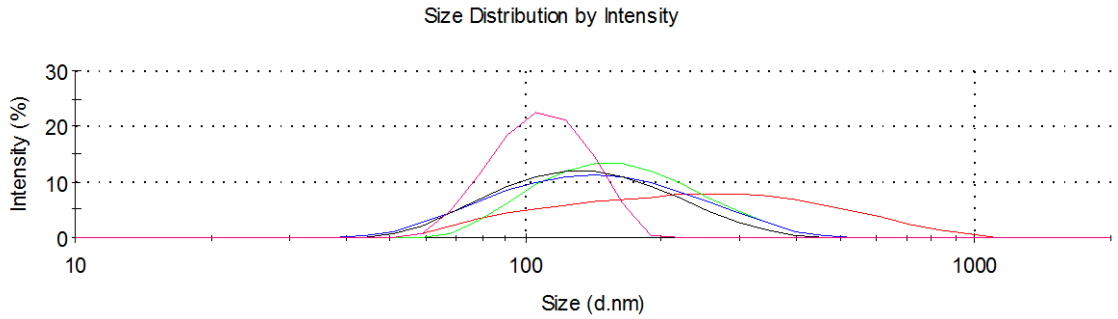

Figure 132: Intensity distribution graph comparing the final measurements of; cyclohexane 3.5Ro (SAXS 25/26, record number 240) red line; octane 3.5Ro (SAXS 43/44, record number 260) green line; heptane 3.5Ro (SAXS 4/5, record number 273) blue line; hexane 2.5Ro (RVe1c 5, record number 281) black line; and pentane 3.5Ro (RVe1c 10, record number 312).

These two sudden changes in size ranges (between the cyclic-alkane systems and the high molecular weight alkanes-pentane systems) may indicate the critical point at which a structural phase transition forms particles other than unilamellar reverse vesicles. However, the range of sizes is still within the expected range for unilamellar reverse vesicles. Therefore, the cause of the difference between the cyclic and high molecular weight alkane solvents may be due to a greater infiltration of solvent into the lipophilic region of the bilayer – increasing curvature and preventing the formation of stable, larger unilamellar reverse vesicles. This would, in effect, restrict the size range of unilamellar reverse vesicles in solution.

This increased infiltration of the bilayer is also likely cause of the monodisperse pentane solution. There must be areas of the lipid tail surface that are too narrow to allow hexane, or other higher molecular weight alkanes, through which pentane molecules can infiltrate. However, from these DLS results alone it is uncertain whether this change in the packing parameter has formed a monodisperse solution of unilamellar reverse vesicles, or a critical point has been reached at which other structures have been formed, for example, reverse cylinders.

6.9.2 Over 1000 nm peak

The structures over 1000 nm diameter are correlated with samples that contain white fluid precipitants or cloudy layers. In Chapter 5, microscopy has revealed the white fluid precipitants to consist of multilamellar reverse vesicles/onions. Therefore, it is sensible to assume the micrometre sized particles that have been detected in these DLS results are multilamellar reverse vesicles/onions.

6.9.3 Signals under 70 nm

There were often fluctuations in the signals arising in the ~40-70 nm size range. This implies that any unilamellar reverse vesicles in this size range are metastable.

6.9.4 Comparison of whole systems

As described above, there was an observed reduction in the polydispersity of particles in the main intensity peak occurring between cyclic and alkane solvents and with a decline in molecular weight of the solvent. When also taking into consideration samples where an intensity distribution curve was not obtained, due high polydispersity in those systems, a broad conclusion emerges: a reduction in the solvents molecular width (cyclic to alkane) and weight increases the overall polydispersity of the system. This may signify that smaller solvent particles not only penetrate the bilayer, increasing curvature and limiting the size range of reverse vesicles in solution, but also may cause the formation of a range of other self-assembled structures. The formation of different structures in solution would account for the invalid intensity distribution data found in some of the samples using lower molecular weight solvents.

6.10 Conclusions

Although the size range of colloidal particles in our systems correlates well with unilamellar reverse vesicles they may also be multilamellar reverse vesicles, compound reverse micelles, reverse cylindrical micelles or disc like reverse bilayers. So to determine the shape and whether lamellar or micellar internal structures are present Studies 7 and 8 were undertaken using the complementary SANS and SAXS techniques.

Chapter 7: Advanced analyses of multi-component amphiphilic-hydrocarbon systems: Synchrotron facility studies using SANS and SAXS

7.1 Introduction

This study evaluates the self assembled particles in multi-component amphiphilic-hydrocarbon systems by small angle scattering using neutrons (SANS) and X-rays (SAXS). Many of the systems studied herein were evaluated by imaging techniques in Chapter 5 and DLS in Chapter 6.

The complementary SANS and SAXS techniques are useful in determining the differences in the size and shape of small colloidal particles and provides information on internal structures. In particular, for our assemblages we focused on the thickness, number and spacing of bilayers for vesicular structures.

Three sample types were analysed using SANS; multi-component, 3.5 Ro, 20 mM, phosphatidylcholine systems in deuterated heptane, hexane, and pentane. There was a large range of sample types analysed by SAXS analyses which are listed in Appendices I and II.

Detailed in Chapter 3 is information regarding sample synthesis; the synchrotron facilities and beamlines (SANS D11 beamline at ILL and SAXS I22 beamline at Diamond); the equipment and methods used to obtain scatter data; the treatment and processing of the raw scatter data; and the SASView software, models and least square (LS) fitting to analyse the scatter data.

Although both these techniques use small angle scattering there are variations in the form factor model parameters and expected scatter intensity profiles due to differences in the regions where contrasts are found in the systems. The main difference in the model parameters is the scatter length densities (SLD); which is the neutron scatter length density for SANS and the electron scatter length density for SAXS. Therefore, the expected shell thickness for SAXS is assumed to be lower than for SANS because SAXS will measure the thickness of the polar interior of the bilayer (due to the strong contrast between the electron scatter length densities of the polar regions of the phospholipids compared to the lipid tails and solvent) and SANS will measure the thickness of the whole bilayer (due to the strong contrast between the neutron scatter length densities of the whole of the phospholipids and the solvent).

The following sections are organised as follows:

- Explanation for the range of values chosen for some of the SASView form factor model parameters.
- Evaluation of the SANS data for the reverse vesicular system published by Tung *et al.* (2008).
- Analysis of the SAXS and SANS scatter data obtained from multi-component amphiphilic-hydrocarbon systems; with sections split into solvent type and then value of the amphiphilic ratio.
- Discussion of main conclusions from these results.

7.2 Parameter limitations for models

7.2.1 Approximate shell thickness

The shell thickness parameter in the form factor model relates to the bilayer in lamellar systems. Using the molecular modelling software *CrystalMaker*, the lengths for the amphiphiles and their respective polar and lipid moieties were approximated.

7.2.1.1 SANS

The shell thickness in the SANS scatter data encompasses the complete cross section of the reverse bilayer; comprising of two phosphatidylcholines end to end. The PC18:2 and lyso-PC18:2 molecules have an approximate length of 20.45 Å, and the PC4:0 molecule has an approximate length of 10.7 Å. Using these lengths, we can approximate the thicknesses for mono- and bi- layers; see Table 62.

Amphiphile	Layer type	Approximate thickness of a sheet of amphiphiles (Å)
PC18:2	Mono layer	~ 20.45
PC18:2	Bilayer	~ 40.9
PC4:0	Mono layer	~ 10.7
PC4:0	Bilayer	~ 21.4
PC18:2 + PC4:0	Mono layer	Between ~ 10.7 and ~ 20.45
PC18:2 + PC4:0	**Bilayer**	**Between ~ 21.4 and ~ 40.9**

Table 62: Table of approximate thicknesses (Å) for sheets of amphiphiles present in the systems studied.

These approximations presume the amphiphiles within bilayers are ordered exactly end to end. However, these estimations ignore factors that may affect the exact bilayer thickness, including potential overlapping polar regions, changing of lipid configuration with temperature, and the inclusion of NaCl. Including these factors we can increase the range of expected bilayer thickness to approximately 19 Å and 43 Å.

7.2.1.2 SAXS

The shell thickness in the SAXS scatter data measures the cross section of the polar interior of the reverse bilayer; comprising of two phosphatidylcholines head groups and NaCl. The thickness of the polar area will depend on the exact configuration of these components; for example, whether the polar moieties between leaflets are situated end to end or overlap (as shown in Figure 133). However, we can estimate the shell thickness from the length of the phosphatidylcholine head groups, the minimum d-spacing (distance between lamellar) for reversed bilayers and the distance between polar regions within a normal bilayer; see Table 63.

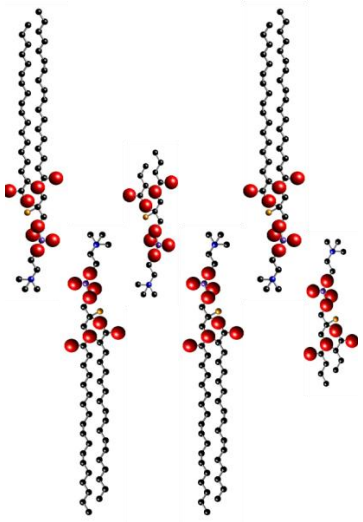

Figure 133: Reversed bilayer with overlapping polar head groups between leaflets.

Structure	Shell components	Estimated shell thickness (Å)
Reverse lamellar	X2 head groups	~15 to 20 Å shell thickness
Reverse multilamellar	X2 head groups separated by 2 lipid tail lengths and layer of solvent	~15 to 20 Å shell thicknesses separated by over 20 Å spacing
Normal lamellar	1 head group separated by 2 lipid tails	~10 Å shell thicknesses separated by ~20 Å spacing

Table 63: Table presenting estimates for shell thickness and d-spacing or distance between polar regions for SAXS data consisting of reversed and normal lamellar.

7.2.2 Incoherent background scatter

The incoherent background scatter (scatter effect of the solvent) was removed from the SAXS scatter data during processing and therefore is set to zero for our SAXS analyses. However, to remove the scatter effect of the solvent for our SANS analyses we used the background parameter of the form factor models. The estimated incoherent background scatter for a fully deuterated solvent with a 1 mm length path, using an incidence wavelength of 6 Å, is 0.05 cm^{-1}. Physically reasonable background parameters for form factor models were therefore limited to a

10^{-2} cm^{-1} magnitude. The actual incoherent background was determined by the plateauing of the scattering data at high Q using the LS fitting function.

7.2.3 Scatter length densities

The scatter length density (SLD) determines the interaction of radiations with materials and a sufficient contrast between the solvent and the particle is required to evaluate structures in solution. The SLD is characterized by the scattering length b_i and its density D:

$$SLD = \Sigma_i^n b_i D N_A / M_m \text{ (Bucknall 1999)}$$

$\Sigma_i^n b_i$ = sum of the coherent scattering lengths of all atoms in the molecule ($_m$)

D = density (g cm^{-3})

N_A = Avogadro's number (mol^{-1})

M_m = molar mass (molecular weight) (g mol^{-1})

Therefore:

$$SLD\ (Å^{-2}) = \Sigma_i^n b_i D N_A / M_m = (m * g\ cm^{-3} * mol^{-1} / g\ mol^{-1}) \times 10^{-14}$$

For X-rays, the photons interact with every electron in the sample, and the scattering length is the Thomson scattering length b=0.282 x 10^{-14} m. For neutrons, the interaction is with the atomic nucleus and the scattering length depends on the type of atoms in the system.

The density for the solvents and NaCl were obtained from the Merck Index (Budavari *et al.* 1989) and the deuterated solvents from Cambridge Isotope Laboratories database. The density of the amphiphiles was calculated from the molar mass (M_m obtained from the Lipid Maps database) and the van der Waals molecular volume. The van der Waals molecular volumes (V_{vdW}) were calculated using functions from Zhao *et al.* (2003) using atomic radii with adjustments for the number of bonds.

$$V_{vdW} = \Sigma \text{ all atom contributions} - 5.92N_B - 14.7R_A - 3.8R_{NR}$$

N_B = number of bonds

R_A = number of aromatic rings

R_{NA} = number of non-aromatic rings

The amphiphiles in our systems do not have rings, and therefore, "$14.7R_A$" and "$3.8R_{NR}$" has a value of zero. So the amphiphilic van der Waals molecular volume can be simplified to:

$$V_{vdW} = \Sigma \text{ all atom contributions} - 5.92N_B$$

Using the NIST SLD calculator the scatter length densities of the compounds found within our samples and those of Tung *et al.* (2008) were calculated; SLDs listed in Tables 64 and 65.

The averaged neutron SLD for a shell/particle in the 2.6 Ro, 3.5 Ro and 4.5 Ro systems (presuming 20 mM of amphiphiles, 3.5 mM of NaCl and a 97wt% PC18:2 and 3wt% lyso-PC18:2 in the C18 95% product) was estimated as 9.9e-7 A^{-2}, 1.01e-6 A^{-2} and 1.02e-6 A^{-2}; respectively.

The lipid tails and the solvent have similar X-ray SLD characteristics and therefore the scatter intensity will differentiate between the high X-ray SLD polar regions (consisting of the lipid polar head groups and NaCl) and the rest of the system. For a shell/particle consisting of a mixture of NaCl and polar head groups, the estimated X-ray SLD is taken as 1.08e-05 A^{-2} and 1.10e-05 A^{-2}, for the 20 mM and 15 mM amphiphilic systems respectively.

Calculating exact SLDs for the amphiphilic-NaCl particles is difficult due to the assumption of an equal composition between particles that might not reflect reality; the ignored effect of solvent infiltration into any bilayers; the mixed nature of the 95% PC18 product (varied fatty acid distribution as set out in Chapter 3); and the possible effect of temperature on SLD. Therefore, although the calculated SLDs for the solvents and mixed amphiphilic-NaCl particles were set as constant parameters the scaling was freely variable to account for these effects.

Compound	Density^{20C} (g cm^3)	Neutron $\Sigma_i^n b_i$ (m)	Neutron SLD (A^{-2})	X-Ray SLD (A^{-2})
d-cyclohexane C6D12	0.89	1.2e-13	**6.68e-6**	-
Cyclohexane C6H12	0.778	-	-	**7.84e-6**
Octane C7H18	0.703	-	-	**7.27e-6**
d-heptane C7D16	0.794	1.53e-13	**6.3e-6**	-
Heptane C7H16	0.684	-	-	**6.99e-6**
d-hexane C6D14	0.767	1.33e-13	**6.14e-6**	-
Hexane C6H14	0.659	-	-	**6.75e-6**
d-pentane C5D12	0.73	1.13e-13	**5.92e-6**	-
Pentane C5H12	0.626	-	-	**6.43e-6**

Table 64: Showing the calculated scatter length densities for the hydrocarbon solvents used in the samples studied with SANS/SAXS.

	Density (g cm^3) [M_m g mol^{-1} /V_{vdW} $Å^3$ mol^{-1}]	Neutron $\Sigma_i^n b_i$ (m)	Neutron SLD (A^{-2})	X-Ray SLD (A^{-2})
Sodium chloride NaCl	2.17	1.32e-14	**2.95e-6**	**1.52e-5**
PC4:0 C16H32NO8P	1.042 [397.187/381.23]	4.761e-14	**7.52e-7**	**9.817e-6**
PC18:2 C44H80NO8P	0.914 [781.562/855.07]	5.4226e-14	**3.82e-7**	**8.845e-6**
Lyso-PC18:2 C26H54NO7P	0.955 [523.364/548.08]	2.6008e-14	**2.86e-7**	**9.214e-6**
Head group for phosphatidylcholines C10H18NO8P	1.093 [341.124/312.03]	-	**1.271e-6**	**1.05e-5**
Tail for PC18:2 (fatty acyl) C34H62O2	0.832 [502.4750/603.78]	-	**0.57e-7**	**8.249e-6**

Table 65: Showing the calculated scatter length densities for the amphiphiles and stabiliser used in the samples studied with SANS/SAXS.

7.2.4 Polydispersity types

The form factor of a monodisperse structure can be smeared with a size distribution function to simulate the effect of a suspension of polydisperse structures. The polydispersity points in the fitting models were set to a 3σ symmetric Gaussian function with 35 points defining the calculated Gaussian curve. Fixing the polydispersity function to these settings enables comparisons between the Chi^2 results of models accurately.

$$\text{Gaussian function} = (1/(\Delta x_o \sqrt{2\pi})) \exp -((x-x_o)^2/2\Delta x_o^2)$$

When evaluating the polydispersity (PD) of a parameter we can use the half width of the Gaussian polydispersity to obtain min and max values for the bulk of the parameter values.

Calculating the half width of a Gaussian function with 3 sigma points:

$$\text{Half width of Gaussian function} = \Gamma = 2\sqrt{(2*\ln 2)}\sigma = 2.3548\sigma$$

$PD = \sigma / x_o$

x_o = mean

σ = standard deviation

Therefore, the standard deviation and the corresponding min/max values of the half width were determined by the fitted mean and PD for a parameter.

7.2.5 Fit engine used in SASView

The least squares fitting engine (Scipy), which employs the Levenberg–Marquardt algorithm was used to find a global minimum in Chi^2 space. For the SANS data the dI was used as the weighting for the Chi^2 calculation to give a greater importance to data points with good statistics and producing a greater accuracy for the Chi^2 value. Errors in intensity were not available for the SAXS data and therefore the weighting for these analyses were set to zero.

In this study the statistical value used to compare the best fits of the form factor models to the scatter intensity data was the averaged Chi^2 statistic, Chi^2/Npts, which divides the total sum of Chi^2 for each data point by the number of data points. This value is a simplified version of a reduced Chi^2 value which was used to compare the fits between models and assist in determining the most appropriate model for the data.

7.3 Evaluation of Tung *et al.* (2008) reverse vesicle SANS data

The original processed scatter intensity data for the research published in Tung *et al.* (2008) was obtained. This study included three deuterated cyclohexane (d-cyclohexane) samples containing C4 and C18 95% at ratios of 0 Ro, 0.5 Ro and 2.6 Ro (total 20 mM amphiphilic concentration) with 3.5 mM NaCl. The measurements were made on the NG-3 beamline at NCNR (NIST Center for Neutron Research) using a 6 Å wavelength at 25 °C. The detector distances used were 1.35 m and 13.18 m which produced a 0.004 to 0.46 $Å^{-1}$ scattering vector range. The scatter intensity data were treated, processed, and placed on an absolute scale using calibration standards provided by NIST.

This section focuses on re-analysing the processed scatter intensity data from the 2.6 Ro system, reported to contain reverse vesicles, using SASView models and the published model parameters as a baseline.

7.3.1 Evaluation of the 2.6 Ro d-cyclohexane SANS data

The published SANS analysis of the 2.6 Ro d-cyclohexane system reported a fit to a unilamellar vesicle form factor model with the parameters; 234 nm diameter, 3.7 nm bilayer thickness and a polydispersity of 0.22. Using these published values and a 6.68e-6 A^{-2} d-cyclohexane SLD as constants in the Vesicle model a Chi^2/Npts value of 16.424 was obtained; see Table 66 and Figure 134.

Fitting the Vesicle model free of the restrictions from the published data but with a fixed thickness polydispersity of 0 resulted in a similar 15.526 Chi^2/Npts value with a 37Å bilayer thickness; see Table 67 and Figure 135. However, there is a 18 Å reduction in core radius that results in an overall diameter of 230 nm which is 4 nm below the value published by Tung *et al.* (2008).

Fitting the Vesicle model free of the restrictions from the published data and thickness polydispersity created a better fit with an 11.383 Chi^2/Npts value; see Table 68 and Figure 135. Compared to the published values this fit had a 22 Å drop in core radius, a 4 Å drop in thickness but an increase in thickness polydispersity. This generates an overall diameter of 229 nm (with 0.22 PD) which is 5 nm less than the published values.

The 33 Å bilayer thickness with 0.28 PD, corresponding to min/max half width values of 22.32 Å and 44.34 Å, fall within acceptable values set out in the preceding subchapter. The high Q region (0.1 $Å^{-1}$ and 0.2 $Å^{-1}$) of the Vesicle model results in Figure 135 illustrate the improved quality of fit for a 33 Å bilayer value with 0.28 PD. This bilayer polydispersity may result from: fluctuations in a flexible, sol (fluid) state, bilayer; a range of bilayer thickness related to the a variation of amphiphilic ratios forming curvature differences responsible for the 0.2 PD in the size of the reverse vesicles; or microdomain differences in the bilayer due to the incorporation of long and short amphiphiles.

There is a quasi-Bragg peak at around 0.05 $Å^{-1}$, corresponding to ~125 Å, which is likely to relate to d-spacing of multilamellar vesicles. Fitting of the Multishell model to this data revealed a poor fit as the model is limited to integers in regards to number of lamellar. This issue was surmounted by fitting the LamellarPCrystal model which resulted in a Chi^2/Npts value of 5.68 using the parameters; 1.1 lamellar, 37 Å bilayer thickness, and a 94 ±1 Å with 0.22 ±0.002 PD d-spacing. This indicates that the system is dominated by unilamellar vesicles, but includes a limited number of multilamellar vesicles.

	Value	Origin of value
Background	0.08354	LS fitting function in SASView.
Core radius (Å)	1133	Tung *et al.* (2008): 234 nm diameter. diameter - 2 * shell thickness / 2 = core radius Therefore: (2340Å -(2*37))/2 = 1133 Å
Scale	0.0093	LS fitting function in SASView.
Shell SLD (A^{-2})	9.9e-7	Estimated shell SLD; see previous section .
Solvent SLD (A^{-2})	6.68e-6	Calculated.
Thickness (Å)	37	Tung *et al.* (2008)
Radius PD	0.22	Tung *et al.* (2008)
Thickness PD	0	Tung *et al.* (2008)
Chi^2/Npts	16.424	Using LS fitting function; with dI weighting.

Table 66: Table of parameter values used to fit the Vesicle model illustrated in Figure 134 to the 2.6 Ro sample scatter intensity data; with the parameters in grey shading being fixed and the resulting Chi^2/Npts value.

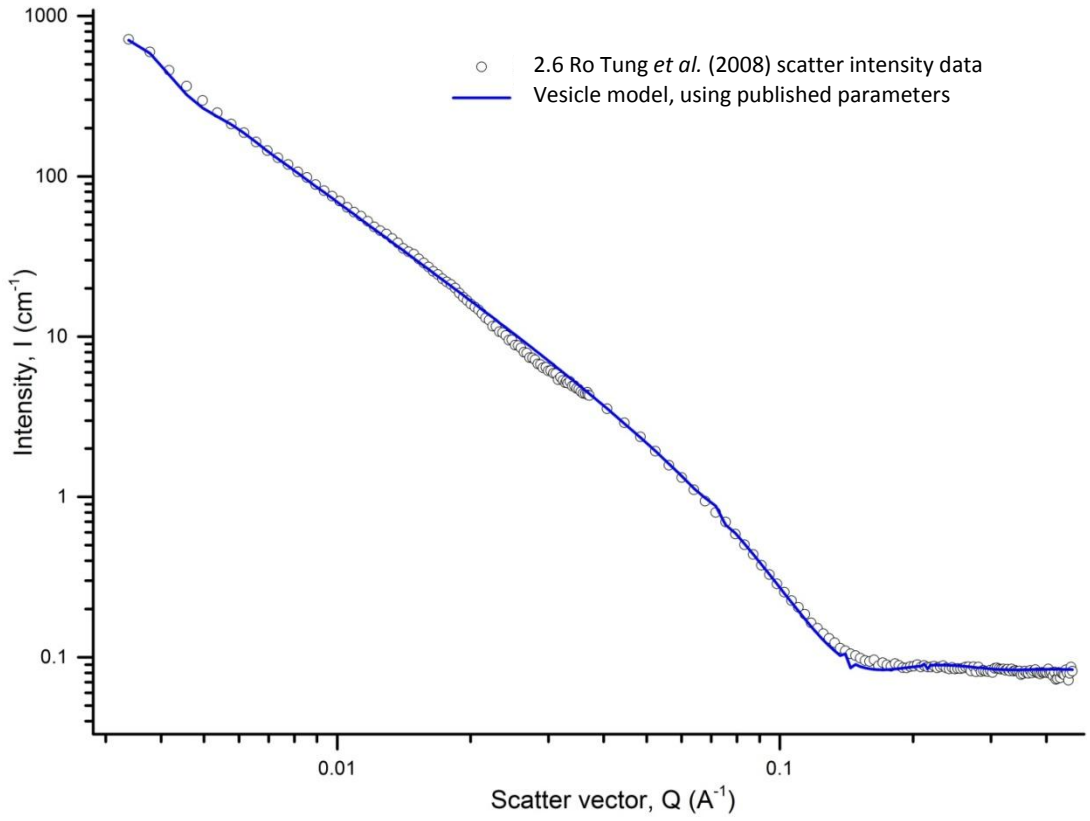

Figure 134: Graph illustrating the scatter intensity curve for Tung *et al.* (2008) 2.6 Ro sample and the Vesicle model fit to the data using fixed radius, thickness and polydiversity values taken from Tung *et al.* (2008) with calculated solvent SLD; as shown in Table 66.

	Value	Origin of value
Background	0.081095	LS fitting function in SASView.
Core radius (Å)	1111.6 Å	LS fitting function in SASView.
Scale	0.0096172	LS fitting function in SASView.
Shell SLD (A^{-2})	9.9e-7 A^{-2}	Estimated shell SLD; see previous section .
Solvent SLD (A^{-2})	6.68e-6 A^{-2}	Calculated.
Thickness (Å)	33.328 Å	LS fitting function in SASView.
Radius PD	0.22324	LS fitting function in SASView.
Thickness PD	0.28052	LS fitting function in SASView.
Chi^2/Npts	11.383	Using LS fitting function with dI weighting.

Table 67: Table of parameter and Chi^2/Npts values for the fit of the Vesicle model (with PD thickness) to the 2.6 Ro sample scatter intensity data; grey shading = fixed value.

	Value	Origin of value
Background	0.083164	LS fitting function in SASView.
Core radius (Å)	1114.7 Å	LS fitting function in SASView.
Scale	0.0093661	LS fitting function in SASView.
Shell SLD (A^{-2})	9.9e-7 A^{-2}	Estimated shell SLD; see previous section.
Solvent SLD (A^{-2})	6.68e-6 A^{-2}	Calculated.
Thickness (Å)	36.596 Å	LS fitting function in SASView.
Radius PD	0.21406	LS fitting function in SASView.
Thickness PD	0	Fixed.
Chi^2/Npts	15.526	Using LS fitting function with dI weighting.

Table 68: Table of parameter and Chi^2/Npts values for the fit of the Vesicle model (without PD thickness) to 2.6 Ro sample scatter intensity data; grey shading = fixed value.

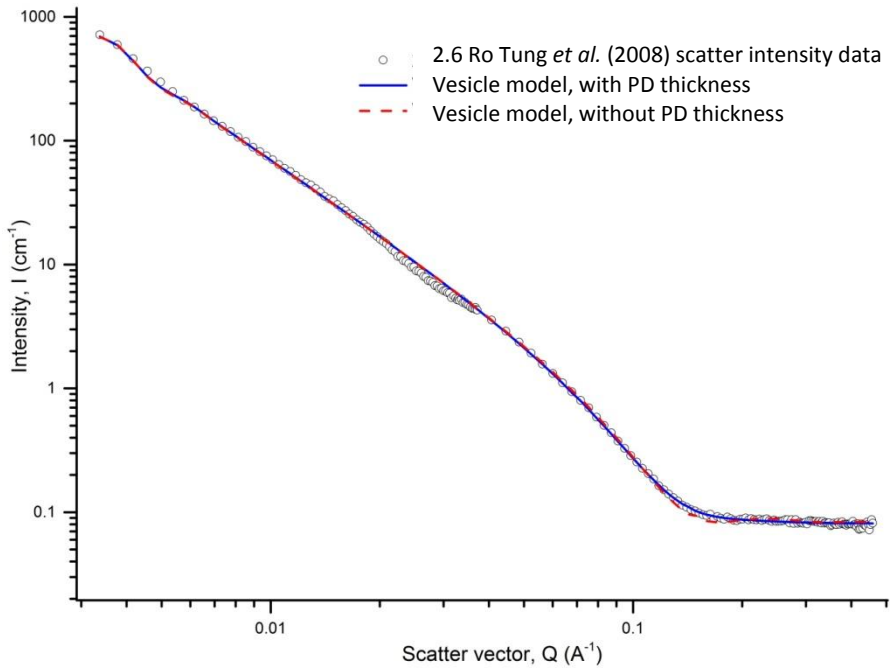

Figure 135: Graph showing the scatter intensity curve for the Tung *et al.* (2008) 2.6 Ro sample and the vesicle model fits to the data using variable parameters except a fixed calculated solvent SLD; with and without PD of bilayer thickness. The parameters for these fits are outlined in Tables 67 and 68.

7.4 SANS and SAXS results for this study

The raw scatter intensity data was treated, reduced, and normalised as detailed in the small angle scattering section of Chapter 3.

For the SAXS results, the viable scatter vector range of the scatter intensity curves was 0.0038 $Å^{-1}$ to 0.1686 $Å^{-1}$. Many of the data swaths requiring masking due to ice crystal formation were removed from this analysis because the remaining scatter intensity data was too diluted at low Q. Also, when repeat experiments showed a discrepancy in sudden reduction of particle scattering it was assumed that radiation damage had altered the system and these too were removed from the analyses.

7.4.1 Cyclohexane 2.5 Ro system

Due to fluctuations at high scatter vectors, the analyses were limited to an upper limit of 0.1 $Å^{-1}$ for the repeat SAXS 23 and SAXS 24 samples. At 258 K, there was no distinct scatter data which is likely to signify the solvent solidifying.

There was a Q^{-2} gradient for this data across the temperature range 298 K to 268 K indicating a thermally stable lamellar system; see Table 69. The scatter vector range was not high enough to indicate the exact bilayer thickness, however, the size of the particles is well constrained with peaks at low Q; see Figure 136. Therefore, the SAXS 23 data swaths were fitted to the Vesicle model with a constrained 10 Å bilayer thickness to obtain the average core radii and corresponding polydispersities listed in Table 70. The average diameter fluctuated slightly between 144 nm and 147 nm with a polydispersity of 0.29 to 0.33 for the 298 K to 278 K data swaths. Due to the large polydispersity, the fluctuations in average diameter are not significant.

The combination of a reduction in intensity at mid to low scatter vectors with reduction in diameter and polydispersity, 142 nm and 0.25 respectively, for the 268 K data swath is likely to be caused by the crystallising of the solvent rather than a transformation of the particle state due to temperature alone.

Data set	Background	Scale	Slope gradient $I(Q)^{-m}$	Chi^2/Npts
SAXS 24 298 K	0	1.24e-09	2.17	1.9e-13
SAXS 23 298 K	0	1.73e-09	2.15	2.2e-13
SAXS 24 288 K	0	1.78e-09	2.10	6.0e-14
SAXS 23 288 K	0	1.55e-09	2.17	6.9e-14
SAXS 24 278 K	0	3.75e-09	1.97	8.7e-14
SAXS 23 278 K	0	1.48e-09	2.15	4.8e-14
SAXS 23 268 K	0	1.70e-09	2.08	3.5e-13

Table 69: Table of parameters and resulting Chi^2/Npts values for the Absolute Power Law model (using constrained background and Q values of 0.005 $Å^{-1}$ to 0.1 $Å^{-1}$) LS fitted to SAXS 23 and SAXS 24 samples at various temperatures.

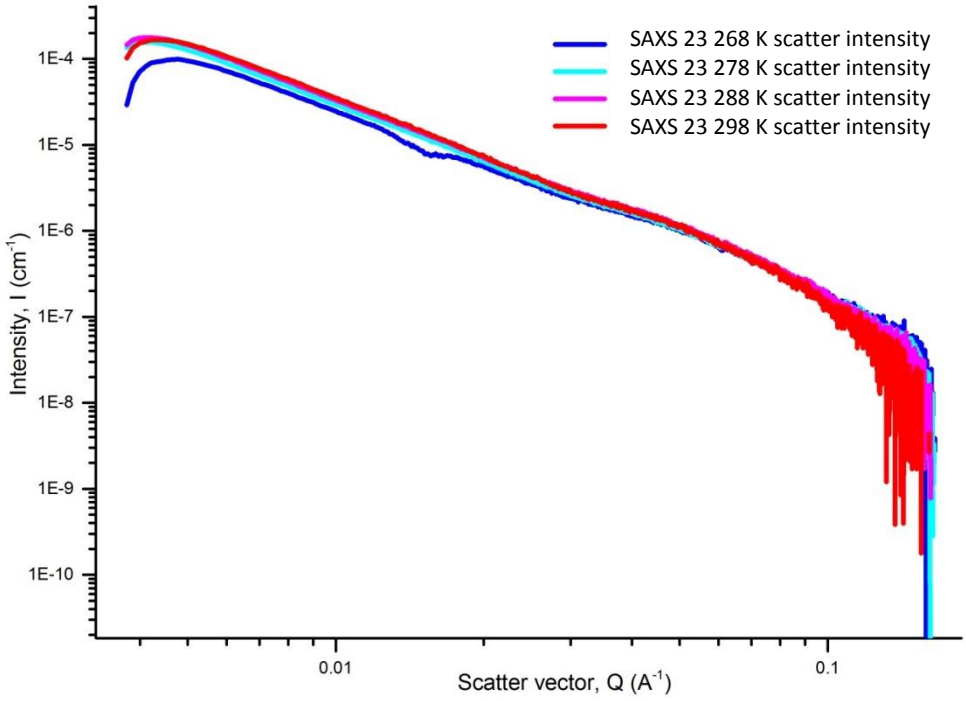

Figure 136: Processed scatter intensity data of SAXS 23 at a range of temperatures; 298 K, 288 K, 278 K, and 268 K.

Data set	Scale	Radius (Å)	Radius PD	Chi^2/Npts
SAXS 23 298 K	6.53e-8	710.9	0.29	9.38e-13
SAXS 23 288 K	6.32e-8	727.2	0.32	6.16e-13
SAXS 23 278 K	5.52e-8	719.8	0.33	3.87e-13
SAXS 23 268 K	4.30e-8	702.4	0.25	9.89e-13

Table 70: Table of parameters and resulting Chi^2/Npts values for the Vesicle model (using constrained background, Q values of 0.0039 $Å^{-1}$ to 0.12 $Å^{-1}$, 1.08e-5 shell SLD and 7.84e-6 solvent SLD, and a 10 Å bilayer thickness) LS fitted to SAXS 23 samples at various temperatures.

7.4.2 Cyclohexane 3.5 Ro system

Due to fluctuations at the extreme scatter vector regions the analyses were limited between 0.005 $Å^{-1}$ and 0.12 $Å^{-1}$ for the repeat SAXS 25 and SAXS 26 samples. At 258 K, there was no distinct scatter data which is likely to signify the solvent solidifying. There was a Q^{-2} gradient for this data across the temperature range 298 K to 268 K indicating a lamellar system; see Table 71.

Data set	Background	Scale	Slope gradient $I(Q)^{-m}$	Chi^2/Npts
SAXS 25 298 K	0	7.73e-10	2.25	1.1e-13
SAXS 26 298 K	0	2.11e-10	2.43	1.02e-13
SAXS 25 288 K	0	5.45e-10	2.33	3.1e-13
SAXS 25 278 K	0	1.36e-9	2.17	9.7e-13
SAXS 25 268 K	0	2.79e-9	1.86	6.9e-13
SAXS 26 268 K	0	3.50e-9	1.90	2.50e-13

Table 71: Table of parameters and resulting Chi^2/Npts values for the Absolute Power Law model (using constrained background and Q values of 0.005 $Å^{-1}$ to 0.12 $Å^{-1}$) LS fitted to SAXS 25 and SAXS 26 samples at various temperatures.

The scatter vector range was not high enough to indicate the bilayer thickness and SAXS 25 298 K was only data swath containing a peak related to the size of these particles at low scatter vectors. The SAXS 25 298 K data was fit to a Vesicle model with a diameter of 162 nm and an estimated thickness of 15 Å; see Table 72 and Figure 137.

The shallow and wide quasi-Bragg peak around 0.05 $Å^{-1}$ is similar to that of the cyclohexane 2.6 Ro Tung *et al.* (2008) data (discussed in the previous section) that corresponds to 94 ±1 Å with 0.22 ±0.002 PD d-spacing for a limited number of multilamellar vesicles. This indicates a system dominated by unilamellar reverse vesicles and a small quantity of multilamellar reverse vesicles.

For temperatures below 298 K, we can say that the particles are over ~170 nms in diameter. The gradient was shown to decrease slightly with temperature reduction which may mean the lamellar curvature was flattening which may have caused the increase in the overall size of particles.

	Value	Origin of value
Radius (Å)	795.18 ±9e+5	LS fitting function in SASView.
Radius PD	0.23 ±935	LS fitting function in SASView.
Thickness (Å)	14.949 ±2.7e+4	LS fitting function in SASView.
Thickness PD	0	Fixed.
Scale	2.99e-8 ±6e-5	LS fitting function in SASView.
Shell SLD (A^{-2})	1.08e-5	Estimated shell SLD; see previous section .
Solvent SLD (A^{-2})	7.84e-6	Calculated.
Chi^2/Npts		Using LS fitting function; with no weighting.

Table 72: Table of parameter values used to fit the Vesicle model illustrated in Figure 137 to the 3.5 Ro cyclohexane SAXS 25 scatter intensity data; with the parameters in grey shading being fixed and the resulting Chi^2/Npts value.

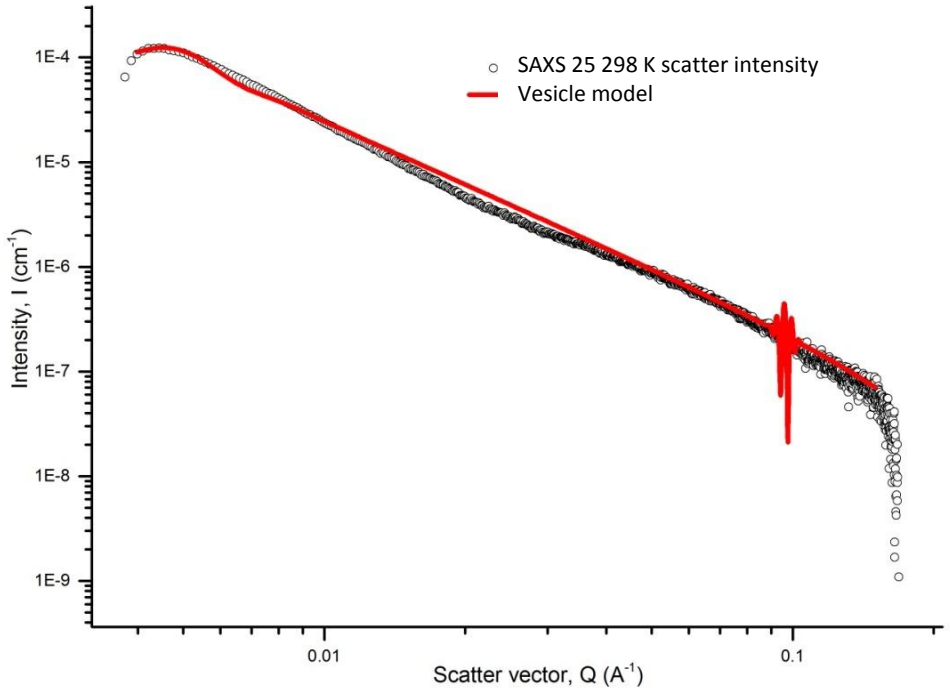

Figure 137: The Vesicle fitted model using the parameters set out in Table 72 to the SAXS 25 data at 298 K.

7.4.3 Cyclohexane 4.5 Ro system

Due to fluctuations at the extreme scatter vector regions the analyses were limited between 0.004 $Å^{-1}$ and 0.1 $Å^{-1}$ for the repeat SAXS 28 and SAXS 29 samples. At 258 K, there was no distinct scatter data which is likely to signify the solvent solidifying.

There was a Q^{-2} gradient for this data across the temperature range 298 K to 268 K indicating a lamellar system; see Table 73. The scatter vector range was not high enough to indicate the bilayer thickness or low enough to find the size of these particles. However, we can say that the particles are over ~170 nm in diameter.

Data set	Background	Scale	Slope gradient $I(Q)^{-m}$	Chi^2/Npts
SAXS 28 298 K	0	5.39e-9	1.61	9.99e-12
SAXS 27 288 K	0	8.43e-11	2.54	3.27e-14
SAXS 28 288 K	0	1.71e-9	1.89	4.38e-12
SAXS 27 278 K	0	2.29e-10	2.40	1.04e-12
SAXS 28 278 K	0	1.11e-8	1.55	4.41e-12
SAXS 27 268 K	0	4.41e-9	1.64	2.42e-12

Table 73: Table of parameters and resulting Chi^2/Npts values for the Absolute Power Law model (using constrained background and Q values of 0.004 $Å^{-1}$ to 0.1 $Å^{-1}$) LS fitted to SAXS 27 and SAXS 28 samples at various temperatures.

7.4.4 Octane 2.5 Ro system

The viable scatter vector range of the scatter intensity curves for the repeat SAXS 41 and SAXS 42 samples was 0.0038 $Å^{-1}$ to 0.1686 $Å^{-1}$. There was a Q^{-2} gradient for this data across the temperature range 298 K to 238 K indicating lamellar systems; see Table 74. The scatter vector range was not high enough to indicate the bilayer thickness or low enough to find the size of most of these particles. However, we can say that the particles are over ~170 nm in diameter. There was very little difference in the curve gradients within the 298 K to 238 K range implying the systems are thermally stable.

Data set	Background	Scale	Slope gradient $I(Q)^{-m}$	Chi^2/Npts
SAXS 41 298 K	0	2.48e-9	2.24	6.43e-12
SAXS 42 298 K	0	3.97e-10	2.59	8.43e-12
SAXS 41 290 K	0	1.56e-9	2.40	2.69e-12
SAXS 41 288 K	0	1.65e-9	2.31	3.77e-12
SAXS 41 278 K	0	1.66e-9	2.31	4.40e-12
SAXS 42 278 K	0	2.56e-9	2.19	7.76e-13
SAXS 41 268 K	0	1.59e-9	2.32	3.55e-12
SAXS 42 268 K	0	4.12e-9	2.23	4.55e-12
SAXS 41 258 K	0	1.22e-9	2.38	2.06e-12
SAXS 41 238 K	0	4.43e-10	2.52	2.60e-13

Table 74: Table of parameters and resulting Chi^2/Npts values for the Absolute Power Law model (using constrained background and Q values of 0.0038 $Å^{-1}$ to 0.1686 $Å^{-1}$) LS fitted to SAXS 41 and SAXS 42 samples at various temperatures.

7.4.5 Octane 4.5 Ro system

Due to fluctuations at high scatter vectors, the analyses were limited to an upper limit of 0.15 $Å^{-1}$ for the repeat SAXS 45 and SAXS 46 samples. Any particles in solution are over ~170 nm in diameter. There was a Q^{-2} gradient for this data across the temperature range 298 K to 238 K indicating a thermally stable lamellar system; see Table 75.

Data set	Background	Scale	Slope gradient $I(Q)^{-m}$	Chi^2/Npts
SAXS 45 298 K	0	3.08e-9	2.15	1.19e-11
SAXS 46 298 K	0	6.79e-10	2.41	1.33e-12
SAXS 45 290 K	0	1.72e-9	2.35	2.78e-12
SAXS 45 288 K	0	2.31e-9	2.19	7.8e-12
SAXS 46 288 K	0	7.78e-10	2.40	2.89e-13
SAXS 45 278 K	0	2.08e-9	2.17	9.61e-12
SAXS 46 278 K	0	8.33e-10	2.41	8.07e-13
SAXS 46 268 K	0	7.60e-10	2.13	3.72e-13
SAXS 45 258 K	0	2.68e-9	2.22	8.44e-12
SAXS 45 238 K	0	1.34e-9	2.34	1.37e-12

Table 75: Table of parameters and resulting Chi^2/Npts values for the Absolute Power Law model (using constrained background and Q values of 0.0038 $Å^{-1}$ to 0.1686 $Å^{-1}$) LS fitted to SAXS 45 and SAXS 46 samples at various temperatures.

7.4.6 Heptane 2.5 Ro system

The viable scatter vector range of the scatter intensity curves for the repeat SAXS 2 and SAXS 3 samples was 0.0038 $Å^{-1}$ to 0.1686 $Å^{-1}$. SAXS 2 measurements were taken from cold to hot temperatures; the low temperatures indicate no particles in solution (in line with freezing of the solvent) and the high temperatures resemble the colder temperature data swaths of SAXS 3. Therefore, SAXS 2 results were ignored in this analysis.

Data swaths for SAXS 3 at temperatures below 258 K showed an exponential increase in gradient at scatter vector values lower than ~0.015 $Å^{-1}$ corresponding to ice crystals forming on the outside of the capillaries; see Figure 138. Therefore, a shorter scatter vector range (0.015 to 0.1686 $Å^{-1}$) was chosen to analyze gradient differences when applying the Absolute Power Law model.

There was a Q^{-2} gradient for this data across the temperature range 298 K to 268 K indicating lamellar systems; see Table 76. The sizes of these lamellar particles were above ~170 nm (outside the detection range of this equipment). There is a gradual decline in gradient at temperatures below 268 K indicating changes in packing parameter and overall shape; by 218 K, the system is likely to be dominated by micellar cylinders.

Data set	Background	Scale	Slope gradient $I(Q)^{-m}$	Chi^2/Npts
SAXS 3 298 K	0	3.29e-9	1.93	4.26e-15
SAXS 3 278 K	0	3.49e-9	1.89	2.64e-15
SAXS 3 268 K	0	2.94e-9	1.87	1.28e-15
SAXS 3 258 K	0	5.50e-9	1.59	1.30e-15
SAXS 3 238 K	0	8.90e-9	1.49	1.63e-15
SAXS 3 218 K	0	1.36e-8	1.37	2.64e-15

Table 76: Table of parameters and resulting Chi^2/Npts values for the Absolute Power Law model (using constrained background and Q values of 0.0015 $Å^{-1}$ to 0.1686 $Å^{-1}$) LS fitted to SAXS 3 at various temperatures.

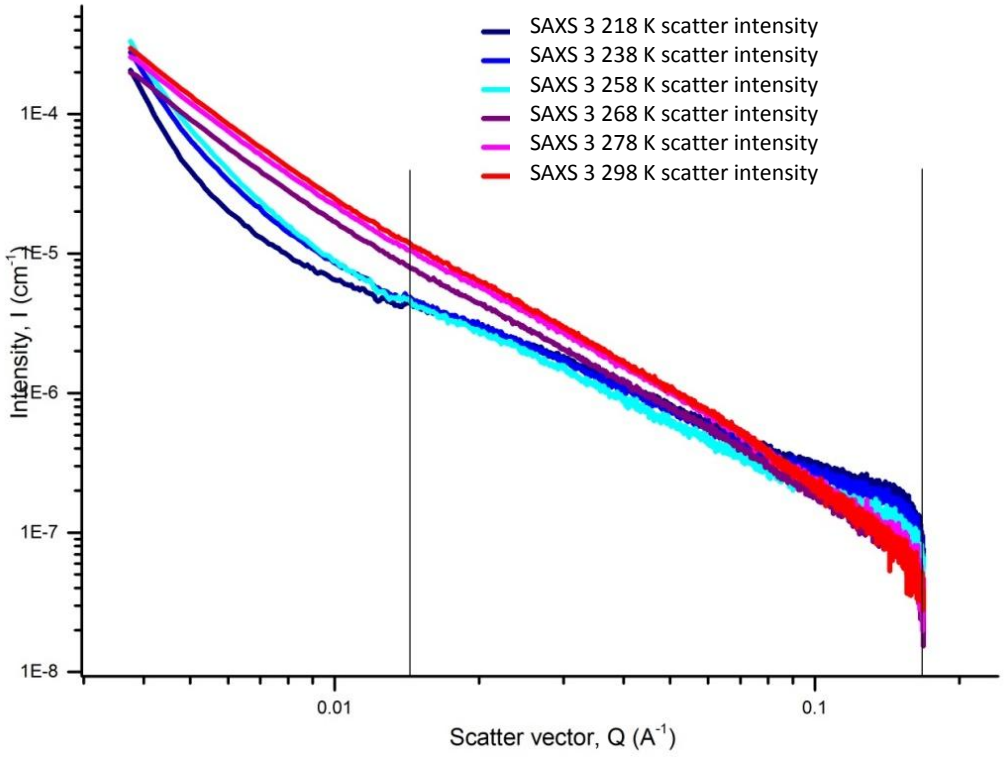

Figure 138: Processed scatter intensity data of SAXS 3 at a range of temperatures (298 K, 278 K, 268 K, 258 K, 238 K and 218 K) with the Q range for fitting the Absolute Power Law models shown between the thin black lines (0.0015 to 0.1686 $Å^{-1}$).

7.4.7 Heptane 3.5 Ro system

7.4.7.1 SAXS results

The viable scatter vector range of the scatter intensity curves for the repeat SAXS 4 and SAXS 5 samples was 0.0038 $Å^{-1}$ to 0.1686 $Å^{-1}$. As can be seen by Figure 139 there is no significant change in morphology with temperature for this data. There was a steady gradient of -2.5 to -2.8 for this data across the temperature range 298 K to 218 K; see Table 77. This implies that this is a lamellar system with some 3D structure; such as would be expected for vesicular forms.

The shallow and wide peak around 0.07 $Å^{-1}$ indicates that there is an average ~90 Å d-spacing which is highly polydisperse. This indicates a system dominated by unilamellar reverse vesicles and a small quantity of multilamellar reverse vesicles which are over ~170 nm in diameter.

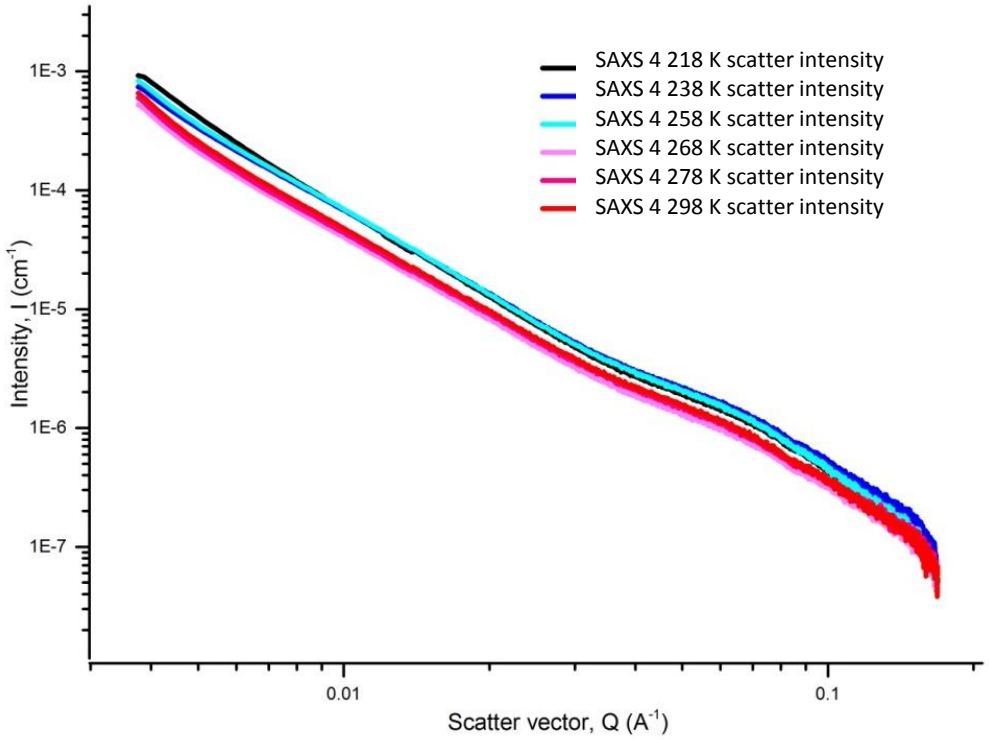

Figure 139: Processed scatter intensity data of SAXS 4 at a range of temperatures (298 K, 278 K, 268 K, 258 K, 238 K and 218 K).

Data set	Background	Scale	Slope gradient $I(Q)^{-m}$	Chi^2/Npts
SAXS 4 298 K	0	1.14e-10	2.78	9.86e-12
SAXS 5 298 K	0	7.26e-11	2.85	7.55e-12
SAXS 4 278 K	0	1.02e-10	2.78	9.39e-12
SAXS 5 278 K	0	9.75e-11	2.77	7.49e-12
SAXS 4 268 K	0	1.31e-10	2.71	6.09e-12
SAXS 5 268 K	0	1.27e-10	2.72	6.85e-12
SAXS 4 258 K	0	4.08e-10	2.59	9.29e-12
SAXS 4 238 K	0	6.99e-10	2.48	5.65e-12
SAXS 4 218 K	0	2.11e-10	2.74	5.24e-12

Table 77: Table of parameters and resulting Chi^2/Npts values for the Absolute Power Law model (using constrained background and Q values of 0.0038 $Å^{-1}$ to 0.15 $Å^{-1}$) LS fitted to SAXS 4 and SAXS 5 samples at various temperatures.

7.4.7.2 SANS room temperature result

The room temperature SANS scatter intensity data from the SANS 2 sample was taken at 290 K (17 °C), at ambient pressure and resulted in a scatter vector range of 0.00132459 $Å^{-1}$ to 0.30273 $Å^{-1}$; see Figure 140.

At high scatter vectors, there is a Q^{-2} gradient which corresponds to bilayer structures; see Figure 141. At low scatter vectors the $Q^{-2.5}$ gradient which implies there are sheet like structures that can expand in three dimensions which corresponds to lamellar vesicular structures.

The closest fit for this data is a LamellarPCrystal model as shown by the Chi^2/Npts values after applying a variety of models with confined SLDs, a 0.2 radius PD, a 0.2 spacing PD, a 0.055 1/cm background value, and using a LS fitting function; as shown in Table 78. Therefore, the majority of the scatter comes from large multilamellar vesicles.

To evaluate the bilayer structure further, the LamellarPCrystal model was fit with variable shell dimensions and polydispersity values; see Figure 142 and Table 79. The mid to high Q regions corresponds well with a 32 Å bilayer thickness, an average of 2.5 lamellar sheets and a 82 Å spacing with a high 0.6 PD. As expected for a multilamellar system the spacing corresponds to the first Bragg peak (Taulier *et al.* 2002) which in this system is a quasi-Bragg peak around 0.06 $Å^{-1}$. The extensive width of this quasi-Bragg peak required a high spacing polydispersity to enable an appropriate fit.

The 32 Å shell thickness falls within the expected range and although this value is 5 Å less than the bilayer thickness of the unilamellar vesicles in cyclohexane reported by Tung *et al.* (2008) it is close to the 33 Å (with 0.28 PD) value obtained with our re-evaluation.

The model diverges from the scatter data at low scatter vector values which implies there is a factor which is not identified by the LamellarPCrystal model. This divergence may indicate that the scatter for the LamellarPCrystal model is dominated by large multilamellar vesicles and low scatter vectors are affected by other nanometre sized particles in solution.

Using the Ellipsoid form factor model (which has the next lowest Chi2/Npts value see Table 78) to fit the low 0.001 $Å^{-1}$ to 0.01 $Å^{-1}$ scatter vector values a radius of (a) 156 Å ±0.3 and (b) 1491 Å ±4.5 is obtained. This low Q data swath was further evaluated with the TriaxialEllipsoid model (using three radius parameters) which fit an ellipsoid with the radii (a) 166 Å ±0.4, (b) 1510 Å ±49.3, and (c) 1449 Å ±46. This correlates with a polydisperse (280.6 nm to 311.8 nm diameter) bicelle that is either vesicular (with some solvent in the core) or an onion with 4-5 lamellar (presuming a thickness between 33 Å and 37 Å and no spacing between bilayers).

Bicelles are known to be precursors for spherical vesicle formation in mixed long-short lipid systems in aqueous systems (Harroun *et al.* 2005). It is likely that these high curvature edges of

these bicelles have a larger proportion of PC4:0 and the low curvature faces have a larger proportion of PC18:2.

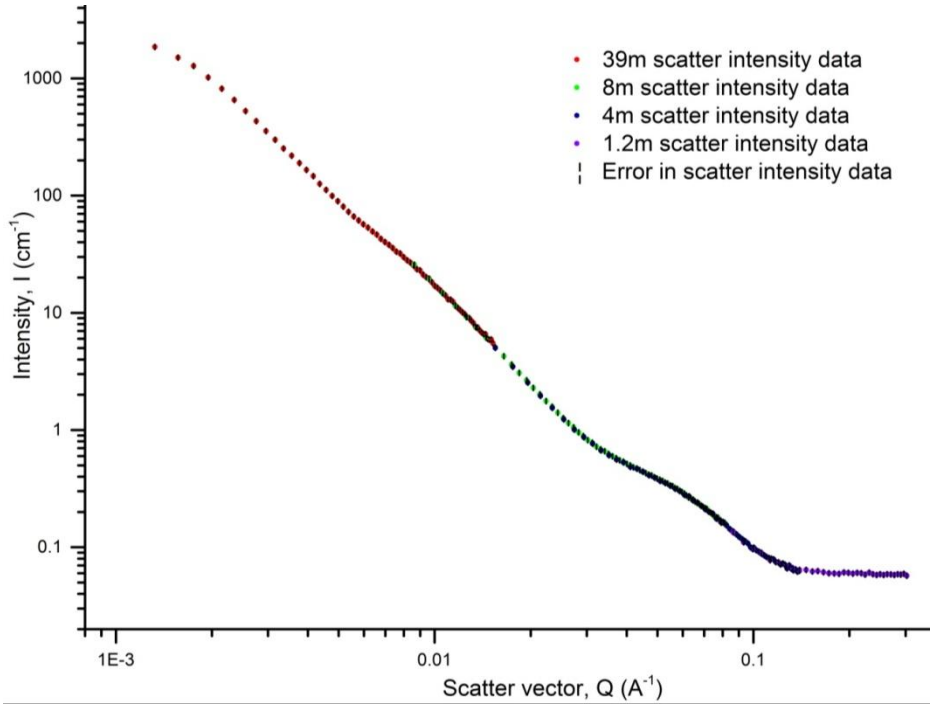

Figure 140: Processed scatter intensity curve for SANS 2 (heptane 3.5 Ro) at 290 K.

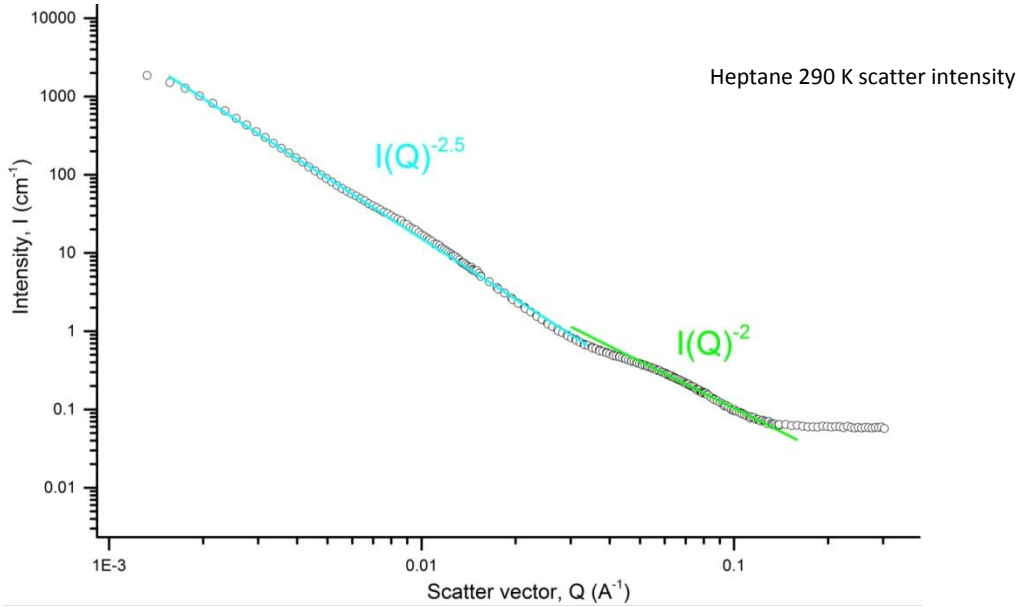

Figure 141: Showing the absolute power law analyses gradients of the d-heptane 3.5 Ro scatter curve; $Q^{-2.5}$ at low scatter vectors and Q^{-2} at high scatter vectors.

Model	Radius (Å)		PD of radius		Shell				Chi^2 /Npts
	a	b	a	b	Thickness (Å)	Number	Spacing (Å)	PD Spacing	
Vesicle	441	-	0.2	-	37	1	-	-	2778
Multishell	736	-	0.2	-	37	3	40	0.2	2446
CoreMultishell	450	-	0.2	-	37	2	-	-	2282
LamellarPCrys	-	-	-	-	37	2	93	0.2	1429
CSBicelle	98	9399	0.2	-	15	-	-	-	5679
Sphere	500	-	0.2	-	-	-	-	-	11897
Ellipsoid	38	1168	0.2	0.2	-	-	-	-	2137
Cylinder	22	9008	0.2	0.2	-	-	-	-	8296
Lamellar	-	-	-	-	37	-	-	-	2648

Table 78: Table of model parameters and resulting Chi^2/Npts values using constrained SLD, background, and polydispersity.

	Value	Origin of value
Background	0.055	LS fitting function in SASView.
Scale	0.062863±4e-5	LS fitting function in SASView.
Layers	2.56±2e-3	LS fitting function in SASView.
Thickness (Å)	31.838±0.06	LS fitting function in SASView.
Spacing (Å)	81.996±0.06	LS fitting function in SASView.
Spacing PD	0.6±8e-4	LS fitting function in SASView.
Shell SLD (A^{-2})	1.01e-6	Estimated shell SLD; see previous section.
Solvent SLD (A^{-2})	6.3e-6	Calculated.
Chi^2/Npts	225.84	Using LS fitting function; with dI weighting.

Table 79: Table of parameter values used to fit the LamellarPCrystal model illustrated in Figure 142 to the 3.5 Ro heptane SANS scatter intensity data; with the parameters in grey shading being fixed and the resulting Chi^2/Npts value.

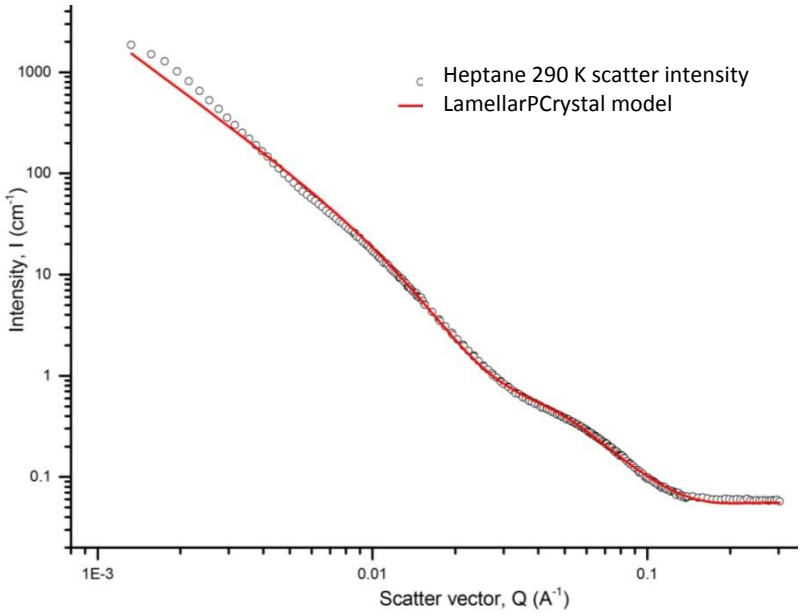

Figure 142: The LamellarPCrystal fitted model using the parameters set out in Table 79 to the SANS 2 data at 290 K.

7.4.7.3 SANS cryogenic results

The raw scatter intensity data from the SANS 2 sample was also obtained at a range of temperatures; 290 K, 270 K, 250 K, 230 K, 210 K and 190 K. Figure 143 illustrates that the overall form of the scatter intensity curves do not change with temperature which supports the conclusions that the forms in the system – large multilamellar vesicles and nanometre sized bicelles – remain the same.

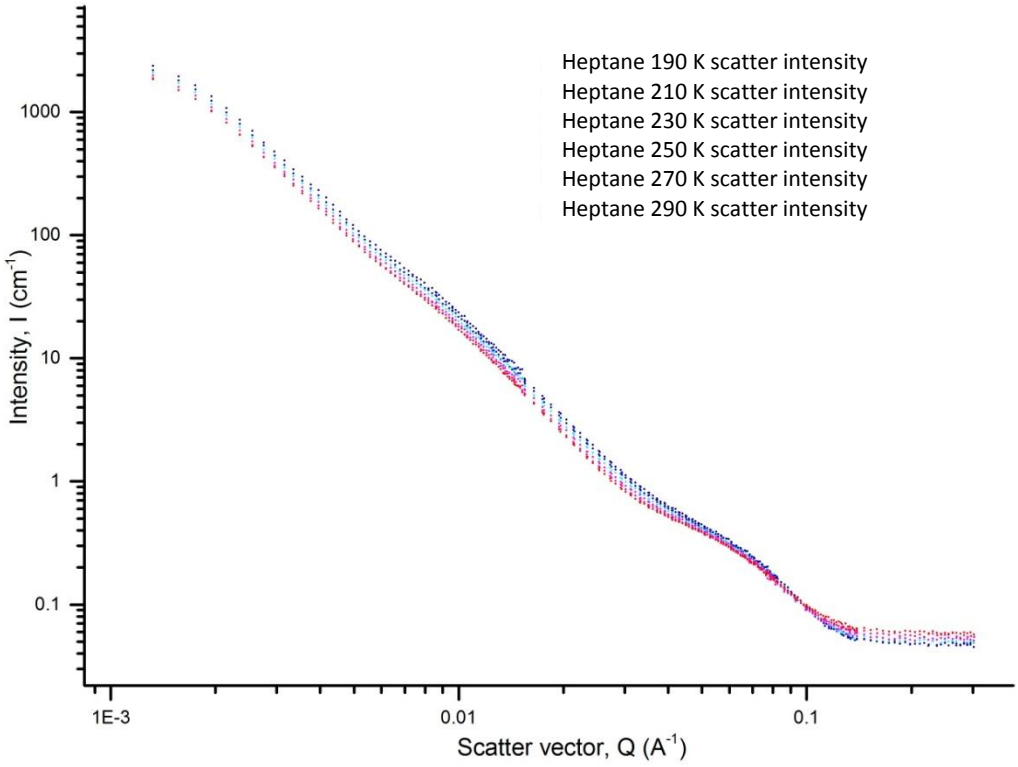

Figure 143: Processed scatter intensity data of SANS 2 at a range of temperatures: 290 K, 270 K, 250 K, 230 K, 210 K and 190 K.

If the lipids of the bilayer had changed their conformity to a gel state at some point in the temperature reduction we would expect distinct Bragg peaks to form; especially in the high scatter vector region (Pabst *et al.* 2010). This evidence supports the bilayer remaining in a bulk liquid crystalline state down to 190 K even if some of the components have transformed into their gel state.

To evaluate the small changes at high scatter vectors and in the quasi-Bragg peak, related to the bilayer thickness and the spacing respectively, the LamellarPCrystal model was fit to the 0.3-0.01 A^{-1} region of these data sets; see Table 80. The scale was allowed to vary to take into consideration small changes in SLD of the materials.

Data set	Background	Scale	Shell				Chi^2 /Npts
			Thickness (Å)	Number	Spacing (Å)	PD Spacing	
290 K	0.0568	0.0579	28.190	2.156	78.765	0.595	12
270 K	0.0536	0.0604	30.261	2.146	79.006	0.607	7
250 K	0.0499	0.0641	30.390	2.138	77.658	0.617	8
230 K	0.0481	0.0672	30.417	2.141	75.119	0.641	9
210 K	0.0458	0.0702	30.746	2.163	72.498	0.672	9
190 K	0.0450	0.0746	30.915	2.160	71.998	0.671	10

Table 80: Table of LamellarPCrystal model parameters and resulting Chi^2/Npts values using constrained SLD (1.01 A^{-2} shell SLD and 6.3 A^{-2} solvent SLD) for fitting to SANS 2 data at various temperatures.

Fitting the LamellarPCrystal model to a limited scatter vector range changed the best fit values. The 290 K data set revealed a 2.15 average lamellar, with 28 Å bilayer thickness and 79 Å spacing with 0.6 PD in comparison to the 2.56 average lamellar, with 32 Å bilayer thickness and 82 Å spacing with 0.6PD resulting from fitting all the data points.

When comparing the bilayer thickness between the highest and lowest temperature swaths there is an increase in bilayer thickness of 3 Å. This could be due to a difference in effective surface areas of the amphiphiles or confirmation changes in the bilayer. The lack of distinct Bragg peaks and the incremental increase of the bilayer thickness with decreasing temperatures support this change being caused by an increase in the effective surface areas of the amphiphiles.

The average number of lamellar remained constant throughout the temperature decrease implying that the overall structure remained constant. The average spacing increases with temperature and the polydispersity decreases. However, as the polydispersity is so high these changes appear insignificant because most of the spacing values overlap; the spacing for 290 K is 23 Å to 134 Å and for 190 K is 15 Å to 128 Å.

7.4.8 Heptane 4.5 Ro system

The viable scatter vector range of the scatter intensity curves for the repeat SAXS 6 and SAXS 7 samples was 0.0038 $Å^{-1}$ to 0.1686 $Å^{-1}$. Many of the data swaths for SAXS 7 seem to be affected by radiation damage, therefore, only SAXS 6 is further analysed. There is little change with temperature for the SAXS 6 data. There was a steady gradient of -2 for this data across the temperature range 298 K to 218 K; see Table 81. This implies that this is a thermally stable lamellar system.

Data set	Background	Scale	Slope gradient $I(Q)^{-m}$	Chi^2/Npts
SAXS 6 298 K	0	1.65e-9	2.13	1.20e-14
SAXS 6 278 K	0	2.01e-9	2.08	1.31e-14
SAXS 6 268 K	0	2.66e-9	1.99	1.26e-14
SAXS 6 258 K	0	1.42e-9	2.21	2.50e-14
SAXS 6 238 K	0	2.41e-9	2.08	2.69e-14
SAXS 6 218 K	0	2.62e-9	2.04	2.28e-14

Table 81: Table of parameters and resulting Chi^2/Npts values for the Absolute Power Law model (using constrained background and Q values of 0.015 $Å^{-1}$ to 0.15 $Å^{-1}$) LS fitted to SAXS 6 at various temperatures.

7.4.9 Hexane 2.5 Ro system

The viable scatter vector range of the scatter intensity curves for the repeat SAXS 16 and SAXS 17 samples was 0.0038 $Å^{-1}$ to 0.1686 $Å^{-1}$. Many of the data swaths for SAXS 17 are anomalous, possibly due to an incorrect set up; therefore, only SAXS 16 is further analysed.

There is little change with temperature for the SAXS 16 data; however, there is a small change that occurs between the 268 K and 258 K measurements. At 258 K and below the intensity is increased and there is no peak at low scatter vectors; see Figure 144. There was a steady gradient of -2 for this data across the temperature range 298 K to 218 K (see Table 82) which implies that this system remains as lamellar with reduction in temperature. However, it is likely that at a temperature between 268 K and 258 K, the size of the reverse vesicles has increased beyond the detection limit of this equipment or bilayers sheets have formed. At these temperatures, the lamellar may be in a gel, or partial gel, state.

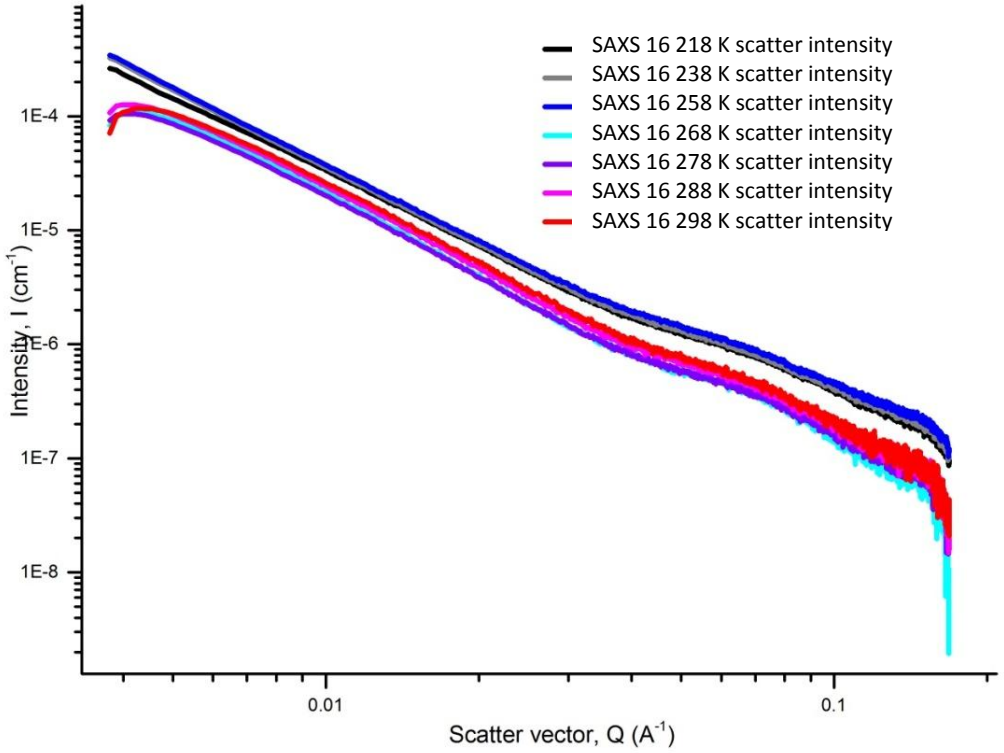

Figure 144: Processed scatter intensity data of SAXS 16 at a range of temperatures; 298 K, 288 K, 278 K, 268 K, 258 K, 238 K and 218 K.

Data set	Background	Scale	Slope gradient $I(Q)^{-m}$	$Chi^2/Npts$
SAXS 16 298 K	0	4.28e-9	1.89	2.51e-12
SAXS 16 288 K	0	2.42e-9	2.00	1.19e-12
SAXS 16 278 K	0	2.02e-9	2.00	8.19e-13
SAXS 16 268 K	0	2.24e-9	1.99	1.29e-12
SAXS 16 258 K	0	1.13e-9	2.26	1.28e-13
SAXS 16 238 K	0	1.12e-9	2.25	6.31e-14
SAXS 16 218 K	0	1.96e-9	2.12	7.76e-14

Table 82: Table of parameters and resulting $Chi^2/Npts$ values for the Absolute Power Law model (using constrained background and Q values of 0.004 $Å^{-1}$ to 0.15 $Å^{-1}$) LS fitted to SAXS 16 at various temperatures.

The low scatter vector peak in the 298 K to 268 K measurements corresponds to an estimated particle diameter of ~146 nms. Using the Vesicle model to fit to the data, we obtain a reverse vesicle diameter and bilayer thickness of 152 nm and 10 Å respectively; see Table 83 and Figure 145. Using the estimated 10 Å bilayer thickness and spacing polydispersity of 0 the LamellarPCrystal model was fit to obtain an 80 Å d-spacing and 1.19 average lamellar; see Table 84 and Figure 145. Together these models indicate that this is a reverse vesicular system with a 152 nm average diameter and 0.24 PD; dominated by unilamellar reverse vesicle with a smaller quantity of multilamellar reverse vesicles with a 80 Å d-spacing.

	Value	Origin of value
Scale	2.4358e-8 ±5e-5	LS fitting function in SASView.
Radius (Å)	763.51 ±1e+6	LS fitting function in SASView.
Radius PD	0.24 ±8805	LS fitting function in SASView.
Thickness (Å)	10.018 ±21853	LS fitting function in SASView.
Thickness PD	0	Fixed
Shell SLD (A^{-2})	1.08e-5	Estimated shell SLD; see previous section .
Solvent SLD (A^{-2})	6.75e-6	Calculated.
Chi^2/Npts	1.16e-12	Using LS fitting function; with no weighting.

Table 83: Table of parameter values used to fit the Vesicle model illustrated in Figure 145 to the SAXS 16 298 K scatter intensity data; with the parameters in grey shading being fixed and the resulting Chi^2/Npts value.

	Value	Origin of value
Scale	2.283e-7 ±7e-4	LS fitting function in SASView.
Layers	1.1892 ±4641	LS fitting function in SASView.
Spacing (Å)	80 ±3488	LS fitting function in SASView.
Spacing PD	0	Fixed
Thickness (Å)	10 ±4e+6	LS fitting function in SASView.
Thickness PD	0	Fixed
Shell SLD (A^{-2})	1.08e-5	Estimated shell SLD; see previous section.
Solvent SLD (A^{-2})	6.75e-6	Calculated.
Chi^2/Npts	7.13e-14	Using LS fitting function; with no weighting.

Table 84: Table of parameter values used to fit the LamellarPCrystal model illustrated in Figure 145 to the SAXS 16 298 K scatter intensity data; with the parameters in grey shading being fixed and the resulting Chi^2/Npts value.

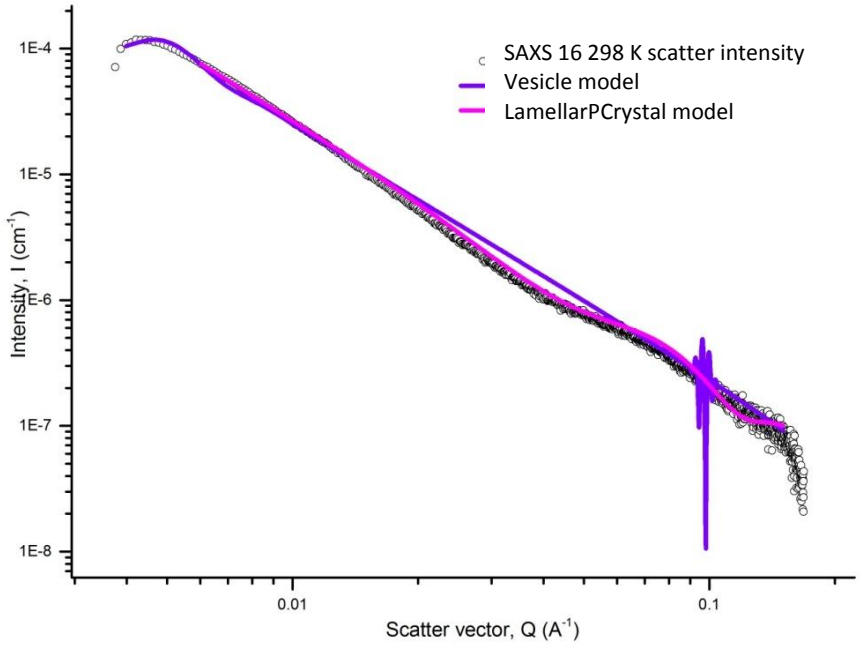

Figure 145: Showing the SAXS 16 scatter curve at 298 K with a fitted Vesicle model with parameters as detailed in Table 83 and a fitted LamellarPCrystal model with parameters as detailed in Table 84.

7.4.10 Hexane 3.5 Ro system

7.4.10.1 SANS result

The SANS scatter intensity data from the SANS 6 sample was taken at 270 K, at ambient pressure and resulted in a scatter vector range of 0.0094007 $Å^{-1}$ to 0.3027440 $Å^{-1}$; see Figure 146.

At low scatter vectors the Q^{-4} (Porod law) gradient indicates interface scattering and in our samples is likely to be from clustering on length scales beyond the detection limits of this equipment (Q_{min} cannot be obtained from this data).

There is a Q^{-1} slope at high scatter vectors, indicative of cylinders. To remove the Porod scattering from the form factor fitting a Cylinder model was fit to a limited, 0.015 $Å^{-1}$ to 0.3 $Å^{-1}$, scatter vector range. The background was taken to start where there was a slight rise in intensity at the 0.15 $Å^{-1}$. This produced a fit for a cylinder with a 77 Å length and an 11 Å radius; see Table 85 and Figure 147. However, the point at which the curve changes to Porod, around 0.01 $Å^{-1}$, indicates a particle with an estimated length of ~630 $Å^{-1}$.

The lack of any Q^{-2} gradients at high scatter vectors signifies there are no lamellar forms in this system. Therefore, this system is likely to be a system of rod like micelles.

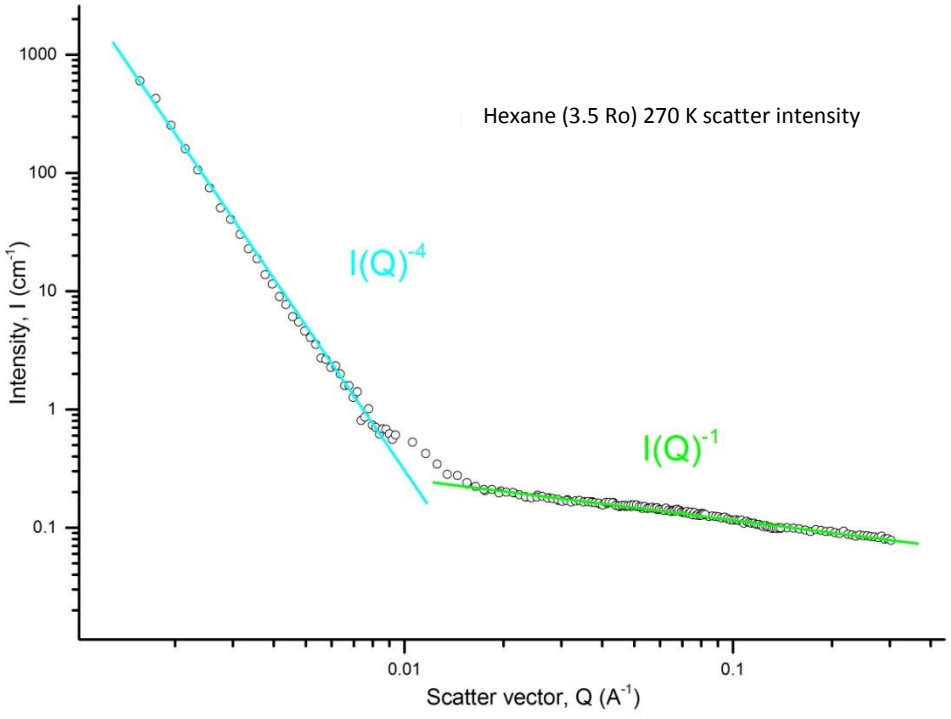

Figure 146: Showing the SANS 6 scatter curve at 270 K and the slope gradients at low and high scatter vectors; Q^{-4} and Q^{-1} respectively.

	Value	Origin of value
Background	0.085	Using slight rise at Q of 0.15 A^{-1} as the start of particle scatter.
Scale	9.298e-8 ±3e-9	LS fitting function in SASView.
Length (Å)	76.961 ±1.429	LS fitting function in SASView.
Radius (Å)	11.237 ±0.252	LS fitting function in SASView.
Shell SLD (A^{-2})	1.01e-6	Estimated shell SLD; see previous section .
Solvent SLD (A^{-2})	6.3e-6	Calculated.
Chi^2/Npts	2.98	Using LS fitting function; with dI weighting.

Table 85: Table of parameter values used to fit the Cylinder model illustrated in Figure 147 to the Q = 0.015 to 0.3 A^{-1} region of the SANS 6 scatter intensity data; with the parameters in grey shading being fixed and the resulting Chi^2/Npts value.

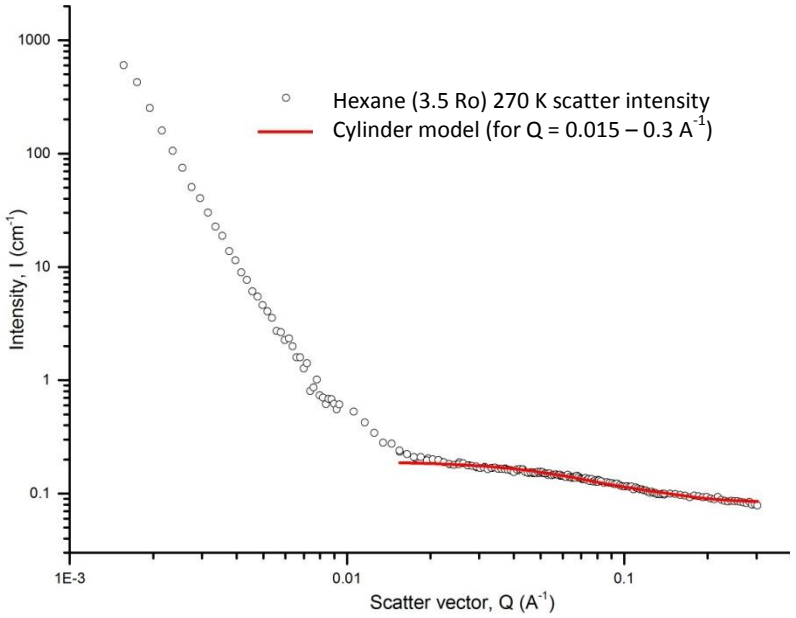

Figure 147: Showing the SANS 6 scatter curve at 270 K with a fitted Cylinder model with parameters as detailed in Table 85.

7.4.11 Pentane 3.5 Ro system

7.4.11.1 SAXS results

The viable scatter vector range of the scatter intensity curves for the repeat SAXS 11 and SAXS 12 samples was 0.0038 $Å^{-1}$ to 0.1686 $Å^{-1}$. Many of the data swaths for SAXS 12 are anomalous, maybe due to an incorrect set up or reverse temperature measurements; therefore only SAXS 11 is further analysed.

The Absolute Power Law model fit was limited to the 0.02 $Å^{-1}$ to 0.15 $Å^{-1}$ scatter vector range as the influence of ice crystal growth on the outside of the capillary was evident in the increase of intensities at low scatter vectors. The low gradient across these data swaths, as shown in Table 86, indicate a system of cylindrical micelles.

Data set	Background	Scale	Slope gradient $I(Q)^{-m}$	Chi^2/Npts
SAXS 11 298 K	0	4.66e-9	1.43	8.49e-16
SAXS 11 288 K	0	3.86e-9	1.35	4.16e-16
SAXS 11 278 K	0	3.86e-9	1.24	3.52e-16
SAXS 11 268 K	0	5.74e-9	1.36	4.77e-16
SAXS 11 218 K	0	3.70e-9	1.47	1.17e-15

Table 86: Table of parameters and resulting Chi^2/Npts values for the Absolute Power Law model (using constrained background and Q values of 0.02 $Å^{-1}$ to 0.15 $Å^{-1}$) LS fitted to SAXS 11 at various temperatures.

7.4.11.2 SANS result

The SANS scatter intensity data from the SANS 4 sample was taken at 280 K, at ambient pressure and resulted in a scatter vector range of 0.00156613 $Å^{-1}$ to 0.302674 $Å^{-1}$; see Figure 148.

There is a lack of any scatter at high scatter vectors indicating any particles in solution are larger than the length scales probed by SANS and those particles do not have any discernible internal structures e.g. lamellar. At low scatter vectors the $I(Q)^{-4}$ (Porod law) gradient indicates interface scattering and in this sample is likely to be from the large particles that are out of the detection length scales of this equipment.

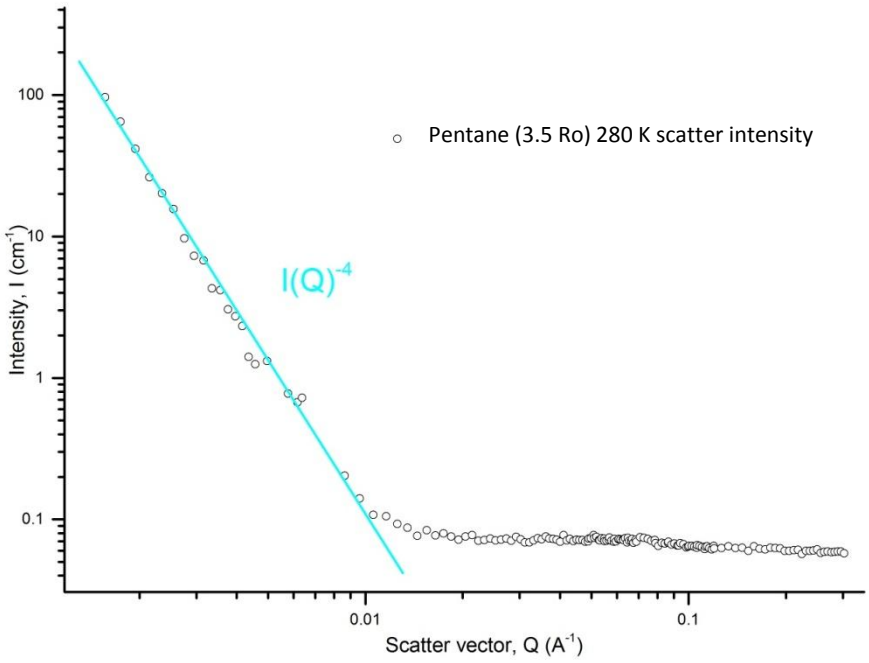

Figure 148: Showing the SANS 4 scatter curve at 280 K and the $I(Q)^{-4}$ slope gradients at low Q.

7.4.12 Butane 3.5 Ro system

The viable scatter vector range of the scatter intensity curves for the SAXS 31 sample was 0.0038 $Å^{-1}$ to 0.1686 $Å^{-1}$. The Absolute Power Law model fit was limited to the 0.02 $Å^{-1}$ to 0.15

$Å^{-1}$ scatter vector range as the influence of ice crystal growth on the outside of the capillary was evident in the increase of intensities at low scatter vectors. The low gradient across these data swaths, as shown in Table 87, indicate a system of cylindrical micelles.

Data set	Background	Scale	Slope gradient $I(Q)^{-m}$	Chi^2/Npts
SAXS 31 260 K	0	5.35e-8	1.08	3.44e-15
SAXS 31 240 K	0	8.36e-8	1.04	8.86e-15
SAXS 31 230 K	0	5.67e-8	1.07	2.34e-15
SAXS 31 220 K	0	6.11e-8	1.03	2.84e-15
SAXS 31 130 K	0	5.12e-8	1.13	5.54e-15

Table 87: Table of parameters and resulting Chi^2/Npts values for the Absolute Power Law model (using constrained background and scatter vector values of 0.02 $Å^{-1}$ to 0.15 $Å^{-1}$) LS fitted to SAXS 31 at various temperatures.

7.4.13 Anomalous SAXS results

Almost all of the SAXS data swaths for the; hexane 3.5 Ro and 4.5 Ro, pentane 2.5 Ro and 4.5 Ro, systems are anomalous; with ice crystals causing exponential scattering at low scatter vectors, occasional lack of any scatter in some data swaths and anomalous fluctuations in the high scatter vector region. Therefore, this data was also deemed unsuitable for model fitting analyses.

These anomalous measurements may have been caused by incorrectly setting up the sample within the beamline or the system has a mixture of coexisting structures that the scatter fluctuates beyond the point to which it can be useful for SAXS analyses. The lack of any clear $I(Q)^{-2}$ gradient at high scatter vectors indicate that if there are any bilayered structures in solution they are coexisting with micellar structures.

7.5 Summary

The evaluation of the SANS cyclohexane 2.6 Ro data from Tung *et al.* (2008) coincides with the published results that this system is dominated by unilamellar vesicles. However, our results imply that their average diameter is 4-5 nm larger than published values, and the bilayer thickness is 4 Å thinner when including a 0.28 bilayer polydispersity parameter; see Tables 66-68. When taking into consideration the 0.2 polydispersity of the core radius this 4 nm difference in the average diameter is not highly significant. Also, in evaluating the quasi-Bragg peak that had been ignored in the published data the system was shown to include some multilamellar vesicles with 94 Å (0.22 PD) d-spacing.

The SAXS results of our cyclohexane 2.5 Ro system indicated smaller, 144 nm (0.29 PD), unilamellar reverse vesicles compared to the 234 nm (0.22 PD) reverse vesicles described in the comparable system by Tung *et al.* (2008); see Figure 136 and Table 70. This could be attributed to the comparatively higher intensity of our sonication process; our samples were probe

sonicated for 3 minutes (using 8 amps) and Tung *et al.* (2008) used an industrial ultrasonic bath for 30 minutes.

Increasing the amphiphilic ratio of the cyclohexane systems created larger unilamellar reverse vesicles; average diameters of 162 nm (0.23 PD) and over ~170 nm, for the 3.5 Ro and 4.5 Ro systems, respectively. These cyclohexane results indicate that the increase in amphiphilic ratio decreases the curvature of the bilayers causing an increase in the average diameter.

In the cyclohexane systems, the d-spacing quasi-Bragg peak corresponds to 94 ±1 Å with 0.22 ±0.002 PD d-spacing for Tung's *et al.* (2008) 2.6 Ro SANS data and our 3.5 Ro SAXS data. However, this quasi-Bragg peak is absent in our 2.5 Ro and 4.5 Ro SAXS data. This implies there are a limited number of multilamellar vesicles in Tung's *et al.* (2008) 2.6 Ro system and our 3.5 Ro system. This is likely due the comparatively lower sonication intensity used by Tung's *et al.* (2008) ultrasonic bath preparation and our 3.5 Ro system receiving, 2 min 30 sec at 8 amps and 30 sec at 6 amps probe sonication, compared to the 3 min at 8 amp probe sonication for the 2.5 Ro and 4.5 Ro systems. Therefore, higher sonication intensities remove any residual multilamellar vesicles in reverse vesicular systems and reduce the average diameter of reverse vesicles.

The octane systems show lamellar systems are prevalent across all the amphiphilic ratios studied; see Tables 74 and 75. These lamellar systems are likely to be unilamellar reverse vesicles over ~170 nm in diameter.

The heptane systems show lamellar systems are prevalent across all the amphiphilic ratios studied; see Table 76-81. The SANS results for the 3.5 Ro system indicate that the lamellar system is a mixture of bicelles (280.6 nm to 311.8 nm in diameter) and large unilamellar and multilamellar reverse vesicles (82 Å with 0.6 PD d-spacing).

The hexane systems show differences in the structural phase between amphiphilic ratios; see Figure 13. The 2.5 Ro system presented reverse vesicles with a 152 nm average diameter and 0.24 PD; dominated by unilamellar reverse vesicle with a smaller quantity of multilamellar reverse vesicles with a 80 Å d-spacing (see Table 82 and Figure 144). However, the 3.5 Ro was a system of rod like micelles (see Figures 146 and 147 and Table 85) and 4.5 Ro was too polydisperse to enable a valid analysis. This indicates that with decreasing molecular weight of alkane solvents reverse vesicular systems are found in mixtures with a lower amphiphilic ratio.

The pentane systems showed very polydisperse, possibly mixed coexisting phase, systems for 2.5 Ro and 4.5 Ro systems. The SANS data for the 3.5 Ro system indicated that the system was likely to consist of rod like micelles (Figure 148), however, this may also coexist with other structures. The single butane 3.5 Ro system also indicated the presence of cylindrical micelles;

see Table 87. Therefore, for these amphiphilic ratios there were no lamellar or reverse vesicular phases.

7.5.1 Summary of temperature depression

Some of the temperature depression results showed sudden drops in scatter intensity data related to the freezing of the solvent, for example, the 258 K cyclohexane SAXS scatter data; see Table 69. It is also difficult to determine whether some of the samples phase separate at very low temperatures or whether the radiation damage from repeat exposure to the beamline destroys the particles.

These results show that temperature reduction did not change the structural phase behaviour of the system. However, in certain lamellar systems there seemed to be a small decrease in diameter with reduction in temperature. This is related to the decrease in curvature of the bilayer. Either the decrease in curvature can be caused by a change of the solvents ability to penetrate the bilayer or there is a change in the geometric packing parameter of the amphiphiles. For a decrease in curvature, the geometric packing parameter would need to increase closer to the 1 value. This can occur from an increase in effective surface area of the polar head groups in respect to the lipid tails or a decrease in the effective surface area lipid tail in respect to the polar head group. A decrease in the effective surface area of the lipid tail often occurs with the sol-gel transition which implies that at least some of the amphiphiles in the bilayer change to a gel configuration at low temperatures. The first to change to a gel configuration are likely to be the small number of long saturated amphiphiles in the C18 95% product.

The cyclohexane mixtures presented a thermally stable system of unilamellar vesicles at 2.5 Ro; 144 nm and 147 nm with a polydispersity of 0.29 to 0.33. However, the equivalent 3.5 Ro system indicated an increase in size of reverse vesicles with temperature; compare Tables 70 and 72. This indicates that the ordering of the amphiphiles in the 2.5 Ro bilayers allow for less solvent penetration than those in the 3.5 Ro bilayers; related to the expected increase in bilayer fluidity for mixture with a greater percentage of PC4:0.

There is no apparent change in the lamellar systems of the octane mixtures across all amphiphilic ratios with decreasing temperature; see Tables 74 and 75. Therefore, any reverse vesicles will be thermally stabile. This could indicate octane is not as efficient as cyclohexane in penetrating bilayers which supports a thermally stable system across all the amphiphilic ratios that form reverse vesicles.

In the heptane 2.5 Ro systems, there was a gradual decline in gradient at temperatures below 268 K indicating changes in packing parameter and overall shape from some amphiphilic sol to gel transitions; see Table 76 and Figure 138. This is the only example where a structural phase transition is observed with temperature reduction where the lamellar system at high

temperatures transform into a system dominated by rod like micelles at low temperatures (by 218 K). This temperature induced phase transition is not observed in the 3.5 Ro and 4.5 Ro systems demonstrating that an increase in PC4:0 form a bilayer with higher overall fluidity and therefore greater thermal stability at very low temperatures.

Therefore, phase changes found with temperature reduction in heptane 3.5 Ro are due to changes in the effective surface area or conformation of the lipid tails of the phosphatidylcholines in the 95% PC18 product. As shown in Table 4 (Chapter 3) the number of unsaturation points of PC18 alters the transition temperature. The transition temperature for a mixed 18:0 and 18:2 phosphatidylcholine bilayer is approximately 257 K but it is known that salts can reduce the transition temperature of reversed bilayers (Lee *et al.* 2013). Therefore, the molecules in the 95% PC18 product may begin to transform to their gel state at temperatures below 258 K. This gel state changes the conformation of the lipid tails and therefore the packing parameters of bilayers are increasingly affected in relation to the quantity of the 95% PC18 product. It is therefore probable that the 2.5 Ro heptane systems underwent a spontaneous phase change when the 18:0 and 18:2 phosphatidylcholines changed to their gel state between 258 K and 218 K.

The hexane 2.5 Ro indicate reverse vesicles (~152 nm diameter) in a sol state at high temperatures, however, at 258 K there is sharp change where the curvature of the bilayers suddenly decrease causing the size of the reverse vesicles to grow beyond the detection range of the equipment; see Figure 144. This sudden change implies that some of the phosphatidylcholines in the 95% PC18 product spontaneously transformed into their gel state between 268 K and 258 K. However, in contrast to the 3.5 Ro heptane system there was no phase change. This may be due to the increased ability for hexane to penetrate the bilayer and therefore keep the overall fluidity of the bilayer higher.

The hexane 3.5 Ro, pentane 3.5 Ro and butane 3.5 Ro systems presented no obvious changes with temperature depression for their systems dominated by cylindrical micelles.

Chapter 8: Discussion

8.1 Introduction

The following sections are organised into two main sections; summaries of the information contained in Chapters 4 to 7 and discussions on the relevance of the conclusions from this research to soft condensed matter topics. The next, and final, chapter contains the discussion of this research in the context of astrobiological research and suggested avenues for further research.

8.2 Summaries for main systems studied

8.2.1 Binary systems

Table 88 below shows which binary systems contained self assembled particles and whether that self assembly produced reverse vesicles (uni- or multi- lamellar and any size).

In the binary systems the only solvent to produce prevalent reverse vesicles, as either colloidal dispersions of nanometre sized unilamellar reverse vesicles or suspensions of micrometer sized uni- or multi- lamellar reverse vesicles, was cyclohexane. The binary cyclohexane systems presenting unilamellar reverse vesicular colloidal dispersions, with prominent Tyndall scattering, were limited to methanol prepared samples with amphiphilic ratios higher than 6 Ro. Without methanol preparation the >7 Ro cyclohexane systems would present a suspension dominated by micrometre sized reverse vesicles (see Figure 149) which included unilamellar, multilamellar and onion formations. This indicates that the methanol preparation facilitated the attachment of Na+ and Cl- ions to the polar moieties of the amphiphiles, allowing a denser polar interior of the reverse bilayers by negating the electrostatic repulsive forces. This methanol facilitated dense polar interior of the reverse bilayers would consequently allow a greater curvature for the reverse vesicles and promote smaller, nanometre sized, reverse vesicles.

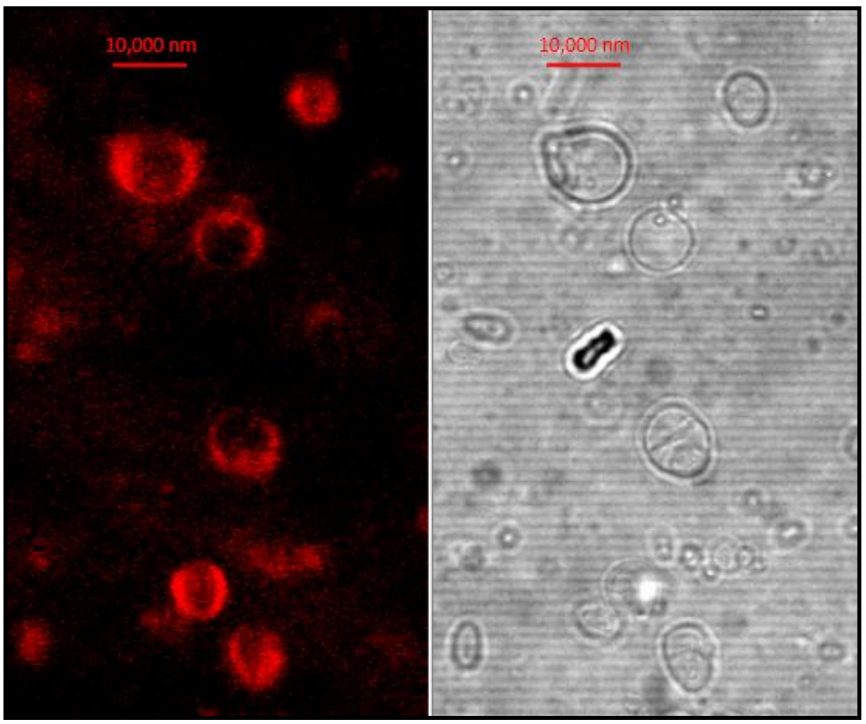

Figure 149: Fluorescence micrograph of binary 7 Ro cyclohexane sample (without methanol preparation), showing giant unilamellar reverse vesicles.

In contrast to the cyclohexane high amphiphilic ratio studies, the 7 Ro alkane systems in presented completely phase separated systems containing liquid crystal precipitants. The heptane and hexane binary systems were dominated by micellar, bicontinuous or phase separated liquid crystal phases. The lowest, 2.5, Ro in the heptane and hexane systems promoted self assembly, however, in pentane systems the higher amphiphilic ratios (> 3.5 Ro) promoted self assembly. This coincides with the theory that the smaller pentane molecules have penetrated between the lipid tails of the amphiphiles, thereby, increasing the effective nonpolar surface area, and increasing the packing parameter.

Although there were no reverse vesicles in the binary alkane systems, a lamellar phase of stacked reverse bilayers was revealed in the 3.5 Ro pentane systems. Temperature reduction did not alter the structure of most of the binary systems, however, the pentane 3.5 Ro system changed from reverse bilayer sheets to a reverse micellar system when -95 °C was reached.

Amphiphilic ratio (Ro)	Methanol preparation	Solvent	Resulting system	Self assembled particles?	Reverse vesicles?
Pure C18 99%	☒	Cyclohexane	PS:LC	☒	☒
Pure C18 99%	☒	Heptane	PS:LC	☒	☒
Pure C18 99%	☒	Pentane	PS:LC	☒	☒
Pure C4	☒	Cyclohexane	MS	☒	☒
Pure C4	☒	Heptane	RM	☑	☒
Pure C4	☒	Pentane	RM	☑	☒
2.5	☒	Cyclohexane	PS:LC+GMRV(some)	Mixed	Mixed
3.5	☒	Cyclohexane	PS:LC+GURV(some)	Mixed	Mixed
5	☒	Cyclohexane	PS:LC+CRM	Mixed	☒
6.5	☒	Cyclohexane	PS:GCRM+GRCM	☑	☒
7	☒	Cyclohexane	PS:GURV	☑	☑
8	☒	Cyclohexane	PS:GURV+MURV+GRVO	☑	☑
2.5	☒	Hexane	PS:Bc	☑	☒
3.5	☒	Hexane	PS:LC	☒	☒
4.5	☒	Hexane	PS:LC	☒	☒
2.5	☒	Pentane	PS:LC	☒	☒
3.5	☒	Pentane	PS:RBi	☑	☒
4.5	☒	Pentane	PS:Bc	☑	☒
2.5	☑	Cyclohexane	GURV	☑	☑
6	☑	Cyclohexane	SURV	☑	☑
7	☑	Cyclohexane	SURV	☑	☑
2.5	☑	Heptane	CRM	☑	☒
2.5	☑	Hexane	PS:Bc	☑	☒

Table 88: This table presents the initial confirmed phase behaviour of the binary systems between 20 mM to 30 mM total amphiphilic concentration, at room temperature, with the mixed systems containing over 3 mM of NaCl. Table key: PS, Phase separated; LC, Liquid crystal precipitant; GMRV, Giant (over micrometre sized) multilamellar reverse vesicle; SMRV, Small (under micrometre sized) multilamellar reverse vesicles; GURV, Giant (over micrometre sized) unilamellar reverse vesicle; SURV, Small (under micrometre sized) unilamellar reverse vesicles; Bc, Bicontinuous; RM, reverse micelles; RBi, Reverse bilayer sheets; CRM, Compound reverse micelles; GCRM, Giant (over micrometre sized) compound reverse micelles; RCM, Reverse cylindrical micelles; GRCM, Giant (over micrometre length) reverse cylindrical micelles; GRVO, Giant (over micrometre diameter) reverse vesicle onions (without a visible internal compartment); MS, Molecular solution.

8.2.2 Multi-component systems

Unlike the binary systems, colloidal dispersions of unilamellar reverse vesicles were prevalent across numerous multi-component systems that had been strongly sonicated; see Figure 150. Table 90 shows which of the probe sonicated multi-component systems contained self assembled particles and whether any reverse vesicles were present (either uni- or multi- lamellar and any size).

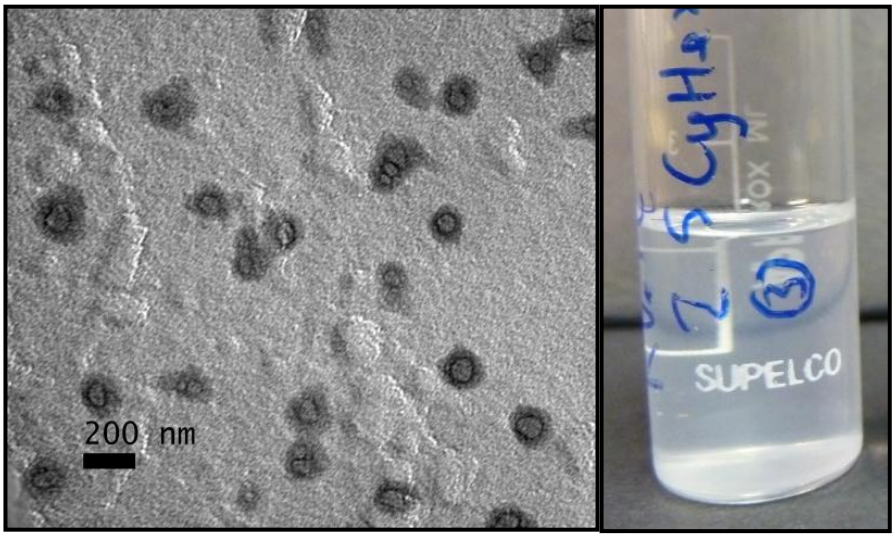

Figure 150: Left image; TEM of unilamellar reverse vesicles found in multi-component cyclohexane 2.5 Ro. Right image; Picture of the blue hue from the Tyndall scattering effect of the unilamellar reverse vesicles in multi-component cyclohexane 2.5 Ro.

Tung's (2008) SANS analysis of the 2.6 Ro d-cyclohexane system reported a fit to a unilamellar vesicle form factor model with the parameters; 234 nm diameter, 3.7 nm bilayer thickness and a size polydispersity of 0.22. There is only a slight decrease (~5 nm) in reverse vesicle diameter and 0.4 nm decrease in bilayer thickness between Tung's published values and my own models; this is an insignificant difference considering the polydispersity of 0.22 and 0.28 for diameter and bilayer thickness respectively. In comparison, my 2.5 Ro results show 178 nm diameter with 0.29 PD from DLS and 144 nm diameter with 0.29 PD from SAXS (see Table 91). This reduction in average vesicle size may have been due to three factors: the 0.1 difference in the amphiphilic ratios between samples, the 5 mM lower total concentration of amphiphiles in the SAXS sample of this study and the difference in the contrast variation method between neutron and X-ray scattering techniques.

Changes in the preparation method have sometimes shown to alter the structures produced. Examples of the cyclohexane results are shown in Table 89 and show that weak sonication of lamellar systems produce large (multi-micrometre), uni- and multi- lamellar reverse vesicles that quickly settle out of solution; stronger sonication methods produce a stable colloidal dispersion of reverse vesicles. Also, as Table 89 indicates, methanol preparation is required in

the multi-component cyclohexane 2.5 Ro systems in order to change from a micellar to a vesicular system.

Amphiphilic ratio (Ro)	Methanol preparation	Sonication	Resulting system	Self assembled particles?	Reverse vesicles?
2.5	☑	Weak water-bath	PS:GMRV+GURV	☑	☑
2.5	☑	Strong water-bath	SURV	☑	☑
2.5	☒	Probe sonication	RCM	☑	☒
2.5	☑	Probe sonication	SURV	☑	☑

Table 89: This table presents the initial confirmed phase behaviour of the multi-component systems with a total amphiphilic concentration of 20 mM, at room temperature, and containing over 3 mM of NaCl. Table key: PS, Phase separated; GMRV, Giant (over micrometre sized) multilamellar reverse vesicle; GURV, Giant (over micrometre sized) unilamellar reverse vesicle; SURV, Small (under micrometre sized) unilamellar reverse vesicles; RCM, Reverse cylindrical micelles.

Due to the large number of colloidal dispersions in the multi-component systems that were probe sonicated various *in situ* scatter techniques were employed to study these systems in further detail. The results of these scattering techniques were presented in Chapters 6 and 7; therefore, the following subchapters summarises each individual system combining and reviewing the results of the imaging studies with the scatter studies. Table 91 summarises the key information retrieved from the DLS, SAXS and SANS analyses at room temperature.

Amphiphilic ratio (Ro)	Methanol preparation	Solvent	Resulting system	Self assembled particles?	Reverse vesicles?
Pure C18 95%	☒	Cyclohexane	MS	☒	☒
Pure C18 95%	☒	Heptane	RM	☑	☒
Pure C18 95%	☒	Pentane	RM	☑	☒
Pure C4	☒	Cyclohexane	MS	☒	☒
Pure C4	☒	Heptane	RM	☑	☒
Pure C4	☒	Pentane	RM	☑	☒
2.5	☑	Cyclohexane	SURV	☑	☑
3.5	☑	Cyclohexane	SURV+SMRV	☑	☑
4.5	☑	Cyclohexane	SURV	☑	☑
7	☑	Cyclohexane	PS:MS+SC(some)	☒	☒
2.5	☑	Octane	SURV+GURV+GMRV	☑	☑
3.5	☑	Octane	SURV+GURV+GMRV	☑	☑
4.5	☑	Octane	SURV+GURV+GMRV	☑	☑
2.5	☑	Heptane	SURV+GURV+GMRV	☑	☑
3.5	☑	Heptane	SURV(disc)+GURV+ GMRV+RCM	☑	☑
4.5	☑	Heptane	SURV+GURV+GMRV	☑	☑
2.5	☑	Hexane	SURV+SMRV+GMRV+ LC	☑	☑
3.5	☑	Hexane	GCRM+RCM(short rods)	☑	☒
4.5	☑	Hexane	Unsure (colloids and precipitant)	☑	Maybe
2.5	☑	Pentane	Unsure(colloids)+ SAS+SC	☑	Maybe
3.5	☑	Pentane	Unsure(precipitant)+ RCM	☑	Maybe
4.5	☑	Pentane	RBi	☑	☒

Table 90: This table presents the initial confirmed phase behaviour of the multi-component systems between 15 mM to 30 mM total amphiphilic concentration, at room temperature, probe sonicated, with the mixed systems containing over 3 mM of NaCl. Table key: PS, Phase separated; LC, Liquid crystal precipitant; GMRV, Giant (over micrometre sized) multilamellar reverse vesicle; SMRV, Small (under micrometre sized) multilamellar reverse vesicles; GURV, Giant (over micrometre sized) unilamellar reverse vesicle; SURV, Small (under micrometre sized) unilamellar reverse vesicles; Bc, Bicontinuous; RM, reverse micelles; RBi, Reverse bilayer sheets; CRM, Compound reverse micelles; GCRM, Giant (over micrometre sized) compound reverse micelles; RCM, Reverse cylindrical micelles; GRCM, Giant (over micrometre length) reverse cylindrical micelles; GRVO, Giant (over micrometre diameter) reverse vesicle onions (without a visible internal compartment); SAS, self assembled structures with undetermined morphology; MS, Molecular solution; SC, Solid crystal precipitant.

Sample	Ro	Solvent	Temperature (K)	DLS results		SANS or SAXS results						Vesicles present?
				Zeta-average diameter (nm)	Diameter PD	Particle shape	Average diameter (nm)	Diameter PD	Bilayering present	Bilayer thickness (A)	d-spacing (A)	
SAXS 23/24	2.5	Cyhex.	298	178	0.29	Sphere	144	0.29	Yes	-	-	☑
SAXS 25/26	3.5	Cyhex.	298	204	0.26	Sphere	162	0.23	Yes	-	94	☑
SAXS 27/28	4.5	Cyhex.	298	194	0.25	Sphere	>170	-	Yes	-	-	☑
SAXS 41/42	2.5	Octane	298	123	0.22	Sphere	>170	-	Yes	-	-	☑
SAXS 43/44	3.5	Octane	298	154	0.19	-	-	-	-	-	-	Maybe
SAXS 45/46	4.5	Octane	298	130	0.23	Sphere	>170	-	Yes	-	-	☑
SAXS 2/3	2.5	Heptane	298	-	-	Sphere	>170	-	Yes	-	-	☑
SAXS 4/5	3.5	Heptane	298	127	0.17	Sphere	>170	-	Yes	-	90	☑
SANS 2	3.5	Heptane	290	-	-	Ellipsoid /Disc	17/151/145	-	Yes	28	78	☑
SAXS 6/7	4.5	Heptane	298	124	0.18	-	-	-	Yes	-	-	☑
RVe1c 5 (DLS) SAXS 16/17	2.5	Hexane	298	138	0.25	Sphere	152	0.24	Yes	-	80	☑
SANS 6	3.5	Hexane	270	-	-	Cylinder	2/8	-	No	-	-	☒
SAXS 9/10	2.5	Pentane	298	100	0.11	-	-	-	-	-	-	Maybe
SAXS 11/12	3.5	Pentane	298	-	-	Cylinder	-	-	No	-	-	☒
SANS 4	3.5	Pentane	280	-	-	-	-	-	No	-	-	☒

Table 91: Table summarising the key results of the room temperature experiments, using the scattering analyses of the multi-component systems. Key: Cyhex, Cyclohexane; PD, polydispersity.

8.2.2.1 Summary of the results for the multi-component systems

8.2.2.1.1 Cyclohexane 2.5 Ro

Strong sonication produces stable (over two years) colloidal particles that produce the Tyndall scattering effect in both 15 mM and 20 mM systems. The DLS results presented a multimodal system, however, the modal 190-200 nm hydrodynamic diameter values do not correlate well with the SAXS data presenting reverse vesicles with 144 nm (0.29 PD) diameters. Therefore, the DLS zeta-average hydrodynamic diameter of 178 nm (0.29 PD) is likely to be more accurate. The difference in the 178 nm and 144 nm diameter values may be due to the SAXS method measuring the diameter in relation to the interior polar core of the bilayer and the DLS measures the size in relation to the Brownian motion which takes into account the whole of the reverse vesicle. However, both of these averages fall within the range of 100-200 nm diameters observed by TEM.

8.2.2.1.2 Cyclohexane 3.5 Ro

Colloidal dispersions with some Tyndall scattering (opalescence or/and blue hue) are formed in both 15 mM and 20 mM systems. Both form some white fluid precipitants early and have a faster flocculation rate than 2.5 Ro, although, particles remained in solution for over 6 months. DLS showed zeta-average diameters of 204 nm (0.27 PD) for the 15 mM sample and 196 nm (0.36 PD) for the 20 mM sample. The SAXS data revealed the colloidal particles of the 15 mM system were dominated by unilamellar reverse vesicles with a diameter of 162 nm; although some multilamellar vesicles with 94 Å (0.22 PD) d-spacing were also present. Similar to the cyclohexane 2.5 Ro results the SAXS data present a smaller diameter than DLS data.

8.2.2.1.3 Cyclohexane 4.5 Ro

Stable (over 1 ½ years) colloidal dispersions with some Tyndall scattering (opalescence or/and blue hue) are formed in both 15 mM and 20 mM amphiphilic concentration systems. Flocculation rates are slightly lower for the 15 mM system. Flocculation forms clusters of micron sized multilamellar reverse vesicles. DLS showed zeta-average diameters of 194 nm (0.25 PD) for the 15 mM sample and 185 nm (0.26 PD) for the 20 mM sample. The SAXS data revealed these particles are in a lamellar form without any d-spacing and therefore it is probable that the system is dominated by unilamellar reverse vesicles. The SAXS data means the average size of the reverse vesicles is over ~170 nm which correlates well with the DLS data.

8.2.2.1.4 Octane 2.5 Ro

The octane 2.5 Ro samples presented coexisting suspension of micron sized multilamellar reverse vesicles that quickly settled out of solution and a colloidal dispersion of unilamellar particles presents. Flocculation of the colloidal particles was slow and many remained in solution for over a year and a half. The slow flocculation rate was associated with cycling of the

particles between suspension and making up the sediment. DLS results of the colloidal dispersion 3 days after preparation show a principally stable system with a zeta-average diameter of 126 nm (0.22 PD). This contradicts with the SAXS data indicating a lamellar system with particles over ~170 nm in diameter. This may be due to some of the large micron sized reverse vesicles of the precipitant dominating the SAXS data due to the disruption of the system during sample transference to the capillary for sample analysis.

8.2.2.1.5 Octane 3.5 Ro

The octane 3.5 Ro samples presented coexisting suspension, of micron sized multilamellar reverse vesicles that quickly settled out of solution, and a colloidal dispersion, presenting Tyndall scattering. There was a relatively fast flocculation of the colloidal particles, removing all particles from the solution within a year. The zeta-average particle diameter of the colloidal suspension was 158 nm (0.19 PD), although, the SAXS measurements showed a system so polydisperse that valid results were unobtainable. This may be due to unintentional mixing of the precipitant and the colloidal particles during sample transport. However, we can extrapolate the presence of unilamellar reverse vesicles due to the presence of Tyndall scattering and the 158 nm zeta-average diameter. Also, we can presume that multilamellar vesicles, like those shown to be present in 2.5 Ro, made up the white fluid precipitant phase.

8.2.2.1.6 Octane 4.5 Ro

The octane 4.5 Ro samples presented coexisting suspension of micron sized multilamellar reverse vesicles that quickly settled out of solution and a colloidal dispersion presenting Tyndall scattering. There was a relatively fast flocculation of the colloidal particles, removing all particles from the solution within a year. DLS presented a 133 nm zeta-average diameter (0.23 PD) for these colloidal particles. This contradicts the >170 nm average diameter reported by SAXS. However, like the other octane samples, this may have resulted from disruption of the sample during transport to the beamline - allowing the micron sized reversed vesicles, which had quickly settled, to be re-suspended and dominate the SAXS results. Although there are discrepancies in size, all of the particles in the system are lamellar according to the SAXS results which indicate the colloidal particles are reverse vesicles.

8.2.2.1.7 Heptane 2.5 Ro

The heptane 2.5 Ro samples presented a coexisting suspension of highly polydisperse, micron sized multilamellar reverse vesicles, which quickly settled out of solution, and a colloidal dispersion presenting Tyndall scattering. There was a slow flocculation rate associated with cycling of the particles between the sediment and suspension. This cycling may have produced the fast aggregation / high polydispersity that caused the anomalous DLS results. The SAXS

data revealed the colloidal particles to have a lamellar structure; however, we can only determine that the diameter of these particles is over ~170 nm.

8.2.2.1.8 Heptane 3.5 Ro

The heptane 3.5 Ro samples presented coexisting suspension of highly polydisperse, micron sized multilamellar reverse vesicles that quickly settled out of solution and a colloidal dispersion presenting Tyndall scattering. The flocculation rate was high in comparison to the 2.5 Ro system and all the particles had settled within 6 months. DLS of an unshaken sample after 3 days presented a 128 nm (0.17 PD) zeta-average diameter for the colloidal particles. The SAXS data presented lamellar particles over ~170 nm and some of these were multilamellar with a d-spacing around 90 Å. It may be that the sample was disturbed before the SAXS measurement took place and the result was dominated by the micron sized multilamellar vesicles. The SANS data also presented a lamellar system with a 32 Å bilayer thickness and an 82 Å spacing with a high 0.6 PD for large multilamellar vesicles. In addition to these structures were 281 nm to 312 nm diameter bicelles which may have also been vesicular due to their 332 Å length. DLS calculates a hydrodynamic diameter presuming a sphere, and therefore, a disc with a length of 33 nm and a diameter between 281 nm to 312 nm could be responsible for the 128 nm zeta-average diameter. So this system is a highly polydisperse system of lamellar structures including reverse vesicles.

8.2.2.1.9 Heptane 4.5 Ro

The heptane 4.5 Ro samples presented coexisting suspension of highly polydisperse, micron sized multilamellar reverse vesicles that quickly settled out of solution, and a colloidal dispersion presenting Tyndall scattering. The flocculation rate was low with colloids remaining in solution for over 1 year and 7 months. DLS results revealed a zeta-average diameter of 124 nm (0.18 PD). The SAXS data revealed the system to be lamellar; however, the particle size was higher than the DLS value which may have resulted from disturbance of the sample before the measurements were taken.

8.2.2.1.10 Hexane 2.5 Ro

The hexane 2.5 Ro samples presented coexisting suspension of: highly polydisperse, micron sized, multilamellar and onion reverse vesicles with liquid crystal particles that quickly settled out of solution; and a colloidal dispersion presenting Tyndall scattering. The flocculation rate was low with a small quantity of colloids remaining in solution for over 1 year and 7 months. DLS measurements reported a 137nm zeta-average diameter (0.25 PD) for the colloidal particles. This coincides with the reverse vesicle 152 nm (0.24 PD) diameter reported by SAXS. The SAXS data also revealed the system has some multilamellar structures that have a 80 Å d-spacing.

8.2.2.1.11 Hexane 3.5 Ro

The hexane 3.5 Ro samples presented a suspension of micron sized compound micelles that quickly settled out of solution and a colloidal dispersion presenting Tyndall scattering. DLS reports a zeta-average of 137 nm (~0.25 PD) for the colloids. The SAXS model fit estimated these colloids were cylindrical micelles with a 77 Å length and 11 Å radius which are too low to correlate with the DLS data. Therefore, it is likely that there is a very polydisperse micellar colloidal dispersion.

8.2.2.1.12 Hexane 4.5 Ro

The hexane 4.5 Ro samples presented both a suspension of large spheres, which were either bicontinuous or aggregated micelles/vesicles, and a colloidal dispersion, presenting Tyndall scattering. The colloidal particles were too polydisperse to be validly analysed with DLS and SAXS data. It is therefore likely that this is a very polydisperse micellar system.

8.2.2.1.13 Pentane 2.5 Ro

The pentane 2.5 Ro samples presented; a suspension of micrometer sized reverse vesicular onions and phase separated crystal regions, along with a colloidal dispersion with fast flocculation (absence of particles within a few months). According to the DLS measurements, the zeta-average diameters of the colloidal particles were 104 nm (0.0024) and 109 nm (0.11 PD) after 1 week and 1 month respectively. Although these diameters are in the acceptable range for unilamellar reverse vesicles, the extremely low polydispersity suggests this may not be the case. Because the SAXS results were anomalous, it is difficult to determine whether these colloidal structures were phase separated crystals or micellar structures.

8.2.2.1.14 Pentane 3.5 Ro

The pentane 3.5 Ro samples presented both a suspension of non-lamellar thick walled 10-60 μm particles, and a colloidal dispersion of 1 μm particles with fast flocculation (absence of particles within a few months). DLS measurements after week indicated the colloidal dispersion was highly polydisperse; however, after a month the polydispersity decreased and reported a zeta-average diameter of 115 nm (0.2 PD). The SAXS measurements revealed the colloidal system contained cylindrical micelles which may correspond to the particles detected by DLS. This system is not lamellar but there may still be large 10-60 μm particles with internal compartments.

8.2.2.1.15 Pentane 4.5 Ro

The pentane 4.5 Ro samples present a lamellar suspension that settles too rapidly to be accurately analysed with scattering techniques.

8.3 Discussion of key differences

8.3.1 Differences between binary and multi-component systems

There was a distinct difference in macroscopic phase behaviour of the pure C18 99% and C18 95% products in cyclic and alkane liquids. C18 99% formed an amorphous liquid crystal precipitant in all solvents and C18 95% presented similar phase behaviour to PC4:0 by forming a molecular solution in cyclohexane and a colloidal solution in alkanes. This showed that the inclusion of lyso-C18 greatly increased the solvability of the C18 95% product in organic solvents.

The studies of mixed amphiphilic systems indicated that the inclusion of a small quantity of lyso-PC18 strongly enables the formation of reverse vesicles in alkanes. This conforms to the theory of geometric packing parameters of micellar systems. Replacing some of the two tailed PC18 with single tailed PC18, decreases the volume occupied by the lipid moiety which consequently decreases the packing parameter. Therefore, a decrease in the number of the short tailed PC4:0 can raise the packing parameter back to a value that encourages vesicular formation.

The inclusion of lyso-C18:2 may also increase the stability of reverse vesicles by increasing the potential for asymmetry between the leaflets of bilayers; which is known to stabilise terrestrial cell membranes (Devaux & Morris 2004).

8.3.2 Differences between solvent types

Both the binary and multi-component cyclohexane systems presented some systems that were dominated by unilamellar reverse vesicles. However, the change from a cyclic to alkane solvent in the binary systems hindered reverse vesicle formation. For multi-component systems, the reduction in molecular weight of the alkane solvent reduced the number of systems dominated by reversed vesicles (in the 2.5 Ro to 4.5 Ro range).

In the binary systems, the lowest amphiphilic ratio promoted self assembly in the heptane and hexane systems; however, the higher amphiphilic ratios (> 3.5 Ro) promoted self assembly in pentane systems. This coincides with the theory that the smaller pentane molecules have penetrated between the lipid tails of the amphiphiles, thereby, increasing the effective nonpolar surface area, and increasing the packing parameter. This indicates that solvent molecules equal to, or below, the size of pentane molecules will have a large influence on the self assembly of amphiphiles. Therefore, mixtures of amphiphiles with large polar moieties and small nonpolar moieties may promote self assembly and reverse vesicle formation in very low molecular weight alkanes, such as ethane and methane.

The multi-component results indicate that a high molecular weight alkane, such as octane, is not as efficient in bilayer penetration as cyclohexane. However, reduction in alkane molecular weight increases the effective bilayer penetration beyond that presented by cyclohexane.

The differences in the phase behaviour of the unmixed systems demonstrate that small amphiphiles undergo a dramatic change with reduction in the solvent's molecular weight. The higher dielectric constants of high molecular weight solvents, such as cyclohexane, can form molecular solutions of PC4:0 due to affiliation between the polar head group of small amphiphiles and the solvent. The low molecular weight solvents, with lower dielectric constants, cause the self assembly of PC4:0 due to the immiscibility of the polar moiety with the solvent.

Therefore, there are two key opposing forces that affect self assembly with reduction in solvent molecular weight; the increased immiscibility of polar moieties drives self assembly and the increased ability of solvent penetration drives phase separation.

8.3.3 Differences between amphiphilic ratios

The amphiphilic ratios influenced the phase behaviours in the binary and multi-component systems. Reverse vesicles dominated multi-component systems in a wide amphiphilic ratio range (2.5 Ro to 4.5 Ro) in the high molecular weight alkanes and cyclohexane systems. High amphiphilic ratios (6-7 Ro) were required for colloidal dispersions of unilamellar reverse vesicles in binary cyclohexane. However, the multi-component 7 Ro cyclohexane systems presented a molecular solution which illustrates the difference in amphiphilic ratios between the binary and multi-component systems.

Tung (2008) reported that methanol prepared multi-component systems over 4 Ro were phase separated; however, our 4.5 Ro samples presented a colloidal dispersion of unilamellar reverse vesicles. Therefore, the boundary for a macroscopic and structural phase transition is actually at a higher amphiphilic ratio than published previously.

The average size of the unilamellar reverse vesicles grew with an increase in amphiphilic ratios in the multi-component cyclohexane systems; see Table 91. This indicates that for these multi-component cyclohexane systems a relative increase in polar surface area (compared to nonpolar surface area) has decreased the curvature of the reverse vesicles; consequently increasing the average reverse vesicle diameter.

In the binary alkane systems, the amphiphilic ratios determined whether the phase was micellar, bicontinuous, liquid crystal, or coexisting.

8.3.4 Differences in bilayer spacing

In the unstable binary cyclohexane 2.5 Ro system a few multilamellar vesicles were found and the spacing of the bilayers was most frequently ~1-5 nm (but in disturbed regions increased to ~50 nm); see Figure 151.

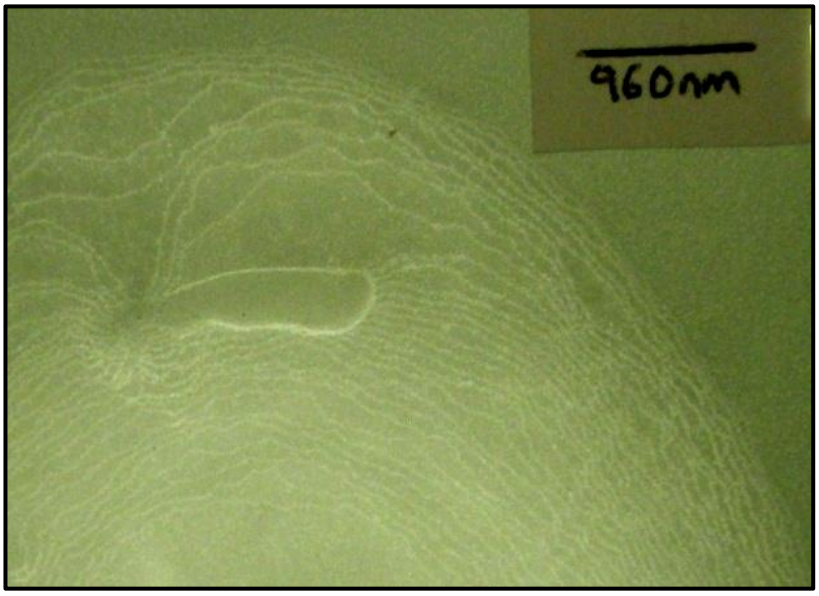

Figure 151: TEM micrograph of the bilayers of the multilamellar reverse vesicles in binary cyclohexane 2.5 Ro system (without methanol preparation).

Stable colloidal dispersions containing some multilamellar reverse vesicles have bilayer spacing that is notably less (under 1 nm) than those of unstable giant multilamellar reverse vesicles; see Table 92. A d-spacing of 94 Å with 0.22 PD for a smaller number of multilamellar reverse vesicles were also found for Tung's (2008) multi-component cyclohexane 2.6 Ro systems. As shown in Table 92 there is a high polydispersity in the bilayer spacing for numerous samples, which makes the slight decrease in bilayer spacing with temperature (SANS heptane 3.5 Ro sample) insignificant.

This tight 0.7 to 5 nm bilayer spacing makes it difficult to distinguish multilamellar reverse vesicles from unilamellar reverse vesicles with microscopy; as a vesicle wall may have multiple bilayers, but they will not be able to be distinguished from one another.

Ro	Solvent	Temperature (K)	Average diameter (nm)	Bilayer thickness (A)	d-spacing (A)	d-spacing PD
3.5	Cyhex.	298	162	-	94	0.22
3.5 SAXS	Heptane	298	>170	-	90	High
3.5 SANS	Heptane	290	17 / 151 / 145	28	78	0.60
		270	Slight increase in mean size with temp reduction	30	79	0.61
		250		30	78	0.62
		230		30	75	0.64
		210		31	72	0.67
		190		31	71	0.67
2.5	Hexane	298➔258	152	-	80	0 (constrained)

Table 92: Table summarising the key room temperature scattering results for the multi-component systems. Key: Cyhex, Cyclohexane; PD, polydispersity.

8.3.5 Differences with temperature reduction

Changes in temperature can alter: the polar and nonpolar effective surface areas of amphiphiles, the phase of the individual amphiphilic components, and their miscibility in mixed systems. All these factors can influence the subsequent form of the self assembled particles. For example, an increase in temperature has been shown to trigger a phase transition from micellar bicelles to unilamellar vesicles due to the increased miscibility between the long and short chained phosphatidylcholines in aqueous systems (Nieh *et al.* 2011). The spacing between bilayers of multilamellar vesicles has also been reported to change with temperature with swelling occurring near the transition temperature of the amphiphile (Mason *et al.* 2001).

The slight increase in bilayer thickness and decrease of bilayer spacing with temperature reduction detected in the multi-component heptane 3.5 Ro sample by SANS may be a result of some of the sol-gel transition of some of the amphiphiles; see Table 93. However, more scatter analyses are required, that focus on larger scatter vectors, to be able to determine the precise state of the lipids.

A reduction in temperature has been shown to change the structural behaviour of particles in a limited number of systems. In the binary systems, the pentane 3.5 Ro sample changed from reverse bilayer sheets to a reverse micellar system when temperature fell below -95 °C. In the multi-component systems only heptane 2.5 Ro was shown to change from a reverse vesicle phase to a cylindrical micellar phase at ~218 K.

In some lamellar phases of the multi-component systems, a reduction in temperature caused an increase in bilayer curvature, and therefore, an increase in the diameter of reverse vesicles; for example, cyclohexane 3.5 Ro, see Table 93. At higher temperatures, the gradual changes are likely to be a result of the penetration ability of the solvent into the bilayer. At temperatures

above ~ 260 K, the systems with lower amphiphilic ratios were more stabile and no changes in curvature or particle diameter were observed. This indicates that the ordering of the amphiphiles at lower amphiphilic ratios increase the rigidity of the structure and reduces the points of entry for solvent penetration.

At temperatures below ~ 260 K, sudden changes are probably a result of sol to gel transitions for some of the bilayer amphiphiles. As shown in Chapter 3 the number of saturation points of PC18 alters the transition temperature of lipids and the bulk phase transition for a mixed 18:0 and 18:2 phosphatidylcholine bilayer is approximately 257 K. Therefore, it is likely that most of the molecules in the 95% PC18 product have transformed into their gel state below 258 K.

The numerous examples of temperature stability in the multi-component systems show that the PC4:0 and lyso-PC18 components keep the bulk phase of bilayers as liquid crystal; for example, a heptane 3.5 Ro system indicated a liquid crystal bilayer at temperatures down to 190 K.

Sample	Ro	Solvent	Temperature (K)	SANS or SAXS results					
				Shape	Average diameter (nm)	Diameter PD	Bilayering	Bilayer thickness (A)	d-spacing (A)
SAXS 23/24	2.5	Cyhex.	298	○	142	0.29	☑	-	-
			288	○	145	0.32	☑	-	-
			278	○	144	0.33	☑	-	-
			268	○	141	0.25	☑	-	-
SAXS 25/26	3.5	Cyhex.	298	○	162	0.23	☑	-	94
			288➔268	○	>170	-	☑	-	94
SAXS 27/28	4.5	Cyhex.	298➔268	○	>170	-	☑	-	-
SAXS 41/42	2.5	Octane	298➔258	○	>170	-	☑	-	-
SAXS 45/46	4.5	Octane	298➔238	○	>170	-	☑	-	-
SAXS 2/3	2.5	Heptane	298➔268	○	>170	-	☑	-	-
			258	-	>170	-	☑	-	-
			238	-	>170	-	☑	-	-
			218	▯	>170	-	☒	-	-
SAXS 4/5	3.5	Heptane	298➔218	○	>170	-	☑	-	~90
SANS 2	3.5	Heptane	290	0	17/151/145	-	☑	28	78
			270	0	Slight increase in mean size with temp reduction	-	☑	30	79
			250	0		-	☑	30	78
			230	0		-	☑	30	75
			210	0		-	☑	31	72
			190	0		-	☑	31	71
SAXS 6/7	4.5	Heptane	298➔218	-	-	-	☑	-	-
SAXS 16/17	2.5	Hexane	298➔258	○	152	0.24	☑	~10	80
			238➔218	○	>170	-	Maybe	-	-
SAXS 31	3.5	Butane	260➔130	▯	-	-	☒	-	-

Table 93: Table summarising the key results of the temperature depression experiments from the scattering analyses of the multi-component systems. Key: Cyhex, Cyclohexane; PD, polydispersity; ○, Sphere; 0, Disc; ▯, Cylinder.

8.3.6 Differences in macroscopic phase behaviour of systems studied over time

Flocculation rates for colloidal dispersions of small reverse vesicles are shown to be lower for systems with lower amphiphilic concentrations; for example, the increased longevity of the colloidal dispersions in the 15 mM multi-component cyclohexane 3.5 Ro and 4.5 Ro systems compared with the 20 mM systems, see Table 94. This is expected due to an increase in the space between particles. Flocculation implies antiparticle forces of attraction but in these systems this is unlikely to be the electrostatic interactions (that often cause clustering in aqueous colloidal dispersions) because the solvent is uncharged and the external surfaces of reversed self assembled particles consist of uncharged lipid tails. Therefore, in our systems it is likely that aggregation forces are caused by van der Waals. The additive character of van der Waals creates a positive correlation between the size of the bodies involved and the strength of the force. This study correlates higher amphiphilic ratios with faster flocculation rates due to increases in the average sizes of nanometre sized particles and therefore supports the theory of flocculation being dominated by van der Waals forces in reverse micellar systems.

Sample num	Ro	Solvent	Total amphiphilic concentration (mM)	Sonication type	Time of complete precipitation (months)
RVe1c 7	3.5	Cyclohexane	20	Probe	~12
SAXS 25/26	3.5	Cyclohexane	15	Probe	19+
RVe1c 11	4.5	Cyclohexane	20	Probe	~12
SAXS 27/28	4.5	Cyclohexane	15	Probe	19+

Table 94: Table displaying the rates of total precipitation for multi-component cyclohexane systems.

In the binary systems, a large NaCl to amphiphile ratios was related to an initial agglomeration of particles due to excess NaCl which caused an attractive force between particles.

Many of the colloidal dispersions in the multi-component systems remained in solution for years. The precipitants of the systems would usually follow a gradual transition to form an amorphous liquid crystal gel with time.

8.3.7 Differences between preparation methods

In general, methanol preparation facilitated the formation of reverse vesicular assemblages. This methanol preparation is likely to have facilitated the disassociation of NaCl and subsequent bonding of the ions into the polar head moieties of the amphiphiles; thereby counteracting any electrostatic repulsion interactions. This is shown in binary cyclohexane systems in which giant reverse unilamellar vesicles were found at low amphiphilic ratios in methanol prepared systems, but exclusive reverse vesicle phases were limited to amphiphilic ratios over 7 Ro for systems prepared without methanol.

There were very different phases in the multi-component cyclohexane 2.5 Ro systems, in which, without methanol preparation cylindrical micelles dominated, but when methanol preparation was used a system of reverse vesicles was produced; see Table 90. This implies that not only does methanol preparation help in stabilising reverse vesicle bilayers, but also, by bonding Na+ and Cl- ions to appropriate parts of the polar moieties of the amphiphiles this increases the effective polar surface area which decreases the packing parameter. This decrease in packing parameter changes the system from being dominated by reverse micellar forms (PP > 1½) to being dominated by reverse vesicular forms (1 < PP < 1½); see Table 2.

In the multi-component cyclohexane 7 Ro systems, the addition of methanol preparation transforms a suspension dominated by micrometre sized reverse vesicles (unilamellar, multilamellar and onion formations) into a colloidal dispersion of unilamellar vesicles. This indicates that methanol preparation facilitates the attachment of Na+ and Cl- ions to the polar moieties of the amphiphiles, allowing a denser polar interior of the reverse bilayers by negating the electrostatic repulsive forces. This methanol facilitated dense polar interior of the reverse bilayers would consequently allow a greater curvature for the reverse vesicles and promote smaller, nanometre sized, reverse vesicles.

An increase in sonication intensity was shown to decrease the particle size. In systems with suspensions, this reduction in particle surface area decreased friction with the solvent and increased the settling rate. However, in systems that could produce nanometre sized unilamellar reverse vesicles the stronger sonication would reduce the average size and slightly increase the longevity of the colloidal dispersions; for example, as evidenced by the reduction in laser reflectivity the longevity of the colloidal dispersions of the multi-component 2.5 Ro cyclohexane systems increased between using a strong water-bath and intense probe sonication; see Table 31.

For lamellar systems in general, weaker sonication would promote the formation of multilamellar and onion reverse vesicles and strong sonication would promote unilamellar reverse vesicles formation.

8.3.8 Macroscopic phase behaviour in relation to microscopic structures

Tyndall scattering has been observed in systems dominated by unilamellar reverse vesicles but weak Tyndall scattering (referred to as opalescence in this study) has also been observed in systems with spherical micellar particles; therefore it is not an indicative sign of reverse vesicles across these systems. Also, the strength of the Tyndall effect has been shown to be dependent on the concentration and size of the colloids.

Chapter 9: Conclusions from research and subsequent consequences for astrobiology

9.1 Considerations of self assembly in relation to astrobiology

It is unlikely that the usefulness of reversed vesicular structures, separating two nonpolar reservoirs, would be limited to being a framework for a functional cell membrane. In the case of Titan, the hydrocarbon lakes are likely to consist of methane-ethane-propane liquids at a ratio consistent with the atmospheric equilibrium. As these lakes are likely to contain more than one alkane liquid, these compartments could be used to discriminately uptake one specific alkane or a ratio of alkanes that differs to that of the surrounding environment. This discriminatory selection process could create a cell with a 'cytoplasm' that differs from its medium, or produce pockets of unique solutions that serve specific purposes within a cell.

These discrete pockets of unique mixtures could be used to elevate the number or rate of chemical processes that are able to take place within the biota. The equivalent of 'organelles' could be encapsulated in reversed vesicles along with different alkanes that facilitate the functions of that particular construct. The size and compounds used in the vesicular construct could also influence the functionality required for the organelle being encapsulated. Multi-compound vesicles with slightly different mixtures in each compartment have the potential to facilitate long chemical processes that require slightly different environments for each step.

It may also be possible to trap some ammonia-water within bilayers, which would decrease the freezing temperature of this polar solvent maybe to the point where it can be used to provide ideal nano-reaction centres for biological process that are facilitated by polar solvents. Bicontinuous phases may also enable nano-channels of liquid ammonia-water to allow ion transport throughout the cell.

These trapped polar liquid regions may derive from short lived cryolava, impact melts, or theoretically, the biota may be able to derive minute quantities of water directly from the icy bed of the hydrocarbon lakes or aquifers by using antifreeze proteins.

Small micellar particles may be ideal for storage of nutrients or facilitate the keeping of energy in a durable chemical form by regulating the surface properties. In terrestrial biota normal micelles are commonly used as reservoirs for accumulating monomers and can change the rate or reverse chemical reaction pathways, for example, oxidation-reduction processes can be reversed by the increase in concentration of localising reagents (Khabibullaev & Saidov 2003).

In these reversed systems, hydrocarbon-based biota could use reverse micelles as reservoirs for polar solutes or be used as a transport vehicle for proteins and enzymes.

These considerations for the biological use of various reversed self assembled systems show that the importance of self assembly is not limited to reverse vesicular structures. Therefore, all the systems presenting reversed micellar, vesicular and bicontinuous phases may have use for nonpolar-based biota across the universe.

For Titan in particular the cylindrical micelles reported for many of the low molecular weight alkanes (pentane and butane) systems may be useful for hydrocarbon-based life to use as storage or mopping up polar solutes that may settle to the base of hydrocarbon habitats. The long lived bicontinuous spheres in the pentane 4.5 Ro system of the binary system may be of use for biota as a skeleton for channelling or filtrating nutrients from one area to another. This may be especially important for hydrocarbon-based life on Titan to allow the transport of nutrients with low solubilities in the alkane habitat.

Some systems presented very polydisperse lamellar or coexisting micellar/lamellar phases. This wide range of structures from a limited amphiphilic range could allow for compartmentalisation from reverse vesicles and storage from micellar structures, for any biota which are restricted to utilizing a limited range of amphiphiles (perhaps due to nutrient deficiency in the immediate environment).

9.2 Considerations of temperature driven phase transitions in relation to astrobiology

There are two main astrobiological concerns regarding compartmentalisation strategies in cold environments: (1) is the formation of a self assembled vesicular compartment possible at low temperatures, and (2) would the phase behaviour of the vesicular compartment allow the vesicular compartment to function as a biological membrane?

The results of these projects indicate that these mixtures of long/short phosphatidylcholines kept the bulk phase of lamellar systems in a liquid crystalline state at very low temperatures; although further X-ray diffraction studies should be carried out to confirm this conclusion. Also, although there was an increase in curvature and therefore reverse vesicles increased in diameter the majority remained as reverse vesicular systems. In fact, only one system presented a change in structural state with temperature reduction. This supports their use as compartmental structures for hydrocarbon-based biota on Titan.

Our studies show that the quantity of small amphiphiles is important in maintaining the fluidity of bilayers at low temperatures; however, only certain long/short amphiphilic ratios produce reverse vesicles which decreased with solvent molecular weights. Therefore, it is likely that

forming reverse vesicles in low molecular solvents in low temperature environments would require a diverse mixture of amphiphiles.

This conclusion is consistent with our knowledge of terrestrial membranes which are composed of a wide range of amphiphiles. The recent work by (Georgiou & Deamer 2014) demonstrates that life utilises a distinct distribution of lipids. It would therefore seem reasonable to take this distribution and transpose it to lower molecular weights in order to study systems of vesicles in low molecular weight solvents that are fluid at low temperatures.

If reverse vesicles are present at low temperatures in hydrocarbon solvents, and if they have gone through the Lc-sol transition (see section 2.5.3 for description), the question remains whether a solid compartment such as this could support life on Titan, or whether a liquid crystal compartment is a requirement for all life in the universe. If the cell membranes on Titan were solid and ordered, rather than liquid-crystalline as terrestrial life uses, there may be coping mechanisms such as special transmembrane transport proteins (similar to those used by terrestrial biota) for nutrient uptake and waste removal, however, there is still the question of replication methods. Conventional budding or binary fission may not be possible with a solid membrane, but an alternative type of sporulation (spore formation) maybe be possible with the 'spores' being created internally and expelled by lysis of the parent cell. There is also the question of growth in cells with a solid membrane; it may be possible that when a cell wants to grow it adds another bilayer over the old one whilst using specialised structures to chemically disintegrate the internal layer. Or the internal layers may remain to allow additional regions of separation within the cell. Benefits of a solid capsule may include not needing to repair the compartment often and have a stable difference between the internal and external functions for the membrane such as is used by terrestrial biota – which is only available because of the minimal transference of lipids from one of the adjoined layers to the other within a bilayer. Of course, what biochemistries can be used as transport proteins etc in these conditions requires a set of other experimental astrobiological studies.

Even if the larger amphiphiles have no configurational freedom (ability to flex parts of a molecule and rotate bonds of carbon backbone) the inclusion of smaller molecules, maybe even from the methane-ethane medium, may allow the structure to have enough flexibility to allow it to function as a membrane in a similar way to those found on Earth. It has been shown that in mixed (long and short chain) phosphatidylcholine aqueous systems that growth and the self-folding of self assembled particles can still occur far below the transition temperature of the long chain phosphatidylcholine; with the long chain phosphatidylcholine in a gel phase and the short chain amphiphile in a liquid crystalline phase (Mahabir *et al.* 2010). This implies that there could be a specific mixture of long and short chained amphiphiles which forms a vesicle.

If the membrane is in a gel or liquid-ordered (liquid translational order but gel configuration of hydrocarbon chains) state can it still function as a compartmental structure? It would be difficult to mediate lipid and component exchange especially without translational freedom. Could there be small liquid-disordered domains within a liquid-ordered or gel dominated bilayer? In terrestrial membranes there are examples of functional domains including 'lipid rafts'; which are small domains of liquid-ordered states in a typical liquid-disordered bilayer (Fielding 2006). In a reversal of this typical lipid raft, phenomena Titan life may utilise 'lipid ponds' - small liquid-disordered domains – within reverse vesicles that are mainly in a gel or liquid-ordered state. This may be possible with the inclusion of smaller molecules with low freezing points into specific locations in a membrane. These lipid ponds may also be extended to form networks around large 'gel plates'. This would also facilitate the inclusion or removal of any gel plates which would in turn allow growth and replication as well as directed vesicular transport. The gel plates themselves would be useful as an anchor for other biological constituents such as a cytoskeleton and the liquid network could serve as a selective permeability barrier.

If a membrane consisting of a network of liquid and gel domains, termed the 'floating plates theory' hereafter, was a plausible strategy for compartmentalisation for hydrocarbon-based biota then they could also function to compartmentalise other biological components such as organelles. Changes of the components in these domains could control the required internal environments to enable characteristic differences that facilitate the function of organelles.

9.3 Importance and suggested avenues for further research

There are three main areas for further investigations connected to this research; synthetic astrobiological research, mission based research and planetary science related research. Synthetic astrobiological research could use experimental and computer modelling to further evaluate amphiphilic self assembly in conditions analogous to those of Titan. Mission based research would test equipment capable of looking for amphiphilic biosignatures or imaging single celled biota in hydrocarbon solvents. Planetary science related research would try to connect the presence of hydrocarbon-based biota with remotely derived data. An example of planetary science related research would be studying the viscosity and consequent wave action between solutions at Titan's atmospheric equilibrium and those containing self assembled structures.

Here we discuss the potential for further synthetic astrobiological research and lessons learnt from this study. The main conclusions we draw from this research can assist in directing further investigating the possibility of self assembled structures forming in Titan's lakes.

9.3.1 Condensed matter research – synthetic astrobiology

There are two avenues for further synthetic astrobiology research – origins vs. biological approach to research. Research into the origins of life on Earth focuses on the plausibility of prebiotic and primitive biotic processes that enabled the eventual evolution of complex life. The studies presented in this thesis fall into this research style. Determining the prebiotic chemical processes that can occur in non-terrestrial settings to gain a greater understanding of habitability would be essential for any non-water medium being scrutinized. However, in the case of Titan's hydrocarbon lakes the simple structures may have a greater importance in the search for hydrocarbon-based life than researching complex, biological systems. This premise stems from the relatively short existence of these hydrocarbon lakes, in comparison to the longevity of terrestrial life, and the prevailing cryogenic temperatures. Billions of years of evolution have produced very complex life on Earth, even when considering extant single celled biota. Therefore, the relatively short age of Titan's hydrocarbon liquid bodies (thousands to millions of years) suggests that extant hydrocarbon-based life will be in a very primitive stage. The low temperatures on Titan's surface may also slow the pace of evolution due to the reduction in the rate of chemical processes.

However, there is an argument for subsurface water-based biota having gradually migrated to the surface and evolved to become a highly complicated, hydrocarbon-based biota. This may be unlikely considering hydrocarbon-based life has not been discovered in oil reserves on Earth, but the high pressures and temperatures for oil reserves may have prevented this evolutionary pathway. If this evolutionary pathway has been followed on Titan, a biological approach to research - studying complex phenomena - may generate greater benefits in the search for hydrocarbon-based biota. However, considering the newness of synthetic astrobiology I will focus the rest of this section on illuminating avenues for further research based on the origins approach.

Lipid biosignatures from cell membranes that have made it into the palaeontological record on Earth can provide taxonomic information about the organisms present at that time, and can even indicate if they were stressed, starved or dormant (e.g. Amir *et al.* 2008; Fang *et al.* 2006). These types of lipid biosignatures also have the potential as extraterrestrial biosignatures if we are able to accurately predict the types of amphiphiles that could serve as membrane components (Georgiou & Deamer 2014). For example, gas chromatography methods (Hart *et al.* 2011; e.g. Stadnitskaia *et al.* 2008) could be used to identify the presence of these characteristic lipid biosignatures on Titan. In order to get an idea of the types of possible compartmentalisation strategies for hydrocarbon-based biota this research should focus on amphiphiles that are more likely to found on the surface of Titan than phospholipids; these may include amphiphiles containing amino (NH_2) or imino (C=NH) hydrophilic groups.

Avenues for further research could include processes such as polymer shielding to decrease flocculation rate and therefore increase the stability of colloidal self assembled particles. An external shield of protruding polymers may work in reverse vesicles the same way it does in normal vesicles; as the contact area between the polymer layers decrease, the concentration of polymers increase, producing an increase in pressure that pushes the two particles away from one another.

Fruitful investigations may also include permeability and solute storage. Solute storage may take place in the core for polar solutes, the palisade layer (between the hydrophilic groups and the first few carbon atoms of the alkyl tail) for amphiphiles, and the lipophilic tails region for nonpolar solutes (Turco Liveri 2006).

The studies of this thesis showed that if reverse vesicles are found in high molecular weight alkanes within a certain range of amphiphilic ratios then it is likely that with reduction in molecular weight of the solvent the likely range of reverse vesicles are at lower amphiphilic ratios. Therefore, for further studies this knowledge can be used to estimate appropriate amphiphilic ratios for low molecular weight alkane solvents in regards to systems that have presented reversed vesicles in common high molecular weight solvents.

In phospholipid systems, a stabiliser and methanol preparation are key to forming stable reverse vesicles. Therefore, further studies for any zwitterionic systems should utilise stabilisers that are well mixed using alcohol solvents.

The low temperatures that transform the amphiphiles from their liquid crystal phase to their solid gel phase could be a problem with using typical terrestrial cell membrane forming amphiphiles for cell membranes on Titan; so it may be that silane based amphiphiles that have lower phase transition temperatures (e.g. Hawkins & Grunlan 2012) are better suited for compartmentalization.

This study highlights the requirements for using a variety of methods to describe a self assembled system fully; therefore, future experiments could include additional methods that were not used in this study such as rheological changes. Investigations could include analysing phase behaviour of bilayers at low temperatures using X-ray diffraction. This method may also be able to investigate the possibility of the ‘floating plates theory’ (discussed in the previous section). FRET could also be used to analyse the distribution of liquid-ordered (rafts) and liquid-disordered states in a membrane and view changes in domain sizes with temperature; similar to the work done for normal bilayers (Silvius 2003). FRAP could also be used to measure the translational freedom of membrane components at low temperatures using a cryo-stage. Raman spectroscopy may also be used to find transition temperature of membranes consisting of mixed components.

9.3.2 Lessons learnt from experimental difficulties

Many of the samples had particles between 2 micrometres and 200 nanometres which were difficult to analyse with the equipment used in these studies. Therefore, access to a high power microscope with a polarizing analyser and fluorescence capabilities would be beneficial for future studies.

Due to the speed that pentane would dissolve the carbon films of the TEM grids further imaging investigations into the nanometre sized particles should use specialised grids with silicon films. The TEM electron beam would often destroy morphological features. Therefore, future TEM work should utilise cryo-TEM to reduce the risk of structures being destroyed or altered by the radiation. Also, a dye suitable for TEM imaging would help in the analysis for structures on a nanometre scale.

For the SAXS studies the detector (HOTSAXS) to enable high Q measurements were asked for on the proposal but was not set up. The results in this thesis show that a high Q range is essential for valid analysis of bilayer thickness and lipid phase transitions. Therefore, in future investigations using SAXS measurements at high Q should be prioritised. Ice crystals growing on SAXS capillaries during temperature reduction was also an issue in this project. Therefore, methods for low temperature measurements in a desiccated environment should be perused.

The inclusion of the fluorescent Rhodamine b dye could have altered the systems being studied. Therefore, further studies of reversed systems should use fluorescent lipids rather than an additional polar dye.

The illumination from microscopy would heat the samples which may alter them, and also, the pentane sample would often evaporate too quickly to analyse them appropriately. Therefore, a cryo-stage for microscopy will be useful for cryogenic experiments and for keeping samples at a consistent temperature during room temperature measurements.

9.4 Conclusion

This is just the beginning for synthetic astrobiological research.

Reference List

Aharonson, O., Hayes, A.G., Lunine, J.I., Lorenz, R.D., Allison, M.D. & Elachi, C. (2009) An asymmetric distribution of lakes on Titan as a possible consequence of orbital forcing. *Nature Geoscience*, **2**, pp. 851-854.

Annous, B.A., Becker, L.A., Bayles, D.O., Labeda, D.P. & Wilkinson, B.J. (1997) Critical role of anteiso-C-15:0 fatty acid in the growth of Listeria monocytogenes at low temperatures. *Applied and Environmental Microbiology*, **63**, pp. 3887-3894.

Ardhammar, M., Lincoln, P. & Nordén, B. (2002) Invisible liposomes: Refractive index matching with sucrose enables flow dichroism assessment of peptide orientation in lipid vesicle membrane. *Proceedings of the National Academy of Sciences*, **99**, pp. 15313-15317.

Artemieva, N. (2003) Cratering on Titan: impact melt, ejecta, and the fate of surface organics. *Icarus*, **164**, pp. 471-480.

Atlas, R.M. (1995) Bioremediation of Petroleum Pollutants. *International Biodeterioration & Biodegradation*, **35**, pp. 317-327.

Atlas, R.M. & Bartha, R. (1992) Hydrocarbon Biodegradation and Oil-Spill Bioremediation. *Advances in Microbial Ecology*, **12**, pp. 287-338.

Atlas, R.M. & Cerniglia, C.E. (1995) Bioremediation of Petroleum Pollutants - Diversity and Environmental Aspects of Hydrocarbon Biodegradation. *BioScience*, **45**, pp.332-338.

Atlas, R.M. & Philp, J. (2005) Bioremediation: Applied Microbial Solutions for Real-World Environmental Cleanup. *Bioremediation: Applied Microbial Solutions for Real-World Environmental Cleanup*. ASM Press: Washington, DC.

Atreya, S.K., Donahue, T.M. & Kuhn, W.R. (1978) Evolution of a Nitrogen Atmosphere on Titan. *Science*, **201**, pp. 611-613.

Bains, W. (2004) Many chemistries could be used to build living systems. *Astrobiology*, **4**, pp. 137-167.

Bangham, A.D., Standish, M.M. & Watkins, J.C. (1965) Diffusion of Univalent Ions Across Lamellae of Swollen Phospholipids. *Journal of Molecular Biology*, **13**, pp. 238-252.

Barnes, J.W., Brown, R.H., Soderblom, L., Sotin, C., Le Mouelic, S., Rodriguez, S., Jaumann, R., Beyer, R.A., Buratti, B.J., Pitman, K., Baines, K.H., Clark, R. & Nicholson, P. (2008) Spectroscopy, morphometry, and photoclinometry of Titan's dunefields from Cassini/VIMS. *Icarus*, **195**, pp. 400-414.

Barnes, J.W., Radebaugh, J., Brown, R.H., Wall, S., Soderblom, L., Lunine, J., Burr, D., Sotin, C., Le Mouélic, S., Rodriguez, S., Buratti, B.J., Clark, R., Baines, K.H., Jaumann, R., Nicholson, P.D., Kirk, R.L., Lopes, R., Lorenz, R.D., Mitchell, K. & Wood, C.A. (2007) Near-infrared spectral mapping of Titan's mountains and channels. *Journal of Geophysical Research-Planets*, **112** (E11), p. E11006.

Beghin, C., Sotin, C. & Hamelin, M. (2010) Titan's native ocean revealed beneath some 45 km of ice by a Schumann-like resonance. *Comptes Rendus Geoscience*, **342**, pp. 425-433.

Benner, S.A., Ricardo, A. & Carrigan, M.A. (2004) Is there a common chemical model for life in the universe? *Current Opinion in Chemical Biology*, **8**, pp. 672-689.

Bergstrom, M., Pedersen, J.S., Schurtenberger, P. & Egelhaaf, S.U. (1999) Small-angle neutron scattering (SANS) study of vesicles and lamellar sheets formed from mixtures of an anionic and a cationic surfactant. *Journal of Physical Chemistry B*, **103**, pp. 9888-9897.

Berteloite, C., Le Picard, S.D., Balucani, N., Canosa, A. & Sims, I.R. (2010a) Low temperature rate coefficients for reactions of the butadiynyl radical, C4H, with various hydrocarbons. Part I: reactions with alkanes (CH4, C2H6, C3H8, C4H10). *Physical Chemistry Chemical Physics*, **12**, pp. 3666-3676.

Berteloite, C., Le Picard, S.D., Balucani, N., Canosa, A. & Sims, I.R. (2010b) Low temperature rate coefficients for reactions of the butadiynyl radical, C4H, with various hydrocarbons. Part II: reactions with alkenes (ethylene, propene, 1-butene), dienes (allene, 1,3-butadiene) and alkynes (acetylene, propyne and 1-butyne). *Physical Chemistry Chemical Physics*, **12**, pp. 3677-3689.

Bills, B.G. & Nimmo, F. (2008) Forced obliquity and moments of inertia of Titan. *Icarus*, **196**, pp.293-297.

Boettcher, C., Schade, B. & Fuhrhop, J.H. (2001) Comparative cryo-electron microscopy of noncovalent N-dodecanoyl- (D- and L-) serine assemblies in vitreous toluene and water. *Langmuir*, **17**, pp. 873-877.

Brook, M.A. (2000) *Silicon in Organic, Organometallic and Polymer Chemistry*. John Wiley & Sons Inc: New York.

Brown, M.E., Bouchez, A.H. & Griffith, C.A. (2002) Direct detection of variable tropospheric clouds near Titan's south pole. *Nature*, **420**, pp. 795-797.

Brown, M.E., Roberts, J.E. & Schaller, E.L. (2010) Clouds on Titan during the Cassini prime mission: A complete analysis of the VIMS data. *Icarus*, **205**, pp. 571-580.

Brown, M.E., Smith, A.L., Chen, C. & Adamkovics, M. (2009) Discovery of Fog at the South Pole of Titan. *Astrophysical Journal Letters*, Vol.706, L110-L113.

Brown, R.H., Soderblom, L.A., Soderblom, J.M., Clark, R.N., Jaumann, R., Barnes, J.W., Sotin, C., Buratti, B., Baines, K.H. & Nicholson, P.D. (2008) The identification of liquid ethane in Titan's Ontario Lacus. *Nature*, **454**, pp. 607-610.

Bucknall, D.G. (1999) Neutron reflection studies of polymers. *In:* Pethrick, R.A. & Dawkins, J.V., *Modern techniques for polymer characterisation*. John Wiley & Sons: Chichester, pp.109-138.

Budavari, S., O'Neal, M.J., Smith, A. & Heckelman, P.E. (1989) The merck index an encyclopedia of chemicals drugs and biologicals. Inc. Rahway: New Jersey.

Carrasco, N., Schmitz-Afonso, I., Bonnet, J.Y., Quirico, E., Thissen, R., Dutuit, O., Bagag, A., Laprevote, O., Buch, A., Giulani, A., Adande, G., Ouni, F., Hadamcik, E., Szopa, C. & Cernogora, G. (2009) Chemical Characterization of Titan's Tholins: Solubility, Morphology and Molecular Structure Revisited. *Journal of Physical Chemistry A*, **113**, pp. 11195-11203.

Castello, J.D. & Rogers, S.O. (2005) *Life in Ancient Ice*. Princeton University Press: Oxford.

Chan, Y.C. & Wiedmann, M. (2009) Physiology and Genetics of Listeria Monocytogenes Survival and Growth at Cold Temperatures. *Critical Reviews in Food Science and Nutrition*, **49**, pp. 237-253.

Chassefiere, E. & Cabane, M. (1995) Two formation regions for Titan's hazes: indirect clues and possible synthesis mechanisms. *Planetary and Space Science Journal*, **43**, pp. 91-103.

Chen, I.A. & Walde, P. (2010) From Self-Assembled Vesicles to Protocells. *Cold Spring Harbor Perspectives in Biology*, **2** (7), pp. 1-13.

Clark, R.N., Curchin, J.M., Barnes, J.W., Jaumann, R., Soderbolm, L., Cruikshank, D.P., Brown, R.H., Rodriguez, S., Lunine, J., Stephan, K., Hoefen, T.M., Le Mouelic, S., Sotin, C., Baines, K.H., Buratti, B.J. & Nicholson, P.D. (2010) Detection and mapping of hydrocarbon deposits on Titan. *Journal of Geophysical Research*, **115**, E10005.

Clarke, D.W. & Ferris, J.P. (1997) Chemical evolution on Titan: comparisons to the prebiotic earth. *Origins of Life and Evolution of the Biosphere*, **27**, pp. 225-248.

Cockell, C.S., Kaltenegger, L. & Raven, J.A. (2009) Cryptic Photosynthesis-Extrasolar Planetary Oxygen Without a Surface Biological Signature. *Astrobiology*, **9**, pp. 623-636.

Coll, P., Ramirez, S.I., Navarro-Gonzalez, R. & Raulin, F. (2001) Chemical and optical behaviour of tholins, laboratory analogues of Titan aerosols. *Space Life Sciences: Life in the Solar System: Prebiotic Chemistry, Chirality and Space Biology*, **27**, pp. 289-297.

Committee on the Limits of Organic Life in Planetary Systems, Committee on the Origins and Evolution of Life, National Research Council. (2007) *The Limits of Organic Life in Planetary Systems*. The National Academies Press: Washington DC.

Cordier, D., Mousis, O., Lunine, J.I., Lavvas, P. & Vuitton, V. (2009) An Estimate of the Chemical Composition of Titan'S Lakes. *Astrophysical Journal Letters*, **707**, pp. L128-L131.

Cordier, D., Mousis, O., Lunine, J.I., Lebonnois, S., Rannou, P., Lavvas, P., Lobo, L.Q. & Ferreira, A.G.M. (2012) Titan's lakes chemical composition: Sources of uncertainties and variability. *Planetary and Space Science*, **61**, pp. 99-107.

Coustenis, A. & Bezard, B. (1995) Titans Atmosphere from Voyager Infrared Observations .4. Latitudinal Variations of Temperature and Composition. *Icarus*, **115**, pp. 126-140.

Coustenis, A., Gendron, E., Lai, O., Veran, J.P., Woillez, J., Combes, M., Vapillon, L., Fusco, T. & Mugnier, L. (2001) Images of Titan at 1.3 and 1.6 mu m with adaptive optics at the CFHT. *Icarus*, **154**, pp. 501-515.

Cruden, D.L., Wolfram, J.H., Rogers, R.D. & Gibson, D.T. (1992) Physiological-Properties of A Pseudomonas Strain Which Grows with Paraxylene in A 2-Phase (Organic-Aqueous) Medium. *Applied and Environmental Microbiology*, **58**, pp. 2723-2729.

Curtis, D.B., Glandorf, D.L., Toon, O.B., Tolbert, M.A., McKay, C.P. & Khare, B.N. (2005) Laboratory studies of butane nucleation on organic haze particles: application to Titan's clouds. *Journal of Physical Chemistry A*, **109**, pp. 1382-1390.

Curtis, D.B., Hatch, C.D., Hasenkopf, C.A., Toon, O.B., Tolbert, M.A., McKay, C.P. & Khare, B.N. (2008) Laboratory studies of methane and ethane adsorption and nucleation onto organic particles: Application to Titan's clouds. *Icarus*, **195**, pp. 792-801.

Czechowski, L. & Kossacki, K. (2009) Thermal convection in the porous methane-soaked regolith of Titan: Investigation of stability. *Icarus*, **202**, pp. 599-606.

Danielso, R.E., Caldwell, J.J. & Larach, D.R. (1973) Inversion in Atmosphere of Titan. *Icarus*, **20**, pp. 437-443.

Deamer, D.W. (1985) Boundary Structures Are Formed by Organic-Components of the Murchison Carbonaceous Chondrite. *Nature*, **317**, pp. 792-794.

Deamer, D.W. & Dworkin, J.P. (2005) *Chemistry and physics of primitive membranes.* Springer-Verlag: Berlin.

Deamer, D.W. & Oro, J. (1980) Role of Lipids in Prebiotic Structures. *Biosystems*, **12**, pp. 167-175.

Deamer, D.W. & Pashley, R.M. (1989) Amphiphilic Components of the Murchison Carbonaceous Chondrite - Surface-Properties and Membrane Formation. *Origins of Life and Evolution of the Biosphere*, **19**, pp. 21-38.

Dermott, S.F. & Sagan, C. (1995) Tidal Effects of Disconnected Hydrocarbon Seas on Titan. *Nature*, **374**, pp. 238-240.

Devaux, P.F. & Morris, R. (2004) Transmembrane asymmetry and lateral domains in biological membranes. *Traffic*, **5**, pp. 241-246.

Dianoux, A. & Lander, G. (2003) *Neutron Data Booklet*. Old City Publishing: Philadelphia.

Dimitriou-Christidis, P., Autenrierh, R.L. & Abraham, M.H. (2008) Quantitative structure-activity relationships for kinetic parameters of polycyclic aromatic hydrocarbon biotransformation. *Environmental Toxicology and Chemistry*, **27**, pp. 1496-1504.

Duarte, F.J. & James, R.O. (2003) Tunable solid-state lasers incorporating dye-doped, polymer-nanoparticle gain media. *Optics Letters*, **28**, pp. 2088-2090.

Dubouloz, N., Raulin, F., Lellouch, E. & Gautier, D. (1989) Titan Hypothesized Ocean Properties - the Influence of Surface-Temperature and Atmospheric Composition Uncertainties. *Icarus*, **82**, pp. 81-96.

Ebbing, M.H.K., Villa, M.J., Valpuesta, J.M., Prados, P. & de Mendoza, J. (2002) Resorcinarenes with 2-benzimidazolone bridges: Self-aggregation, self-assembled dimeric capsules, and guest encapsulation. *Proceedings of the National Academy of Sciences of the United States of America*, **99**, pp. 4962-4966.

Elachi, C., Wall, S., Allison, M., Anderson, Y., Boehmer, R., Callahan, P., Encrenaz, P., Flamini, E., Franceschetti, G., Gim, Y., Hamilton, G., Hensley, S., Janssen, M., Johnson, W., Kelleher, K., Kirk, R., Lopes, R., Lorenz, R., Lunine, J., Muhleman, D., Ostro, S., Paganelli, F., Picardi, G., Posa, F., Roth, L., Seu, R., Shaffer, S., Soderblom, L., Stiles, B., Stofan, E., Vetrella, S., West, R., Wood, C., Wye, L. & Zebker, H. (2005) Cassini radar views the surface of Titan. *Science*, **308**, pp. 970-974.

Elsayed, M.M., Abdallah, O.Y., Naggar, V.F. & Khalafallah, N.M. (2007) Lipid vesicles for skin delivery of drugs: Reviewing three decades of research. *International Journal of Pharmaceutics*, **332**, pp. 1-16.

Fielding, C.J. (2006) *Lipid Rafts and Caveolae - From Membrane Biophysics to Cell Biology*. John Wiley & Sons: New York.

Flasar, F.M. (1983) Oceans on Titan? *Science*, **221**, pp. 55-57.

Fortes, A.D. (2000) Exobiological implications of a possible ammonia-water ocean inside Titan. *Icarus*, **146**, pp. 444-452.

Fortes, A.D., Grindrod, P.M., Trickett, S.K. & Vocadlo, L. (2007) Ammonium sulfate on Titan: Possible origin and role in cryovolcanism. *Icarus*, **188**, pp. 139-153.

Fukuoka, T., Yanagihara, T., Ito, S., Imura, T., Morita, T., Sakai, H., Abe, M. & Kitamoto, D. (2012) Reverse vesicle formation from the yeast glycolipid biosurfactant mannosylerythritol lipid-D. *Journal of Oleo Science*, **61**, pp. 285-289.

Gautier, D. (1995) Titan's atmosphere composition: certainties and speculations. *Advances in Space Research Journal*, **15**, pp. 295-301.

Georgiou, C.D. & Deamer, D.W. (2014) Lipids as universal biomarkers of extraterrestrial life. *Astrobiology*, **14**, pp. 541-549.

Gilichinsky, D.A., Soina, V.S. & Petrova, M.A. (1993) Cryoprotective Properties of Water in the Earth Cryolithosphere and Its Role in Exobiology. *Origins of Life and Evolution of the Biosphere*, **23**, pp. 65-75.

Gilichinsky, D.A., Vorobyova, E.A., Erokhina, L.G., Fyordorovdayvdov, D.G. & Chaikovskaya, N.R. (1992) Long-Term Preservation of Microbial Ecosystems in Permafrost. *Life Sciences and Space Research Xxiv (3) : Planetary Biology and Origins of Life*, **12**, pp. 255-263.

Glindemann, D., Edwards, M. & Schrems, O. (2004) Phosphine and methylphosphine production by simulated lightning - a study for the volatile phosphorus cycle and cloud formation in the earth atmosphere. *Atmospheric Environment*, **38**, pp. 6867-6874.

Gregoriadis, G. (2008) Liposome research in drug delivery: The early days. *Journal of Drug Targeting*, **16**, pp. 520-524.

Griffith, C.A., Hall, J.L. & Geballe, T.R. (2000) Detection of daily clouds on Titan. *Science*, **290**, pp. 509-513.

Griffith, C.A., McKay, C.P. & Ferri, F. (2008) Titan'S Tropical Storms in An Evolving Atmosphere. *Astrophysical Journal Letters*, **687**, pp. L41-L44.

Griffith, C.A., Penteado, P., Rannou, P., Brown, R., Boudon, V., Baines, K.H., Clark, R., Drossart, P., Buratti, B., Nicholson, P., McKay, C.P., Coustenis, A., Negrao, A. & Jaumann, R. (2006) Evidence for a polar ethane cloud on Titan. *Science*, **313**, pp. 1620-1622.

Griffith, C.A., Penteado, P., Rodriguez, S., Le Mouelic, S., Baines, K.H., Buratti, B., Clark, R., Nicholson, P., Jaumann, R. & Sotin, C. (2009) Characterization of Clouds in Titan'S Tropical Atmosphere. *Astrophysical Journal Letters*, **702**, pp. L105-L109.

Griffith, C.A., Lora, J.M., Turner, J., Penteado, P.F., Brown, R.H., Tomasko, M.G., Doose, L. & See, C. (2012) Possible tropical lakes on Titan from observations of dark terrain. *Nature*, **486**, pp. 237-239.

Grindrod, P.M., Fortes, A.D., Nimmo, F., Feltham, D.L., Brodholt, J.P. & Vocadlo, L. (2008) The long-term stability of a possible aqueous ammonium sulfate ocean inside Titan. *Icarus*, **197**, pp. 137-151.

Hargreaves, W.R., Mulvihill, S.J. & Deamer, D.W. (1977) Synthesis of Phospholipids and Membranes in Prebiotic Conditions. *Nature*, **266**, pp. 78-80.

Harris, J.K., Rose, G.D. & Bruening, M.L. (2002) Spontaneous Generation of Multilamellar Vesicles from Ethylene Oxide/Butylene Oxide Diblock Copolymers. *Langmuir*, **18**, pp. 5337-5342.

Harroun, T.A., Koslowsky, M., Nieh, M.P., de Lannoy, C.F., Raghunathan, V.A. & Katsaras, J. (2005) Comprehensive examination of mesophases formed by DMPC and DHPC mixtures. *Langmuir*, **21**, pp. 5356-5361.

Hartley, G.S. (1936) *Aqueous Solution of Paraffinic-Chain Salts. A Study of Micelle Formation.* Herman: Paris.

Hawkins, M.L. & Grunlan, M.A. (2012) The protein resistance of silicones prepared with a PEO-silane amphiphile. *Journal of Materials Chemistry*, **22**, pp. 19540-19546.

Hayes, A., Aharonson, O., Callahan, P., Elachi, C., Gim, Y., Kirk, R., Lewis, K., Lopes, R., Lorenz, R., Lunine, J., Mitchell, K., Mitri, G., Stofan, E. & Wall, S. (2008) Hydrocarbon lakes on Titan: Distribution and interaction with a porous regolith. *Geophysical Research Letters*, **35** (9), L09204.

Haynes, W.M. & Lide, D.R. (2011) *CRC Handbook of Chemistry and Physics: a ready-reference book of chemical and physical data*. CRC Press: London.

Hazel, J.R. (1995) Thermal Adaptation in Biological-Membranes - Is Homeoviscous Adaptation the Explanation. *Annual Review of Physiology*, **57**, pp. 19-42.

Heipieper, H.J. & Debont, J.A.M. (1994) Adaptation of Pseudomonas-Putida S12 to Ethanol and Toluene at the Level of Fatty-Acid Composition of Membranes. *Applied and Environmental Microbiology*, **60**, pp. 4440-4444.

Heipieper, H.J., Weber, F.J., Sikkema, J., Keweloh, H. & Debont, J.A.M. (1994) Mechanisms of Resistance of Whole Cells to Toxic Organic-Solvents. *Trends in Biotechnology*, **12**, pp. 409-415.

Higgins, C.F. & Gottesman, M.M. (1992) Is the Multidrug Transporter A Flippase. *Trends in Biochemical Sciences*, **17**, pp. 18-21.

Horst, S., Vuitton, V. & Yelle, R., V. (2008) Origin of oxygen species in Titan's atmosphere. *Journal of Geophysical Research-Planets*, **113** (E10), p. E10006.

Hunten, D. M., Tomasko, M. G., Flasar, F. M., Samuelson, R. E., Strobel, D. F. and Stevenson, D. J. (1984) Titan. *In: Saturn*, edited by T. Gehrels and M. S. Matthews. University of Arizona Press: Tucson, pp. 671-759.

Hutzell, W.T., McKay, C.P., Toon, O.B. & Hourdin, F. (1996) Simulations of Titan's brightness by a two-dimensional haze model. *Icarus*, **119**, pp. 112-129.

Ibsen, S., Benchimol, M., Simberg, D., Schutt, C., Steiner, J. & Esener, S. (2011) A novel nested liposome drug delivery vehicle capable of ultrasound triggered release of its payload. *Journal of Controlled Release*, **155**, pp. 358-366.

Iess, L., Rappaport, N.J., Jacobson, R.A., Racioppa, P., Stevenson, D.J., Tortora, P., Armstrong, J.W. & Asmar, S.W. (2010) Gravity Field, Shape, and Moment of Inertia of Titan. *Science*, **327**, pp. 1367-1369.

Imanaka, H. & Smith, M.A. (2010) Formation of nitrogenated organic aerosols in the Titan upper atmosphere. *Proceedings of the National Academy of Sciences of the United States of America*, **107**, pp. 12423-12428.

Inoue, A., Yamamoto, M. & Horikoshi, K. (1991) Pseudomonas-Putida Which Can Grow in the Presence of Toluene. *Applied and Environmental Microbiology*, **57**, pp. 1560-1562.

Isken, S. & de Bont, J.A.M. (1998) Bacteria tolerant to organic solvents. *Extremophiles*, **2**, pp. 229-238.

Isken, S. & Debont, J.A.M. (1996) Active efflux of toluene in a solvent-resistant bacterium. *Journal of Bacteriology*, **178**, pp. 6056-6058.

Israelachvili, J.N. (1991) *Intermolecular and surface forces*. Academic Press: London.

Jennings, D., Cottini, V., Nixon, C., Flasar, F., Kunde, V., Samuelson, R., Romani, P., Hesman, B., Carlson, R., Gorius, N., Coustenis, A. & Tokano, T. (2011) Seasonal Changes in Titan's Surface Temperatures. *Astrophysical Journal Letters*, **737** (1), pp. L15.

Jennings, D.E., Flasar, F.M., Kunde, V.G., Samuelson, R.E., Pearl, J.C., Nixon, C.A., Carlson, R.C., Mamoutkine, A.A., Brasunas, J.C., Guandique, E., Achterberg, R.K., Bjoraker, G.L., Romani, P.N., Segura, M.E., Albright, S.A., Elliott, M.H., Tingley, J.S., Calcutt, S., Coustenis, A. & Courtin, R. (2009) Titan'S Surface Brightness Temperatures. *Astrophysical Journal Letters*, **691**, pp. L103-L105.

Jorgensen, A., Giessing, A.M.B., Rasmussen, L.J. & Andersen, O. (2005) Biotransformation of the polycyclic aromatic hydrocarbon pyrene in the marine polychaete Nereis virens. *Environmental Toxicology and Chemistry*, **24**, pp. 2796-2805.

Jost, P.C. & Griffith, O.H. (1982) *Lipid-protein interactions*. Wiley: New York.

Karkoschka, E. & Tomasko, M.G. (2009) Rain and dewdrops on titan based on in situ imaging. *Icarus*, **199**, pp. 442-448.

Katsaras, J., Harroun, T.A., Pencer, J. & Nieh, M.P. (2005) "Bicellar" lipid mixtures as used in biochemical and biophysical studies. *Naturwissenschaften*, **92**, pp. 355-366.

Keweloh, H. & Heipieper, H.J. (1996) Trans unsaturated fatty acids in bacteria. *Lipids*, **31**, pp. 129-137.

Khabibullaev, P.K. & Saidov, A.A. (2003) *Phase separation in soft matter physics, micellar solutions, microemulsions, critical phenomena*. Springer-Verlag: Berlin.

Khare, B.N., McKay, C.P., Cruikshank, D.P., Sekine, Y., Wilhite, P. & Ishihara, T. (2008) Optical and chemical properties of tholins. *Iau: Organic Matter in Space*, **4**, pp. 441-442.

Kim, K., Lee, S.J., Lee, K.H. & Lim, D.B. (1998) Isolation and characterization of toluene-sensitive mutants from the toluene-resistant bacterium Pseudomonas putida GM73. *Journal of Bacteriology*, **180**, pp. 3692-3696.

King, S.M. (1999) Small-angle Neutron Scattering. *In:* Pethrick, R.A. & Dawkins, J.V., *Modern Techniques for Polymer Characterisation*. John Wiley & Sons: Chichester, pp. 171-222.

Kratky, O. & Porod, G. (1949) Diffuse Small-Angle Scattering of X-Rays in Colloid Systems. *Journal of Colloid Science*, **4**, pp. 35-70.

Kuiper, G.P. (1944) Titan: a Satellite with an Atmosphere. *Astrophysical Journal*, **100**, pp. 378-388.

Kunieda, H., Akimaru, M., Ushio, N. & Nakamura, K. (1993a) Reverse Vesicles - Counter Structure of Biological-Membranes. *Journal of Colloid and Interface Science*, **156**, pp. 446-453.

Kunieda, H., Kanei, N., Uemoto, A. & Tobita, I. (1994) Structure of Reverse Vesicles in A Sucrose Monoalkanoate System. *Langmuir*, **10**, pp. 4006-4011.

Kunieda, H., Makino, S. & Ushio, N. (1991a) Anionic Reversed Vesicles. *Journal of Colloid and Interface Science*, **147**, pp. 286-288.

Kunieda, H., Nakamura, K., Davis, H.T. & Evans, D.F. (1991b) Formation of Vesicles and Microemulsions in A Water Tetraethylene Glycol Dodecyl Ether Dodecane System. *Langmuir*, **7**, pp. 1915-1919.

Kunieda, H., Nakamura, K. & Evans, D.F. (1991c) Formation of Reversed Vesicles. *Journal of the American Chemical Society*, **113**, pp. 1051-1052.

Kunieda, H., Nakamura, K., Infante, M.R. & Solans, C. (1992) Reversed Vesicles from Biocompatible Surfactants. *Advanced Materials*, **4**, pp. 291-293.

Kunieda, H., Nakamura, K., Olsson, U. & Lindman, B. (1993b) Spontaneous Formation of Reverse Vesicles. *Journal of Physical Chemistry*, **97**, pp. 9525-9531.

Kunieda, H., Shigeta, K. & Suzuki, M. (1999) Phase behavior and formation of reverse vesicles in long-polyoxyethylene-chain nonionic surfactant systems. *Langmuir*, **15**, pp. 3118-3122.

Kunieda, H., Ushio, N., Nakano, A. & Miura, M. (1993c) 3-Phase Behavior in A Mixed Sucrose Alkanoate and Polyethyleneglycol Alkyl Ether System. *Journal of Colloid and Interface Science*, **159**, pp. 37-44.

Kuruma, Y. (2007) Biosynthesis of phosphatidic acid in liposome compartments - Toward the self-reproduction of minimal cells. *Origins of Life and Evolution of Biospheres*, **37**, pp. 409-413.

Le Corre, L., Le Mouelic, S., Sotin, C., Combe, J.P., Rodriguez, S., Barnes, J.W., Brown, R.H., Buratti, B.J., Jaumann, R., Soderblom, J., Soderblom, L.A., Clark, R., Baines, K.H. & Nicholson, P.D. (2009) Analysis of a cryolava flow-like feature on Titan. *Planetary and Space Science*, **57**, pp. 870-879.

Le Mouelic, S., Paillou, P., Janssen, M.A., Barnes, J.W., Rodriguez, S., Sotin, C., Brown, R.H., Baines, K.H., Buratti, B.J., Clark, R.N., Crapeau, M., Encrenaz, P.J., Jaumann, R., Geudtner, D., Paganelli, F., Soderblom, L., Tobie, G. & Wall, S. (2008) Mapping and interpretation of Sinlap crater on Titan using Cassini VIMS and RADAR data. *Journal of Geophysical Research-Planets*, **113** (4), p. 4003.

LeBard, D.N., Levine, B.G., DeVane, R., Shinoda, W. & Klein, M.L. (2012) Premicelles and monomer exchange in aqueous surfactant solutions above and below the critical micelle concentration. *Chemical Physics Letters*, **522**, pp. 38-42.

Lebreton, J.P., Coustenis, A., Lunine, J., Raulin, F., Owen, T. & Strobel, D. (2009) Results from the Huygens probe on Titan. *Astronomy and Astrophysics Review*, **17**, pp. 149-179.

Lee, H.Y., Diehn, K.K., Ko, S.W., Tung, S.H. & Raghavan, S.R. (2010) Can Simple Salts Influence Self-Assembly in Oil? Multivalent Cations as Efficient Gelators of Lecithin Organosols. *Langmuir*, **26**, pp. 13831-13838.

Lee, H.Y., Hashizaki, K., Diehn, K. & Raghavan, S.R. (2013) Reverse self-assembly of lipid onions induced by gadolinium and calcium ions. *Soft Matter*, **9**, pp. 200-207.

Lee, S., Lee, J. & Choi, Y.W. (2007) Characterization and evaluation of freeze-dried liposomes loaded with ascorbyl palmitate enabling anti-aging therapy of the skin. *Bulletin of the Korean Chemical Society*, **28**, pp. 99-102.

Lellouch, E., Coustenis, A., Gautier, D., Raulin, F., Dubouloz, N. & Frere, C. (1989a) Titans Atmosphere and Hypothesized Ocean - A Reanalysis of the Voyager-1 Radio-Occultation and Iris 7.7-Mu-M Data. *Icarus*, **79**, pp. 328-349.

Leonov, A.V., Pishchal'nik, V.M. & Chicherina, O.V. (2010) Modeling of the marine environmental pollution by petroleum hydrocarbons and their biotransformation in Tatar Strait waters. *Water Resources*, **37**, pp. 220-233.

Li, H.G. & Hao, J.C. (2007) Reverse vesicles of salt-free catanionic surfactants in toluene/water mixtures. *Chemistry Letters*, **36**, pp. 702-703.

Li, H.G., Hao, J.C. & Wu, Z.H. (2008) Phase behavior and properties of reverse vesicles in salt-free catanionic surfactant mixtures. *Journal of Physical Chemistry B*, **112**, pp. 3705-3710.

Li, H.G., Xin, X., Kalwarczyk, T., Kalwarczyk, E., Niton, P., Holyst, R. & Hao, J.C. (2010) Reverse Vesicles from a Salt-Free Catanionic Surfactant System: A Confocal Fluorescence Microscopy Study. *Langmuir*, **26**, pp. 15210-15218.

Li, W., Li, B., Wang, Y.L., Zhang, J., Wang, S. & Wu, L.X. (2010) Vesicular assemblies of modified Mn-12 single molecular magnets. *Chemical Communications*, **46**, pp. 6548-6550.

Lindal, G.F., Wood, G.E., Hotz, H.B., Sweetnam, D.N., Eshleman, V.R. & Tyler, G.L. (1983) The Atmosphere of Titan - An Analysis of the Voyager-1 Radio Occultation Measurements. *Icarus*, **53**, pp. 348-363.

Lopes, R.M.C., Mitchell, K.L., Stofan, E.R., Lunine, J.I., Lorenz, R., Paganelli, F., Kirk, R.L., Wood, C.A., Wall, S.D., Robshaw, L.E., Fortes, A.D., Neish, C.D., Radebaugh, J., Reffet, E., Ostro, S.J., Elachi, C., Allison, M.D., Anderson, Y., Boehmer, R., Boubin, G., Callahan, P., Encrenaz, P., Flamini, E., Francescetti, G., Gim, Y., Hamilton, G., Hensley, S., Janssen, M.A., Johnson, W.T.K., Kelleher, K., Muhleman, D.O., Ori, G., Orosei, R., Picardi, G., Posa, F., Roth, L.E., Seu, R., Shaffer, S., Soderblom, L.A., Stiles, B., Vetrella, S., West, R.D., Wye, L. & Zebker, H.A. (2007) Cryovolcanic features on Titan's surface as revealed by the Cassini Titan Radar Mapper. *Icarus*, **186**, pp. 395-412.

Lopes, R.M.C., Stofan, E.R., Peckyno, R., Radebaugh, J., Mitchell, K.L., Mitri, G., Wood, C.A., Kirk, R.L., Wall, S.D., Lunine, J.I., Hayes, A., Lorenz, R., Farr, T., Wye, L., Craig, J., Ollerenshaw, R.J., Janssen, M., LeGall, A., Paganelli, F., West, R., Stiles, B., Callahan, P., Anderson, Y., Valora, P., Soderblom, L. & Cassini RADAR Team. (2010) Distribution and interplay of geologic processes on Titan from Cassini radar data. *Icarus*, **205**, pp. 540-558.

Lorenz, R.D., Mitchell, K.L., Kirk, R.L., Hayes, A.G., Aharonson, O., Zebker, H.A., Paillou, P., Radebaugh, J., Lunine, J.I., Janssen, M.A., Wall, S.D., Lopes, R.M., Stiles, B., Ostro, S., Mitri, G. & Stofan, E.R. (2008) Titan's inventory of organic surface materials. *Geophysical Research Letters*, **L35**, p. L02206.

Lorenz, R.D., Niemann, H.B., Harpold, D.N., Way, S.H. & Zarnecki, J.C. (2006a) Titan's damp ground: Constraints on Titan surface thermal properties from the temperature evolution of the Huygens GCMS inlet. *Meteoritics & Planetary Science*, **41**, pp. 1705-1714.

Lorenz, R.D., Wall, S., Radebaugh, J., Boubin, G., Reffet, E., Janssen, M., Stofan, E., Lopes, R., Kirk, R., Elachi, C., Lunine, J., Mitchell, K., Paganelli, F., Soderblom, L., Wood, C., Wye, L., Zebker, H., Anderson, Y., Ostro, S., Allison, M., Boehmer, R., Callahan, P., Encrenaz, P., Ori, G.G., Francescetti, G., Gim, Y., Hamilton, G., Hensley, S., Johnson, W., Kelleher, K., Muhleman, D., Picardi, G., Posa, F., Roth, L., Seu, R., Shaffer, S., Stiles, B., Vetrella, S., Flamini, E. & West, R. (2006b) The sand seas of Titan: Cassini RADAR observations of longitudinal dunes. *Science*, **312**, pp. 724-727.

Lorenz, R.D., Wood, C.A., Lunine, J.I., Wall, S.D., Lopes, R.M., Mitchell, K.L., Paganelli, F., Anderson, Y.Z., Wye, L., Tsai, C., Zebker, H. & Stofan, E.R. (2007) Titan's young surface: Initial impact crater survey by Cassini RADAR and model comparison. *Geophysical Research Letters*, **34**, pp. L07204.

Luisi, P.L., Stano, P., Rasi, S. & Mavelli, F. (2004) A possible route to prebiotic vesicle reproduction. *Artificial Life*, **10**, pp. 297-308.

Luisi, P.L., Walde, P. & Oberholzer, T. (1999) Lipid vesicles as possible intermediates in the origin of life. *Current Opinion in Colloid & Interface Science*, **4**, pp. 33-39.

Lunine, J.I. (2009) Saturn's Titan: A Strict Test for Life's Cosmic Ubiquity. *Proceedings of the American Philosophical Society*, **153**, pp. 403-418.

Lunine, J.I., Stevenson, D.J. & Yung, Y.L. (1983) Ethane Ocean on Titan. *Science*, **222**, pp. 1229-1230.

Mahabir, S., Wan, W., Katsaras, J. & Nieh, M.P. (2010) Effects of Charge Density and Thermal History on the Morphologies of Spontaneously Formed Unilamellar Vesicles. *Journal of Physical Chemistry B*, **114**, pp. 5729-5735.

Mahjoub, A., Carrasco, N., Dahoo, P.R., Gautier, T., Szopa, C. & Cernogora, G. (2012) Influence of methane concentration on the optical indices of Titan's aerosols analogues. *Icarus*, **221**, pp. 670-677.

Malheiros, P.d.S., Daroit, D.J. & Brandelli, A. (2010) Food applications of liposome-encapsulated antimicrobial peptides. *Trends in Food Science & Technology*, **21**, pp. 284-292.

Mason, P.C., Nagle, J.F., Epand, R.M. & Katsaras, J. (2001) Anomalous swelling in phospholipid bilayers is not coupled to the formation of a ripple phase. *Physical Review E*, **6303** (3), p. 0902

Mayo, L.A. & Samuelson, R.E. (2005) Condensate clouds in Titan's north polar stratosphere. *Icarus*, **176**, pp. 316-330.

Mays, H., Almgren, M., Dedinaite, A. & Claesson, P.M. (1999) Spontaneous formation of reverse vesicles with soybean phosphatidyl ethanolamine in mixture with triglyceride and some water. *Langmuir*, **15**, pp. 8072-8079.

McClay, K., Fox, B.G. & Steffan, R.J. (2000) Toluene monooxygenase-catalyzed epoxidation of alkenes. *Applied and Environmental Microbiology*, **66**, pp. 1877-1882.

McDonald, G.D., Khare, B.N., Thompson, W.R. & Sagan, C. (1991) $CH_4/NH_3/H_2O$ spark tholin: chemical analysis and interaction with Jovian aqueous clouds. *Icarus*, **94**, pp. 354-367.

McKay, C.P., Coustenis, A., Samuelson, R.E., Lemmon, M.T., Lorenz, R.D., Cabane, M., Rannou, P. & Drossart, P. (2001) Physical properties of the organic aerosols and clouds on Titan. *Planetary and Space Science*, **49**, pp. 79-99.

McKay, C.P., Pollack, J.B. & Courtin, R. (1989) The thermal structure of Titan's atmosphere. *Icarus*, **80**, pp. 23-53.

McKay, C.P., Pollack, J.B. & Courtin, R. (1991) The greenhouse and antigreenhouse effects on Titan. *Science*, **253**, pp. 1118-1121.

McKay, C.P. & Smith, H.D. (2005) Possibilities for methanogenic life in liquid methane on the surface of Titan. *Icarus*, **178**, pp. 274-276.

Menger, F.M. & Peresypkin, A.V. (2001) A combinatorially-derived structural phase diagram for 42 zwitterionic geminis. *Journal of the American Chemical Society*, **123**, pp. 5614-5615.

Mitri, G., Bland, M.T., Showman, A.P., Radebaugh, J., Stiles, B., Lopes, R.M.C., Lunine, J.I. & Pappalardo, R.T. (2010) Mountains on Titan: Modeling and observations. *Journal of Geophysical Research-Planets*, **115** (10), p. E10002

Mitri, G., Showman, A.P., Lunine, J.I. & Lorenz, R.D. (2007) Hydrocarbon lakes on Titan. *Icarus*, **186**, pp. 385-394.

Mollee, H., De Vrind, J. & De Vringer, T. (2000) Stable reversed vesicles in oil: Characterization studies and encapsulation of model compounds. *Journal of Pharmaceutical Sciences*, **89**, pp. 930-939.

Monnard, P.A. & Deamer, D.W. (2001) Nutrient uptake by protocells: A liposome model system. *Origins of Life and Evolution of the Biosphere*, **31**, pp. 147-155.

Monnard, P.A., Luptak, A. & Deamer, D.W. (2007) Models of primitive cellular life: polymerases and templates in liposomes. *Philosophical Transactions of the Royal Society B-Biological Sciences*, **362**, pp. 1741-1750.

Mori, K., Tsunemi, H., Katayama, H., Burrows, D.N., Garmire, G.P. & Metzger, A.E. (2004) An X-ray measurement of titan's atmospheric extent from its transit of the Crab nebula. *Astrophysical Journal*, **607**, pp. 1065-1069.

Morowitz, H.J., Heinz, B. & Deamer, D.W. (1988) The Chemical Logic of A Minimum Protocell. *Origins of Life and Evolution of the Biosphere*, **18**, pp. 281-287.

Mumma, M.J., Villanueva, G.L., Novak, R.E., Hewagama, T., Bonev, B.P., DiSanti, M.A., Mandell, A.M. & Smith, M.D. (2009) Strong Release of Methane on Mars in Northern Summer 2003. *Science*, **323**, pp. 1041-1045.

Murdan, S., Gregoriadis, G. & Florence, A.T. (1999) Inverse toroidal vesicles: precursors of tubules in sorbitan monostearate organogels. *International Journal of Pharmaceutics*, **183**, pp. 47-49.

Nagarajan, R. (2002) Molecular packing parameter and surfactant self-assembly: The neglected role of the surfactant tail. *Langmuir*, **18**, pp. 31-38.

Nakamura, K., Uemoto, A., Imae, T., Solans, C. & Kunieda, H. (1995) Stability and Size Control of Reverse Vesicles. *Journal of Colloid and Interface Science*, **170**, pp. 367-373.

Nieh, M.P., Raghunathan, V., Pabst, G., Harroun, T., Nagashima, K., Morales, H., Katsaras, J. & Macdonald, P. (2011) Temperature Driven Annealing of Perforations in Bicellar Model Membranes. *Langmuir*, **27**, pp. 4838-4847.

Niemann, H.B., Atreya, S.K., Bauer, S.J., Carignan, G.R., Demick, J.E., Frost, R.L., Gautier, D., Haberman, J.A., Harpold, D.N., Hunten, D.M., Israel, G., Lunine, J.I., Kasprzak, W.T., Owen, T.C., Paulkovich, M., Raulin, F., Raaen, E. & Way, S.H. (2005) The abundances of constituents of Titan's atmosphere from the GCMS instrument on the Huygens probe. *Nature*, **438**, pp. 779-784.

Nixon, C.A., Temelso, B., Vinatier, S., Teanby, N.A., Bezard, B., Achterberg, R.K., Mandt, K.E., Sherrill, C.D., Irwin, P.G.J., Jennings, D.E., Romani, P.N., Coustenis, A. & Flasar, F.M. (2012) Isotopic Ratios in Titan'S Methane: Measurements and Modeling. *Astrophysical Journal*, **749** (2) p.15.

Norman, L.H. & Fortes, A.D. (2011) Is there life on ... Titan? *Astronomy & Geophysics*, **52**, pp. 39-42.

Oda, Y., Suzuki, R., Utoguchi, N. & Maruyama, K. (2010) Drug and Gene Delivery System Using Liposome Technology. *Yakuzaigaku*, **70**, pp. 21-26.

Olsson, U., Nakamura, K., Kunieda, H. & Strey, R. (1996) Normal and reverse vesicles with nonionic surfactant: Solvent diffusion and permeability. *Langmuir*, **12**, pp. 3045-3054.

Ostwald, W. (1917) *An introduction to theorectical and applied colloid chemistry*. John Wiley & Sons: New York.

Owen, T. (1982) The atmosphere of Titan. *Journal of Molecular Evolution*, **18**, pp. 150-156.

Owen, T. (2005) Planetary science: Huygens rediscovers Titan. *Nature*, **438**, pp. 756-757.

Pabst, G., Kucerka, N., Nieh, M.P., Rheinstadter, M.C. & Katsaras, J. (2010) Applications of neutron and X-ray scattering to the study of biologically relevant model membranes. *Chemistry and Physics of Lipids*, **163**, pp. 460-479.

Pasek, M.A., Mousis, O. & Lunine, J.I. (2011) Phosphorus chemistry on Titan. *Icarus*, **212**, pp. 751-761.

Penteado, P.F., Griffith, C.A., Tomasko, M.G., Engel, S., See, C., Doose, L., Baines, K.H., Brown, R.H., Buratti, B.J., Clark, R., Nicholson, P. & Sotin, C. (2010) Latitudinal variations in Titan's methane and haze from Cassini VIMS observations. *Icarus*, **206**, pp. 352-365.

Pereira-Lachataignerais, J., Pons, R., Panizza, P., Courbin, L., Rouch, J. & Lopez, O. (2006) Study and formation of vesicle systems with low polydispersity index by ultrasound method. *Chemistry and Physics of Lipids*, **140**, pp. 88-97.

Peresypkin, A., Clavel, C. & Menger, F.M. (2007) Ambidextrous 'hybrid' fluorinated zwitterionic geminis: self-assembly in both organic and aqueous media. *Mendeleev Communications*, **17**, pp. 82-84.

Pershan, P.S. (1982) Lyotropic Liquid-Crystals. *Physics Today*, **35**, pp. 34-39.

Pilling, S., Andrade, D.P.P., Neto, A.C., Rittner, R. & de Brito, A.N. (2009) DNA Nucleobase Synthesis at Titan Atmosphere Analog by Soft X-rays. *Journal of Physical Chemistry A*, **113**, pp. 11161-11166.

Pinkart, H.C., Wolfram, J.W., Rogers, R. & White, D.C. (1996) Cell envelope changes in solvent-tolerant and solvent-sensitive Pseudomonas putida strains following exposure to o-xylene. *Applied and Environmental Microbiology*, **62**, pp. 1129-1132.

Prince, R. & Atlas, R.M. (2005) Bioremediation of marine oil spills. *Bioremediation: Applied Microbial Solutions for Real-World Environmental Cleanup*, pp. 269-292.

Quinn, P.J. & Cherry, R.J. (1992) *Structural and dynamic properties of lipids and membranes / edited by Peter J. Quinn, Richard J. Cherry*. Portland Press: Portland.

Rangelov, S., Almgren, M., Edwards, K. & Tsvetanov, C. (2004) Formation of normal and reverse bilayer structures by self-assembly of nonionic block copolymers bearing lipid-mimetic units. *Journal of Physical Chemistry B*, **108**, pp. 7542-7552.

Raulin, F. (1987) Organic chemistry in the oceans of Titan. *Advances in Space Research*, **7**, pp. 71-81.

Raulin, F., Bruston, P., Coll, P., Coscia, D., Gazeau, M.C., Guez, L. & Devanssay, E. (1994) Exobiology on Titan - A Reference Laboratory for Studying Prebiotic Chemistry on A Planetary Scale. *Journal of Biological Physics*, **20**, pp. 39-53.

Raulin, F., Cerceau, F., Hakdaoui, M. & Vargas, A. (1986) Prebiotic Chemical Evolution in Titans Ocean. *Origins of Life and Evolution of the Biosphere*, **16**, pp. 401-402.

Raulin, F., Dubouloz, N. & Frere, C. (1989) Titan's Ocean. *Origins of Life and Evolution of Biospheres*, **19**, pp. 471-472.

Raulin, F., Frere, C., Paillous, P., De, V.E., Do, L. & Khlifi, M. (1992) Titan and exobiological aspects of the Cassini-Huygens mission. *Journal of the British Interplanetary Society*, **45**, pp. 257-271.

Raymond, K. (2008) *General, organic, and biological chemistry : an integrated approach / Kenneth W. Raymond*. Wiley :New York.

Rivkina, E.M., Friedmann, E.I., McKay, C.P. & Gilichinsky, D.A. (2000) Metabolic activity of permafrost bacteria below the freezing point. *Applied and Environmental Microbiology*, **66**, pp. 3230-3233.

Rodriguez, S., Le Mouelic, S., Rannou, P., Tobie, G., Baines, K.H., Barnes, J.W., Griffith, C.A., Hirtzig, M., Pitman, K.M., Sotin, C., Brown, R.H., Buratti, B.J., Clark, R.N. & Nicholson, P.D. (2009) Global circulation as the main source of cloud activity on Titan. *Nature*, **459**, pp. 678-682.

Roe, H.G., de Pater, I. & McKay, C.P. (2004) Seasonal variation of Titan's stratospheric ethylene (C2H4) observed. *Icarus*, **169**, pp. 440-461.

Roos-Serote, M. (2005) The changing face of Titan's haze: Is it all dynamics? *Space Science Reviews*, **116**, pp. 201-210.

Rosenberg, E. (1993) Exploiting Microbial-Growth on Hydrocarbons - New Markets. *Trends in Biotechnology*, **11**, pp. 419-424.

Ruckenstein, E. & Nagarajan, R. (1980) Aggregation of amphiphiles in nonaqueous media. *The Journal of Physical Chemistry*, **84**, pp. 1349-1358.

Ruiz-Bermejo, M., Menor-Salvan, C., de la Fuente, J.L., Mateo-Marti, E., Osuna-Esteban, S., Martin-Gago, J.A. & Veintemillas-Verdaguer, S. (2009) CH4/N-2/H-2-spark hydrophobic tholins: A systematic approach to the characterisation of tholins. Part II. *Icarus*, **204**, pp. 672-680.

Russell, N.J. (1989) Functions of Lipids: Structural roles and membrane functions. *In:* Ratledge, C. & Wilkinson, S.G., *Microbial Lipids*. Academic Press: London, pp. 279-365.

Russell, N.J. (1992) Physiology and molecular biology of psychrophilic micro-organisms. *In:* Herbert, R.A. & Sharpe, R.J., *Molecular Biology and Biotechnology of Extremophiles.* Blackie: Glasgow, pp. 203-224.

Russell, N.J. & Nichols, D.S. (1999) Polyunsaturated fatty acids in marine bacteria - a dogma rewritten. *Microbiology-Sgm*, **145**, pp.767-779.

Sagan, C. & Dermott, S.F. (1982) The Tide in the Seas of Titan. *Nature*, **300**, pp. 731-733.

Sagan, C., Thompson, W.R. & Khare, B.N. (1992) Titan - A Laboratory for Prebiological Organic-Chemistry. *Accounts of Chemical Research*, **25**, pp. 286-292.

Salabat, A., Eastoe, J., Mutch, K.J. & Tabor, R.F. (2008) Tuning aggregation of microemulsion droplets and silica nanoparticles using solvent mixtures. *Journal of Colloid and Interface Science*, **318**, pp. 244-251.

Samuelson, R.E. & Mayo, L.A. (1991) Thermal Infrared Properties of Titans Stratospheric Aerosol. *Icarus*, **91**, pp. 207-219.

Sanchez-ferrer, A. & Garcia-carmona, F. (1992) Reverse Vesicles As A New System for Studying Enzymes in Organic-Solvents. *Biochemical Journal*, **285**, pp. 373-376.

Sanchez-ferrer, A. & Garcia-carmona, F. (1994) Biocatalysis in Reverse Self-Assembling Structures - Reverse Micelles and Reverse Vesicles. *Enzyme and Microbial Technology*, **16**, pp. 409-415.

Schaller, E.L., Brown, M.E., Roe, H.G. & Bouchez, A.H. (2006) A large cloud outburst at Titan's south pole. *Icarus*, **182**, pp. 224-229.

Schaller, E.L., Roe, H.G., Schneider, T. & Brown, M.E. (2009) Storms in the tropics of Titan. *Nature*, **460**, pp. 873-875.

Schneider, T., Graves, S., Schaller, E. & Brown, M. (2012) Polar methane accumulation and rainstorms on Titan from simulations of the methane cycle. *Nature*, **481**, pp. 58-61.

Schulze-Makuch, D. & Grinspoon, D.H. (2005) Biologically enhanced energy and carbon cycling on Titan? *Astrobiology.*, **5**, pp. 560-567.

Schulze-Makuch, D. & Grinspoon, D.H. (2006) Plausible metabolic pathways and energy cycling on Titan. *Origins of Life and Evolution of the Biosphere*, **36**, pp. 324-325.

Schulze-Makuch, D. & Irwin, L.N. (2006) The prospect of alien life in exotic forms on other worlds. *Naturwissenschaften*, **93**, pp. 155-172.

Sciamma-O'Brien, E., Carrasco, N., Szopa, C., Buch, A. & Cernogora, G. (2010) Titan's atmosphere: An optimal gas mixture for aerosol production? *Icarus*, **209**, pp. 704-714.

Segre, D., Ben-Eli, D., Deamer, D.W. & Lancet, D. (2001) The lipid world. *Origins of Life and Evolution of the Biosphere*, **31**, pp. 119-145.

Shrestha, L.K. & Aramaki, K. (2007) Phase Behavior of diglycerol monomyristate in different nonpolar organic solvent systems. *Journal of Dispersion Science and Technology*, **28**, pp. 1236-1241.

Shrestha, L.K., Kaneko, M., Sato, T., Acharya, D.P., Iwanaga, T. & Kunieda, H. (2006) Phase behavior of diglycerol fatty acid esters - Nonpolar oil systems. *Langmuir*, **22**, pp. 1449-1454.

Shrestha, L.K., Shrestha, R.G. & Aramaki, K. (2009) Self-Assembled Structures of Diglycerol Monolaurate- and Monomyristate in Olive Oil. *Journal of Dispersion Science and Technology*, **30**, pp. 1525-1532.

Sikkema, J., Debont, J.A.M. & Poolman, B. (1995) Mechanisms of Membrane Toxicity of Hydrocarbons. *Microbiological Reviews*, **59**, pp. 201-222.

Silva, B.F., Marques, E.F. & Olsson, U. (2008) Unusual vesicle-micelle transitions in a salt-free catanionic surfactant: Temperature and concentration effects. *Langmuir*, **24**, pp. 10746-10754.

Silvius, J.R. (2003) Fluorescence energy transfer reveals microdomain formation at physiological temperatures in lipid mixtures modeling the outer leaflet of the plasma membrane. *Biophysical Journal*, **85**, pp. 1034-1045.

Smith, G.N., Brown, P., Rogers, S.E. & Eastoe, J. (2013) Evidence for a Critical Micelle Concentration of Surfactants in Hydrocarbon Solvents. *Langmuir*, **29**, pp. 3252-3258.

Smith, P.H., Lemmon, M.T., Lorenz, R.D., Sromovsky, L.A., Caldwell, J.J. & Allison, M.D. (1996) Titan's surface, revealed by HST imaging. *Icarus*, **119**, pp. 336-349.

Soderblom, L.A., Tomasko, M.G., Archinal, B.A., Becker, T.L., Bushroe, M.W., Cook, D.A., Doose, L.R., Galuszka, D.M., Hare, T.M., Howington-Kraus, E., Karkoschka, E., Kirk, R.L., Lunine, J.I., McFarlane, E.A., Redding, B.L., Rizk, B., Rosiek, M.R., See, C. & Smith, P.H. (2007) Topography and geomorphology of the Huygens landing site on Titan. *Planetary and Space Science*, **55**, pp. 2015-2024.

Stan-Lotter, H. & Fendrihan, S. (2012) Adaption of Microbial Life to Environmental Extremes: Novel Research Results and Application. Springer: Vienna.

Stephan, K., Jaumann, R., Brown, R.H., Soderblom, J.M., Soderblom, L.A., Barnes, J.W., Sotin, C., Griffith, C.A., Kirk, R.L., Baines, K.H., Buratti, B.J., Clark, R.N., Lytle, D.M., Nelson, R.M. & Nicholson, P.D. (2010) Specular reflection on Titan: Liquids in Kraken Mare. *Geophysical Research Letters*, **37**, p. L07104.

Stofan, E.R., Elachi, C., Lunine, J.I., Lorenz, R.D., Stiles, B., Mitchell, K.L., Ostro, S., Soderblom, L., Wood, C., Zebker, H., Wall, S., Janssen, M., Kirk, R., Lopes, R., Paganelli, F., Radebaugh, J., Wye, L., Anderson, Y., Allison, M., Boehmer, R., Callahan, P., Encrenaz, P., Flamini, E., Francescetti, G., Gim, Y., Hamilton, G., Hensley, S., Johnson, W.T., Kelleher, K., Muhleman, D., Paillou, P., Picardi, G., Posa, F., Roth, L., Seu, R., Shaffer, S., Vetrella, S. & West, R. (2007) The lakes of Titan. *Nature*, **445**, pp. 61-64.

Stoker, C.R., Boston, P.J., Mancinelli, R.L., Segal, W., Khare, B.N. & Sagan, C. (1990) Microbial metabolism of tholin. *Icarus*, **85**, pp. 241-256.

Strobel, D.F. (2010) Molecular hydrogen in Titan's atmosphere: Implications of the measured tropospheric and thermospheric mole fractions. *Icarus*, **208**, pp. 878-886.

Strobel, D.F. (2012) Hydrogen and methane in Titan's atmosphere: chemistry, diffusion, escape, and the Hunten limiting flux principle. *Canadian Journal of Physics*, **90**, pp. 795-805.

Takajo, Y., Matsuki, H., Matsubara, H., Tsuchiya, K., Aratono, M. & Yamanaka, M. (2010) Structural and morphological transition of long-chain phospholipid vesicles induced by mixing with short-chain phospholipid. *Colloids Surf B Biointerfaces*, **76**, pp. 571-576.

Tanford, C. (1980) *The Hydrophobic Effect*. Wiley: New York.

Taulier, N., Ober, R., Gouzy, M.F., Guidetti, B., Rico-lattes, I. & Urbach, W. (2002) Behavior of a reverse lamellar phase in the presence of low molecular weight triblock molecules. *Langmuir*, **18**, pp. 68-73.

Teanby, N.A., de Kok, R., Irwin, P.G.J., Osprey, S., Vinatier, S., Gierasch, P.J., Read, P.L., Flasar, F.M., Conrath, B.J., Achterberg, R.K., Bezard, B., Nixon, C.A. & Calcutt, S.B. (2008a) Titan's winter polar vortex structure revealed by chemical tracers. *Journal of Geophysical Research-Planets*, **113**, p. E12003.

Teanby, N.A., Irwin, P.G.J., de Kok, R., Nixon, C.A., Coustenis, A., Royer, E., Calcutt, S.B., Bowles, N.E., Fletcher, L., Howett, C. & Taylor, F.W. (2008b) Global and temporal variations in hydrocarbons and nitriles in Titan's stratosphere for northern winter observed by Cassini/CIRS. *Icarus*, **193**, pp. 595-611.

Thompson, W.R., Zollweg, J.A. & Gabis, D.H. (1992) Vapor-Liquid-Equilibrium Thermodynamics of N2 + Ch4 - Model and Titan Applications. *Icarus*, **97**, pp. 187-199.

Tobie, G., Grasset, O., Lunine, J.I., Mocquet, A. & Sotin, C. (2005) Titan's internal structure inferred from a coupled thermal-orbital model. *Icarus*, **175**, pp. 496-502.

Tobie, G., Lunine, J.I. & Sotin, C. (2006) Episodic outgassing as the origin of atmospheric methane on Titan. *Nature*, **440**, pp. 61-64.

Tokano, T. (2005a) Meteorological assessment of the surface temperatures on Titan: constraints on the surface type. *Icarus*, **173**, pp. 222-242.

Tokano, T. (2005b) Thermal structure of putative hydrocarbon lakes on Titan. *Space Life Sciences: Astrobiology: Steps Toward Origin of Life and Titan Before Cassini*, **36**, pp. 286-294.

Tokano, T. (2009) Impact of seas/lakes on polar meteorology of Titan: Simulation by a coupled GCM-Sea model. *Icarus*, **204**, pp. 619-636.

Tokano, T., McKay, C.P., Neubauer, F.M., Atreya, S.K., Ferri, F., Fulchignoni, M. & Niemann, H.B. (2006) Methane drizzle on Titan. *Nature*, **442**, pp. 432-435.

Tomasko, M.G., Archinal, B., Becker, T., Bezard, B., Bushroe, M., Combes, M., Cook, D., Coustenis, A., DE, B.C., Dafoe, L.E., Doose, L., Doute, S., Eibl, A., Engel, S., Gliem, F., Grieger, B., Holso, K., Howington-Kraus, E., Karkoschka, E., Keller, H.U., Kirk, R., Kramm, R., Kuppers, M., Lanagan, P., Lellouch, E., Lemmon, M., Lunine, J., McFarlane, E., Moores, J., Prout, G.M., Rizk, B., Rosiek, M., Rueffer, P., Schroder, S.E., Schmitt, B., See, C., Smith, P., Soderblom, L., Thomas, N. & West, R. (2005) Rain, winds and haze during the Huygens probe's descent to Titan's surface. *Nature*, **438**, pp. 765-778.

Toon, O.B., McKay, C.P., Courtin, R. & Ackerman, T.P. (1988) Methane Rain on Titan. *Icarus*, **75**, pp. 255-284.

Torres, S., Pandey, A. & Castro, G.R. (2011) Organic solvent adaptation of Gram positive bacteria: Applications and biotechnological potentials. *Biotechnology Advances*, **29**, pp. 442-452.

Trainer, M.G., Pavlov, A.A., DeWitt, H.L., Jimenez, J.L., McKay, C.P., Toon, O.B. & Tolbert, M.A. (2006) Organic haze on Titan and the early Earth, *Proceedings of the National Academy of Sciences of the United States of America*, **103**, pp. 18035-18042.

Tung, S.H., Lee, H.Y. & Raghavan, S.R. (2008) A facile route for creating "Reverse" vesicles: Insights into "Reverse" self-assembly in organic liquids. *Journal of the American Chemical Society*, **130**, pp. 8813-8817.

Turco Liveri, V. (2006) *Controlled Synthesis of Nanoparticles in Microheterogeneous Systems*. Springer: *Dordrecht Heidelberg London* New York.

Turtle, E., Perry, J., Hayes, A., Lorenz, R., Barnes, J., McEwen, A., West, R., Del Genio, A., Barbara, J., Lunine, J., I, Schaller, E., Ray, T., Lopes, R. & Stofan, E. (2011) Rapid and Extensive Surface Changes Near Titan's Equator: Evidence of April Showers. *Science*, **331**, pp. 1414-1417.

Turtle, E.P., Perry, J.E., McEwen, A.S., DelGenio, A.D., Barbara, J., West, R.A., Dawson, D.D. & Porco, C.C. (2009) Cassini imaging of Titan's high-latitude lakes, clouds, and south-polar surface changes. *Geophysical Research Letters*, **36**, p. L02204,

Venkatraman, S.S., Ma, L.L., Natarajan, J.V. & Chattopadhyay, S. (2010) Polymer- and liposome-based nanoparticles in targeted drug delivery. *Frontiers in bioscience (Scholar edition)*, **2**, pp. 801-814.

Vervack, R.J., Sandel, B.R. & Strobel, D.F. (2004) New perspectives on Titan's upper atmosphere from a reanalysis of the Voyager 1 UVS solar occultations. *Icarus*, **170**, pp. 91-112.

Wall, S., Hayes, A., Bristow, C., Lorenz, R., Stofan, E., Lunine, J., Le Gall, A., Janssen, M., Lopes, R., Wye, L., Soderblom, L., Paillou, P., Aharonson, O., Zebker, H., Farr, T., Mitri, G., Kirk, R., Mitchell, K., Notarnicola, C., Casarano, D. & Ventura, B. (2010) Active shoreline of Ontario Lacus, Titan: A morphological study of the lake and its surroundings. *Geophysical Research Letters*, 37, p. L05252.

Wang, C.C., Atreya, S.K. & Signorell, R. (2010) Evidence for layered methane clouds in Titan's troposphere. *Icarus*, **206**, pp. 787-790.

Weber, F.J., Isken, S. & Debont, J.A.M. (1994) Cis-Trans Isomerization of Fatty-Acids As A Defense-Mechanism of Pseudomonas-Putida Strains to Toxic Concentrations of Toluene. *Microbiology-Uk*, **140**, pp. 2013-2017.

Wilson, E.H. & Atreya, S.K. (2004) Current state of modeling the photochemistry of Titan's mutually dependent atmosphere and ionosphere. *Journal of Geophysical Research-Planets*, **109** (6), p. E06002

Woon, D.E. (2006) Modeling chemical growth processes in Titan's atmosphere: 1. Theoretical rates for reactions between benzene and the ethynyl (C_2H) and cyano (CN) radicals at low temperature and pressure. *Chemical Physics*, **331**, pp. 67-76.

Woon, D.E. & Park, J.Y. (2009) Modeling chemical growth processes in Titan's atmosphere 2. Theoretical study of reactions between C2H and ethene, propene, 1-butene, 2-butene, isobutene, trimethylethene, and tetramethylethene. *Icarus*, **202**, pp. 642-655.

Wu, W.G., Chi, L.M., Yang, T.S. & Fang, S.Y. (1991) Freezing of Phosphocholine Headgroup in Fully Hydrated Sphingomyelin Bilayers and its Effect on the Dynamics of Nonfreezable Water at Subzero Temperatures. *Journal of Biological Chemistry*, **266**, pp. 13602-13606.

Xu, X.N., Wang, L. & Li, Z.T. (2009) Reverse vesicles formed by hydrogen bonded arylamide-derived triammonium cyclophanes and hexaammonium capsule. *Chemical Communications*, **43,** pp. 6634-6636.

Yan, Y., Li, B., Li, W., Li, H.L. & Wu, L.X. (2009) Controllable vesicular structure and reversal of a surfactant-encapsulated polyoxometalate complex. *Soft Matter*, **5**, pp. 4047-4053.

Yelle, R.V., Strobel, D.F., Lellouch, E. & Gautier, D. (1997) Engineering models for Titan's atmosphere. *In:* Lebreton, J.P., *Huygens Science, Payload and Mission*. ESA SP, pp. 243-256.

Young, C.L., Fogg, P.G.T., Clever, H.L. & Hayduk, W. (1985) *Ammonia, Amines, Phosphine, Arsine, Stibine, Silane, Germane and Stannane in Organic Solvents.* Pergamon Press: Oxford.

Zdziennicka, A., Szymczyk, K., Krawczyk, J. & Janczuk, B. (2012) Critical micelle concentration of some surfactants and thermodynamic parameters of their micellization. *Fluid Phase Equilibria*, **322**, pp. 126-134.

Zhang, J., Song, A., Li, Z., Xu, G. & Hao, J. (2010a) Phase Behaviors and Self-Assembly Properties of Two Catanionic Surfactant Systems: $C_{(8)}F_{(17)}COOH/TTAOH/H_{(2)}O$ and $C_{(8)}H_{(17)}COOH/TTAOH/H_{(2)}O$. *Journal of Physical Chemistry B*, **114**, pp. 13128-13135.

Zhang, Y.H.P., Sun, J.B. & Zhong, J.J. (2010b) Biofuel production by *in vitro* synthetic enzymatic pathway biotransformation. *Current Opinion in Biotechnology*, **21**, pp. 663-669.

Zhao, Y.H., Abraham, M.H. & Zissimos, A.M. (2003) Fast calculation of van der Waals volume as a sum of atomic and bond contributions and its application to drug compounds. *Journal of Organic Chemistry*, **68**, pp. 7368-7373.

Appendix I: List of synthesised samples

Date Finished Initial Prep. = date of first sonication.

Refer to Appendix II for sonication details and history for each sample.

RVe1a: Amphiphiles used in RVe1a were PC18 99% and PC4:0.

RVe1a Sample 99% C18 / C4	Date Finished Initial Prep.	Ratio (Ro)		Solvent		Concentration (mM)		NaCl concentration (mM)	
		Aim	Measured	Type	Quantity (ml)	Aim	Measured	Aim	Measured
A1	19 Jan 11	2.5	2.7	CyHex	4	30	30.1	10	10
A 1:1ml	22 Jan 11	2.5	2.7	CyHex	1	15	-	10	10
A 1:3ml	22 Jan 11	2.5	2.7	CyHex	3	22.5	-	10	10
B2	19 Jan 11	3.5	3.6	CyHex	4	30	29.7	10	10
C3	19 Jan 11	4.5	5	CyHex	4	30	31	10	10
A4	8 Nov 10	2.5	2.4	CyHex	4	30	28.5	5	5→~1000
B5	8 Nov 10	3.5	3.7	CyHex	4	30	30.4	5	5→~1000
C6	8 Nov 10	4.5	5.1	CyHex	4	30	31.6	5	5→~1000
A7	20 Jan 11	2.5	2.55	Hexane	4	30	29.8	10	10
B8	20 Jan 11	3.5	3.6	Hexane	4	30	29.7	10	10
C9	20 Jan 11	4.5	5.1	Hexane	4	30	29.4	10	10
A10	8 Nov 2010	2.5	2.2	Hexane	4	30	29.2	5	5→~1000
B11	8 Nov 2010	3.5	3.5	Hexane	4	30	30.7	5	5→~1000
C12	8 Nov 2010	4.5	4.9	Hexane	4	30	30.3	5	5→~1000
A13	27 Jan 11	2.5	2.55	Pentane	4	30	29.8	10	10
B14	27 Jan 11	3.5	3.7	Pentane	4	30	30.4	10	10
C15	27 Jan 11	4.5	5.6	Pentane	4	30	29.7	10	10
A16	8 Nov 2010	2.5	2.3	Pentane	4	30	27.3	5	5→~1000

B17	8 Nov 2010	3.5	3.7	Pentane	4	30	31.9	5	5→~1000
C18	8 Nov 2010	4.5	5.1	Pentane	4	30	31.6	5	5→~1000
A4b	19 Jan 2011	2.5	2.7	CyHex	4	30	30.1	10	10
B5b	19 Jan 2011	3.5	3.7	CyHex	4	30	31.9	10	10
C6b	19 Jan 2011	4.5	8.1	CyHex	4	30	29.6	10	10
22	31 Jan 2011	2.5	2.4	Butane	4	30	29.5	10	10
23	31 Jan 2011	3.5	3.3	Butane	4	30	29.4	10	10
24	31 Jan 2011	4.5	4.3	Butane	4	30	31	10	10
25	1 Feb 2011	2.5	2.7	Propane	2	30	65.9	10	20
27	1 Feb 2011	4.5	5.2	Propane	3	30	40	10	13
RVe1a(fl) 28	18 Jun 2014	2.5	2.5	CyHex	2	10	10	5	5
RVe1a(fl) 29	18 Jun 2014	3.5	3.5	CyHex	2	30	30	5	5
RVe1a(fl) 30	18 Jun 2014	7	7	CyHex	2	20	19.9	5	11
RVe1a(fl) 6rep	18 Jun 2014	8	6.5	CyHex	2	30	30	10	10
RVe1a(fl) 31	18 Jun 2014	2.5	2.5	Hexane	2	30	30.1	5	6.8
RVe1a(fl) 32	18 Jun 2014	8	7.7	CyHex	2	20	20.1	10	13
RVe1a(fl) 33	18 Jun 2014	4.5	4.5	Hexane	2	30	30	10	12
RVe1a(fl) 16rep	18 Jun 2014	2.5	2.5	Pentane	2	30	30	5	5

RVe1b: Amphiphiles used in RVe1b were PC18 99% and PC4:0.

RVe1b Sample 99% C18 / C4	Date Finished Initial Prep.	Ratio (Ro)		Solvent		Concentration (mM)		NaCl concentration (mM)	
		Aim	Measured	Type	Quantity (ml)	Aim	Measured	Aim	Measured
T2Hep	6 Feb 12	2.5	2.57	Heptane	2	30	30.4	3.5	4.5
T3CyHex	6 Feb 12	2.5	2.57	CyHex	2	30	30.4	3.5	4.5
T4Hex	6 Feb 12	2.5	2.57	Hexane	2	30	30.4	3.5	4.5
CyHex4	10 Feb 12	4	4	CyHex	2	20	20.1	5	5

CyHex5	10 Feb 12	5	5	CyHex	2	20	20	5	5
CyHex6	10 Feb 12	6	6	CyHex	2	20	19.9	5	5
CyHex7	10 Feb 12	7	6.8	CyHex	2	20	20.1	5	5
CyHex8	10 Feb 12	8	8	CyHex	2	20	20.2	5	5
RVe1b(fl) T3rep	18 Jun 2014	2.5	2.5	CyHex	2	30	30	5	12
RVe1b(fl) T2rep	18 Jun 2014	2.5	2.5	Heptane	2	30	30	5	5
RVe1b(fl) T4rep	18 Jun 2014	2.5	2.5	Hexane	2	30	30.1	5	17

RVe1c: Amphiphiles used in RVe1c were PC18 95% and PC4:0.

RVe1c Sample 95% C18 / C4	Date Finished Initial Prep.	Ratio (Ro)		Solvent		Concentration (mM)		NaCl concentration (mM)	
		Aim	Measured	Type	Quantity (ml)	Aim	Measured	Aim	Measured
RVe1c 1	1 Mar 12	2.5	2.6	CyHex	2	20	20.0	5	6.8
RVe1c 2	8 Mar 12	2.5	2.6	CyHex	2	20	20.0	5	6.0
RVe1c 3	30 Mar 12	2.5	2.5	CyHex	4	20	20.3	3.5	3.5
RVe1c 4	30 Mar 12	2.5	2.5	Heptane	4	20	20.3	3.5	3.5
RVe1c 5	30 Mar 12	2.5	2.5	Hexane	4	20	20.3	3.5	3.5
RVe1c 6	30 Mar 12	2.5	2.5	Pentane	4	20	20.3	3.5	3.5
RVe1c 7	30 Mar 12	3.5	3.3	CyHex	2	20	19.6	3.5	3.5
RVe1c 8	30 Mar 12	3.5	3.3	Heptane	2	20	19.6	3.5	3.5
RVe1c 9	30 Mar 12	3.5	3.3	Hexane	2	20	19.6	3.5	3.5
RVe1c 10	30 Mar 12	3.5	3.3	Pentane	2	20	19.6	3.5	3.5
RVe1c 11	30 Mar 12	4.5	4.2	CyHex	2	20	20.2	3.5	3.5
RVe1c 12	30 Mar 12	4.5	4.2	Heptane	2	20	20.2	3.5	3.5
RVe1c 13	30 Mar 12	4.5	4.2	Hexane	2	20	20.2	3.5	3.5
RVe1c 14	30 Mar 12	4.5	4.2	Pentane	2	20	20.2	3.5	3.5
RVe1c 15	18 Jun 2014	7	7.1	CyHex	4	20	20	5	11

SANS

SANS Sample 95% C18 / C4	Date Finished Initial Prep.	Ratio (Ro)		Solvent		Concentration (mM)		NaCl concentration (mM)	
		Aim	Measured	Type	Quantity (ml)	Aim	Measured	Aim	Measured
SANS 1	-	-	-	Deuterated heptane	0.35	-	-	-	-
SANS 2	16 Nov 12	3.5	3.4	Deuterated heptane	1	20	19.9	3.5	5.6
SANS 3	-	-	-	Deuterated pentane	0.35	-	-	-	-
SANS 4	21 Nov 12	3.5	3.4	Deuterated pentane	1	20	19.9	3.5	5.6
SANS 5	-	-	-	Deuterated hexane	0.35	-	-	-	-
SANS 6	16 Nov 12	3.5	3.4	Deuterated hexane	1	20	19.9	3.5	5.6
SANS 7	-	-	-	Deuterated cyclohexane	0.35	-	-	-	-
SANS 8	21 Nov 12	3.5	3.4	Deuterated cyclohexane	1	20	19.9	3.5	5.6

SAXS

SANS Sample 95% C18 / C4	Date Finished Initial Prep.	Ratio (Ro)		Solvent		Concentration (mM)		NaCl concentration (mM)	
		Aim	Measured	Type	Quantity (ml)	Aim	Measured	Aim	Measured
SAXS 1	16 Nov 2012	-	-	Heptane	4	-	-	-	-
SAXS 2	16 Nov 2012	2.5	2.5	Heptane	4	20	20.0	3.5	4.0

SAXS 3									
SAXS 4	16 Nov 2012	3.5	3.5	Heptane	4	20	20.0	3.5	4.1
SAXS 5									
SAXS 6	16 Nov 2012	4.5	4.5	Heptane	4	20	20.0	3.5	3.4
SAXS 7									
SAXS 8	16 Nov 2012	-	-	Pentane	4	-	-	-	-
SAXS 9	16 Nov 2012	2.5	2.5	Pentane	4	20	20.0	3.5	4.0
SAXS 10									
SAXS 11	16 Nov 2012	3.5	3.5	Pentane	4	20	20.0	3.5	4.1
SAXS 12									
SAXS 13	16 Nov 2012	4.5	4.5	Pentane	4	20	20.0	3.5	3.4
SAXS 14									
SAXS 15	16 Nov 2012	-	-	Hexane	4	-	-	-	-
SAXS 16	16 Nov 2012	2.5	2.5	Hexane	4	20	20.0	3.5	4.0
SAXS 17									
SAXS 18	16 Nov 2012	3.5	3.5	Hexane	4	20	20.0	3.5	4.1
SAXS 19									
SAXS 20	16 Nov 2012	4.5	4.5	Hexane	4	20	20.0	3.5	3.4
SAXS 21									
SAXS 22	16 Nov 2012	-	-	CyHex	4	-	-	-	-
SAXS 23	16 Nov 2012	2.5	2.6	CyHex	4	15	15.0	3.5	7.5
SAXS 24									
SAXS 25	16 Nov 2012	3.5	3.5	CyHex	4	15	15.1	3.5	7.5
SAXS 26									
SAXS 27	16 Nov 2012	4.5	4.6	CyHex	4	15	15.0	3.5	7.5
SAXS 28									
SAXS 29	4 Dec 12	-	-	Butane	0.5	-	-	-	-
SAXS 30	4 Dec 12	3.5	3.5	Butane	2	20	? due to evaporation	3.5	4.1
SAXS 31									

SAXS 32	4 Dec 12	2.5	2.5	Butane	2	20	? due to evaporation	3.5	4.0
SAXS 33									
SAXS 34	4 Dec 12	-	-	Propane	0.5	-	-	-	-
SAXS 35	4 Dec 12	3.5	3.5	Propane	2	20	? due to evaporation	3.5	4.1
SAXS 36									
SAXS 37	4 Dec 12	2.5	2.5	Propane	2	20	? due to evaporation	3.5	4.0
SAXS 38									
SAXS 40	16 Nov 2012	-	-	Octane	4	-	-	-	-
SAXS 41	16 Nov 2012	2.5	2.5	Octane	4	20	20.0	3.5	7.5
SAXS 42									
SAXS 43	16 Nov 2012	3.5	3.5	Octane	4	20	19.9	3.5	5.6
SAXS 44									
SAXS 45	16 Nov 2012	4.5	4.5	Octane	4	20	19.9	3.5	6.4
SAXS 46									

Appendix II: List of sample preparation methods

Key:

CyHex = Cyclohexane

Evap = Evaporation

RVe1a experiments

RVe1a Sample 99% C18 / C4	Date Finished Prep.	Solvent	Methanol Prep?	Glove bag Prep?	Hydrocarbon mixing			Sonication			Notes
					Time (hrs)	Temp (°C)	RPM	Type	Time (min)	Setting/ Reactivity	
A1	19 Jan 11	CyHex	No	Yes	41	30	250	Small Bath	25	Weak	A1 transformed into A1:1 and A1:3 samples.
A 1:1ml	19 Jan 11	CyHex	-	-	-	-	-	Small Bath	+20	Weak	
	22 Mar 12				-	-	-	Large bath	30	Strong	
A 1:3ml	19 Jan 11	CyHex	-	-	-	-	-	Small Bath	+20	Weak	
	22 Mar 12				-	-	-	Large bath	30	Strong	
B2	19 Jan 11	CyHex	No	Yes	41	30	250	Small Bath	25	Weak	
C3	19 Jan 11	CyHex	No	Yes	41	30	250	Small Bath	25	Weak	
A4	8 Nov 10	CyHex	No	Yes	3	60	250	Probe	10	~5amps	
B5	8 Nov 10	CyHex	No	Yes	2	60	250	Probe	10	~5amps	
C6	8 Nov 10	CyHex	No	Yes	3	60	250	Probe	5	~5amps	
A7	20 Jan 11	Hexane	No	Yes	23	37	250	Small Bath	30	Weak	
B8	20 Jan 11	Hexane	No	Yes	23	37	250	Small Bath	30	Weak	
C9	20 Jan 11	Hexane	No	Yes	23	37	250	Small Bath	30	Weak	
A10	8 Nov 2010	Hexane	No	Yes	2	60	250	Probe	5	~5amps	
B11	8 Nov 2010	Hexane	No	Yes	2	60	250	Probe	5	~5amps	
C12	8 Nov 2010	Hexane	No	Yes	2	60	250	Probe	5	~5amps	

A13	27 Jan 11	Pentane	No	Yes	6	30	250	Small Bath	30	Weak	Ice in sonicating bath.
B14	27 Jan 11	Pentane	No	Yes	6	30	250	Small Bath	30	Weak	Ice in sonicating bath.
C15	27 Jan 11	Pentane	No	Yes	6	30	250	Small Bath	30	Weak	Ice in sonicating bath.
A16	8 Nov 2010	Pentane	No	Yes	2	30	250	Probe	5	~5amps	
B17	8 Nov 2010	Pentane	No	Yes	2	30	250	Probe	5	~5amps	
C18	8 Nov 2010	Pentane	No	Yes	2	30	250	Probe	5	~5amps	
A4b	19 Jan 11	CyHex	No	Yes	1	50	250	Small Bath	30	Weak	
	22 Mar 12				-	-	-	Large bath	30	Strong	
	3 April 12				-	-	-	Probe	10	8-12 amps	
B5b	19 Jan 11	CyHex	No	Yes	1	50	250	Small Bath	30	Weak	
	22 Mar 12				-	-	-	Large bath	30	Strong	
	3 April 12				-	-	-	Probe	5	10-12 amps	
C6b	19 Jan 11	CyHex	No	Yes	1	50	250	Small Bath	30	Weak	
	22 Mar 12				-	-	-	Large bath	30	Strong	
	3 April 12				-	-	-	Probe	5	10 amps	
22	31 Jan 11	Butane	No	Yes	1min hand shaken			Small Bath	120	Weak	Sonication: 1hr NaCl + ice (-20°C) and 1hr CaCl2 · 6H2O + ice (-55°C). Some evap when taking TEM samples.
23	31 Jan 11	Butane	No	Yes	1min hand shaken			Small Bath	120	Weak	
24	31 Jan 11	Butane	No	Yes	1min hand shaken			Small Bath	120	Weak	
25	1 Feb 11	Propane	No	Yes	-	-	-	Small Bath	36	Weak	Sonication: 1hr acetonitrile + dry ice (-40°C). Total evap of 26 and some evap of 27 when taking TEM samples.
26	-	Propane	No	Yes	No solvent for this sample			-	-	-	
27	1 Feb 11	Propane	No	Yes	-	-	-	Small Bath	36	Weak	
RVe1a(fl) 28	18 Jun 14	CyHex	No	No	24	30	250	Small Bath	30	Weak	Rhodamine b included
RVe1a(fl) 29	18 Jun 14	CyHex	No	No	1	60	250	Probe	10	5 amps	Rhodamine b included
RVe1a(fl) 30	18 Jun 14	CyHex	No	No	24	60	250	Small Bath	30	Weak	Rhodamine b included
RVe1a(fl) 6rep	18 Jun 14	CyHex	No	No	1	60	250	Small Beth	30	Weak	Rhodamine b included

RVe1a(fl) 31	18 Jun 14	Hexane	No	No	2	60	250	Small Bath	30	Weak	Rhodamine b included
RVe1a(fl) 32	18 Jun 14	CyHex	No	No	1	60	250	Small Bath	30	Weak	Rhodamine b included
RVe1a(fl) 33	18 Jun 14	Hexane	No	No	2	60	250	Probe	5	8 amps	Rhodamine b included
RVe1a(fl) 16rep	18 Jun 14	Pentane	No	No	2	30	250	Probe	5	8 amps	Rhodamine b included

RVe1b experiments

RVe1b Sample 99% C18 / C4	Date Finished Prep.	Solvent	Methanol preparation				Hydrocarbon mixing			Sonication			Notes
			Mix order	Evaporation			Time (hrs)	Temp (°C)	RPM	Probe/Bath	Time (min)	Setting/ Reactivity	
				Time (hrs)	Temp (°C)	RPM							
T2Hep	6 Feb 12	Heptane	C18+C4→NaCl	92	50-55	60	Submerged in boiled water and hand shaken for 10mins			Small bath	45	Weak	After methanol evaporation the amphiphilic gel film was yellow (rather than the transparent film of the CyHex samples).
	22 Mar 12		-	-	-	-				Large bath	30	Strong	
	3 April 12		-	-	-	-				Probe	10	8-15 amps	
T3CyHex	6 Feb 12	CyHex	C18+C4→NaCl	92	50-55	60	Submerged in boiled water and hand shaken for 10mins			Small bath	45	Weak	
	22 Mar 12		-	-	-	-				Large bath	30	Strong	
	3 April 12		-	-	-	-				Probe	10	8-15 amps	
T4Hex	6 Feb 12	Hexane	C18+C4→NaCl	92	50-55	60	Submerged in boiled water and hand shaken for 10mins			Small bath	45	Weak	
	22 Mar 12		-	-	-	-				Large bath	30	Strong	
	3 April 12		-	-	-	-				Probe	8	10 amps	
CyHex4	10 Feb 12	CyHex	C18+C4→NaCl	12	40	60	55	60	190	Small bath	30	Weak	After methanol evaporation the amphiphilic gel film was transparent (rather than the
	22 Mar 12		-	-	-	-	-	-	-	Large bath	30	Strong	
	3 April 12		-	-	-	-	-	-	-	Probe	5	8-10 amps	
CyHex5	10 Feb 12	CyHex	C18+C4→NaCl	12	40	60	55	60	190	Small bath	30	Weak	
	22 Mar 12		-	-	-	-	-	-	-	Large bath	30	Strong	
	3 April 12		-	-	-	-	-	-	-	Probe	5	8-11 amps	

													yellow film of the T samples).
CyHex6	10 Feb 12	CyHex	C18+C4→NaCl	12	40	60	55	60	190	Small bath	30	Weak	
	22 Mar 12		-	-	-	-	-	-	-	Large bath	30	Strong	
	3 April 12		-	-	-	-	-	-	-	Probe	5	8-12 amps	
CyHex7	10 Feb 12	CyHex	C18+C4→NaCl	12	40	60	55	60	190	Small bath	30	Weak	
	22 Mar 12		-	-	-	-	-	-	-	Large bath	30	Strong	
	3 April 12		-	-	-	-	-	-	-	Probe	5	8-12 amps	
CyHex8	10 Feb 12	CyHex	C18+C4→NaCl	12	40	60	55	60	190	Small bath	30	Weak	
	22 Mar 12		-	-	-	-	-	-	-	Large bath	30	Strong	
	3 April 12		-	-	-	-	-	-	-	Probe	5	8-12 amps	
RVe1b(fl) T3rep	18 Jun 2014	CyHex	C18+C4→NaCl	24	60	60	2	60	250	Small bath	45	Weak	
RVe1b(fl) T2rep	18 Jun 2014	Heptane	C18+C4→NaCl	24	60	60	2	60	250	Probe	5	8 amps	
RVe1b(fl) T4rep	18 Jun 2014	Hexane	C18+C4→NaCl	24	60	60	2	60	250	Probe	5	8 amps	

RVe1c experiments

RVe1c Sample 95% C18 / C4	Date Finished Prep.	Solvent	Methanol preparation				Hydrocarbon mixing			Sonication			Notes
			Mix order	Evaporation			Time (hrs)	Temp (°C)	RPM	Probe/Bath	Time (min)	Setting/ Reactivity	
				Time (hrs)	Temp (°C)	RPM							
RVe1c 1	1 Mar 12	CyHex	C18+C4→NaCl	54	60	90	0.30	60	150-200	Small bath	30	Weak	
	22 Mar 12		-	-	-	-	-	-	-	Large bath	60	Strong	

RVe1c 2	8 Mar 12	CyHex	C18+C4→NaCl	24 + 96 (120)	60	90	49	60	300	Small bath	30	Weak	120hrs evap time because added more methanol by mistake.
RVe1c 3	30 Mar 12	CyHex	C18+C4→NaCl	20	45	90	2	45	250	Probe	10	8 amps	
RVe1c 4	30 Mar 12	Heptane	C18+C4→NaCl	20	45	90	2	45	250	Probe	10	8 amps	
RVe1c 5	30 Mar 12	Hexane	C18+C4→NaCl	20	45	90	2	45	250	Probe	10	8 amps	
RVe1c 6	3 April 12	Pentane	C18+C4→NaCl	20	45	90	80	45	250	Probe	8	8 amps	Evap noted during sonication
RVe1c 7	3 April 12	CyHex	C18+C4→NaCl	20	45	90	80	45	250	Probe	10	8 amps	
RVe1c 8	3 April 12	Heptane	C18+C4→NaCl	20	45	90	80	45	250	Probe	10	8-12 amps	
RVe1c 9	3 April 12	Hexane	C18+C4→NaCl	20	45	90	80	45	250	Probe	10	12 amps	
RVe1c 10	3 April 12	Pentane	C18+C4→NaCl	20	45	90	80	45	250	Probe	6	8-12 amps	
RVe1c 11	3 April 12	CyHex	C18+C4→NaCl	20	45	90	80	45	250	Probe	5+5 (10)	10+12 amps	
RVe1c 12	3 April 12	Heptane	C18+C4→NaCl	20	45	90	80	45	250	Probe	10	10-11 amps	
RVe1c 13	3 April 12	Hexane	C18+C4→NaCl	20	45	90	80	45	250	Probe	10	10-11 amps	Top damaged by shaking incubator. 5 May 12 solution lost, more solvent added to precipitant left and sonicated.
RVe1c 14	3 April 12	Pentane	C18+C4→NaCl	20	45	90	80	45	250	Probe	10	6-8amps	
RVe1c 15	18 Jun 14	CyHex	C18+C4→NaCl	24	60	60	24	60	250	Probe	5	8 amps	

SANS

SANS Sample 95% C18 / C4	Date Finished Prep.	Solvent	Methanol preparation				Hydrocarbon mixing			Sonication		
			Mix order	Evaporation			Time (hrs)	Temp (°C)	RPM	Probe/Bath	Time (min)	Setting/ Reactivity
				Time (hrs)	Temp (°C)	RPM						
SANS 2	16 Nov 12	Deuterated heptane	NaCl+C4→C18	24	60	100	4.10	40	260	Probe	1	5 amps
SANS 4	21 Nov 12	Deuterated pentane	NaCl+C4→C18	24	60	100	3.40	40	260	Large bath	40	Strong
SANS 6	16 Nov 12	Deuterated hexane	NaCl+C4→C18	24	60	100	4.10	40	260	Probe	1	5 amps
SANS 8	21 Nov 12	Deuterated cyclohexane	NaCl+C4→C18	24	60	100	-	-	-	Large bath	40	Strong

SAXS

SAXS Sample 95% C18 / C4	Date Finished Prep.	Solvent	Methanol preparation				Hydrocarbon mixing			Sonication			Notes
			Mix order	Evaporation			Time (hrs)	Temp (°C)	RPM	Probe/ Bath	Time (min)	Setting/ Reactivity	
				Time (hrs)	Temp (°C)	RPM							
SAXS 2/3	16 Nov 12	Heptane	C18+C4→NaCl	24	60	100	2.40	25	260	Probe	3	8 amps	
SAXS 4/5	16 Nov 12	Heptane	NaCl+C4→C18	24	60	100	2.40	25	260	Probe	4	8 amps	
SAXS 6/7	16 Nov 12	Heptane	NaCl+C4→C18	24	60	100	2.40	25	260	Probe	5	8 amps	
SAXS 9/10	16 Nov 12	Pentane	C18+C4→NaCl	24	60	100	3.25	40	260	Probe	3	5 amps	Problems with evaporation during transport
SAXS 11/12	16 Nov 12	Pentane	NaCl+C4→C18	24	60	100	3.25	40	260	Probe	3	5 amps	
SAXS 13/14	16 Nov 12	Pentane	NaCl+C4→C18	24	60	100	3.25	40	260	Probe	1+2	8+5 amps	
SAXS 16/17	16 Nov 12	Hexane	C18+C4→NaCl	24	60	100	3.40	40	260	Probe	1+2	8+6 amps	
SAXS 18/19	16 Nov 12	Hexane	NaCl+C4→C18	24	60	100	3.40	40	260	Probe	1+2	8+6 amps	
SAXS 20/21	16 Nov 12	Hexane	NaCl+C4→C18	24	60	100	3.40	40	260	Probe	4	6 amps	

SAXS 23/24	16 Nov 12	CyHex	NaCl+C4→C18	24	60	100	3.10	40	260	Probe	3	8 amps	
SAXS 25/26	16 Nov 12	CyHex	NaCl+C4→C18	24	60	100	3.10	40	260	Probe	2.30+ 0.30	8+6 amps	
SAXS 27/28	16 Nov 12	CyHex	NaCl+C4→C18	24	60	100	3.10	40	260	Probe	3	8 amps	
SAXS 30/31	4 Dec 12	Butane	NaCl+C4→C18	24	60	100	-	-	-	Small bath	90	Weak	Problems with evaporation during transference to capillaries
SAXS 32/33	4 Dec 12	Butane	C18+C4→NaCl	24	60	100	-	-	-	Small bath	90	Weak	
SAXS 35/36	4 Dec 12	Propane	NaCl+C4→C18	24	60	100	-	-	-	Small bath	30	Weak	
SAXS 37/38	4 Dec 12	Propane	C18+C4→NaCl	24	60	100	-	-	-	Small bath	30	Weak	
SAXS 41/42	16 Nov 12	Octane	NaCl+C4→C18	24	60	100	3.55	40	260	Probe	3	8 amps	
SAXS 43/44	16 Nov 12	Octane	NaCl+C4→C18	24	60	100	3.55	40	260	Probe	3	8 amps	
SAXS 45/46	16 Nov 12	Octane	NaCl+C4→C18	24	60	100	3.55	40	260	Probe	3	8 amps	

Appendix III: Key and examples to explain the phase behaviour terminology used in this body of work.

Term	Explanation	Term	Explanation	Term	Explanation
Opaque	White opaque solution. Cannot see through the solution.	SL	Strong laser reflection.	WFP	White (translucent) fluid precipitant.
Cl or Cl(s)	Cloudy solution, (s) symbol signifies after being shaken by hand. A cloudy solution has some transparency unlike those that are characterised as 'Opaque'.	WL	Weak laser reflection.	YFP	Yellow (translucent) fluid precipitant.
O or O(s)	Opalescent solution, (s) symbol signifies after being shaken by hand. Opalescent solution is translucent with an intense shine and can range of slight hues from grey (Gr), grey/yellow (Gr/Y) and grey/blue (Gr/B).	WSL	Widely scattered laser reflection.	TFP	Transparent fluid precipitant.
B	Solution has a blue hue - substantial Tyndall Scattering occurring.	WWSL	Weak widely scattered laser reflection.	WGP	White (translucent) gel precipitant.
T	Transparent solution.	NL	No laser reflection.	YGP	Yellow (translucent) gel precipitant.
Ph	Phase separated solution – the separate phases are characterised individually.			TGP	Transparent gel precipitant.
CLay	White cloudy layer, at the base of the container unless stated otherwise.			YWGP	Milky yellow (translucent) gel precipitant.
BLay	Bluish, opalescent layer, at the base of the container unless stated otherwise.			WSP	White solid precipitant.
Fla(x)	Visible opaque flakes in solution, temporarily after being hand shaken (x=colour; w=white, y=yellow, wy=milky yellow).			Mot	Mottled transparent and white precipitant with solid and fluid characteristics.
Glo	Spherical and translucent gel globules in solution after being shaken by hand.			NaClCem (x)	NaCl crystals cemented with a gel, colour of gel in brackets.

Key explaining the abbreviations used in describing the phase behaviour of samples.

Term	Explanation	Term	Explanation	Term	Explanation	Term	Explanation
BPS	Before probe sonication	BWS	Before weak water-bath sonication	BSS	Before strong water-bath sonication	AHS	After hand shaking
APS	After probe sonication	AWS	After weak water-bath sonication	ASS	After strong water-bath sonication		

Key explaining the non-descriptive abbreviations used in the phase behaviour tables.

Term	Explanation of characteristic	Image of characteristic	Term	Explanation of characteristic	Image of characteristic
Opaque	White opaque solution. Cannot see through the solution.		Cl + Cl(s)	Cloudy solution, (s) symbol signifies after being shaken by hand. A cloudy solution has some transparency unlike those that are characterised as 'Opaque'.	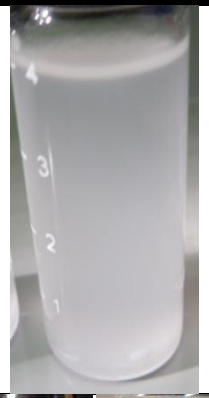
O + O(s)	Opalescent solution, (s) symbol signifies after being shaken by hand. Opalescent solution is translucent with an intense shine and can range of slight hues from grey (Gr), grey/yellow (Gr/Y) and grey/blue (Gr/B).	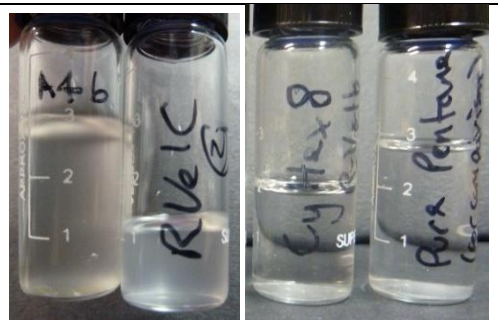 Left photo: Left sample is opalescent with a grey/yellow hue and the right sample is opalescent with a grey/blue hue. Right photo: Left sample is opalescent with grey hue, being compared to a transparent sample featured on the right.	B	Solution has a blue hue - substantial Tyndall Scattering occurring.	 Left photo: Transparent solution with blue hue. Right photo: Opalescent solution with blue hue.

T	Transparent solution.	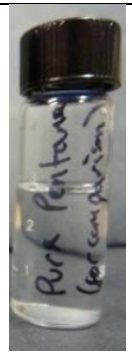 Example of pure, transparent pentane.	Ph	Phase separated solution – the separate phases are characterised individually.	 Example of a phase separated solution with the top fourth of the volume being transparent and below this is opaque.
Fla(x)	Visible opaque flakes in solution, temporarily after being hand shaken (x=colour; w=white, y=yellow, wy=milky yellow).	 Example of white flakes in solution after being shaken by hand.			

Table presenting photographic images that demonstrate the corresponding solution characteristics used in describing the phase behaviour of samples.

Term	Explanation of characteristic	Image of characteristic	Term	Explanation of characteristic	Image of characteristic
WFP	White fluid precipitant.	 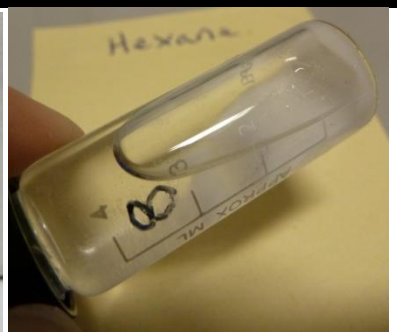 The photos show the same sample presenting an opalescent solution with a white fluid precipitant from different angles.	YFP	Yellow (translucent) fluid precipitant.	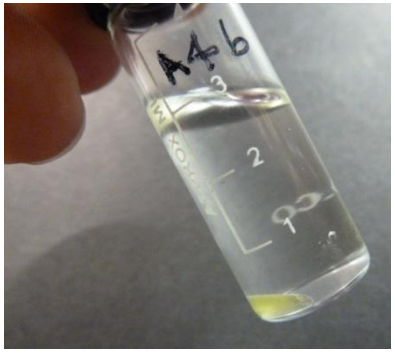 O+YGP
TFP	Transparent fluid precipitant.	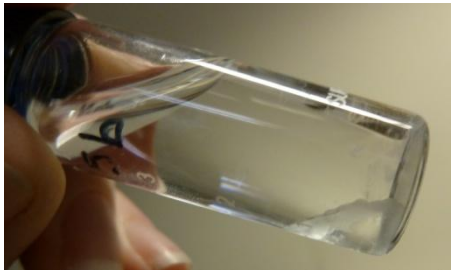 T+TFP	WGP	White gel precipitant.	  T+WGP
YGP	Yellow (translucent) gel precipitant.	 T+YGP	TGP	Transparent gel precipitant.	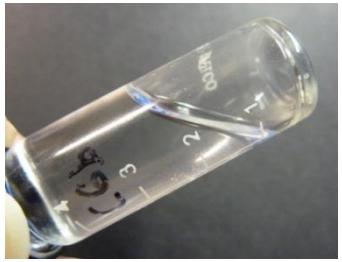 O+TGP

TFP+YFP (precipitant types phase separated)	Phase separated precipitant, with both transparent and yellow fluid precipitants.	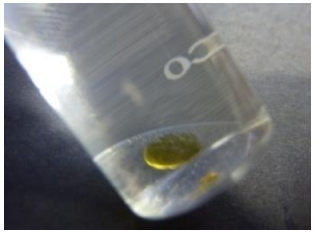 T+TFP+YFP	YWGP and YWGP (wavy pattern)	Milky yellow (translucent) gel precipitant. Some have a wavy pattern from a phase separated transparent gel.	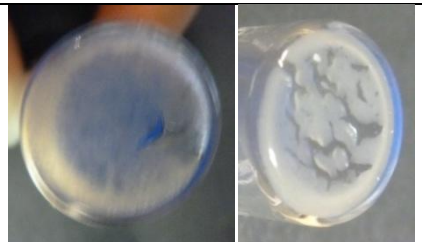 Left photo: YWGP Right photo: YWGP(wavy pattern)
WSP	White solid precipitant. Flaky or grainy texture.	 T+WSP	NaClCry (x)	NaCl crystals cemented with a gel, colour of gel in brackets.	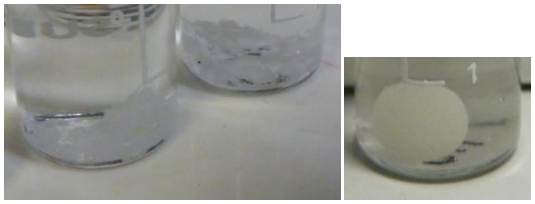 Left photo: T+NaClCry Right photo: T+NaClCry(milky yellow)
Mot(x)	Precipitant has a mottled appearance, details written in brackets. Often white grains/flakes in a transparent gel matrix.	 Left photo: T+Mot(TGP + NaClCry(W)) Centre photo: T+Mot(TFP + some WGP) Right photo: T+Mot(TFP + WGP)			

Table presenting photographic images that demonstrate the corresponding precipitant characteristics used to describe sample phase behaviour.